NASA SP-511

Arctic and Antarctic Sea Ice, 1978 - 1987

Satellite Passive-Microwave Observations and Analysis

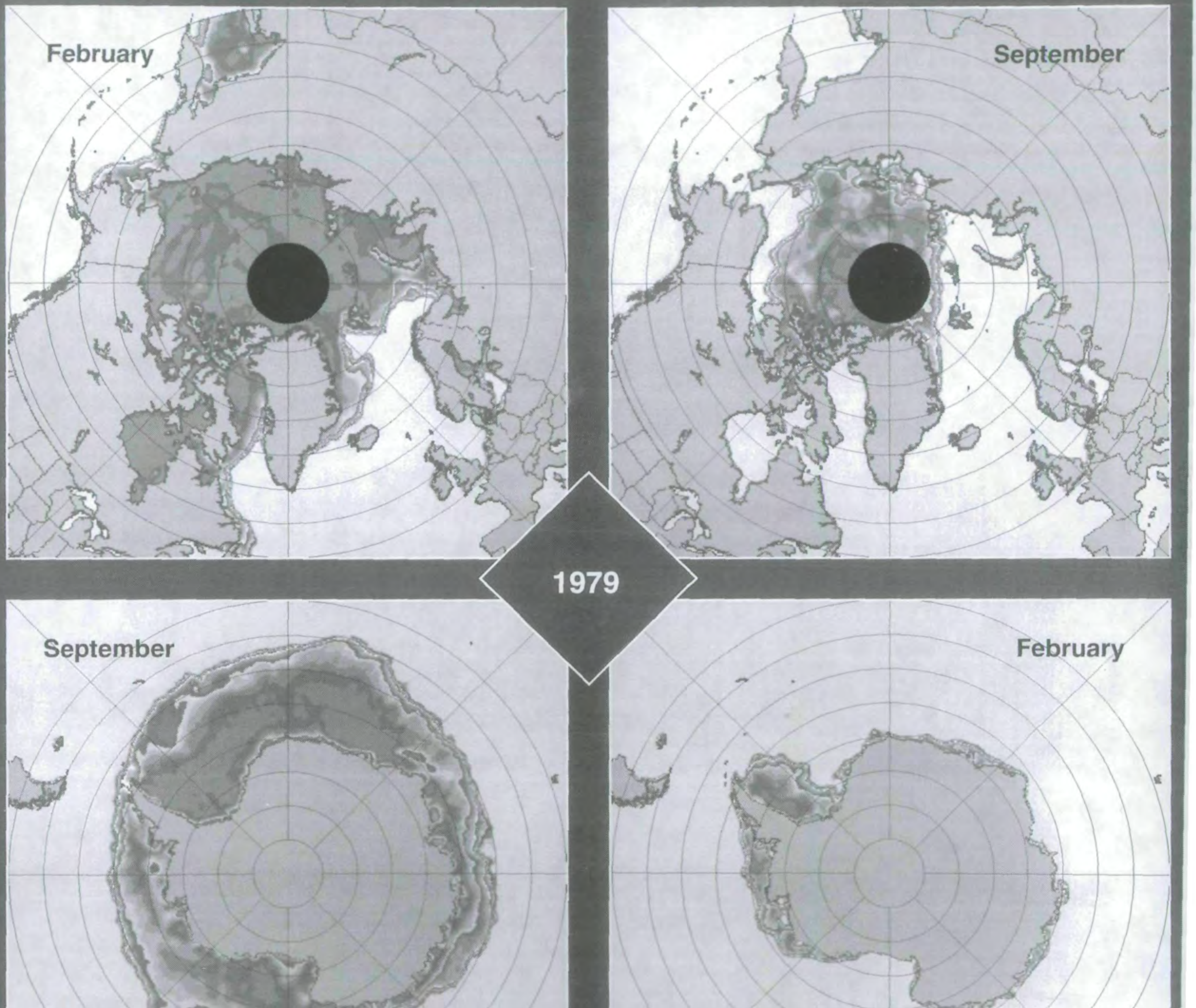

National Aeronautics and Space Administration

ARCTIC AND ANTARCTIC SEA ICE, 1978-1987:

SATELLITE PASSIVE-MICROWAVE OBSERVATIONS AND ANALYSIS

(NASA-SP-511) ARCTIC AND ANTARCTIC SEA ICE, 1978-1987: SATELLITE PASSIVE-MICROWAVE OBSERVATIONS AND ANALYSIS (NASA) 306 p

N94-17439

Unclas

H1/48 0191484

NASA SP-511

ARCTIC AND ANTARCTIC SEA ICE, 1978-1987:

SATELLITE PASSIVE-MICROWAVE OBSERVATIONS AND ANALYSIS

Per Gloersen
Laboratory for Hydrospheric Processes
NASA Goddard Space Flight Center
Greenbelt, Maryland 20771

William J. Campbell
United States Geological Survey
Ice and Climate Project
University of Puget Sound
Tacoma, Washington 98416

Donald J. Cavalieri, Josefino C. Comiso,
Claire L. Parkinson, H. Jay Zwally
Laboratory for Hydrospheric Processes
NASA Goddard Space Flight Center
Greenbelt, Maryland 20771

Scientific and Technical Information Program
National Aeronautics and Space Administration
Washington, D.C. 1992

Library of Congress Cataloging-in-Publication Data

Arctic and Antarctic sea ice, 1978-1987 : satellite passive-microwave
observations and analysis / Per Gloersen, William J. Campbell ;
[with] Donald J. Cavalleri ... [et al.].
p. cm. -- (NASA SP ; no. 511)
Includes bibliographical references and index.
1. Sea ice--Polar regions--Remote sensing. 2. Microwave remote sensing.
I. Gloersen, Per. II. Campbell, William Joseph, 1930-. III. Series.
GB2595.A72 1993
551.3'43'0911--dc20 93-22329
CIP

IN MEMORIAM

William J. Campbell 1930 -1992

We grieve the sudden and untimely loss of our beloved friend and colleague, Bill Campbell (1930-1992). We shall always remember Bill as one of the warmest human beings, as well as one of the most enthusiastic scientists we have ever encountered. Bill constantly reminded us that "we are human beings first and scientists second." Friendship was always a primary consideration in Bill's interactions with colleagues. Bill Campbell was a forceful advocate of polar region research. He pioneered microwave remote sensing of sea ice from aircraft, and contributed greatly to the evolution of satellite microwave remote sensing. Bill's many contributions, both written and unwritten, are reflected throughout this book. Bill will be sorely missed.

FOREWORD

This volume is the third in a series of NASA publications on the results of passive-microwave observations of sea ice in the polar regions, made from polar orbiting satellites. The casual reader will open this volume and be impressed by the magnificent multicolored maps of the Arctic and Antarctic, showing the changes in distributions of sea ice with season and from year to year. Those who have been waiting for a comprehensive analysis of what has been happening in the polar regions in the past decade or so will surely hail the publication of this volume as a major event.

The history of these satellite observation is detailed in the text, but let me remind the readers of this volume that the first passive-microwave maps for sea ice were drawn as a result of flights over the Arctic Ocean in a NASA Convair-990 aircraft during the period of 1967-1972, under the direction of the late Dr. William Nordberg. It is to William Nordberg that this volume is dedicated. Deeply involved in these pioneering flights were two of the present authors—Drs. William Campbell and Per Gloersen—and Dr. Thomas Wilheit. These flights proved convincingly that it was indeed possible to monitor remotely sea ice distribution in the dark of the polar night and through clouds. The instrument used in the aircraft, the Electrically Scanning Microwave Radiometer (ESMR), served as the model for a scaled-up and redesigned version for space flight, manufactured by the Aerojet Corporation and flown on Nimbus 5 during the period 1973 to 1976. The ESMR observations have been summarized in the publications by Zwally et al. (1983a) for the Antarctic, and by Campbell et al. (1984) and Parkinson et al. (1987) for the Arctic.

Encouraged by the success of ESMR, NASA scientists and engineers developed a greatly improved instrument system—the Scanning Multichannel Microwave Radiometer (SMMR)—flown on Nimbus 7 and Seasat A. The observations from the Nimbus 7 SMMR from November 1978 to August 1987 (8.8 years) are the subject of this treatise.

SMMR received microwave radiation at five different wavelengths, from 0.8 to 4.5 cm (37 to 6.6 GHz), and detected separately both vertically and horizontally polarized radiation at each wavelength. This additional information allowed the analysis to go far beyond that possible with ESMR, and to distinguish between, for example, first-year and multiyear sea ice.

There were some problems with the SMMR. While ESMR had an electrically scanning antenna (a phased array) that did not have to move, SMMR had a mechanically scanning antenna that promised to have better performance. There was a known problem of polarization mixing, caused by the design requirement of fixed receiving horns coupled with an oscillating parabolic dish antenna. However, an unanticipated additional complication in polarization mixing occurred as a result of leakage (cross-talk) in some of the microwave wave guide switches. Therefore, during the first several years of data acquisition, the data contained serious calibration errors. The SMMR Team overcame these problems through an intense analysis of the Nimbus 7 data and experiments with the SMMR engineering model over a lake at NASA/Goddard Space Flight Center (GSFC). Persistence and ingenuity paid off handsomely, and the SMMR stayed on the air longer than any other microwave instrument ever launched on a satellite.

What an extraordinary step forward this observational technique represents from the days of the early explorers and mariners who braved the oceans of the Arctic and Antarctic, or who drifted on ice stations for months and years! (Some of the routes of those early explorers are recorded in Figure 3.2.2.) Their accounts tell the world about the mysterious realm of ice and snow, but their observations were limited by their close horizons. Modern technology permitted SMMR to map both polar regions from space every 2 days in greater detail than ever before. Readers of this volume should keep that awesome sense of historical perspective in mind. It seems quite fair to refer to these new results as technological "breakthroughs."

A good part of the breakthroughs must be credited to the development of instruments capable of mapping the extraordinarily weak signals emitted by the Earth and its atmosphere in the microwave part of the spectrum, a feat deemed impossible in the early days of satellites. The SMMR instrument system did not spring full-blown overnight, of course, but it was the culmination of several years of development efforts at the Massachusetts Institute of Technology, the Goddard Space Flight Center, the Jet Propulsion Laboratory (JPL, where SMMR was built), and a number of other institutions.

Much as we must admire the magnificent gold-plated hardware that flew on Nimbus 7, an even larger and equally crucial effort has been devoted to the analysis of the SMMR observations and the development of computer algorithms on which to base the interpretations given in this volume. The list of references will give some idea of the large team of scientists and programmers, both at the GSFC and elsewhere, who spent years working on the microwave observations in order to understand what they really mean. Note also the attention paid to an analysis of both instrument and algorithm errors given in this treatise. We must not forget that the dedicated and unsung servants of the space flight program are largely responsible for its success.

There is a saying in the space science community about "a solution looking for a problem"—a marvel of technology making observations that nobody really cares about. Nothing could be farther from the mark in the case of SMMR. Its observations of the seasonal growth and decay of sea ice through the years are of immense importance as we try to detect global change and the greenhouse effect on the Earth, a warming trend that now seems likely as the concentrations of carbon dioxide, methane, chlorofluorocarbons (CFCs), and other greenhouse gases continue to increase, and as the circulation patterns in both atmosphere and oceans are gradually modified. The nearly 9-year lifetime of SMMR is too short to demonstrate conclusively a long-term trend by itself, but it provides an invaluable baseline for climate-related studies.

What have the ESMR and SMMR observations shown us so far? Scientists are still sifting through the evidence. During the ESMR period of observation, there was a suggestion that the extent of polar sea ice was decreasing slightly, as might be expected, as the Earth was growing warmer. During the SMMR period, the Arctic sea ice extent has a statistically significant negative trend of 2.1±0.9%, and open water within the ice pack boundaries has a negative trend of 3.5±2.0%. During the same period, the Antarctic sea ice pack shows no significant trends in these two parameters. These trends are consistent with the observation that the global average surface temperature has been rising rapidly in the past 20 years, and that stratospheric temperatures have been falling, both trends predicted by the greenhouse theory.

We are increasingly aware of the fact that our climate system is much too complex to respond in a simple way to greenhouse warming. The regional changes are often just as dramatic and fascinating as the overall average global change. In the past several decades, the North Atlantic and the North Pacific have actually been getting somewhat colder in winter, while the land masses have generally become significantly warmer. Does this mean that the greenhouse theory and the climate models based on it are wrong? Of course not, but the early models have tended to give us an *oversimplified* view of what to expect.

Consider two recent climate model experiments that went a couple of steps farther than previous model experiments to try to capture another level of complexity in the climate system. In one of these model experiments, the National Center for Atmospheric Research (NCAR) Community Climate Model was run with a steadily increasing concentration of greenhouse gases, which is a realistic assumption. (The carbon dioxide will not increase instantaneously, as assumed in most previous model experiments.) Furthermore, in this climate model, the general circulation model (GCM) atmosphere was coupled to a five-layer ocean circulation model that transported heat horizontally and displayed vertical mixing (Washington and Meehl, 1989). All this required an enormous amount of computer time, but the model experiment had to be tried.

In the second decade of the experiment (in model time) a curious phenomenon took place: while the land areas continued to grow warmer, the North Atlantic and (to a lesser degree) the North Pacific became significantly cooler in winter. In short, the model world seemed to behave more or less the same way as the real one, albeit in a complex and unexpected way. Apparently the regional changes, partly driven by changes in circulation in both atmosphere and oceans, did not keep in step everywhere with the global changes. Similar results obtained in a dynamic experiment with the Geophysical Fluid Dynamics Laboratory (GFDL) climate model, with a circulating ocean, show that the response to a progressive climate change is complex and different between the two hemispheres (Stouffer et al., 1989).

With those lessons in mind, let us look again at the SMMR results. To be sure, there were only small changes in the overall Arctic sea ice extent and the open water within the pack during the 9-year period, but consider the changes in the various regions around the Arctic. Stronger decreasing trends occurred in the Sea of Okhotsk, the Greenland Sea, and the Kara and Barents Seas, but the sea ice extent increased in the Bering Sea, Hudson Bay, and Baffin Bay and Davis Strait.

The important point is that we now have an opportunity to study these SMMR results in the light of global surface observations and our improved climate modeling capability. This combined theoretical and observational approach to the analysis of a most complex situation is science at its best. We should not expect a simple picture to emerge, but one that portrays nature in all her enigmatic splendor.

The authors of this volume appreciated this important point. The Arctic Ocean data attracted their attention especially. Section 3.2 covers much more than the maps of sea ice distribution; it includes an analysis of the variations both in sea ice concentration and in multiyear ice distribution in the ice pack for selected periods, comparing the ice drift with the surface pressure and wind distributions (as given by the buoys from the Arctic Ocean Buoy Program). One significant finding was that areas of persistent reduced ice concentration, or polynyas, were not simply a result of wind-induced ice divergence, but also a result of oceanographic forcing such as upwelling—a fact already suspected but previously difficult to observe.

Appendix A provides a surface-based record of Arctic buoy observations of pressure, temperature, and position (provided by Roger Colony of the University of Washington Polar Science Center), and ice temperatures (derived from SMMR data, averaged for each month of the SMMR period) for the purpose of aiding the subsequent analysis of the SMMR data. I wonder how many Ph.D. theses will be based on the information contained in this one volume.

The satellite data that will be obtained in the future may not be made available as completely and elegantly as in this volume for SMMR, but nevertheless the National Oceanic and Atmospheric Administration (NOAA) World Data Center/National Snow and Ice Data Center in Boulder, Colorado, has computer-based files of both Nimbus 7 SMMR and the first years of the Defense Meteorological Satellite Program (DMSP) Special Sensor Microwave/Imager (SSMI—an instrument similar to SMMR) brightness temperatures on polar stereographic grid maps for both regions. Computer programs are provided for extracting the grid files from the data stored on sets of CD ROMs.

This scientific quest will continue to unfold in the years to come and will build on the exemplary record of SMMR as observations from the SSMI and future global observation systems extend the period of observation.

William W. Kellogg
Senior Scientist (Retired)
National Center for Atmospheric Research
Boulder, Colorado

Page intentionally left blank

DEDICATION

The last two decades have been an exciting and fruitful time in the development and utilization of techniques for the passive-microwave remote sensing of sea ice. The generative event that caused this scientific advance occurred in June 1967, when some of us who had manned the drifting ice Station Alpha in the Arctic Ocean during the International Geophysical Year (1957-1958) met with the late Dr. William Nordberg of the NASA Goddard Space Flight Center to discuss our results. He was a man of great vision, knowledge, and energy, and it was serendipitous that he became interested in sea ice at the time he was developing the 19-GHz Electrically Scanning Microwave Radiometer (ESMR) made by the Aerojet Corporation, which was to be the first aircraft-borne passive-microwave imager. Within a few months of our meeting, we were testing the ESMR over the Beaufort Sea in the NASA Galileo I CV-990 Airborne Laboratory. Under Bill Nordberg's leadership and drive, the system was flown during the late 1960s and early 1970s with great success. This success led to the launching of ESMR onboard the Nimbus 5 satellite, which acquired useful sea ice data for almost 4 years. Subsequently, Bill Nordberg was one of the key leaders who worked for the development and launching of the Scanning Multichannel Microwave Radiometer (SMMR), and he gave unstinting encouragement and help to the SMMR Team. On the day before he died in August 1976, he heartily wished us an even greater success with SMMR than we had with ESMR. His wish has been fulfilled. SMMR has been extraordinarily successful during its nearly 9-year lifetime. Bill was our friend and mentor. Still missing him deeply, we dedicate this book to his memory.

Page Intentionally Left Blank

PROLOGUE

"I am the eye through which the Earth beholds itself," proclaimed Shelley's Apollo as he flew aloft and surveyed the Greek landscape and seascape from his Pegasus-borne chariot. A century and a half after the writing of this line, the Apollo astronauts had the wonderful opportunity to be the "eye" by which Earth once again beheld itself. These men were both preceded and followed by inanimate electronic "eyes" that have given and will continue to give mankind many new perspectives of his planet. With these eyes, we have greatly and rapidly expanded the breadth and depth of our vision of Earth. We now know that because of the revolutionary tool of artificial satellites our relationship with nature has reached a new threshold of understanding. Of all the aspects of nature that have been revealed with a new clarity and richness by satellite remote sensing, none has surpassed that of the polar sea ice covers. Passive-microwave observations acquired by the Nimbus 5 and 7 satellites have given us the first synoptic views of these vast dynamic ice masses. A decade of this new information has given us a greater understanding of their large-scale structure, motion, and variability than was ever obtained throughout the long history of mankind's difficult and dangerous polar explorations. These passive-microwave observations have broken the polar observational barrier. This book presents the results from the most successful so far of the passive-microwave sensors launched into space, the Nimbus 7 Scanning Multichannel Microwave Radiometer (SMMR). Would not Shelley's Apollo have exulted to behold Earth with eyes such as SMMR?

Page intentionally left blank

ACKNOWLEDGEMENTS

The authors wish to express their appreciation to those involved with the data processing, program managers, and the reviewers of this treatise whose valuable suggestions contributed significantly to the successful completion of this effort. Paul Hubanks and Bill Abbott of Research and Data Systems, and Hugh Powell of General Sciences Corporation were central in the processing of the SMMR data through the various stages required, including the final ones of producing color separation negatives directly from computer compatible tapes on the Scitex image-setting facility operated under the skillful direction of Ralph Gioseffi at Applied Graphics, Inc. We also appreciate the additional programming support provided by Jamila Saleh and Mike Martino of Hughes-STX Corporation. There were eight scientists who officially reviewed this treatise: Will Kellogg (who also wrote the Foreword), Kirk Bryan, Frank Carsey, Stan Jacobs, Seelye Martin, Gary Maykut, Koni Steffen, and Cal Swift. All of these reviewers provided valuable suggestions that have greatly enhanced this book. Subsequently, the revised manuscript was reviewed internally by Rob Massom and Bob Bindschadler, and also by Cheryll Madison and Renny Greenstone of Hughes-STX Corporation, resulting in additional improvements. The NASA/Goddard Space Flight Center authors are particularly grateful for the support of their organization, the Oceans and Ice Branch, and its several leaders that have spanned the time consumed by this large undertaking, notably Erik Mollo-Christensen, Nancy Maynard, Tony Busalacchi, and Chet Koblinsky. The U.S. Geological Survey author heartily thanks his agency for its steadfast support throughout the long SMMR program and specifically commends two of its leaders, John Conomos and Roger Wolff, for their encouragement and help. Bob Thomas of the NASA/Headquarters Climate and Hydrologic Systems Branch has provided the encouragement and funding that made this work possible.

Page Intentionally Left Blank

CONTENTS

APPENDIX A

APPENDIX B

LIST OF FIGURES

SUMMARY

This book contains a description and analysis of the spatial and temporal variations in the Arctic and Antarctic sea ice covers from October 26, 1978 through August 20, 1987. It is based on data collected by the Scanning Multichannel Microwave Radiometer (SMMR) onboard the NASA Nimbus 7 satellite. The 8.8-year period, together with the 4 years of the Nimbus 5 Electrically Scanning Microwave Radiometer (ESMR) observations presented in two earlier volumes *(Antarctic Sea Ice, 1973-1976: Satellite Passive-Microwave Observations* and *Arctic Sea Ice, 1973-1976: Satellite Passive-Microwave Observations)* comprises a sea ice record spanning almost 15 years.

The sea ice measurements presented in this volume represent a distinct advance over the Nimbus 5 data used in the earlier books. This advance results from the improved characteristics of the SMMR, compared to the ESMR:

- ESMR was a single-frequency, singly polarized sensor; SMMR was a multifrequency, dual-polarized sensor.
- ESMR had cross-track scanning and a varying incidence angle; SMMR had conical scanning and a constant incidence angle.

The multifrequency, dual-polarized constant incidence-angle characteristics of the SMMR have permitted

- A more accurate calculation of total sea ice concentrations (fraction of ocean area covered by sea ice).
- Determination, for the first time, of both multiyear sea ice concentrations and the physical temperatures of the sea ice.
- An overall accuracy of ±7% for the SMMR total ice concentrations. This compares with estimated accuracies of ±25% in the Arctic and ±15% in the Antarctic for the ESMR.
- More accurate measurements of the sea ice extents (areas enclosed by 15% ice-concentration boundaries), sea ice areas, and open water areas within the ice margins.

SMMR measures vertically and horizontally polarized radiances at five wavelengths, ranging from 0.81 cm to 4.5 cm, and provides a total of ten channels of radiance data. The spatial resolution of the SMMR varies with wavelength and ranges from 30 to 150 km. The 0.8- and 1.7-cm channels are used for calculating ice concentrations and have integrated fields of view of 30 and 55 km, respectively. In this volume, the 55-km spatial resolution of the SMMR ice concentrations is maintained by mapping the SMMR radiances onto a polar stereographic projection with a grid spacing of about 25 km.

A description of the sea ice cover is provided by a variety of maps and plots:

- Monthly averaged maps of total sea ice concentrations produced from SMMR data for the Arctic and Antarctic for each month from November 1978 through August 1987.
- The 8- or 9-year averages by month over the SMMR lifetime.
- Monthly anomalies with respect to these averages.
- Time series of the ice extents, the areal coverage by ice, and the open water within the ice-ocean boundary.
- Maps of monthly averaged multiyear sea ice concentrations, along with their long-term averages and anomalies (Arctic only).
- Maps of monthly averaged sea ice temperatures, with the additional use of the vertically polarized 4.6-cm channel.

For the purpose of examining regional differences, the Arctic is divided into nine regions and the Antarctic into five. We provide

- Time-series analyses for each region and the hemispheric and global totals.
- Selected single-day Arctic ice-concentration maps to illustrate the rapid changes in the sea ice distributions.

Analysis of the Arctic SMMR time series for the nine regions combined reveals that the Arctic seasonal cycle ranges, on average, from a minimum of 9 x 10^6 km^2 in September to a maximum of 16 x 10^6 km^2 in March. The Arctic Ocean contributes about 14% of the 7 x 10^6 km^2 seasonal range and the balance is contributed by the perimeter seas. The interannual variability of the ice extent areas is much larger for the perimeter seas than for the Arctic as a whole; some regions exhibit decreasing trends, while others exhibit increasing trends. Negative trends in the Sea of Okhotsk, the Greenland Sea, and the Kara and Barents Seas are countered in part by positive trends in the Arctic Ocean, Bering Sea, Hudson Bay, and Baffin Bay, Davis Strait, and Labrador Sea, resulting in a small but statistically significant negative trend (-2.1±0.9%) over the 8.8-year record. Ice-free areas within the sea ice pack are also found to have a negative trend (-3.5±2.0%). The confidence level for each of these trends is better than 90%.

The 8.8-year SMMR record also reveals that the Arctic Ocean ice pack at the height of the summer melt season usually assumes one of two different positions over the years of SMMR coverage:

- The Siberian mode, characterized by the ice pack being distant from the Alaskan coastline, leaving extensive open water areas along its shoreline.
- The Alaskan mode, characterized by the ice pack impinging on or being close to the Alaskan coastline.

A relationship between this bimodal behavior of the summer ice distribution and the general oceanic circulation patterns in the Arctic Ocean can be inferred from the Arctic Ocean Buoy Program (AOBP) data:

- The Siberian mode occurs when the general circulation pattern assumes its long-term state, i.e., with a well-developed Beaufort Gyre and Transpolar Drift Stream.
- The Alaskan mode occurs when the long-term state breaks down.

These two modes are evenly divided over the 1979-1987 time span (1981 had an ambiguous ice distribution). This equal division contrasts with the earlier ESMR years when the Siberian mode persisted for 3 of the 4 years.

The higher accuracy of the SMMR ice concentrations has increased the confidence in the observation of areas of reduced concentration (polynyas) that occur in the Arctic Ocean from November through April. These winter polynyas have typical lifetimes on the order of months; the summer polynyas persist days or weeks. The areas, or zones, where polynyas occur most often are the southern Beaufort Sea (adjacent to the McKenzie Delta and Alaskan coast), near the center of the usual location of the Beaufort Gyre, and along the Siberian sector of the Transpolar Drift Stream. These winter polynyas do not form with any regularity in any zone.

The ability to determine multiyear sea ice concentration in winter leads to

- Removal of some ambiguities in calculating the multiyear ice distribution within the central Arctic during the winter months.
- An estimate of the accuracy of the derived multiyear ice concentrations of almost 11%, almost twice the error in the total ice-concentration calculations.
- The observation that multiyear ice concentrations in winter are as high as 96%-100% north of the Canadian Archipelago.
- The observation of lower and more variable concentrations in other regions of the central Arctic, where the average concentration is about 60%.
- The ability to analyze large-scale motions of the Arctic ice pack.
- The observation that widely different distributions of the multiyear ice from one year to the next are related to the bimodal nature of the summertime location of the Arctic ice pack.
- Evidence that multiyear ice flows from the Arctic Ocean into the channels of the Canadian Archipelago during winter, at rates consistent with independent observations at the surface and from Landsat images.

There is a difference between the area of multiyear ice in midwinter and the total ice area in the previous September. The SMMR record indicates that only about 3 x 10^6 km^2 of the 5 x 10^6 km^2 ice area at the mid-September ice minimum becomes multiyear ice. Most of the difference is explained by the fact that ice in mid-September includes not only ice that becomes multiyear ice the following winter, but also new ice that persists into the winter as first-year ice and some ice that will melt prior to the winter season. Since the entire ice pack does not make the transition from melting to freezing simultaneously, the ice present at the September ice minimum is not a good estimate of the multiyear ice area the following winter.

In the Antarctic, the most dissimilar observation in the SMMR lifetime as compared to the ESMR is the absence of the Weddell Polynya, which had persisted throughout 3 of the 4 austral winters during the ESMR lifetime. The range in the SMMR Antarctic ice extents is about 16 x 10^6 km^2, with a seasonal minimum of 3.5 x 10^6 km^2 and a seasonal maximum of 19 x 10^6 km^2.

As in the Arctic, the individual sectors have larger interannual differences than in the Antarctic as a whole, implying compensating relationships in the various regions. For instance, a 7-year undulation in the sea ice extent maxima of the Weddell, Amundsen, and Bellingshausen Seas is countered by a similar but out-of-phase undulation in the Western Pacific.

Although the ice extents in the Weddell Sea have a large downward trend during the 8.8-year SMMR record, this negative trend is countered by positive trends in the Ross Sea and Indian Ocean. The Antarctic ice extents as a whole have no statistically significant trend.

Globally, the combined Arctic and Antarctic sea ice extent varies from a minimum of about 20 x 10^6 km^2 to a maximum of about 30 x 10^6 km^2 and is roughly in phase with the Antarctic oscillation. Thus, the average global oceanic albedo has an appreciable seasonal variation in spite of the out-of-phase characteristic of the boreal and austral seasons. The 2.1% negative trend in the Arctic sea ice extent, combined with the lack of a trend in the Antarctic, results in an overall negative trend of about 1% in global sea ice during the SMMR lifetime.

Monthly averaged ice temperatures derived from the SMMR data are given in Appendix A, which also includes coincident data from the AOBP. While not validated, the SMMR sea ice temperature data provide information not available from any other source, and may be potentially useful for surface-atmosphere heat transfer studies in the polar regions. The SMMR and AOBP temperature data sets have important differences in their interpretation. The AOBP temperatures are point measurements that approximate surface-air temperatures in winter. In contrast, the SMMR ice temperatures are a spatially averaged measure of the physical temperature of the radiating portion of the ice, typical of the snow-ice interface for first-year ice and of a weighted-mean temperature of the freeboard layer for multiyear ice. A linear regression analysis of the wintertime SMMR and AOBP temperatures shows the SMMR temperatures to be 5 K to 13 K warmer, on average, with the larger biases over regions of thick multiyear ice. The standard error of estimate between the two data sets is 4.7 K.

This volume serves as a summary of the sea ice parameters derived from the 8.8-year SMMR polar data set. It is a companion to a series of 12 compact disk-read only memories (CD-ROMs) containing the SMMR polar data set. These CD-ROMs have been made available by the NASA/Goddard Space Flight Center (GSFC) in Greenbelt, Maryland, and are archived at and distributed by the National Oceanic and Atmospheric Administration (NOAA) World Data Center/National Snow and Ice Data Center (NSIDC) in Boulder, Colorado. The CD-ROMs contain brightness temperature and ice concentration maps for every other day, all on the same polar stereographic grids used in this book. The radiance data are for eight of the ten horizontally and vertically polarized channels, with the 1.4-cm channels not included because of severe instrument drift. An additional CD-ROM is planned that will include the monthly averaged ice concentrations and ice temperatures as they appear in this book, along with tables of values for the curves. Similar brightness temperature and sea ice concentration maps are being created and distributed on CD-ROMs by NSIDC for the Defense Meteorological Satellite Program Special Sensor Microwave/ Imager (SSMI), launched on June 19, 1987. For the purpose of providing a consistent set of sea ice parameters, a comparison was undertaken that shows that concentration differences (SMMR-SSMI) during the 2 months of overlap are 0.2%±5% during austral winter and 0.5%±5% during boreal summer. This measure of consistency between the two data sets should encourage the use of the combined data sets, which provide well over a decade of continuous global, multispectral passive-microwave observations.

1

INTRODUCTION

Sea ice forms through the freezing of sea water over large areas of the polar oceans in both hemispheres and covers as much as 30 x 10^6 km^2 of the Earth's surface. This large expanse of ice greatly reduces the exchanges of heat, mass, and momentum between ocean and atmosphere, and decreases the amount of solar radiation absorbed at the surface. These processes depend strongly on time and location because of the high temporal and spatial variability of the sea ice cover in each hemisphere.

In the Northern Hemisphere, sea ice extent (area enclosed by the ice boundary) fluctuates each year from a minimum in September, when most of the ice is confined to the central Arctic Ocean, Greenland Sea, and Canadian Archipelago, to a maximum in March, when the ice covers almost the entire Arctic Ocean, Canadian Archipelago, Hudson Bay, Baffin Bay, and Kara Sea, as well as major portions of the Sea of Okhotsk, Bering Sea, Davis Strait, Greenland Sea, Barents Sea, and smaller portions of the Sea of Japan and Labrador Sea.

In the Southern Hemisphere, the annual fluctuation is even greater, from a minimum in February, when the ice is confined largely to the western Weddell, the Amundsen, and the Bellingshausen Seas, to a maximum in September, when the ice surrounds the Antarctic continent and extends equatorward to 55°-65° S.

The first satellite sensors providing views of the large-scale structure and motion of sea ice utilized visible and infrared band channels (e.g., Sissala et al., 1972), such as those onboard the early Nimbus, Tiros, and Earth Resources and Technology Satellite (ERTS, later renamed Landsat). By the late 1960s, it was apparent that the sequential synoptic observations needed for sea ice and climate studies could not be acquired by satellite-borne visible sensors, which are limited to cloud-free and well-illuminated conditions, not frequently met in the polar regions. Sea ice exists in regions that are dark for several months of the year and very frequently cloudy in the remaining months. The ability of microwave sensors to view the Earth's surface under all weather conditions, day or night, provides the opportunity to obtain the required sea ice and ocean observations. Furthermore, these measurements can be made frequently enough to obtain nearly complete polar coverage within a day, thereby enhancing the analyses of ice-ocean-atmosphere processes.

The first satellite passive-microwave remote sensing of the Earth began with the Russian satellites Cosmos 243 and Cosmos 384 in 1968 and 1970, respectively. In the U.S., passive-microwave technology was first used in the remote sensing of sea ice during the late 1960s and early 1970s, when a prototype of the Electrically Scanning Microwave Radiometer (ESMR) was flown over the Arctic (Wilheit et al., 1972; Campbell, 1973; Gloersen et al., 1973). The period since 1970 has been one of great advancement in the remote sensing of sea ice, starting with the full-scale flight model of the ESMR, which operated onboard the NASA Nimbus 5 satellite during 1973-1976 (Gloersen et al., 1974a,b). The experience gained from the ESMR and subsequent airborne experiments led to the development of a more advanced satellite instrument, the Scanning Multichannel Microwave Radiometer (SMMR). The SMMR operated on NASA's Nimbus 7 satellite (Figure 1.0.1) from October 26, 1978 to August 20, 1987, the longest continuous period of observation yet obtained by a satellite-borne passive-microwave instrument.

The Nimbus 7 transmitted SMMR radiance data every other day for most of its 8.8-year span of operation, well past its design lifetime of 2 years. Its multichannel nature allowed the calculation not only of sea ice concentration (the fraction of an area covered by sea ice), but also of multiyear ice (ice that has survived at least one summer melt season) concentration and ice temperature (Svendsen et al., 1983; Cavalieri et al., 1984; Swift et al., 1985; Gloersen and Cavalieri, 1986; Comiso, 1986). The ice parameters presented in this volume were derived from the SMMR observations with the algorithm developed by Cavalieri et al. (1984) and Gloersen and Cavalieri (1986), as discussed in Chapter 2.

In this document, we present a detailed description and analysis of the growth, decay, and interannual variations of the Arctic and Antarctic sea ice covers on regional, hemispheric, and global scales, based on the data obtained by SMMR. This volume follows two earlier books that contained compilations and analyses of global sea ice observations using ESMR data for much of the 4-year period 1973-1976. These two atlases, entitled *Antarctic Sea Ice, 1973-1976: Satellite Passive-Microwave Observations* (Zwally et al., 1983a) and *Arctic Sea Ice, 1973-1976: Satellite Passive-Microwave Observations* (Parkinson et al., 1987), respectively, will hereafter be referred to as the ESMR Antarctic atlas and the ESMR Arctic atlas.

1.1 Sea Ice Processes and Climate

Sea ice has many roles in the global climate system. For one, it serves as an effective insulator between the ocean and the atmosphere, restricting exchanges of heat, mass, momentum, and chemical constituents. During winter when there is a large temperature difference between the cold atmosphere and the relatively warm ocean surface, ocean-to-atmosphere heat transfer is essentially limited to areas of open water and thin ice within the pack. The winter flux of oceanic heat to the atmosphere from open water can exceed by two orders of magnitude the heat flux through an adjacent thick ice cover (Badgley, 1966; Maykut, 1978). As a result, the distribution of open water and thin ice is particularly important to the regional heat balance.

Another important role of sea ice in the global climate system is that it affects surface albedo. Ice-free ocean generally has albedos of 10%-15% (Lamb, 1982), whereas sea ice albedos average about 80% (Grenfell, 1983). A fresh snow cover on the ice can increase the surface albedo to values as high as 98% (Vowinckel and Orvig, 1970), whereas melt ponds can decrease the ice albedo to 20%-60% (Grenfell and Maykut, 1977). Because the albedo of sea ice is high, relative to that of the open ocean, the presence of sea ice considerably reduces the amount of solar radiation absorbed at the Earth's surface. This is most significant in summer, when the insolation, or solar heating, is high. Both the insulation and the albedo effects have important implications for climate change scenarios, because they contribute to positive feedback mechanisms (e.g., Kellogg, 1975).

Sea ice processes also affect oceanic circulation directly by the rejection of salt to the underlying ocean during ice growth. This increases the density of the water directly under the ice, thereby inducing convection that tends to deepen the mixed layer. This convection contributes to driving the thermohaline circulation of the ocean (Bryan et al., 1975) and, in regions with density structures that were initially weak or unstable, can lead to overturning and, at times, to deep-water and bottom-water formation. Much of the world's deep and bottom water is believed to be formed in polar latitudes by these mechanisms (Stommel, 1962; Gordon, 1978; Killworth, 1983). Conversely, the input of relatively fresh water to the ocean during ice melt periods tends to increase the stability of the upper mixed layer, inhibiting convection. Furthermore, the net equatorward transport of the ice in each hemisphere produces a positive freshwater transport and a negative heat transport.

The location of the ice edge influences regional weather. The presence of the sharp thermal and surface stress boundary between winter sea ice and the open ocean gives rise to violent weather patterns known as polar lows. The pronounced change in energy exchange that takes place at the ice margin can, under the appropriate atmospheric conditions, trigger the cyclogenesis of polar lows (Carleton, 1985, 1989; Businger and Reed, 1989; Gloersen et al., 1989). A summary of the present understanding of these cyclogenesis events has been given elsewhere (Kellogg and Twitchell, 1986; Twitchell et al., 1989).

The distribution of sea ice is affected by the oceans and atmosphere in many ways. On an hemispheric scale, the seasonal growth and decay of the sea ice cover are controlled by atmospheric and oceanic forcing, including ocean temperatures and salinities, and atmospheric temperatures and winds.

On a regional scale, surface roughness of the ice and its drag coefficient depend upon ridging and rafting, both of which can be produced by wind- or wave-induced ice convergence. Numerical models have amply demonstrated the influence of the atmosphere on the ice (e.g., Parkinson and Kellogg, 1979; Parkinson and Bindschadler, 1984), the impact of the ice on the atmosphere (e.g., Ledley, 1988; Simmonds and Budd, 1990), and the importance of the full ice-ocean-atmosphere coupling (e.g., Washington and Meehl, 1989; Manabe et al., 1990).

In addition to its importance in climate processes, sea ice also plays an important role in the oceanic biome, including location of certain fisheries and species. Further, the distribution and strength of sea ice affect maritime navigation.

1.2 Passive-Microwave Remote Sensing of Sea Ice

Although images of sea ice acquired by satellite-borne visible and infrared wavelength sensors during the 1960s proved useful for mesoscale studies in cloud-free regions, only microwave sensors could acquire surface observations at regular and frequent time and space intervals. The relatively coarse resolution of the passive-microwave sensors limits delineation of the small-scale features of the ice pack. These instruments, however, provide an integrated measure of the open water amount within the ice packs and the distribution of ice types.

The recognition of the importance of obtaining sea ice parameters from space was based on the Arctic experience of scientists beginning with Station Alpha (Reed and Campbell, 1962) during the International Geophysical Year (IGY) in 1957-1958, and continuing during the 1960s with the Arctic Research Laboratory Ice Stations (ARLIS). As a direct result of this pre-ESMR work, Dr. William Nordberg and his team at Goddard had constructed in 1967 the first passive-microwave imager, the prototype of the Electrically Scanning Microwave Radiometer (ESMR) operating at the single wavelength of 1.55 cm (19.35 GHz).

Prior to the launch of ESMR on Nimbus 5 in December 1972, in the late 1960s and early 1970s, several experiments, including coordinated international Arctic missions, provided the requisite data for developing and testing the ESMR (and later SMMR) sea ice algorithms. The first aircraft mission

Figure 1.0.1. Nimbus 7 satellite, showing the SMMR onboard. The oscillating SMMR antenna receiving dish can be seen near the center of the figure above the sensory ring, which contains the SMMR radiometers and components of other instruments.

for the ESMR occurred onboard the NASA Galileo I CV-990 Airborne Laboratory under Nordberg's direction, with the first flights over the Beaufort Sea in May 1967 and June 1970. These suggested several of the important microwave characteristics of the ice cover (Wilheit et al., 1972; Campbell, 1973). The flights of 1967-1970 clearly demonstrated the ability to distinguish between open water and sea ice with passive-microwave data. The 1970 observations also led to an hypothesis that there are at least two radiometrically distinct sea ice types: first-year and multiyear. This hypothesis was confirmed during the Arctic Ice Dynamics Joint Experiments (AIDJEX) in subsequent wintertime aircraft expeditions flown in conjunction with major expeditions on the ice, prior to the launch of ESMR (Campbell, 1973; Gloersen et al., 1973, 1974b; Meeks et al., 1974; Ramseier et al., 1974).

Valuable synoptic and large-scale information on the oceanic and atmospheric processes was also acquired during AIDJEX and other field programs. These programs included

- AIDJEX, Spring 1971, 1972, and Spring 1975 through Spring 1976.
- BESEX (Joint US/USSR Bering Sea Experiment), Spring 1973.
- Skylab Snow and Ice Experiment, Winter and Spring 1973 and 1974.
- SURSAT (Canadian Surveillance Satellite Experiment), Winter-Spring 1978 and 1979.
- NASA CV 990 Underflight Mission for the Nimbus 7 SMMR, Oct-Nov. 1978.
- NORSEX (Norwegian Remote Sensing Experiment), Autumn 1978 and 1979.
- MIZEX-East (Marginal Ice Zone Experiments in the Greenland Sea), Summer 1983 and 1984, and Winter 1987.
- MIZEX-West (Marginal Ice Zone Experiments in the Bering Sea), Winter 1983.
- Winter-Weddell Sea Project, July-December 1986.
- NASA P3/Submarine Arctic Experiment, May 1987.

During the BESEX, AIDJEX, and Skylab programs, aircraft microwave observations, coordinated with in-situ snow and ice observations, were obtained over various parts of the western Arctic Ocean, the Bering Sea, and the Gulf of St. Lawrence. Aircraft and simultaneous Nimbus 5 ESMR observations obtained during the AIDJEX were analyzed to yield the first seasonal view of the variations in multiyear ice in the Arctic Ocean (Campbell et al., 1978, 1984; Gloersen et al., 1978; Carleton, 1984; Carsey, 1985).

These projects led to a series of additional papers on the measurements of sea ice extent, concentration, thickness, type, motion, and comparisons with L-band Synthetic Aperture Radar (SAR) data (e.g., Campbell et al., 1974, 1975a,b, 1976a,b, 1977a,b, 1980a,b, 1981, 1984; Gloersen et al., 1974a, 1975a,b; Kondratyev et al., 1975; Ramseier et al., 1975; Zwally and Gloersen, 1977; Carsey, 1982; and Crane et al., 1982). Large-scale comparisons have also been made between ESMR data and data from other satellite instruments (e.g., Comiso and Zwally, 1982, and Campbell et al., 1984).

In addition to providing valuable corroborative information in support of ESMR, the foregoing experiments also provided the basis for the development of the sea ice algorithm used for SMMR data. The CV-990 carried not only the airborne ESMR, but also fixed-beam radiometers obtaining both polarized radiation components at wavelengths from 0.3 to 21 cm (Gloersen et al., 1973). Thus, it was possible to select the most appropriate wavelengths for the SMMR sea ice channels and to design the SMMR sea ice algorithm based on the data from these early experiments. The first experiment carried out with SMMR was the NASA CV-990 Underflight Mission (Gloersen et al., 1980a), which covered observational areas not only in the Arctic, but also in the Norwegian Sea and the Pacific Ocean. Then followed the large international sea ice experiments, all of which involved coordinated surface, aircraft, and satellite observational programs. Utilization of the results from these observations is described in Chapters 2 and 3.

The launches of the Nimbus 5 ESMR in December 1972, the Nimbus 7 SMMR in October 1978, and most recently, the Defense Meteorological Satellite Program (DMSP) Special Sensor Microwave/Imagers (SSMI) in 1987, 1990, and 1991, resulted in data for analyzing the global sea ice cover for most of the period from December 1972 until the present. In addition to the research directed towards improving the microwave remote sensing of sea ice (including the development of algorithms for calculating areal coverage and ice type distribution from the microwave radiances), the ESMR and SMMR data have been utilized to study oceanic processes and to examine the role of sea ice in the global climate system.

1.3 Prior Analyses of Satellite Passive-Microwave Observations

A simple linear relationship between sea ice concentration and radiometric brightness temperature was used to calculate sea ice concentrations (the percentage of ice coverage) from observations obtained with the single-channel ESMR. These concentrations were mapped onto a polar stereographic projection with a grid spacing of 30- by 30-km for both the Arctic and Antarctic for the 4-year period of ESMR data, 1973 through 1976 (Gloersen et al., 1974a; Zwally et al., 1983a; Campbell et al., 1984; Parkinson et al., 1987). These data could not be used to determine ice type distributions unambiguously, because the ESMR observations were limited to a single frequency and polarization. Nevertheless, by making the reasonable assumption of high ice concentration in the central Arctic during the winter months, the ESMR data were used to obtain a measure of the distribution of multiyear ice across the Arctic basin (Gloersen et al., 1973; Campbell et al., 1978; Parkinson et al., 1987). The ambiguity between the first-year and the multiyear ice concentrations limits the accuracy of the derived total ice concentrations.

Even though the compiled ESMR ice concentrations covered only a 4-year period and were less accurate than those derived from the SMMR data, the ESMR data revealed previously unrecognized features that reflected unusual large-scale oceanic events as well as significant regional and interannual variations. An unexpected discovery was a major opening in the Weddell ice pack (the Weddell Polynya), which was found to have occurred in 3 of the 4 ESMR years. Its extent and duration were recorded and examined in conjunction with atmospheric and oceanic data (Zwally et al., 1976, 1983a; Zwally and Gloersen, 1977; Gordon, 1978; Carsey, 1980; Parkinson, 1983). Further analysis showed significant decreases in ice extent in the Weddell and Ross Seas during the 1970s. The maximum extent of sea ice in the southern ocean as a whole was found to have decreased by 6% over the 4 ESMR years (Zwally et al., 1983b). Large areas of reduced ice concentration were found in the Arctic Ocean (Gloersen et al., 1978; Campbell et al., 1984; Parkinson et al., 1987). Out-of-phase fluctuations between the adjacent Bering and Okhotsk Seas were determined and analyzed (Campbell et al., 1981; Cavalieri and Parkinson, 1987). Many other studies of ice-atmosphere and ice-ocean interactions were also undertaken with the ESMR data set (e.g., Cavalieri and Parkinson, 1981; Crane et al., 1982; Parkinson and Cavalieri, 1982; Crane, 1983; Parkinson, 1983; Parkinson and Gratz, 1983; Zwally et al., 1985; Parkinson, 1990; Comiso and Zwally, 1984; Cahalan and Chiu, 1986).

With the launch of the Nimbus 7 SMMR on October 24, 1978, the requisite multichannel passive-microwave data set for obtaining more accurate sea ice concentrations, multiyear ice concentrations, and sea ice temperatures began to be collected. This book provides a systematic analysis of the spatial and temporal variations in the global sea ice cover from October 26, 1978 through August 20, 1987, using sea ice concentrations and extents derived from the SMMR data. A summary of the initial results obtained by the SMMR Team of the Nimbus Project is provided by Gloersen et al. (1984).

Previous analyses of the SMMR data examined

- The variability of sea ice and multiyear ice (e.g., Cavalieri and Zwally, 1985; Comiso, 1986; Zwally and Walsh, 1987; Parkinson, 1991, 1992).
- Time series of sea ice extents (e.g., Gloersen and Campbell, 1988a; Parkinson and Cavalieri, 1989; Gloersen and Campbell, 1991a,b).
- Characteristics of melting snow (Anderson et al., 1985; Anderson, 1987).
- Ice-ocean and ice-atmosphere interactions (e.g., Cavalieri and Martin, 1985; Zwally et al., 1985; Alfultis and Martin, 1987; Comiso and Gordon, 1987; Gordon and Comiso, 1988; Gloersen et al., 1989; Jacobs and Comiso, 1989; Martin and Cavalieri, 1989; Parkinson, 1990).
- Correlation of melt water production from sea ice (inferred from SMMR data) with phytoplankton blooms (derived from ocean color satellite data) (Sullivan et al., 1988; Comiso et al., 1990; Mitchell et al., 1992).

1.4 Synopsis

This volume extends by nearly 9 years the data record provided by the two ESMR Atlases. Monthly average maps of sea ice concentrations from the SMMR data in the north and south polar regions are presented for each month from November 1978 through August 1987, mapped onto polar stereographic projections with an approximately 25-km grid spacing. A variety of time series plots has been generated for both polar regions, for the global total, and for nine subregions within the Arctic and five subregions within the Antarctic. These maps and plots, along with the associated analyses, form the core of this volume. Chapter 2 describes the SMMR instrument, the microwave properties of sea ice, and the algorithm used for determination of sea ice concentrations, multiyear ice concentrations, and ice temperatures.

The ability to distinguish unambiguously between first-year and multiyear ice was not possible before SMMR, and is important both from the standpoint of long-term studies of ice production, destruction, and distribution, and from the inherent increase in the accuracy of total ice-concentration calculations resulting from this information. Also in Chapter 2 are the results of comparisons between field data, airborne observations, and satellite observations to provide estimates of the accuracy of the sea ice algorithm.

Chapter 3 contains monthly maps of Arctic sea ice concentrations and multiyear ice concentrations, additional maps and time series of the Arctic data, and an analysis of the 9 years of Arctic sea ice coverage (both regionally and as a whole). Chapter 4 contains the corresponding maps, plots, and analyses for the Antarctic, but without the multiyear concentrations (for reasons given in Chapter 2). Chapter 5 examines the regional, interannual, and global variations of sea ice. Appendix A contains monthly mean pressure, temperature, and buoy-drift data from the Arctic Ocean Buoy Program (courtesy of R. Colony) and the SMMR ice temperatures mapped onto the Arctic and Antarctic polar stereographic grids.

Page Intentionally Left Blank

2

MICROWAVE THEORY AND THE SMMR INSTRUMENT

This chapter describes the relevant microwave properties of sea ice and ice-free ocean, the characteristics of the SMMR instrument pertinent to the observation of sea ice over a long time span, the algorithm used to calculate sea ice concentration, multiyear ice concentration, and ice temperature, and the accuracies and sources of error of the calculated parameters.

2.1 Microwave Properties of Sea Ice and Ice-Free Ocean

The SMMR record consists of dual-polarized components of multi-frequency radiance data from the surface of the Earth and its atmosphere. In the polar regions, the contributions from the atmosphere are low, in the absence of storms, for the wavelength span of SMMR (0.8 cm to 4.5 cm), and are implicitly treated as constant in this book. The contributions from the surface are expressed as a product of the emissivity and the physical temperature of the radiating layer. This linear relationship holds because the Rayleigh-Jeans approximation to the Planck blackbody law is valid for the SMMR wavelength interval over the range of physical temperatures encountered on the Earth. Radiances are frequently described in terms of brightness temperature. Depending on the polarized component and the wavelength of the radiation, the emissivities of ice-free open water lie in the range 0.28-0.75, and those of sea ice lie in the range 0.52-0.96. Except at wavelengths shorter than 1 cm, there is no overlap in the water versus ice emissivity ranges, and sea ice can readily be discerned against the background of open ocean. Moreover, sea ice emissivities vary with ice type, allowing some ice types to be distinguished, within certain limitations, by multichannel microwave observations.

The two major types of sea ice that are known (Wilheit et al., 1972; Gloersen et al., 1973; Campbell et al., 1974) to have distinctly different microwave emissivities are first-year ice (ice that is at least 30 cm thick but has not undergone a melt season) and multiyear ice (ice that has survived at least one melt season). The World Meteorological Organization (WMO) has produced a glossary of new and young ice types (WMO, 1970). Among these types, new and young ice (under 30 cm thick) are known to have distinctly different microwave emissivities from first-year ice and have been observed in coastal polynyas (Ramseier et al., 1975; Gloersen et al., 1975a; Cavalieri et al., 1986; Grenfell and Comiso, 1986; Comiso et al., 1989). New and young ice are further categorized by WMO as

- Frazil ice—fine spicules or plates of ice, suspended in water.
- Grease ice—a soupy surface layer of coagulated crystals formed during a later stage of freezing than frazil ice, having a matte appearance.
- Nilas—A thin elastic crust of ice, up to 10 cm in thickness, frequently displaying finger rafting.
- Pancake ice—Predominantly circular pieces of ice from 30 cm to 3 m in diameter and up to about 10 cm in thickness, with raised rims.
- Young ice—ice of 10-30 cm in thickness.

As discussed in Section 2.3.4, the presence of these additional ice types within the SMMR field of view cannot be determined unambiguously and thus contributes to the error of the calculated ice concentrations. Another ice type that has not been resolved with satellite multichannel radiometers is second-year ice, classified here as multiyear ice. Second-year ice has been reported to have an emissivity intermediate between first-year ice and multiyear ice (Livingstone et al., 1983; Tooma et al., 1975) and also contributes to the error budget. The focus of the discussion here is on the multispectral and polarization characteristics of the two major ice types, first-year ice and multiyear ice, including their seasonal and regional variability.

Arctic maps of microwave brightness temperatures averaged for February, 1979, for four of the ten SMMR channels, are shown in Figure 2.1.1a-d and are used to illustrate some of the radiometric properties of sea ice and ice-free ocean utilized in the development of the sea ice algorithm discussed in Section 2.3. In addition to the obvious differences in the range in brightness temperature for each of the four radiance maps, there are numerous more subtle differences. For instance, the vertically polarized 0.8-cm (37-GHz) map shows greater spatial variability within the ice pack than its counterpart at 1.7 cm (18 GHz). This difference results from a greater sensitivity to ice type and snow cover and a smaller integrated field of view at 0.8 cm. Over the ice-free ocean, the greater variability arises from a greater sensitivity to cloud liquid water. The 1.7-cm horizontally polarized channel has an even greater spatial variability over the open ocean than the vertically polarized channels. This is not apparent in Figure 2.1.1a because all values less than 120 K are assigned the same color. The greater variability results from the greater sensitivity to atmospheric variation, caused by the higher reflectivity of the ocean for that channel. The highest brightness temperatures for each of the

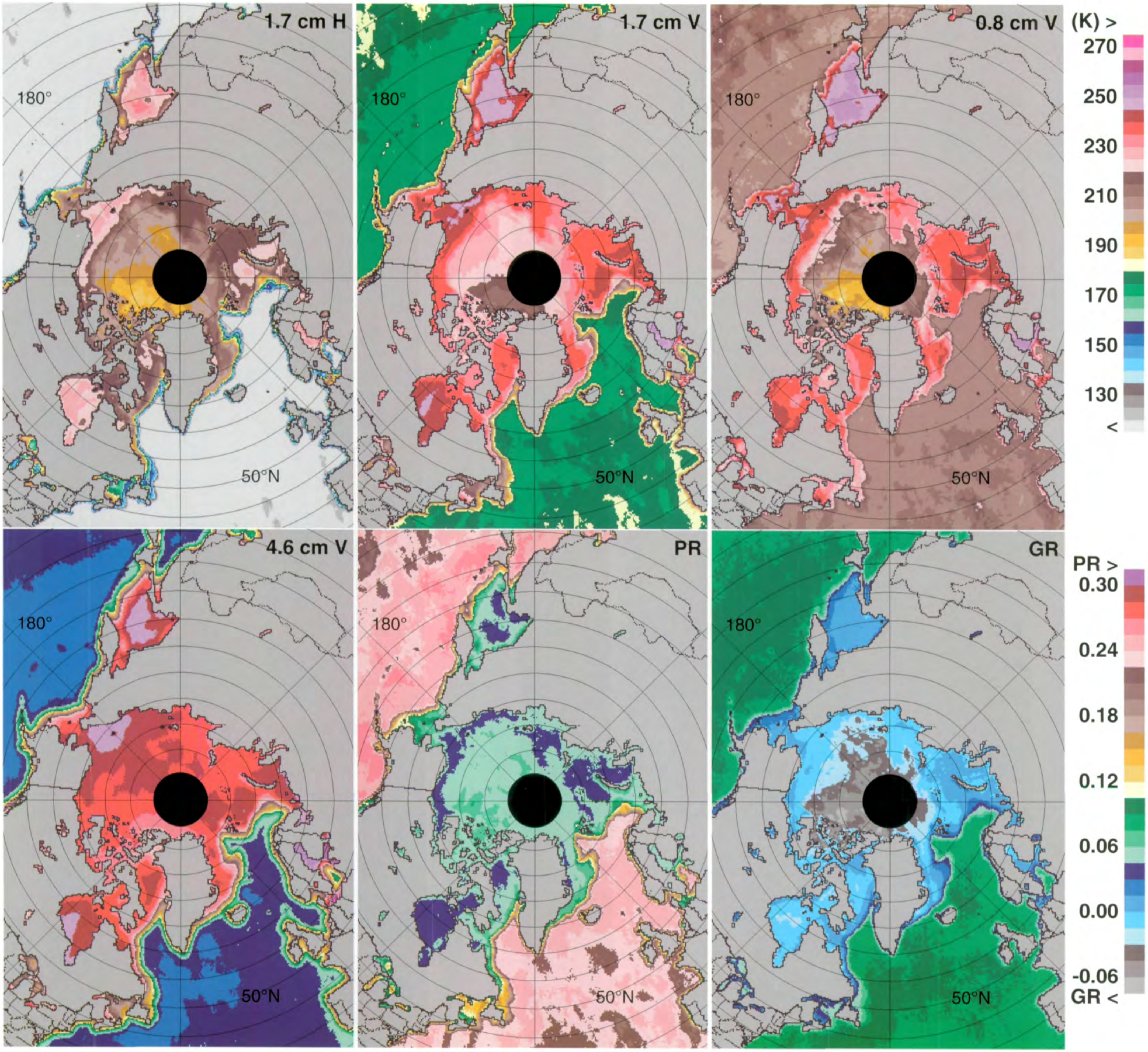

Figure 2.1.1. SMMR radiances and radiance ratios averaged for February 1979.

channels are found in the various peripheral ice-covered seas and bays, i.e., the Bering, Chukchi, East Siberian, Laptev, Kara, Barents, Greenland, and Labrador Seas, the Seas of Okhotsk and Japan, Baffin Bay, and Hudson Bay. Each of these areas includes a seasonal sea ice zone consisting primarily of first-year sea ice. Depending on wavelength and polarization, the brightness temperatures range from about 180 to about 255 K in the ice-covered portions of these regions. In contrast, the central Arctic has a perennial ice cover of multiyear ice that has a characteristically lower brightness temperature than first-year ice, except under melt conditions. This brightness temperature difference increases with decreasing wavelength, as is apparent from a comparison between the predominantly first-year ice area of the Chukchi Sea and the predominantly multiyear ice area north of the Canadian Archipelago (Figure 2.1.1b-d).

2.1.1. Polarization and spectral gradient ratio

Two ratios derived from three of the four SMMR channels shown in Figure 2.1.1a-d are used as the independent variables in the sea ice algorithm described in Section 2.3. These radiance ratios are the polarization PR, defined as

$$PR = (1.7V - 1.7H)/(1.7V + 1.7H) \qquad (2.1.1)$$

and the spectral gradient ratio GR, defined as

$$GR = (0.8V - 1.7V)/(0.8V + 1.7V) \qquad (2.1.2)$$

Maps of these ratios over the February 1979 time period are shown in Figure 2.1.1 e-f. PR values typically range from 0.03 to 0.09 in the central Arctic, while exhibiting higher values and ranging from 0.2 to 0.27 over open ocean (Figure 2.1.1e). Open ocean differences result from the variability of ocean-surface roughness and the variability of atmospheric water vapor, cloud liquid water, and rain. The GR values also differ for ice and water (Figure 2.1.1f). Open water areas have positive values of GR. Fully ice-covered areas have values ranging from nearly zero for first-year ice to more negative for multiyear ice. It is the observed variation in GR across the Arctic that provides the basis for deriving multiyear ice concentrations. Other properties of these two parameters are discussed below.

The annual variations of sea ice brightness temperatures from three of the SMMR channels are illustrated in Figure 2.1.2a-b for a 500- x 500-km Arctic Ocean area in the Canadian Basin, centered on 79.7° N and 140.8° W, in 1984. Also illustrated are the corresponding time series for PR, GR, the ice concentrations, and the ice temperature (Figure 2.1.2 c-f). Throughout the winter and early spring, the difference between the vertically polarized 1.7-cm and 0.8-cm brightness temperatures is about 25 K. This difference between the two brightness temperatures is important in determining the relative amounts of first-year and multiyear ice concentrations in Section 2.3. Beginning about April 10 (Julian day 100 in Figure 2.1.2), the brightness temperatures at each of the three channels begin to increase as a result of the seasonal warming of the ice. On or about June 18 (Julian day 169), there is a very sharp increase in the brightness temperatures caused by the onset of summer melt (Campbell et al., 1978, 1984; Gloersen and Campbell, 1988b; Cavalieri et al., 1990), followed by prominent but nonuniform decreases until about day 250. The brightness temperatures then return to their wintertime values. During summer, the difference between the vertically polarized 0.8- and 1.7-cm channels is considerably less than in winter and spring, as is the corresponding ice-type information, for reasons discussed later in this section.

The PR time series of Figure 2.1.2c is relatively level during the first 5 months of the year, then begins to fluctuate much more strongly with the onset of melt on or about June 18 (Julian day 169). PR increases during the summer months as the amount of surface water increases, then decreases starting in September with the formation of new ice. In comparison to PR, the GR time series is more highly correlated with the brightness temperature time series during the winter months, suggesting that some of the variation in GR may result from the different temperature dependencies of the 0.8-cm and 1.7-cm brightness temperatures, caused by the difference in optical depth (the distance in the medium over which all but 1/e of the radiation is absorbed) at these wavelengths. Algorithm error associated with this temperature dependence is discussed in Section 2.4.

Since part of the seasonal variation of the SMMR brightness temperatures shown in Figure 2.1.2a-b is caused directly by the seasonal cycle in the physical temperature of the ice, it is more meaningful to describe the radiometric properties of sea ice in terms of its emissivity, defined as the ratio of its radiometric and physical temperatures. The wavelength and polarization dependence of ocean and sea ice emissivities measured at the surface (Svendsen et al., 1983) is shown in Figure 2.1.3. The curves reveal very different trends for first-year ice, multiyear ice, and open water. The emissivity of first-year ice is almost constant as a function of wavelength, that of multiyear ice increases with wavelength, and that of open water decreases with wavelength. The largest emissivity difference between ocean and either first-year or multiyear sea ice occurs at the longer wavelengths, whereas the difference between first-year ice and multiyear ice emissivities is very small at long wavelengths but much larger at shorter wavelengths.

Many of the characteristics depicted in Figure 2.1.3 can be explained in terms of the physical characteristics of the ice. The lack of sensitivity of the first-year ice emissivity to wavelength results from the microwave radiation emanating mainly from a layer of sea ice containing liquid brine cells. This layer is opaque over the range of microwave wavelengths observed by SMMR and lies immediately below a snow cover overlying the ice. The microwave penetration (optical) depth in this layer of first-year sea ice is estimated to be of the order of a wavelength (Gloersen et al., 1975b).

For multiyear ice, the average salinity of the freeboard layer is much less than 1‰, compared to a salinity exceeding 5‰ for first-year ice (Ramseier et al., 1974; Tucker et al., 1991). While desalinization occurs all year, the

(a) 1.7-cm

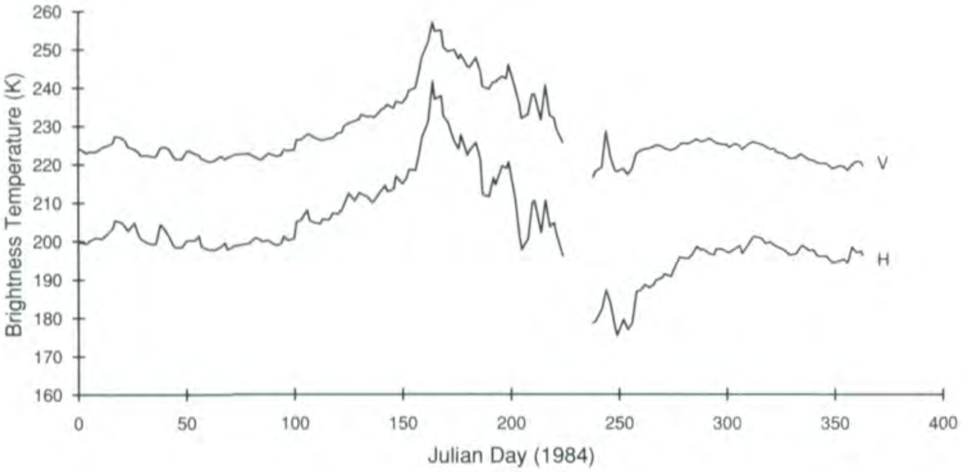

(b) 0.8-cm V

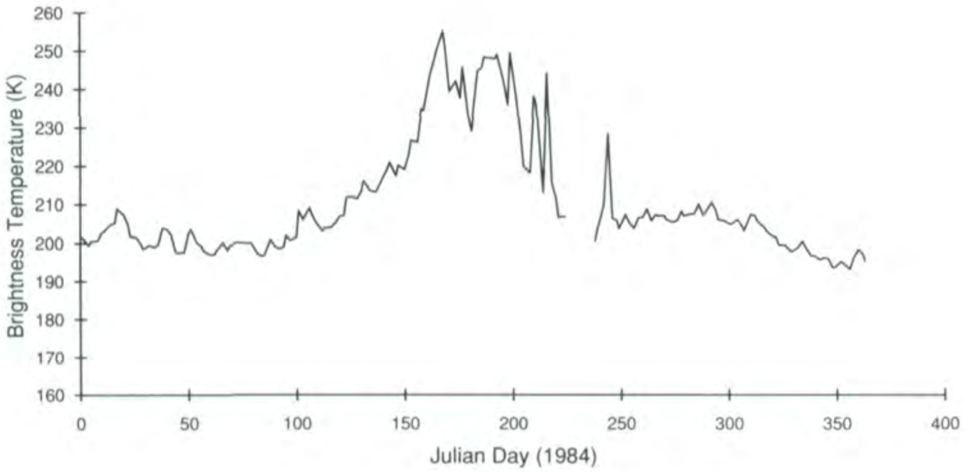

(c) PR

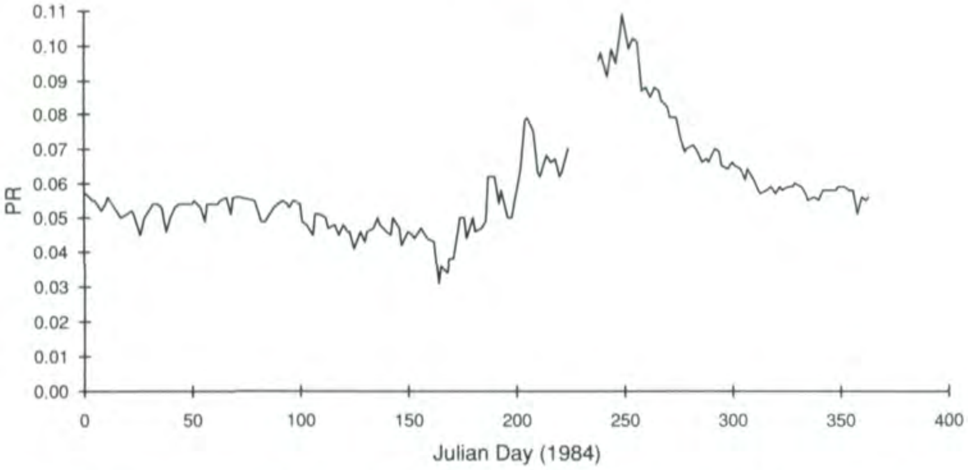

(d) GR

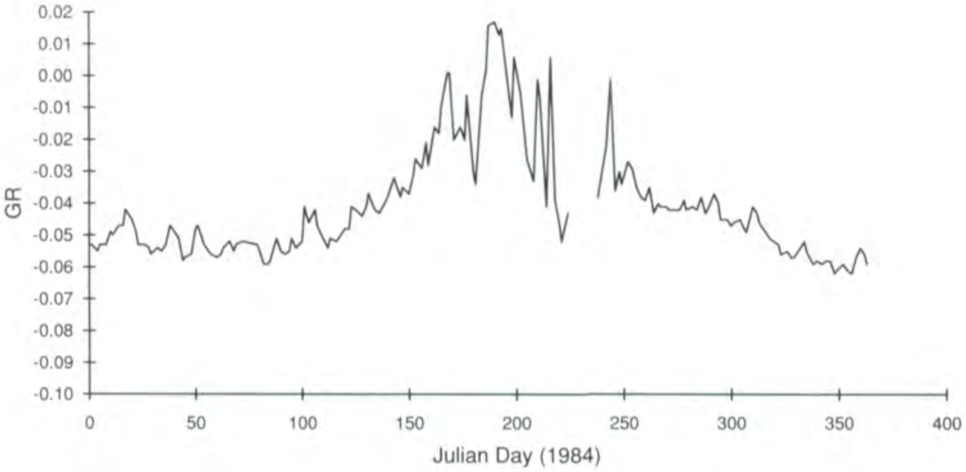

(e) Ice Concentrations

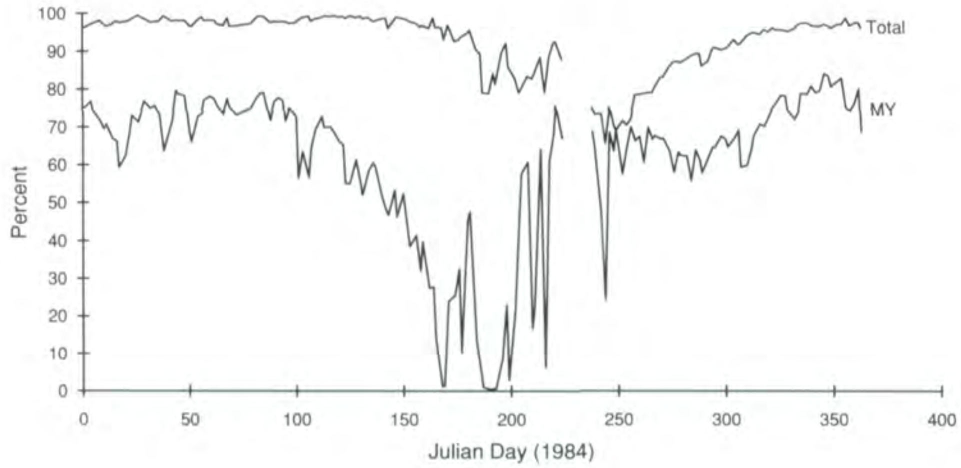

(f) Ice Temperature

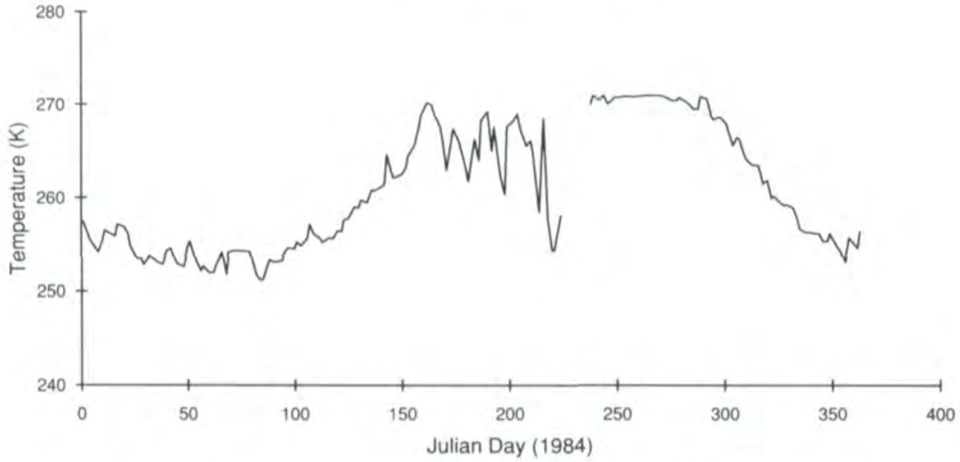

Figure 2.1.2 . SMMR data from a 500- x 500-km region north of the Canadian Archipelago for 1984: (a) 1.7-cm H and V, (b) 0.8-cm V, (c) polarization at 1.7 cm, (d) spectral gradient ratio of 0.8- and 1.7-cm V, (e) total sea ice concentration and multiyear sea ice concentration, and (f) ice temperature. See text for discussion of summertime multiyear ice concentrations. The ice-temperature oscillations in (f) appear to be anticorrelated with those for the total ice concentration, maybe indicative of imperfect compensation in the ice temperature algorithm for variations in ice concentration. This leads to unrealistic values during the summer. However, the ice-temperature fluctuations are within the stated accuracy for the algorithm (see Section 2.3.4).

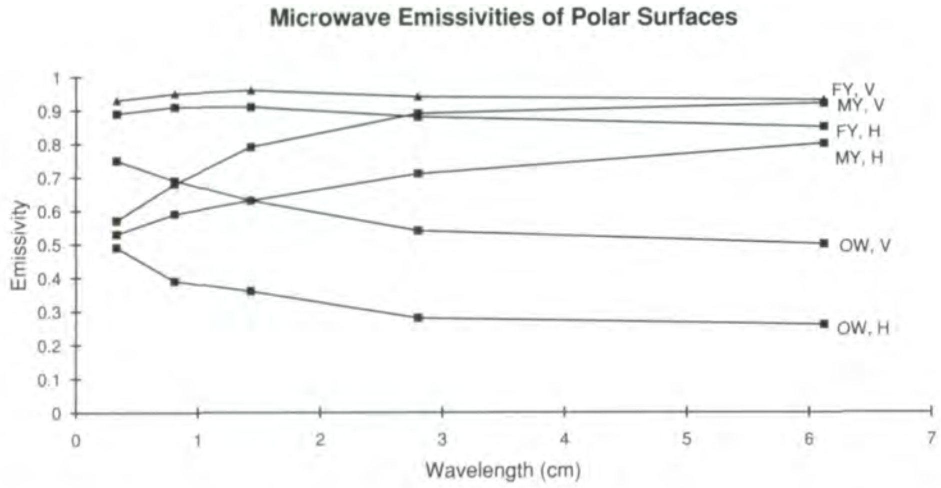

Figure 2.1.3. Emissivity of first-year ice, multiyear ice, and open water as a function of wavelength and polarization (from Svendsen et al., 1983).

process is accelerated during the summer months (Meeks et al., 1974). As a result of the desalinization, the dielectric loss in the multiyear ice freeboard layer is low, making the layer transparent in winter. Therefore, most of the observed radiation is emitted from a brine-bearing layer of ice near sea level, rather than from the layer immediately below the snow cover as with first-year ice. Another result of the brine drainage during summer is the creation of empty brine pockets in the freeboard layer of the ice. This results in a lower emissivity than for first-year ice because of volume scattering caused by the empty brine cells, which serve to trap part of the radiation emanating from the ice near sea level. Since the cross-section of the scattering centers is of the order of millimeters, the short wavelength radiation is scattered more than the long wavelength radiation (Chang et al., 1976; Gloersen and Larabee, 1981), explaining the upward trend in the emissivity of multiyear ice as a function of wavelength (Figure 2.1.3). It should be noted, however, that in the winter marginal sea ice zone, flooded multiyear sea ice has been observed to lose its characteristic microwave emissivity, as the freeboard salinity can be as high as 10‰ (Tucker et al., 1991).

The decrease of open water emissivity with wavelength (Figure 2.1.3) results from the dependence of the complex index of refraction of water on wavelength (Lane and Saxton, 1952). This dependency enters into the Fresnel equations for reflectivity used to calculate emissivities for calm weather conditions. Under windy conditions, the emissivity increases with increases in foam coverage and surface roughness (Nordberg et al., 1969 and 1971; Hollinger, 1971; Webster et al., 1975, 1976; Gloersen and Barath, 1977; Swift, 1980; Jones et al., 1981).

In order to understand the spatial variations, ratios of SMMR and Temperature-Humidity Infrared Radiometer (THIR, also onboard Nimbus 7) brightness temperatures were used to obtain approximate values of sea ice emissivities (Comiso, 1983). The emissivities so estimated are considered independent, to first order, of the spatial variation in physical temperature. Scatter plots of these calculated emissivities for data at the same polarization (vertical) but different wavelengths are shown in Figure 2.1.4a-c. The data shown come from a rectangular area that includes the central Arctic, Chukchi Sea, and part of the Bering Sea. In these plots, the location of multiyear ice, first-year ice, and open ocean data are indicated by M, F, and O, respectively. The data points located between M and F come from regions of high ice concentrations, with a mixture of first-year and multiyear ice, and are presumed to represent ice at 100% concentration. Similarly, data points between M and O are presumed to represent mixtures of multiyear ice and open water, and data points between F and O are presumed to represent mixtures of first-year ice and open water. This simplifies the real situation to one in which only three types of surfaces are assumed to exist in the field of view: first-year ice, multiyear ice, and open water. Data points corresponding to mixtures of the three surface types fall inside the triangle defined by M, F, and O as vertices. A hook pattern is prominent near the label M in Figure 2.1.4a-b, with the bottom of the hook indicating much greater variation in emissivity at 0.8 cm than at either 1.7 cm or 4.5 cm, possibly because of the wavelength dependence of scattering in snow and ice, or of spatial variability in the thickness of the snow cover.

Horizontally polarized emissivities versus vertically polarized emissivities at the three relevant SMMR wavelengths are also shown in Figure 2.1.4. The range in emissivity for the high ice-concentration data points (the points between M and F) decreases with increasing wavelength (Figure 2.1.4d-f), with the slope of the line formed by the high ice-concentration points in each of the three cases being approximately unity. The slopes remain approximately unity throughout the winter and from one year to the next.

2.1.2. Effects of snow cover

The microwave properties of sea ice are affected by the presence of a snow cover on the ice. The snow cover (a) insulates the ice from colder winter air, (b) prevents the formation through sublimation of a brine film on the surface, (c) when below freezing, decreases the surface emissivity because the microwave radiation emanating from below is trapped by scattering, and (d) increases the emissivity when the temperature is near the melting point. The magnitude of these effects depends on the snow grain size, the depth of the snow cover, and its moisture content.

Plots of emissivity over an annual cycle for both perennial (labeled multiyear) and seasonal (labeled first-year) ice areas are shown in Figure 2.1.5 for each of the ten SMMR channels. The emissivities are stable during most winter months at all SMMR channels, but in late spring and early summer, a marked increase occurs in the multiyear ice emissivity, followed by a comparably sharp decrease in midsummer. The spring onset of melting increases the snow-cover emissivity (Campbell et al., 1978, 1984; Grenfell and Lohanick, 1985), accounting for the temporary rise in multiyear ice emissivities. During this time, the emissivity is independent of the type of

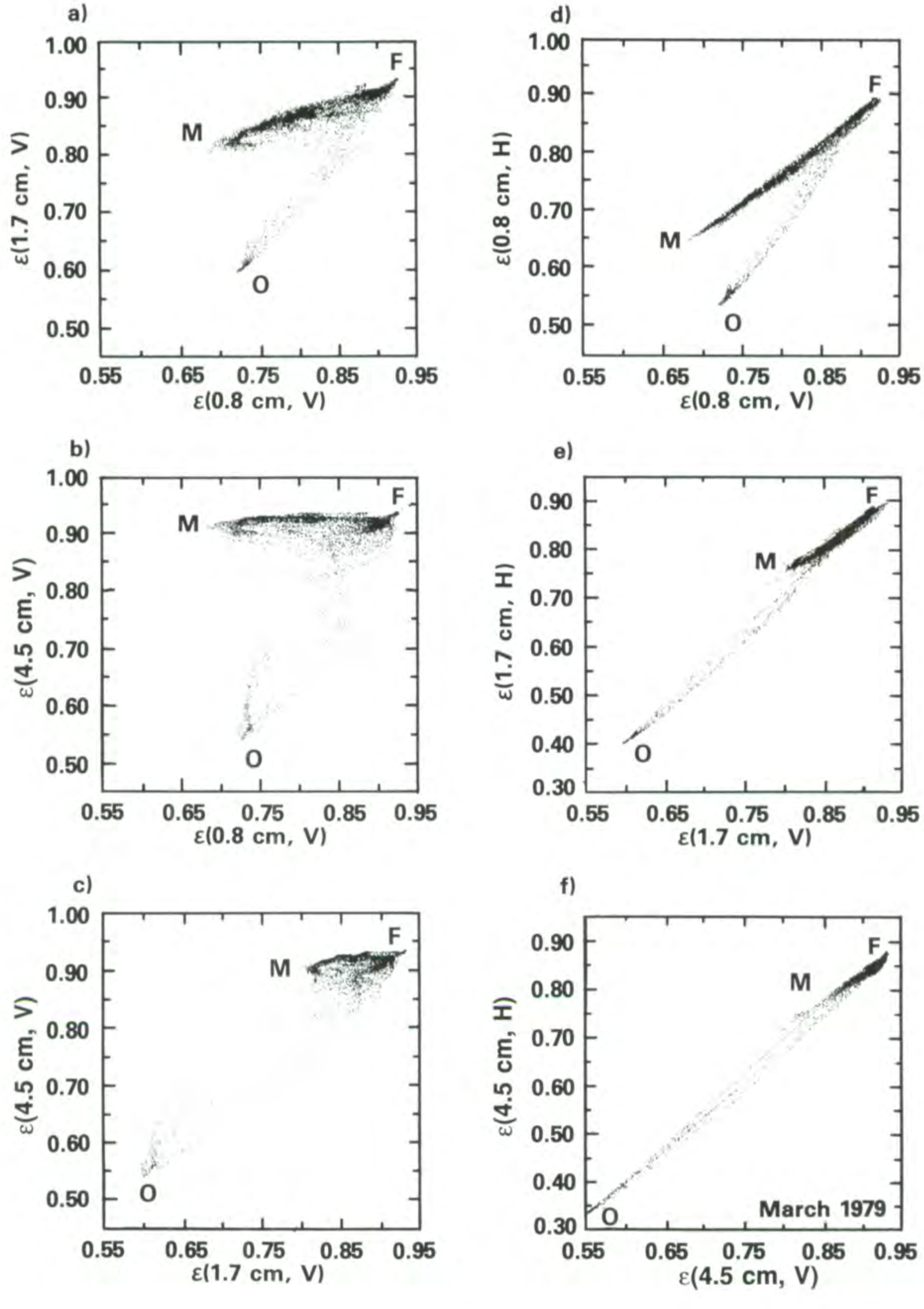

Figure 2.1.4. Emissivity scatter plots for the vertically polarized channels at wavelengths of (a) 1.7 vs. 0.8 cm, (b) 4.5 vs. 0.8 cm, (c) 4.5 vs. 1.7 cm, and for vertically vs. horizontally polarized channels at wavelengths of (d) 0.8 cm, (e) 1.7 cm, and (f) 4.5 cm. The data are from the central Arctic, Chukchi Sea, and part of the Bering Sea, for February 25, 1979 (after Comiso, 1986).

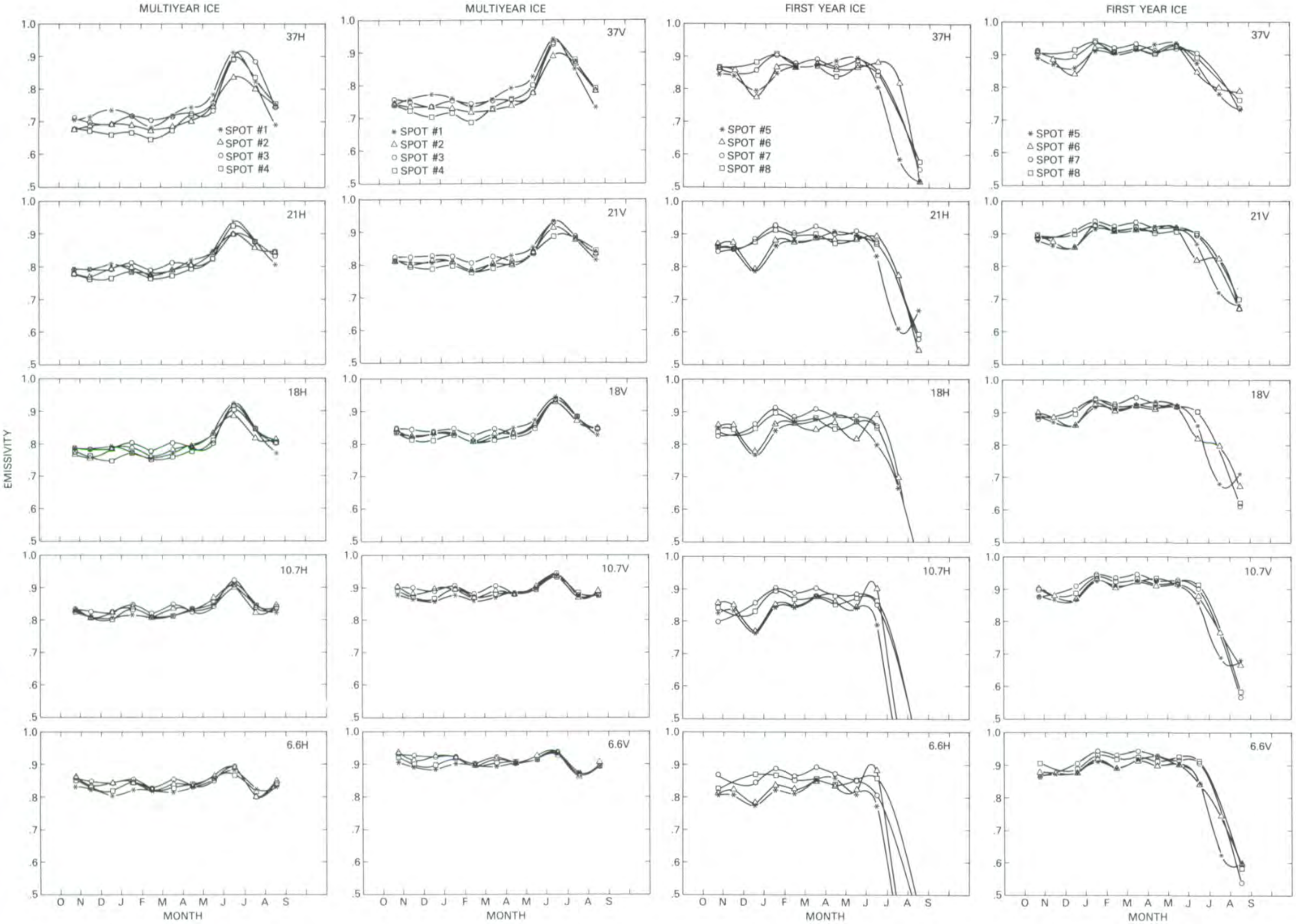

Figure 2.1.5 . Time series of emissivity for all SMMR channels in the Central Arctic from November 4, 1978 to August 29, 1979 (after Comiso, 1983). Channels are designated in frequency (GHz); see Table 2.2.1.

ice underneath the snow, since the radiation emanates primarily from the wet snow layer. This phenomenon is not evident in the first-year ice curves in Figure 2.1.5 because of ice breakup. Edgerton et al. (1971) and Stiles and Ulaby (1980) found a snow cover over land of 15 cm or greater thickness with about 1%-3% water content to be optically opaque, with very high emissivities. Campbell et al. (1978) and Grenfell and Lohanick (1985) report similar observations in the Arctic for first-year and multiyear ice during summer. Furthermore, analysis of single-day data sequences reveals evidence of freeze-thaw cycles during spring when the surface physical temperature is close to freezing (e.g., Gloersen and Campbell, 1988b). When the physical temperature is at the freezing point, the moist snow causes the emissivity to increase, but when the temperature drops to below freezing, the snow recrystallizes, forming larger grains that become very effective scatterers, causing the emissivity of the snow-laden ice to decrease. In cases where the snow is fine-grained (ca. 0.2 mm radius), the scattering is small and the emissivity is basically independent of wavelength (Chang et al., 1976).

The range of wintertime snow depth, in the absence of ridges, is about 5-30 cm in the Arctic (Barry, 1983). However, in the vicinity of ridges, snow depths of more than 1 m are common and affect the microwave emissions. There are no reliable estimates of the ratio of the areas of deep snow and unridged sea ice, but this ratio is presumed to be small in the central Arctic. The decreases in the first-year ice emissivities in Figure 2.1.5. during midwinter have been attributed to a deepening of the snow pack (Comiso, 1983). The scattering from deep snow is important near the perimeter of the ice pack, where the snow can have depths up to 65 cm and a grain size larger than in the interior (Tucker et al., 1987), resulting in signatures similar to those of multiyear sea ice. Brightness temperature differences as large as 8-10 K have been observed between the 0.8- and 1.7-cm aircraft microwave data over first-year ice in the Beaufort and Chukchi seas (Cavalieri et al., 1991). Errors in the calculation of multiyear ice concentration associated with this effect are discussed in Section 2.4.

(a) Microwave Emissivity vs. Sea Ice Thickness

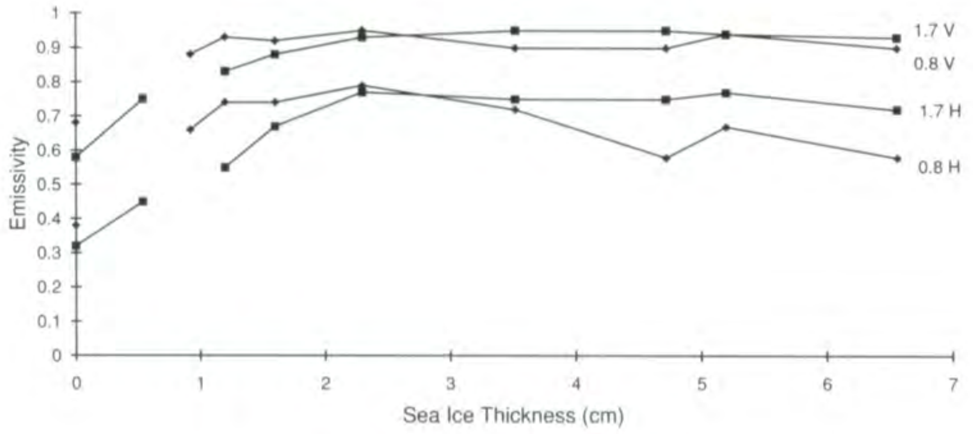

(b) Microwave Radiance Ratios vs. Sea Ice Thickness

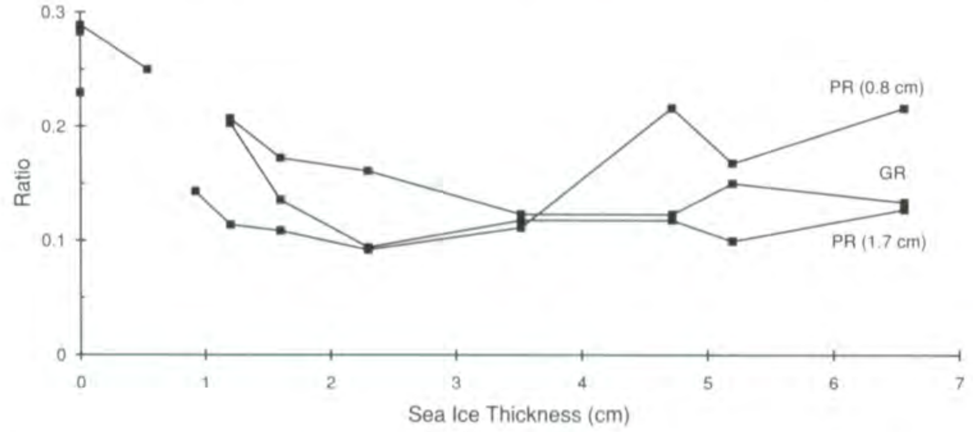

Figure 2.1.6. (a) Emissivities of sea ice vs. thickness in cm for horizontally (H) and vertically (V) polarized radiation at wavelengths of 0.8 and 1.7 cm, and (b) polarizations (PR) at the same two wavelengths and the spectral gradient ratio (GR), both vs. thickness. Data courtesy of T. Grenfell (unpublished data).

2.1.3. Thin ice types

The microwave emissivity of sea ice is also affected by the ice thickness, as recognized both theoretically, from radiative transfer models (Fung and Chen, 1981; Gloersen and Larabee, 1981), and observationally, from direct measurements (Gloersen et al., 1975b; Grenfell and Comiso, 1986; Comiso et al., 1989). The emissivity of very thin ice combines contributions from the underlying water with those from the ice, the contribution from the water decreasing with increasing ice thickness. The change from an open water emissivity to a first-year ice emissivity is gradual over the ice-thickness range of 0-1.5 cm, with the ice emissivity reaching the first-year sea ice value at a thickness of approximately 1.5 cm (Figure 2.1.6a.). The data shown in Figure 2.1.6 are from a controlled laboratory study of the variation of polarization (PR), gradient ratio (GR), and emissivity with ice thickness at wavelengths of 0.8 and 1.7 cm (Grenfell and Comiso, 1986). Under actual polar ocean conditions, because of wave and wind action and the rapid wintertime growth of thin ice, ice thicknesses as low as 1.5 cm are rarely encountered over large areas within the ice cover. Furthermore, a frequent property of new ice not incorporated in the laboratory conditions is the existence of a moist, highly saline film on top of the ice, reducing its emissivity and helping to explain why relatively thick ice, in the range of 10 to 20 cm, has also been observed to have the low emissivity characteristic of thinner ice in the laboratory measurements (Gloersen et al., 1975b; Cavalieri et al., 1986; Grenfell, 1986; Comiso et al., 1989). The 1.7-cm polarization values for new ice decrease exponentially with thickness, approaching an asymptotic value at a thickness of about 2 to 3 cm (Figure 2.1.6b). The polarization at 0.8 cm and the spectral gradient ratio have some unexplained excursions (Figure 2.1.6b).

2.2 The SMMR Instrument

Among the objectives of the Nimbus 7 SMMR were the measurement of sea ice concentrations with improved accuracy over previous measurements, the differentiation of sea ice types, and the measurement over the oceans of rainfall rates, sea-surface temperatures, scalar winds, cloud water, and water vapor (Gloersen et al., 1984). These objectives expand upon those of the Nimbus 5 and Nimbus 6 ESMRs, the primary objectives of which were the determination of rainfall rates over the oceans and the determination of polar sea ice concentrations.

2.2.1. Instrument design

The conceptual design for the Nimbus 7 SMMR was developed at Goddard, based on ideas originated by C. R. Laughlin and K. Richter; the instrument was subsequently adapted for use also on the NASA Seasat A satellite. The radiometers, control electronics, power supply, data, and data-sequencer subsystems of the SMMR are derivatives of the Nimbus E Microwave Spectrometer (NEMS) on Nimbus 5 and the Scanning Microwave Spectrometer (SCAMS) on Nimbus 6, with minor modifications to take advantage of improved state-of-the-art components. A team led by J. Johnston did the final design and fabrication at the Jet Propulsion Laboratory for both the Nimbus 7 and Seasat A SMMR instruments (Gloersen and Barath, 1977).

The SMMR is a 10-channel instrument receiving both horizontally and vertically polarized radiation at each of 5 wavelengths: 0.8, 1.4, 1.7, 2.8, and 4.5 cm (Gloersen and Barath, 1977). Microwave radiation from the Earth and its atmosphere is reflected by an off-axis parabolic mirror into a multifrequency receiving horn that distributes the various radiometric components to appropriate radiometers. Scanning is accomplished by oscillating the parabolic reflector about a vertical axis between local azimuth angles of ±25°, with a period of 4.096 s, comprising two scans. The various integrate-and-dump (dwell) times of the radiometers, combined with the oval instantaneous fields of view (defined as the 3 dB beam width), result in roughly circular beam spots ranging in diameter from about 30 km for the 0.8-cm channels to 150 km for the 4.5-cm channels. Cross-track and along-track sampling intervals range from 14 x 14 km to 56 x 28 km. Since there is an integer number of dwell times in the scan period for each of the channels, the beam spots fall in a repeated pattern across the swath of SMMR observations on the Earth's surface. The incoming microwave beam is at a constant angle of 42° from nadir, corresponding to an Earth incidence angle of 50.2°. The SMMR scanning arrangement results in a nearly circular intersection of the cone swept out by the oscillating optic axis with the surface of the Earth. The swath of the observations along the suborbital track is about 780 km wide. The oscillating reflector feeds a single, fixed multispectral receiving horn, causing the orthogonally polarized components of the incoming radiation to rotate with respect to the fixed polarized axes of the receiving horn. The rotation causes polarized-component mixing that occurs increasingly toward the end of each scan and must be corrected during data processing.

The SMMR consists of six separate radiometers, one for each polarized component at 0.8 cm, and one for both polarized components at each of the other four wavelengths. The horizontally and vertically polarized components of the radiation are observed on alternate scans at the four longest wavelengths and on each scan at the 0.8-cm wavelength. In order to provide reference signals for gain variation adjustments in the data processing, small microwave receiving horns are aimed into space for low-radiance (cold) references. Totally absorbing waveguide terminations at the ambient temperature provide high-radiance (warm) references for each radiometer. The reference signals are switched into the radiometric data stream alternately near each extreme of the scan. To conserve power, the scan is sinusoidal. The SMMR operating characteristics are summarized in Table 2.2.1.

Table 2.2.1. SMMR Operating Characteristics

(from Gloersen and Barath, 1977)

Frequency, GHz	6.6	10.69	18.0	21.0	37.0
Wavelength, cm	4.55	2.81	1.67	1.43	0.81
3db Beamwidth	4.2°	2.6°	1.6°	1.4°	0.8°
Integration Time (ms)*	126	62	62	62	30
Instrument Noise (K)+	0.4	0.5	0.7	0.7	1.1
Integrated fov (km)	148	91	55	46	27
IF Range			10-110 MHz		
RF Range Bandwidth			250 MHz		
Dynamic Range			10-330 K		
Antenna Beam Efficiency			>90%		
Projected Antenna Aperture			79 cm		
Scan Period (back and forth)			4.096 sec.		
View Angle			42°		
Scan Range			-25° to +25°		
Earth Incidence Angle			50.2°		
Satellite Altitude			955 km		
Swath Width			780 km		
Subsatellite Velocity			6.414 km/sec.		

*An additional 2 ms is used to dump and reset the integrator.

+For the integration times above, including all losses, and for a 150-K target.

2.2.2. SMMR calibration

Background

The procedure for converting raw SMMR antenna signals (counts) to microwave radiances entails taking the instrument output data stored as digital counts on tapes called TATs (a misnomer originally meaning Antenna Temperature Tapes) and applying a series of calibrations and corrections. First, a prelaunch calibration was carried out based on tests done in a thermal vacuum chamber at the Jet Propulsion Laboratory. These tests measured the response of each of the ten SMMR channels to a blackbody target operated at a variety of temperatures ranging from 100 K to 350 K. The tests are described in Gloersen and Barath (1977) for the Nimbus 7 SMMR and in greater detail in Njoku et al. (1980) for the Seasat SMMR. Second, a semiempirical correction was made for the observed polarization mixing, described in Gloersen et al. (1980b). A third correction, described in detail in the following subsection, is an adjustment to the prelaunch calibration that forces the observations to conform with model calculations of oceanic radiances. The resulting data, incorporating these first three procedures, are stored on tapes of calibrated brightness temperatures (TCTs). The data are then further adjusted for two additional corrections, one for long-term instrument drift and one for instrument errors dependent on ecliptic angle. These final two corrections are described in the subsections following the discussion of the postlaunch calibration.

Before the production of the TCTs, SMMR radiances were averaged into cells with larger sampling intervals, approximately equal to the integrated fields of view, and recorded on CELL tapes. The CELL data format was designed primarily to produce sea-surface temperatures from SMMR radiances, and for this purpose, the additional averaging was deemed advantageous. However, the CELL data have also been used by a number of investigators in the polar regions. These data, not corrected for all aspects of cross-polarization leakage (described in the next section), instrument drift, and ecliptic-angle dependent instrument errors, were previously mapped onto polar stereographic grids and are archived at the National Snow and Ice Data Center (Comiso and Zwally, 1989). We have chosen to use the TCTs in preference to the CELL tapes, since the TCTs store SMMR data for each sampling interval, which is at most half the diameter of the integrated field of view for a given channel, thereby preserving the inherent spatial resolution of the SMMR data.

Postlaunch calibration

Subsequent to launch, the SMMR calibration algorithm was modified to ensure that the minimum SMMR brightness temperatures for the ocean agreed with model calculations of oceanic brightness temperatures in regions where, and at times when, atmospheric and wind contributions were minimal (Gloersen, 1987). A primary contributor to the prelaunch calibration error is the cross-polarization leakage that occurs between the horizontal (H) and vertical (V) channels at each of the five SMMR wavelengths. This unanticipated cross-polarization leakage was discovered during the course of testing the anticipated and purely geometric polarization mixing.

Since prelaunch tests had confirmed the expected linearity of the SMMR electronics, and the Rayleigh-Jeans approximation to the radiation law pertains over the range of radiances emitted by the global surface, the postlaunch calibration was based on the selection of two reference points, a warm reference and a cold reference. The warm reference point is obtained by using the physical temperature of the internal warm reference (a waveguide termination load inside the radiometer box) adjusted for the portion of the beam spilling over the horizon into space, termed the space spillover factor. The cold reference point is obtained by using the signal from the cold reference horns aimed into space and is adjusted so that oceanic observations correspond to model calculations of the radiation from a zonal area of the oceans selected, among other things, for low spatial variation in climatological sea-surface temperatures. For the cold reference point, the space spillover fraction is automatically taken into consideration when adjusting the observed signal to correspond to the modeled oceanic radiances described below.

The raw data from the satellite are the antenna counts, C_A, the warm reference counts, C_H, and the space-horn reference counts, C_C. These are used to calculate normalized counts

$$N = (C_A - C_H)/(C_C - C_H), \qquad (2.2.1)$$

from which the brightness temperatures, T_B, are calculated as follows:

$$T_B = A(t_h) + B(t_h) \cdot N \qquad (2.2.2)$$

where $A(t_h) = a_0 + a_1 \cdot t_h + a_3 \cdot (t_h - t_{h0})^2$

$B(t_h) = a_2 \cdot (t_c - t_h) + a_4 \cdot (t_h - t_{h0})^2$

$t_c = 2.7$ K, the assumed background temperature of outer space

t_h = measured ambient instrument temperature (the warm load)

t_{h0} = nominal instrument temperature, different for each channel and the a_i are empirically determined constants.

The a_i were determined for each SMMR channel in the thermal-vacuum test chamber prior to launch, with the aid of a blackbody radiation source operated at several temperature levels between 100 K and 350 K, and at several instrument temperatures in the range 270 K to 320 K (Gloersen et al., 1984).

The corrected brightness temperatures, T_B', are calculated from T_B with the use of offset and gain correction factors, a and b, as follows:

$$T_B' = a + b \cdot T_B = A' + B' \cdot N \qquad (2.2.3)$$

where $A' = a + b \cdot A$ and $B' = b \cdot B$. The correction factors a and b are obtained by solving simultaneously the following two equations, which represent the cold and warm reference points, respectively:

$$T_{Bm} = a + b{\cdot}T_{Bo} \tag{2.2.4}$$
$$A' = a + b{\cdot}A$$

The first equation in (2.2.4) is obtained by setting $T_B' = T_{Bm}$ and $T_B = T_{Bo}$ in Equation 2.2.3. T_{Bm} is the model oceanic brightness temperature, calculated for zero surface winds, zero cloudiness, and 1.0-cm columnar water vapor, based on the minimum climatological values from the U.S. Navy Climatic Atlas of the World (NAVAIR 50-1C-54, 1969), and T_{Bo} is the minimum observed brightness temperature in the latitude zone 30-40° S for the month of December 1978 (Gloersen, 1987). Solving (2.2.4) yields

$$a = T_{Bm} - b{\cdot}T_{Bo} \tag{2.2.5}$$
$$b = (T_{Bm} - A')/(T_{Bo} - A)$$

A' is calculated by taking into account the space spillover fraction, SF, as follows:

$$A' = (A - 2.7{\cdot}SF)/(1 - SF) \tag{2.2.6}$$

SF is determined for each channel from antenna pattern measurements made prior to launch at an antenna range. These values are listed in Table 2.2.2 and are assumed to remain constant throughout the 9-year period. The coefficients a and b in (2.2.5) are evaluated for a fixed value of A based on instrument parameters recorded for the latitude zone 30°-40° S during December 1978. The resultant values for a and b, also listed in Table 2.2.2, are used as constants throughout the data period.

Table 2.2.2. Calibration Adjustment Coefficients and Spillover Fraction

Channel	*a*	*b*	*SF*
4.5 H	04.9	1.068	0.049646
4.5 V	15.5	1.017	0.065527
2.7 H	01.9	1.042	0.034773
2.7 V	15.5	0.990	0.040192
1.7 H	07.6	1.047	0.021596
1.7 V	22.4	0.948	0.022590
1.4 H	27.0	1.113	0.022840
1.4 V	14.8	0.974	0.023250
0.81 H	08.8	1.040	0.010807
0.81 V	27.9	0.920	0.013304

The corrected TCT brightness temperatures for December 1978 are estimated, based on climatological ocean surface and atmospheric parameters, to give values accurate to within 2 K for the 1.7-, 2.7-, and 4.5-cm channels and within 5 K for the 0.8- and 1.4-cm channels (Gloersen, 1987). Accuracies for the other months may be different. As a final note, the differences between the horizontally polarized and vertically polarized brightness temperatures over open ocean in the north polar region have been found to be in good agreement (within 2 K) with radiometric measurements obtained during the Norwegian Remote Sensing Experiment in 1979 (NORSEX-79) (Mätzler et al., 1984) and with measurements from the DMSP SSMI instrument (Gloersen, unpublished data), which does not suffer cross-polarization leakages.

Correction for long-term instrument drift

In order to assure that the calculations of ice concentrations and temperatures accurately reflect changes with time and location, it was necessary to correct for long-term instrument drift and variations with ecliptic angle, described in the next section. In this book, we present only the results from the horizontally and vertically polarized channels of the wavelengths used in the sea ice calculations, i.e., at 0.8, 1.7, and 4.5 cm.

Variations in instrument sensitivity are most easily observed over low-radiance targets because the SMMR consists of Dicke radiometers (Gloersen and Barath, 1977) and therefore utilizes warm comparison signals. The only low-radiance target on the Earth's surface that provides widely distributed and uniform radiances is an averaged oceanic surface. Hence, for the purpose of determining instrument drift relevant to the sea ice calculations, we have used high-latitude oceans, averaging the SMMR oceanic radiances from 50° latitude poleward to the ice edge.

Brightness temperatures averaged over the selected regions of the polar oceans are shown in Figure 2.2.1 for the 1.7-cm horizontally polarized channel (1.7H), with results presented separately for the four cases of Arctic and Antarctic, northbound and southbound portions of the orbits. In order to remove the seasonal oscillation, the amplitudes and phases of the first two harmonics of the annual cycle were determined and used to approximate the seasonal cycle, which was then subtracted from the averaged oceanic brightness temperatures, resulting in the curves shown in Figure 2.2.2a-d. This procedure also subtracts the 8.8-year means. The four curves in Figure 2.2.2a-d nearly superimpose except for short-term fluctuations and are averaged together in order to reduce these short-term fluctuations, which are caused by variations in weather conditions. The resulting curve (Figure 2.2.2e) is then smoothed with an annual running mean, and the smoothed curve is taken as the observed drift for the 1.7H channel. This smoothed curve, along with the similarly created smoothed curves for the other five relevant SMMR channels, is presented in Figure 2.2.3.

In an effort to determine whether the drift in Figure 2.2.3 is instrumental or geophysical, various possible geophysical causes were considered. Oceanic warming was eliminated as a possible cause based on the similarity of the drifts for the Northern and Southern Hemispheres, the lack of a pattern

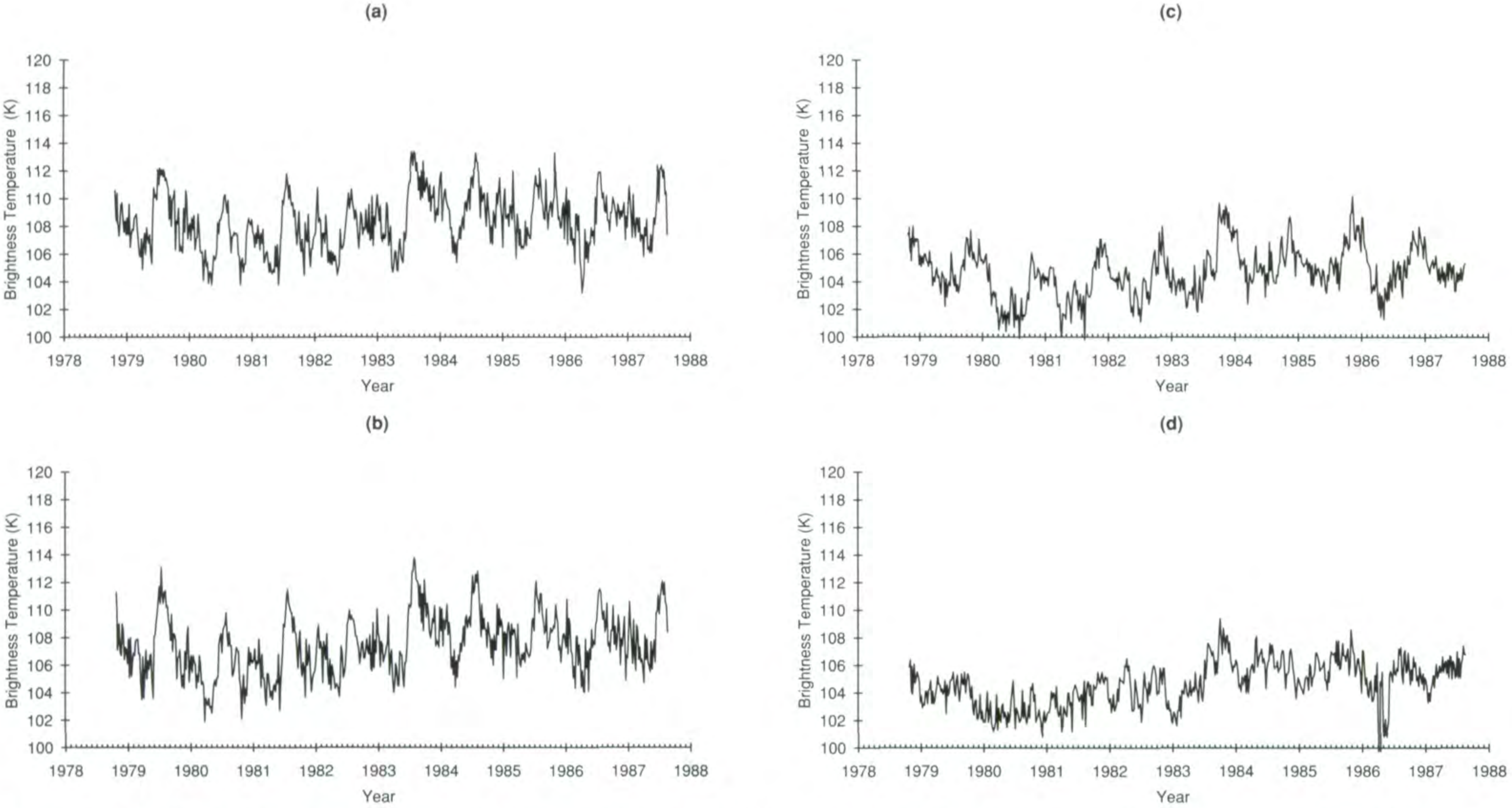

Figure 2.2.1. Temporal variation in the raw and uncorrected oceanic averages for the SMMR channel at a wavelength of 1.7 cm, horizontally polarized for: (a) north polar ascending, (b) north polar descending, (c) south polar ascending, and (d) south polar descending orbital nodes.

consistent with oceanic temperature change in the SMMR data, and the lack of evidence from independent determinations of oceanic surface temperatures. Rather than showing a warming trend, zonally averaged sea-surface temperatures obtained from the Advanced Very High Resolution Radiometer (AVHRR) during the SMMR lifetime showed an oscillation with a period of about 5 years and an amplitude of about 0.2 K (Reynolds et al., 1989), a pattern not observed in the SMMR data. Furthermore, compared to other sources of error, a variation of 0.2 K is insignificant in the calculation of sea ice concentrations and temperatures.

In order to consider other possible geophysical causes of the radiance drifts, the 9-year drifts in the polarizations (Figure 2.2.4) were calculated similarly to the drifts in brightness temperatures (Figure 2.2.3), the polarizations being independent to first order of the physical temperatures on the Earth's surface. Changing cloudiness, if observable in the north and south polar averages of Figure 2.2.4, should be reflected in polarization changes that are inversely proportional to increasing cloudiness and directly proportional to the square of the wavelength, because of the spectral dependence of Rayleigh absorption. Since such relationships in the patterns are not evident in Figure 2.2.3, cloudiness is eliminated as a possible major cause of the observed drift. Finally, a gradual change in wind patterns averaged over the north and south polar zones would result in polarization changes in the opposite sense at each of the three wavelengths and by about the same amount for each. Since no such systematic pattern is evident in Figure 2.2.4, changes in wind patterns are also eliminated as possible causes of the observed drift. Thus, we conclude that the curves represent instrument drifts (Figure 2.2.3). The data were consequently corrected by removing these drifts. (The data not smoothed by the running mean at the ends of the curves in Figure 2.2.3 were smoothed by eye.) This adjustment for instrument drift is important for obtaining the correct long-term variations in sea ice extent (areal coverage with ice concentrations exceeding 15%) and open water areas within the pack discussed in Chapters 3, 4, and 5.

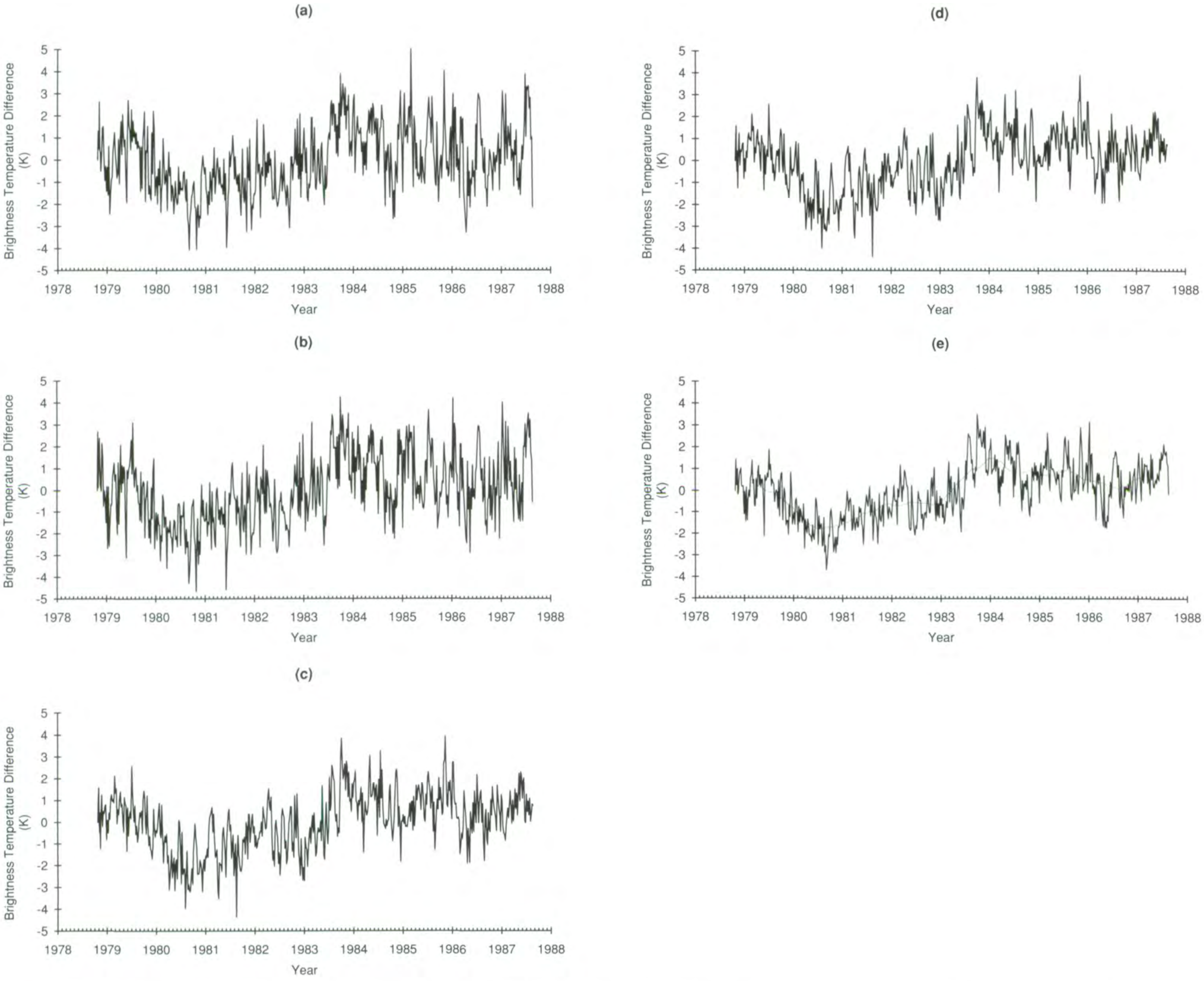

Figure 2.2.2. (a)-(d) Same as Figure 2.2.1, except the 8.8-year average and the first two harmonics of the annual cycle have been removed. (e) The average of the data in curves (a)-(d), with an annual running mean superimposed.

(a) 4.5 H

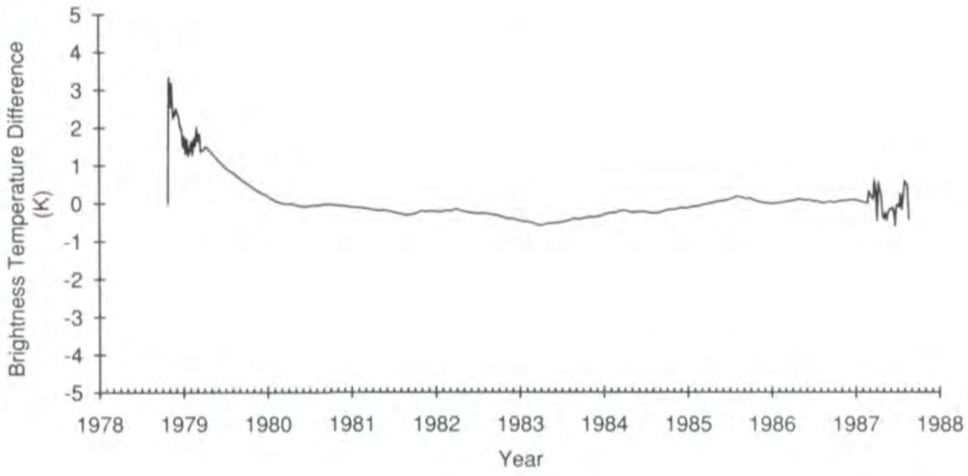

(b) 4.5 V

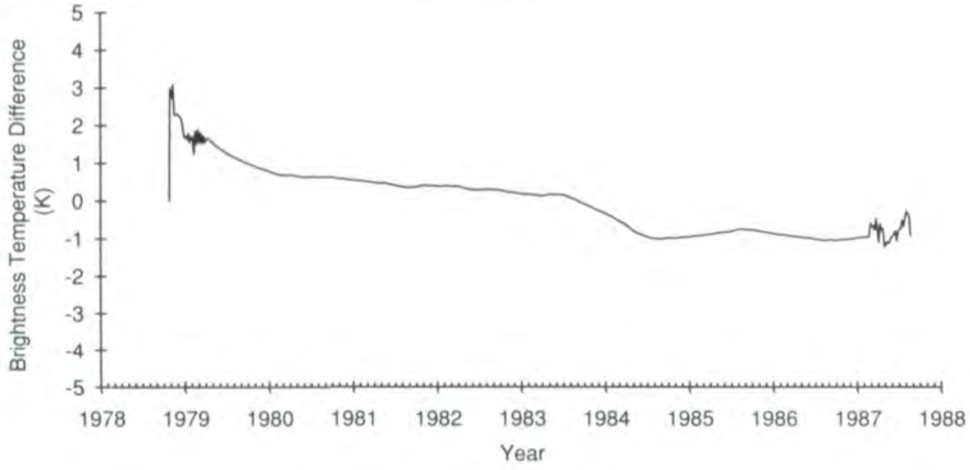

(c) 1.7 H

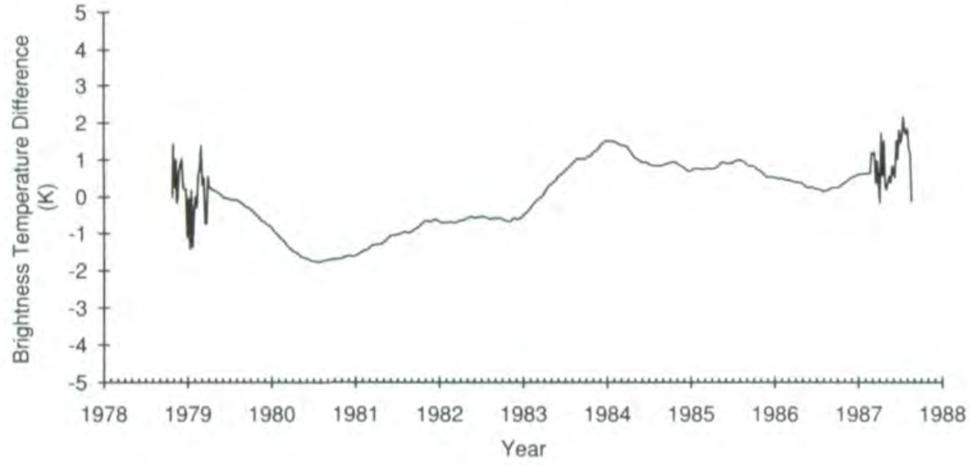

(d) 1.7 V

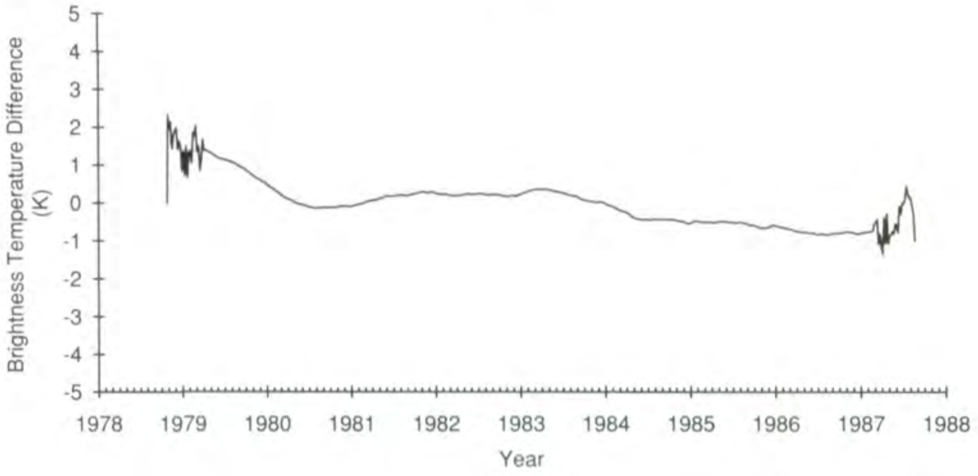

(e) 0.8 H

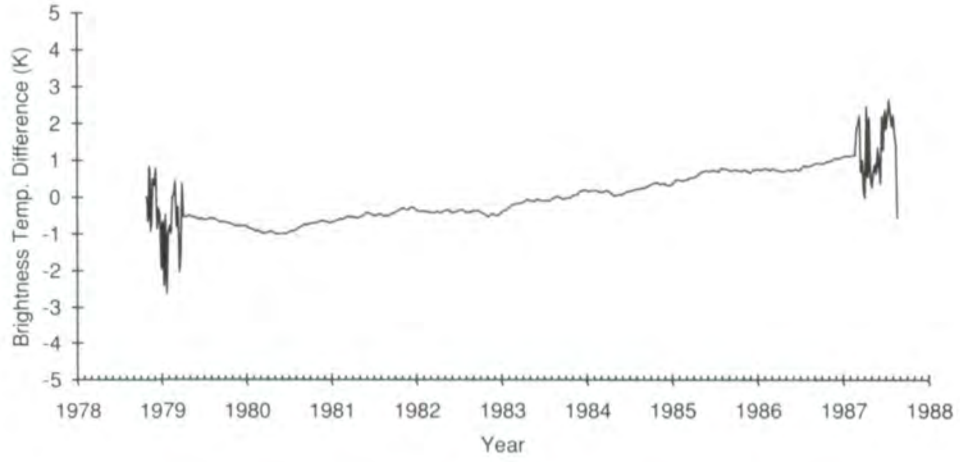

(f) 0.8 V

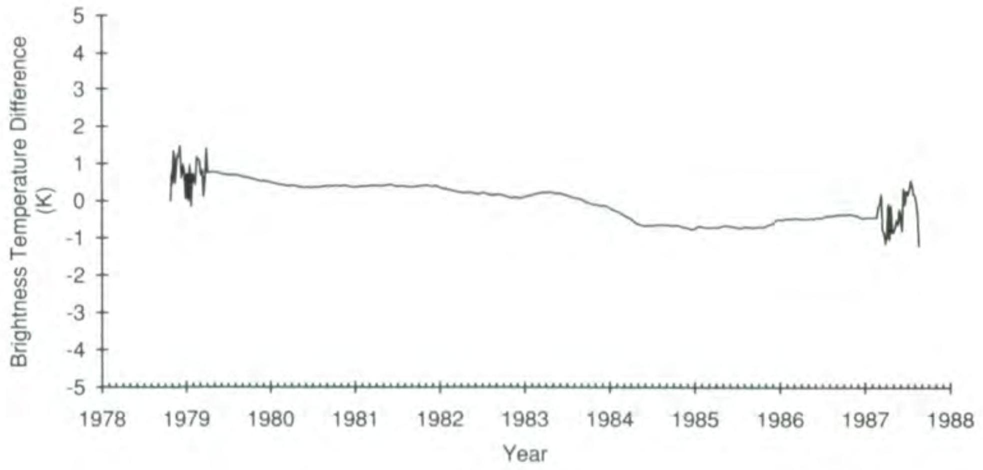

Figure 2.2.3. Temporal variation in the average uncorrected polar oceanic radiances smoothed with an annual running mean for six of the SMMR channels: (a) 4.5-cm wavelength, horizontally polarized, (b) 4.5-cm, vertically polarized, (c) 1.7-cm, horizontally polarized, (d) 1.7-cm, vertically polarized, (e) 0.8-cm, horizontally polarized, and (f) 0.8-cm, vertically polarized. The annual running mean did not operate upon the first and last 6 months of the data series.

(a) PR 4.5

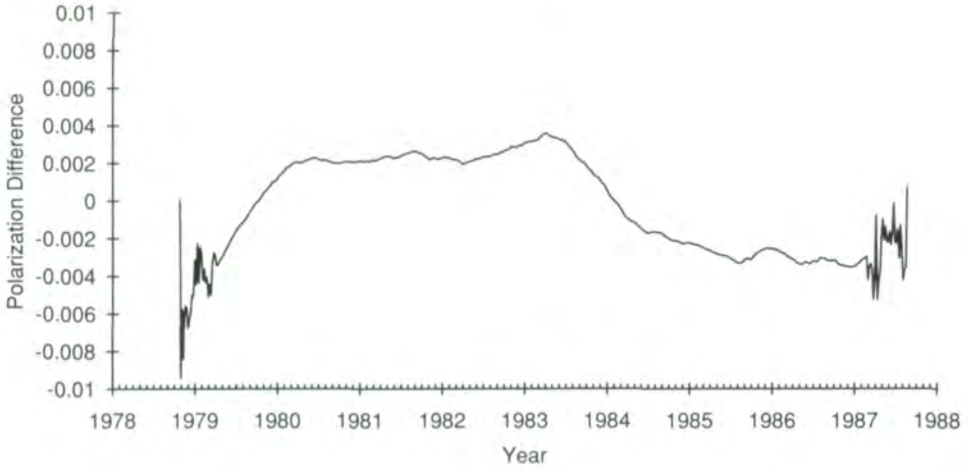

(b) PR 1.7

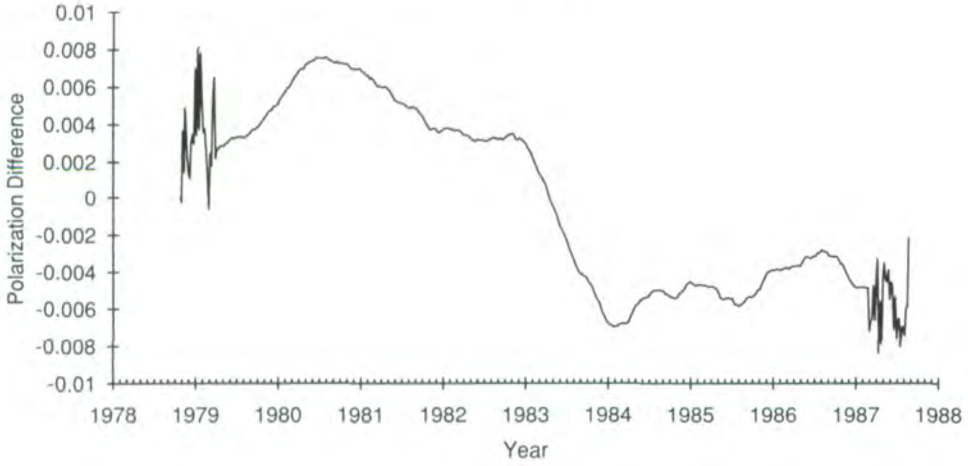

(c) PR 0.8

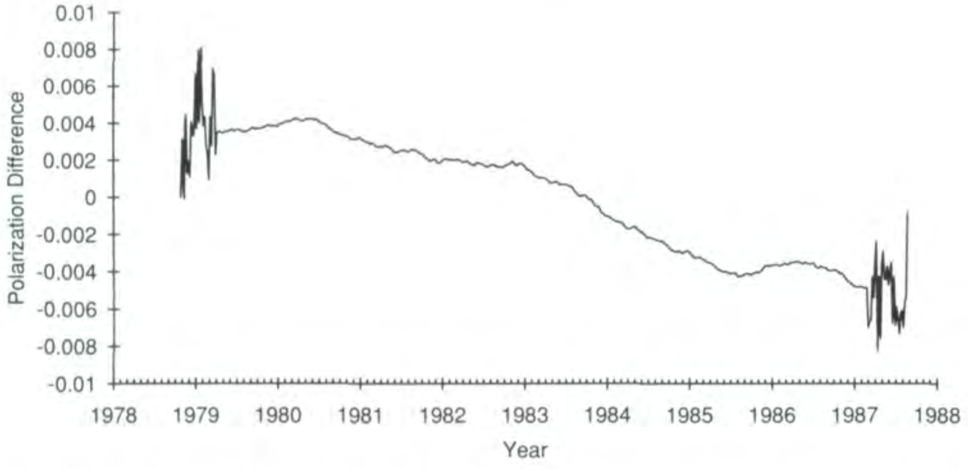

Figure 2.2.4. Temporal variation in the average uncorrected polar oceanic polarizations smoothed with an annual running mean for three of the SMMR wavelengths: (a) 4.5-cm, (b) 1.7-cm, and (c) 0.8-cm. The annual running mean did not operate upon the first and last 6 months of the data series.

Correction for instrument errors dependent on ecliptic angle

The determination of instrument errors dependent on ecliptic angle (defined as the angular position of the spacecraft in its orbital plane with respect to the south-pointing perpendicular to the earth-sun centerline) utilizes average oceanic brightness temperatures, for the entire open ocean region poleward to 68°. The method is an adaptation of one used by Francis (1987) for a portion of the SMMR data set. The first step is to average open oceanic areas into 2° latitude bands from 68° N to 68° S, with northbound and southbound portions of the orbit separated. Although consideration of these averages over half an annual cycle permits observations at all ecliptic angles (albeit sparsely near the poles), complete annual cycles are used for the analysis.

The underlying premise of the ecliptic angle correction is that geophysical differences in the values of the oceanic brightness temperatures for the northbound and southbound portions of the orbit should average out to nearly zero, so that any observed differences can be considered instrumental. If $E1(\varphi,t)$ and $E2(\varphi,t)$ are the northbound and southbound orbital ecliptic angles corresponding to latitude φ and time t (in increments of one day, with the time of day differing for E1 and E2), and R is the oceanic brightness temperature error, then the brightness temperature differences $\Delta(\varphi,t)$ are

$$\Delta(\varphi,t) = R(E1(\varphi,t)) - R(E2(\varphi,t)) \tag{2.2.7}$$

This may be written in matrix form as

$$\underline{\Delta} = \underline{\mathbf{A}} \cdot \underline{\mathbf{R}} \tag{2.2.8}$$

where $\underline{\mathbf{A}}$ is a matrix composed of 0's everywhere except for one +1 and one -1 in each row, corresponding to the differences in Equation 2.2.7. Each row of $\underline{\mathbf{A}}$ corresponds to a different (φ,t) pair, while the columns are arranged in increasing order of ecliptic angle in 2° bins. $\underline{\mathbf{A}}$ is therefore a 4148 (68·61) by 180 matrix, when we restrict ourselves to 2° oceanic zonal band averages between 68° N and 68° S and to the 61 (or 60, depending on the year) six-day SMMR repeat periods in a year. Equation 2.2.8 is an over determined set of simultaneous equations relating the observables, $\underline{\Delta}$, to the average brightness temperature error, $\underline{\mathbf{R}}$, at a given ecliptic angle for a given annual cycle. The formal solution for $\underline{\mathbf{R}}$ is

$$\underline{\mathbf{R}} = ((\underline{\mathbf{A}}^{T} \cdot \underline{\mathbf{A}})^{-1} \cdot \underline{\mathbf{A}}^{T}) \cdot \underline{\Delta} \tag{2.2.9}$$

where the T superscript signifies the matrix transpose. The triple matrix product in Equation 2.2.9 is the same for each SMMR channel.

Equation 2.2.9 was used to obtain the brightness temperature errors for six SMMR channels, including the four used for the sea ice calculations, for each year of SMMR operation after 1978, when there were only just over 2 months of data. The year 1987 had significantly fewer rows in the $\underline{\mathbf{A}}$ and $\underline{\Delta}$ matrices, because of the unavailability of 1987 data after mid-August. Shorter data gaps in other years were similarly taken into account by removing the corresponding rows in $\underline{\mathbf{A}}$ and $\underline{\Delta}$. As expected, the brightness temperature error as a function of ecliptic angle did not change noticeably from year to year. The results averaged for the nine separate determinations are shown in Figure 2.2.5 and were used to correct the SMMR brightness temperatures for ecliptic angle dependencies similarly to the use of the results in Figure 2.2.3 to correct the brightness temperatures for instrument drift. In each case, the zero-points were chosen to correspond to the time and place for which the sea ice algorithm reference points were chosen, namely, February of 1979.

2.2.3. Mapping of SMMR data

In order to facilitate comparisons with passive-microwave polar data acquired by the Defense Meteorological Satellite Program (DMSP) Special Sensor Microwave Imagers (SSMIs), the SMMR data have been mapped onto the same polar grids that are being used to archive the SSMI data on CD-ROMs at the National Snow and Ice Data Center (NSIDC). The grid is a rectangular grid placed over a polar stereographic projection, with the projection plane cutting the globe at a latitude of 70°. The area distortion (i.e., change in the scale factor) is 28% from the north pole to 50° N and 74% from the north pole to 31° N, which is the lowest latitude on the north polar grid. The north polar grid size is 304 x 448 pixels. The pole is located at x,y = 154, 234, (referenced to x,y = 0, 0 at the upper left corner), the common corner of four adjacent pixels. The 50° N parallel has a diameter of 359.28 pixels on this projection, compared to 293 pixels for the ESMR mapping. In the Southern Hemisphere, the grid size is 316 x 332, with the pole located at x,y = 158, 174 and the scale the same as for the Northern Hemisphere. A diagram illustrating how these projections are produced is shown in Figure 2.2.6. The governing equation for the projection is given in terms of the distance r of the point P from the pole on the projection plane (refer to Figure 2.2.6 for the meanings of the terms):

$$r = [R_p + R\cdot\sin(70°)]\cdot\tan[(90° - \varphi)/2] \qquad (2.2.10)$$

where

$$R = R_e\cdot R_p/[\mathrm{sqrt}(R_p^2\cos^2\varphi + R_e^2\sin^2\varphi)] \qquad (2.2.11)$$

and R_e, R_p are the earth radii at the equator and pole, respectively, and φ is the latitude. Note that r is in units of km. It may be expressed in terms of pixels by noting that when $\varphi = 50°$, $r = 180.44$ pixels. The projected longitude (θ) equals the longitude on the globe.

The area scale factor is given by

$$S = \frac{2\cdot[R_p^2\cdot\cos^2(\varphi)+R_e^2\cdot\sin^2(\varphi)]\cdot\tan[(90° - \varphi)/2]}{R_e^2\cdot\cos(\varphi)\cdot\cos^2[(90° - \varphi)/2]} \qquad (2.2.12)$$

Some words of caution regarding the effects of antenna patterns on mapping SMMR data are in order. The map grid size (about 25 km) is nominally half the size of the integrated field of view of the 1.7-cm channels. This, plus the fact that the size of the integrated field of view is determined from the half-power points on an approximately Gaussian-shaped antenna beam pattern, the integrate-and-dump time of the scan, and the spacecraft motion, results in high-radiance objects such as land or sea ice spilling over onto areas of lower radiance such as open water. The land mask used in the SMMR maps does not take this into account, and therefore land signals will appear outside the land mask, giving false impressions of sea ice within 50-100 km of the coastal boundaries. In summer, when coastlines are ice-free, the land signals are high and give a misleading indication of ice. For example, the summertime minima in the Bering, and Okhotsk and Japan regions (Figures 3.4.3 and 3.3.3) show this effect. This should be kept in mind when studying curves of ice extent and area in Chapters 3 to 5. In addition, the 50° incidence angle for SMMR means that a large portion of the backward-looking wings of the SMMR antenna pattern intercepts the surface of the Earth. This gives rise to large differences in the SMMR response to ocean-land and ocean-ice boundaries during the northbound and southbound portions of the spacecraft orbit. These land-ocean and ice-ocean spillover effects are most dramatically illustrated by the differences in the daily northbound/southbound sea ice extents for the Antarctic during austral winter. These differences are on average about 0.8×10^6 km^2, or about 4% of the total extent (see Chapter 4). In the Arctic, the overall wintertime northbound/southbound differences are about 0.2×10^6 km^2, about one-fourth the values in the Antarctic. This contrast results from the fact that the entire perimeter of the Antarctic ice cover is bounded by open ocean whereas in the Arctic much of the perimeter is bounded by land. The northbound/southbound differences are absent in the images in this book, since the data were averaged over the two portions of the orbits.

The land mask is created as follows: First, a high-resolution coastline file [adapted from the Central Intelligence Agency (CIA) World Data Set II] is used to produce land boundaries on a high-resolution map with twice the resolution (four times as many pixels) of the projections used here, and with all pixels initially designated as ocean. Next, the high-resolution pixels containing a boundary are designated as coastline, and the areas within the coastline are designated as land. The latter is done semiautomatically by seeding the enclosed areas and allowing the seeds to grow until they encounter the coastline, with visual inspection of the map image to determine when the process is complete. The pixels in the higher-resolution map are then grouped into 2 x 2 arrays, corresponding to the single pixels in the lower-resolution map. The determination of the proper designations for the pixels in the lower-resolution map involves performing two classifications of each 2 x 2 higher-resolution array and storing the results in two separate 2 x 2 arrays. In both arrays, land pixels remain land and ocean pixels remain ocean; but in the first array, coastline pixels are designated as land, whereas in the second array they are designated as ocean. Next, the number of ocean and land pixels is tallied over the 8 values, and the category with the highest population is selected as the category for the corresponding lower-resolution pixel. Tie scores are set to coastline. Finally, the land pixels adjacent to ocean

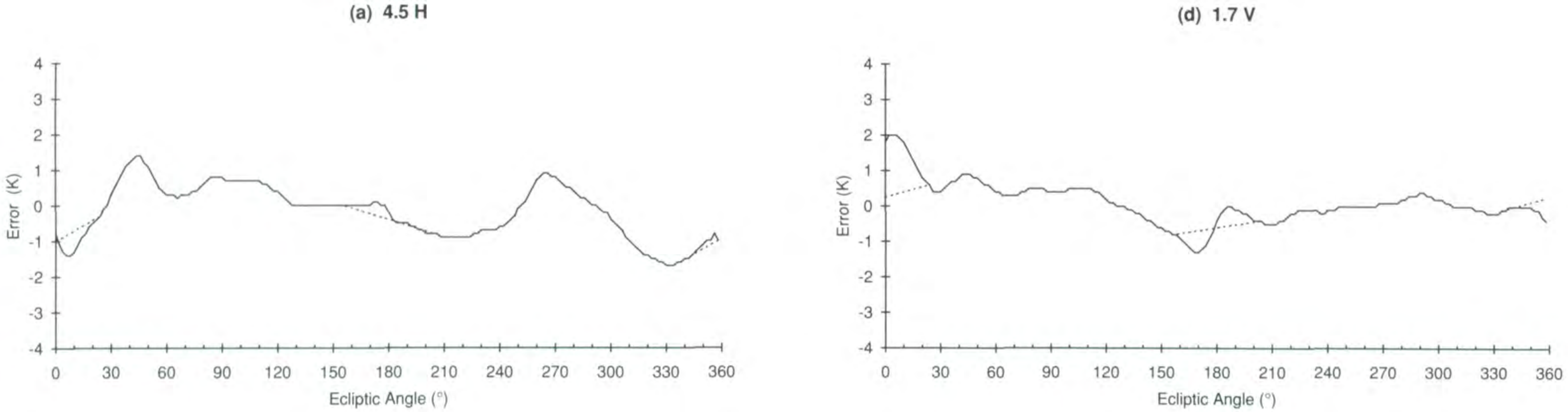
(a) 4.5 H

(d) 1.7 V

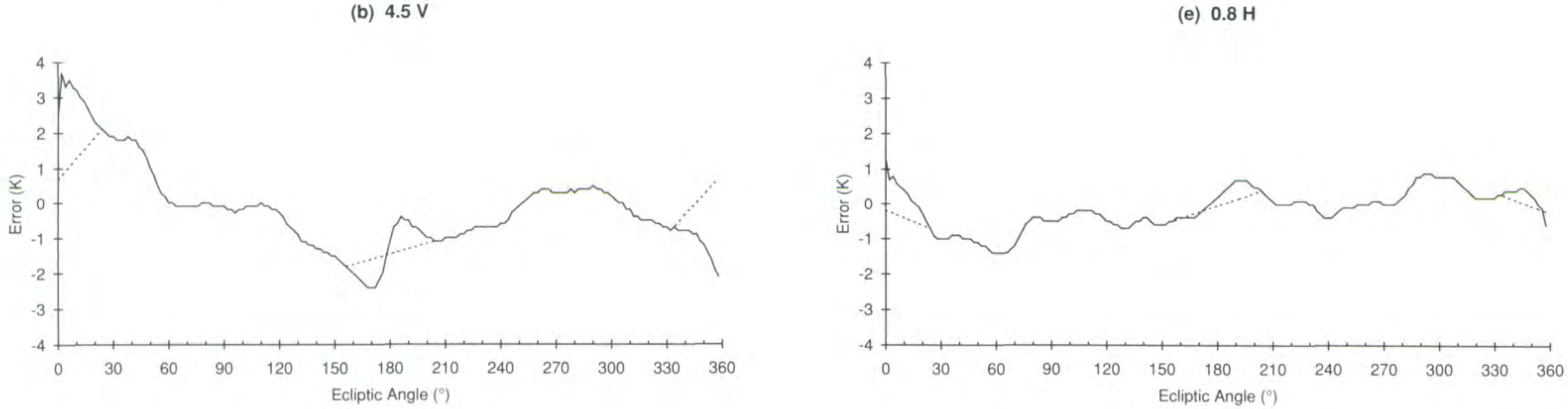
(b) 4.5 V

(e) 0.8 H

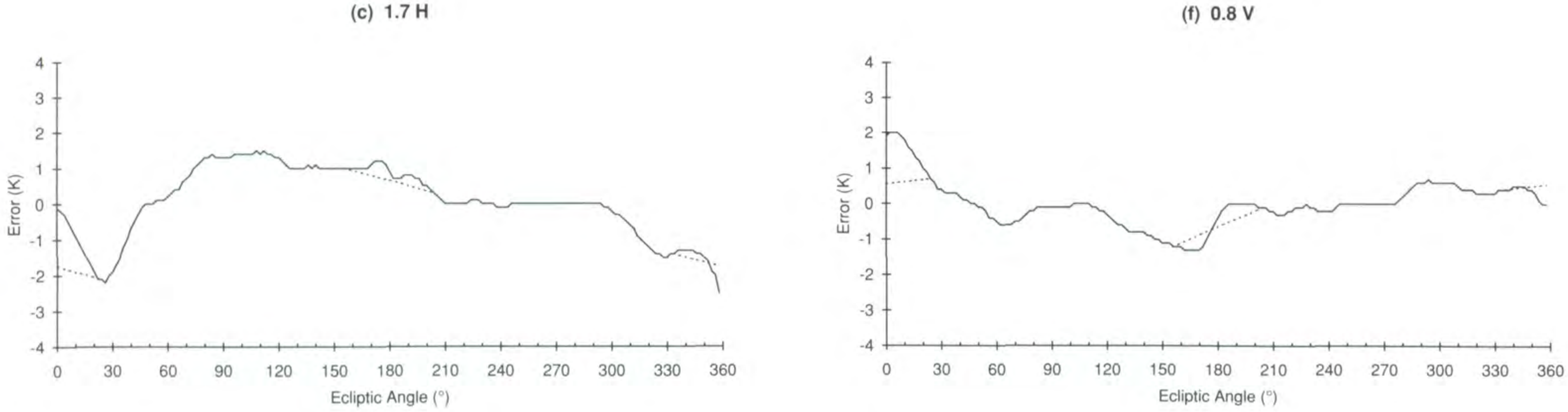
(c) 1.7 H

(f) 0.8 V

Figure 2.2.5. Radiance error vs. ecliptic angle for six of the SMMR channels: (a) 4.5-cm wavelength, horizontally polarized, (b) 4.5-cm, vertically, (c) 1.7-cm, horizontally, (d) 1.7-cm, vertically, (e) 0.8-cm, horizontally, and (f) 0.8-cm, vertically polarized. The thin lines are linear interpolations between ecliptic angles of 335° to 25° and 155° to 205°, where the paucity of data results in unreliable values.

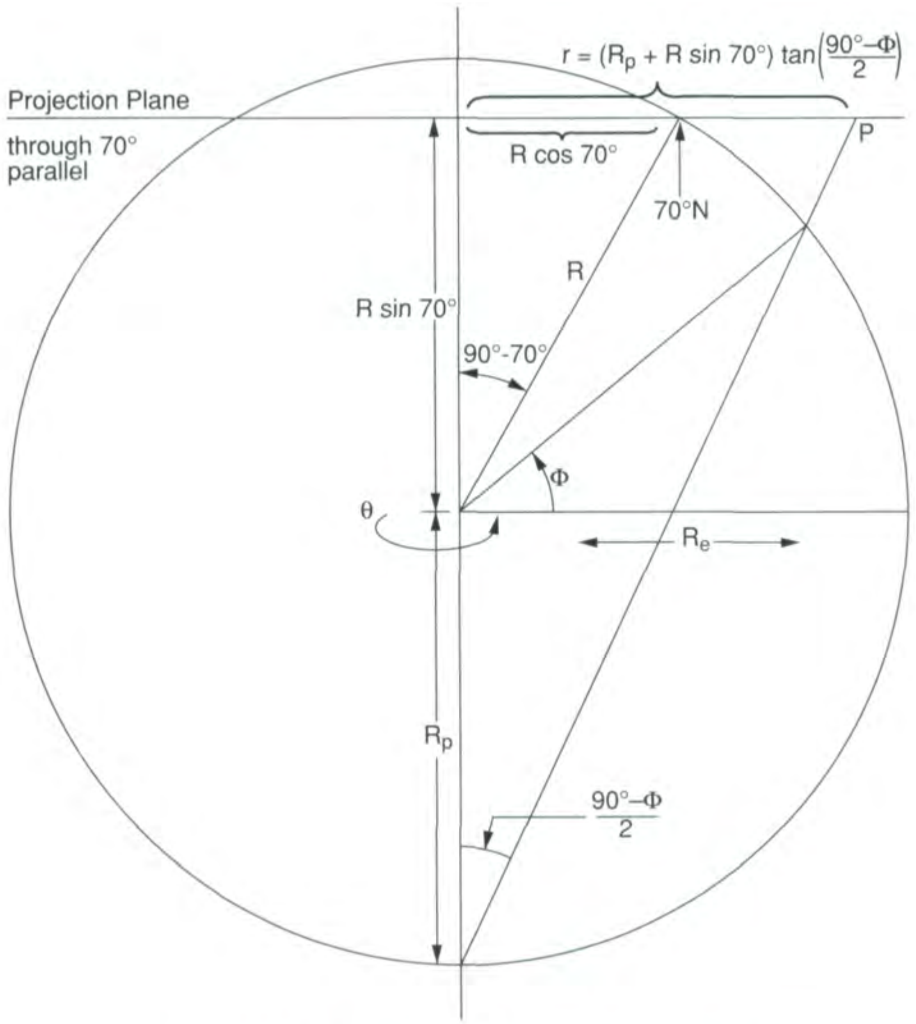

Figure 2.2.6. Schematic of the stereographic projection.

in the lower-resolution array are reset to coastline. In designing the SMMR land mask, the temptation to reduce land contamination effects at boundaries by subjectively increasing the size of the land mask was avoided in the interest of retaining a realistic land mask on the color images and not artificially decreasing the calculated areal extents of the ice cover. This will also facilitate comparison with data from future, higher resolution instruments using the same land mask.

In the case of the ESMR atlases, the land masks were also based on the high-resolution CIA land/sea boundaries, although overlaid with a 293 x 293 square grid extending equatorward to 50° latitude. Grid cells with over half their area covered by land were considered land and were masked out on the ice-concentration images and in the calculations for ice extents. This resulted in a land mask visually similar to the SMMR land mask. However, in the ESMR case, adjustments were made in the Arctic ice-extent calculations in order to reduce the land-contamination effect caused by ocean grid cells containing fractional land coverage. The adjustments involved estimating the brightness temperature of the land within the mixed grid cells and using that estimate along with the observed brightness temperature in order, through a linear formulation, to determine the brightness temperature of the oceanic portion of the cell. This latter brightness temperature was then used to calculate the ice concentration and areal ice coverage within the oceanic portion of the cell, and it was only this area that provided this cell's contribution to the total calculated ice area. Similarly, the grid cell contributed to the total ice extent only the area of its oceanic portion and then only when the calculated ice concentration in that portion exceeded 15%. This resulted in lower land spillover effects in the ESMR Arctic calculations (Parkinson et al., 1987) than in the SMMR Arctic calculations (current volume). Before adjustment, the ESMR spillovers were closer to those of SMMR.

Another difference with the ESMR Arctic calculations concerns the area poleward of 84°, where there are no SMMR data because of the 99° orientation of the spacecraft orbit and the 780-km swath width of the SMMR, necessitating an approximation in the calculation of Arctic ice areas. The lack of data poleward of 84° is of no consequence for the Antarctic sea ice calculations, since the missing area is entirely within continental Antarctica. However, in the Arctic, the missing area is in the Arctic Ocean. It was assumed in the calculation of Arctic ice area that 84°-90° N is 100% sea ice-covered. The 4-year ESMR record shows that the average ice concentration in that region was 90% or greater, except in September, when it averaged about 85% (Parkinson et al., 1987). Since the area north of 84° represents only 20% of the minimum total Arctic ice cover, the result of the assumption of 100% ice coverage is an overestimate of the total ice area by, at most, 2% for all months except September, when the overestimation could be as high as 3%.

It should be noted that the number of observations represented in a given grid element in the present projection depends on latitude. The latitude bands completely covered by the SMMR during the course of 1 day are only 72°-84° N and 72°-84° S. Diamond-shaped data gaps occur on the 1-day maps equatorwards of 72°; near the equator almost all of the data are updated twice every 6 calendar days. In the monthly averages shown in Chapters 3 and 4, and Appendix A, the data gaps are filled in as a result of the longer averaging period. Polewards of 72°, there is increasing overlap in the SMMR orbital swaths in which data were collected. Rather than averaging the data acquired in the overlap areas, the separate northbound and southbound data used for a given location are the values from the last observation of the individual day. The northbound and southbound values are averaged to produce single-day maps used for generating the monthly maps and time series plots in Chapters 3-5.

2.3 The SMMR Sea Ice Algorithm

SMMR provides ten channels of information, but it cannot unambiguously provide ten different ice or ocean parameters, because of the high correlation of information content between channels. A coplanarity test applied to the SMMR data indicates that practically all the points in a 3-D emissivity plot (using vertically polarized data at wavelengths of 0.8, 1.7, and 4.5 cm) lie close to or on a plane defined by the clusters formed by consolidated first-year ice, multiyear ice, and open water (Comiso, 1986). This means that the data are essentially two-dimensional, and that a mixing formalism would enable unambiguous identification of only three independent ice or ocean parameters. An independent investigation using a principal component analysis (Rothrock et al., 1988) similarly determined that the information content of the ten channels is equivalent to, at most, three independent channels, thereby limiting the number of independent variables that can be inferred from the multichannel data to three. We have selected multiyear and first-year ice as two of the independent variables, based on their predominance, and ice temperature as the third. Ice types with emissivities different from those of first-year and multiyear ice, such as new ice and second-year ice, apparently cannot be unambiguously discriminated with the SMMR data. The Rothrock et al. (1988) analysis also showed that PR and GR, used as the independent variables in the sea ice algorithm discussed in Section 2.3, have the same functional forms as principal components, differing in that PR and GR are functions of normalized variables, and that the triplet of channels used in defining PR and GR accounts for over 99% of the total variance of the SMMR data set.

This section describes the procedure for calculating sea ice concentrations and temperatures (Cavalieri et al., 1984; Gloersen and Cavalieri, 1986). The procedure was developed under the auspices of the NASA/Nimbus 7 SMMR Experiment Team (Gloersen et al., 1984), and is referred to as the SMMR Team sea ice algorithm. The calculations are based upon the radiative transfer equation, the contrasting emission characteristics of ice and ocean, and the assumption that the observed brightness temperature can be linearly related to the brightness temperatures of three surface types (open ocean and two ice types, the latter being first-year and multiyear ice in the Arctic and less specific "Type A" and "Type B" ice in the Antarctic). In order to reduce the effect of physical temperature, the ice-concentration formulations are based upon the polarization and spectral gradient ratio introduced in Section 2.1, rather than directly on the brightness temperatures themselves.

2.3.1. The radiative transfer equation

The microwave radiances received by a satellite instrument are a composite of contributions from the earth, atmosphere and space, as illustrated schematically in Figure 2.3.1. The received radiation expressed as a brightness temperature T_{Bij}, with subscripts i and j referring to wavelength and polarized component, respectively, is given by

$$T_{Bij} = \varepsilon_{ij} \cdot T_S \cdot \exp(-\tau_i) + T_{upi} + (1 - \varepsilon_{ij}) \cdot T_{downi} \cdot \exp(-\tau_i) + (1 - \varepsilon_{ij}) \cdot T_{sp} \cdot \exp(-2 \cdot \tau_i) \tag{2.3.1}$$

where ε_{ij} is the surface emissivity, T_S is the physical temperature of the radiating portion of the surface, τ_i is the atmospheric opacity, T_{upi} is the atmospheric upwelling radiation, T_{downi} is the atmospheric downwelling radiation, and T_{sp} is the cosmic background component. Equation 2.3.1 is the fundamental radiative transfer equation, which serves as the basis for developing algorithms for converting satellite radiance data into geophysical parameters. Both T_{upi} and T_{downi} may be expressed as products of a constant weighted average atmospheric temperature and the atmospheric emissivity. To first order (neglecting the temperature dependence of ε_{ij}), T_{Bij} depends linearly on T_S.

2.3.2. Calculation of ice concentrations

The three quantities for which percentage areal coverages are determined by the sea ice algorithm are ice-free ocean (open ocean), first-year ice, and multiyear ice (ice that has survived at least one melt season); these are the three types of surface that are assumed to dominate the polar ocean environment. By neglecting the atmospheric and cosmic contributions in Equation 2.3.1, we obtain the following simplified model for received radiation expressed as a brightness temperature:

$$T_{Bij} = C_W \cdot T_{Wij} + C_{FY} \cdot T_{FYij} + C_{MY} \cdot T_{MYij} \tag{2.3.2}$$

where T_{Wij}, T_{FYij}, and T_{MYij} are the brightness temperatures of ice-free ocean, first-year sea ice, and multiyear sea ice, respectively, and C_W, C_{FY}, and C_{MY} are the fractions of each of the three components within the field of view of the instrument. In this three-component system, C_W, C_{FY}, and C_{MY} add to unity. Equation 2.3.2 is the fundamental equation for the development of the sea ice algorithm.

Spectra for both the horizontally and vertically polarized radiations at each of the SMMR wavelengths and for each of the three surface types presumed present are shown in Figure 2.3.2. These spectra illustrate the physical basis of the algorithm's ability to distinguish among the three ocean components. The spectra were obtained from SMMR observations over three regions of the Arctic during February 3-7, 1979. The curves are representative of first-year ice (sampled in Baffin Bay), multiyear ice (sampled in the Canadian Basin), and open ocean (sampled in the Norwegian Sea), respectively. The widths of the bands indicate the range for ±1 standard deviation about the mean. Two important characteristics are immediately apparent from Figure 2.3.2: first, that the difference between the vertically and horizontally polarized radiances is small for either ice type in comparison to that for the ocean; and second, that the discrimination

RADIATIVE TRANSFER EQUATION

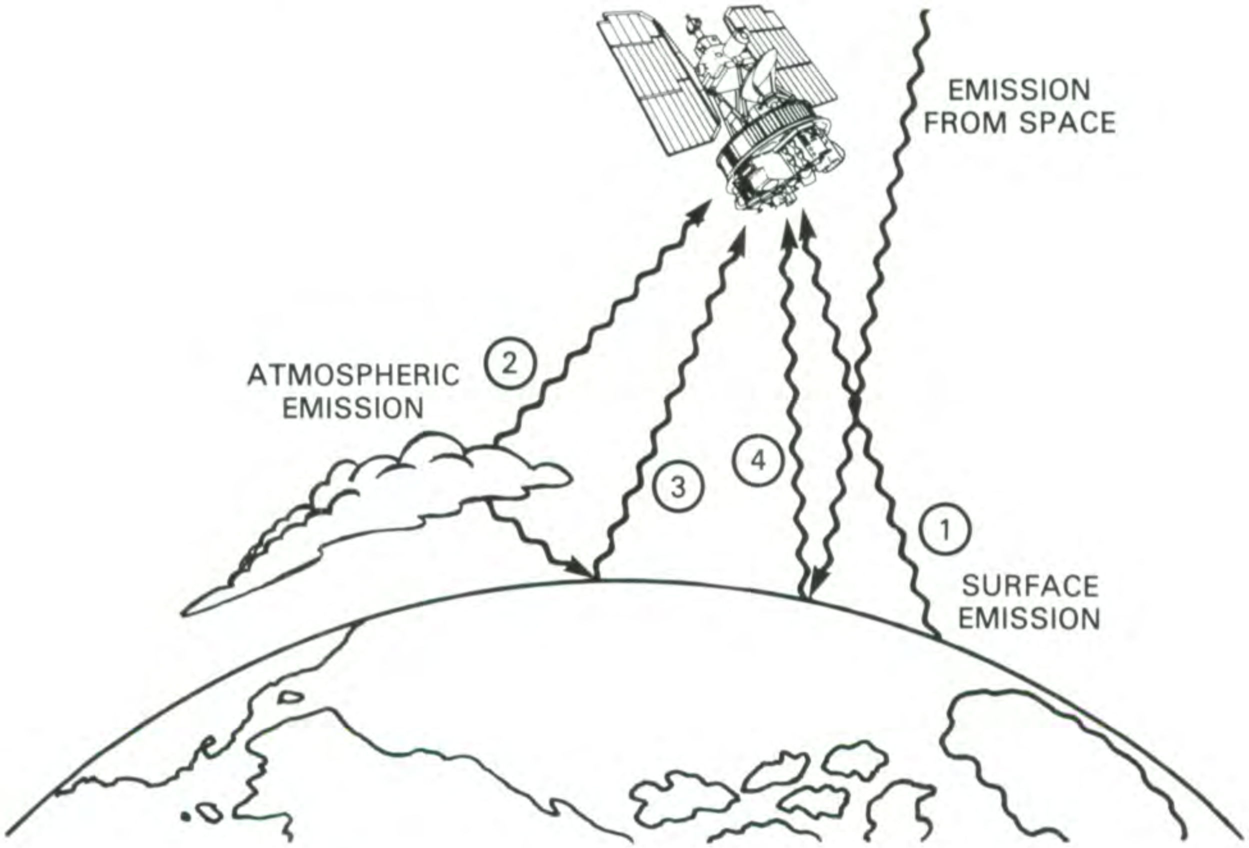

		①		②		③		④
BRIGHTNESS TEMPERATURE	=	(SURFACE EMISSIVITY) x x (PHYS. SURFACE TEMP) x (ATMOSPHERIC ABSORPTION)	+	(UPWELLING ATMOSPHERIC RADIATION)	+	(REFLECTED DOWNWELLING ATMOSPHERIC RADIATION) x x (ATMOSPHERIC ABSORPTION)	+	(REFLECTED SPACE RADIATION) x x (DOUBLE ATMOSPHERIC ABSORPTION)

$$T_B = \varepsilon T_S e^{-\tau} + \underbrace{T_{UP} + (1-\varepsilon) T_{DOWN} e^{-\tau} + (1-\varepsilon) T_{SP} e^{-2\tau}}_{\text{ATMOSPHERIC CORRECTION TERM}}$$

Figure 2.3.1 . Schematic illustrating radiative transfer equation used to derive geophysical parameters from spacecraft microwave radiometer data (after Swift and Cavalieri, 1985).

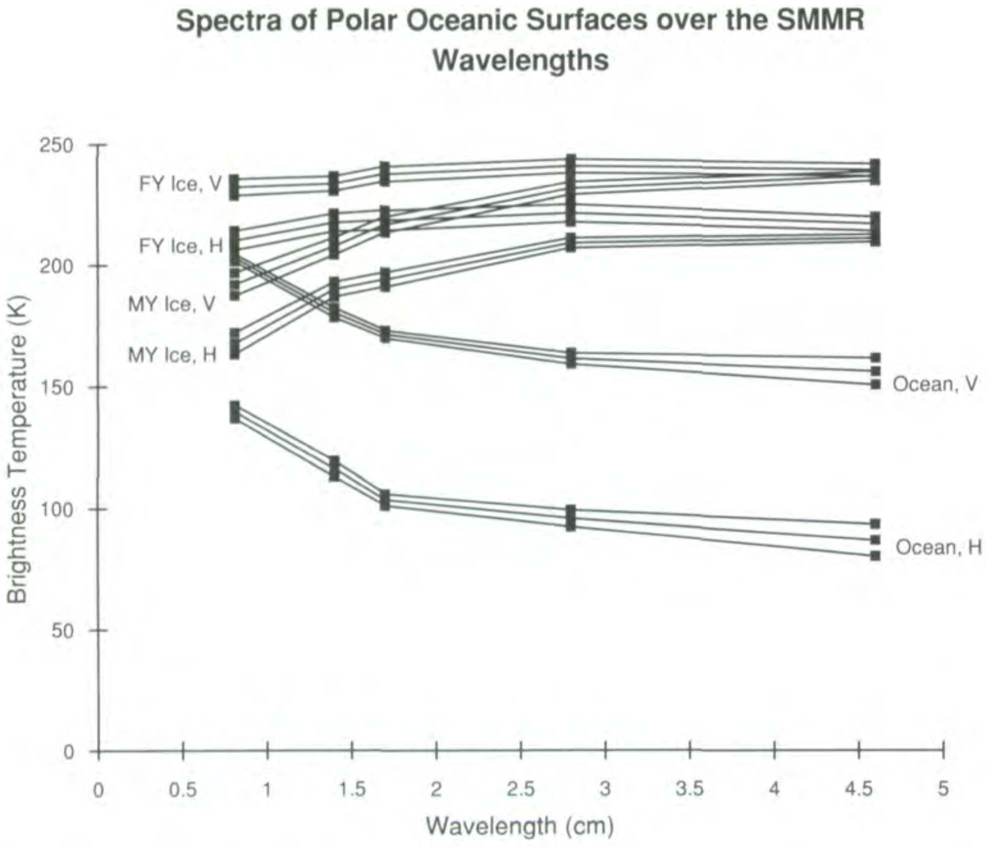

Figure 2.3.2. Microwave spectra of first-year (FY) and multiyear (MY) sea ice, and ice-free ocean for horizontal (H) and vertical (V) polarizations. The closely spaced curves are separated by two standard deviations of the observations (after Cavalieri et al., 1984). The CELL values (ibid.) were converted to TCTs (after Gloersen, 1987).

between ice types increases with decreasing wavelength, being greatest therefore at the 0.8-cm wavelength. The algorithm parameterizes these two characteristics through two radiance ratios that are used as independent variables (Cavalieri et al., 1984). These are the polarization (PR) and the spectral gradient ratio(GR) defined in Equations 2.1.1 and 2.1.2 (Section 2.1). As mentioned earlier, the advantage of using radiance ratios is that the calculated ice concentrations are largely independent of ice temperature variations, which eliminates the problem of estimating ice temperatures both temporally (e.g., day-to-day and seasonal) and spatially (e.g., temperature gradients across the Arctic basin). Following Gloersen and Cavalieri (1986), Equation 2.3.2 is used with the definitions of PR and GR [Equations 2.1.1 and 2.1.2] to solve for the first-year and multiyear ice concentrations, C_{FY} and C_{MY}, respectively. The resultant expressions are

$$C_{FY} = (F_0 + F_1 \cdot PR + F_2 \cdot GR + F_3 \cdot PR \cdot GR)/D \qquad (2.3.3)$$

$$C_{MY} = (M_0 + M_1 \cdot PR + M_2 \cdot GR + M_3 \cdot PR \cdot GR)/D \qquad (2.3.4)$$

where

$$D = D_0 + D_1 \cdot PR + D_2 \cdot GR + D_3 \cdot PR \cdot GR \qquad (2.3.5)$$

The coefficients for the Arctic are

$F_0 = 2782.3$, $F_1 = -20044$, $F_2 = 18835$, $F_3 = 41660$
$M_0 = -690.38$, $M_1 = 14990$, $M_2 = -27579$, $M_3 = -43260$
$D_0 = 1648.2$, $D_1 = 7735.6$, $D_2 = -4112.2$, $D_3 = -10200$

and for the Antarctic are

$F_0 = 2871.7$, $F_1 = -20790$, $F_2 = 19674$, $F_3 = 43335$
$M_0 = -569.75$, $M_1 = 15142$, $M_2 = -29096$, $M_3 = -44808$
$D_0 = 1950.5$, $D_1 = 6585.7$, $D_2 = -417.6$, $D_3 = -5052.8$

The total sea ice concentration is

$$C_T = C_{FY} + C_{MY} \qquad (2.3.6)$$

In the Arctic, the coefficients in Equations 2.3.3 through 2.3.5 were determined from characteristic brightness temperatures T_{Wij}, T_{FYij}, and T_{MYij} for open ocean, first-year ice and multiyear ice, based on SMMR data in areas selected with the aid of aircraft observations made earlier the same winter during the NASA CV-990 Underflight Mission (Gloersen et al., 1980a). In the Antarctic, the coefficients were also based on SMMR data, although the characteristic brightness temperatures were determined for open ocean and two ice types, labeled Type A and Type B, that are radiometrically different from the Arctic first-year and multiyear ice types. In each case, the characteristic brightness temperatures are referred to as algorithm tie-points and are given in Table 2.3.1.

Table 2.3.1. Nimbus-7 SMMR Team Sea Ice Algorithm Tie-Points

NORTHERN HEMISPHERE			
Channel	*OW*	*FY ICE*	*MY ICE*
	(K)	(K)	(K)
1.7-cm (18 GHz) H	098.5	225.2	186.8
1.7-cm (18 GHz) V	168.7	242.2	210.2
0.8-cm (37 GHz) V	199.4	239.8	180.8
SOUTHERN HEMISPHERE			
Channel	*OW*	*TYPE A ICE*	*TYPE B ICE*
	(K)	(K)	(K)
1.7-cm (18 GHz) H	098.5	232.2	205.2
1.7-cm (18 GHz) V	168.7	247.1	237.0
0.8-cm (37 GHz) V	199.4	245.5	210.0

The concentrations calculated from Equations 2.3.3 through 2.3.6 have a spatial resolution of about 55 km, being determined by the size of the field of view of the 1.7-cm SMMR channels. The polarization at 0.8 cm can also be used to obtain ice concentrations (using a different set of coefficients in Equations 2.3.3 to 2.3.5) at an improved spatial resolution (30 km), but at the expense of greater atmospheric interference (Gloersen and Cavalieri, 1986).

A convenient way of illustrating some of the properties of the algorithm is through the use of a schematic representation of the algorithm in PR vs. GR space, following Gloersen and Cavalieri (1986). Figure 2.3.3 shows typical PR vs. GR plots for both the Arctic (for February 3-7, 1979) and Antarctic (for October 27-31, 1986). The algorithm is represented in each figure as a curvilinear triangle superimposed on the PR vs. GR scatter plot. The three points that define the Arctic triangle in Figure 2.3.3a are labeled OW, FY, and MY and correspond to regions of open water, first-year ice, and multiyear ice, respectively. In Figure 2.3.3b, the points defining the Antarctic triangle are labeled OW, A, and B, since the first-year/multiyear ice nomenclature is inappropriate (see discussion below).

Physically meaningful solutions for Arctic and Antarctic sea ice concentrations lie within the triangles of Figure 2.3.3. The approximately elliptically shaped cluster of points near the label OW in each plot corresponds to contributions primarily from ice-free ocean areas. The cluster of points between FY and MY in the Arctic (or between A and B in the Antarctic) consists of an elongated distribution corresponding to high concentrations of sea ice. Areas of first-year ice (or Type A ice) correspond to points having GR values close to zero, whereas areas of mostly multiyear ice (or Type B ice) correspond to points having large negative values of GR. This ice cluster is separated from the OW cluster by a factor of 6 in PR. The sparsely populated band of points connecting the ice-free water and sea ice clusters in the Arctic case corresponds to the transition regions of the Arctic marginal ice zones where the ice concentration goes from zero (high PR) to near 100% (low PR). In contrast, in the Antarctic case, a higher proportion of points lies within the triangle, indicating a lower ice concentration on average. One reason for the difference in the Arctic and Antarctic PR vs. GR distributions stems from the fact that the wintertime Arctic Basin ice pack is largely confined, whereas the Antarctic ice pack is free to expand to the open ocean. This divergent condition in the Antarctic is enhanced by the prevailing circumpolar winds. Another possible factor giving rise to the hemispheric differences in the PR vs. GR diagrams is the difference in physical characteristics of Arctic and Antarctic sea ice, as observed by Ackley et al. (1980) and Wadhams et al. (1987), implying a corresponding difference in microwave radiance characteristics for the two ice covers.

Points that fall outside the algorithm triangle in Figure 2.3.3 correspond to calculated ice concentrations of less than 0% or greater than 100%, i.e., to geophysically impossible situations. The algorithm sets to 0% all total ice concentrations calculated to be less than 0% and to 100% all total ice concentrations calculated to exceed 100%. Multiyear ice concentrations exceeding the corresponding total ice concentration are set equal to the total ice concentration. For the purpose of illustrating how the points outside the triangle affect the concentration distribution, the algorithm was modified to allow total ice concentrations to exceed 100%. Histograms of the resulting total ice concentrations for March 15, 1979 in the Arctic and July 29, 1987 in the Antarctic are shown in Figure 2.3.4. Both the Arctic and Antarctic histograms show the ice peak but not the open water peak, because a weather filter (described later) has largely eliminated very low calculated ice concentrations at high latitudes. The remaining concentrations below 8% result from residual weather effects at low latitudes. For the Arctic, the ice-concentration peak is centered at 97%, and the maximum ice concentration occurs at 115%. For the Antarctic, the peak center and maximum concentrations are 93% and 117%, respectively. Reasons for points falling outside the triangle include (1) fluctuations of microwave emissivity over consolidated single-type ice (first-year or multiyear ice in the Arctic; Type A or Type B ice in the Antarctic), and (2) the presence of radiometrically different ice types than the two identified ones (first-year and multiyear, or Type A and Type B). A quantitative estimate of the errors associated with these factors is presented in the next section.

The large spread of points in the vicinity of OW in both hemispheres (Figure 2.3.3) is caused by atmospheric effects, including water vapor, cloud liquid water, and roughening of the sea surface by wind, all of which tend to increase the recorded radiances, with attendant changes in PR and GR. This spread decreases from point OW to point FY in Figure 2.3.3a, as the sea ice coverage increases and the weather effects, more noticeable over open water, decrease. To help understand the open water cluster, we have superimposed on Figure 2.3.3 square boxes located at GR-PR values calculated for specific atmospheric and oceanic conditions on the basis of the radiative transfer equation, following Gloersen and Cavalieri (1986). Each of these conditions corresponds to a selected sea-surface temperature (SST) in units of K, near-surface wind (NSW) in units of m/s, total column atmospheric water vapor (W) in units of cm, and cloud liquid water content (L) in units of cm, integrated along the SMMR line of sight. For example, the point with associated values (271, 0, 0, 0) represents the PR vs. GR value corresponding to an ocean at the freezing point with no winds, atmospheric water vapor, or clouds. As shown in the figure, increasing W from 0 to 8 cm and leaving the other three variables at 271, 0, and 0 decreases the PR greatly, but the spectral gradient ratio only slightly. The 8-cm value for W is abnormally high globally and is never observed in polar regions, but the points in the vicinity of this box are believed to result from stormy conditions near the ice edge and beyond. A more typical value for W is 0.5 cm, although values as high as 1.5 cm occur on occasion in the marginal ice zones. Increasing NSW also decreases PR and has a much lesser effect on GR, and increasing L decreases PR but increases GR. Interestingly, the only parameter that by itself decreases GR below the 0.07 level is SST, for values of SST not found in polar regions. A similar situation occurs in the Antarctic.

Elimination of most of the spurious ice concentrations associated with weather effects, which sometimes yield calculated ice concentrations as high

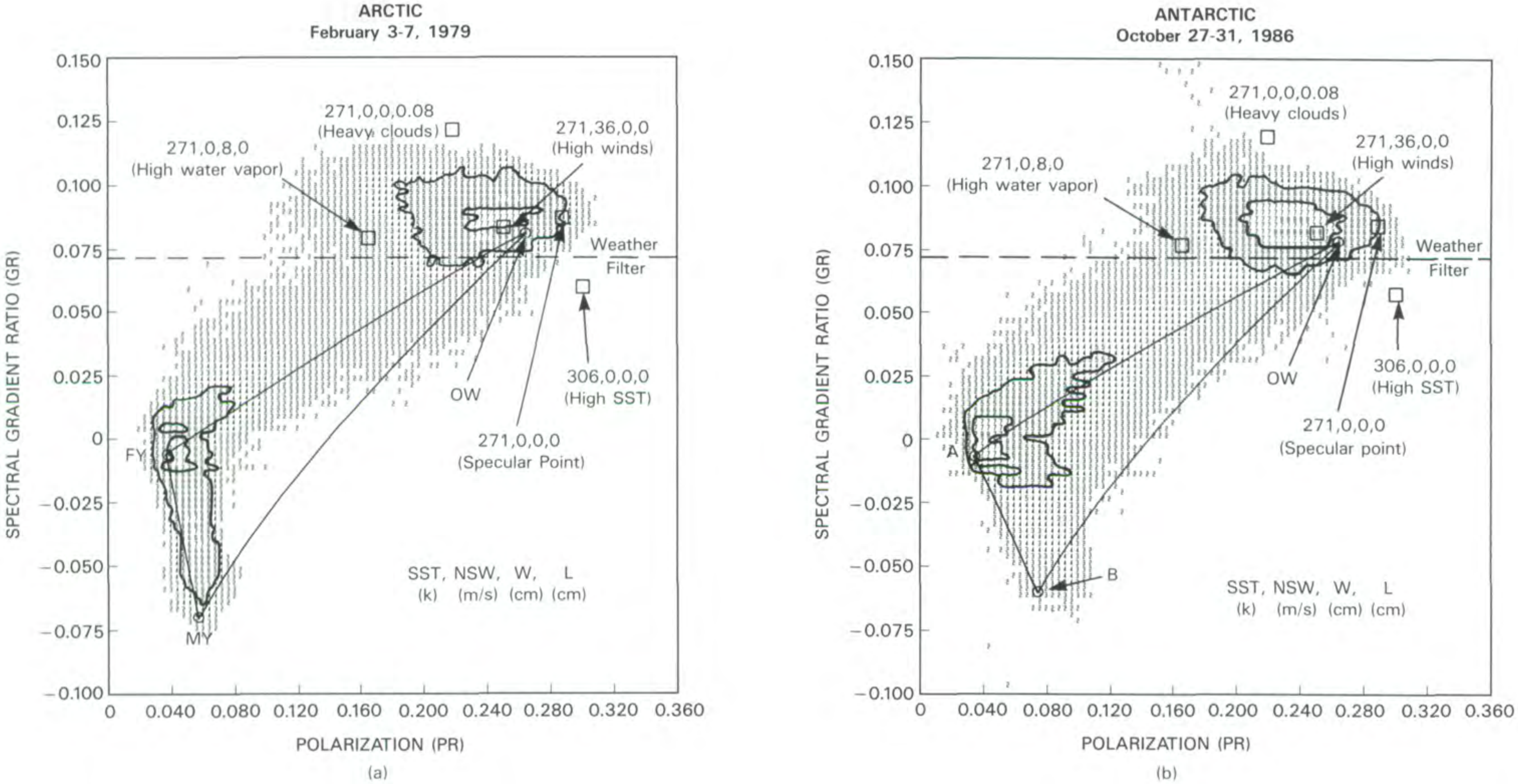

Figure 2.3.3. Spectral gradient ratio (GR) vs. polarization (PR) at the 1.7-cm wavelength for (a) the Arctic for February 3-7, 1979, and (b) the Antarctic for October 27-31, 1986, showing the effects of ocean temperature, winds, and atmospheric water. The points labeled with SST, NSW, W, and L values are model calculations. In (a), the three corners of the triangle correspond to the sea ice algorithm calculations for open water (OW), 100% first-year (FY) sea ice, and 100% multiyear (MY) ice; in (b), A corresponds to FY, and B corresponds to another ice type, possibly FY with a heavy snow cover; in both cases, the curved sides of the triangle also correspond to algorithm calculations. The small numbers in the scatter diagrams represent the truncated natural logarithm of the number of observations, plus 1. Contours are drawn around the boundaries of regions of >55 and >403 observations. The populations were obtained by summing the observations from the separate northbound and southbound orbital nodes of each of the 3 data days. (After Gloersen and Cavalieri, 1986.)

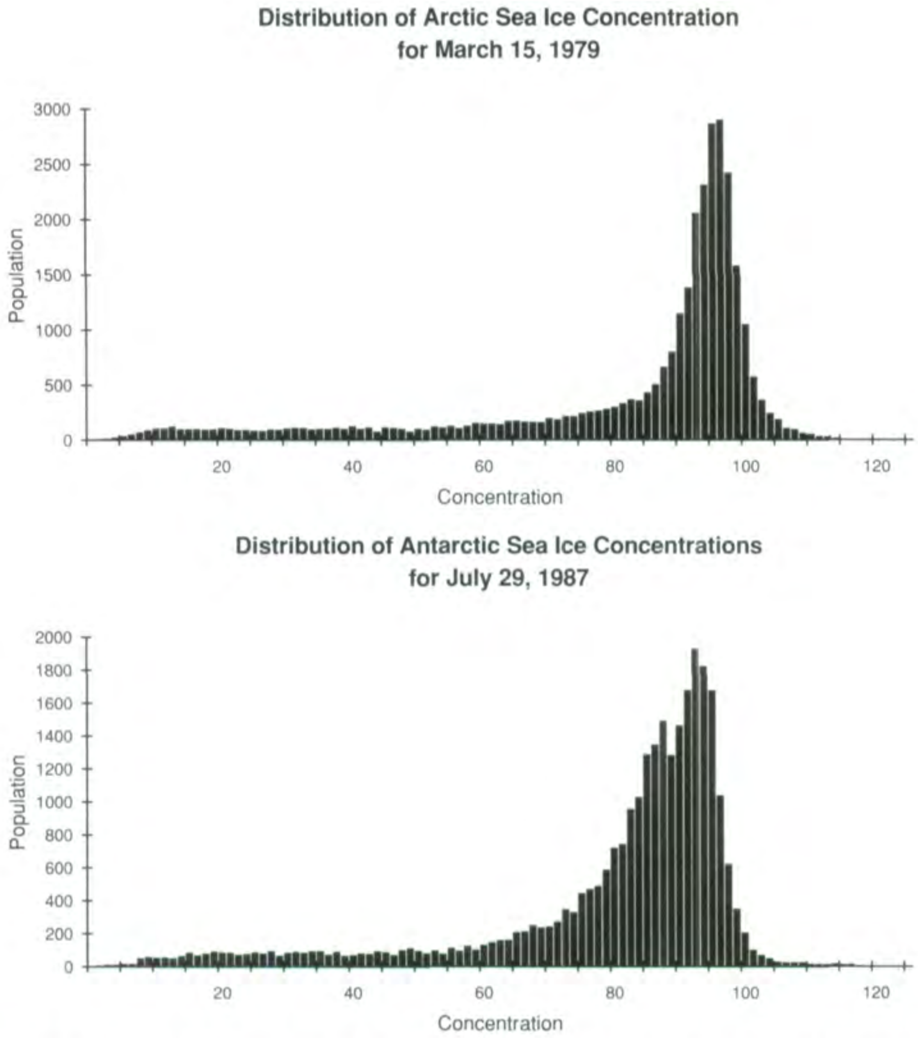

Figure 2.3.4. Distribution of sea ice concentrations for (a) the Arctic on March 15, 1979, and (b) the Antarctic on July 29, 1987.

as 60% in temperate waters (Gloersen and Cavalieri, 1986), is achieved by placing an upper limit on GR. If GR is greater than 0.07, then the ice concentration is set to zero. By placing a limit on GR, we also eliminate concentrations less than about 12% in first-year ice regions and 8% in multiyear ice regions. This so-called weather filter, which has been used in the processing of all the data in this volume, is described in detail by Gloersen and Cavalieri (1986). Residual weather effects that might be present at higher ice concentrations and their associated errors are discussed in the next section.

A need for different Arctic and Antarctic tie-points is suggested by an examination of the PR vs. GR scatter plots in Figure 2.3.3. The principal difference is the shape of the ice clusters. The Arctic FY-MY cluster is elongated and almost vertical and extends to more negative GR values than does the corresponding Antarctic cluster, which is skewed to the right. Also, there are more points distributed along and scattered about the upper leg of the Antarctic triangle than that of the Arctic. This is caused in part by the greater amount of ocean area covered by the Southern Hemisphere grid and in part to the more diffuse nature of the Antarctic marginal ice zone, compared to the Arctic. More points are distributed within the Antarctic triangle at concentrations less than 90% than within the Arctic triangle. For both the Arctic and Antarctic, the tie-point selection was made by adjusting points FY and A so that the PR values corresponding to those points (Figure 2.3.3a,b) fall near the 2-sigma position on the nearly Gaussian distribution of points along PR.

The rationale for the selection of different tie-points for MY and Type B ice in the Arctic and Antarctic cases is based on the significantly different distribution of points for the lowest observed GR values in the PR vs. GR scatter plots (Figure 2.3.3). Selection of point B was somewhat more subjective than the selection of MY because of the absence of appropriate in situ observations, with point B being based on simultaneous minimum values of GR and PR during the austral spring (late October). Both the Arctic and Antarctic SMMR tie-points were fine-tuned using the constraint that the total ice concentrations obtained from the SMMR and SSMI instruments agree during the overlap period of July-August 1987.

The primary reason for the difference between the Arctic MY tie-point and the Antarctic Type B tie-point is that, in the Antarctic, the radiometric distinction between first-year (seasonal) ice and multiyear (perennial) ice is lost. Unlike the Arctic, where the predominant source of negative gradient ratios is the volume scattering by the empty brine pockets in the freeboard portion of multiyear ice, in the Antarctic the main source of volume scattering appears to be from sources other than multiyear ice, although corroborating evidence is very limited. We have produced unpublished trial Antarctic "multiyear" ice maps only to find that the distribution and area of this "multiyear" ice are considerably different in midwinter from the distribution and area of ice remaining at summer's end. One very likely source of the additional volume scattering in the Antarctic is the snow cover on the sea ice. As mentioned in Section 2.1, snow cover of sufficient depth and of sufficiently large grain size will mimic the signature of multiyear ice. Because of these various factors, we present only total sea ice concentrations for the Antarctic.

Finally, it is important to keep in mind potential ambiguities when interpreting the sea ice concentration maps presented in the following chapters. These ambiguities result from the limitation of the SMMR algorithm in distinguishing no more than two radiometrically distinct ice types. For example, in winter, the presence of new ice within the SMMR field of view results in an overestimation of open water because of the strong variation of PR with ice thickness in the range of 0-20 cm (e.g., see Gloersen et al. 1975b; Tucker et al., 1991; Figure 2.1.6). While the latter is clearly a limitation of microwave sensors regarding the determination of ice concentrations, it has a potentially very positive aspect in that it may allow an upper limit to be placed on the ice thickness contributing to the open water-thin ice ambiguity. Nonetheless, it must be kept in mind that the so-called open water areas within the pack during winter months are likely to be mixtures of new ice and open water. The calculated total sea ice concentration is subject to large errors when the surface temperature is near the melting point. During summer, the algorithm cannot discriminate between open water areas and melt ponds on the ice. Regarding the multiyear ice concentration maps, it is difficult from satellite observations alone to obtain unambiguous signatures of multiyear ice. Variability of the signature over areas of the central Arctic is considerable (Campbell et al., 1976a; Campbell et al., 1978; Comiso, 1990). Nevertheless, there is strong evidence that the spatial gradients observed in GR across the Canadian Arctic represent real variations in the mixture of first-year and multiyear ice (Campbell et al., 1976a; Cavalieri et al., 1991).

2.3.3. Calculation of ice temperatures

Sea ice temperatures are calculated from a single channel of microwave radiation, the 4.5-cm vertically polarized brightness temperatures, and the sea ice concentrations. For this channel, the microwave emissions of first-year and multiyear ice types are indistinguishable (see Figure 2.3.2), so that a single ice emissivity is appropriate for both ice types. On the basis of a study of Arctic sea ice emissivities derived from a combination of SMMR and infrared radiances of the ice (Comiso, 1983), the emissivity, ε, of the ice is set at 0.96. Ice temperatures are then calculated from a simple linear relationship between the observed brightness temperature and its ice and open-water components:

$$T_{ice} = \frac{T_{B4.5Vobs} - T_{B4.5Vw} \cdot (1 - C_T)}{\varepsilon_{4.5V} \cdot C_T} \qquad (2.3.7)$$

where $T_{B4.5Vobs}$ and $T_{B4.5Vw}$ are the observed and open water brightness temperatures, respectively, at 4.5V.

In order to adjust for the difference between the 150 km resolution of the 4.5V brightness temperatures (Table 2.2.1) and the 55 km resolution of the C_T maps, the following procedure is used in calculating T_{ice}. First, a 7 by 7 array of grid elements is constructed with normalized weighting factors approximating a Gaussian with a full width of 150 km at 1/e height, corresponding to the 4.5V channel resolution. Next, the C_T maps are smoothed with this filter, reducing the C_T values to the 150-km resolution. The $T_{B4.5Vobs}$ values are also smoothed with this same filter before Equation 2.3.7 is used to calculate T_{ice}. The calculation of T_{ice} is limited to regions where the total ice concentration C_T is 80% or greater, because of the large errors at smaller concentrations and the fact that ice temperatures in areas with 20% or greater open water are likely to be near the melting point. Hence, for concentrations less than 80%, T_{ice} is set to 271 K. Finally, calculated ice temperatures that extend beyond the ice edge, due to the larger field of view of the 4.5-cm channel, are reset to the open ocean value.

It is important to note that the derived ice temperature is not a surface temperature, but the physical temperature of the radiating portion of the ice. This is close to the snow-ice interface temperature for first-year ice, but for multiyear ice, it more nearly approximates a weighted temperature of the upper portion of the ice, with most of the contribution from near sea level. Monthly averages of Arctic and Antarctic sea ice temperatures derived using Equation 2.3.7 are presented in Appendix A.

2.3.4. Algorithm sensitivity and sea ice parameter accuracies

The purpose of this section is to provide a quantitative estimate of algorithm sensitivity and sea ice product accuracies. First, we present a discussion of the algorithm sensitivity to variations of brightness temperatures, PRs, and GRs. Next, the principal sources of error in the calculation of ice concentration are discussed, and then ice-concentration accuracies are estimated from comparisons with independent sources of data for different regions and seasons. This is followed by an estimate of the uncertainties in the calculated sea ice extent and ice areas. Finally, comparisons of the derived sea ice temperatures with climatological surface-air temperature data and Arctic buoy temperature data are presented.

Algorithm sensitivity

Random and systematic errors in the algorithm are described in terms of algorithm sensitivity coefficients for total and multiyear ice concentrations following the methods described earlier for CELL data by Swift and Cavalieri (1985). The sensitivity analysis was redone using TCT brightness temperatures based on the calibration described in Section 2.2.2. The new algorithm sensitivities for both total and multiyear ice concentrations are given in Table 2.3.2.

The sensitivities were calculated for three different ice concentrations, 15%, 50% and 100%, in regions of both first-year and multiyear ice. The values are in units of percentage concentration per Kelvin change in brightness temperature for each of the three channels used by the algorithm. The total sensitivity (the square root of the sum of the squares) is also given for each ice-concentration category. These values may be used to obtain an estimate of the ice-concentration error incurred by variations in the radiometric brightness of the ice surface. For example, consider a random variation in ice emissivity of ±0.01 over an area with 100% coverage of first-year ice. This corresponds to a variation in brightness temperature of 2.5K, assuming a value of 250K for the physical temperature of the radiating portion of the ice. If a random fluctuation of this magnitude is present in each of the three channels, then from Table 2.3.2, the error (obtained from the total sensitivity) in C_T will be ±4.5%.

Another way of examining the sensitivity of the algorithm is through the use of a PR *vs* GR plot. To illustrate how ice concentration is calculated, we have replotted in Figure 2.3.5 the triangle first shown in Figure 2.3.3. The distance along the top leg of the triangle starting from the upper right apex represents variations in first-year ice concentration from open water to a 100% first-year ice cover. Similarly, the lower leg represents variations in multiyear ice concentration. The points on and inside the triangle represent all possible values obtainable from the algorithm. The groups of dashes within the triangle connecting the upper and lower legs represent lines of constant total ice concentration. The figure illustrates the nonlinearity in ice concentration sensitivity through the pairs of vertical and horizontal lines that represent a ±2% change in concentration. Three pairs of dashed lines are drawn at first-year sea ice concentrations of 15%, 50%, and 95% on the upper

Table 2.3.2. Algorithm Sensitivity Coefficients* for Both First-year and Multiyear Sea Ice Regions at Different Concentrations

	100%		*50%*		*15%*	
FIRST-YEAR ICE						
	δC_T	δC_{MY}	δC_T	δC_{MY}	δC_T	δC_{MY}
δT_{B18H}	1.5	1.7	1.2	1.7	0.9	1.7
δT_{B18V}	0.9	4.8	0.3	4.7	0.2	4.7
δT_{B37V}	0.5	3.1	0.6	3.1	0.7	3.1
$[\Sigma(\delta T_B)^2]^{1/2}$	1.8	6.0	1.4	5.9	1.2	5.9
MULTIYEAR ICE						
	100%		*50%*		*15%*	
	δC_T	δC_{MY}	δC_T	δC_{MY}	δC_T	δC_{MY}
δT_{B18H}	1.5	1.0	1.1	1.3	0.8	1.4
δT_{B18V}	0.9	3.4	0.3	3.9	0.2	4.0
δT_{B37V}	0.5	2.8	0.6	2.9	0.6	2.7
$[\Sigma(\delta T_B)^2]^{1/2}$	1.8	4.5	1.3	5.0	1.0	5.

*Each coefficient represents the uncertainty (d) in ice concentration in units of percent per 1 K uncertainty in brightness temperature.

leg of the triangle. The separation of these lines along the PR axis becomes smaller at higher concentrations, indicating a greater sensitivity to variations in PR. For example, at 15%, a 4% change in first-year ice concentration corresponds to a change in PR of -0.012, while at a 95% concentration, the change is only -0.006. This sensitivity is slightly less for multiyear ice concentration, as an examination of the figure will show. The separation of the lines along the GR axis varies in a similar way.

The error in the calculated ice concentrations caused by ice temperature variations is greatly reduced through the use of the radiance ratios PR and GR (Cavalieri et al., 1984; Swift and Cavalieri, 1985). Except at the onset of melt, there is no apparent correlation between PR and the increasing T_{ice} due to the seasonal warming (Figure 2.1.2), whereas GR shows a correlation as discussed in Section 2.1. This correlation may result either from multiyear ice concentration variations, or directly from a temperature dependency of GR on the physical temperature. If we presume that the ±0.005 variations observed in GR are entirely because of temperature variations (see GR plot in Figure 2.1.2), then using Figure 2.3.5, we find that the corresponding uncertainty in total ice concentration is about ±1%, while that in multiyear ice concentration is about ±9%, for 95% consolidated ice. These estimates are illustrated by two warming events in the ice temperature curve in Figure 2.1.2, occurring between Julian days 40 to 50. The GR and C_{MY} are clearly correlated with the ice temperature in these two events. The two positive excursions of 0.01 in GR result in corresponding 15% decreases in C_{MY}. However, only the second of these events has a corresponding decrease in C_T of 1%-2%; C_T actually increases by 1%-2% in the first example.

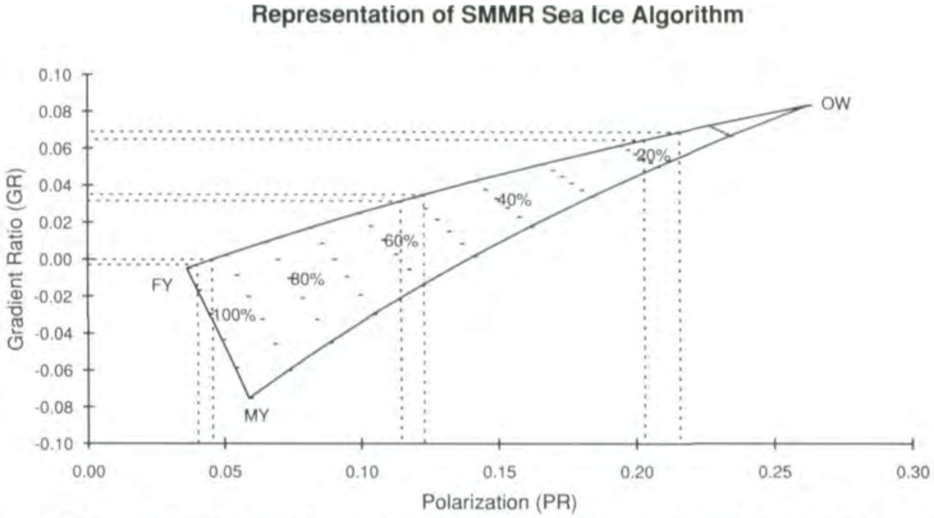

Figure 2.3.5. Sensitivity of ice-concentration calculations to gradient ratio and polarization variations. The pairs of horizontal and vertical dashed lines correspond to changes in PR and GR, which result in 4% changes in the total ice concentration at three different concentration levels. The triangle corresponds to the one in Figure 2.3.3a. Within the triangle, the ten groups of dashes represent total ice concentration (C_T) from 10% to 100% in steps of 10%. The dashes within each group are values of multiyear sea ice fraction, defined as the ratio C_{MY}/C_T, from 0 to 1.0 in steps of 0.2.

The accuracy of the sea ice temperatures derived with Equation 2.3.1 depends on the accuracies of the 4.5-cm vertically polarized brightness temperature, the assumed ice emissivity of 0.96, and the calculated ice concentration. The uncertainty in T_{ice} is given by

$$\Delta T_{ice} = \{(\frac{1}{\varepsilon_{ice} C_T} \delta T_B)^2 + (\frac{T_B - T_{BW}}{\varepsilon_{ice} C_T^2} \delta C_T)^2 + [(\frac{T_B - T_{BW}}{\varepsilon_{ice}^2 C_T} + \frac{T_{BW}}{\varepsilon_{ice}^2}) \delta\varepsilon_{ice}]^2\}^{1/2} \tag{2.3.8}$$

where the coefficients of δT_B, $\delta\varepsilon_{ice}$, and δC_T are measures of the sensitivity of T_{ice} to each parameter. Instrument noise equivalent δT at 4.5-cm is 0.4K (see Table 2.2.1), the variability in ε_{ice} over the Arctic Ocean is about ±0.02 (Comiso, 1983), and the observed standard deviation in computed ice concentration over the central Arctic in winter varies from 2% to 4% (Cavalieri et al., 1984). Although the concentration values contain both fluctuations in ice emissivity and real variability in ice concentration, we use the 4% value as an estimate of ice-concentration uncertainty for this purpose. Using Equation (2.3.8), we find that the uncertainty in T_{ice} for concentrations of 80% or greater, the range for which T_{ice} is calculated, is 7 K.

Principal sources of error

Sources of sea ice concentration error in decreasing order of importance are (a) inability of the algorithm to discriminate among more than two radiometrically different sea ice types, (b) seasonal variations in sea ice emissivities, (c) nonseasonal variations in sea ice emissivities, (d) weather effects at concentrations greater than 8%-12%, and (e) random and systematic instrument error. Each of these sources of error is discussed below.

(a) Radiometrically different sea ice types

The high correlation of information content among the ten SMMR channels limits the number of sea ice types determined by the algorithm to two: first-year ice and multiyear ice (Rothrock et al., 1988, in the Arctic). The broad categories of radiometrically different sea ice types are new ice, first-year ice, and multiyear (or, in the Antarctic, type "B") ice. Since it was assumed in deriving the algorithm that only first-year and multiyear ice types are present, the largest source of error in the determination of total ice concentration is caused by the presence of newly formed sea ice. Of course, both first-year and multiyear ice exhibit radiometric variability, which also results in algorithm error, but this variability is largely due to different surface conditions as is discussed below.

New ice, which is most commonly found in the marginal sea ice zones and coastal polynyas during winter, is characterized by polarization difference values between those of open water and thick first-year ice. PR for thin ice will vary in proportion to ice thickness (Campbell et al., 1975b; Gloersen et al., 1975b; Cavalieri et al., 1986; Grenfell and Comiso, 1986) and will increase in proportion to the fraction of new ice filling the SMMR field-of-view. For example, if we use the PR and GR values obtained by Tucker et al. (1991) for 5-cm pancake ice and scale the values to the SMMR calibration, then PR becomes 0.095 and GR becomes 0.0126. If this ice accounts for 5% of the area within the SMMR FOV and first-year ice accounts for 95%, then the increase in PR and GR results in an underestimate of about 2% in total ice concentration. Larger areas of new ice within the sensor FOV, as in the marginal ice zones or in large polynyas, will result in proportionally larger underestimates by the algorithm.

(b) Seasonal variations in microwave characteristics of sea ice

Seasonal variations in microwave sea ice characteristics can be extremely large. For example, multiyear ice loses its characteristic negative GR during spring and summer and becomes indistinguishable from first-year ice (see Figures 2.1.2 and 2.1.5). In the Canadian Basin example shown in Figure 2.1.2, this process begins in mid April 1984 (Julian Day 100) and becomes complete in mid June (JD 170). Thereafter, until the beginning of September (JD 145), there are oscillations in the multiyear characteristics, probably resulting from alternate freezing and melting conditions at the surface that may be caused by variable cloudiness (Gloersen and Campbell, 1988b). The typical multiyear sea ice characteristics are resumed by October for the remainder of the following winter, while the ice temperature (Figure 2.1.2f) remains near the melting point until mid October (JD 295). In this predominantly multiyear-ice region, correlation between the GR and sea ice temperature in the spring, and no correlation in the autumn, can be explained as follows: In the spring, thawing begins at the surface of the snow-covered ice and progresses slowly downward to sea-level in the ice, resulting in a gradual masking of the volume scattering (and the GR characteristic of multiyear ice) as the moist layer becomes more opaque to microwave radiation. In the autumn, freezing begins at the surface now free of snow, and the frozen layer expands more rapidly towards sea level because of the higher heat conductivity in the ice compared to the springtime snow layer. As autumn progresses, the microwave signature characteristic of multiyear ice, caused by empty brine pockets, is restored. The ice temperature (Figure 2.1.2f) remains stationary for a time while the freezing layer continues to expand below sea level, keeping the ice temperature near the freezing point during the change of state.

Melt ponds on the ice surface are indistinguishable from open water, resulting in large errors in total ice concentration in late spring and summer. While the areal extent of ponding is not well known, Carsey (1982) cites unpublished data that show that for the summer of 1975, 20% or less of the Arctic ice was covered by ponds and that ponding reached maximum areal extent in early July. During the International Geophysical Year (1957 - 1958), the ice in the vicinity of Ice Station Alpha was observed in mid-July of 1958 to be 30% covered by ponds (Campbell et al., 1978, 1984). The extent to which surface moisture and ponding affect the summer ice concentrations remains uncertain. These melt effects vary spatially and temporally across the Arctic. Even less is known about the summertime behavior of the sea ice around Antarctica, prior to the time of its minimum extent.

The variation of the PR and GR parameters over one annual cycle is illustrated in Figure 2.3.6, as the ice characteristics change (Cavalieri et al. 1990). The PR and GR values, averaged over a similar central Arctic region used in Figure 2.1.2, are plotted every 10 days from March 30 through December 15, 1984. Each point has associated with it a temperature shown in parentheses, obtained from Arctic Ocean buoys 3835 and 3849 located within the 600- x 600-km^2 region. Although the reported temperatures (Colony and Muñoz, 1986) are from a sensor within the buoy, they are believed to be within a few degrees of the ambient surface-air temperature during winter (Martin and Clarke, 1978). From March 30 through May 29, the temperatures are well below freezing, but by mid-June, the temperatures reach the freezing point and the PR and GR values approach zero (June 18). This is consistent with the sequence of events described in Section 2.1, whereby, at some time in early to mid-summer, there is a period when the snow cover becomes very nearly a perfect blackbody emitter and the ice emissivity approaches unity. In an earlier study of SMMR brightness temperatures and Arctic Ocean buoy temperature data for the summers of 1979 through 1982, Maslanik and Barry (1989) find that the rapid increase in brightness temperature typically occurs around June 20, which is within 2 days of what is shown in Figure 2.3.6. By June 28, the PR value has increased to wintertime values, but GR has not yet decreased to its wintertime values, indicating a loss of ice type information. From June 29 until September 17, there is considerable variability in both PR and GR, indicating a complicated mix of surface conditions, including wet snow, surface melt ponds, and open water. From September to mid-December, the

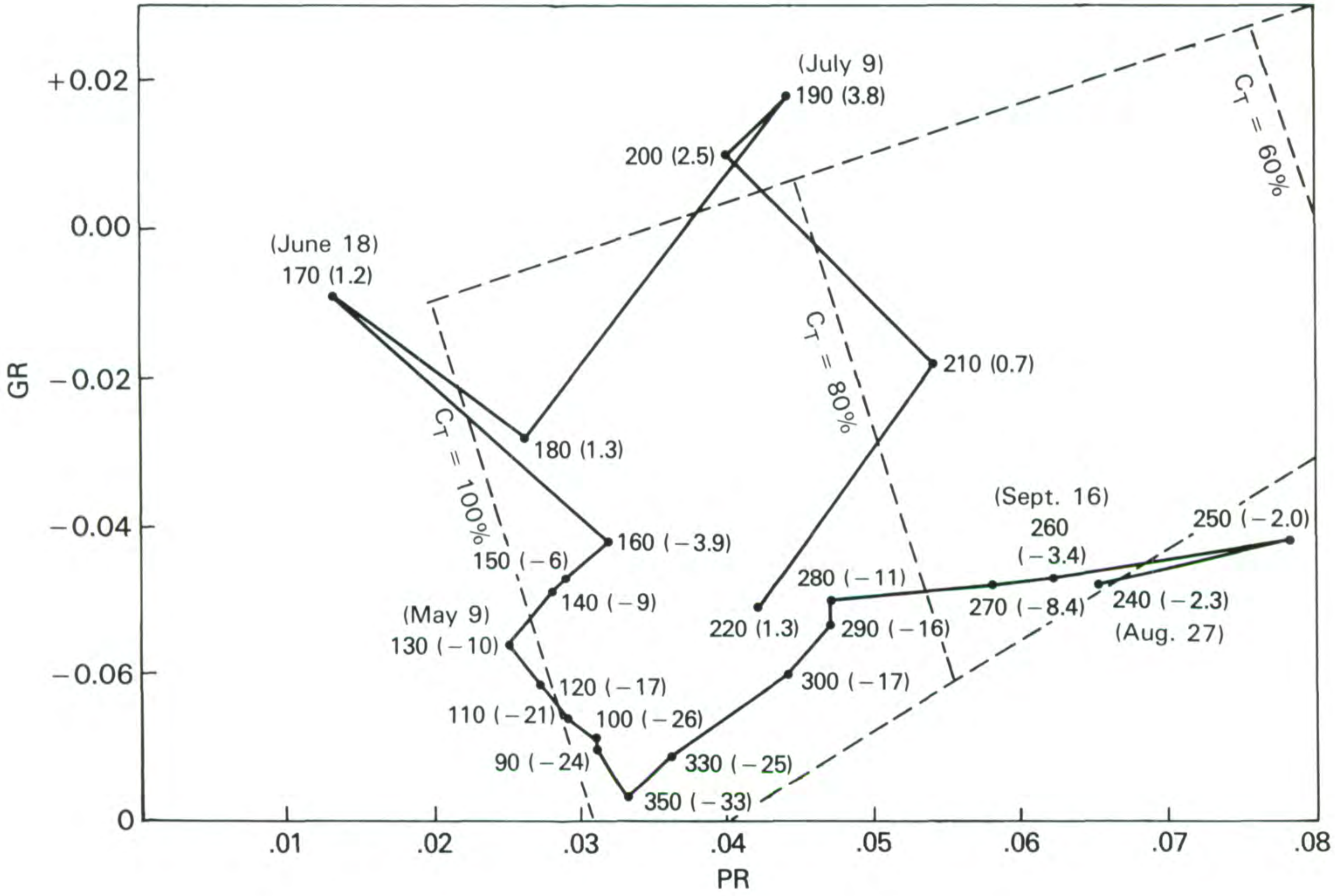

Figure 2.3.6. Average values of GR and PR plotted every tenth day in 1984 from Julian day 90 through Julian day 350, together with corresponding Arctic Ocean buoy temperatures shown in parentheses (from Cavalieri et al., 1990). A portion of the triangle representing the sea ice algorithm domain is shown in dashed lines (from Gloersen and Cavalieri, 1986). As in the references, the values shown are based on CELL data.

temperature decreases and the PRs and GRs return to their wintertime values. To aid in the interpretation of these events, a portion of the triangle representing the algorithm is also shown in Figure 2.3.6. Changes in ice type fall along lines of constant C_T, whereas, the events related to changes in ice concentration or coverage by melt ponds fall along lines perpendicular to these. It is noteworthy that following freeze-up (about JD 330), the variations of PR and GR are generally within 10% of the 100% concentration leg of the triangle. This condition persists until the pack again begins to diverge at the end of June (JD 180).

Similar variations in PR and GR during summer have been observed with aircraft data in the marginal ice zone (Gloersen and Campbell, 1988b). The total ice-concentration determination is only slightly affected by moisture in the freeboard portion of the sea ice, whereas the multiyear ice concentrations drop to zero over a narrow range of temperatures near the melting point (Figure 2.3.7). In a related study of individual ice floes in the marginal ice zone, Cavalieri et al. (1990) show that the ice concentration is accurate to within 10% for ice floes with wet surfaces (not yet ponded), but the concentration drops to 60%-65% for ponded floes. In another study (Barry and Maslanik, 1989), large areas of low ice concentrations in the central Arctic observed during summer were compared with the combination of AVHRR and drifting buoy data (the latter to confirm melting conditions) and found to correspond to open water in many cases.

Finally, it should be noted here that the examples discussed are averages of northbound and southbound satellite passes, corresponding to daytime and nighttime observations in the spring and autumn. Thus, during these times, the observations are likely to be combinations of diurnal or weather-related freeze-thaw cycles, which are unresolved in the averages presented here.

(c) Nonseasonal variations in microwave characteristics of sea ice

Nonseasonal variations in sea ice characteristics include local variations resulting from fluctuations in the physical and chemical properties of sea ice and regional variations resulting from environmental differences. A measure of the local variability in sea ice concentration is provided by calculating the ice-concentration standard deviation over areas of 3.6×10^4 km^2 across the central Arctic in midwinter (Cavalieri et al., 1984). The standard deviations range from 2% to 4%. Although this is, strictly speaking, a measure of the spatial variability of the ice concentration itself, it serves as an estimate of the upper limit on the ice-concentration precision. Except for the summer months, this level of precision is maintained throughout the year (ibid.). This estimate of algorithm precision is consistent with recent comparisons of SSMI ice concentrations with high-resolution aircraft microwave imagery (Cavalieri, et al., 1991). The total ice concentration determined from the aircraft imagery over areas in the Beaufort and Chukchi Seas in March 1988 was 100%, whereas the spatially and temporally coincident SSMI values ranged from 94% to 100%. The overall standard deviation of the total ice concentration differences obtained was 2.4% (see Table 2.3.4).

Observed variability in the emissivity of multiyear ice (Tooma et al., 1975; Comiso, 1990; Comiso et al, 1991; Grenfell, 1991; Tucker et al., 1991) contributes to the large standard errors of estimate obtained in multiyear ice validation studies (Cavalieri et al., 1991). An unknown fraction of the variability is caused by the presence of second year ice, which has an emissivity intermediate between those of first-year and multiyear ice (Tooma et al., 1975).

Earlier studies have shown differences between Arctic and Antarctic sea ice properties (Ackley, 1979) that translate into differences between their microwave emissivities, which are apparent from the differences in the PR *vs* GR distributions noted in Section 2.3.2. Our decision to use different sets of algorithm tie-points for each hemisphere takes these differences into account.

In the seasonal sea ice region, the emissivity of first-year sea ice also varies because of the presence of a thick snow layer that can give false indications of multiyear sea ice under freezing conditions, when large snow grains are present. Under melting conditions, moisture in the snow layer can increase the emissivity of the pack compared to the nominal value for first-year sea ice.

Errors in ice concentration resulting from regionally different ice emissivities can be reduced by using locally chosen tie-points. From a series of SSMI-Landsat comparisons of ice concentrations, Steffen and Schweiger (1991) reduced the concentration difference from -3.6%±6.6%, using hemispherically defined tie-points, to -1.5%±4.5%, using locally defined tie-points (see Table 2.3.4). The hemispheric tie-points we have selected, however, are better suited than local ones for global studies.

(d) Weather effects

Weather effects, including roughening of the sea surface by near surface winds, cloud liquid water, and atmospheric water vapor, all increase the oceanic radiance measured by the SMMR. The purpose of the algorithm weather filter is to reduce the spurious sea ice concentrations over open ocean areas caused by these weather effects. As discussed in Section 2.3.2, Gloersen and Cavalieri (1986) show that for the SMMR, while the weather filter is especially effective at latitudes greater than 45°, it cuts off sea ice concentrations below 8%-12%.

The question remains: are there significant errors associated with weather effects at concentrations greater than 12%? To answer this question, we cite the results of an earlier analysis (Cavalieri et al., 1984) that makes use of the radiative transfer equation illustrated in Figure 2.3.1. This analysis concludes that wind effects near the ice edge are of most importance — a 6-m/s change in wind speed results in a 16% ice concentration change over the open ocean, typical of values near the ice edge observed by Gloersen and Cavalieri (1986) before application of the weather filter. It also shows that nonraining clouds with a water content of 0.04 cm, associated with storms near the ice edge, give 1% errors over the ocean. Finally, this analysis shows that variations of 0.2 cm of atmospheric water vapor about 0.5 cm, a typical average near the Arctic ice edge, result in an ice-concentration variation of 0.5% over open ocean. The variation is substantially less over consolidated ice. These effects may be neglected over 100% ice-covered ocean.

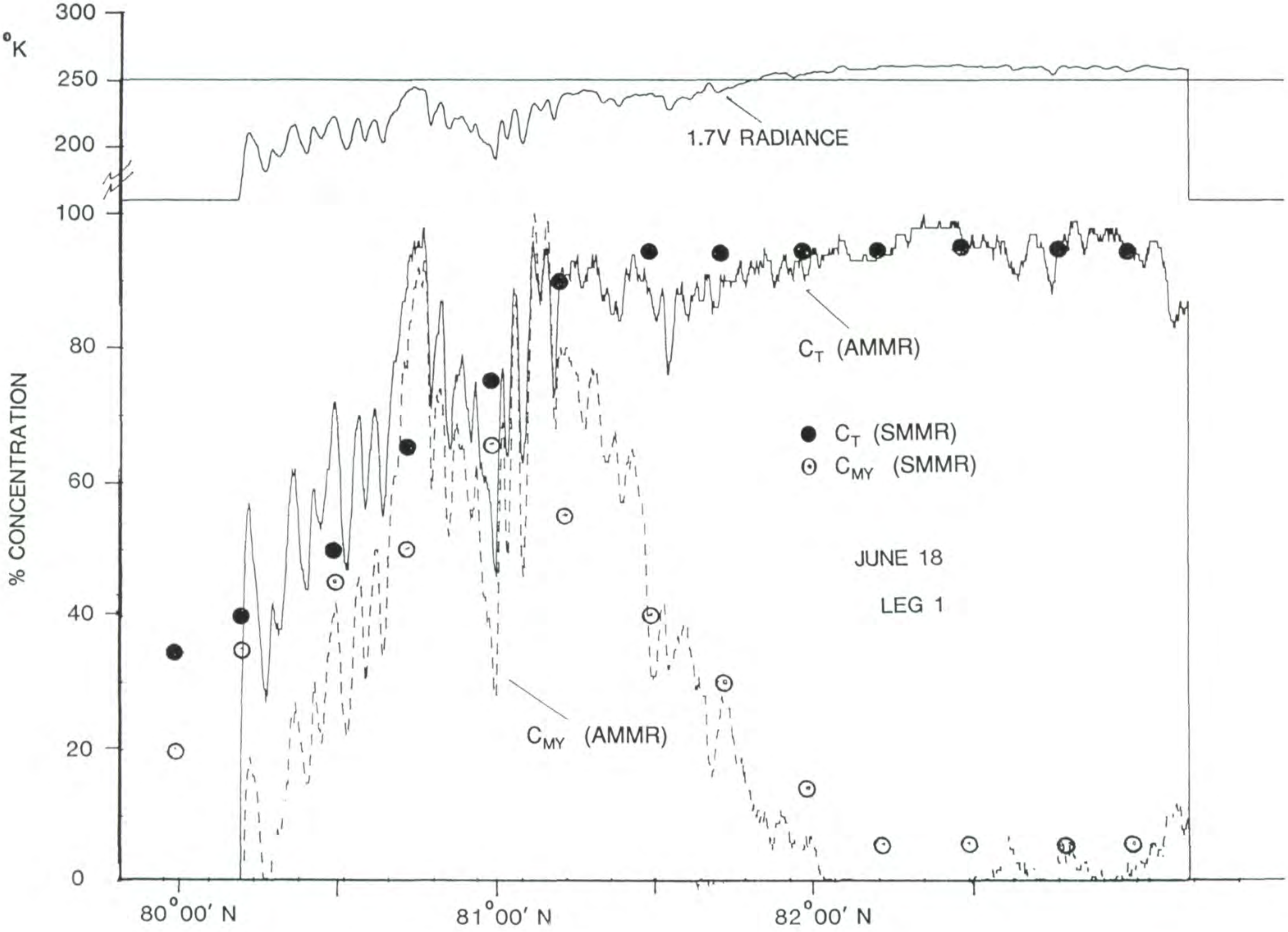

Figure 2.3.7. Comparison ice concentration data along a transect ("Leg 1") of the Fram Strait region for June 18, 1984, obtained with the Airborne Multichannel Microwave Radiometer (AMMR) onboard the NASA Convair 990. The AMMR channels used for calculating ice concentrations are the same polarized components and wavelengths as used with the SMMR data. The solid and dashed curves represent AMMR data for total and multiyear ice concentrations, respectively, and the solid and open points, coincident SMMR data for each pixel along the transect, again, for total (CT) and multiyear (C_{MY}) ice concentrations, respectively. Note the low values of calculated multiyear ice concentrations when the 1.7-cm V-polarized brightness temperature exceeds 250 K (on a relative scale). Visual weather observations onboard the CV-990 are recorded as clear in the southern portion of the transect and cloudy in the northern portion.

For concentrations between 0% and 100%, these effects may be linearly scaled for an upper limit to the errors, because the wind effects are less in water near the freezing point, and in low ice concentration areas with limited fetch. It is important to note that no weather filter was applied to the ESMR data, a point that must be kept in mind when comparing the two data sets.

(e) Random and systematic instrument error

Uncertainties in the ice products associated with random and systematic instrument error are calculated using algorithm sensitivities (Table 2.3.2). The problem of systematic errors resulting from long-term drifts and ecliptic angle errors in the measured radiances is minimized through the calibration procedure described in Section 2.2.2 This leaves the problem of random instrument errors. On the basis of prelaunch measurements and observed radiances (or brightness temperatures) over relatively stable targets such as areas of the Antarctic ice sheet where temporal and spatial variability in the geophysical parameters is small, the error due to instrument noise for each of the four SMMR channels used in the algorithm is less than 1 K. Assuming a 1-K level of random instrument noise in each channel, the upper limit of the rms uncertainty in the individual calculated concentrations, these upper limits range from about 1% to 1.8% for total ice concentration and from 4.5% to 6% for multiyear ice concentration, depending on surface type and concentration. The actual error contributed by random noise is considerably less because of the large number of measurements averaged to obtain the daily and monthly maps presented here.

Sea ice extent and ice-area errors

The uncertainties in the calculated ice extents and ice areas result from both systematic and random errors. The major source of error is the systematic error, because the calculation of ice area involves an integration over a large number of pixels and the random error is reduced by 1 divided by the square root of the number of pixels. Potential sources of systematic error include biases in the chosen algorithm tie-points, a bias in the selected GR value for the weather filter, remaining instrument errors, and integrated field-of-view effects over ocean near land (see Section 2.2.3). The contribution from each of these potential errors is indeterminate. Thus, the approach taken here is to use the observed variability of the calculated ice areas to serve as an upper limit of our ice-area error.

In Chapter 5, we discuss residuals in the Arctic and Antarctic sea ice extents and areas obtained by subtracting a model seasonal cycle from the values in the single-day time series. The observed variability is taken to be the standard deviations of these residual values about the trend lines through them. These standard deviations are listed in Table 2.3.3, along with the percentage of the maxima and minima of the sea ice extents and areas that the standard deviations represent. These percentages serve as an estimate of the upper limit to the uncertainty in the ice areas discussed in Chapters 3, 4, and 5.

Table 2.3.3. Standard Deviations of Residual Ice Extents and Areas for Both the Arctic and Antarctic

REGION	*ICE EXTENT*			*ICE AREA*		
	Std. Dev. (10^6 Km^2)	% of Max.	% of Min.	Std. Dev. (10^6 Km^2)	% of Max.	% of Min.
Arctic	0.14	0.9	1.6	0.14	1.0	2.0
Antarctic	0.13	0.7	3.5	0.15	1.0	7.0

Sea ice concentration accuracies

In contrast to the precision (relative error) of the sea ice parameters discussed in the previous paragraphs, sea ice parameter accuracies (absolute errors) are estimated from comparisons with other corresponding but independent parameters. Comparisons of aircraft SAR and ESMR mesoscale ice concentration maps with concurrent SMMR maps have given agreements to within 10%-20% (Campbell et al., 1987). Comparison of data from the Airborne Multichannel Microwave Radiometer (AMMR) transects within SMMR footprints (e.g., Figure 2.3.7) with SMMR data has yielded agreements within 10% for both C_T and C_{MY} (Gloersen and Campbell, 1988b). Only two papers have provided spatially coincident comparisons between SMMR ice concentrations and concentrations derived from other spacecraft sensors. The first paper compared SMMR concentrations with concentrations derived from imagery obtained with the Shuttle Imaging Radar-B (SIR-B) in the Weddell Sea during October 1984 (Martin et al., 1987), while the second compared SMMR and Landsat ice concentrations in Baffin Bay for days in March, April, May, and June (Steffen and Maslanik, 1988). Results from these two papers are presented in Figures 2.3.8 and 2.3.9.

We also summarize the results from two SSMI validation studies, because the SMMR quantitative studies are so few. These results are deemed relevant here because the SSMI sea ice products were derived using the SMMR Team sea ice algorithm, although with algorithm tie-points that reflect the SSMI sensor characteristics and calibration. The first study (Steffen and Schweiger, 1991) provided over 100 case studies of Landsat/SSMI comparisons for total ice concentration, while the second (Cavalieri et al., 1991) provided direct SSMI multiyear ice concentration comparisons using wide-swath, high-resolution active- and passive-microwave imagery from aircraft underflights. Results from these SMMR and SSMI validation studies are summarized in Table 2.3.4.

For total ice concentration, the mean difference between the reference data and the microwave-satellite data is generally less than 5%, with standard deviations of the differences ranging from 1% to 7%. The largest standard deviations in the Arctic are from the September and October Landsat

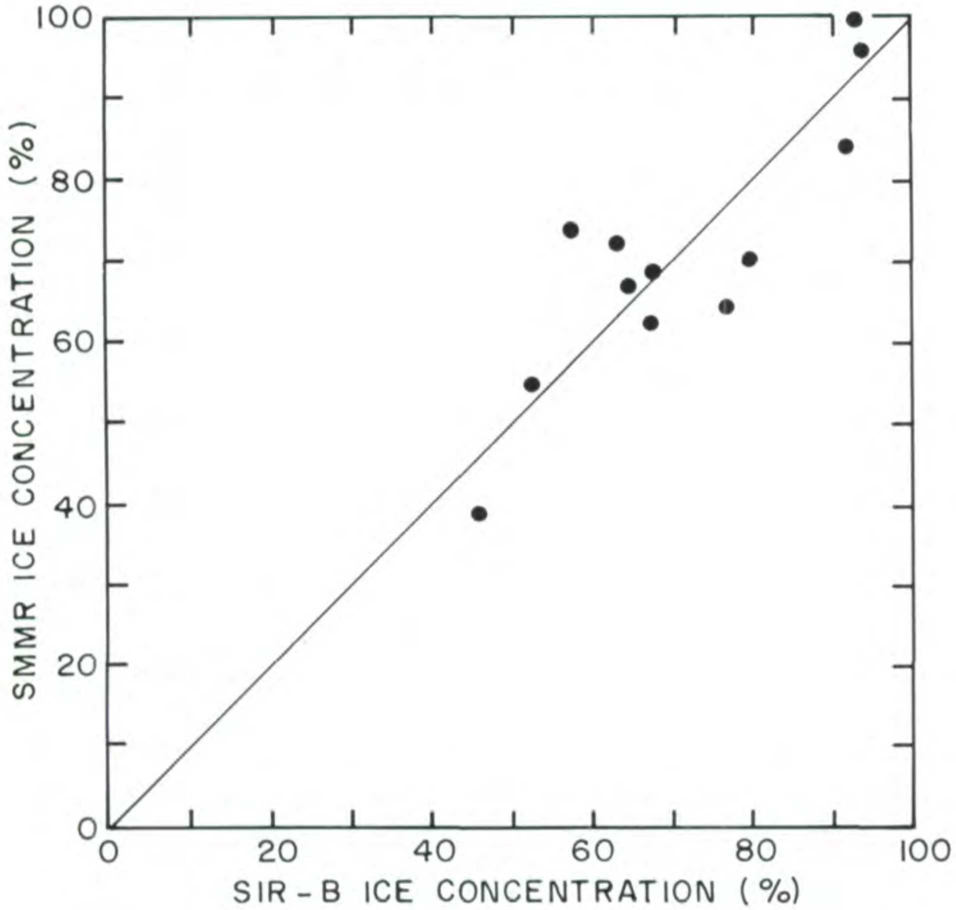

Figure 2.3.8. SMMR ice concentrations vs. SIR-B ice concentrations in the Weddell Sea (from Martin et al., 1987).

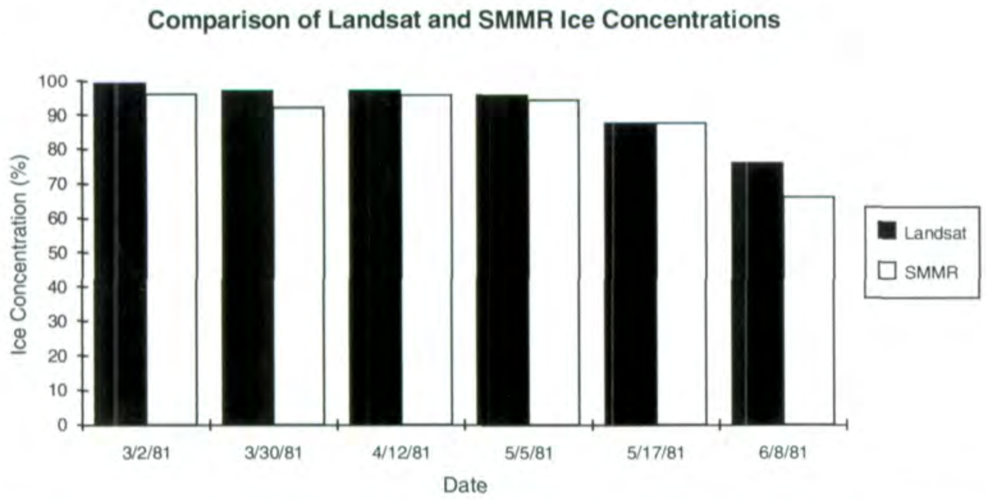

Figure 2.3.9. Total ice concentrations for northern Baffin Bay derived from SMMR data compared to those derived from Landsat data on 6 different days in 1981 (from Steffen and Maslanik, 1988).

Table 2.3.4. Quantitative Estimates of Algorithm[+] Accuracy Based on Comparisons With Other Sources of Ice-Concentration Measurements

REGION	MONTH	SENSOR	MEAN DIFF. ±1 SD	REF. DATA SET	REF.
Total Ice Concentration					
Bering Sea	Feb	SMMR	±5% (Thick FY)	Ship reports	(1)
Baffin Bay	Mar-May	SMMR	-3.5%	Landsat MSS	(2)
Baffin Bay	Jun	SMMR	-10%	Landsat MSS	(2)
Beaufort Sea	Oct	SMMR	-1.5%±2.6%	Landsat MSS	(3)
Weddell Sea	Oct	SMMR	0.3%±7.6%	SIR-B	(4)
Beaufort & Chukchi Seas	Sep-Nov	SSMI	0.6%±7.4%	Landsat MSS	(5)
Beaufort Sea	Mar	SSMI	-2.1%±3.1%	Landsat MSS	(5)
Bering Sea	Mar	SSMI	-9.4%±6.1%[++]	Landsat MSS	(5)
Greenland Sea	Sep	SSMI	-3.7%±1.4%	Landsat MSS	(5)
Weddell Sea	Nov	SSMI	-1.1%±3.1%	Landsat MSS	(5)
Summary		SSMI	-3.6%±6.6%	Landsat MSS	(5)
Amundsen Sea	Dec	SSMI	1.3%±3.6%	Landsat MSS	(5)
Beaufort & Chukchi Seas	Mar	SSMI	-2.4%±2.4%	NADC/ERIM SAR & NOARL	(6)
				KRMS	(6)
Multiyear Ice Concentration					
Beaufort & Chukchi Seas	Mar	SSMI	5%±4%* 12%±11%**	NADC/ ERIMSAR & NOARL KRMS	(6)
Beaufort Sea	Mar	AMMR	-6.0%±14%	JPL C-band SAR	(6)

(1) Cavalieri et al. (1986)
(2) Steffen and Maslanik (1988)
(3) Steffen, unpubl. data (1990)
(4) Martin et al. (1987)
(5) Steffen and Schweiger (1991)
(6) Cavalieri et al. (1991)

[+] The algorithm has been used with SMMR, SSMI, and AMMR data

[++] Including new ice

.*Excluding data from 1 of the 4 flights which gave anomalously large and unexplained biases.

**Including data from all 4 flights.

comparisons in the Beaufort and Chukchi sea regions. Factors contributing to this large variability are likely to be residual melt effects in September and new ice growth in October-November. Both the Bering Sea Landsat comparison (Steffen and Schweiger, 1991) and the Baffin Bay summer Landsat comparison (Steffen and Maslanik, 1988) confirm that large amounts of new ice, wet surfaces, and melt ponds will result in significant negative concentration biases. An estimate of overall total ice-concentration accuracy based on Landsat-SSMI comparisons (Steffen and Schweiger, 1991) in Table 2.3.4 is ±7%, based on a standard deviation of ±6.6% (with an offset of -3.6% under frozen conditions, and as large as 10% under melt conditions). A higher accuracy of about ±3%, based on a standard deviation of ±3.1% (with an offset of -2.1%), is obtained from the Landsat-SSMI comparisons for the Beaufort Sea in March. The three Antarctic comparisons in Table 2.3.4 show that the accuracies based on the standard deviation are about ±3% for the Landsat comparisons and about ±8% for the SIR-B comparison.

The multiyear ice concentration comparisons presented in Table 2.3.4 are relatively few, but they provide the only coincident airborne and spacecraft microwave-sensor observations of multiyear ice concentrations obtained in the central Arctic with the SMMR Team algorithm. From a direct comparison of SSMI and these spatially and temporally coincident aircraft data, an estimate of 5%±4% is obtained using the data from three of the four flights, but a larger estimate of 12%±11% is obtained when including the fourth flight, which had anomalously large positive biases (Cavalieri et al., 1991). A region of anomalously large negative bias was found in a shear zone with predominantly small floes along the northern shore of Ellesmere Island (Cavalieri et al., 1991). The multiyear ice concentration results show a considerable spread in the mean differences, as well as in the standard deviations. While more comparisons are clearly needed, these limited results suggest that the algorithm used on the SSMI data calculates too large a multiyear ice concentration and with a large variability. Also included in Table 2.3.4 are the results from comparisons of multiyear ice concentrations derived using a SMMR-type algorithm on data from the Aircraft Multifrequency Microwave Radiometer (AMMR) onboard the NASA DC-8 Airborne Laboratory and those derived from data from the C-band Synthetic Aperture Radar (SAR) onboard the same aircraft. The difference was found to be within -6%±14% this time, with the algorithm, on average, underestimating the SAR concentrations. In summary, we estimate the accuracy of the multiyear ice concentrations to be ±11%, based on the standard deviation of the SSMI/aircraft C_{MY} differences from all four flights (Table 2.3.4).

Finally, studies utilizing aircraft and ship observations have determined that the SMMR ice-concentration maps correctly locate the ice-edge position to within the resolution limitation of the microwave data (Cavalieri et al., 1983, 1986; Campbell et al., 1987; Gloersen and Campbell, 1988b). Campbell et al. (1987) show that for a diffuse ice edge, the 30% SMMR ice-concentration contour corresponds best with the ice edge. For a compact edge, the ice-edge location correlates best with the 40%-50% isopleths. More recent ice-edge comparisons were made as part of the NASA and Navy SSMI underflights in March 1988 (Cavalieri et al., 1991). The NASA DC-8 aircraft flew over the Bering Sea ice edge and, through the aid of a Global Positioning Satellite navigation system, provided the precise location of ice-edge features for determining the appropriate SSMI ice-concentration contour to use for locating the ice edge on the 25-km SSMI grid. Results from these comparisons showed that, on average, an SSMI ice concentration of 15% corresponds to the position of the initial ice bands as determined from the aircraft, while the location of the edge of the main ice pack corresponds to an SSMI concentration of about 40%, which is consistent with the Campbell et al. (1987) result. The importance of these results is that they suggest that the SSMI 15% ice-concentration contour, on average, locates the outer ice-edge position.

Sea ice temperature accuracies

Sources of error affecting the calculation of sea ice temperatures and the sensitivity of the calculated temperatures to these errors were summarized in Section 2.3.4. For the purpose of obtaining an estimate of the accuracy of the ice temperatures, comparisons are made between the 9-year average ice-temperature map for March (Figure 2.3.10a) and climatological surface-air temperatures for the same month (Figure 2.3.10b). Comparisons are also made with Arctic Ocean buoy temperatures (Figure 2.3.11). These comparisons provide only a rough estimate of the SMMR temperature accuracies, since the SMMR temperature is neither a surface-air temperature nor a temperature corresponding to the internal temperature of Arctic buoys.

In Figure 2.3.10a, ice temperatures across the central Arctic are observed to range from 260 K in the Chukchi Sea, to 248 K just off the coast of Ellesmere Island, and to 262 K in the Kara Sea. Other large ice-temperature gradients are observed from southern Hudson Bay (264 K) to northern Fox Basin (252 K) and from Davis Strait (266 K) to northern Baffin Bay (252 K). The warmest ice temperatures are observed in the Bering, Okhotsk, Greenland, and Labrador Seas and range from about 260 K to 271 K at the ice edge.

For the purpose of examining similarities between the 9-year averages and climatology, we show the climatological surface-air temperature for the month of March in Figure 2.3.10b. A comparison of Figures 2.3.10a and 2.3.10b shows that there are large-scale similarities between the two ice-temperature distributions. The coldest temperature in the March climatology map is 235 K located north of Ellesmere Island in the Canadian Archipelago, while the warmest temperatures are found in the peripheral seas. A tongue of warmer temperature (250 K) in the Chukchi Sea is also apparent in the SMMR sea ice temperature. The ice temperature gradients from southern Hudson Bay to Foxe Basin and from Davis Strait to northern Baffin Bay are also observed in the climatological map. The SMMR temperatures are generally warmer, by about 5 K in the Chukchi Sea to about 13 K north of the Canadian Archipelago. Since the SMMR temperatures represent values close to the snow-ice interface for first-year ice and to some weighted mean portion of the freeboard and near sea level layers for multiyear ice, it is not

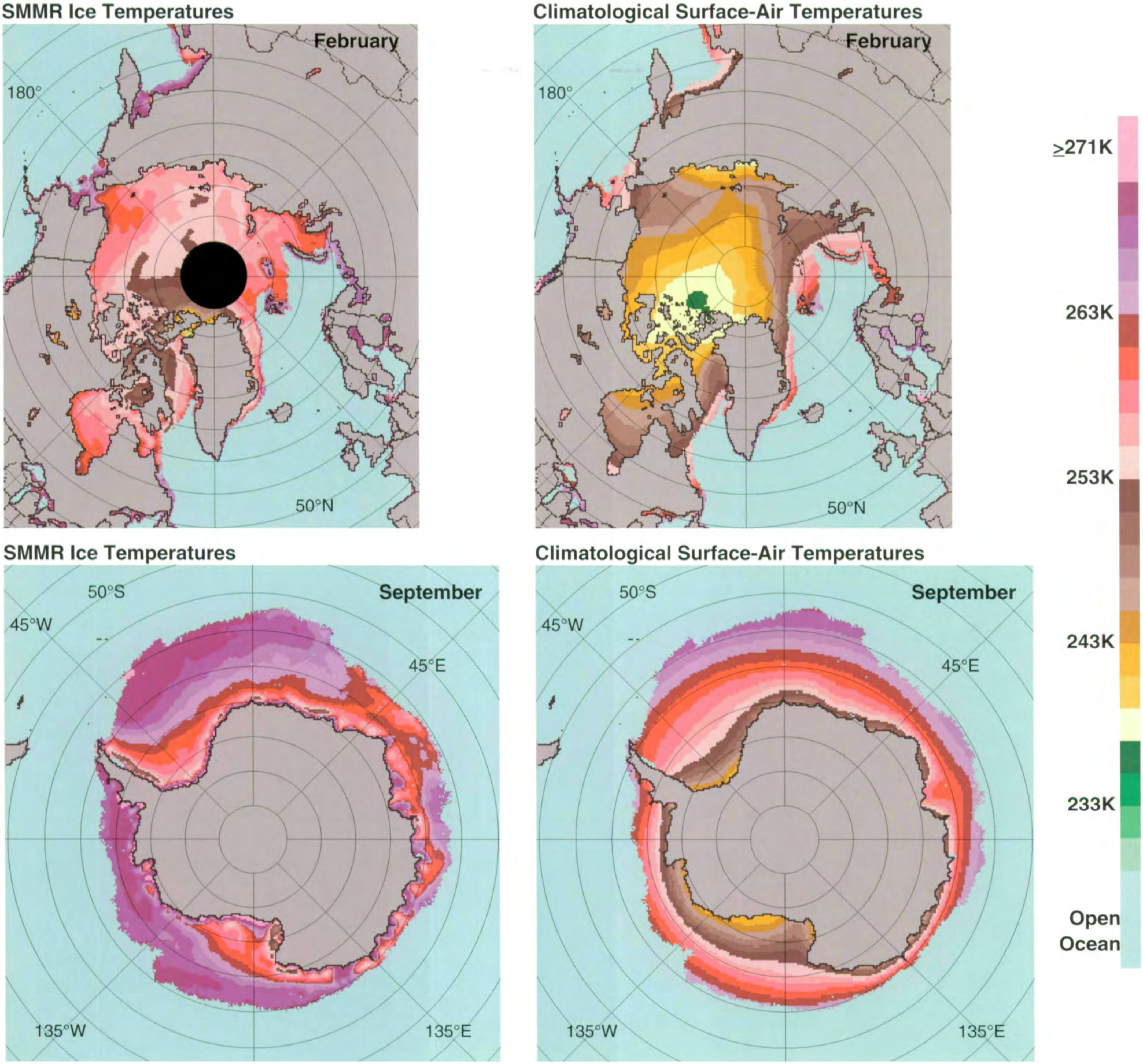

SMMR Ice Temperatures

Climatological Surface-Air Temperatures

SMMR Ice Temperatures

Climatological Surface-Air Temperatures

Figure 2.3.10. SMMR-lifetime average of ice temperatures and mean climatological surface-air temperatures for the Arctic in February, and for the Antarctic in September.

surprising that larger biases are found over the areas of multiyear ice. The largest temperature difference of about 13 K occurs north of the Canadian Archipelago where the multiyear ice is the thickest. These differences result from the insulating properties of the snow cover and the temperature gradient in the ice, and are in fair agreement with modeled temperature profiles during this time of year (Maykut and Untersteiner, 1971).

Another measure of the SMMR ice-temperature accuracy on a different time scale is provided through a comparison of single-day SMMR values with corresponding Arctic Ocean buoy temperatures. A detailed description of the Arctic Ocean Buoy Program (AOBP) data set is given elsewhere (Thorndike and Colony, 1980). This 8-year comparison is limited to the 7 months, October through April, to avoid the incorporation of inaccurate temperature readings that occur when solar heating causes the interior of the buoys, where the temperature sensors are located, to become appreciably warmer than the outside air temperatures. Also excluded from the comparison are data from buoys that have either zero, or inordinately large, standard deviations about their daily averages, indicative of faulty buoy operation. A plot of SMMR ice temperatures and corresponding buoy temperatures is presented in Figure 2.3.11. Examination of the figure shows considerable scatter between the two data sets. A linear least-squares fit of the data gives a slope of 0.39 and an intercept of 160.8 K. The fact that the slope is less than 1 is consistent with the SMMR ice temperatures representing subsurface values and the buoy temperatures representing surface values. The standard error of estimate is 4.1 K, which is less than the estimated SMMR ice-temperature precision of 7 K (obtained in winter). The errors become larger in summer when ice-concentration fluctuations become larger (Figure 2.1.2). There are a number of factors contributing in unknown proportions to these temperature differences. These include uncertainty in ice concentration and ice emissivity, the fact that the comparison is between point measurements and the large SMMR footprint averages, and the deviations of the Arctic buoy temperatures from surface air temperatures (Thorndike and Colony, 1981).

In summary, the comparison with the climatological data for March (Figure 2.3.10) suggests that the SMMR temperatures are 5 K to 13 K higher, as would be expected since SMMR sea ice temperatures represent subsurface temperatures. The larger biases are over regions of thick multiyear ice. For first-year sea ice, the subsurface temperature corresponds to the snow-ice interface temperature. For multiyear ice, it corresponds to a weighted ice temperature within the ice, with most of the contribution from near sea level. The comparison with the AOBP data suggests that the SMMR temperatures are 17 K higher at the low end of the scale (Figure 2.3.11) and 4 K lower at the high end. While the SMMR-climatology-AOBP comparisons appear reasonable, further studies are required to quantify SMMR temperature accuracies—a difficult task, since a true validation of the data set will require in situ sea ice temperature-profile measurements over the satellite sensor field of view.

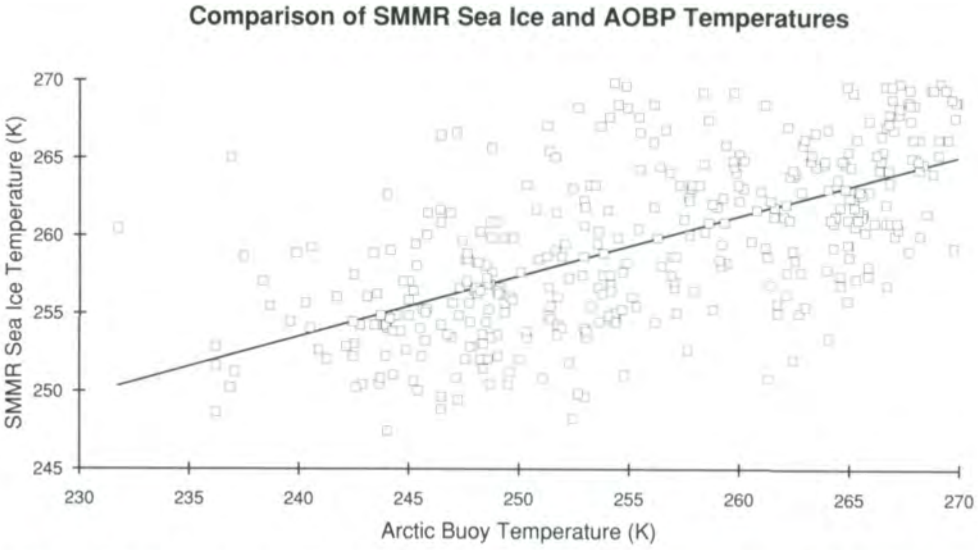

Figure 2.3.11. Comparison of SMMR ice temperatures with the Arctic Ocean Buoy temperatures.

Page Intentionally Left Blank

3

ARCTIC SEA ICE

3.1 Introduction

The structure and dynamics of the sea ice cover in the Northern Hemisphere (Figure 3.1.1) are complex and variable. Unlike the Southern Hemisphere, where most of the ice is bounded on the south by land and open on the north to the ocean, the Northern Hemisphere ice has vast areas where it is bounded by land masses, such as in the Arctic Ocean, Baffin Bay, Hudson Bay, and the Canadian Archipelago. In other areas, it is open to the oceans, as in the Bering, Greenland, Barents Seas, and the Sea of Japan. Confinement of the Arctic Ocean ice pack by land limits its drift and divergence and strongly influences the distributions of ice types, growth/decay rates, and thicknesses. A distinguishing characteristic of the Arctic Ocean is the persistence of a perennial pack of multiyear sea ice. The region of thickest sea ice is located north of the Canadian Arctic, where the ice drift toward land causes extensive ice ridging and retention of thick ice from year to year.

The seasonal cycle of sea ice is driven predominantly by the annual cycle of solar insolation and atmospheric conditions and lags the solar cycle by about 3 months. At the end of the melt season, the northern pack retains about 60% of the ice-covered area occurring at the winter maximum, whereas the southern ice pack largely disappears in summer, retaining only 13% of its maximum ice area. Almost all of the summer ice in the Northern Hemisphere resides in the central Arctic Ocean. Because the peripheral seas are open to the oceans, ice divergence generally produces more open water within the pack and more thin ice that does not survive the summer, compared to the Arctic Ocean.

Major long-term features in the Arctic basin ocean circulation (Figure 3.2.2) include a counterclockwise gyre centered in the Beaufort Sea and a Transpolar Drift Stream across the Arctic basin. The latter transports ice southward through Fram Strait, accounting for approximately 90% of the total ice export from the Arctic basin (Aagaard and Carmack, 1989). The ice continues southward in the East Greenland Current, transporting sea ice and cold Arctic water along the east coast of Greenland. In contrast, the north-flowing Norwegian Current (to the west and north of Norway) transports warm water into the Barents Sea, leading to the presence of a considerable amount of open water all year in spite of the high latitudes. Similarly, the warm waters in the West Greenland Current, in the eastern Davis Strait, and in the West Kamchatka Current (in the eastern Sea of Okhotsk) cause the ice edge to be located farther north in the western portions of these regions. A more detailed description of Arctic oceanic circulation, water temperatures, salinities, and ocean bathymetry, as well as their relations to the sea ice distribution, is given in the ESMR Arctic atlas (Parkinson et al., 1987).

In this chapter, the distribution of the Northern Hemisphere sea ice cover is described for each of nine regions and for their total. The regions, as defined in Figure 3.1.2., include essentially its entire sea ice-covered area. Six of the regions are nearly the same as those in the ESMR Arctic atlas, specifically the Bering Sea and Hudson Bay regions, which have seasonal sea ice covers, and the Greenland Sea, Kara and Barents Seas, Arctic Ocean, and Canadian Archipelago regions, which all contain some perennial sea ice cover. The Sea of Okhotsk and Baffin Bay/Davis Strait regions, which are the two other regions described in the ESMR Arctic atlas, have been extended southward to include the greater spatial coverage of the larger SSMI grid used here. The Sea of Okhotsk region now includes a portion of the Sea of Japan, and the Baffin Bay/Davis Strait region extends southward beyond Newfoundland to include the Labrador Sea. A new region, the Gulf of St. Lawrence, has been added. For the six unchanged regions, the small differences between the areas defined for the ESMR Arctic atlas and those for this volume range from -0.075×10^6 km^2 in the Canadian Archipelago region to $+0.15 \times 10^6$ km^2 in the Kara/Barents Seas region (Table 3.1.1.). These differences result principally from the different logic used to decide whether map pixels that contain both land and ocean are counted as land or ocean and from the differing map grid sizes (see Chapter 2). Part of the difference in area, which amounts to about 1% of the respective areas, is attributed to the use here of the latitude-dependent radius of the Earth, rather than the equatorial radius used in the ESMR atlases.

Table 3.1.1. Areas of the Nine Arctic Regions

(in 10^6 sq km)

Arctic Ocean	7.084
Seas of Okhotsk and Japan	2.021
Bering Sea	2.230
Hudson Bay	1.162
Baffin Bay/Davis Strait/Labrador Sea	2.751
Gulf of St. Lawrence	0.642
Greenland Sea	2.914
Kara and Barents Seas	2.500
Canadian Archipelago	0.714
Total area	22.016

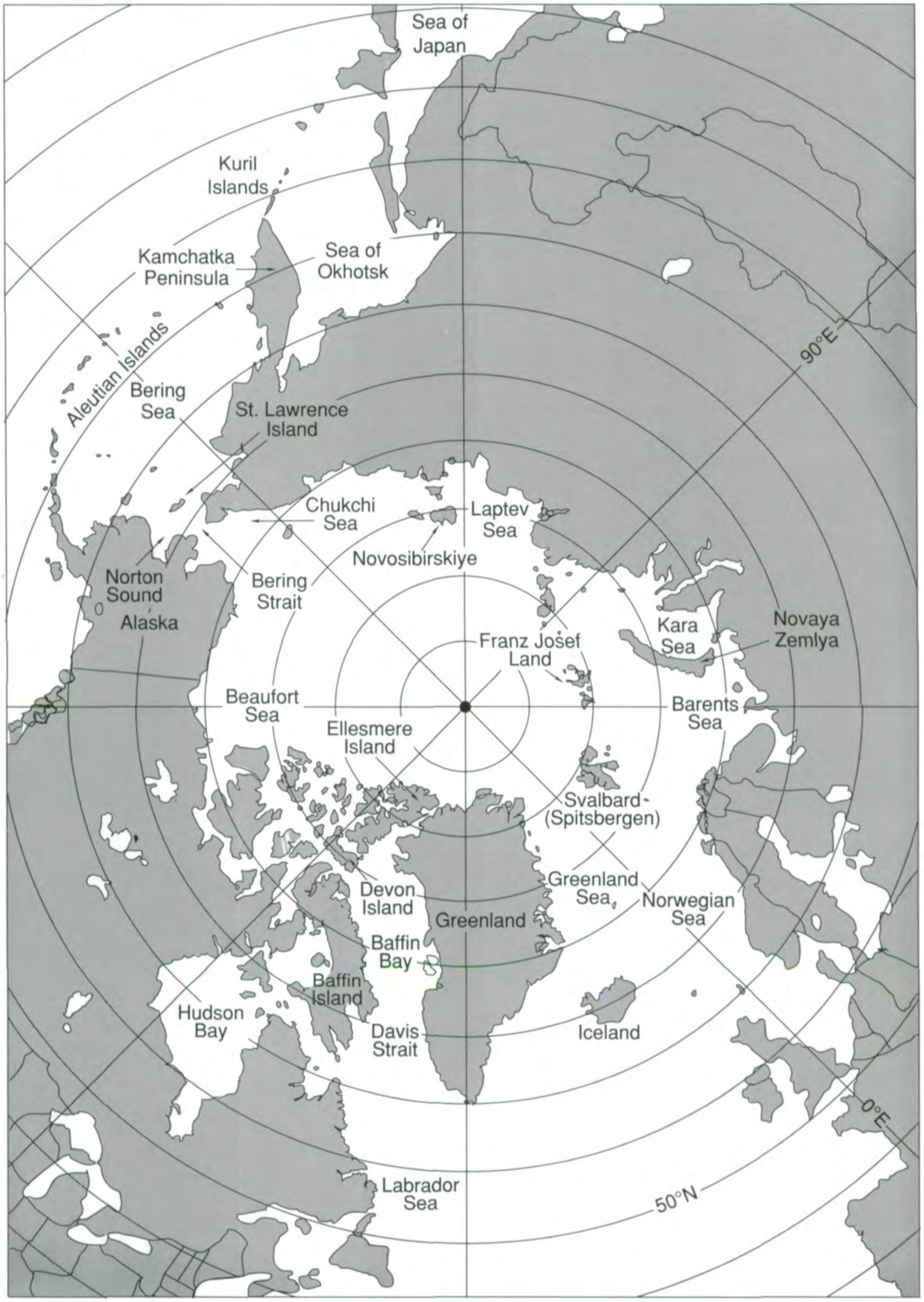

Figure 3.1.1. Arctic location map.

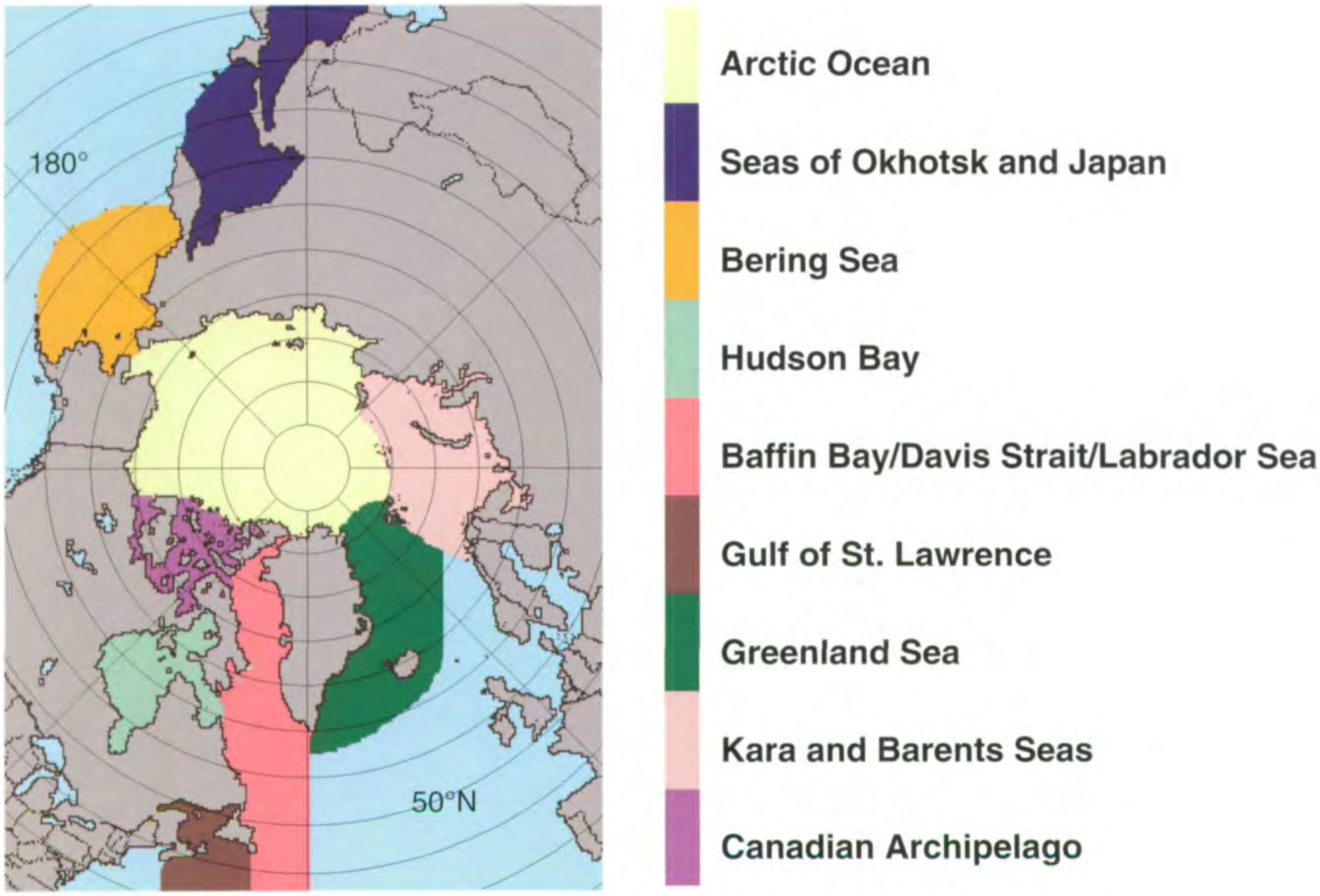

Figure 3.1.2. Arctic region map.

Monthly averages of the Arctic sea ice concentrations are given in Figures 3.1.3-3.1.14. Averages of these monthly averages over the October 1978-August 1987 period form Figure 3.1.15. Maps of monthly anomalies in ice concentration are produced by subtracting the corresponding long-term average from each monthly concentration map (Figures 3.1.16-3.1.27). Finally, month-to-month change maps (averaged over the 9 years) provide an indication of spatial patterns of the monthly ice growth and decay rates (Figure 3.1.28). Generally, the ice concentration in a single pixel in a daily map has an estimated accuracy of ±7% (Chapter 2.4). Since some of the error is reduced by temporal averaging, the estimated accuracy of the monthly average concentration is likely to be better than ±7%.

The multispectral information is an important feature of the SMMR measurements, since it can be used for calculating multiyear ice concentrations (C_{MY}) in the Arctic basin. Monthly average C_{MY} maps (Figures 3.1.29-3.1.35) are produced only for October through April, because of the inability to distinguish between first-year and multiyear in the passive-microwave data during the melt season (Chapter 2). Since the characteristic microwave signature of winter multiyear sea ice does not become fully established until late autumn, the October maps, in some cases, may not include all of the multiyear ice cover (compare Figure 3.1.29 and Figure 3.1.30).

The C_{MY} maps are averaged to produce 8- or 9-year averages for each month (Figure 3.1.36). These are then subtracted from the monthly maps to produce wintertime monthly anomalies (Figures 3.1.37-3.1.43), similar to those for total concentrations. Changes in the multiyear ice distributions that occur between December and April are displayed in Figure 3.1.44, in place of the monthly difference maps of the total concentrations. The multiyear ice concentrations have an estimated accuracy of ±11% (see Chapter 2), but concentration steps finer than the accuracy of the C_{MY} are presented to permit the analysis of smaller relative changes with time and location that may be significant.

Time series of the sea ice extent, sea ice area, and open water within the pack are calculated by spatial integration of the sea ice concentration data in the single-day maps of ice concentration. Specifically, the ice extent is obtained by summing the areas of the pixels with at least 15% ice concentration. The area of sea ice is the sum of ice concentration per pixel times the pixel area. The open water within the pack is the difference between sea ice extent and sea ice area. Each of the area curves has 1607 single-day values. The area curves for the entire Northern Hemisphere are shown in Figure 3.1.45. Similar curves for the individual regions appear in the later sections of this chapter. An interesting aspect of the sea ice extent cycle is the change

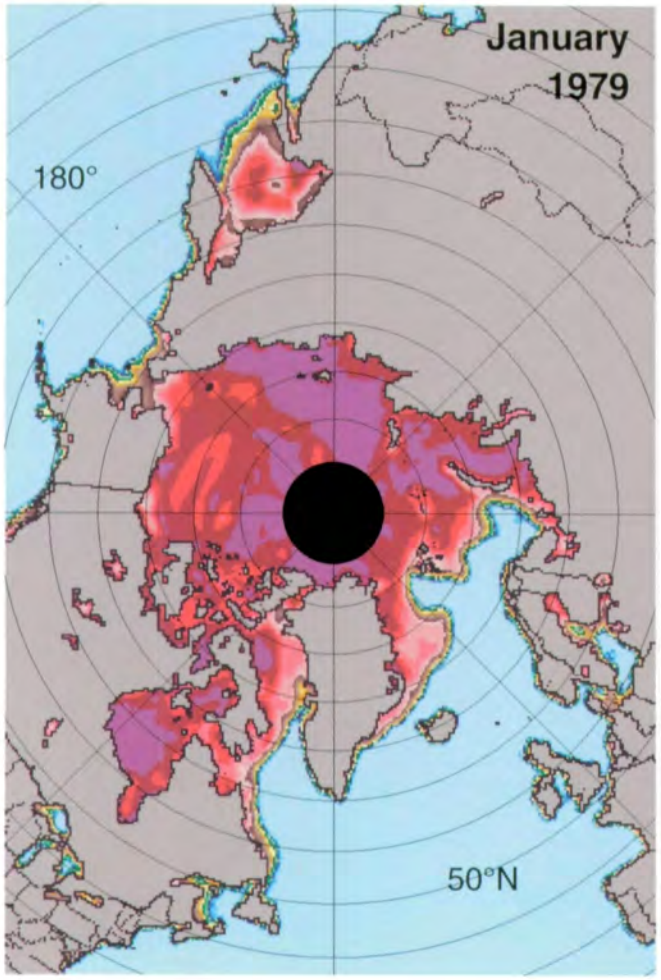
January
1979
180°
50°N

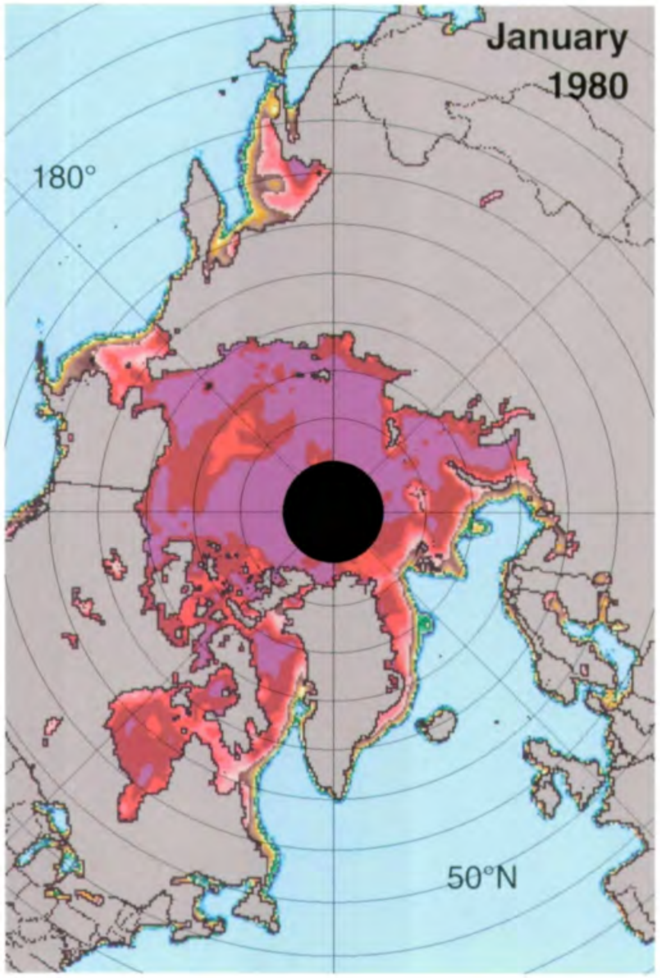
January
1980
180°
50°N

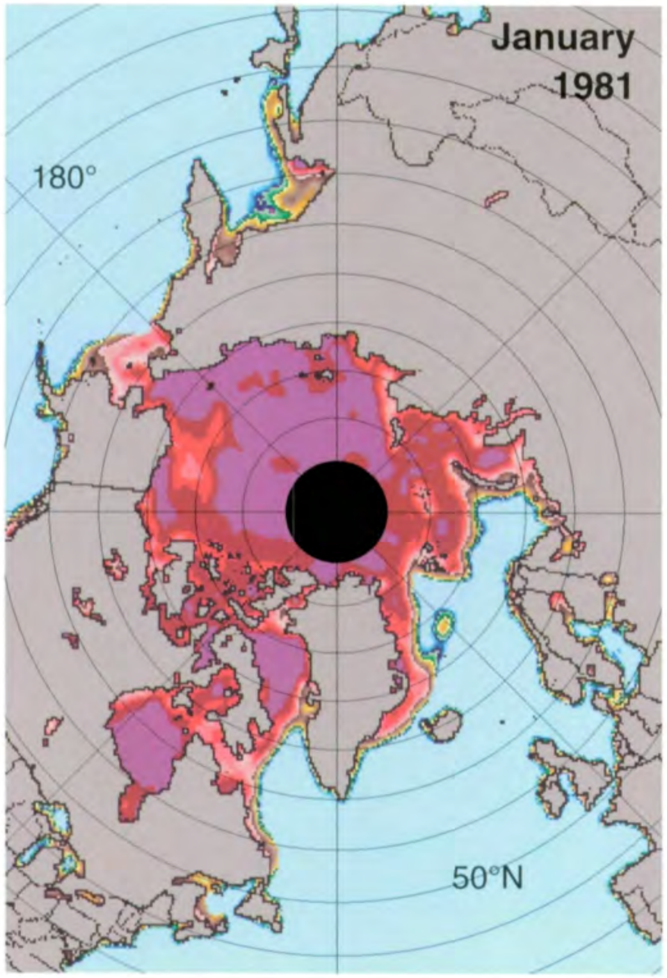
January
1981
180°
50°N

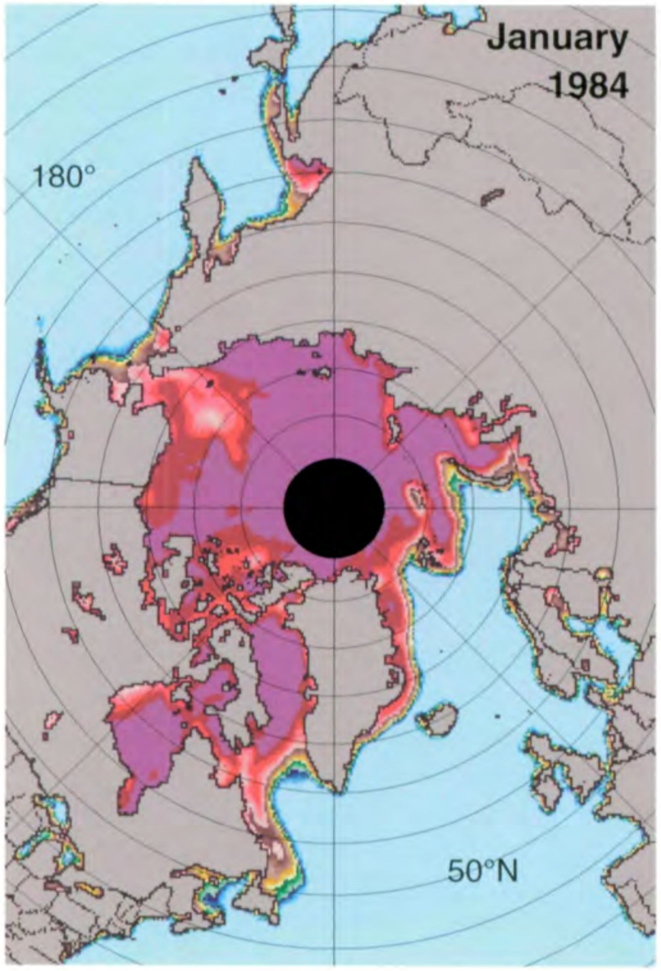
January
1984
180°
50°N

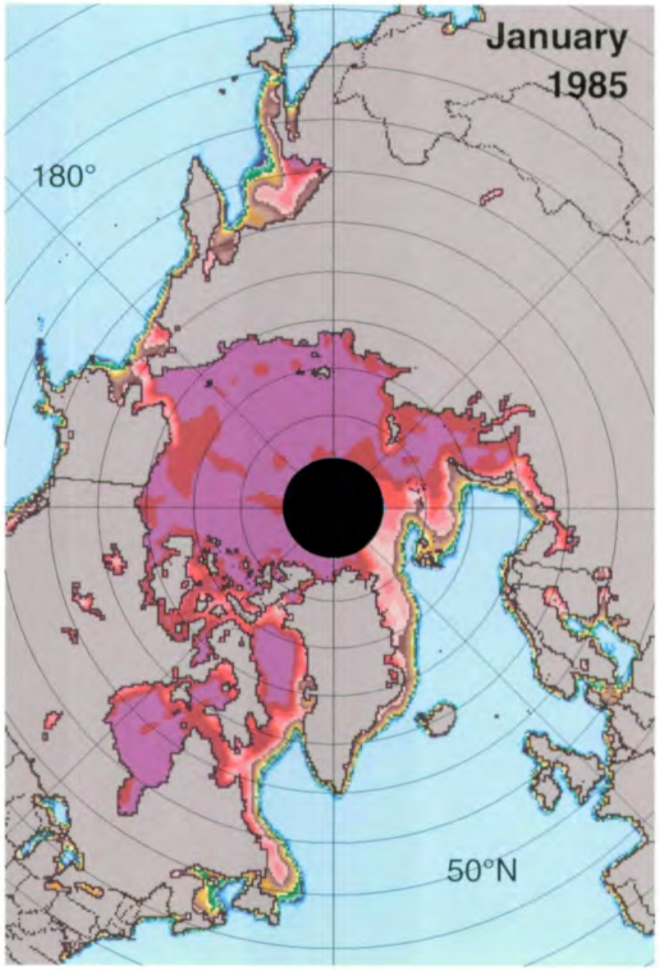
January
1985
180°
50°N

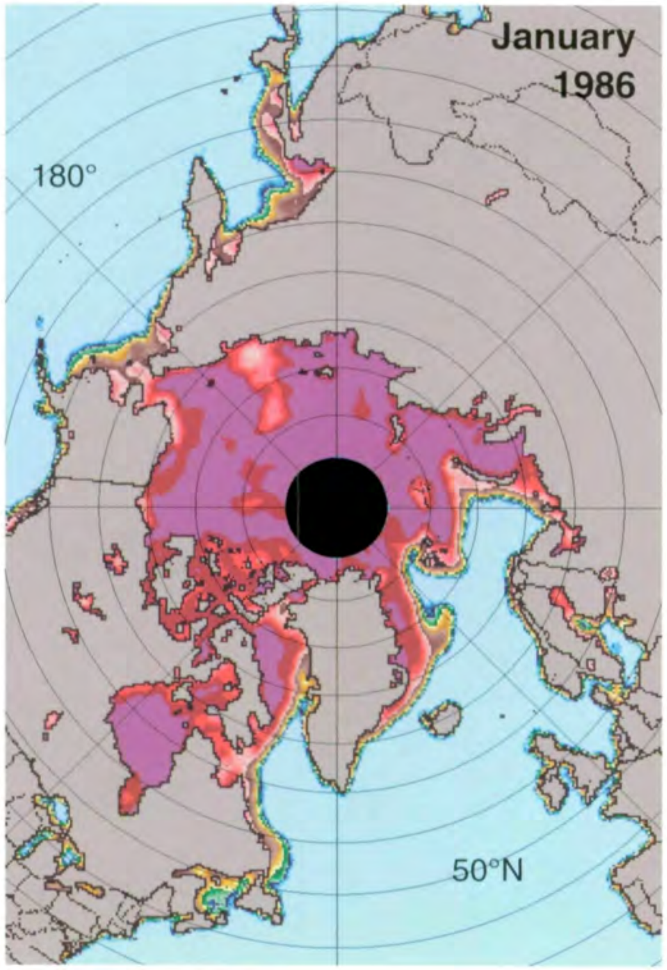
January
1986
180°
50°N

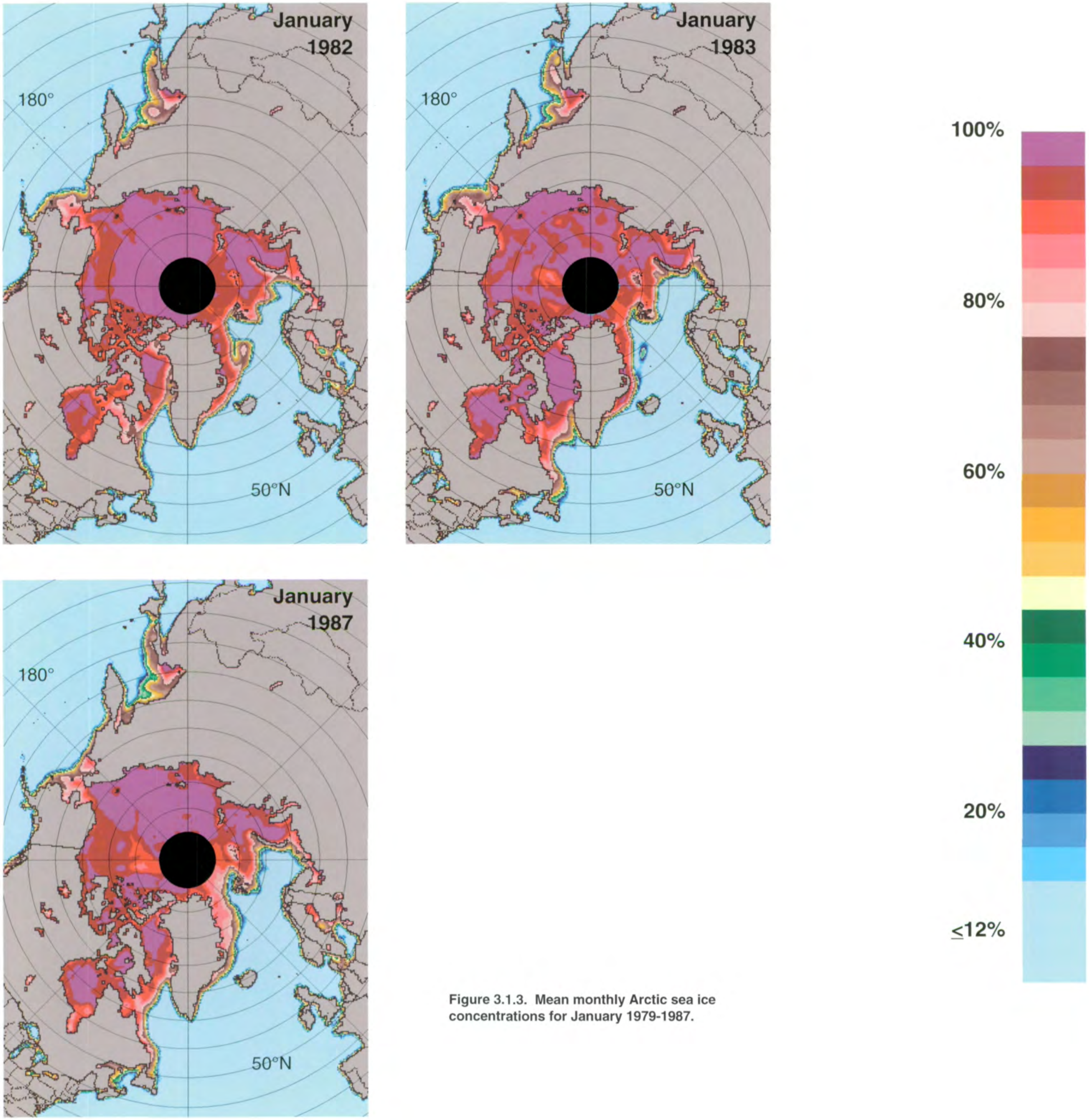

Figure 3.1.3. Mean monthly Arctic sea ice concentrations for January 1979-1987.

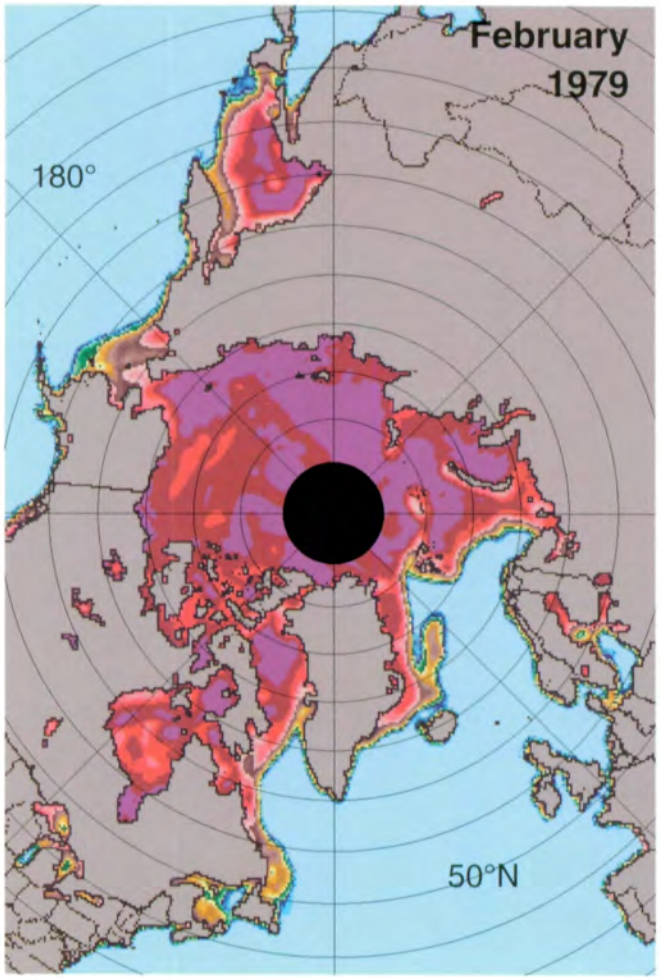
February
1979
180°
50°N

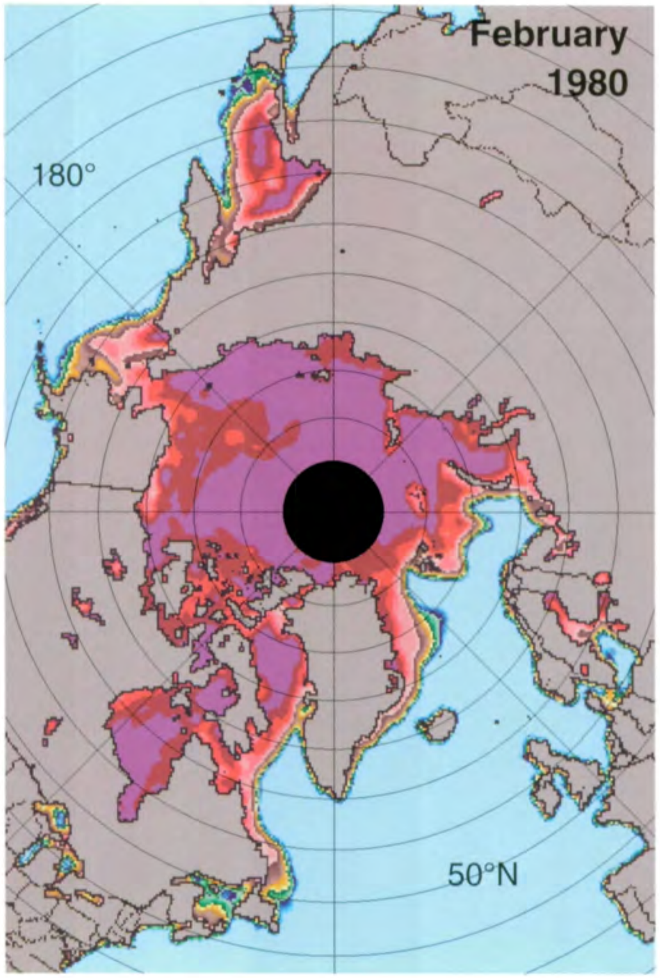
February
1980
180°
50°N

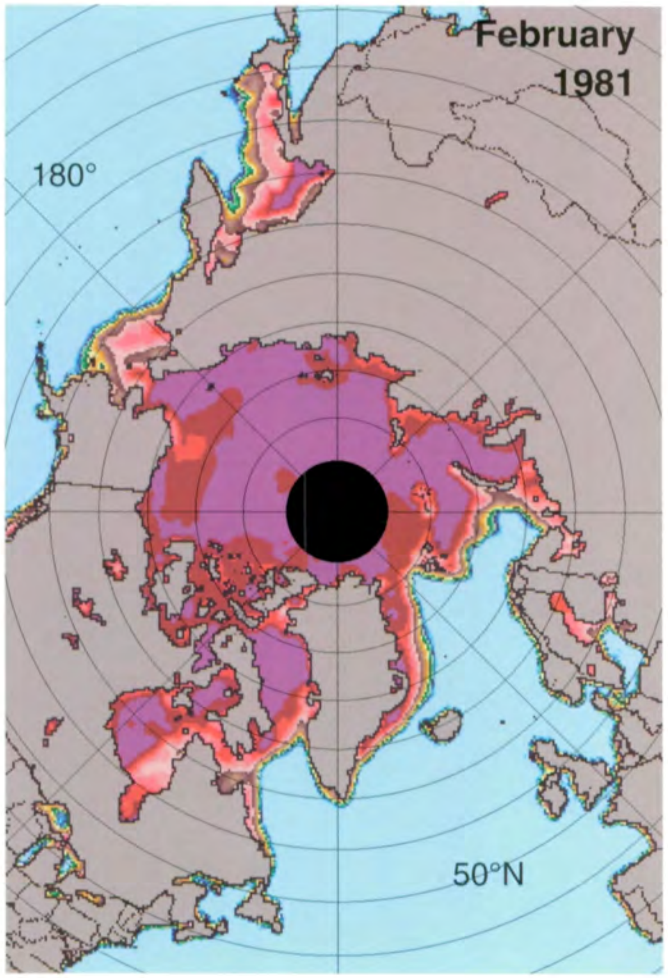
February
1981
180°
50°N

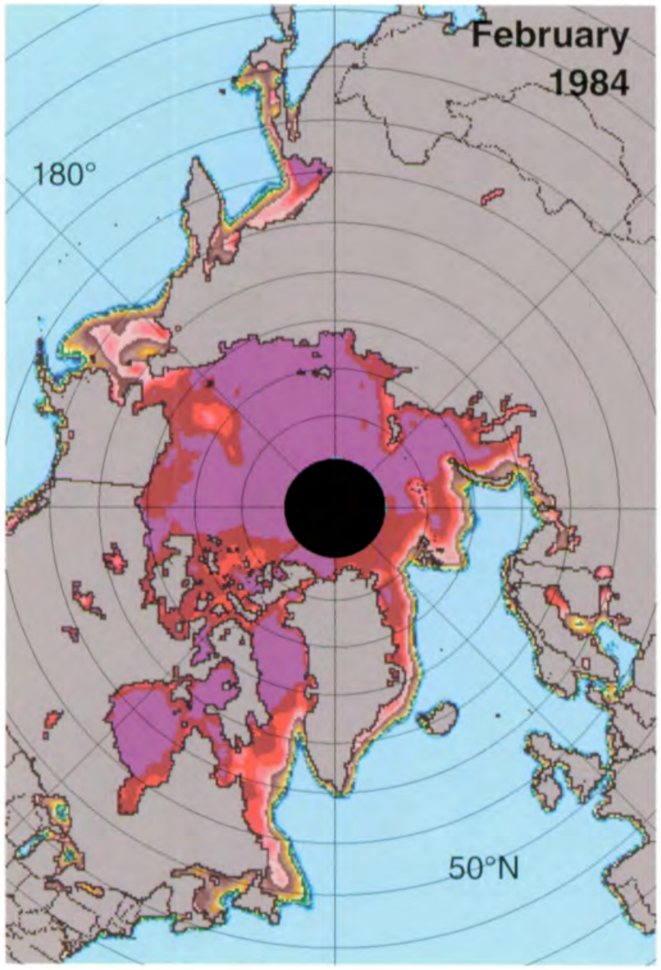
February
1984
180°
50°N

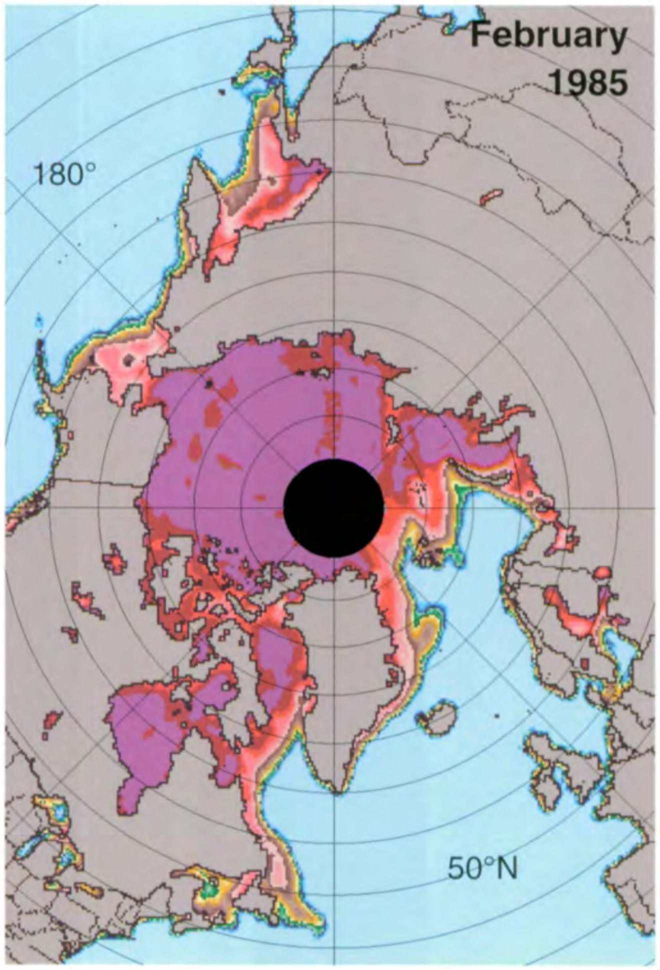
February
1985
180°
50°N

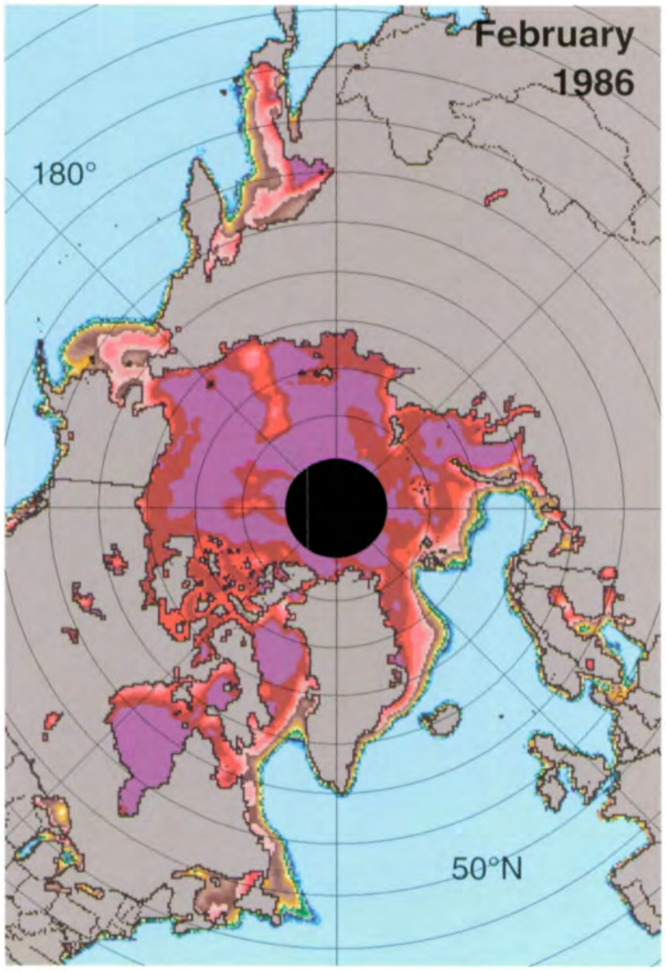
February
1986
180°
50°N

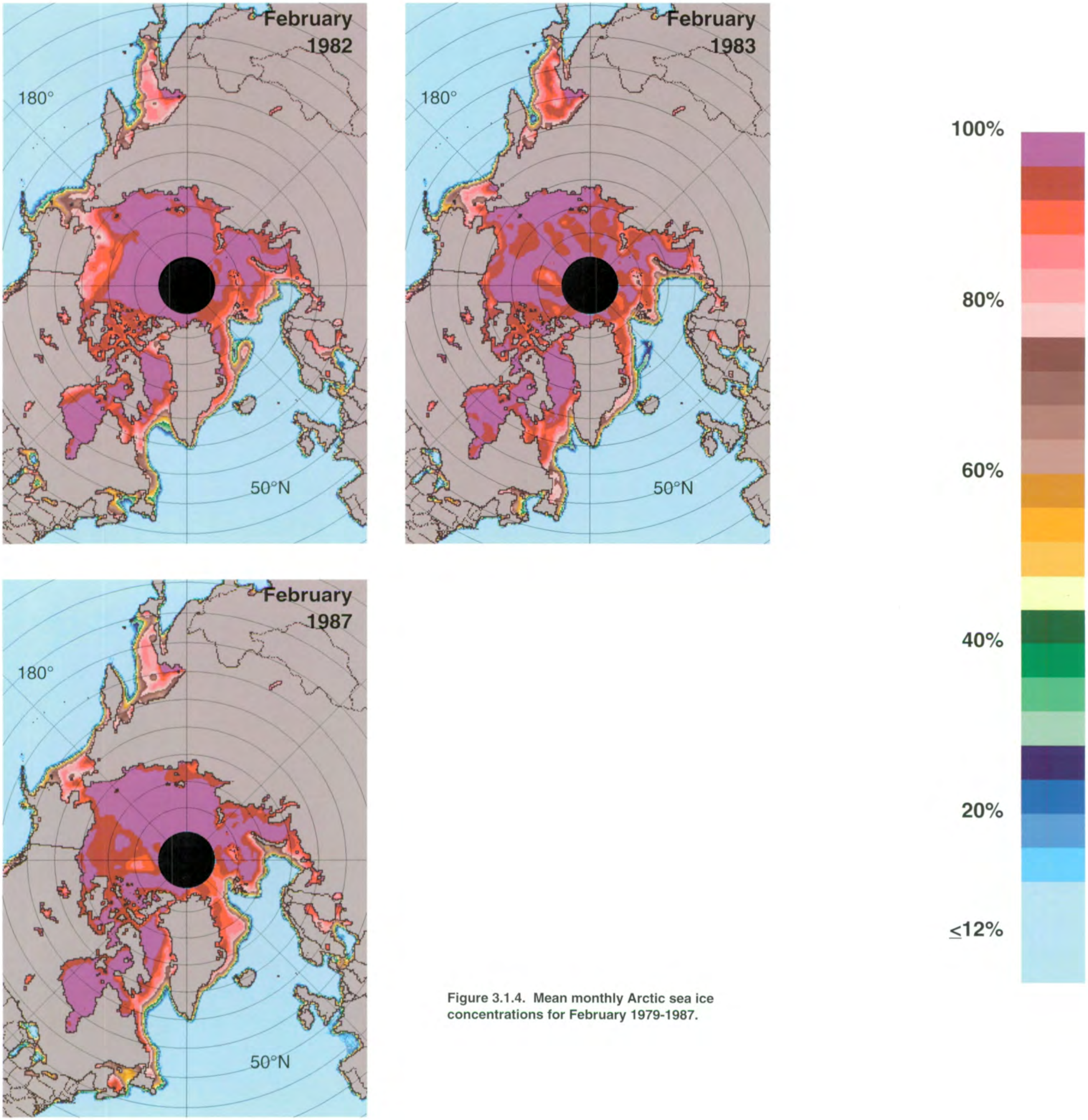

Figure 3.1.4. Mean monthly Arctic sea ice concentrations for February 1979-1987.

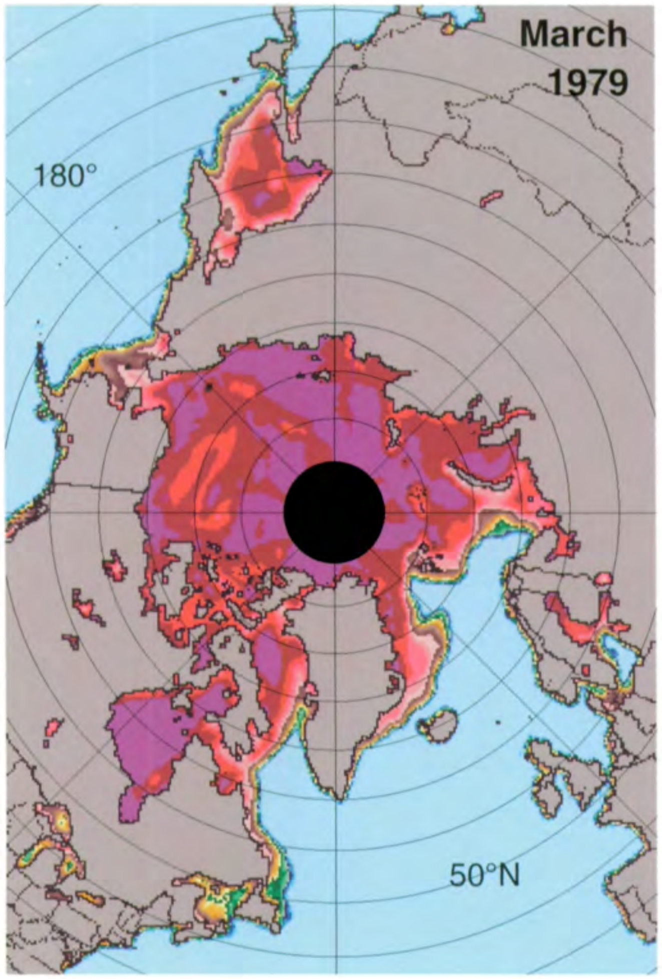
March
1979
180°
50°N

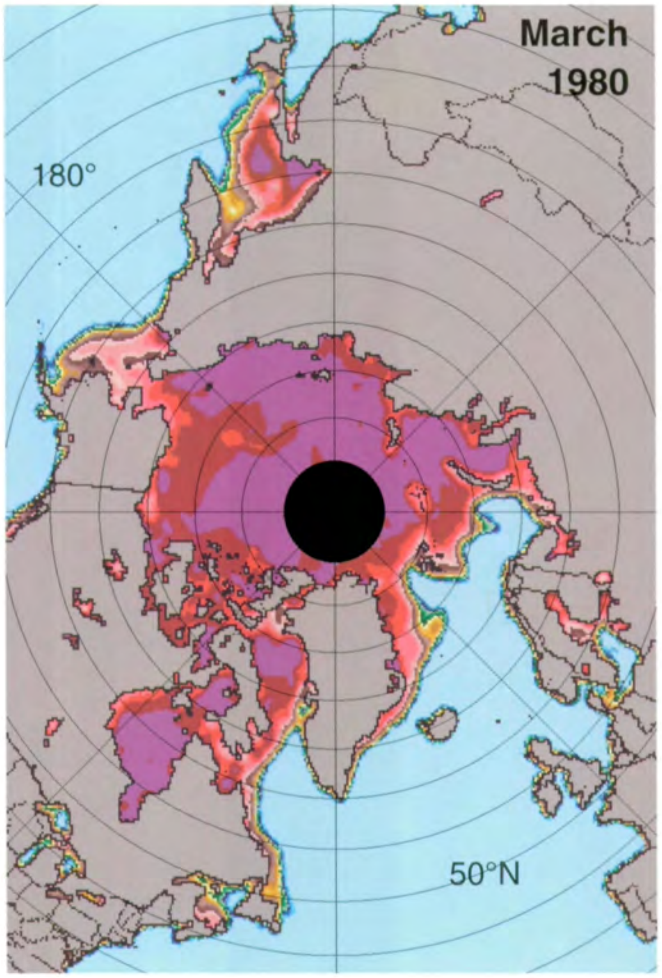
March
1980
180°
50°N

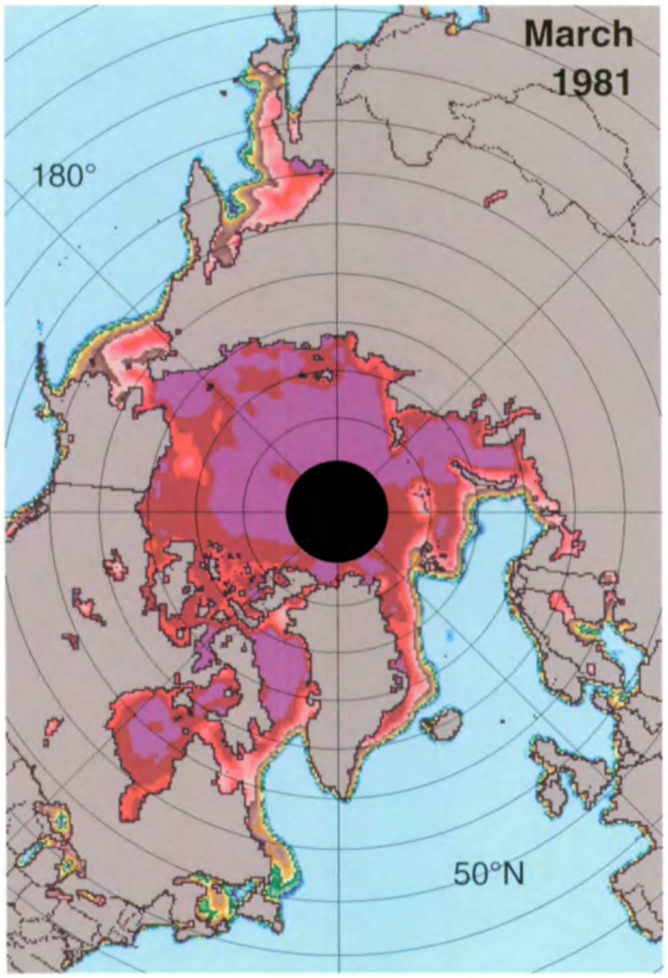
March
1981
180°
50°N

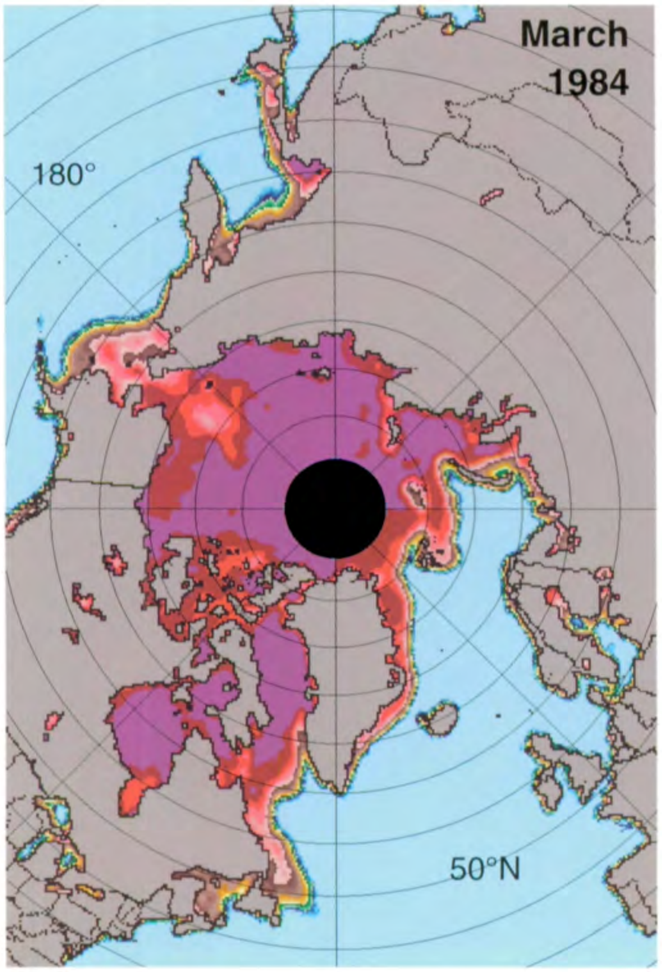
March
1984
180°
50°N

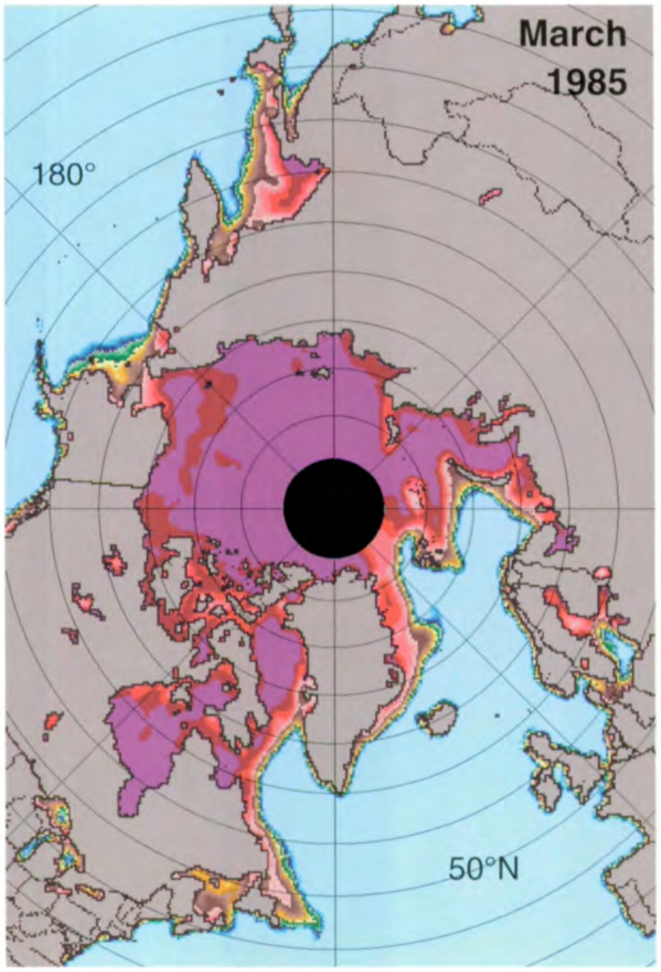
March
1985
180°
50°N

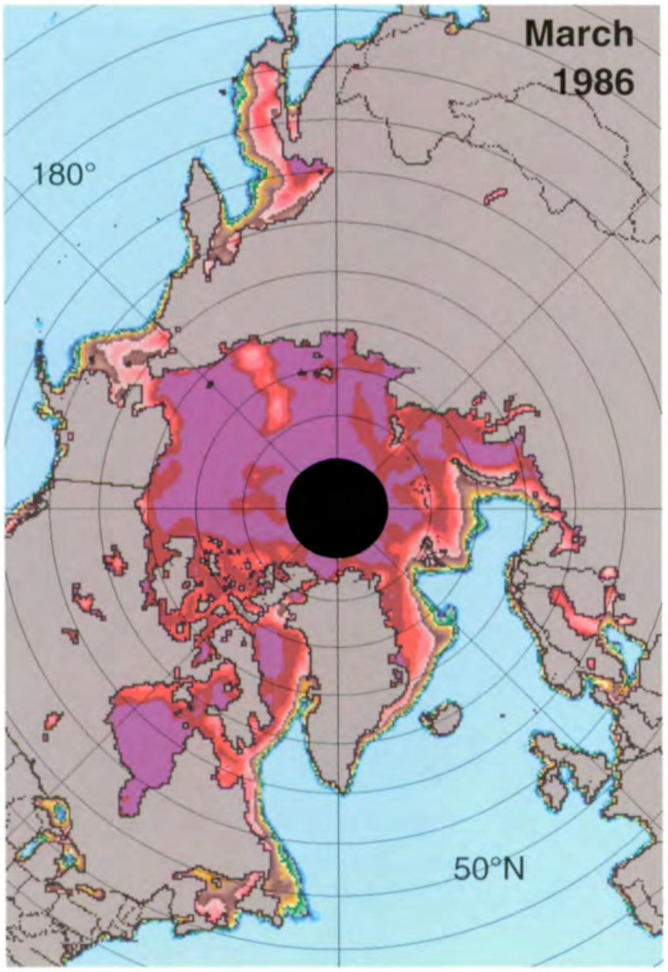
March
1986
180°
50°N

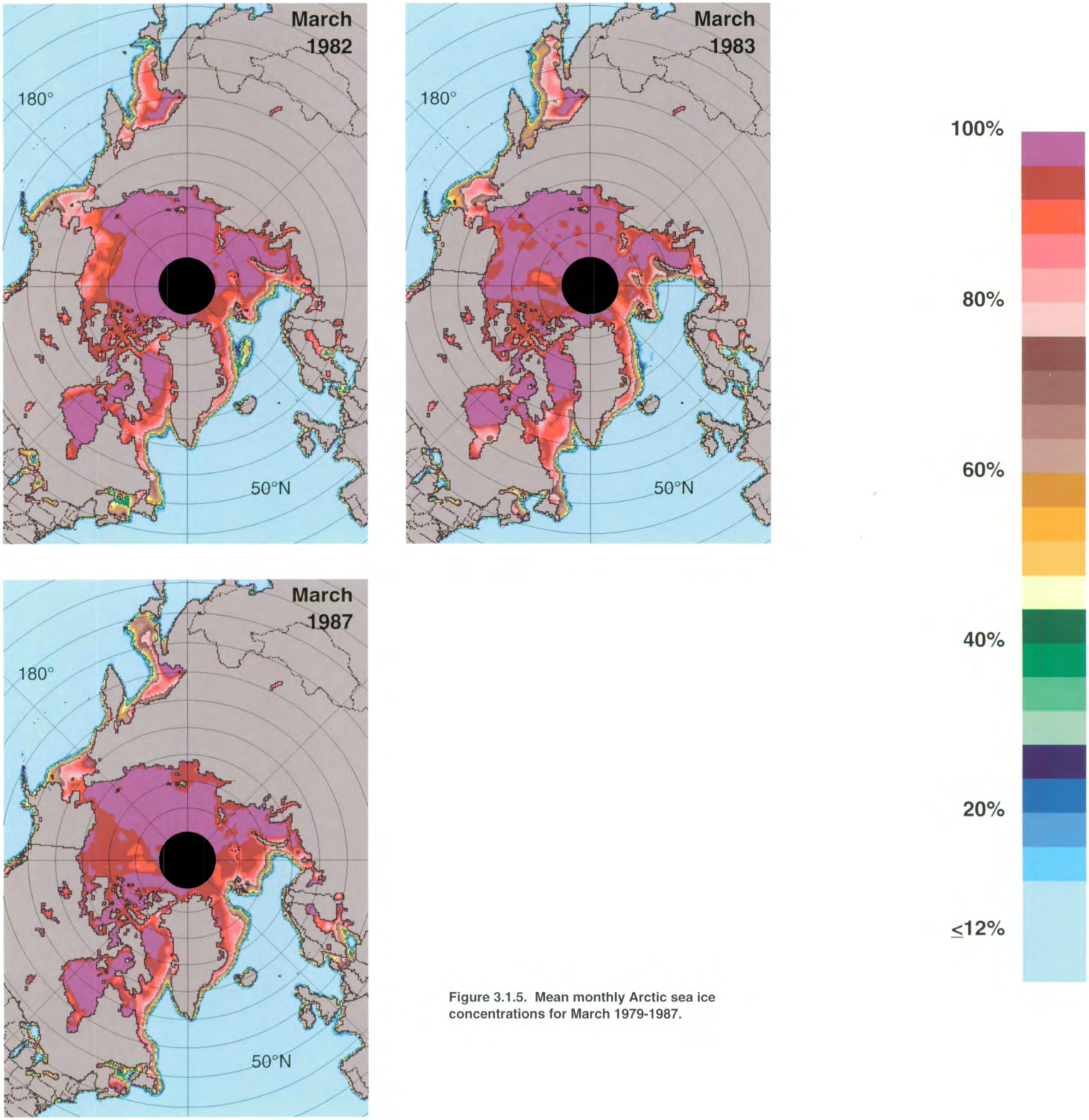

Figure 3.1.5. Mean monthly Arctic sea ice concentrations for March 1979-1987.

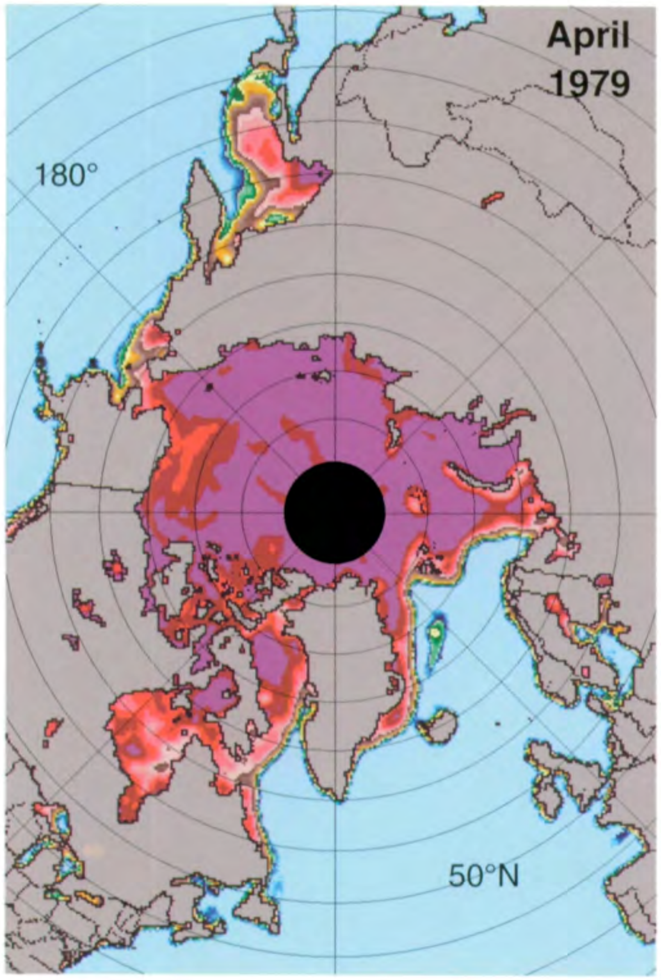
April
1979
180°
50°N

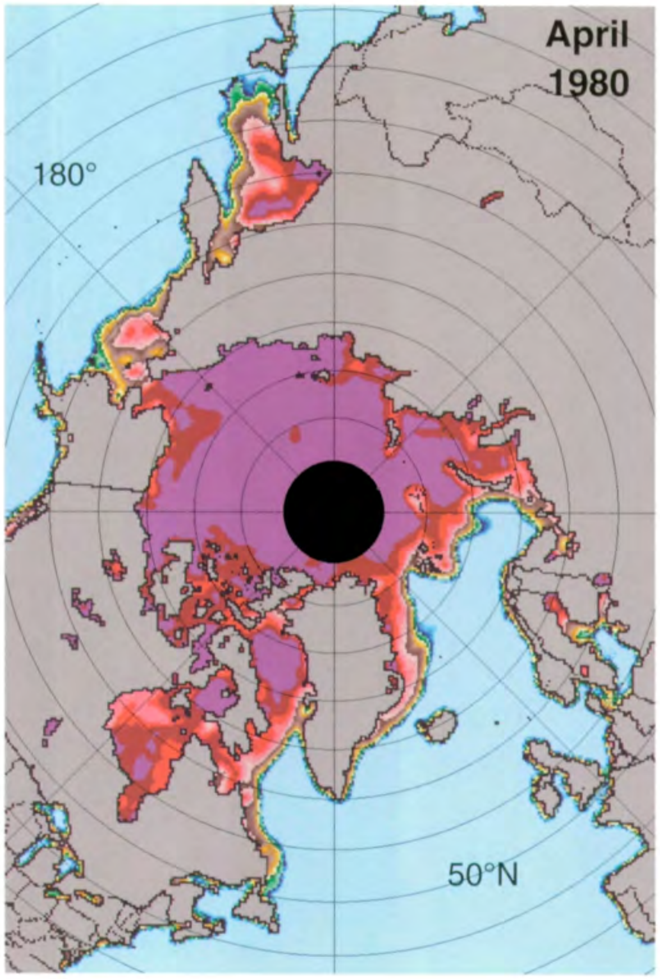
April
1980
180°
50°N

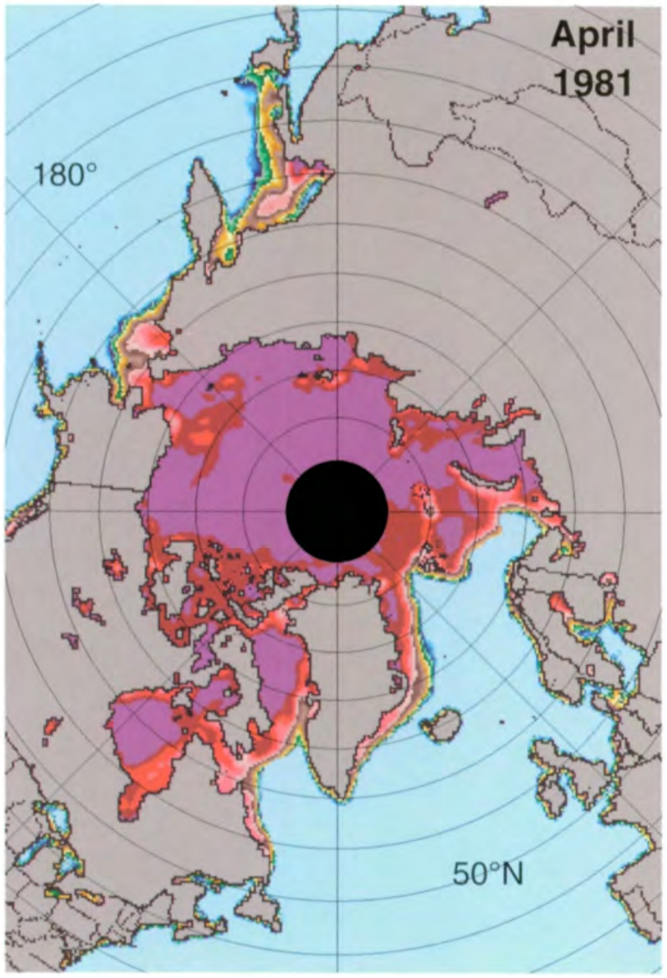
April
1981
180°
50°N

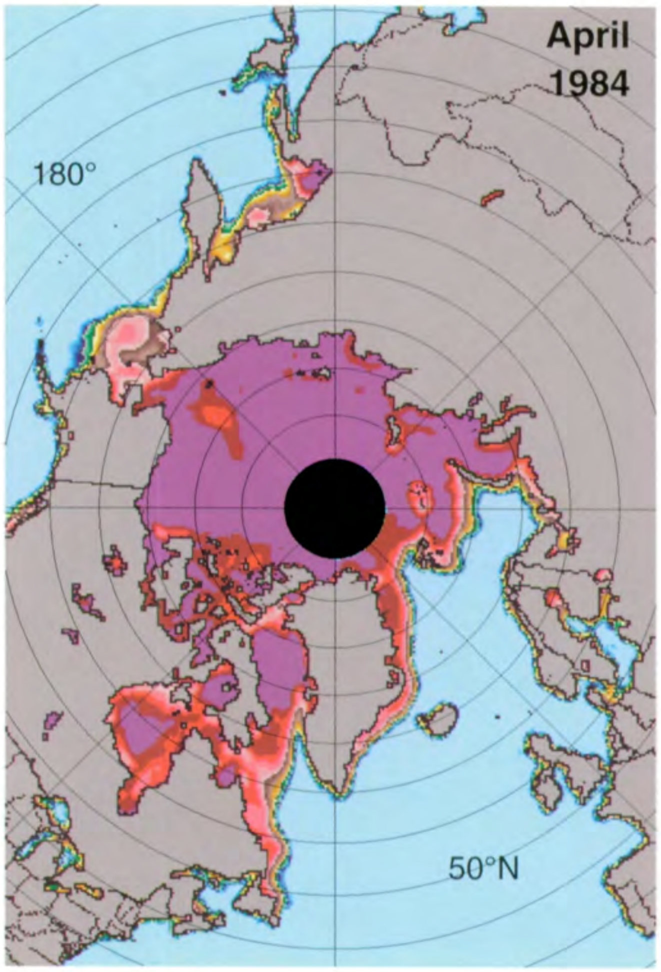
April
1984
180°
50°N

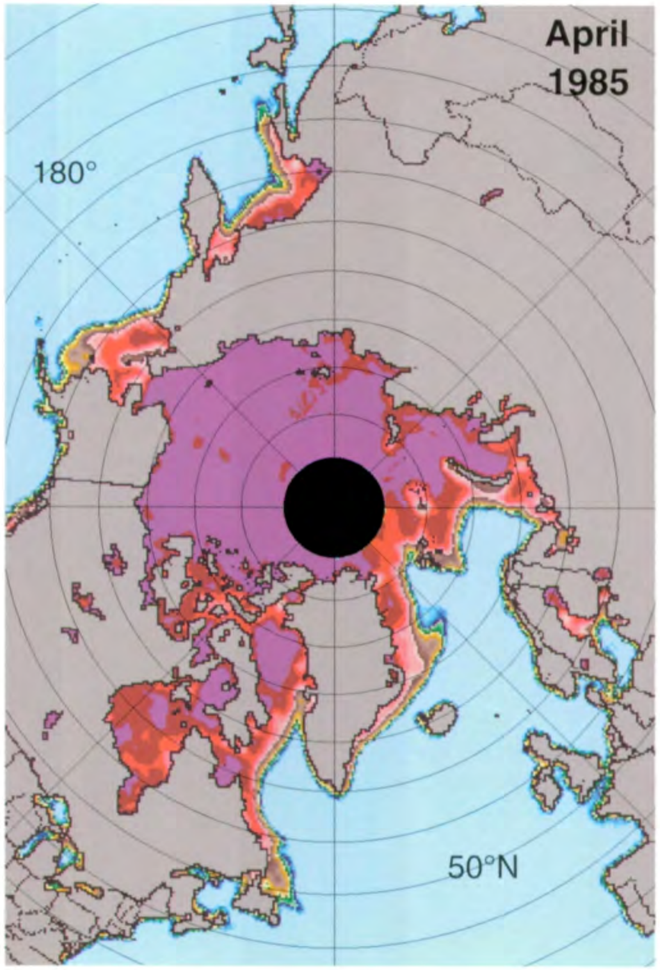
April
1985
180°
50°N

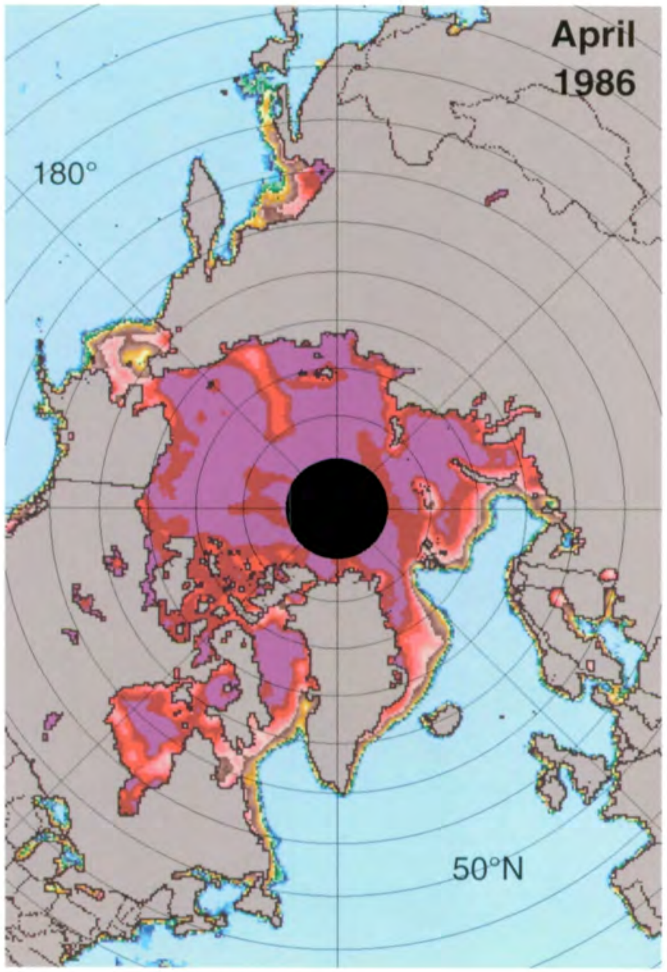
April
1986
180°
50°N

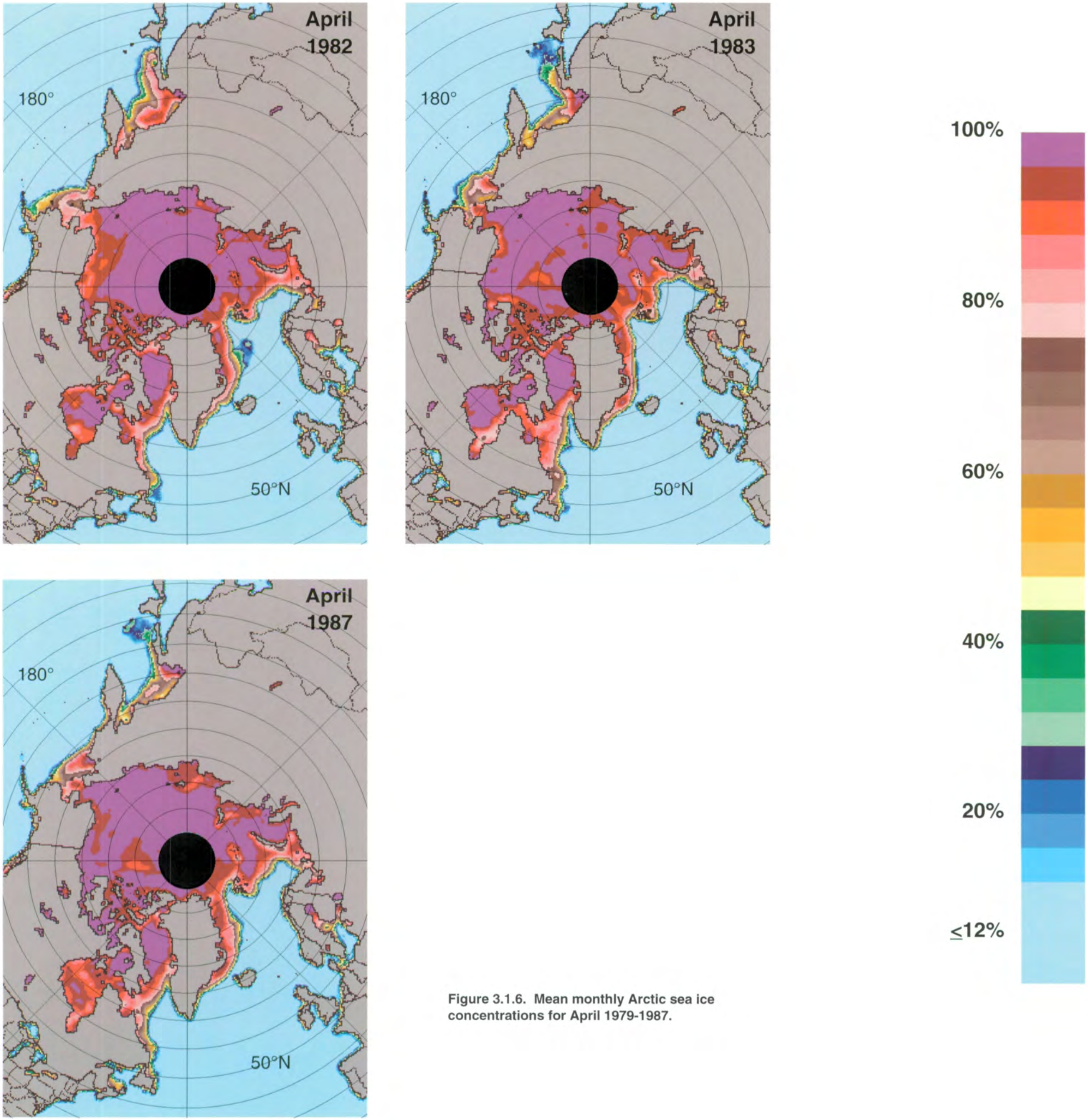

Figure 3.1.6. Mean monthly Arctic sea ice concentrations for April 1979-1987.

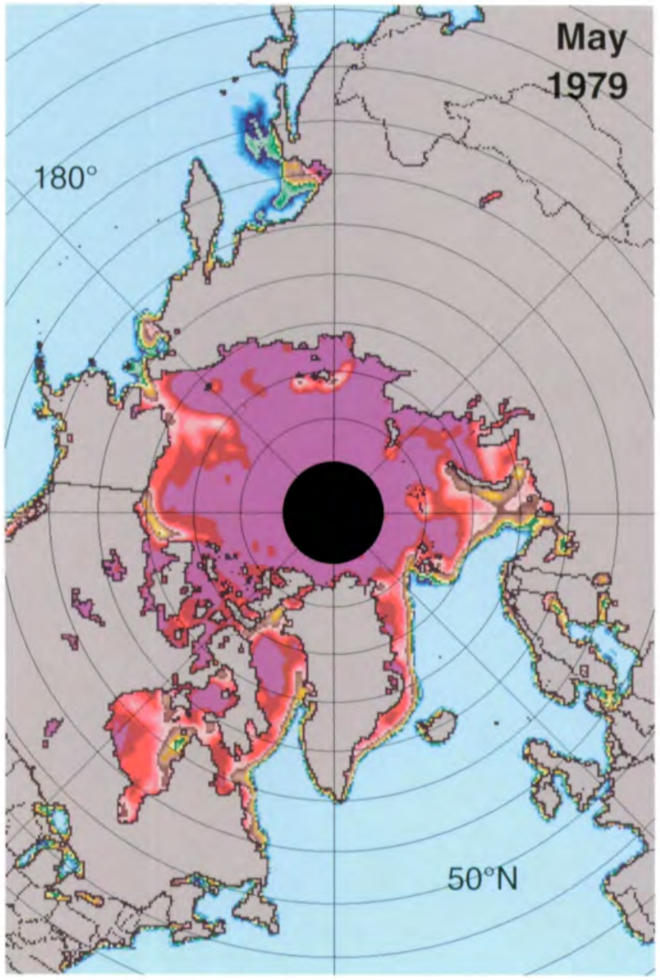
May
1979
180°
50°N

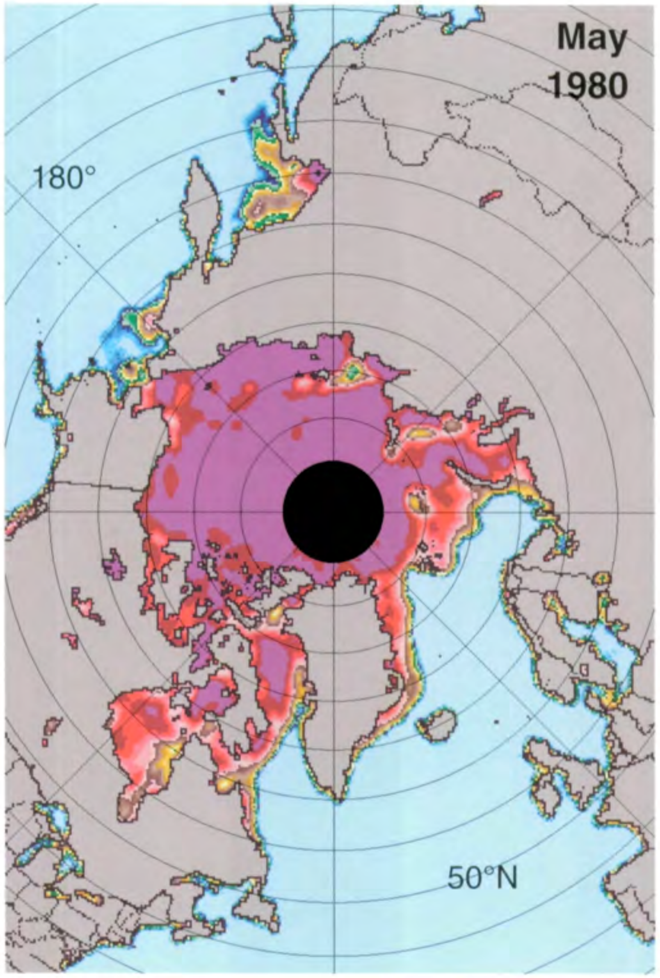
May
1980
180°
50°N

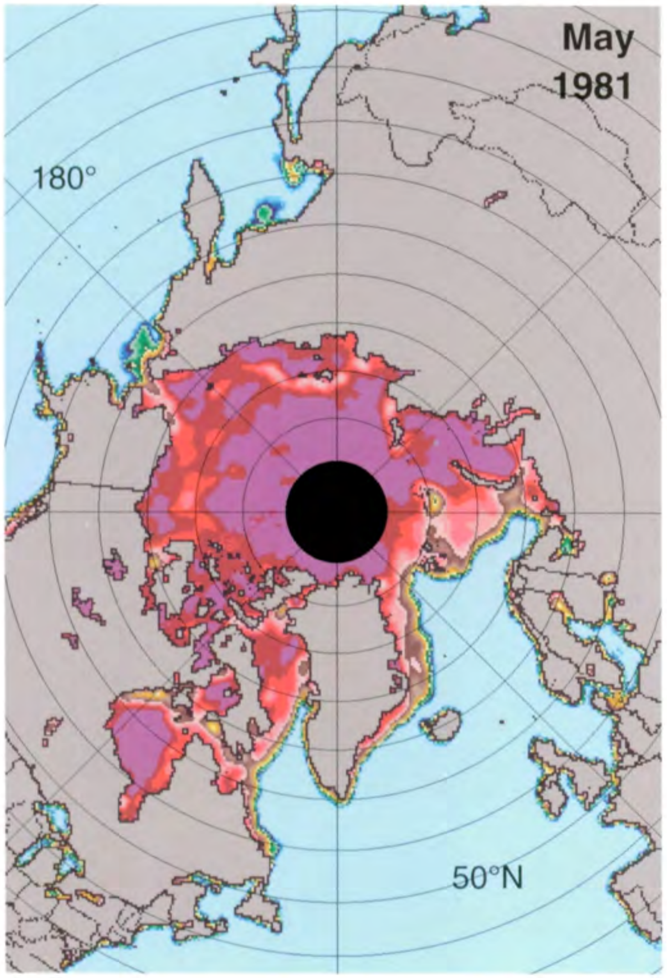
May
1981
180°
50°N

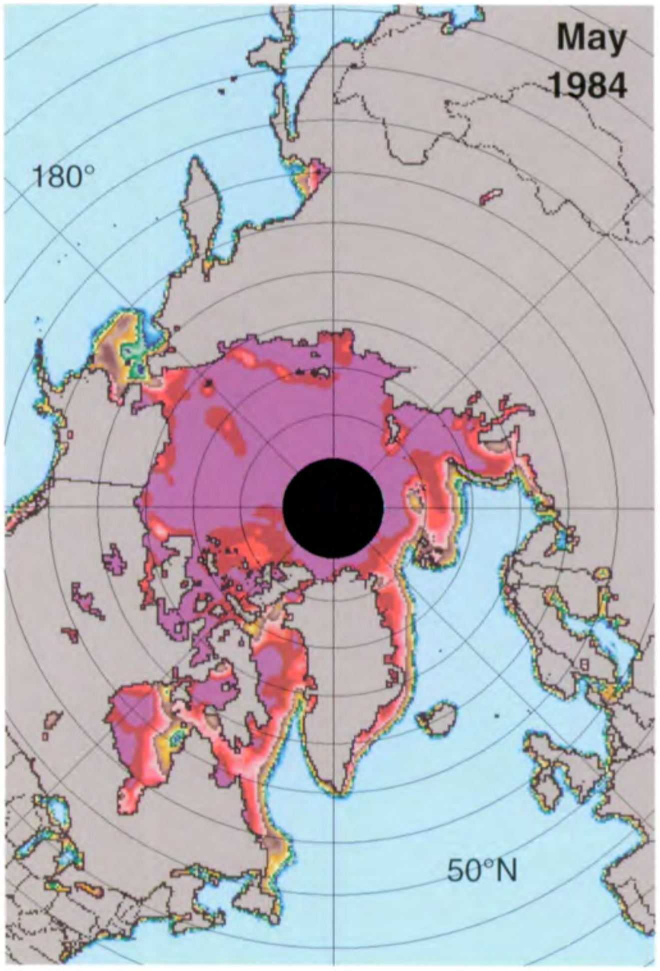
May
1984
180°
50°N

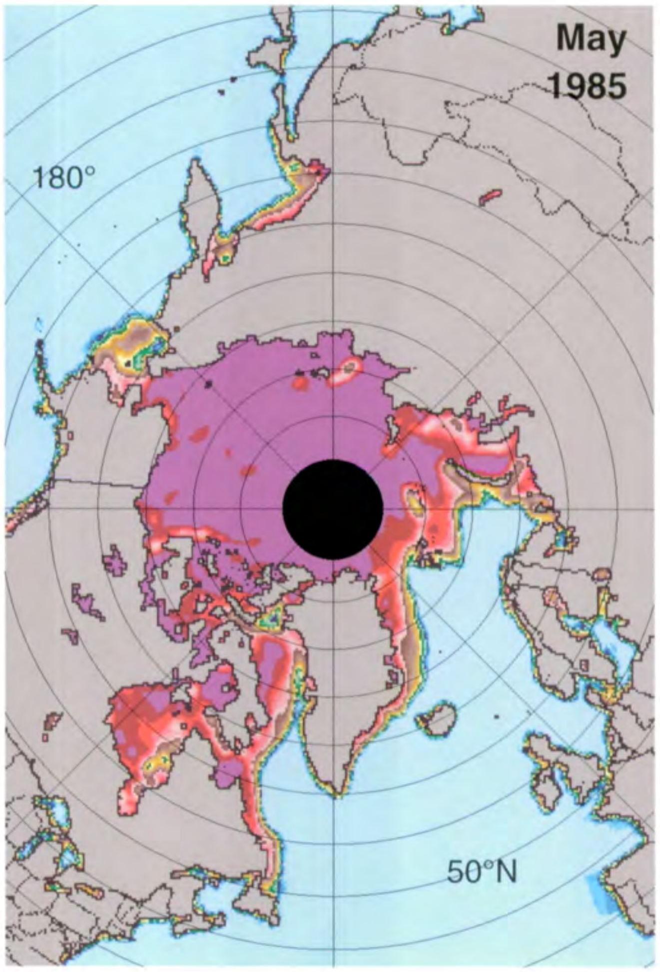
May
1985
180°
50°N

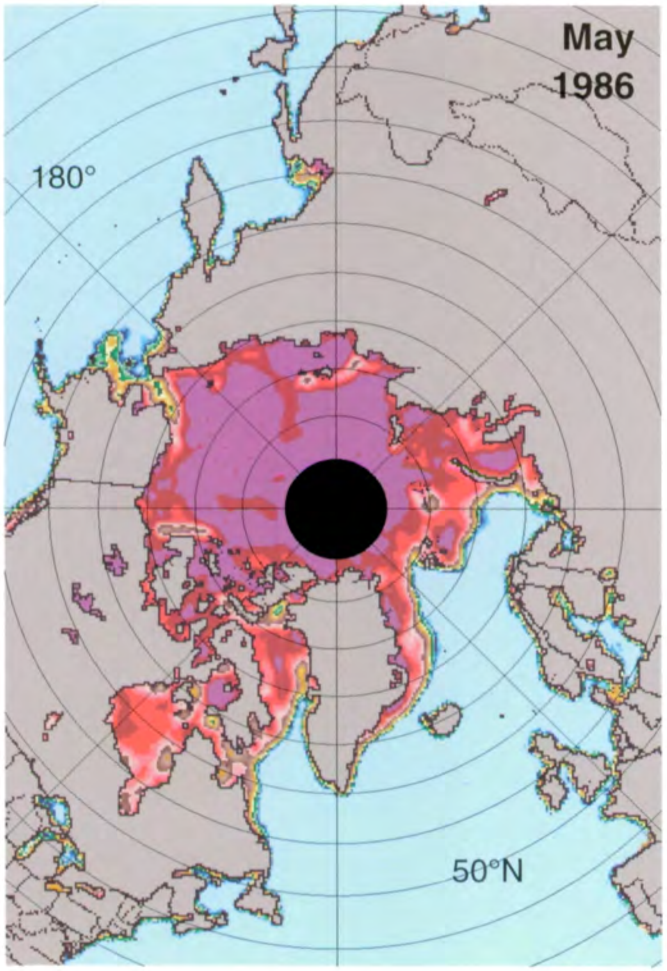
May
1986
180°
50°N

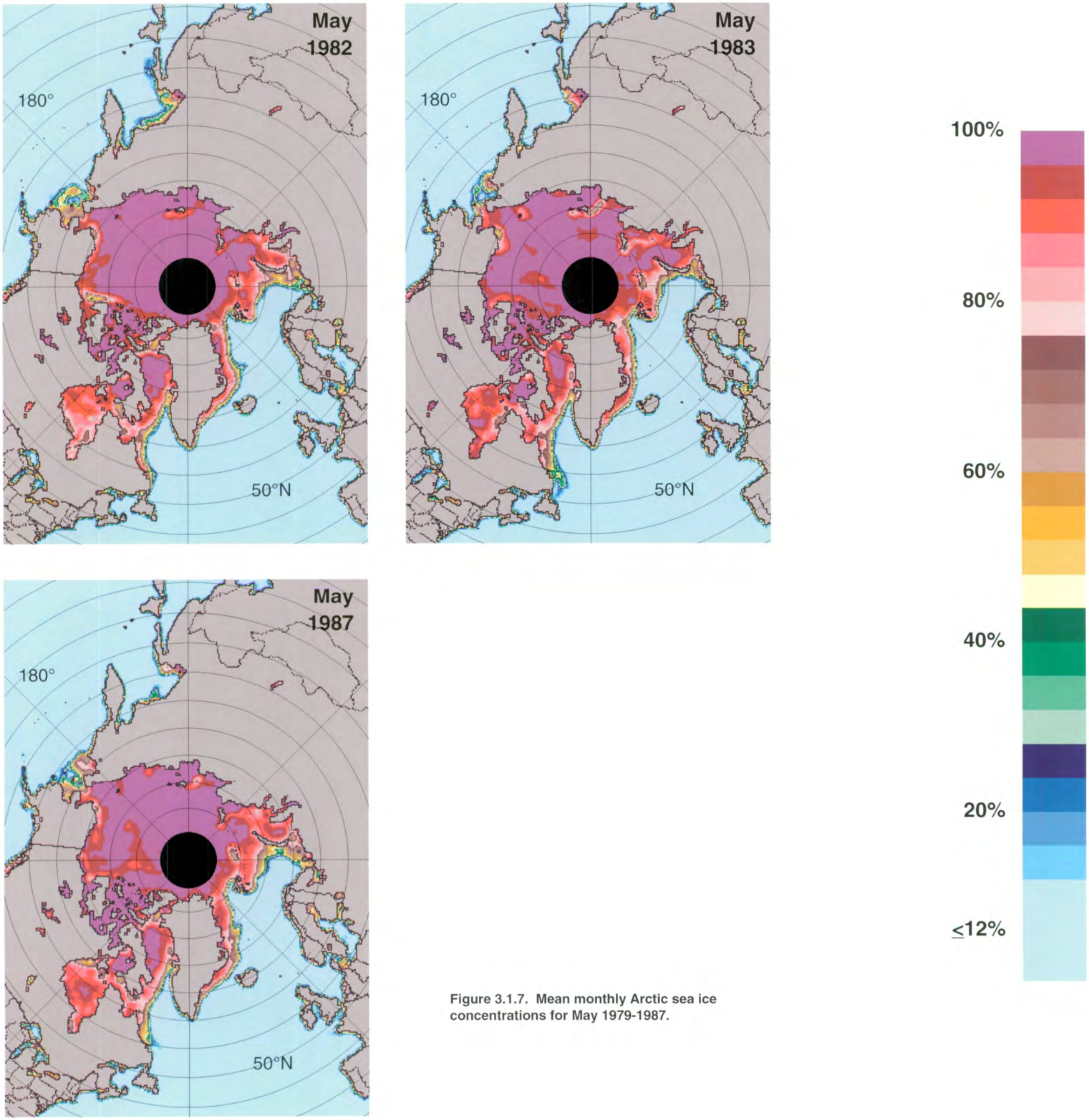

Figure 3.1.7. Mean monthly Arctic sea ice concentrations for May 1979-1987.

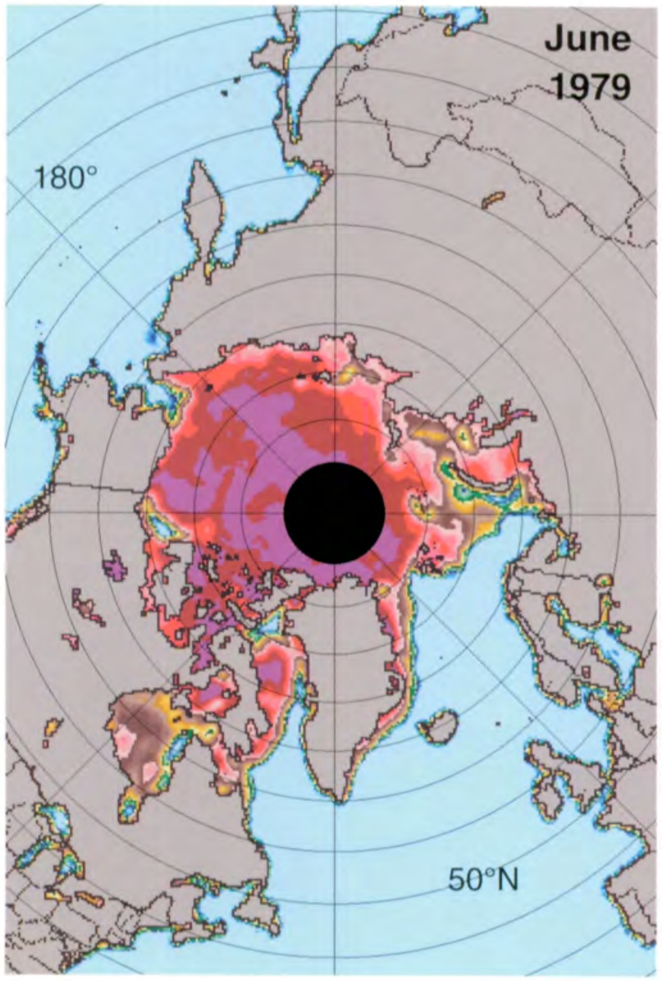
June
1979
180°
50°N

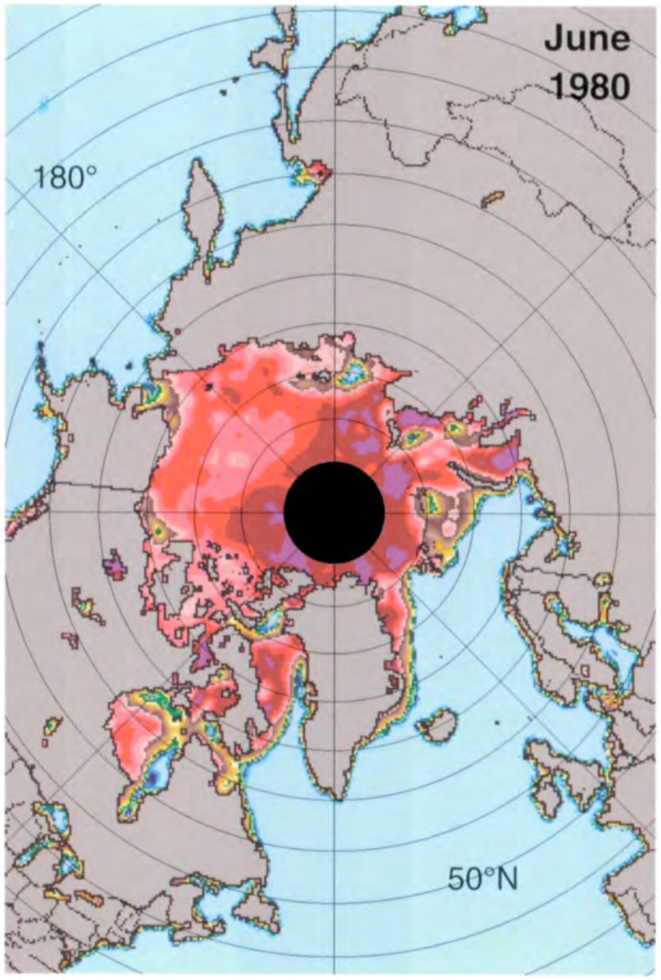
June
1980
180°
50°N

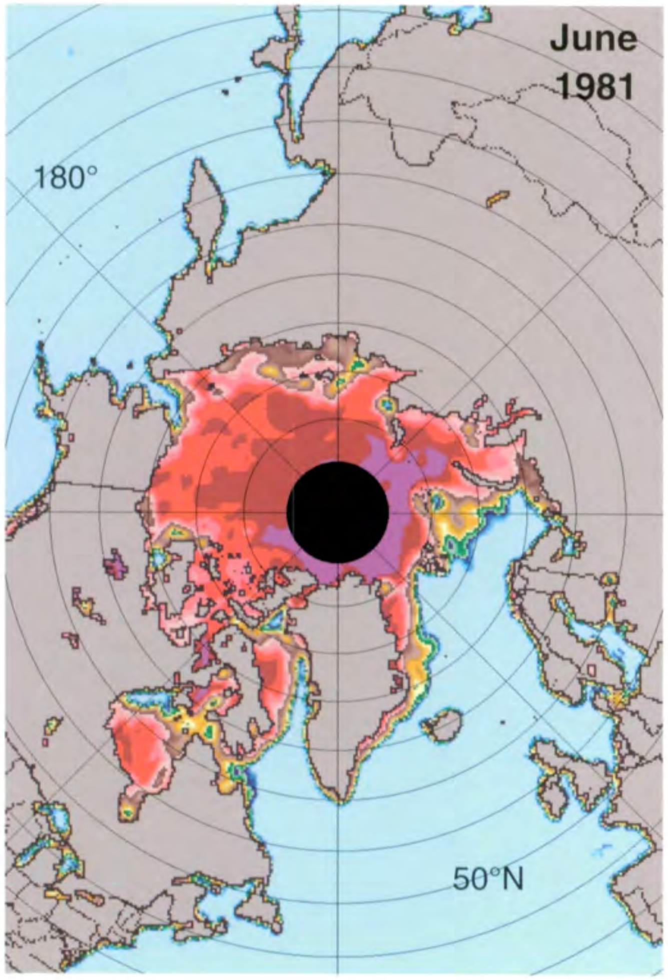
June
1981
180°
50°N

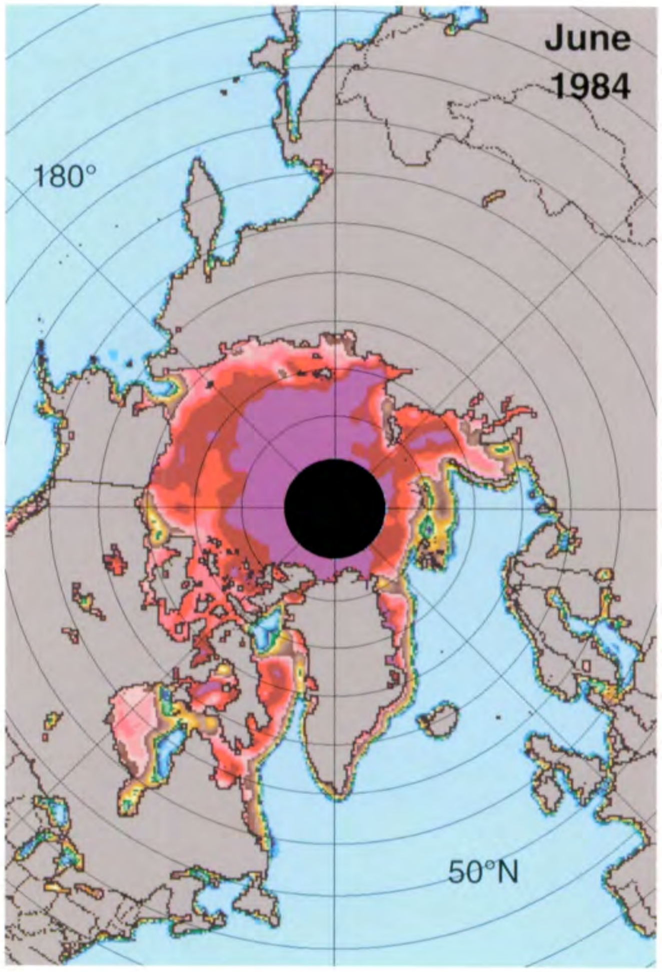
June
1984
180°
50°N

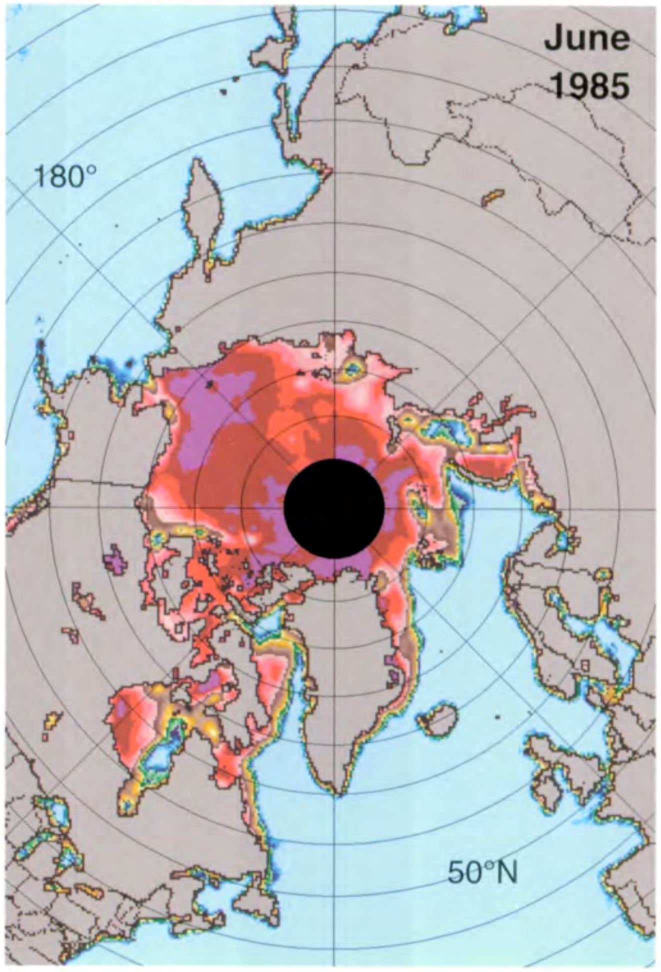
June
1985
180°
50°N

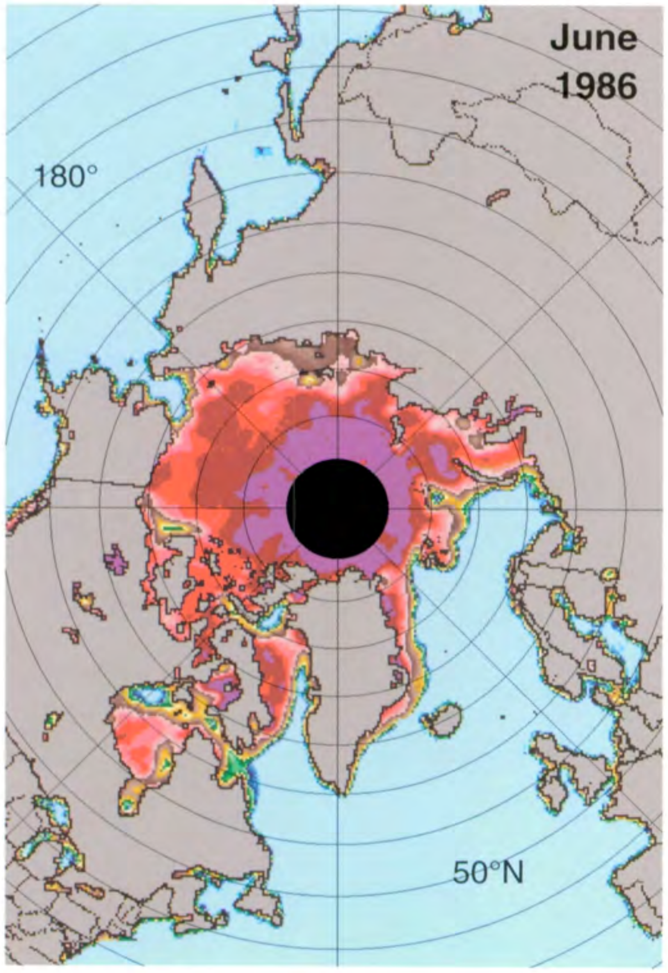
June
1986
180°
50°N

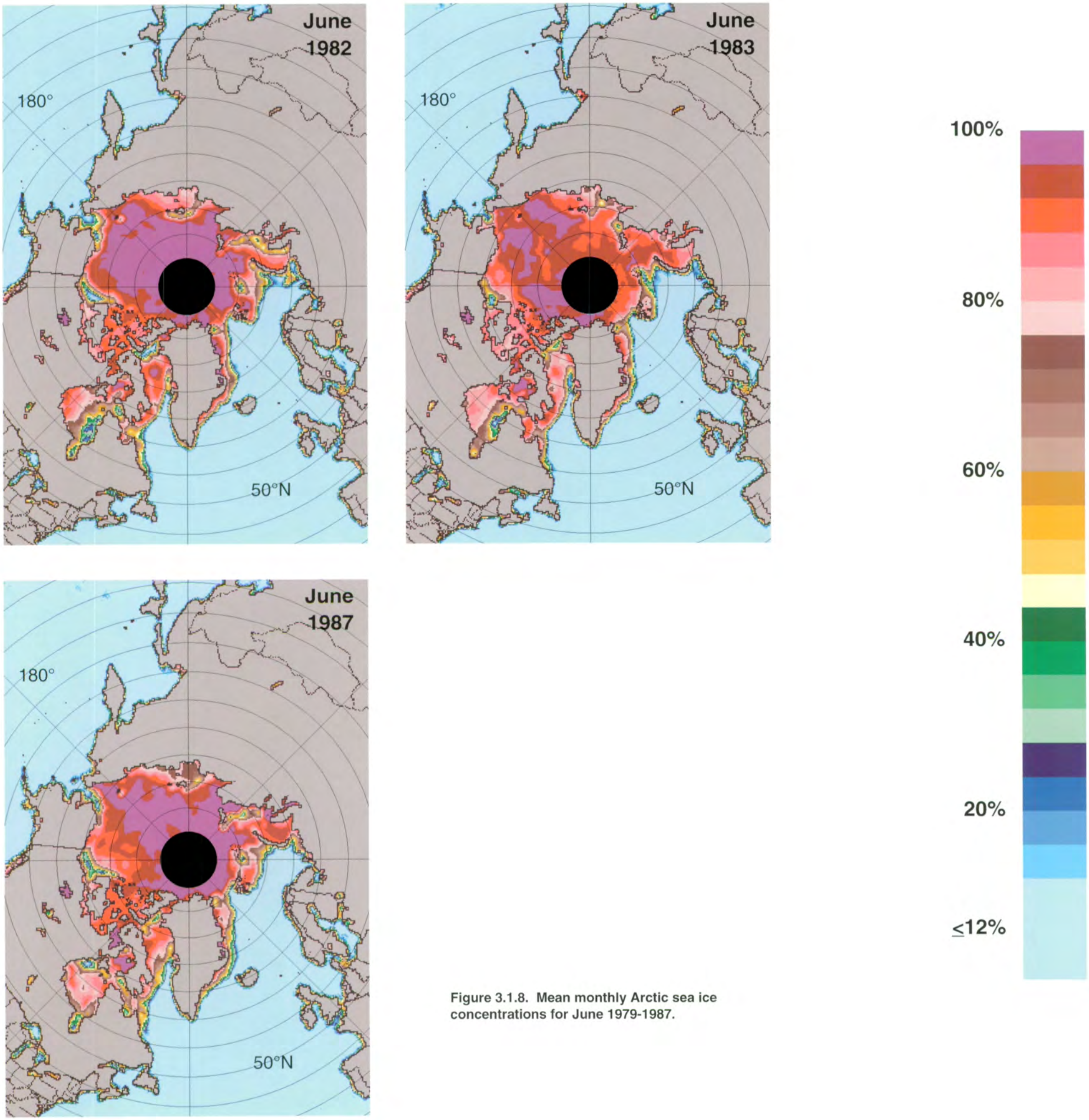

Figure 3.1.8. Mean monthly Arctic sea ice concentrations for June 1979-1987.

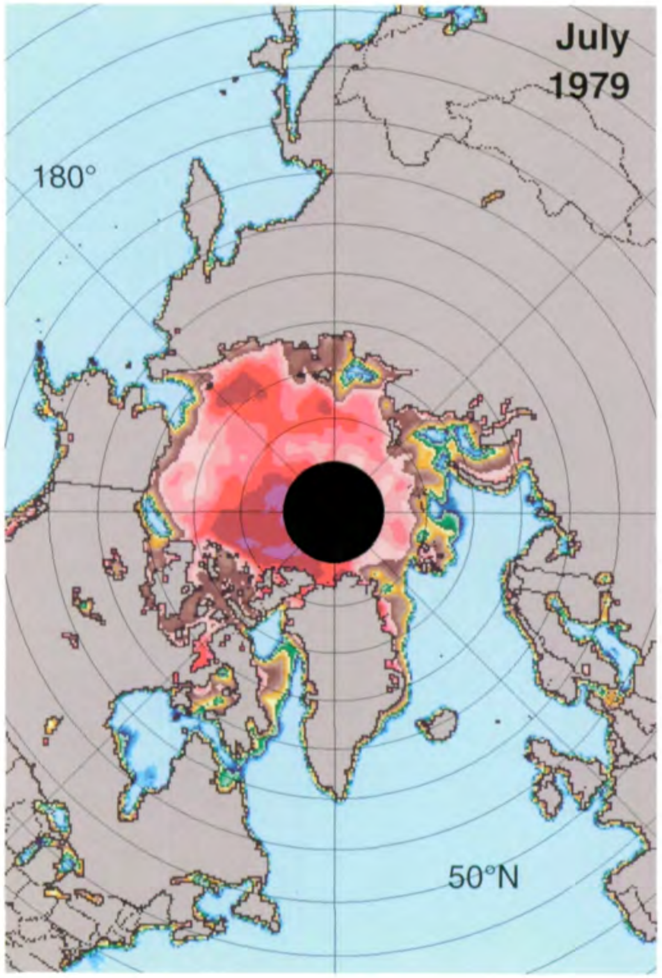
July
1979
180°
50°N

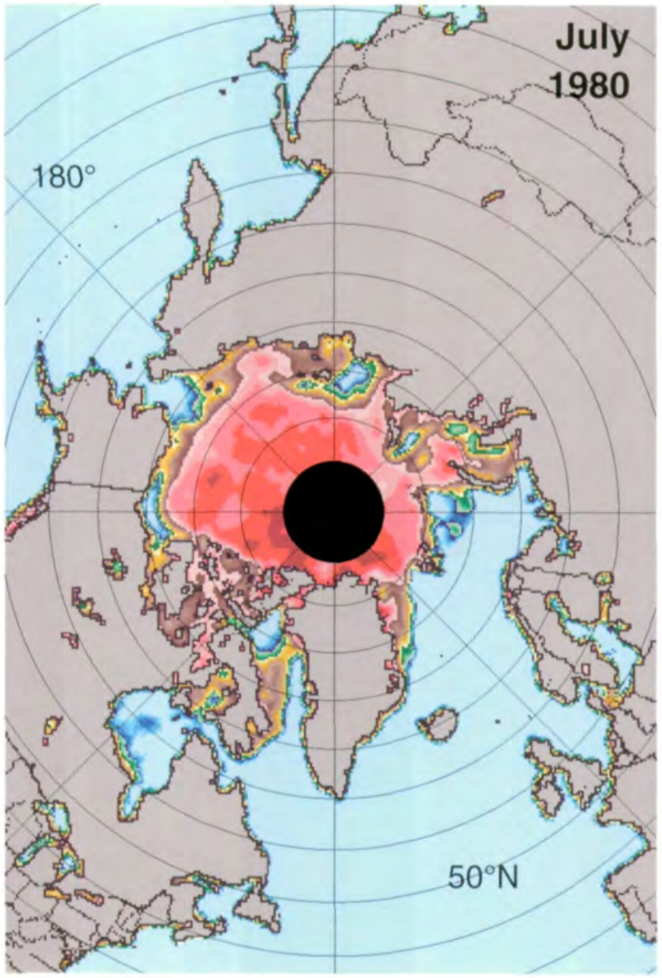
July
1980
180°
50°N

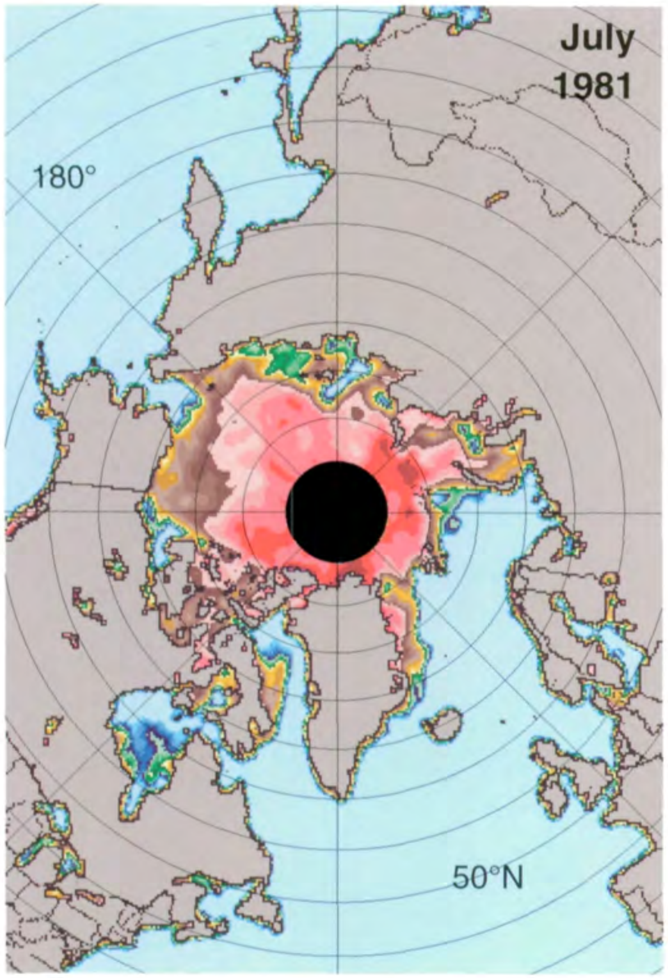
July
1981
180°
50°N

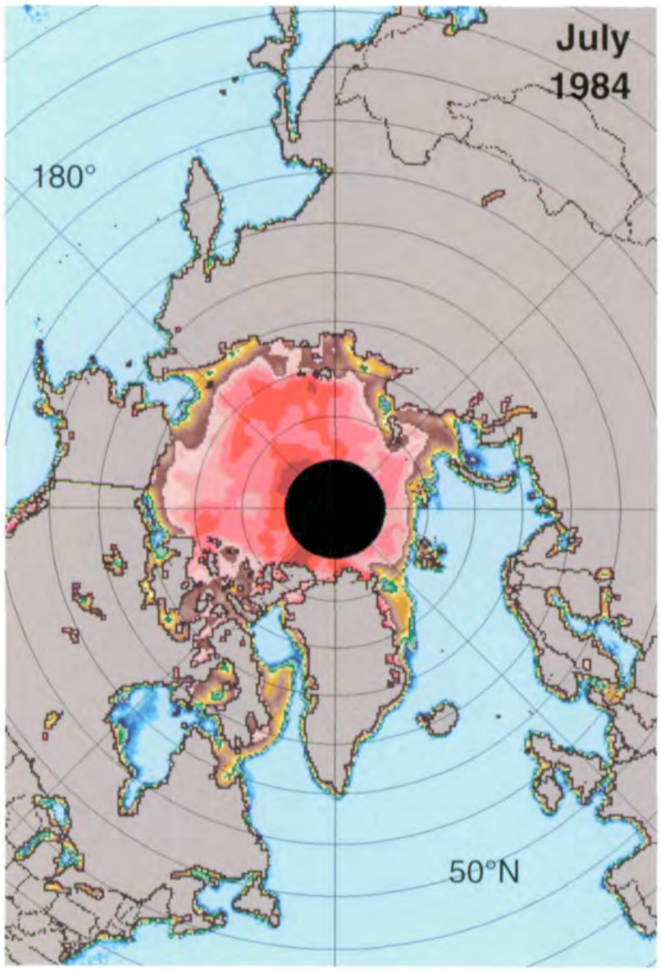
July
1984
180°
50°N

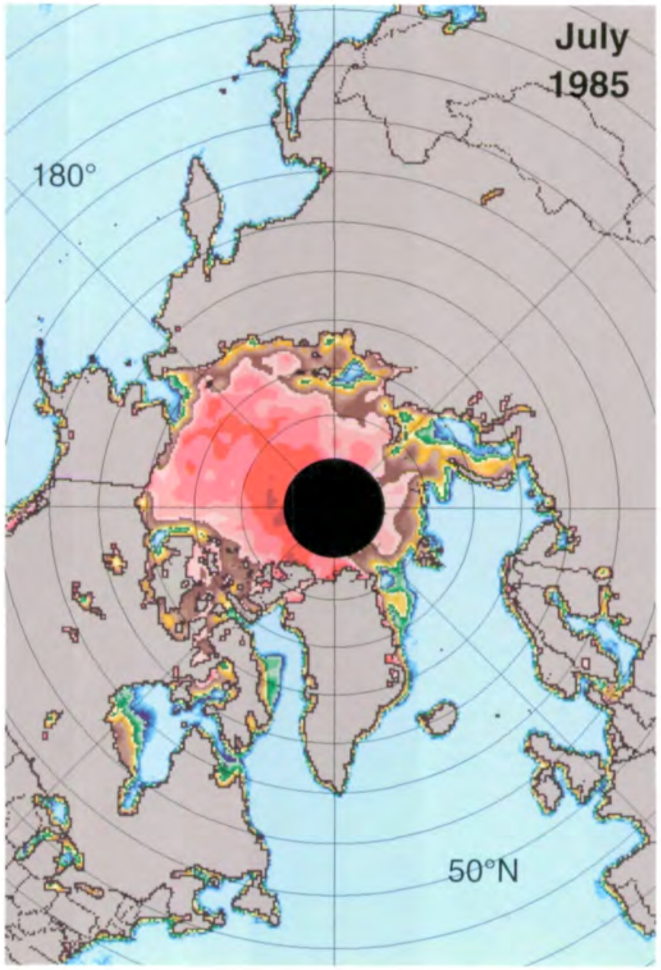
July
1985
180°
50°N

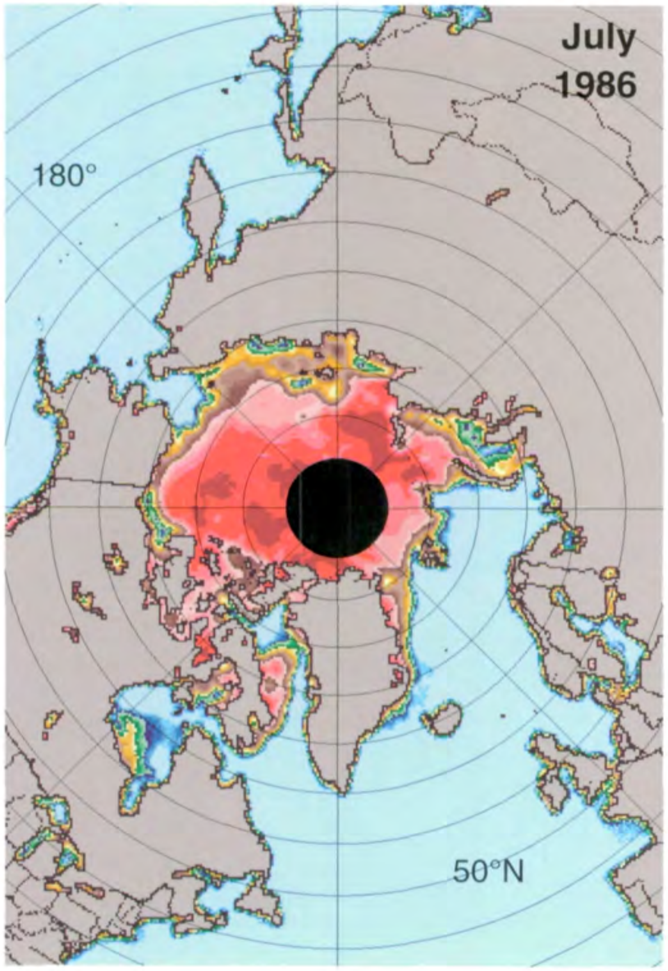
July
1986
180°
50°N

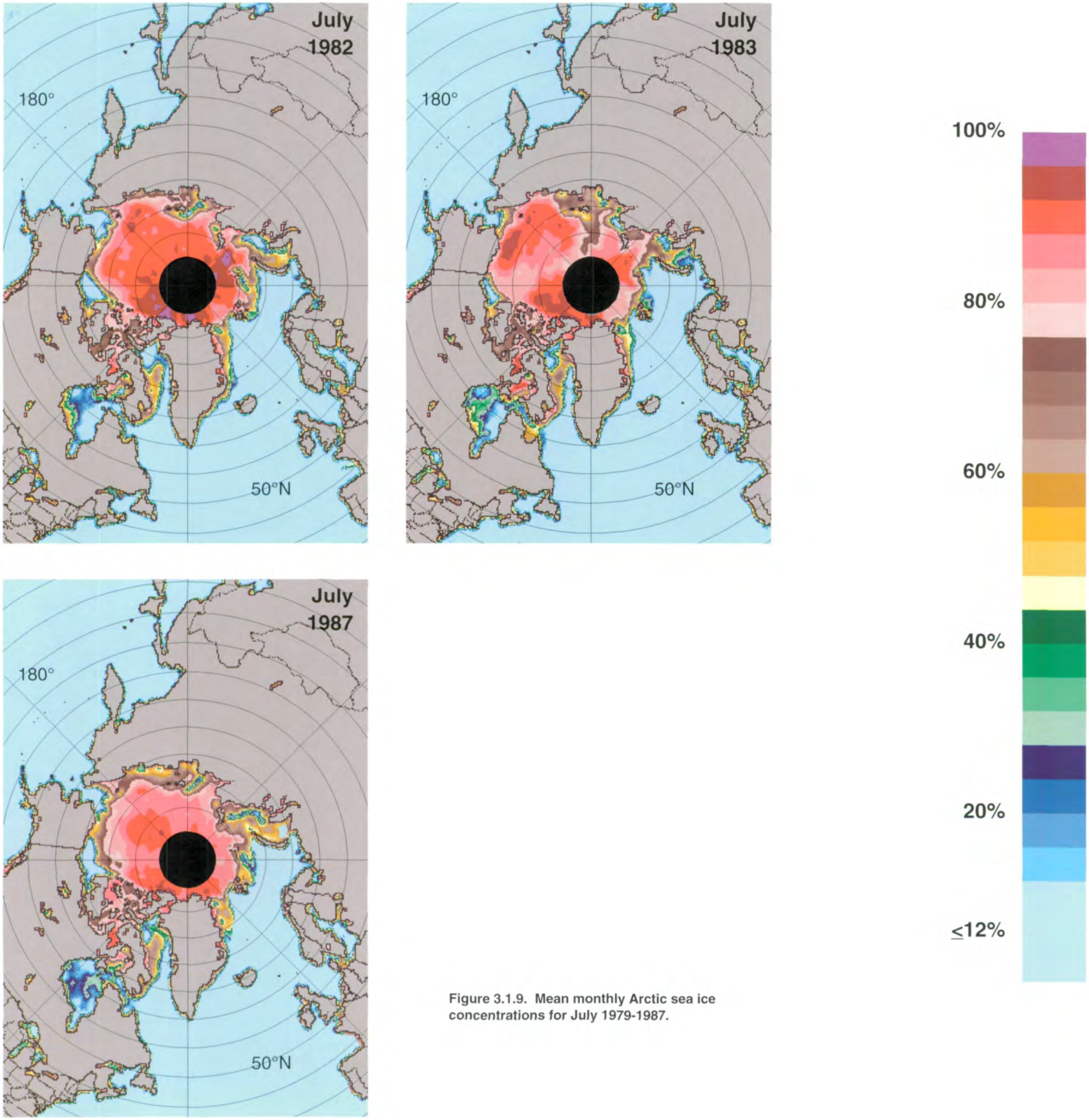

Figure 3.1.9. Mean monthly Arctic sea ice concentrations for July 1979-1987.

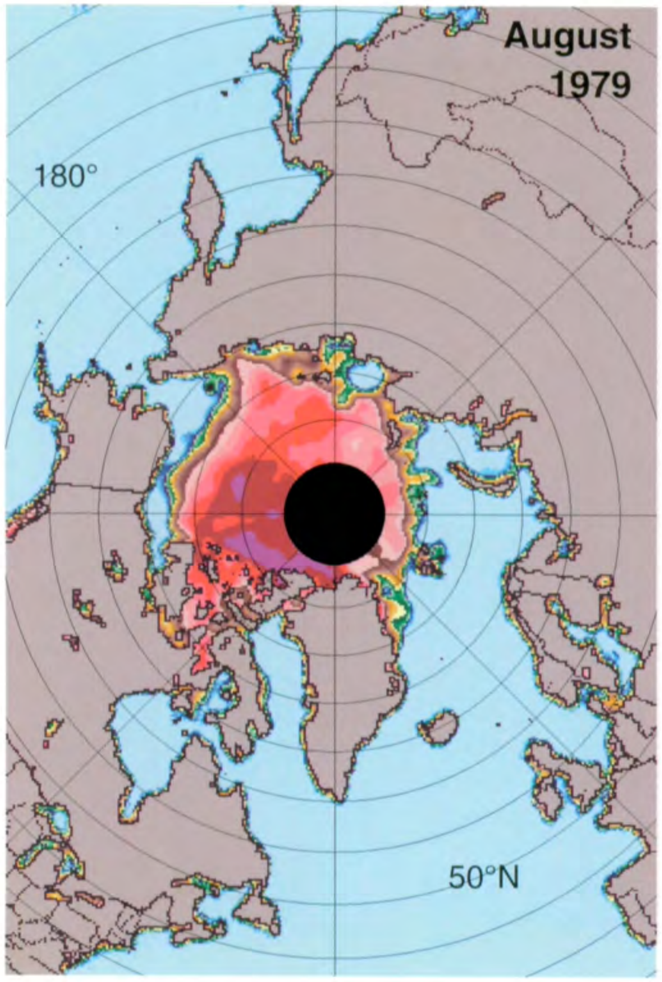
August
1979
180°
50°N

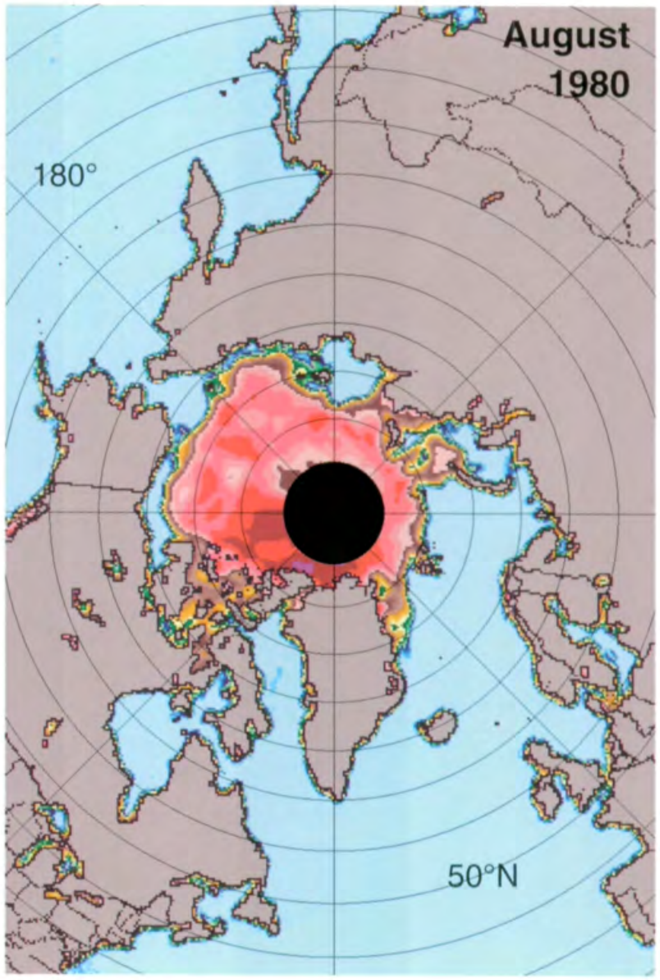
August
1980
180°
50°N

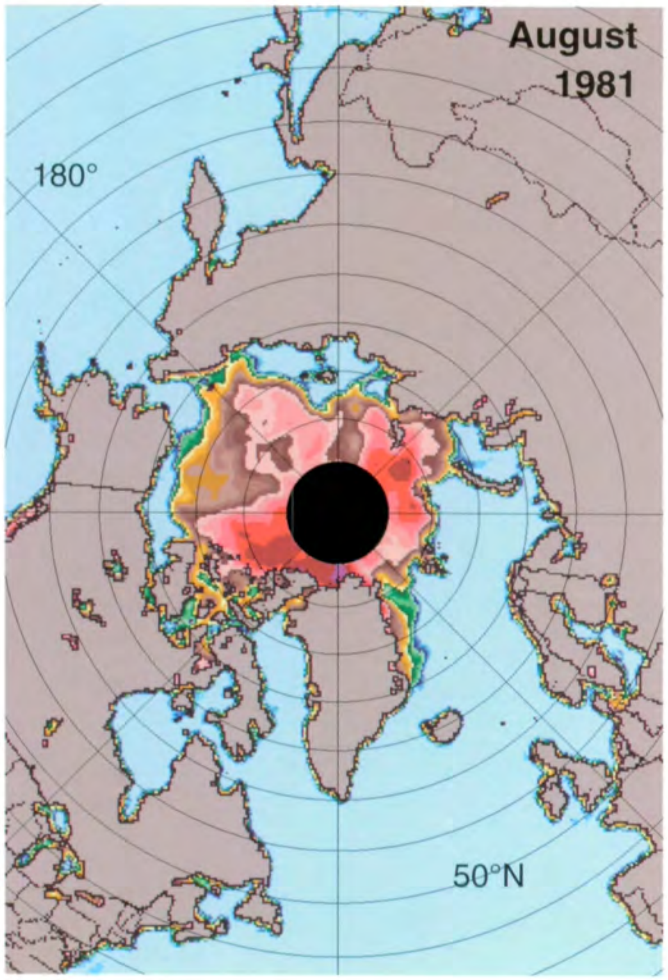
August
1981
180°
50°N

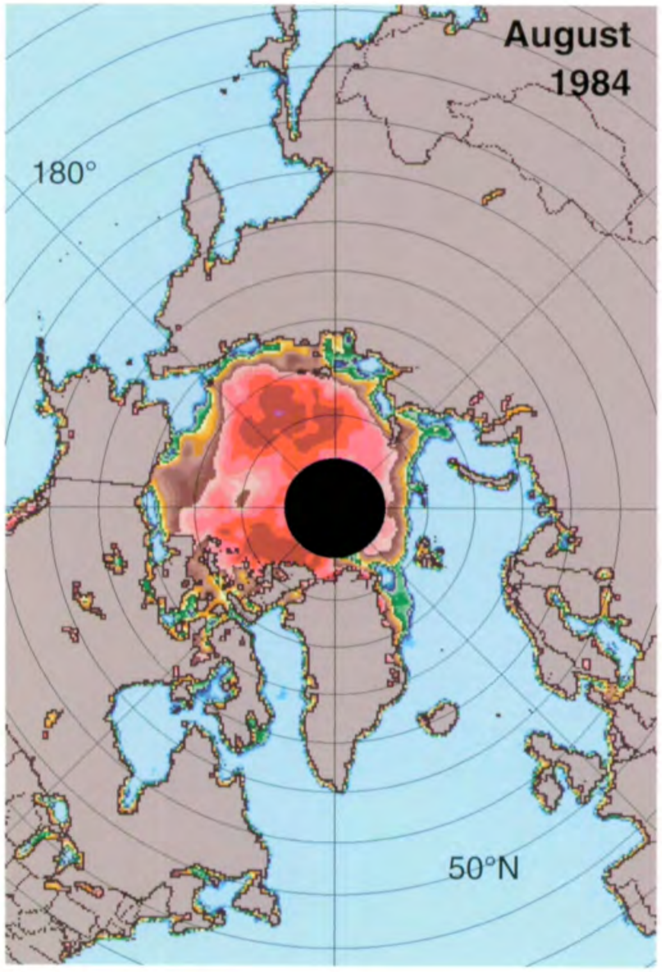
August
1984
180°
50°N

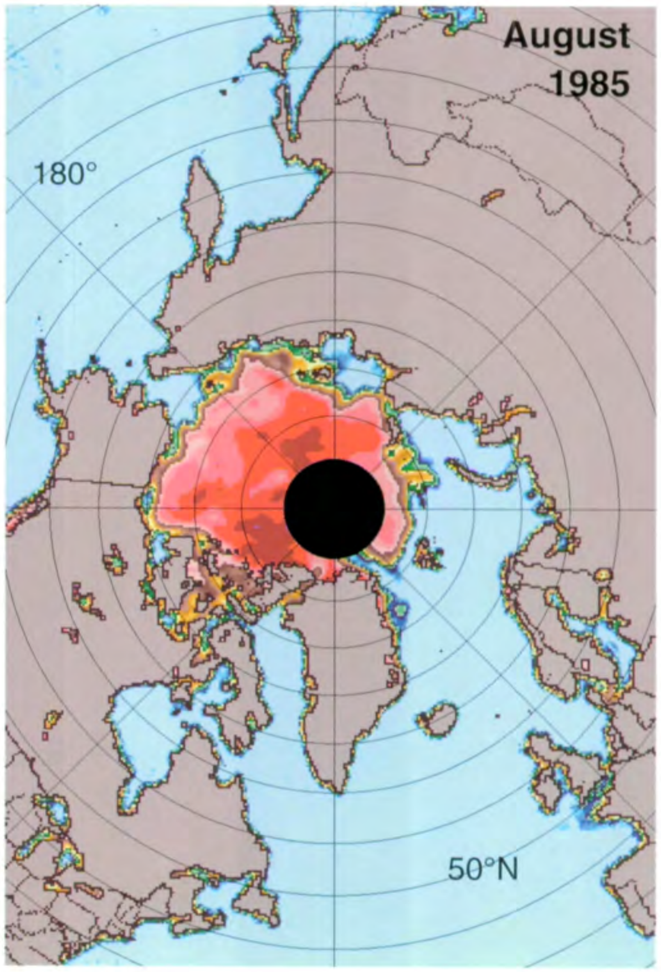
August
1985
180°
50°N

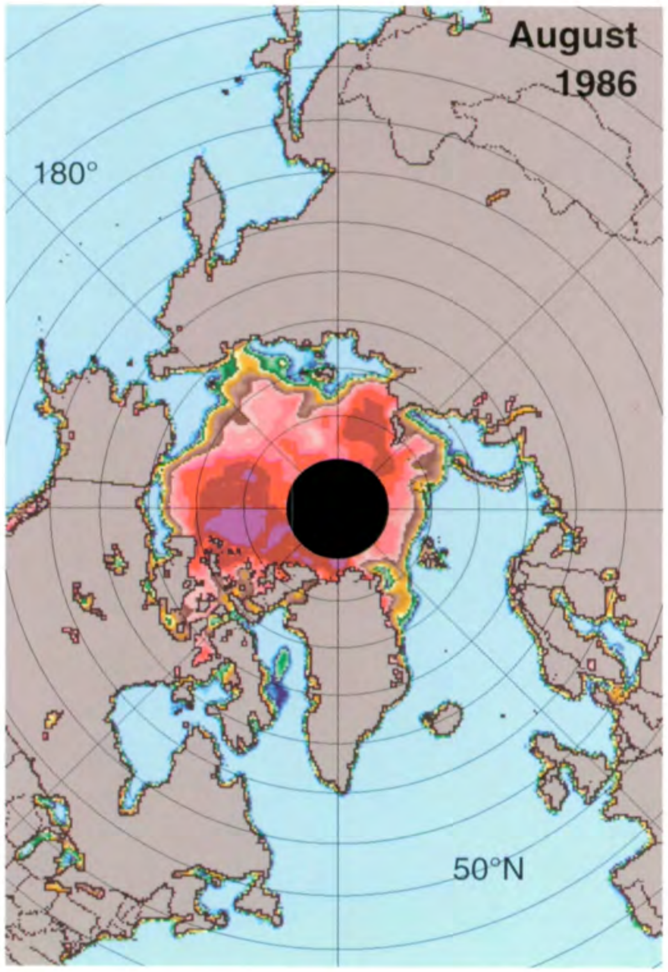
August
1986
180°
50°N

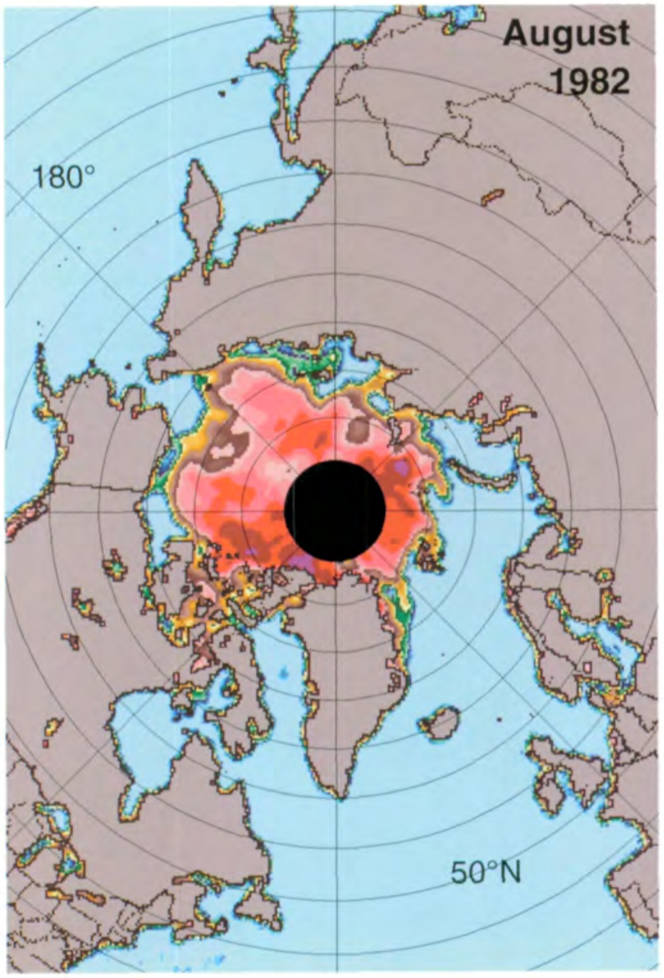

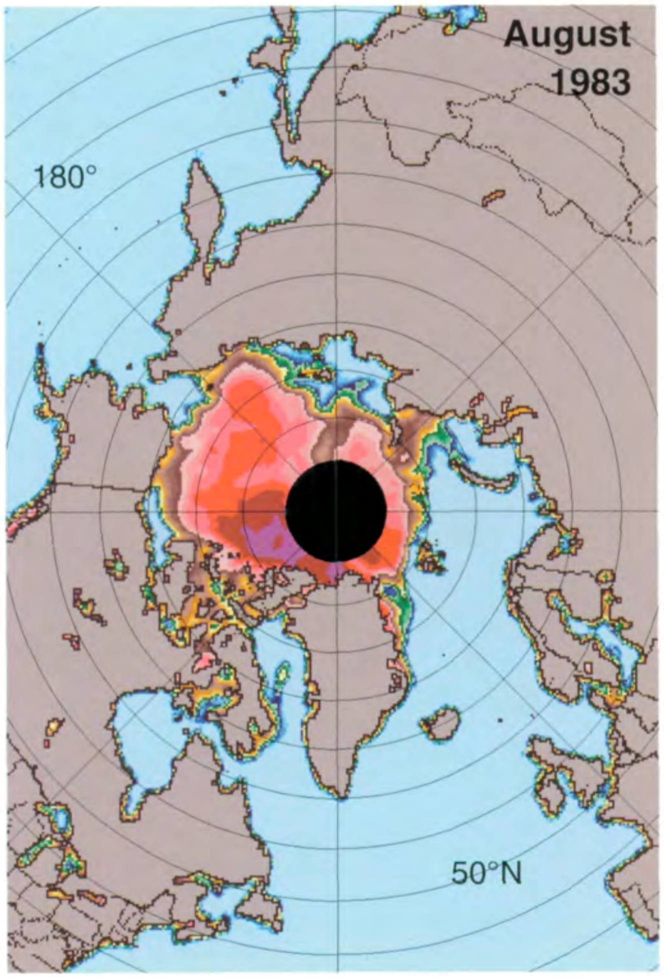

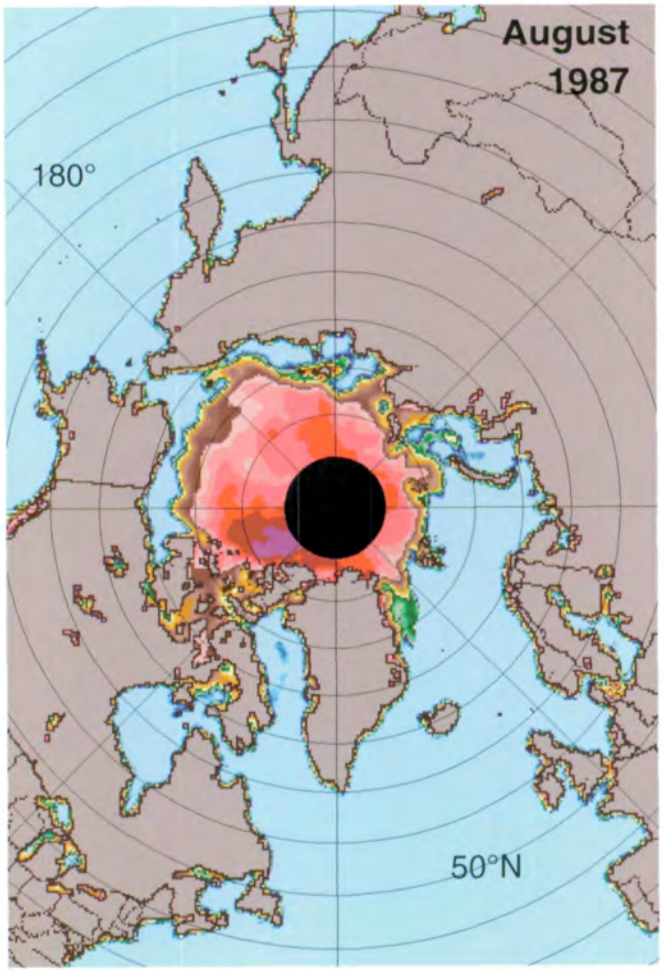

Figure 3.1.10. Mean monthly Arctic sea ice concentrations for August 1979-1987.

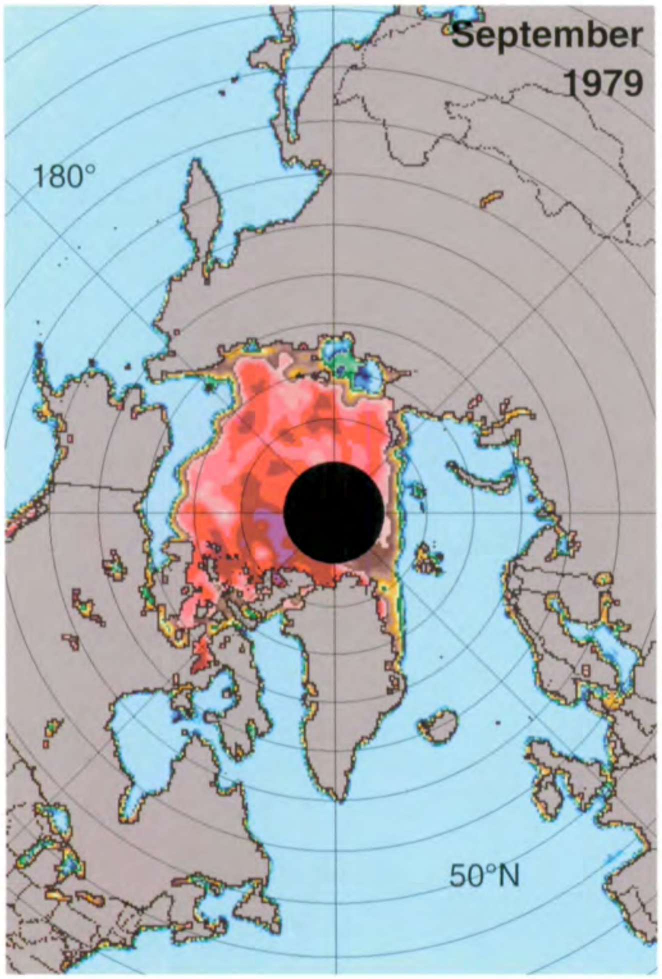
September
1979
180°
50°N

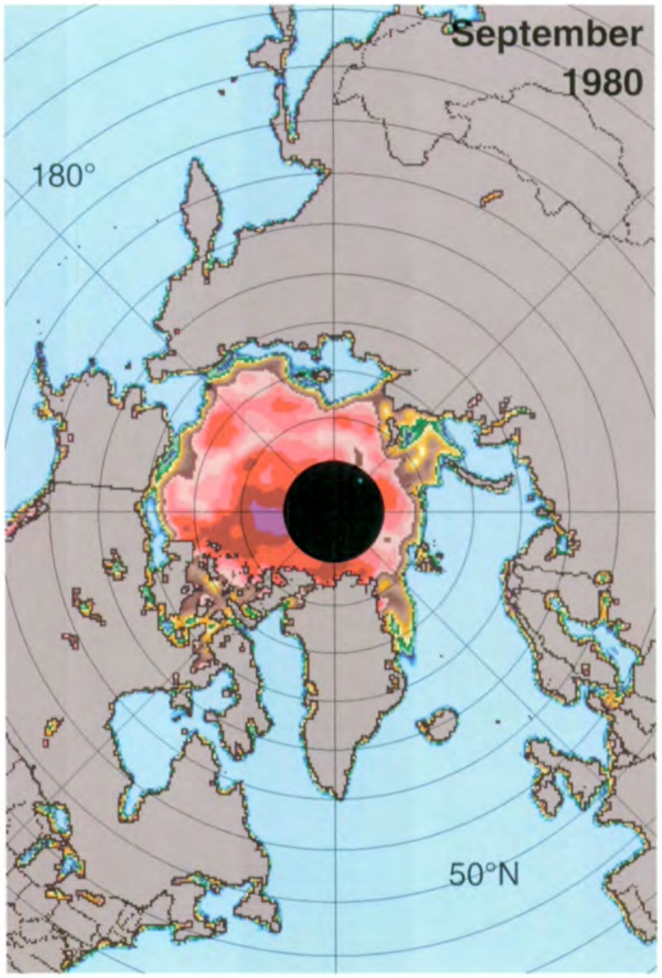
September
1980
180°
50°N

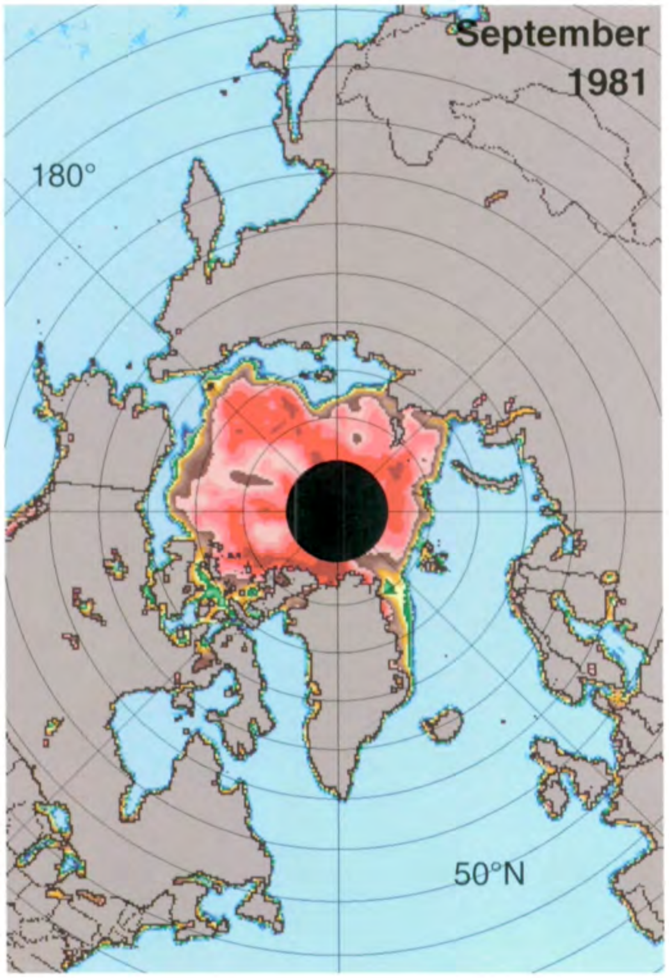
September
1981
180°
50°N

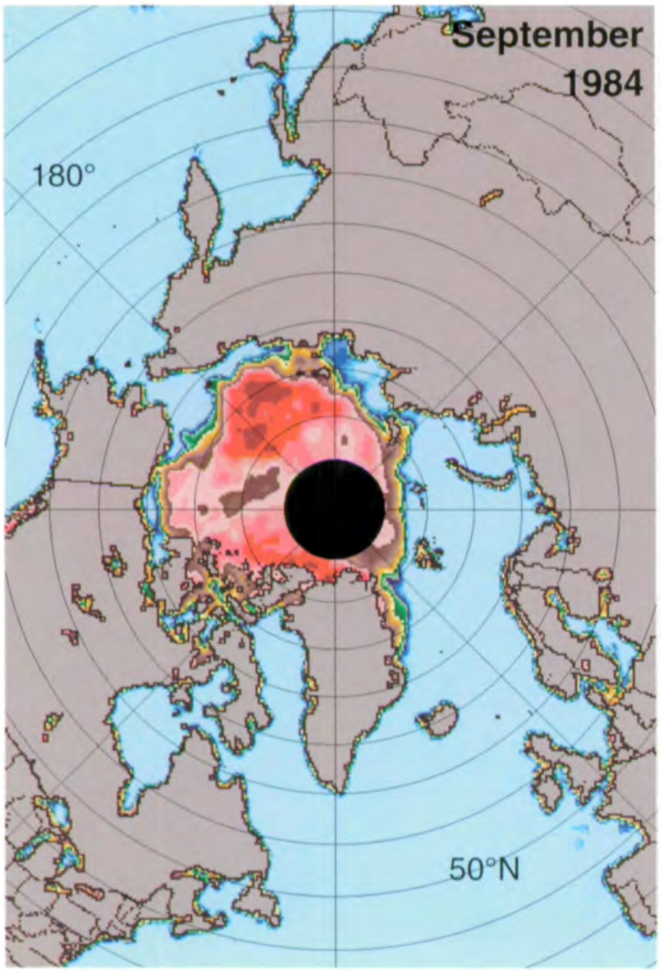
September
1984
180°
50°N

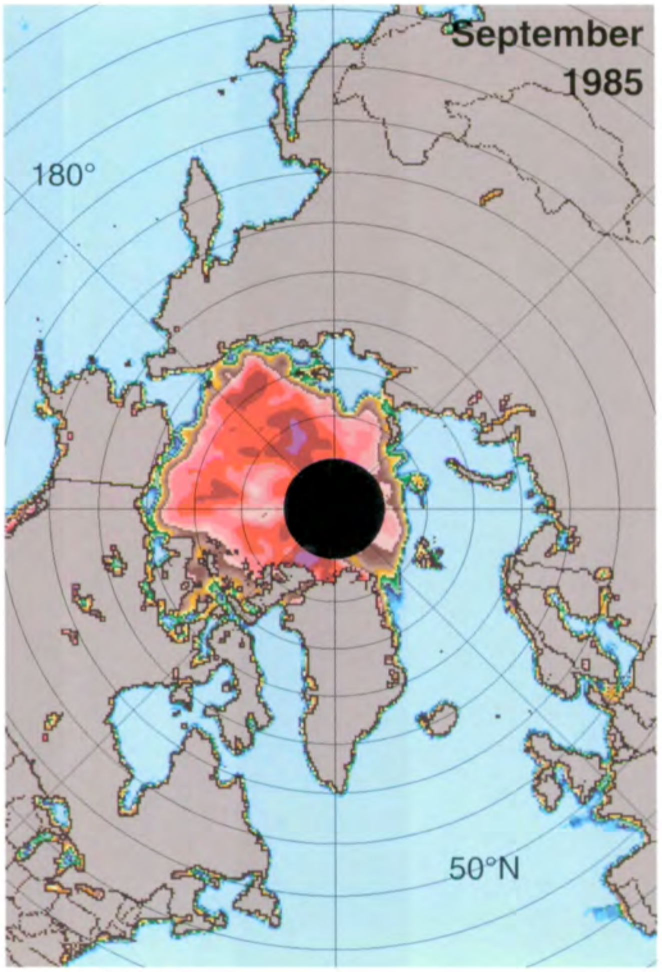
September
1985
180°
50°N

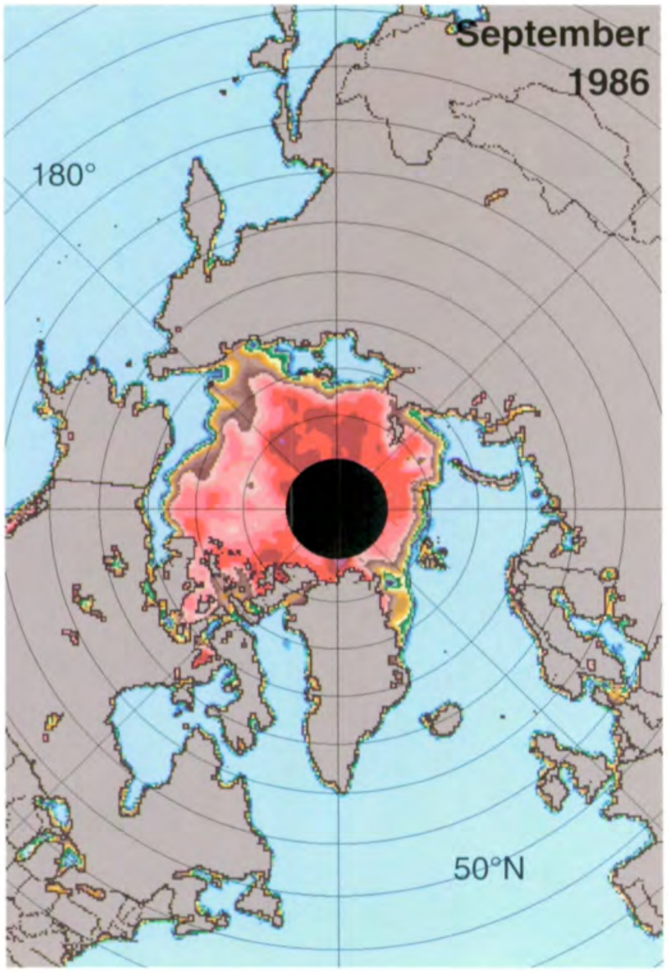
September
1986
180°
50°N

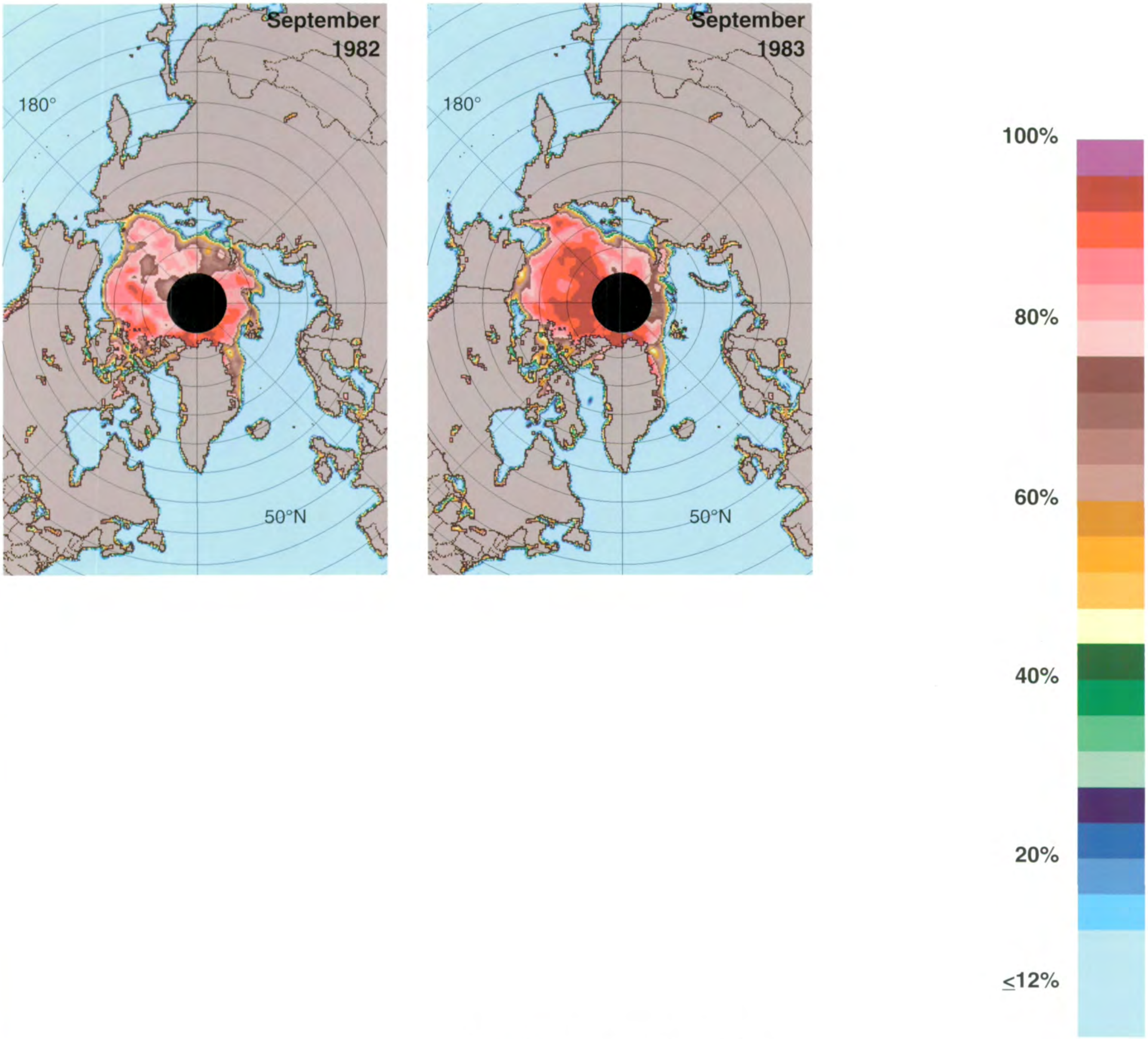

Figure 3.1.11. Mean monthly Arctic sea ice concentrations for September 1979-1986.

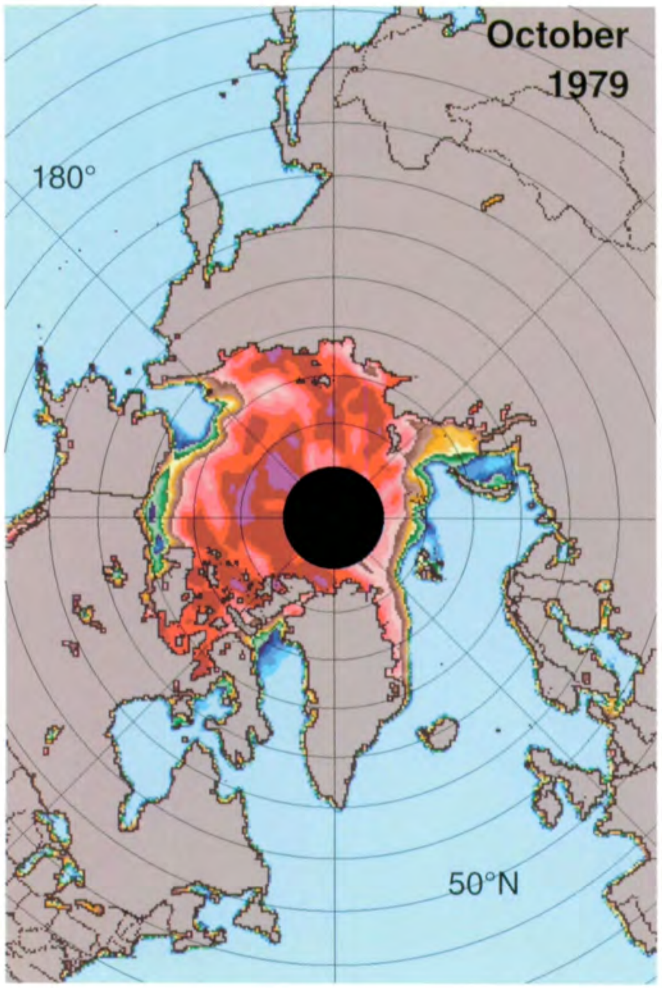
October
1979
180°
50°N

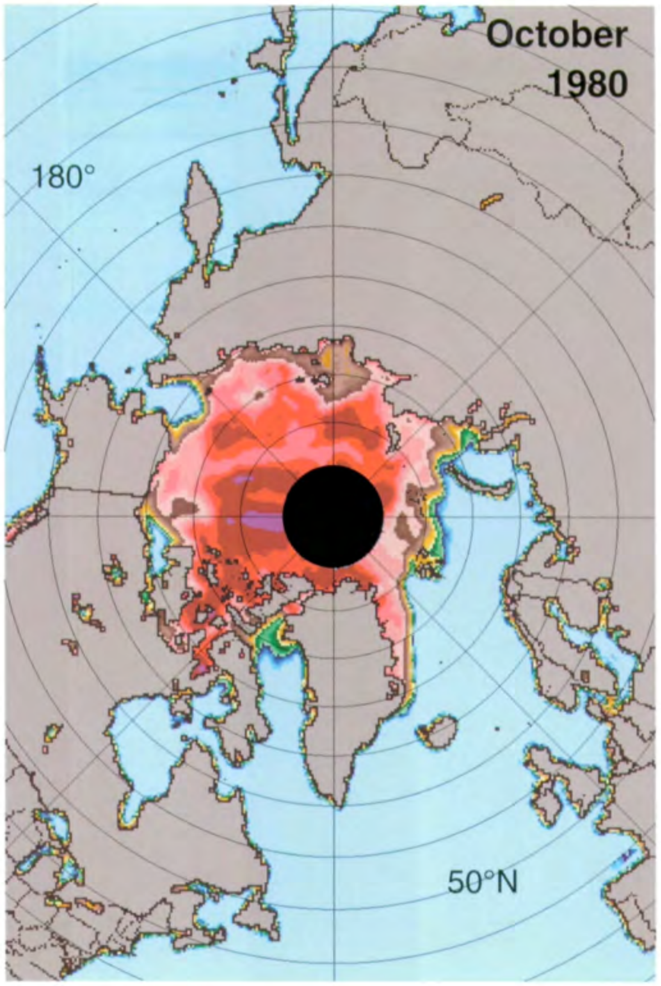
October
1980
180°
50°N

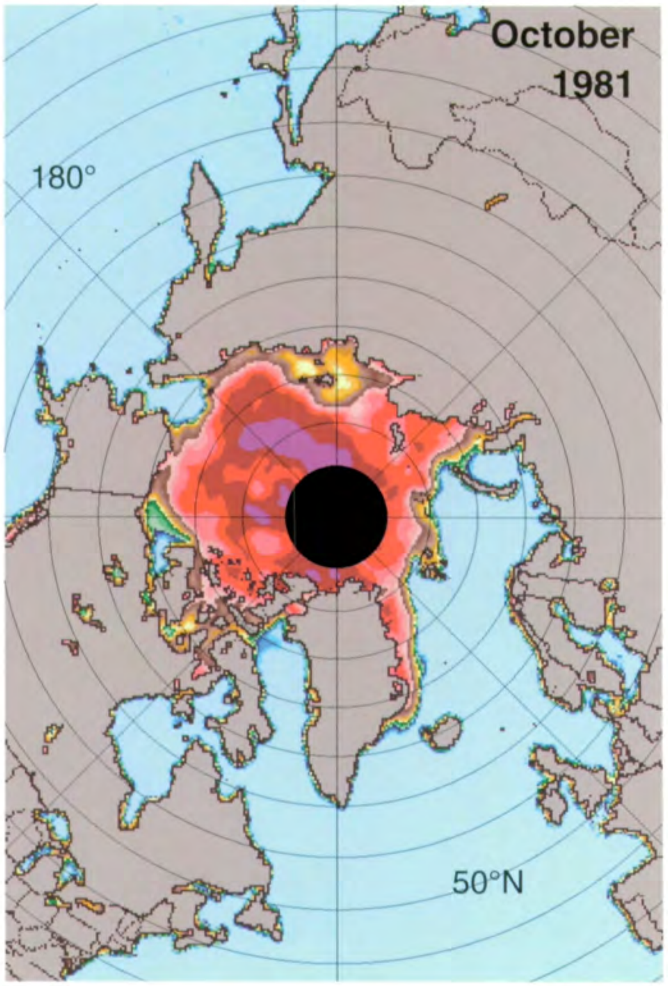
October
1981
180°
50°N

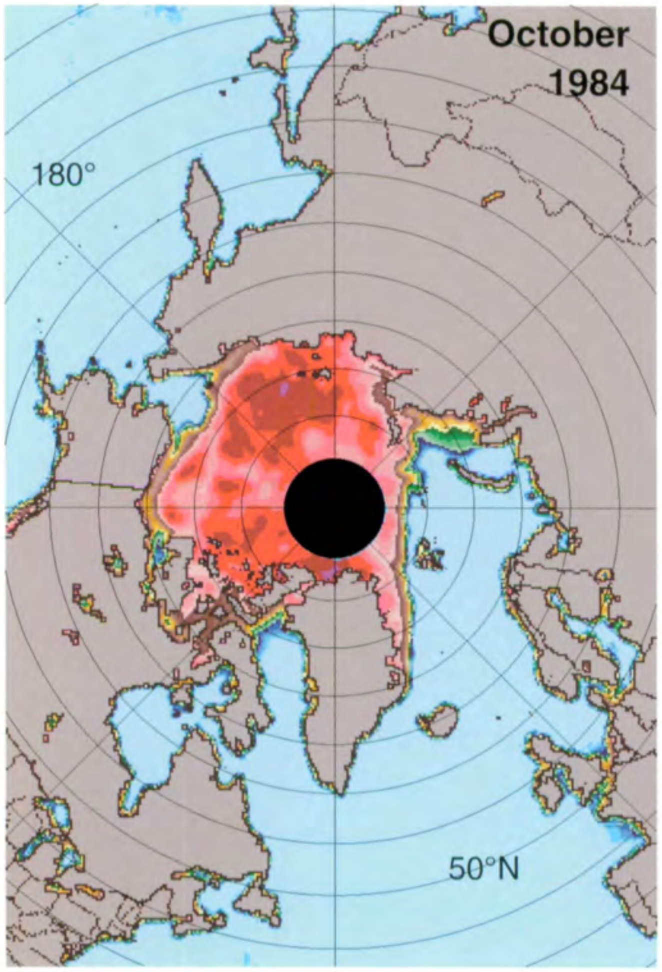
October
1984
180°
50°N

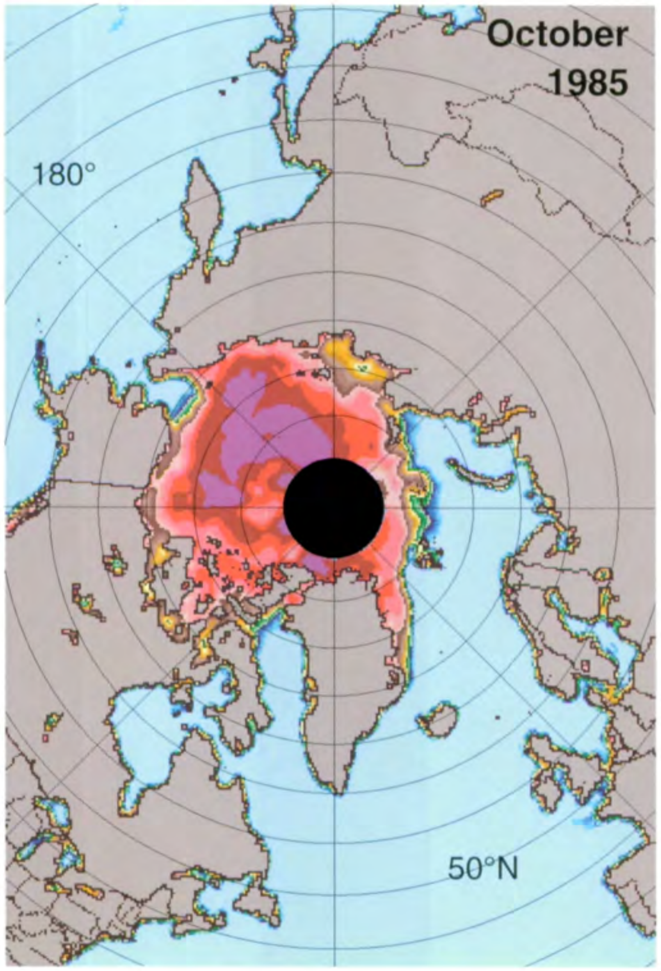
October
1985
180°
50°N

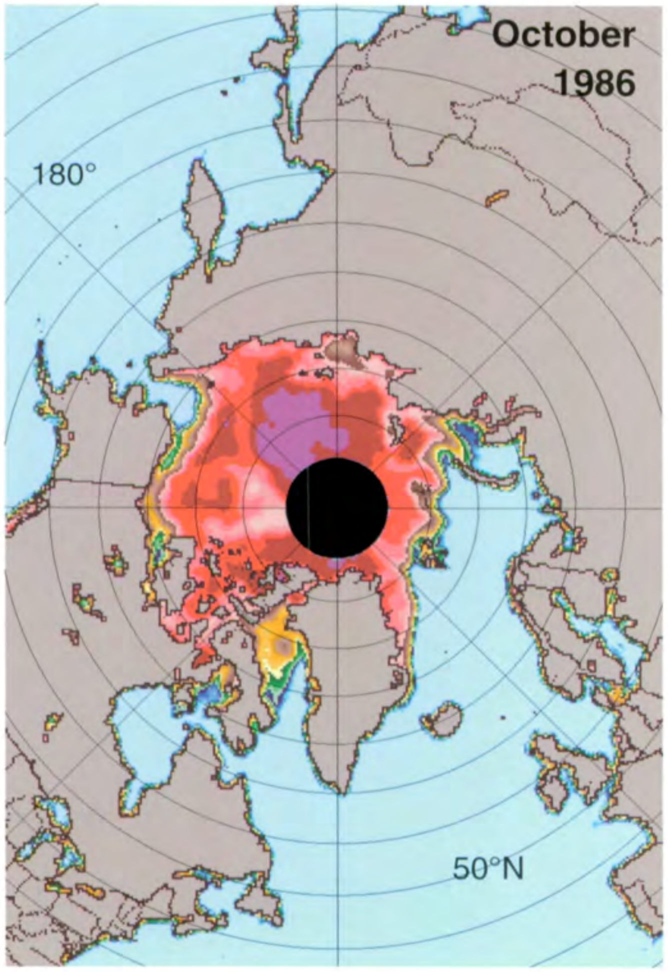
October
1986
180°
50°N

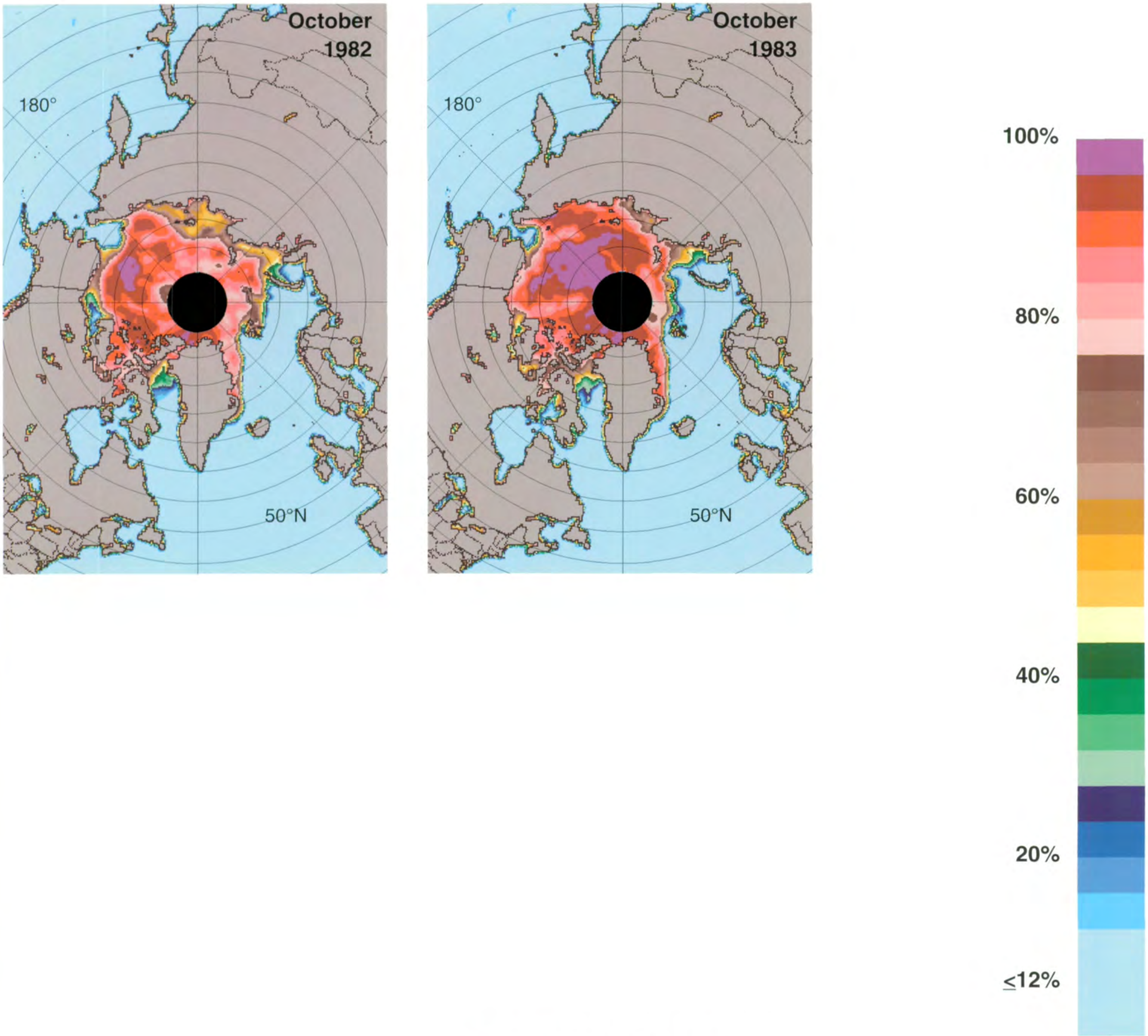

Figure 3.1.12. Mean monthly Arctic sea ice concentrations for October 1979-1986.

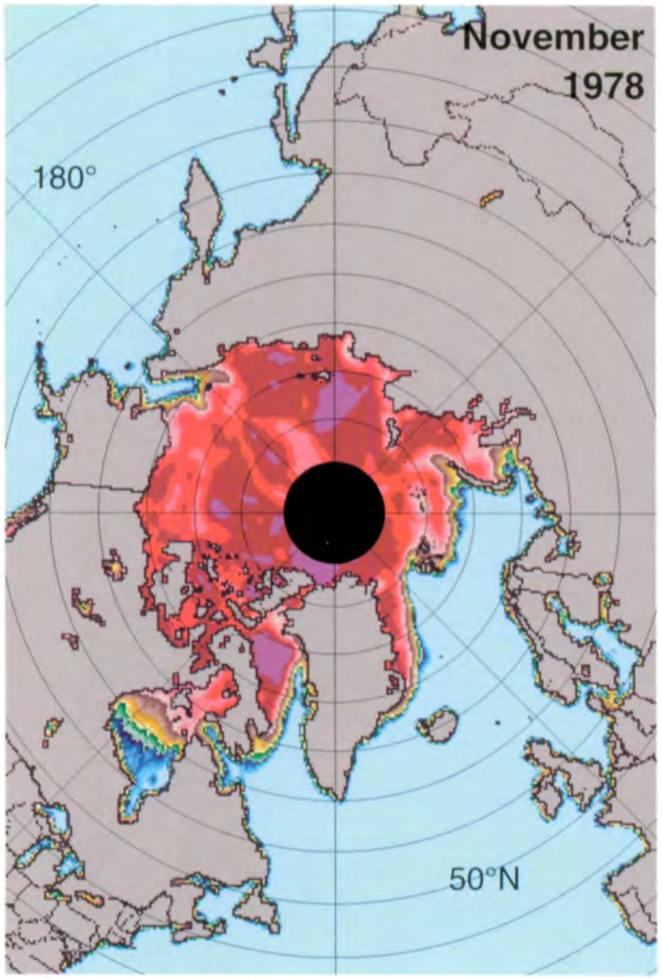
November
1978
180°
50°N

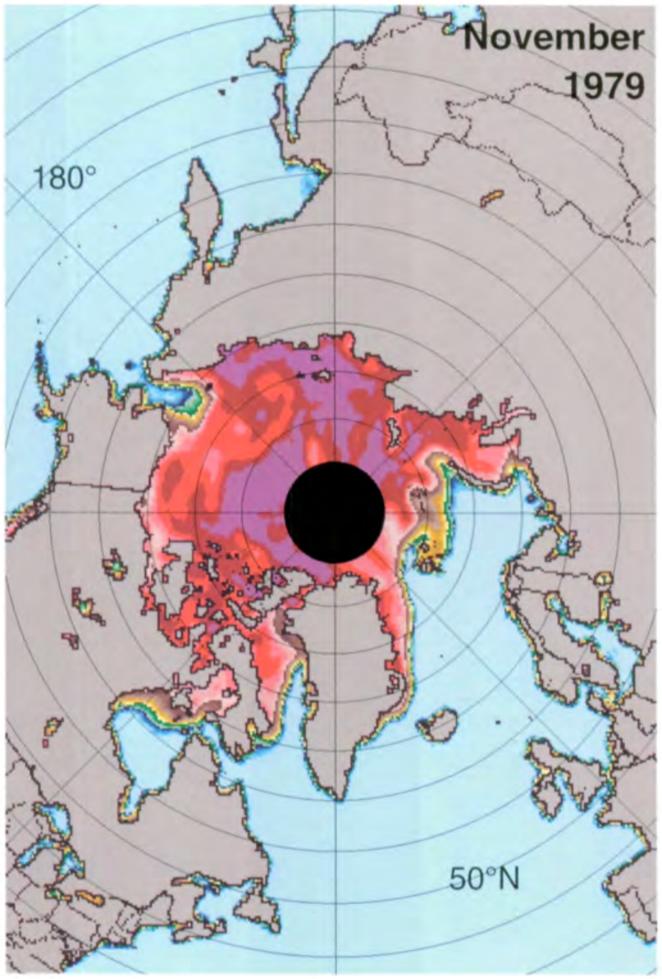
November
1979
180°
50°N

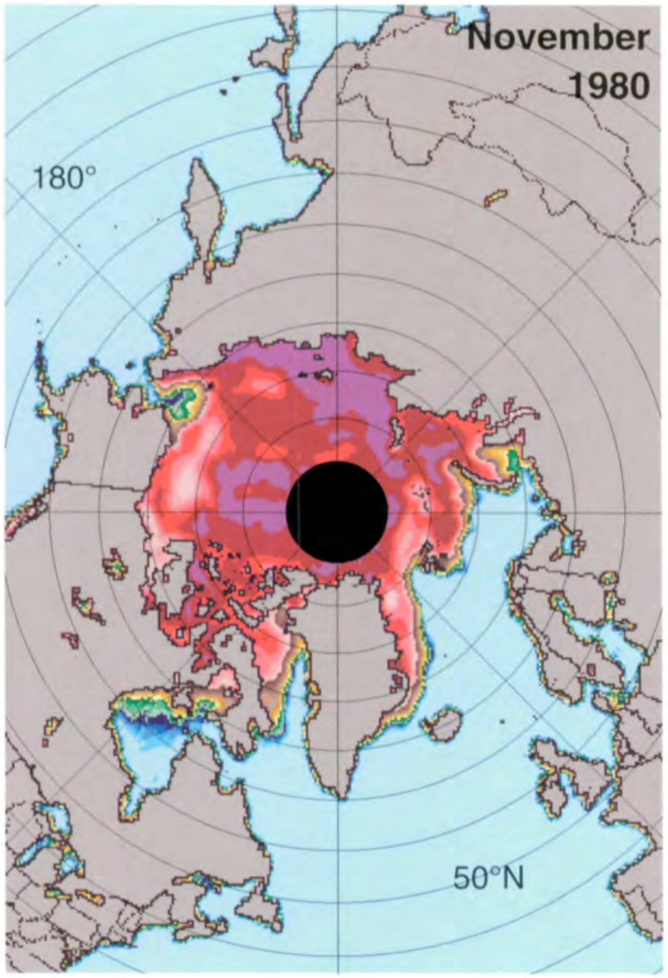
November
1980
180°
50°N

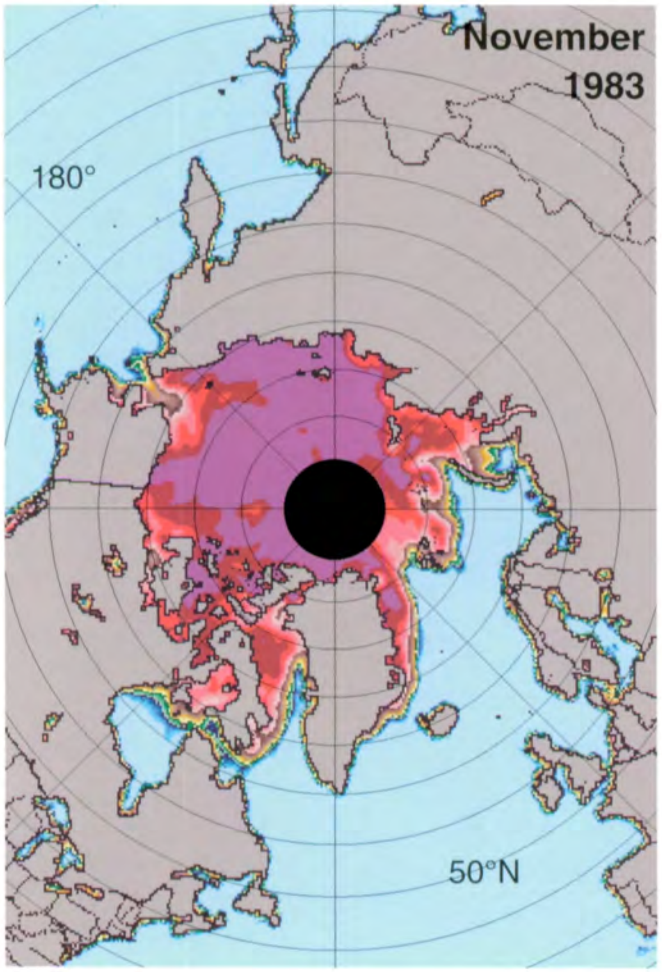
November
1983
180°
50°N

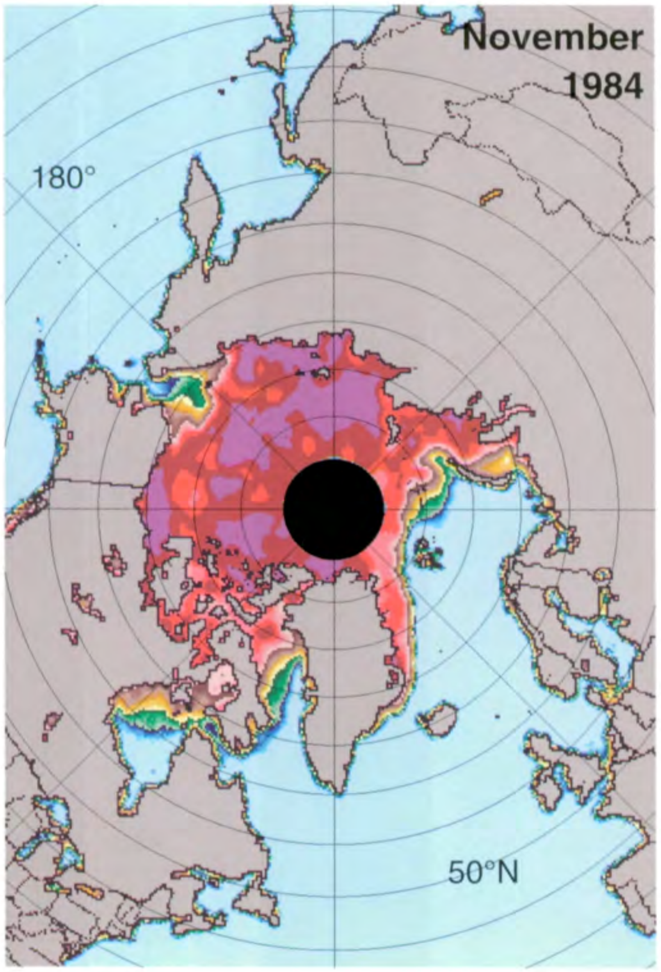
November
1984
180°
50°N

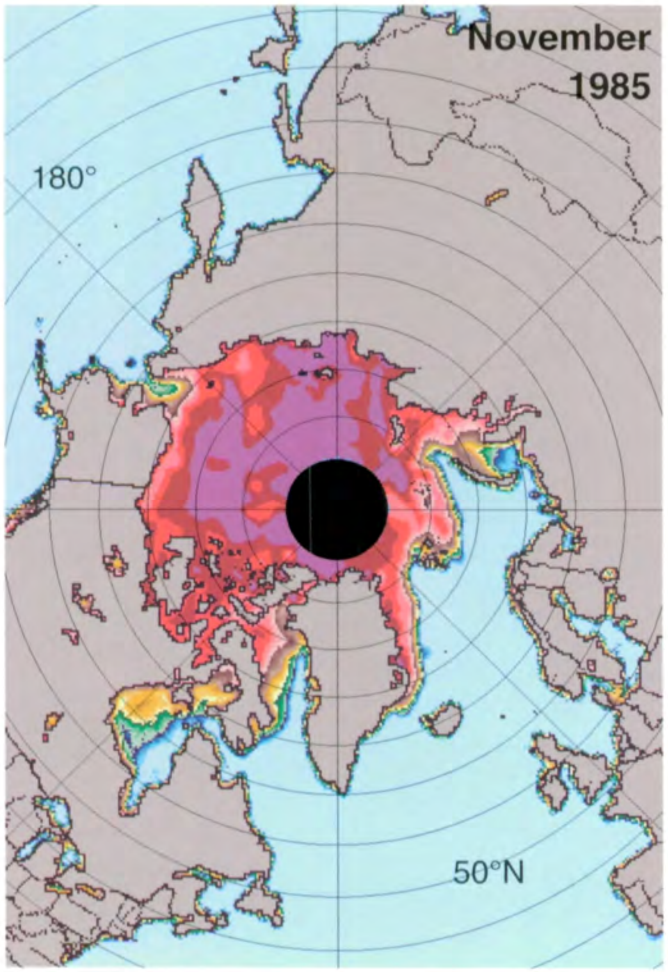
November
1985
180°
50°N

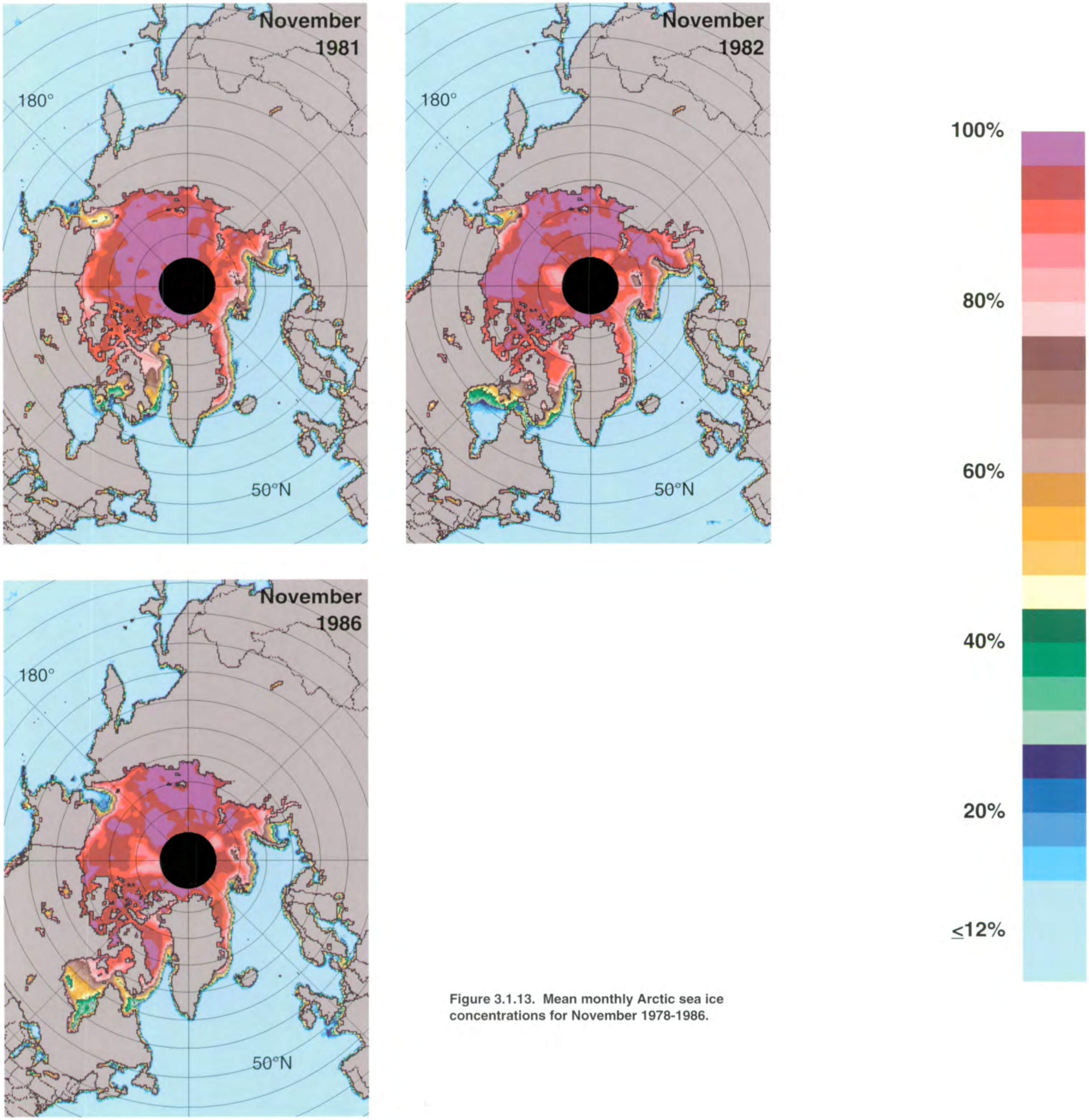

Figure 3.1.13. Mean monthly Arctic sea ice concentrations for November 1978-1986.

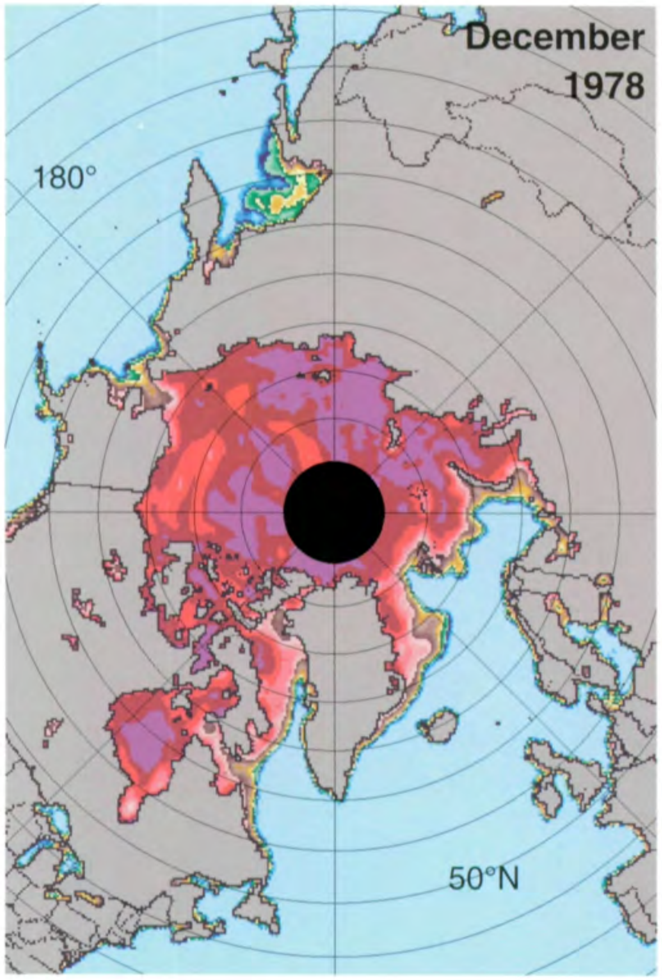
December
1978
180°
50°N

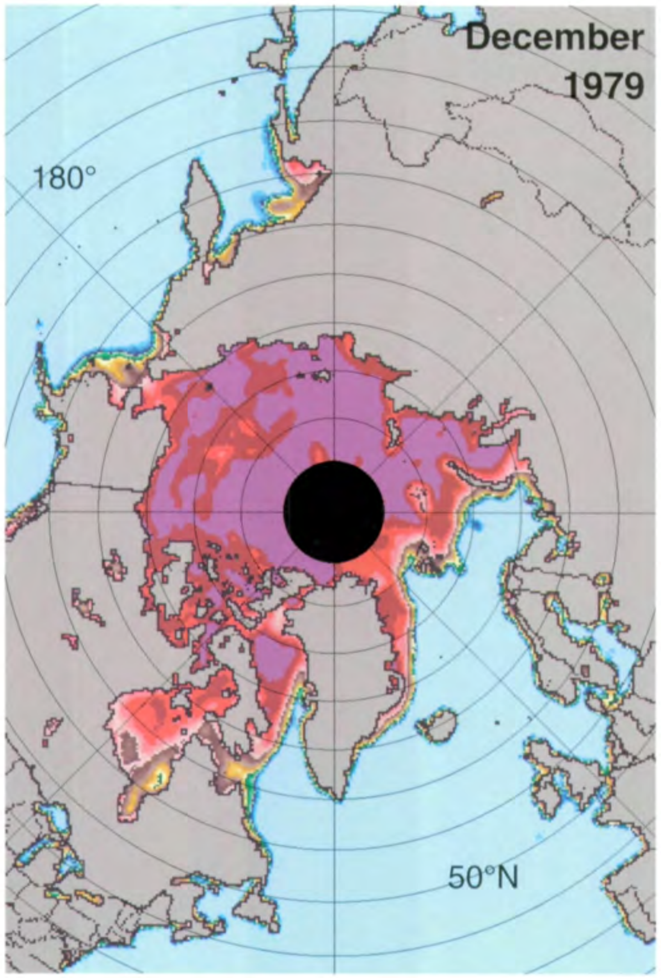
December
1979
180°
50°N

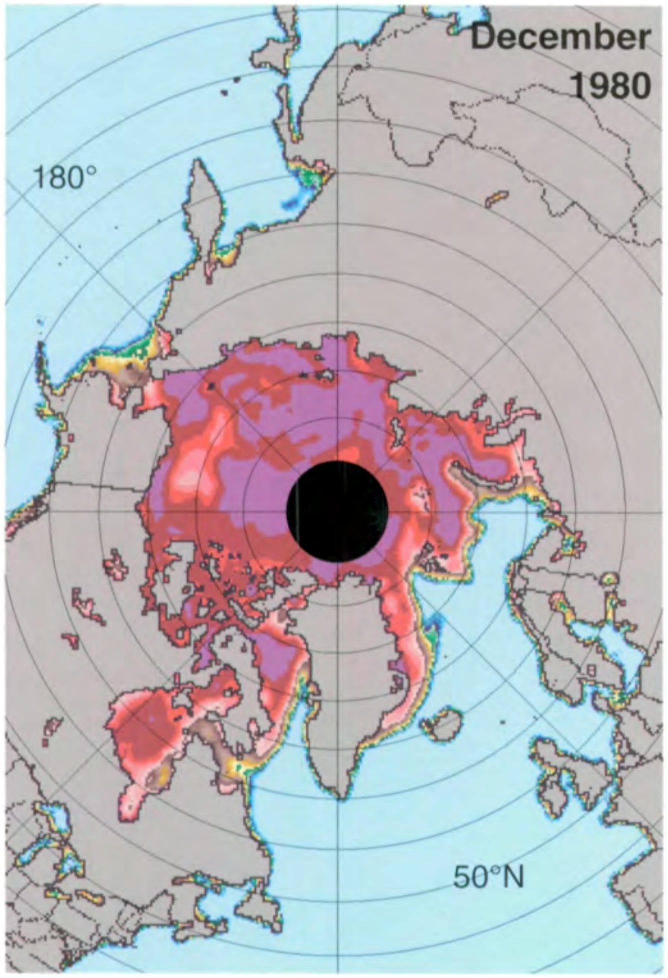
December
1980
180°
50°N

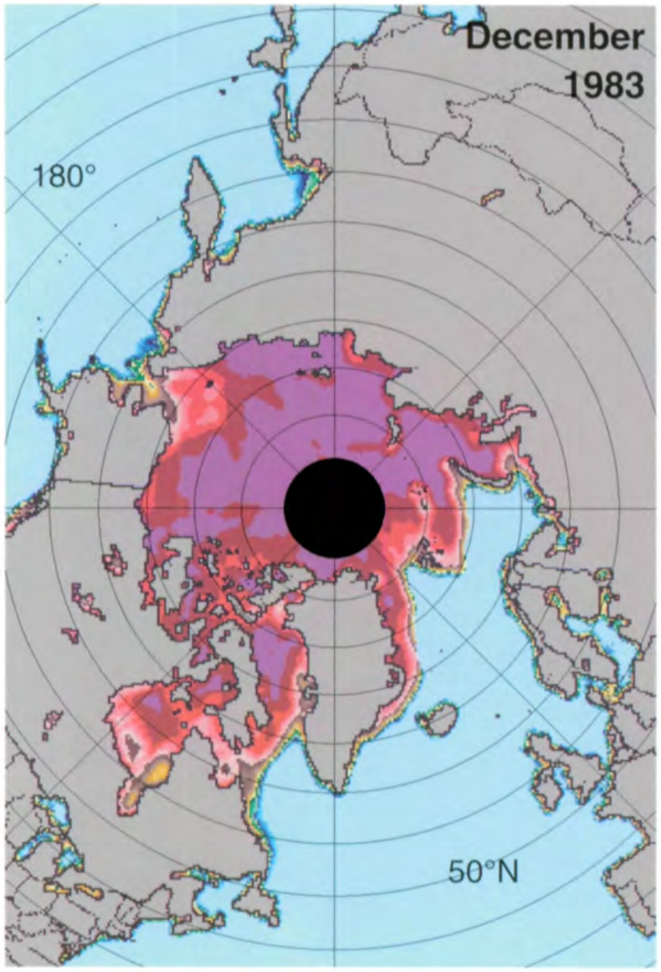
December
1983
180°
50°N

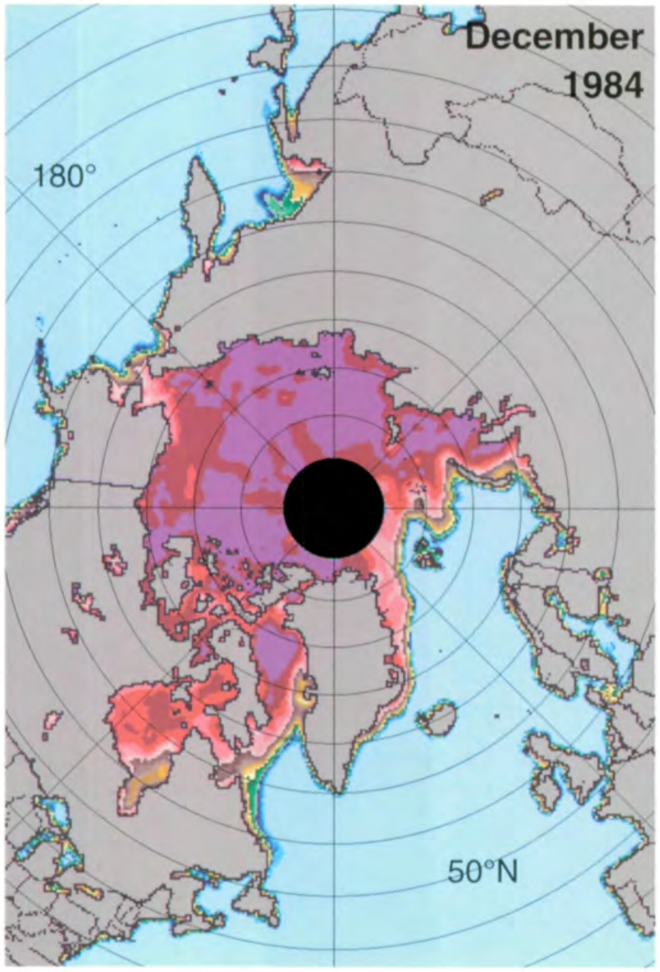
December
1984
180°
50°N

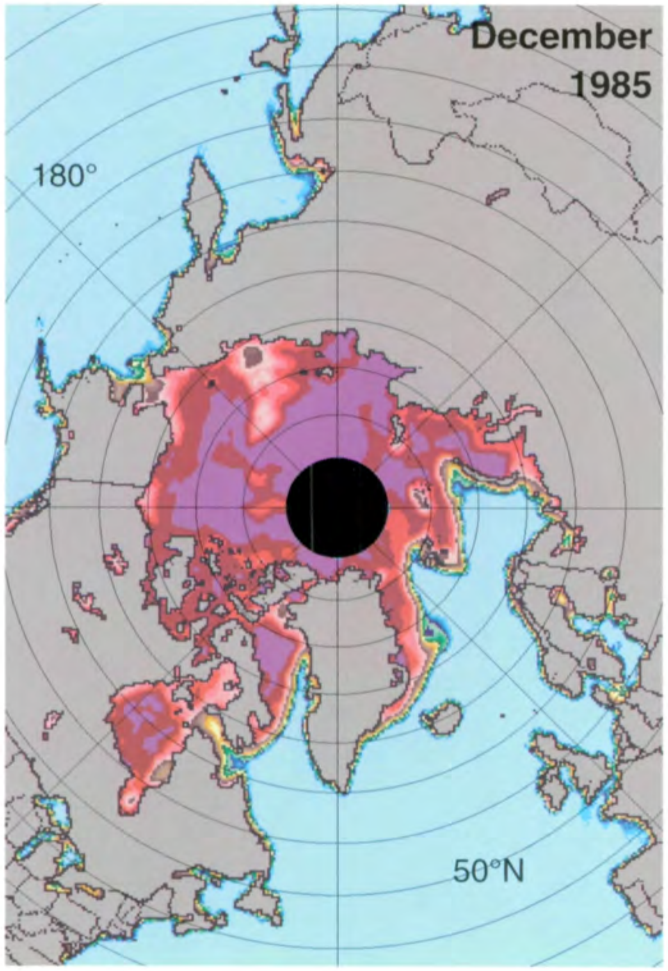
December
1985
180°
50°N

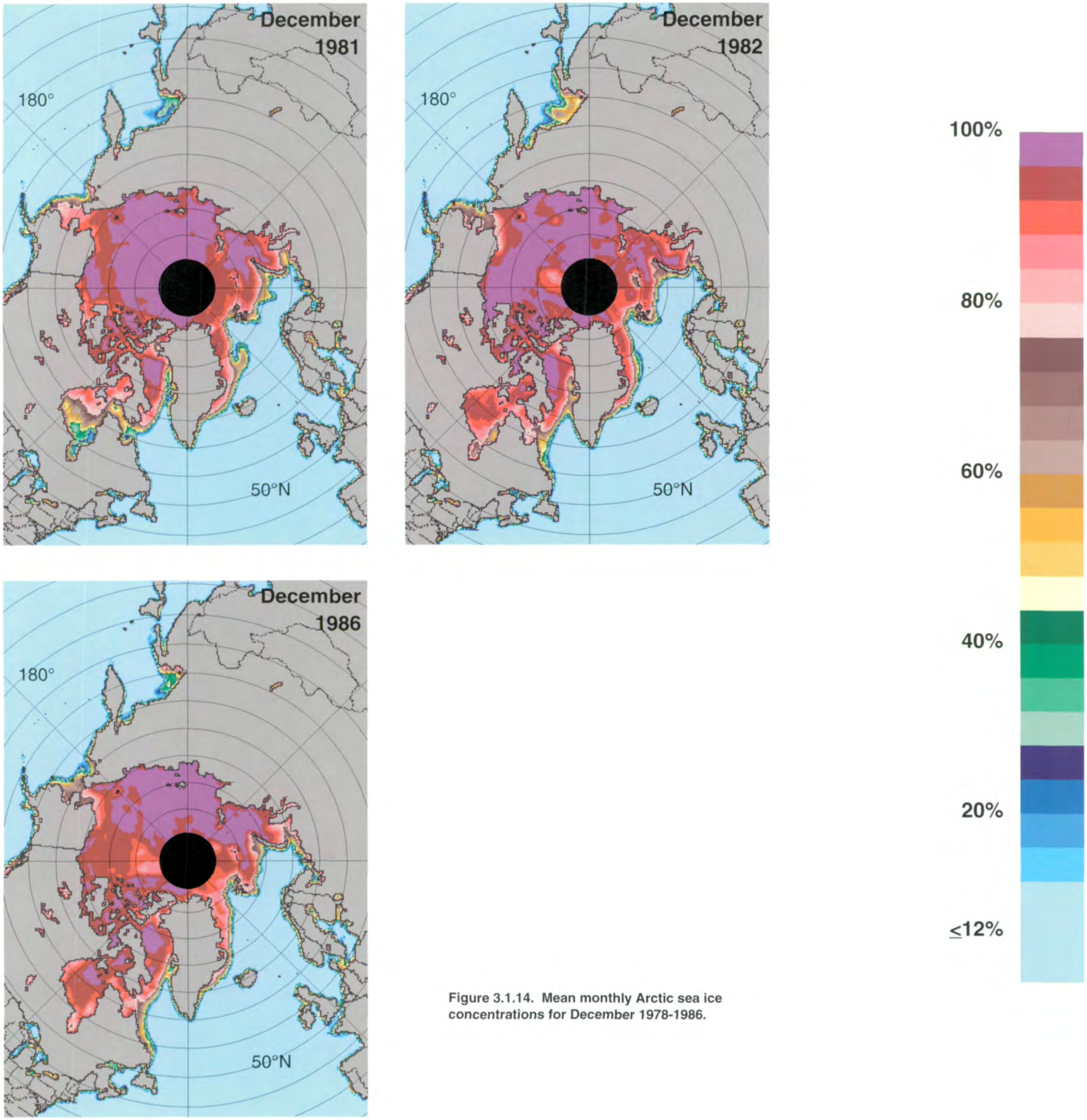

Figure 3.1.14. Mean monthly Arctic sea ice concentrations for December 1978-1986.

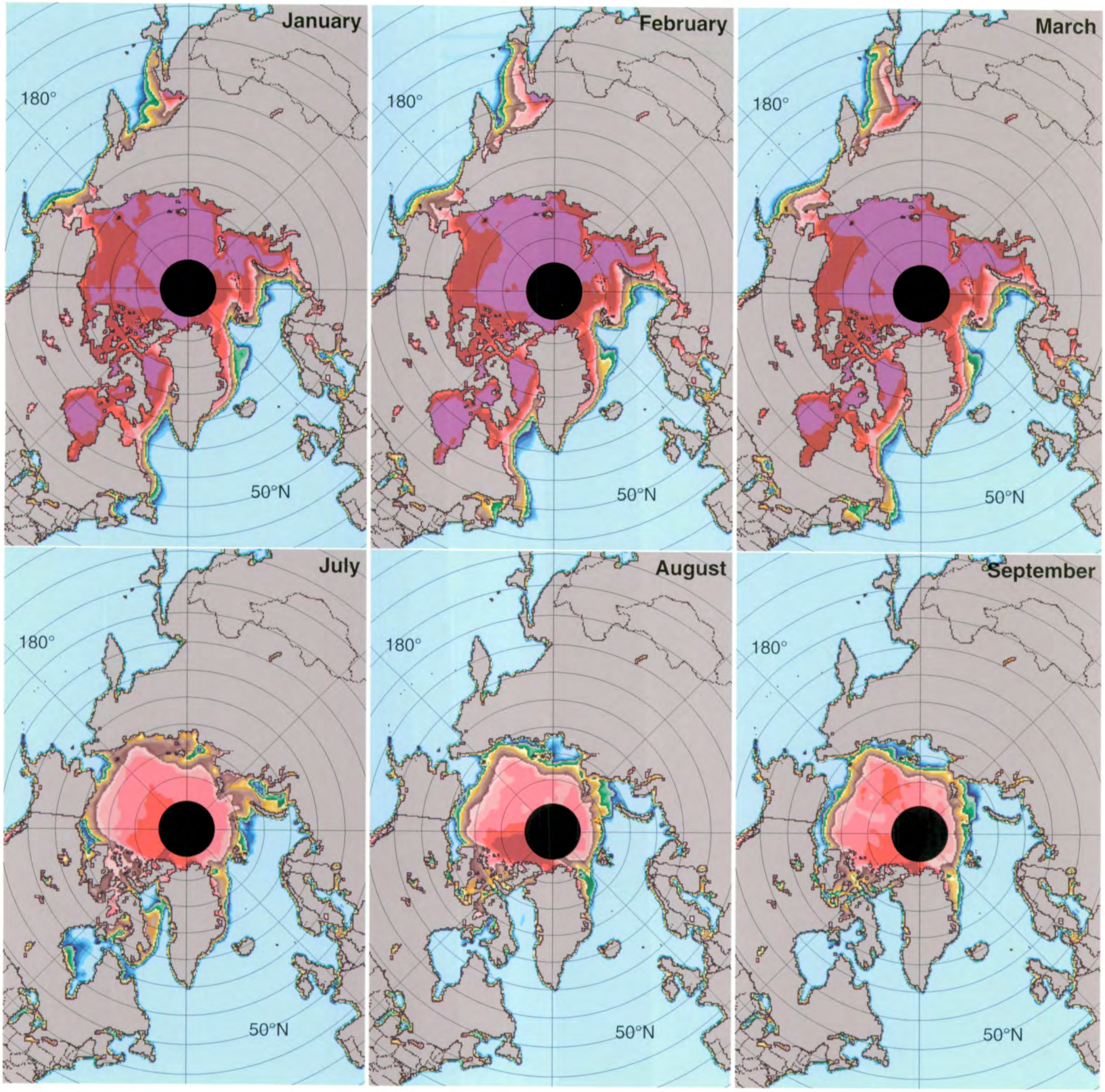
January
180°
50°N
February
180°
50°N
March
180°
50°N
July
180°
50°N
August
180°
50°N
September
180°
50°N

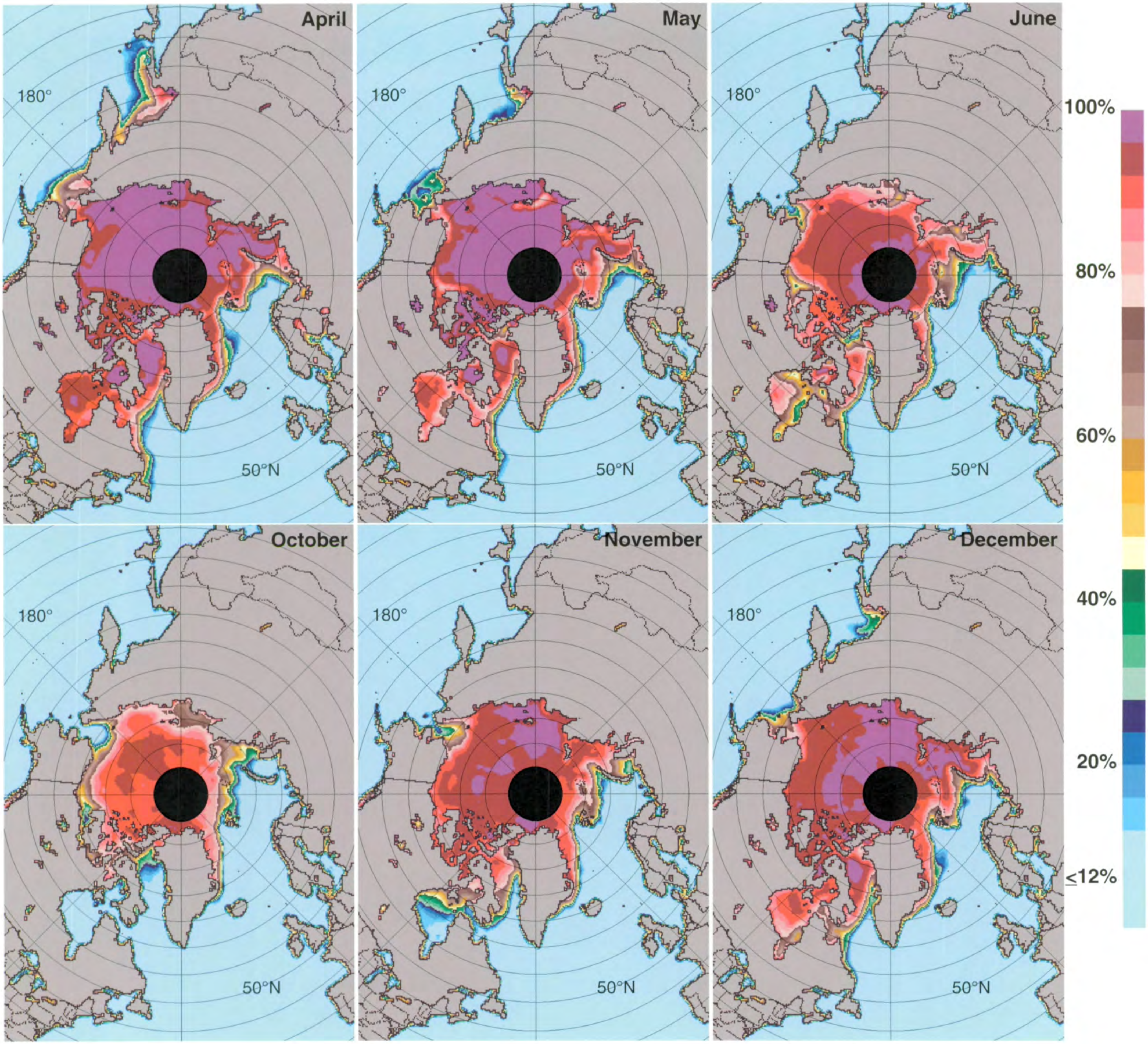

Figure 3.1.15. Monthly Arctic sea ice concentrations averaged over the SMMR lifetime.

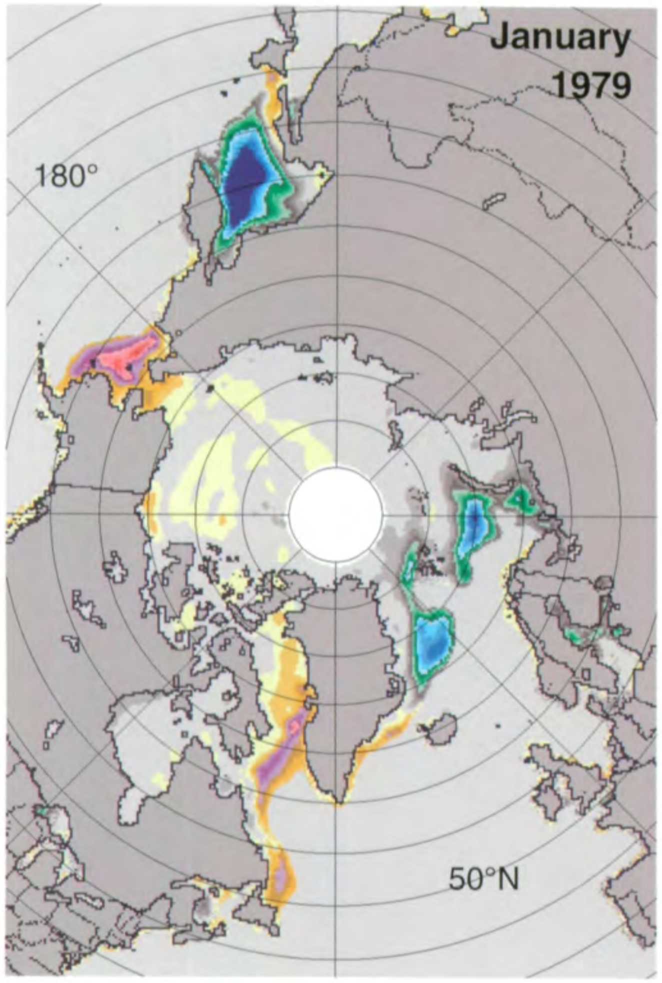
January
1979
180°
50°N

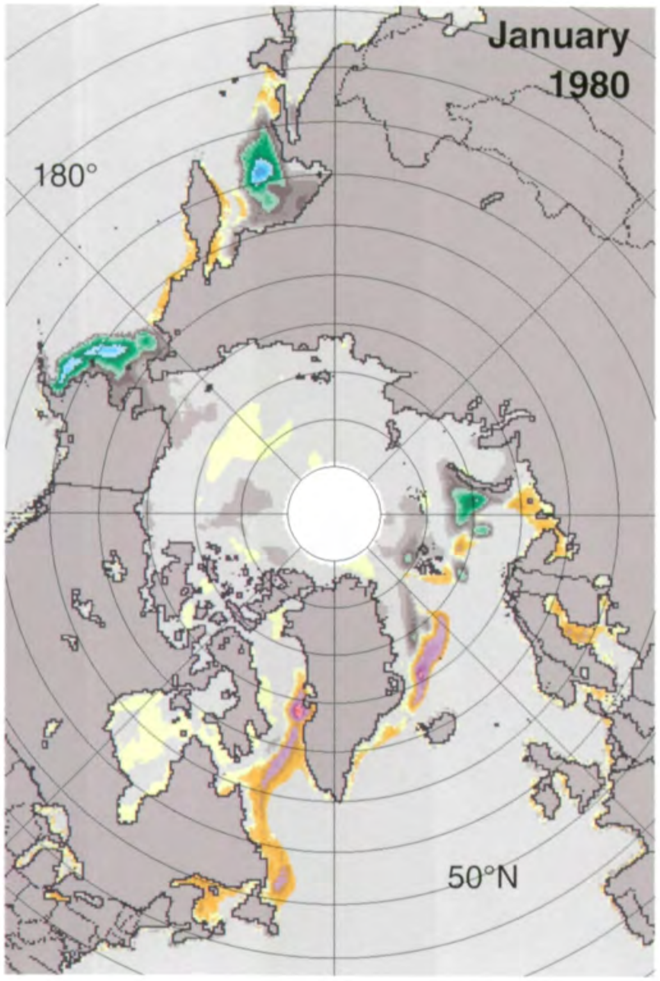
January
1980
180°
50°N

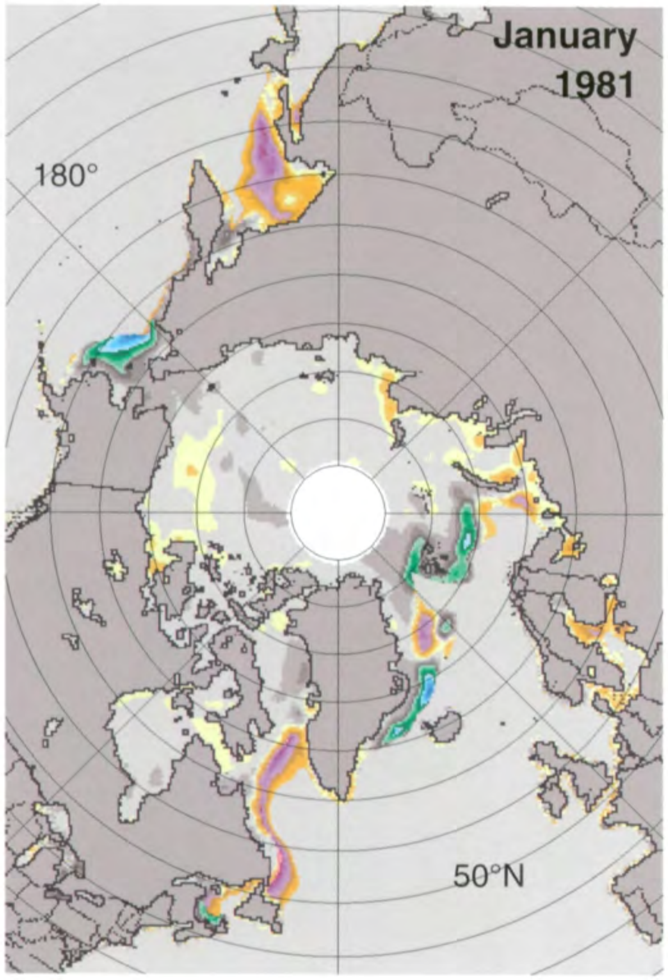
January
1981
180°
50°N

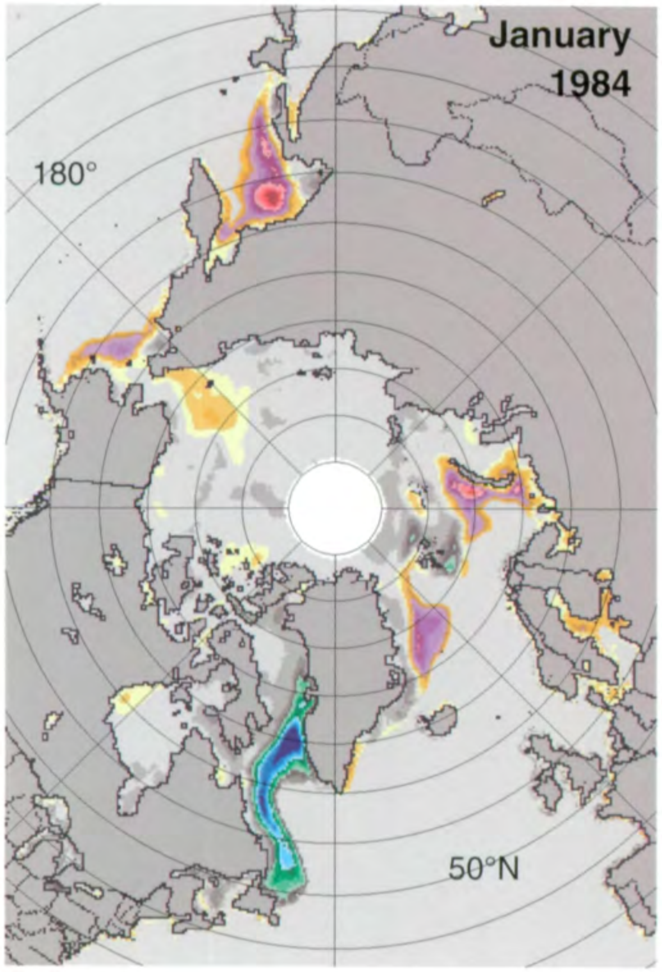
January
1984
180°
50°N

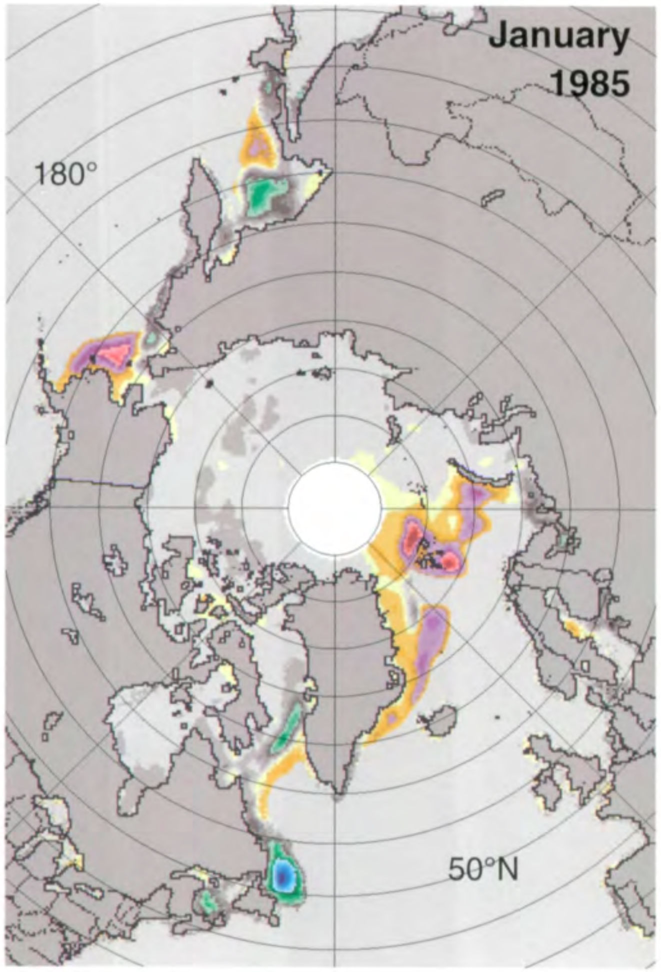
January
1985
180°
50°N

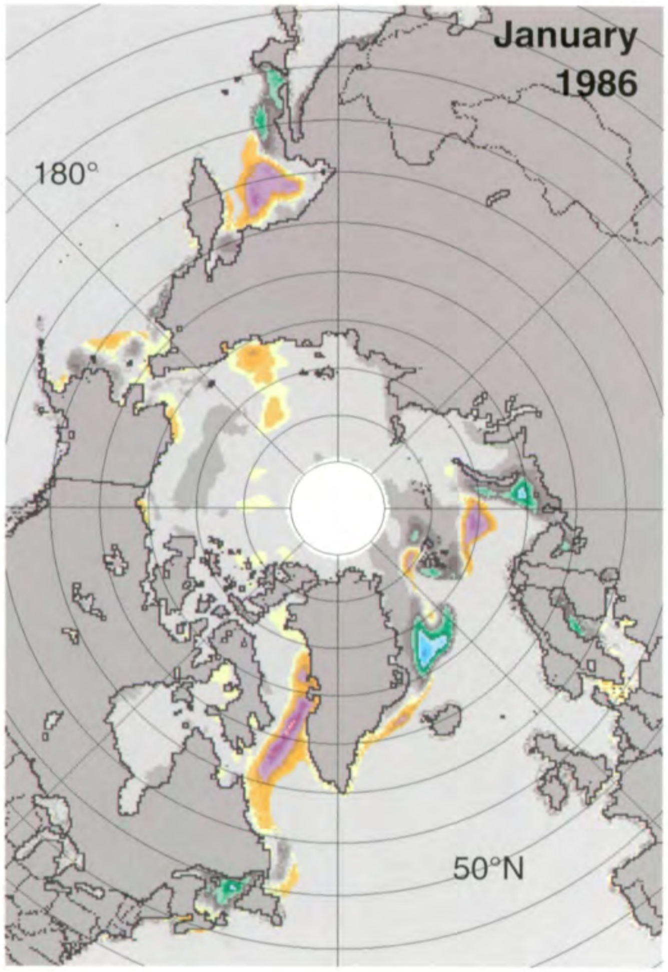
January
1986
180°
50°N

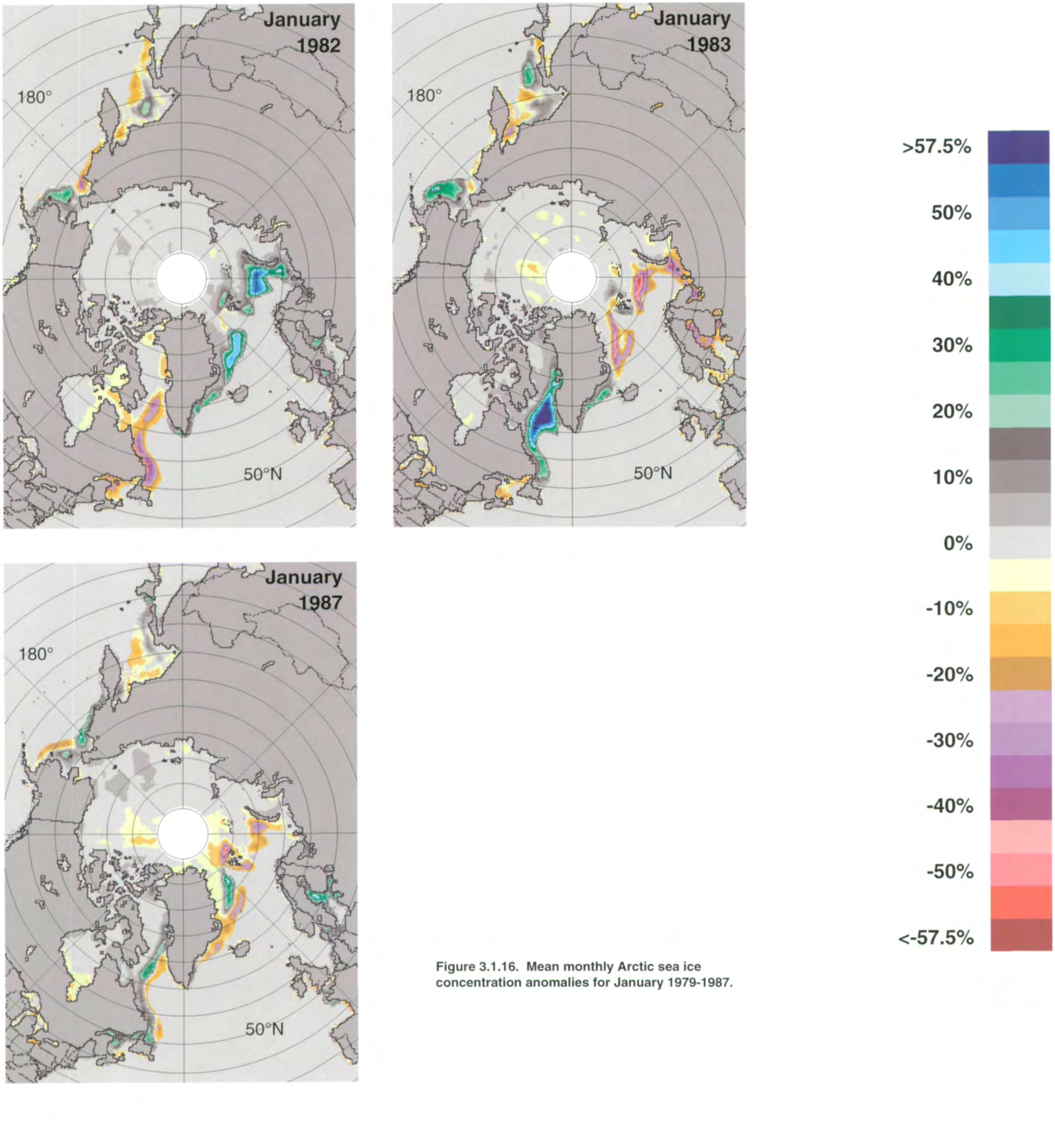

Figure 3.1.16. Mean monthly Arctic sea ice concentration anomalies for January 1979-1987.

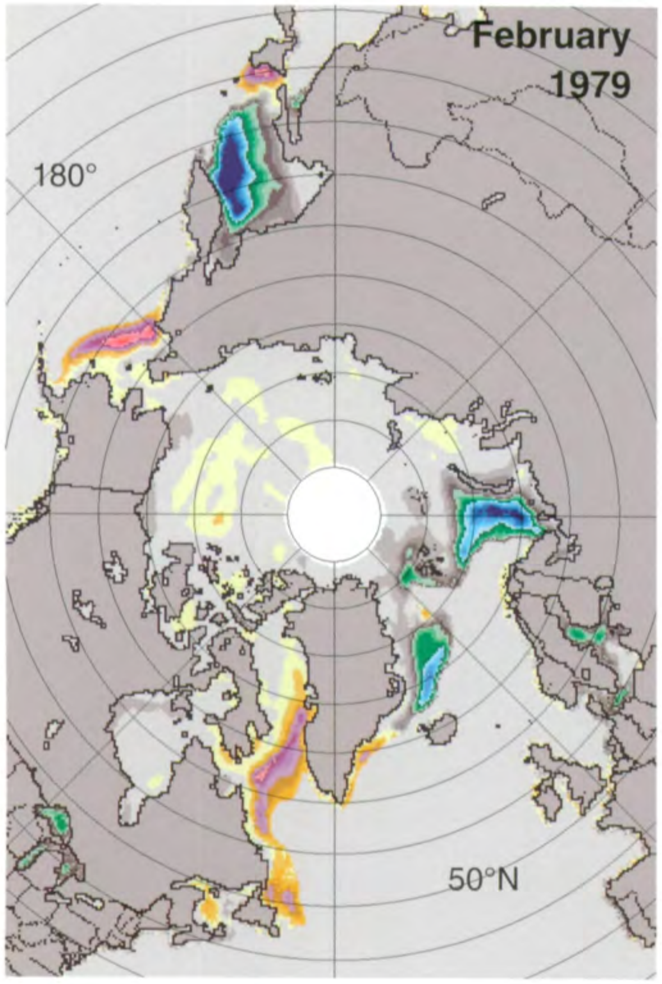
February 1979
180°
50°N

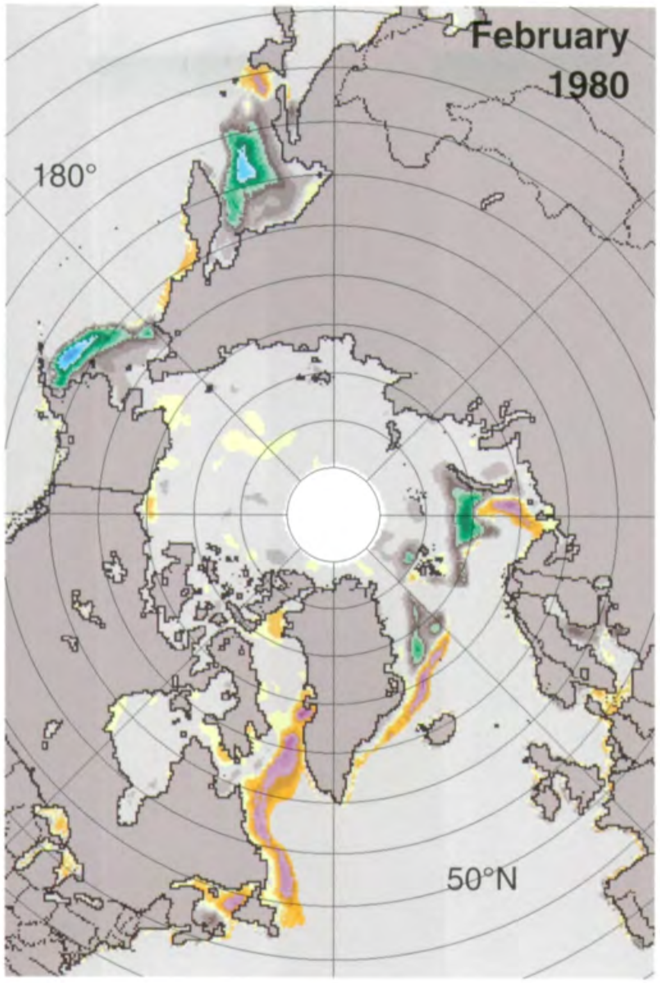
February 1980
180°
50°N

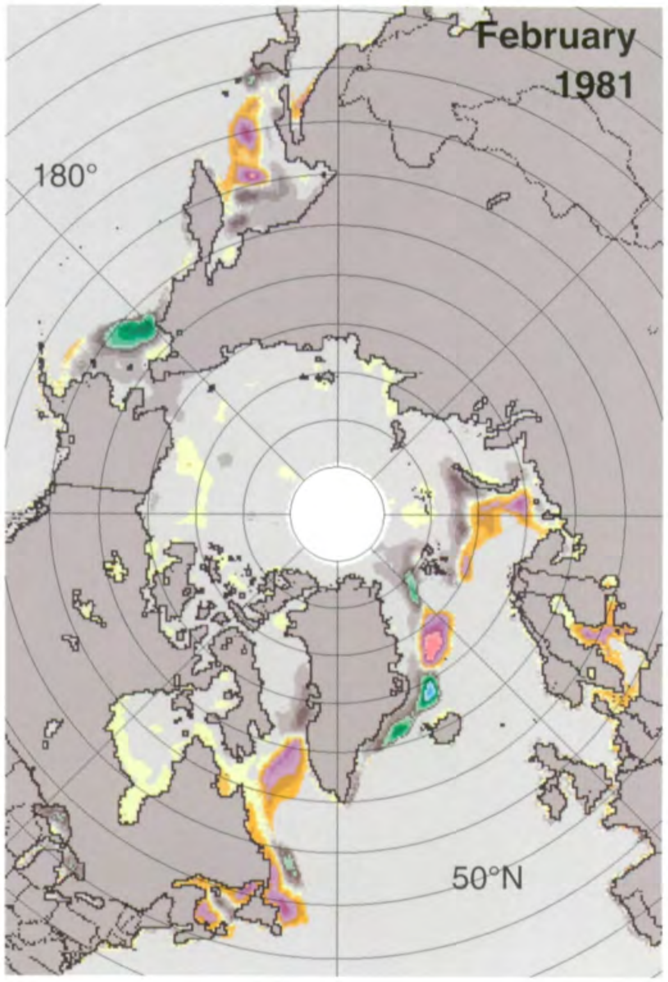
February 1981
180°
50°N

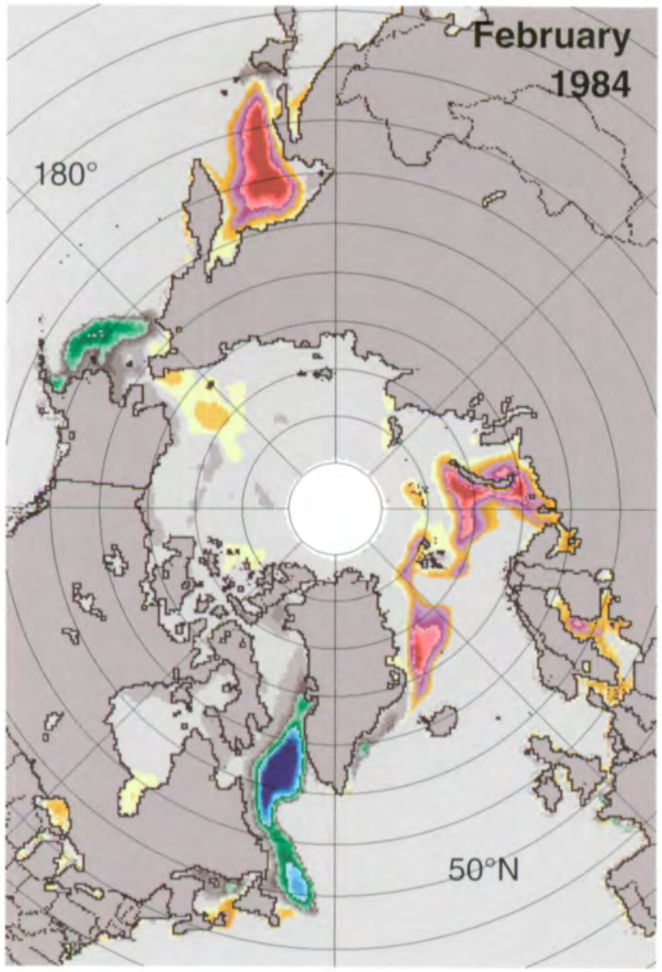
February 1984
180°
50°N

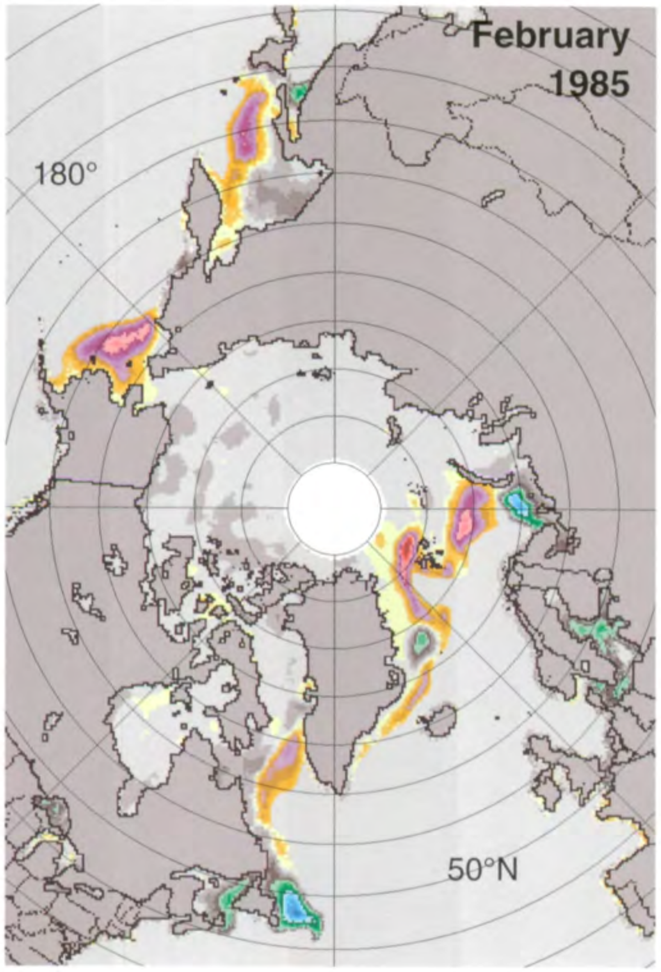
February 1985
180°
50°N

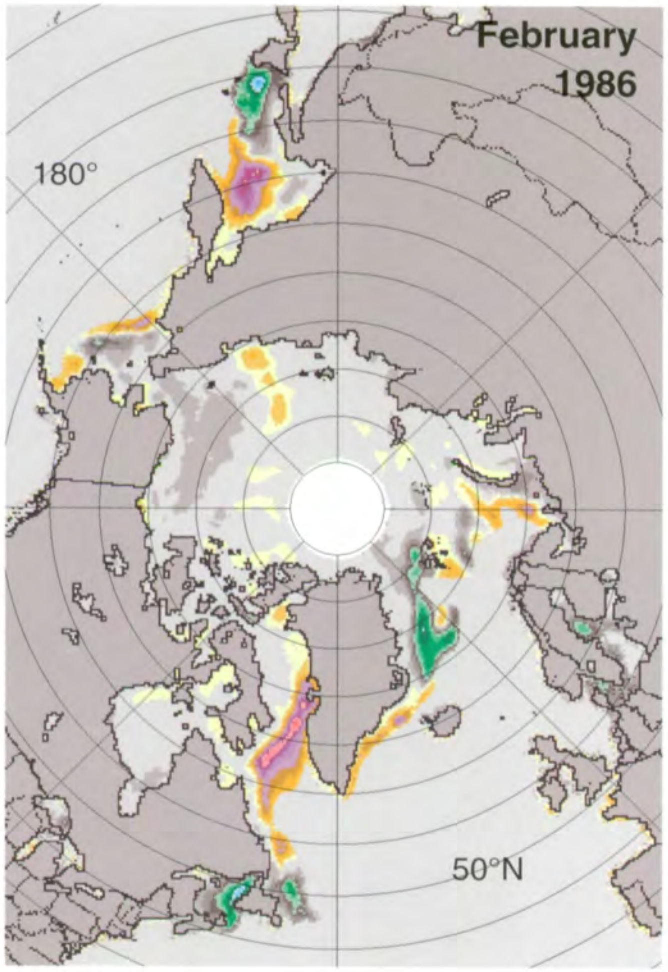
February 1986
180°
50°N

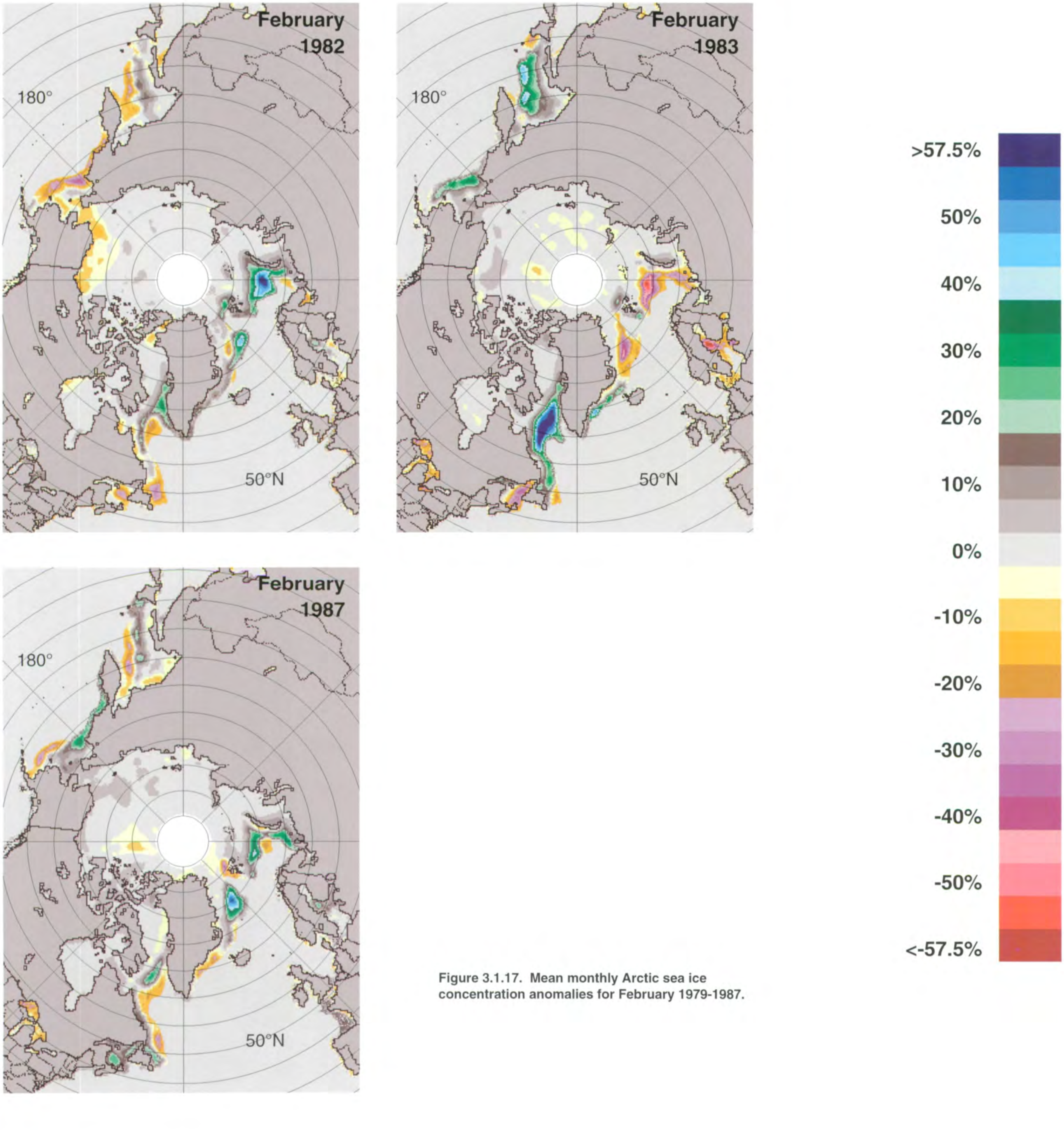

Figure 3.1.17. Mean monthly Arctic sea ice concentration anomalies for February 1979-1987.

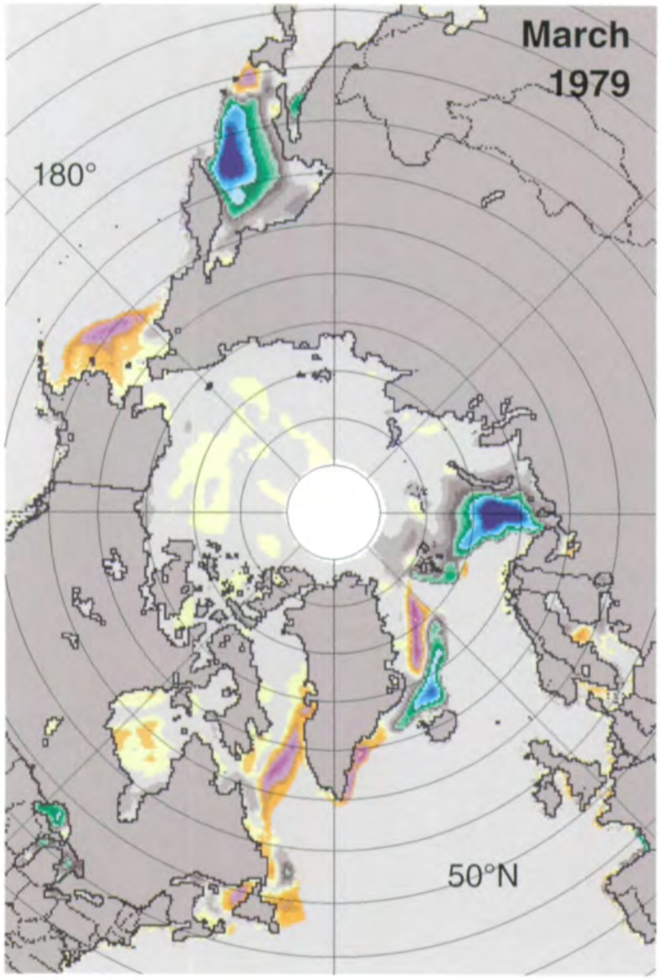
March
1979
180°
50°N

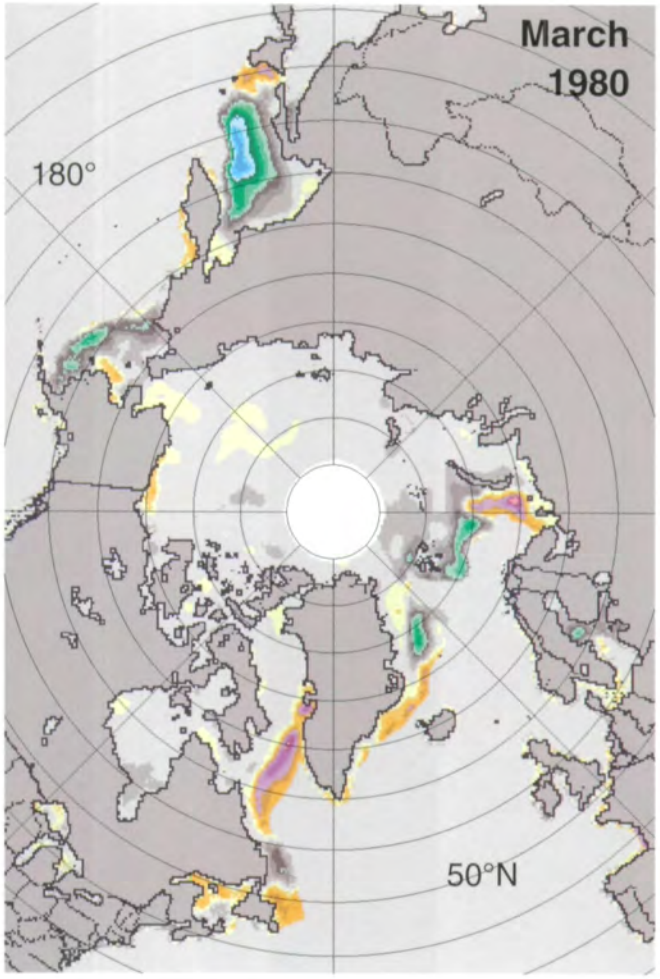
March
1980
180°
50°N

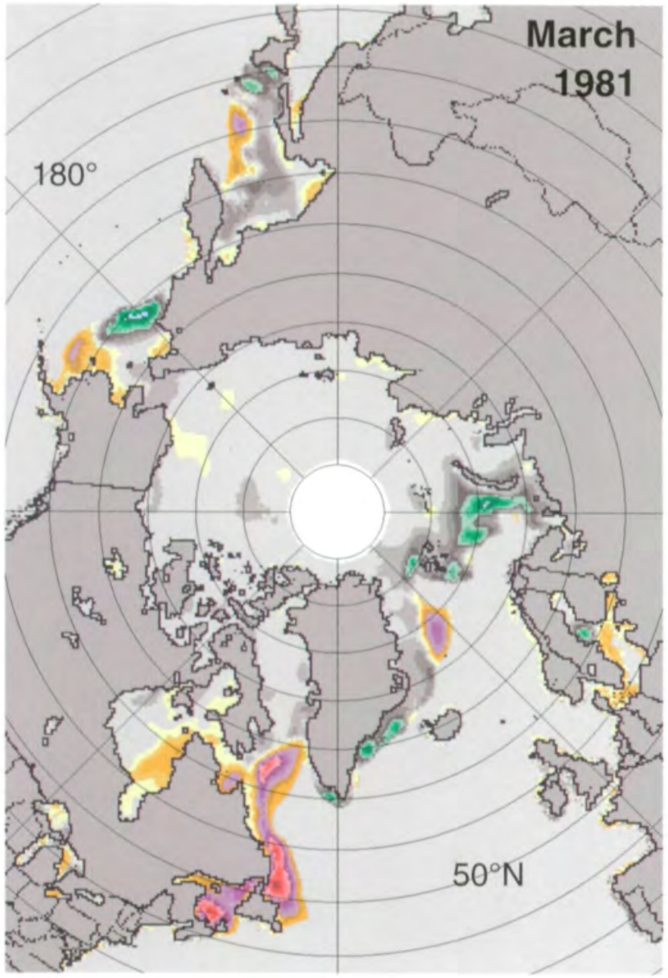
March
1981
180°
50°N

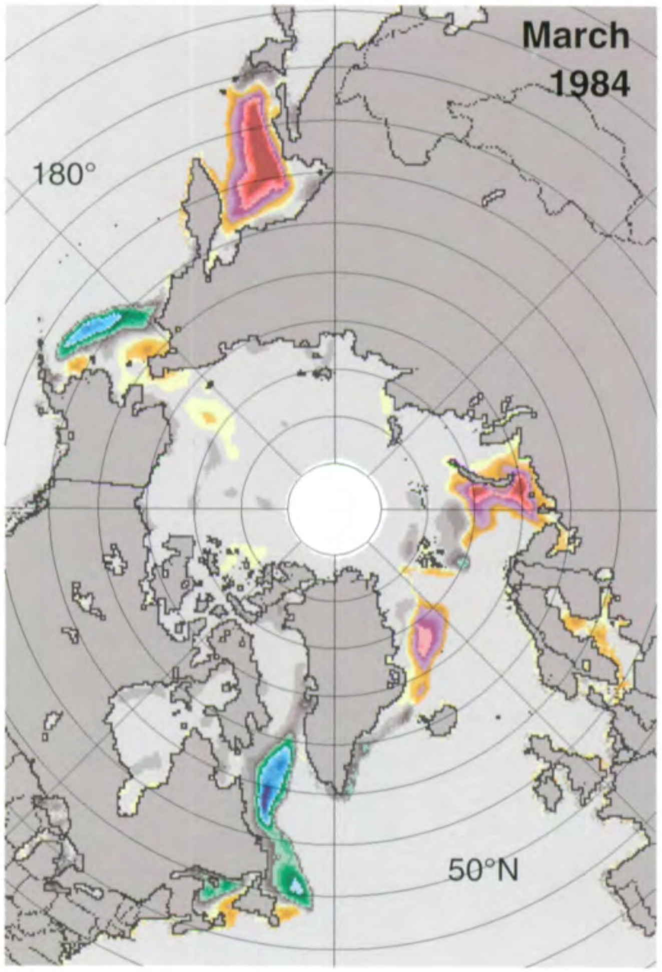
March
1984
180°
50°N

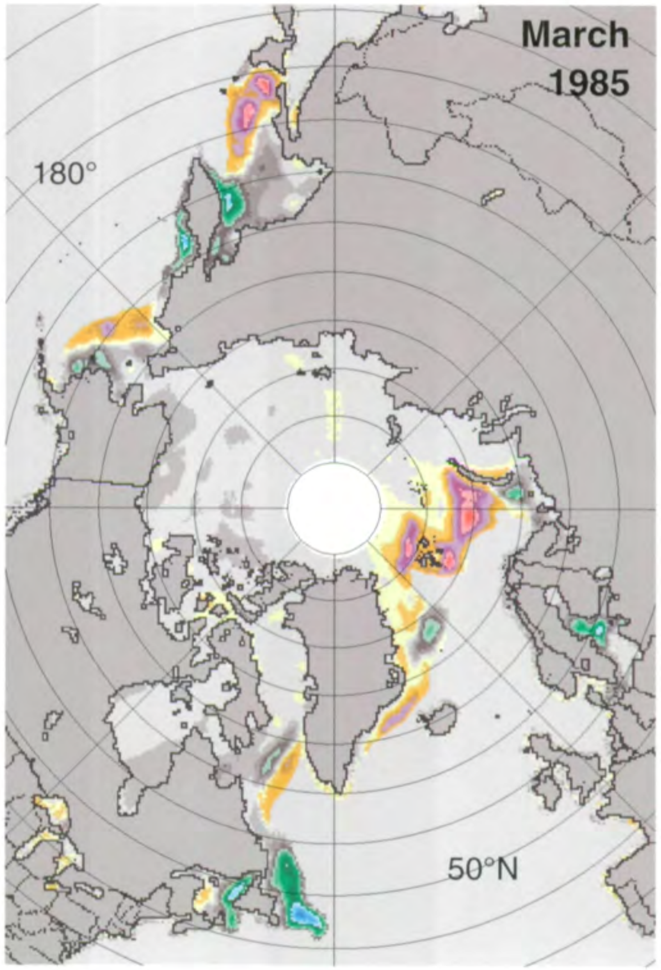
March
1985
180°
50°N

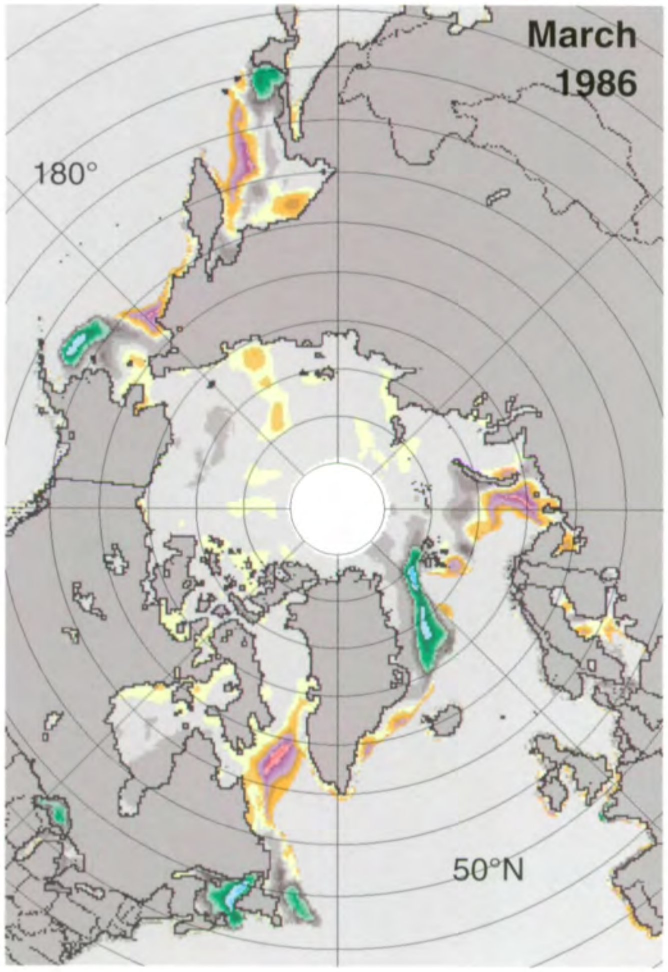
March
1986
180°
50°N

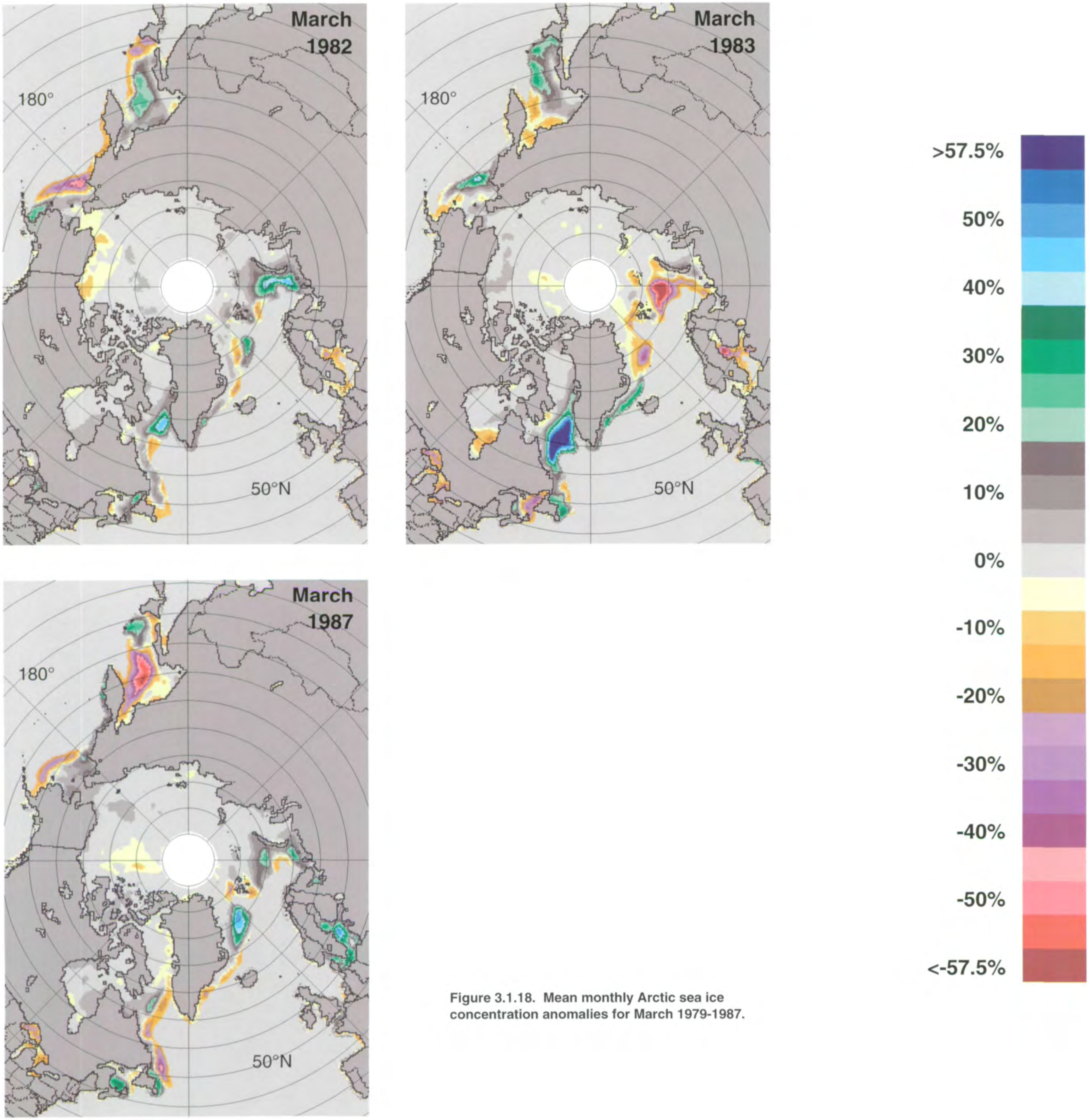

Figure 3.1.18. Mean monthly Arctic sea ice concentration anomalies for March 1979-1987.

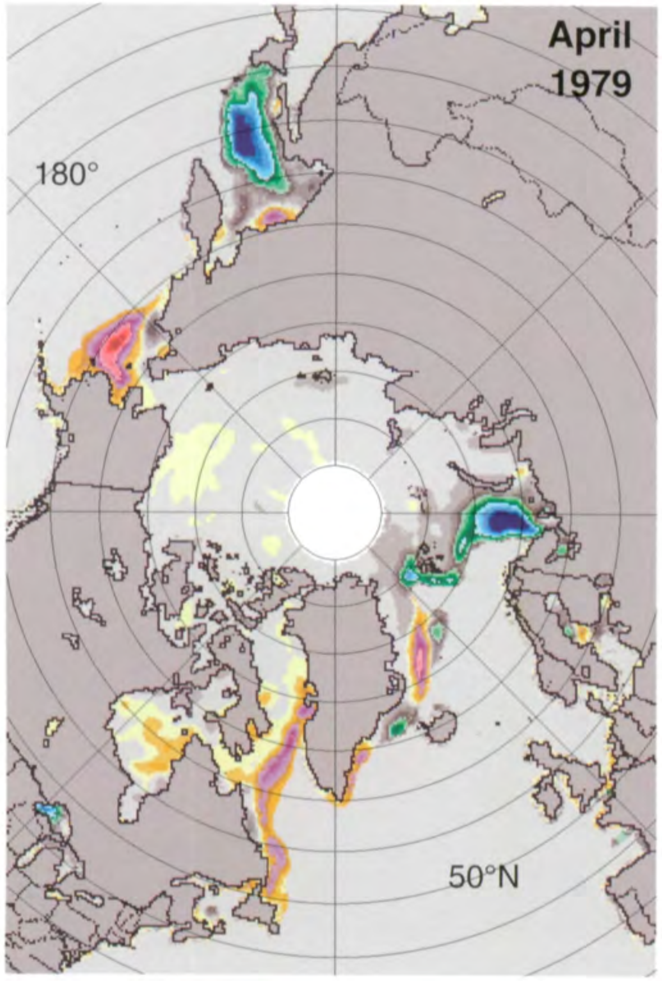
April
1979
180°
50°N

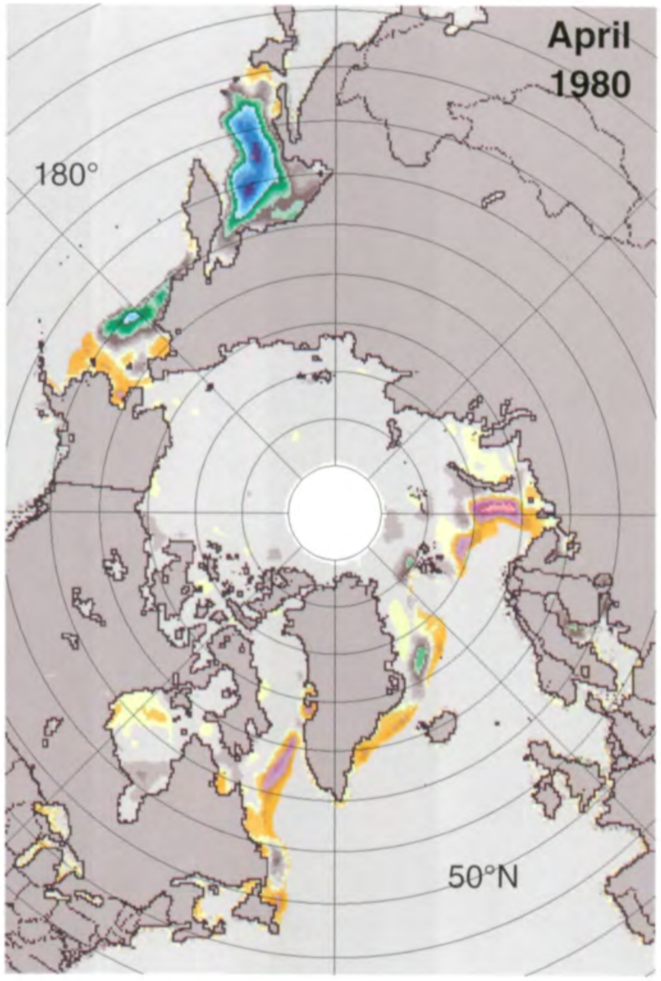
April
1980
180°
50°N

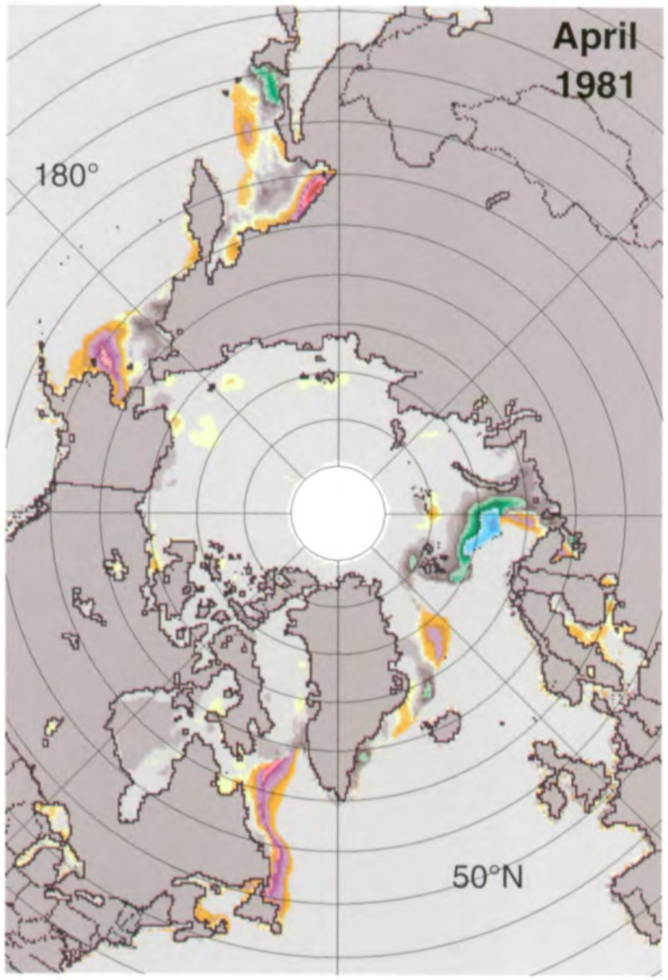
April
1981
180°
50°N

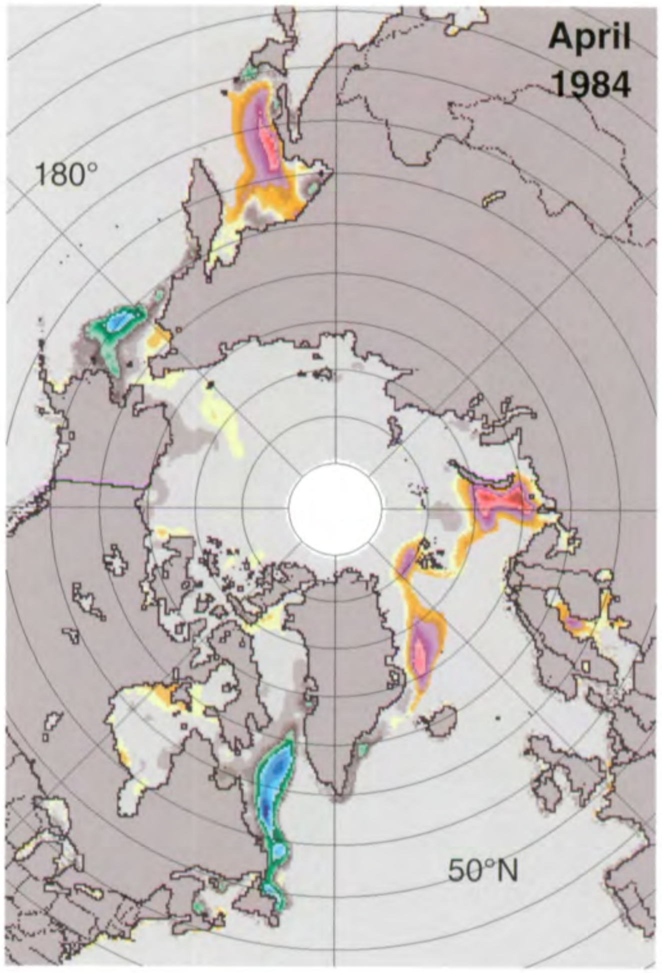
April
1984
180°
50°N

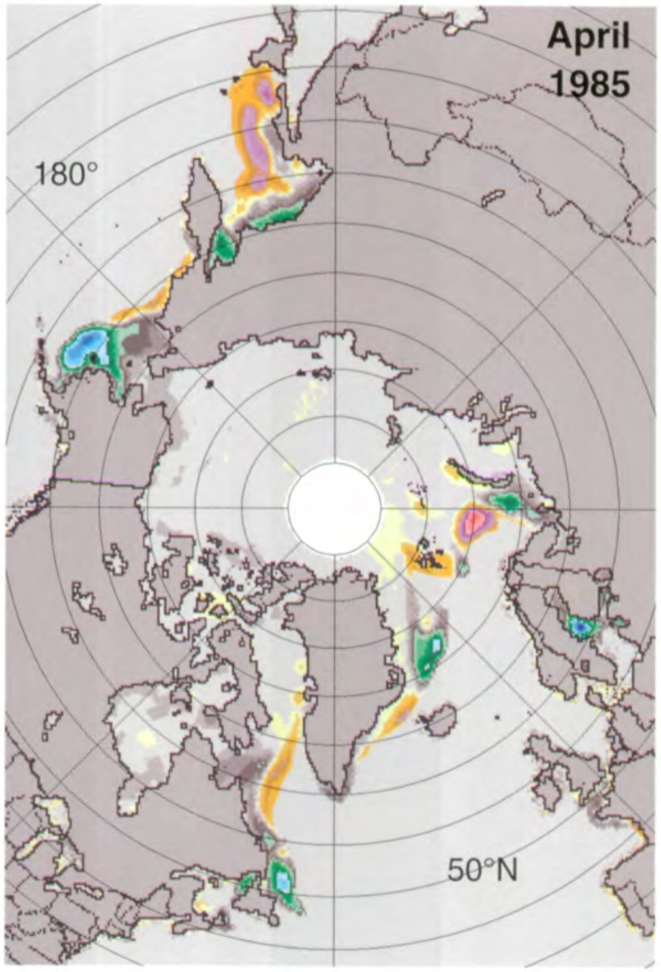
April
1985
180°
50°N

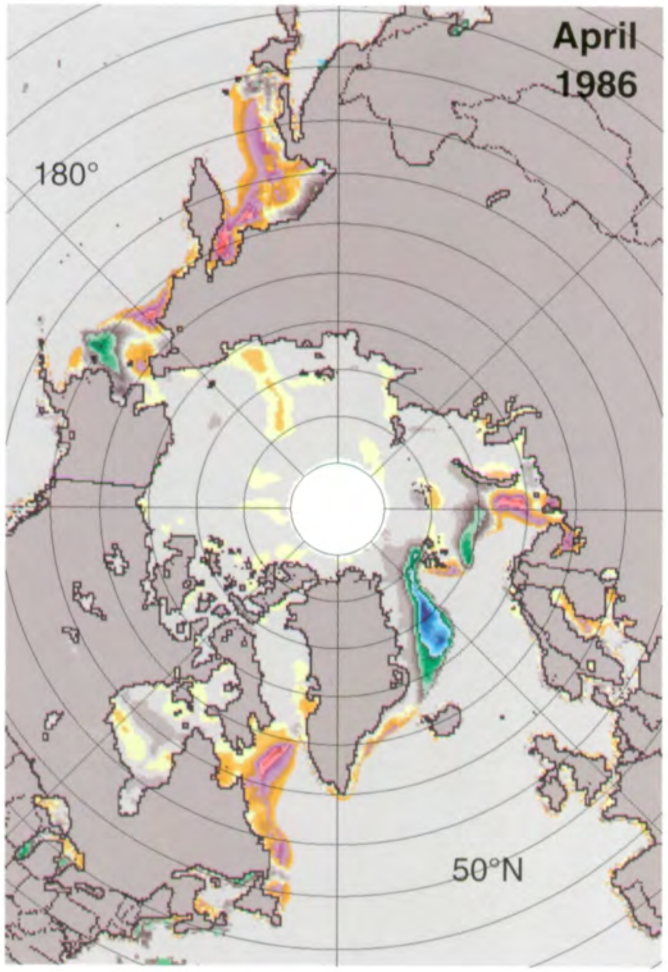
April
1986
180°
50°N

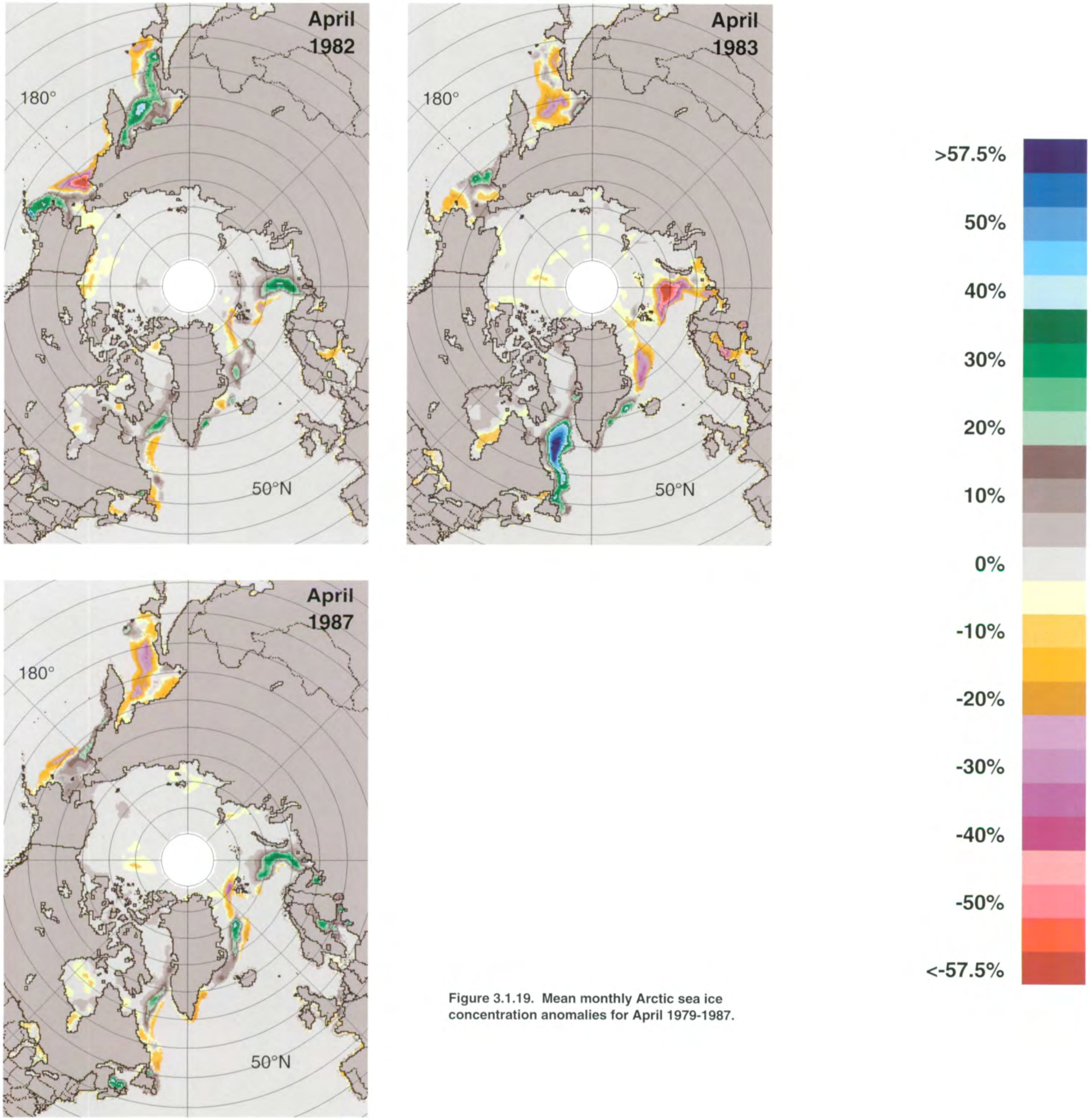

Figure 3.1.19. Mean monthly Arctic sea ice concentration anomalies for April 1979-1987.

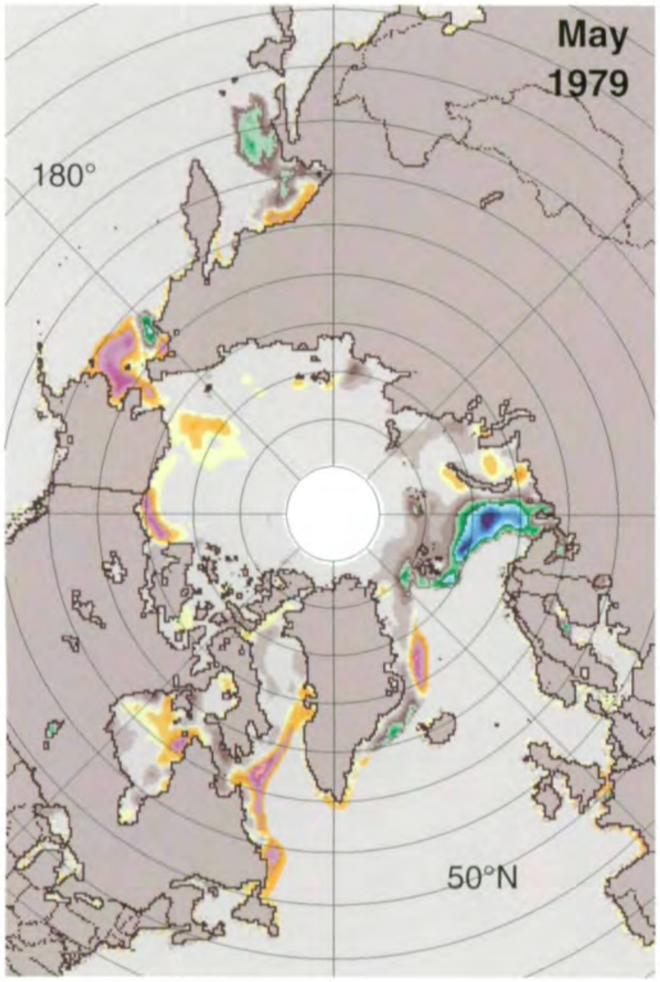
May
1979
180°
50°N

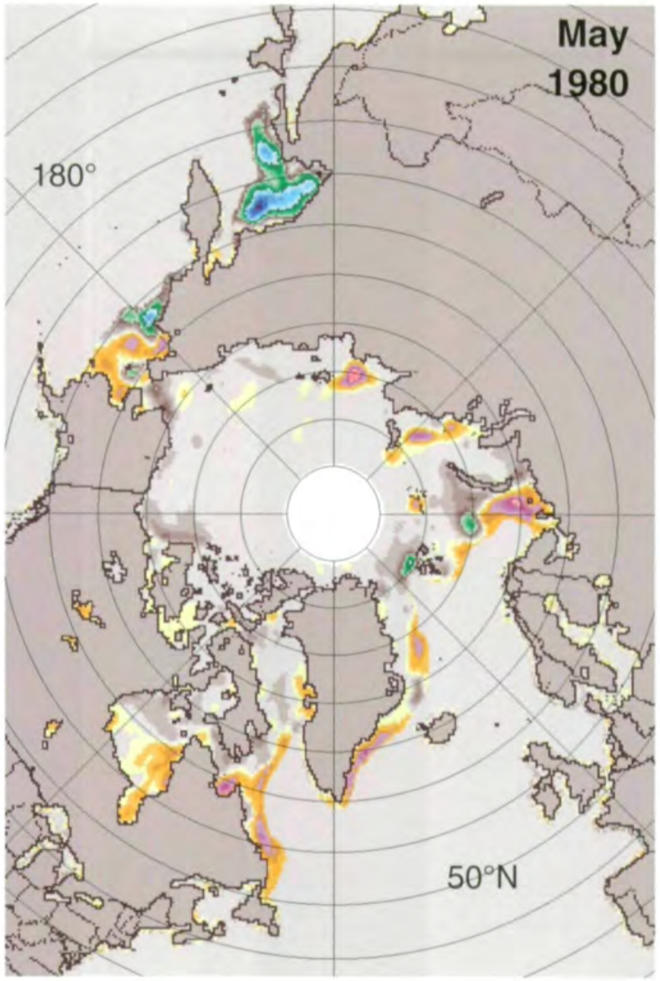
May
1980
180°
50°N

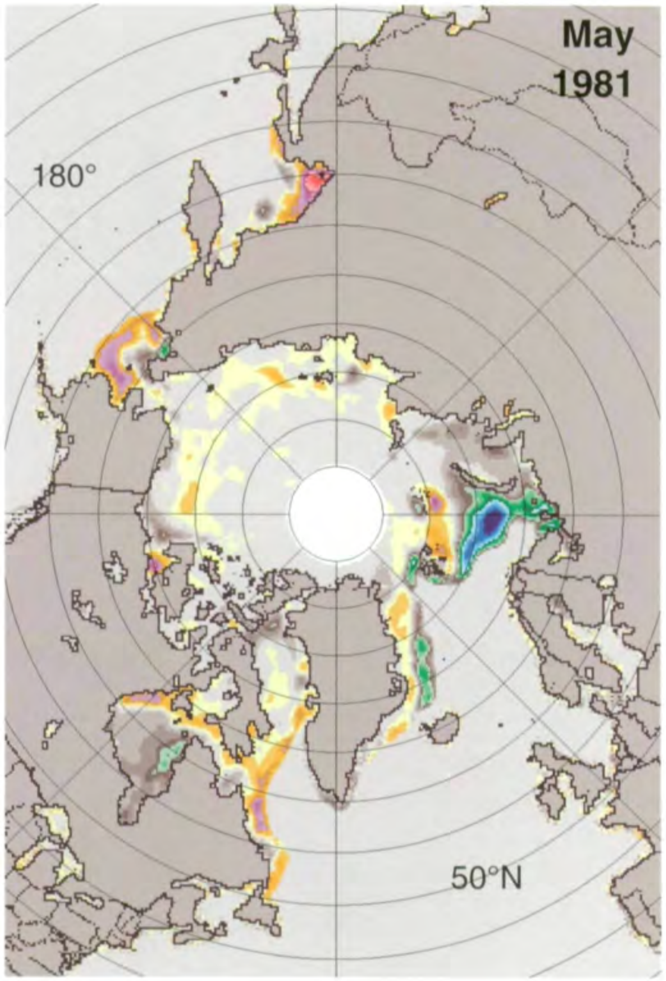
May
1981
180°
50°N

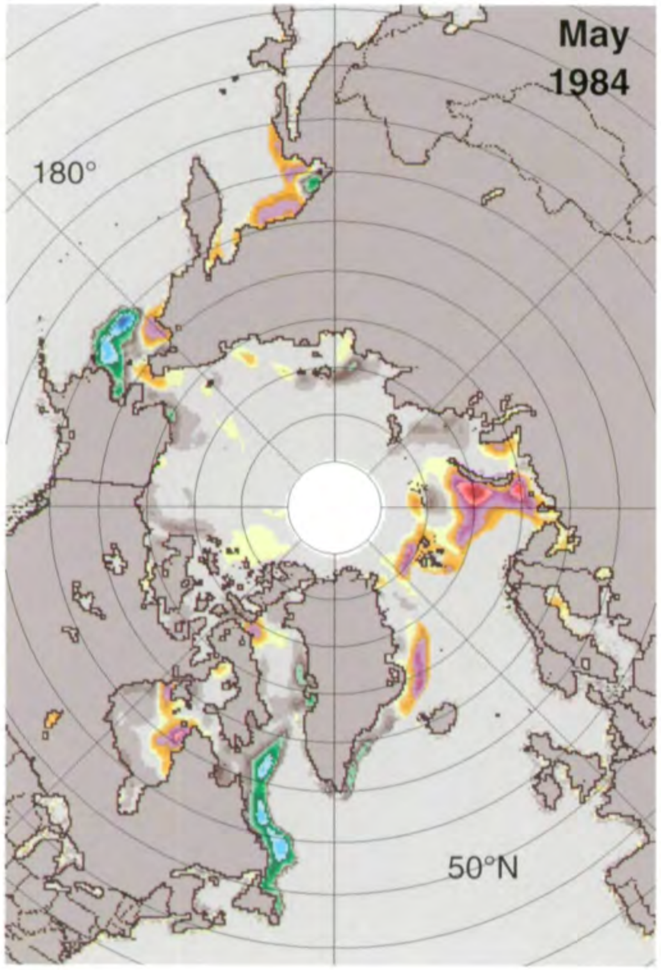
May
1984
180°
50°N

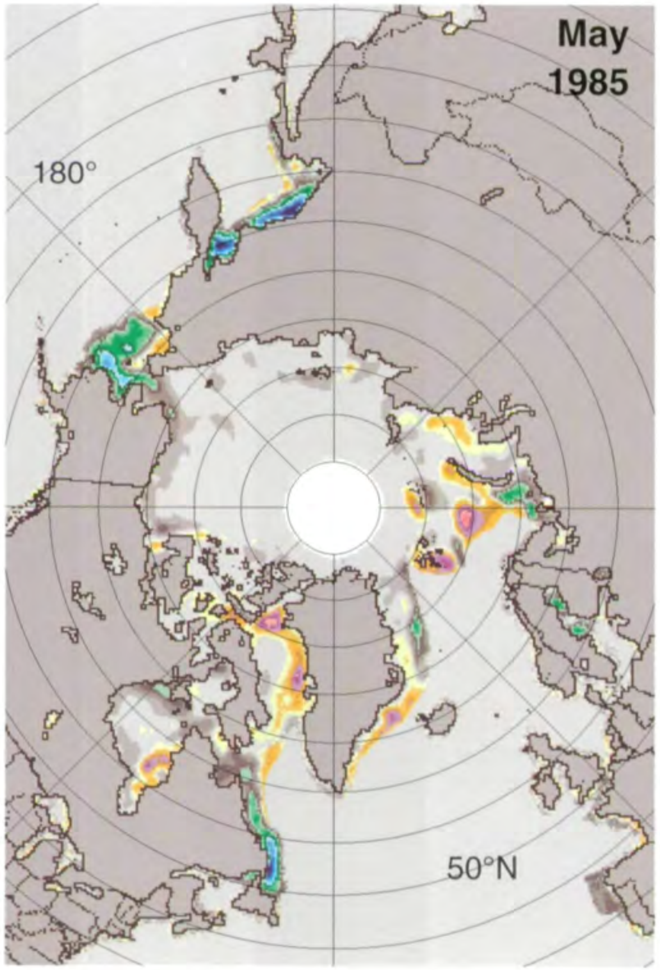
May
1985
180°
50°N

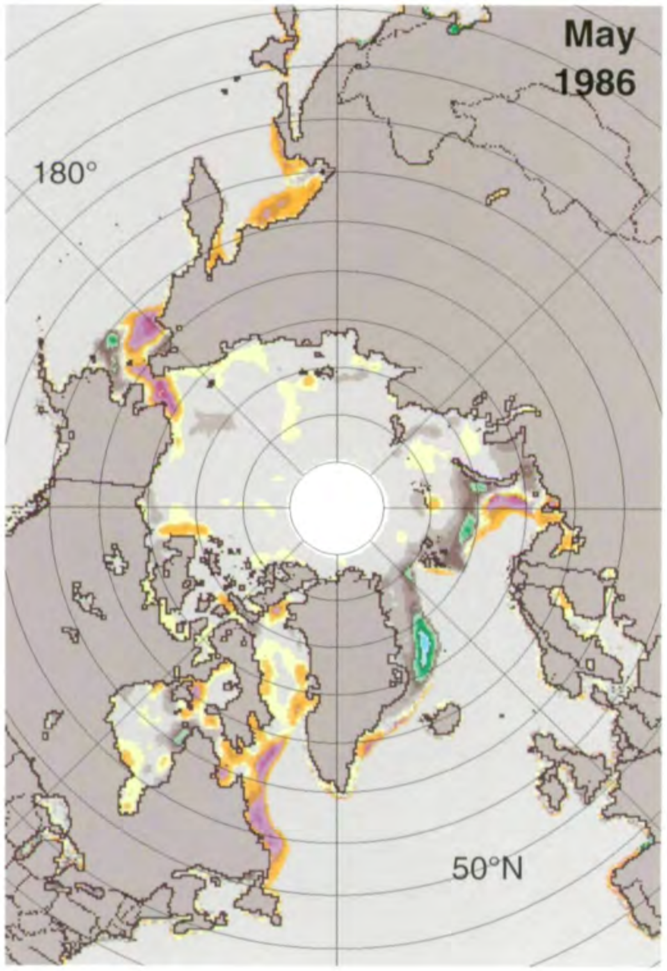
May
1986
180°
50°N

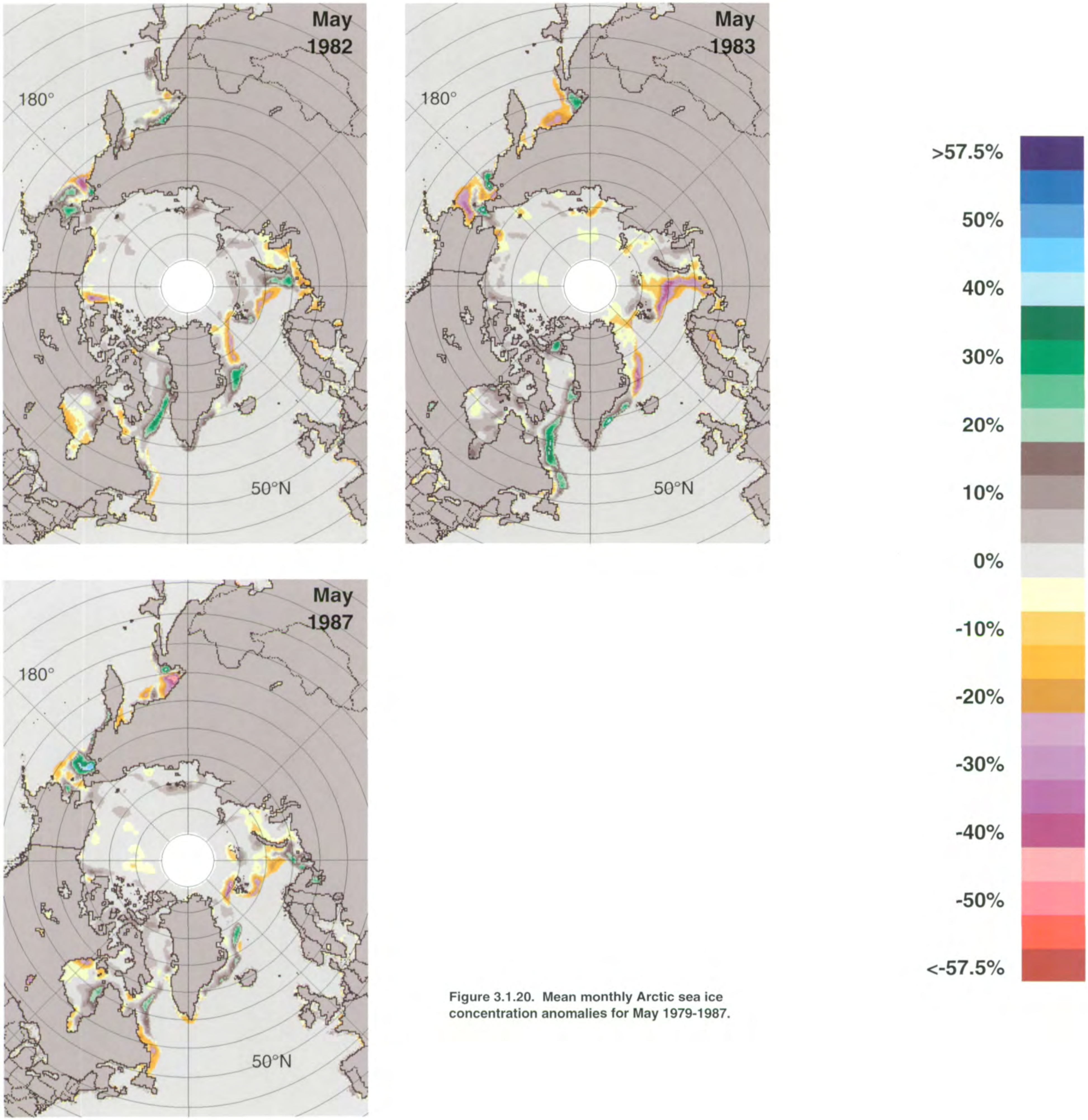

Figure 3.1.20. Mean monthly Arctic sea ice concentration anomalies for May 1979-1987.

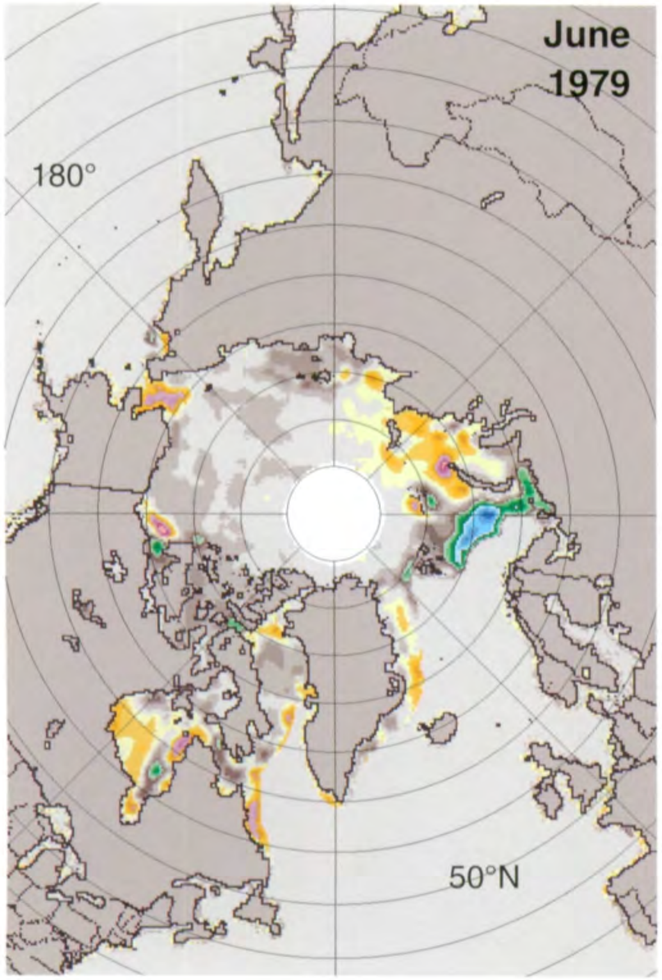
June
1979
180°
50°N

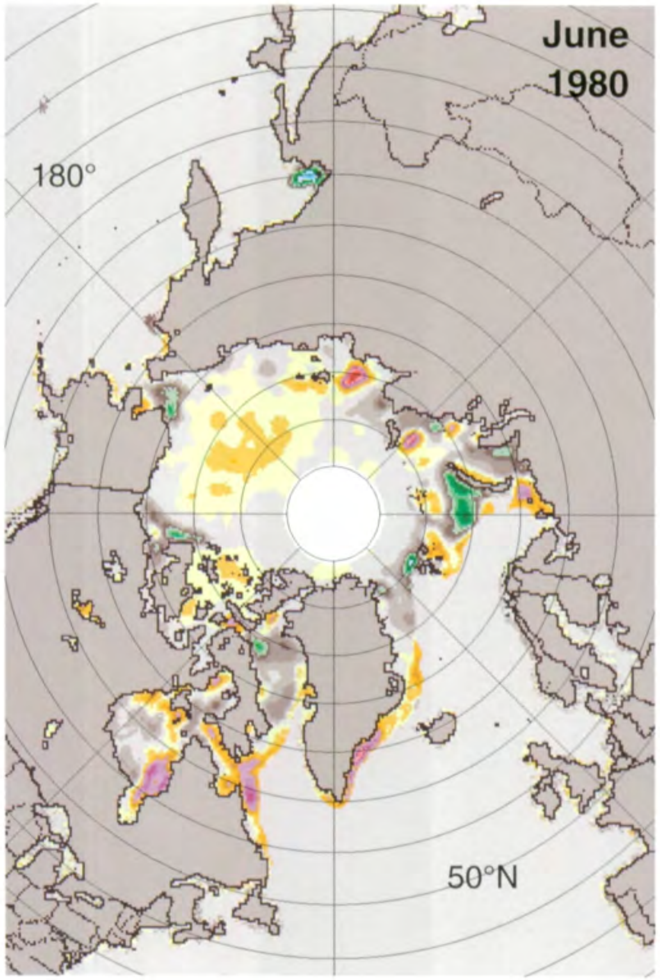
June
1980
180°
50°N

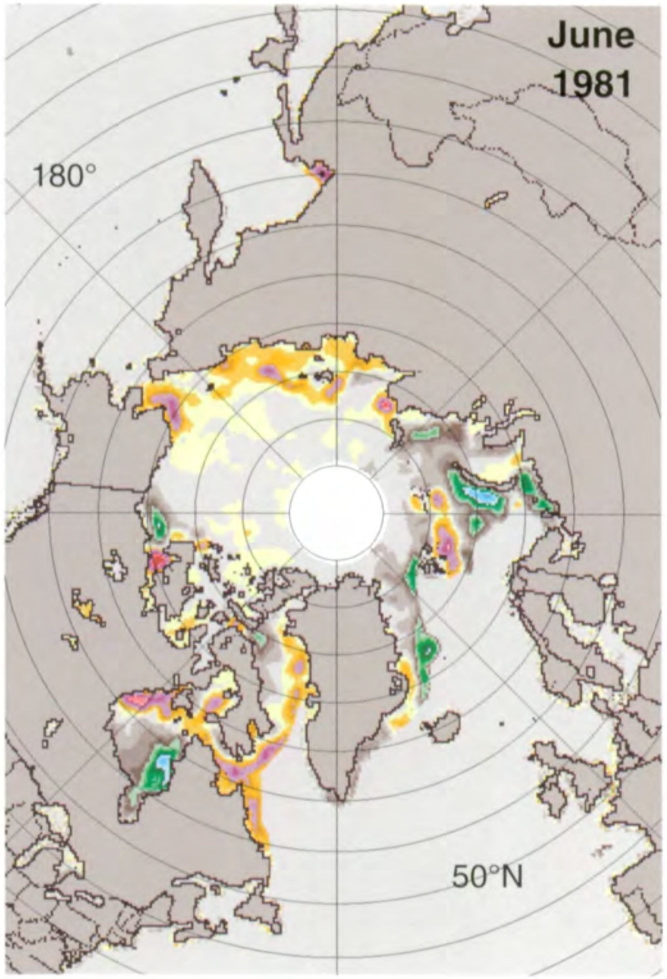
June
1981
180°
50°N

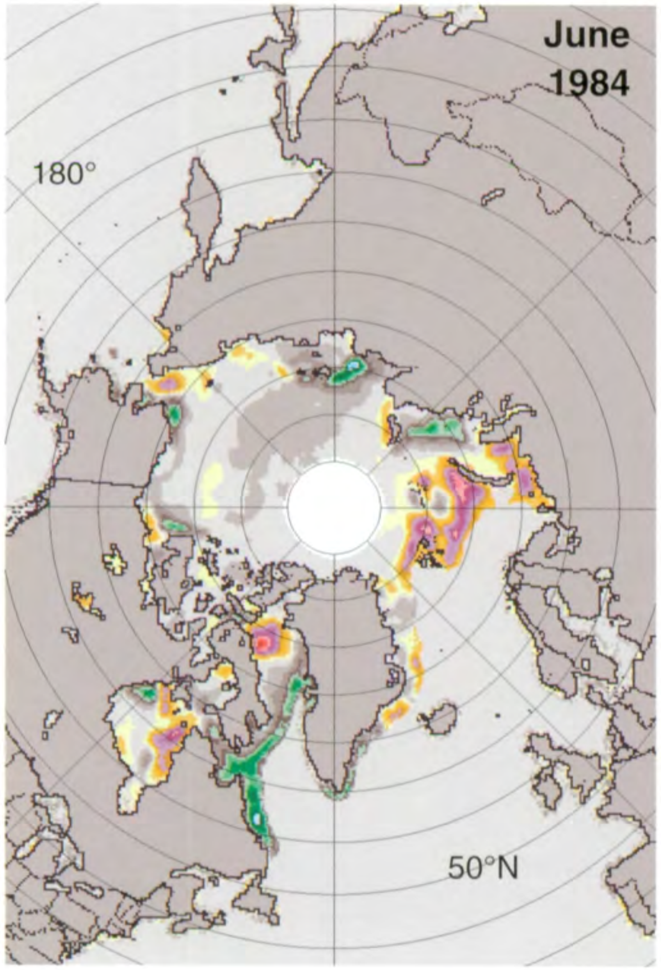
June
1984
180°
50°N

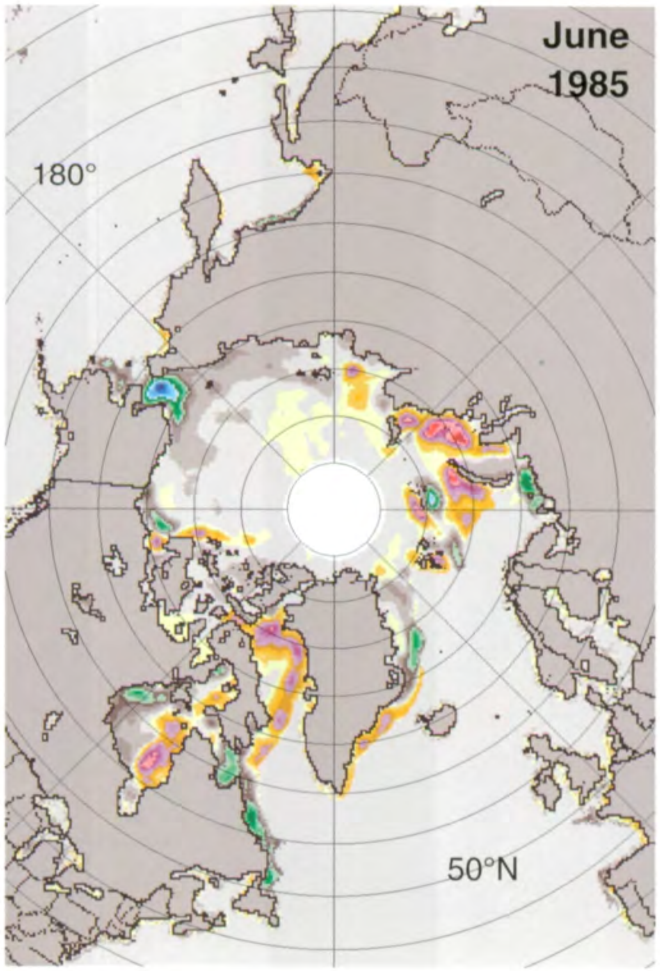
June
1985
180°
50°N

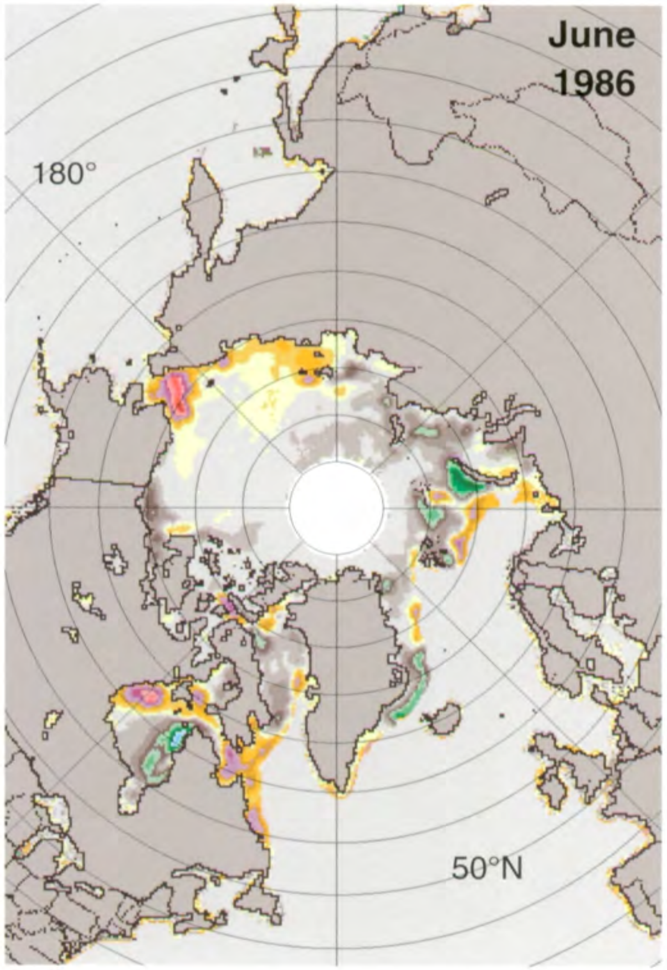
June
1986
180°
50°N

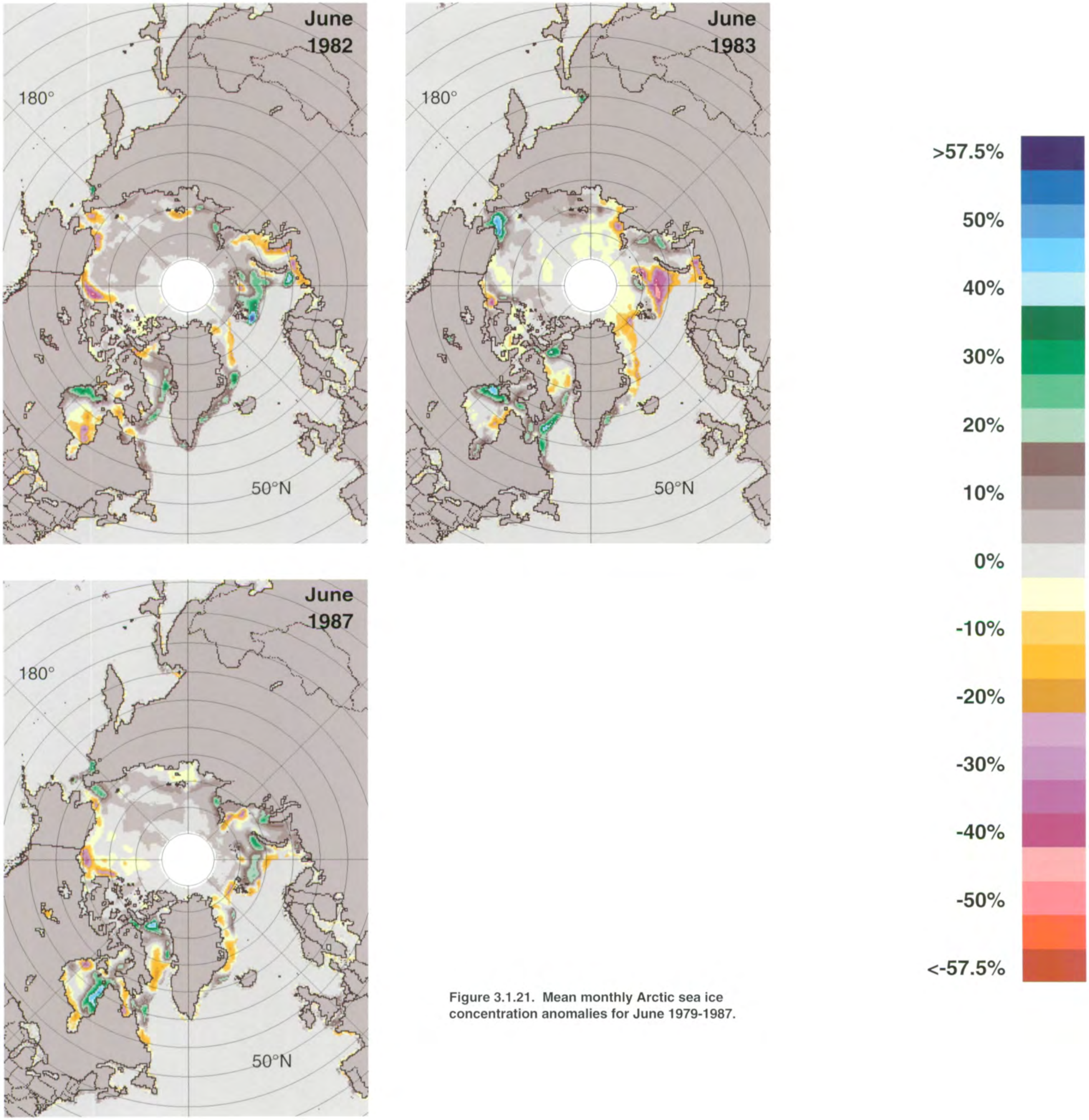

Figure 3.1.21. Mean monthly Arctic sea ice concentration anomalies for June 1979-1987.

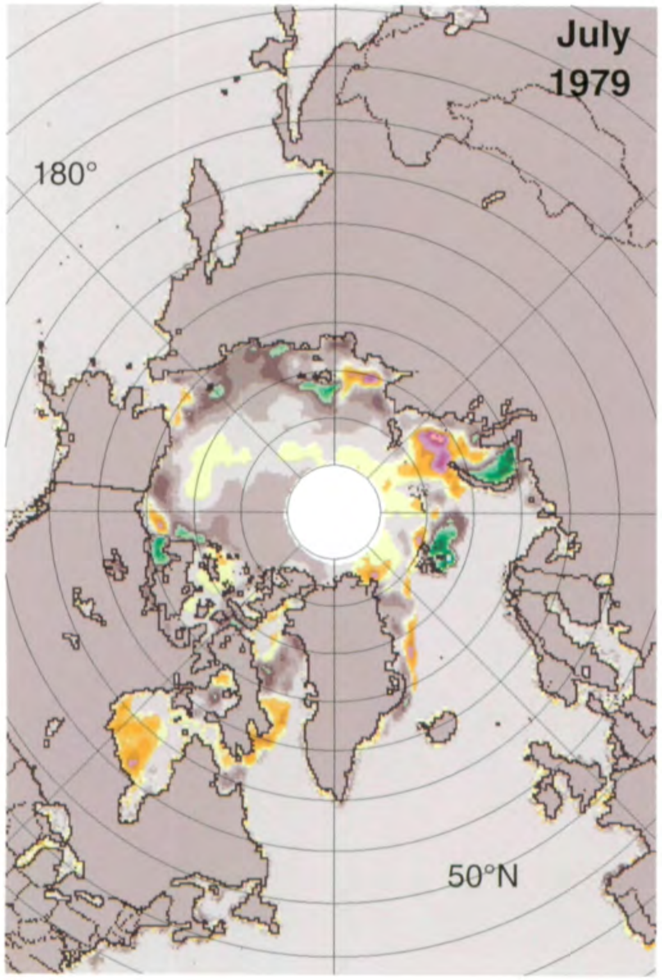
July
1979
180°
50°N

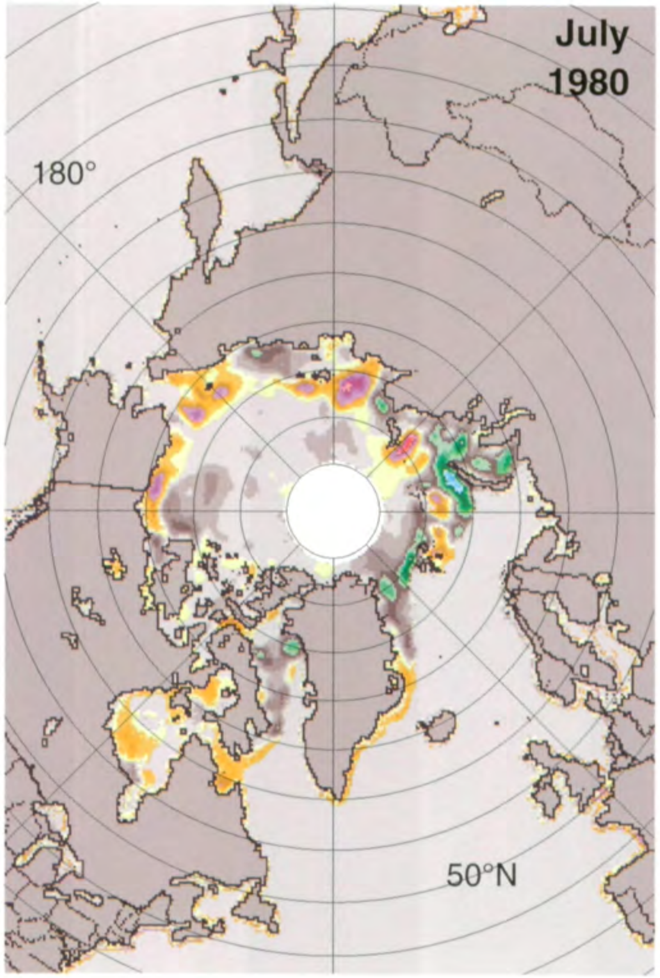
July
1980
180°
50°N

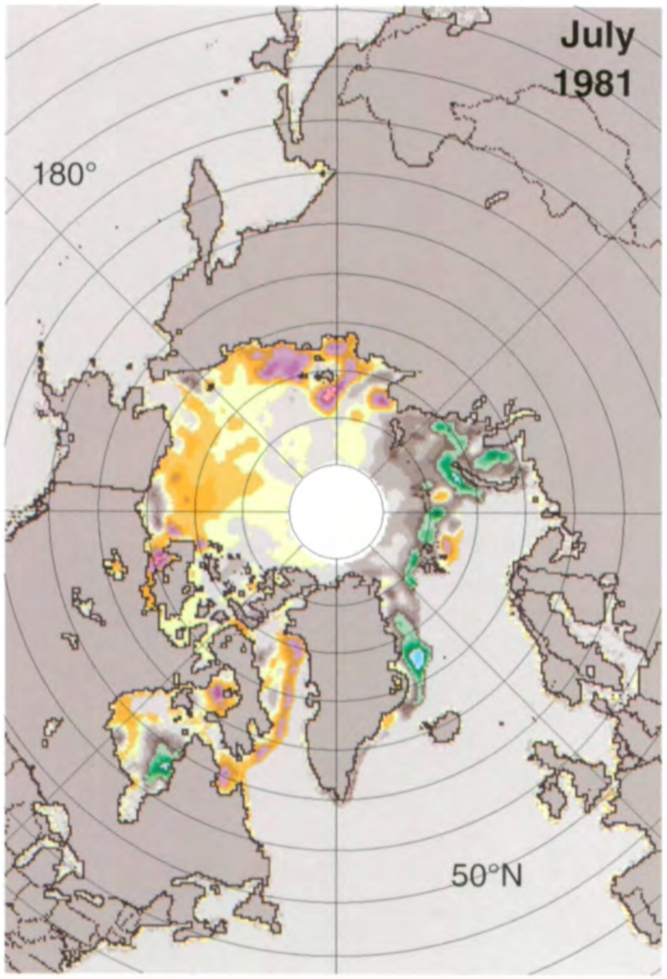
July
1981
180°
50°N

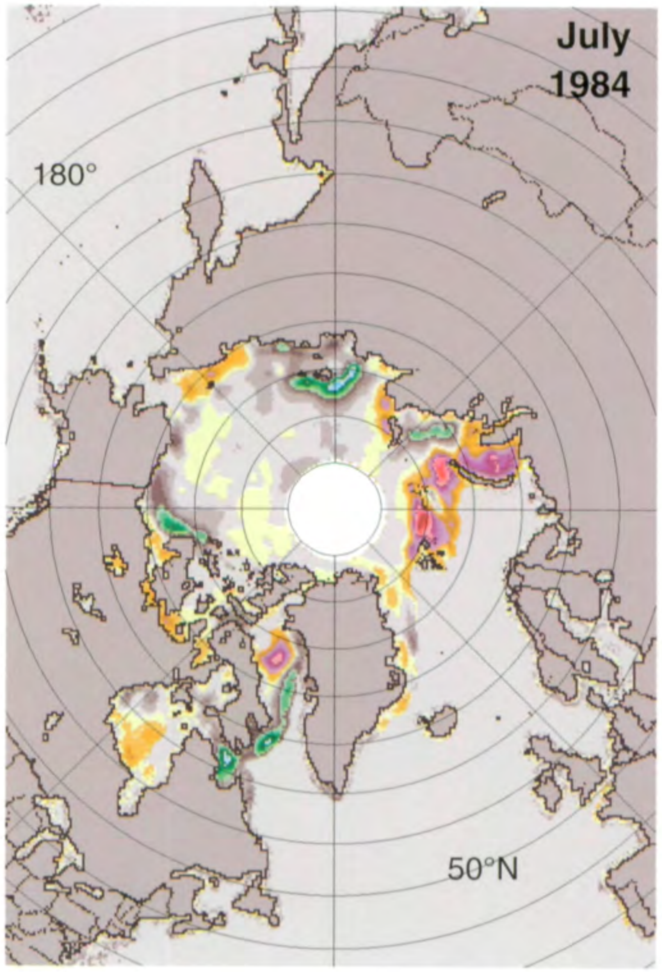
July
1984
180°
50°N

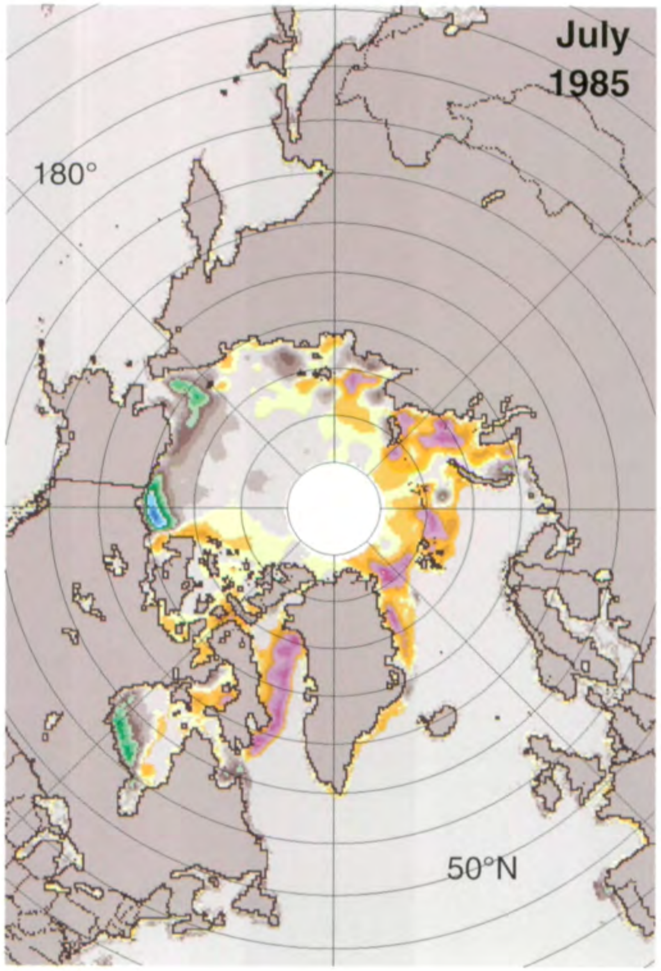
July
1985
180°
50°N

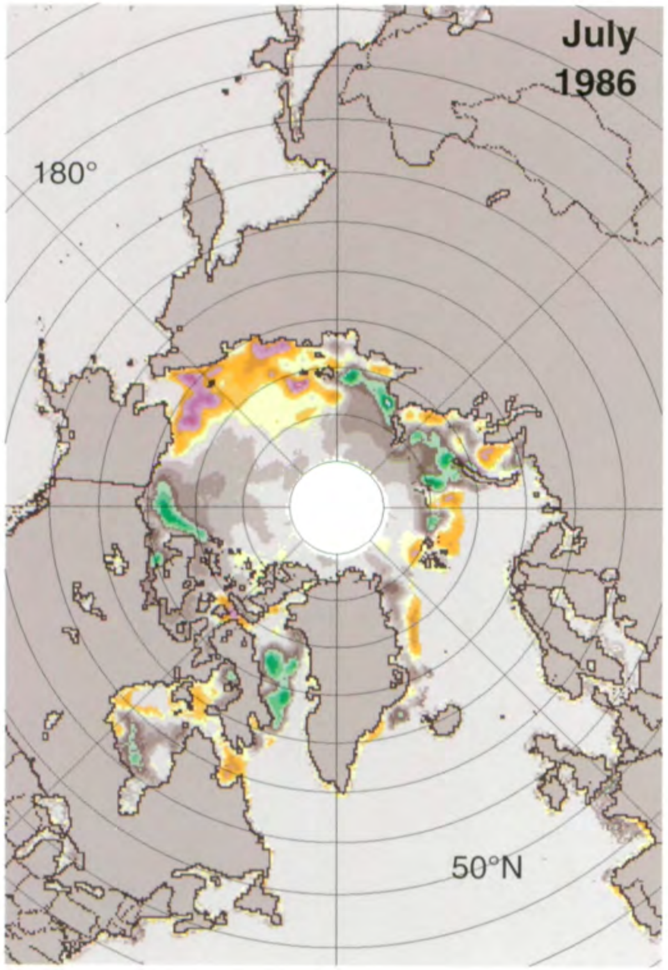
July
1986
180°
50°N

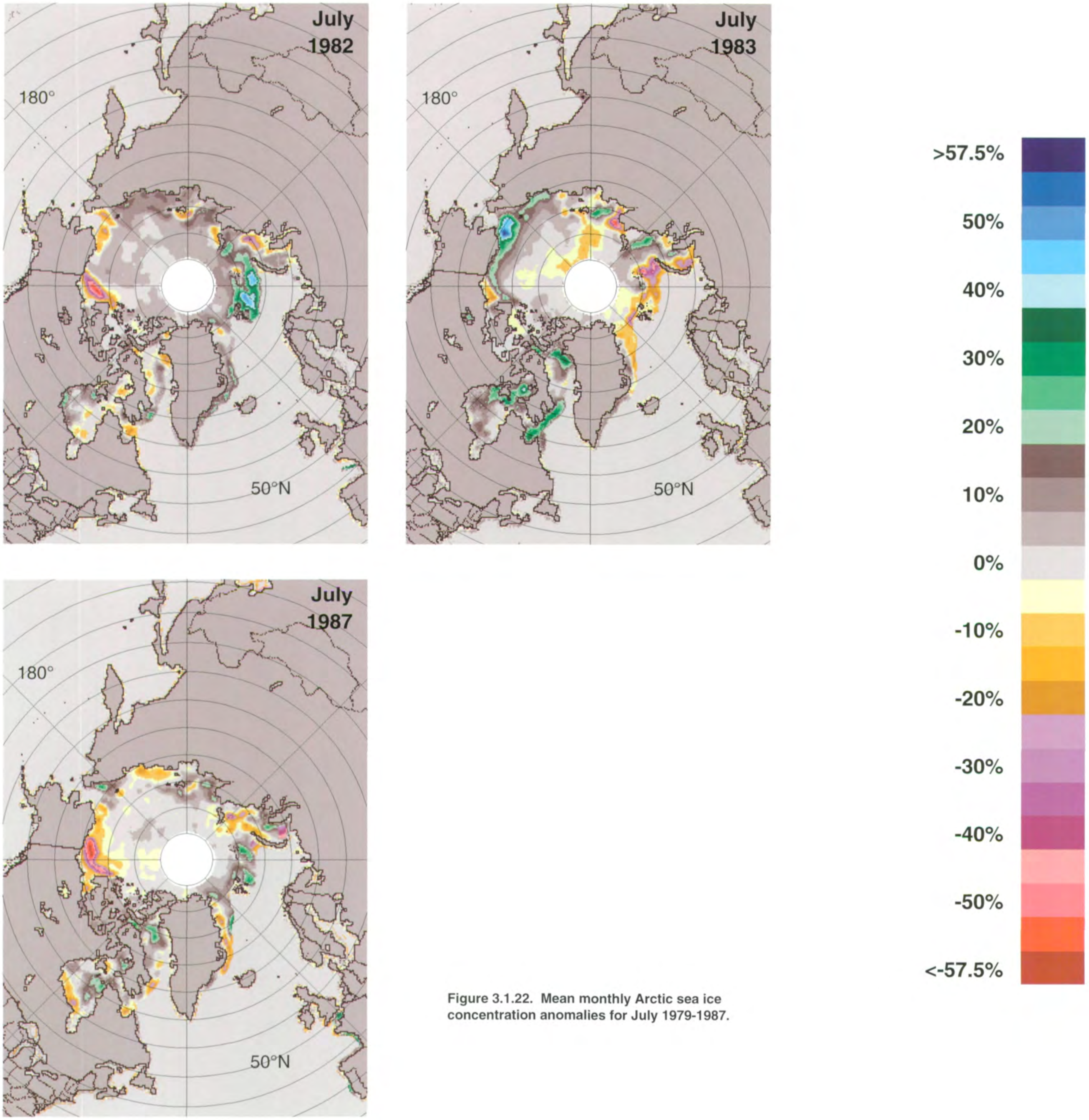

Figure 3.1.22. Mean monthly Arctic sea ice concentration anomalies for July 1979-1987.

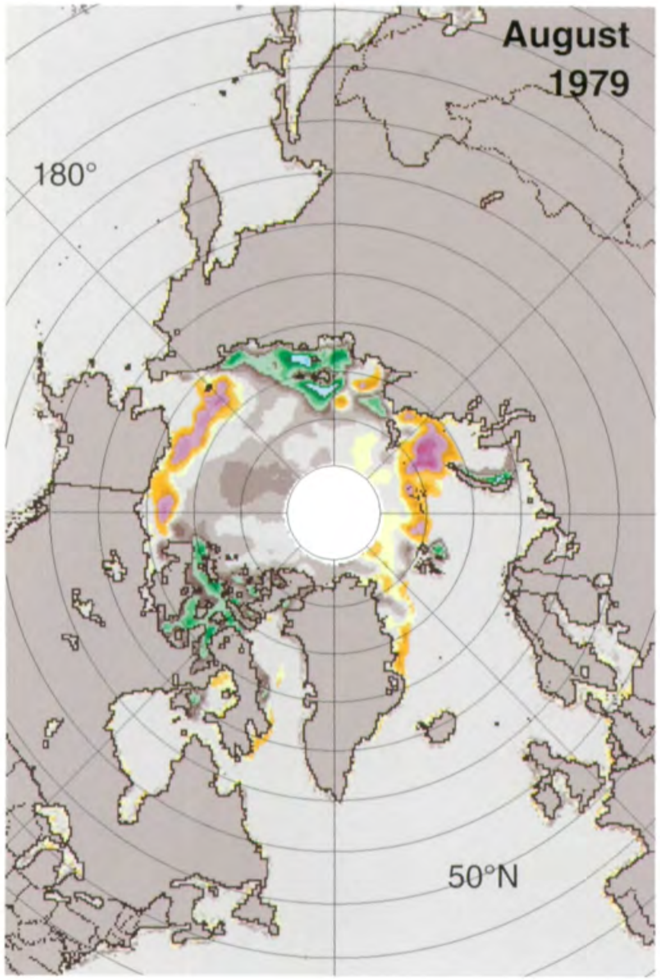
August
1979
180°
50°N

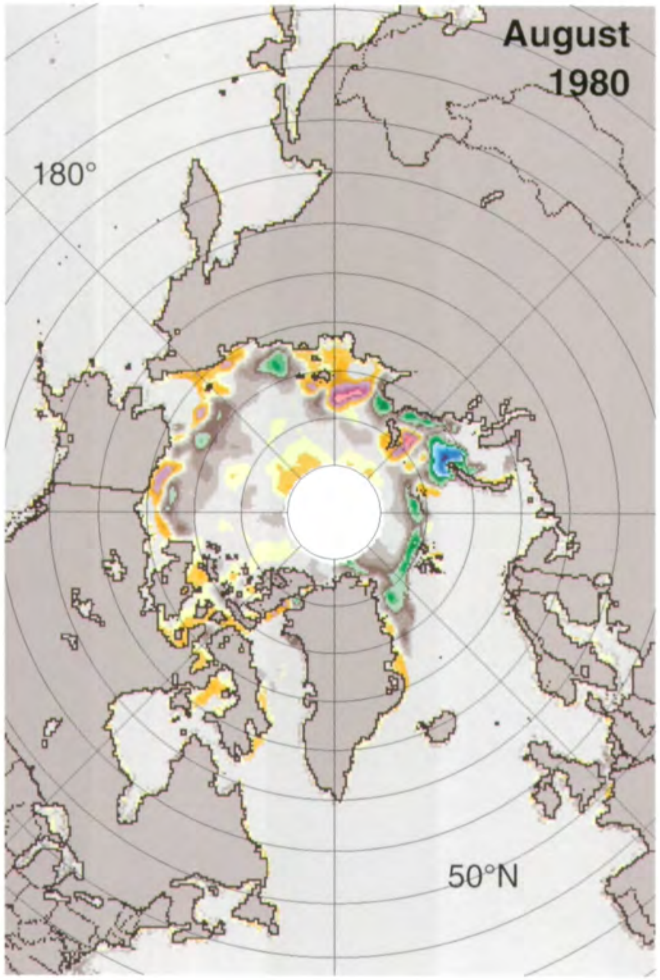
August
1980
180°
50°N

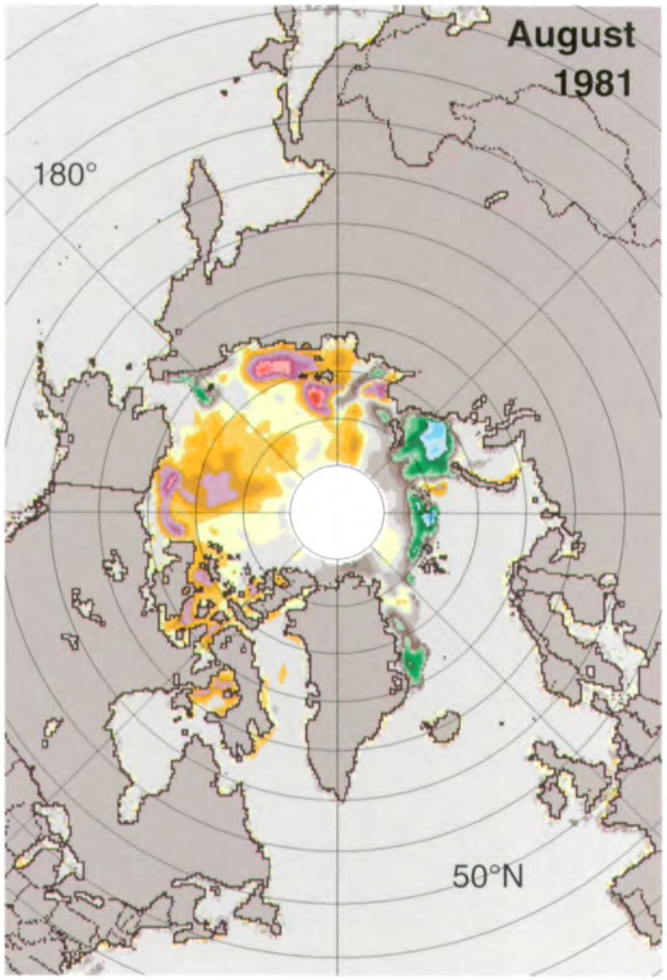
August
1981
180°
50°N

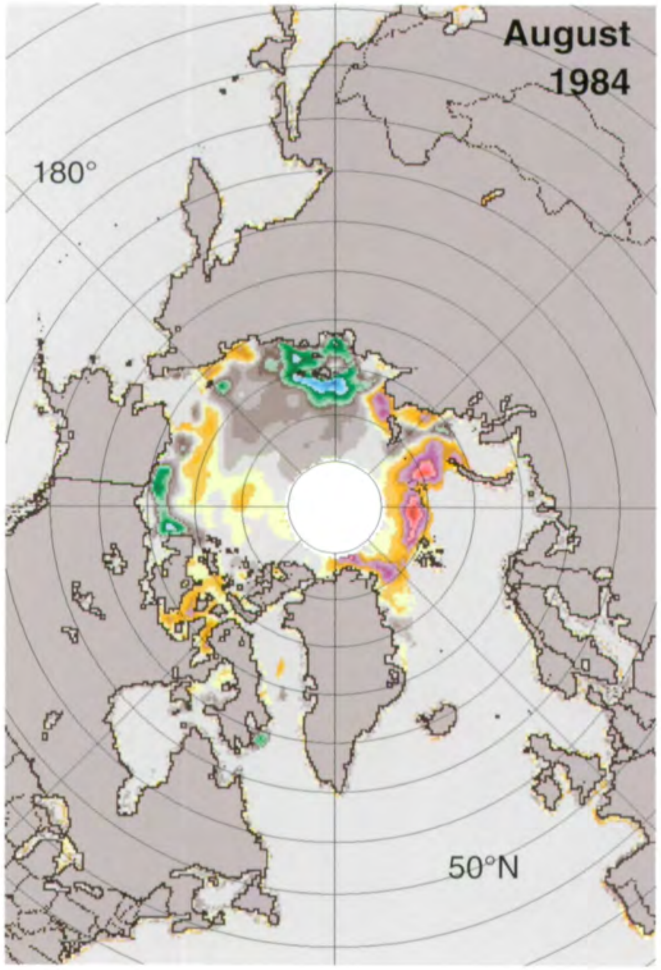
August
1984
180°
50°N

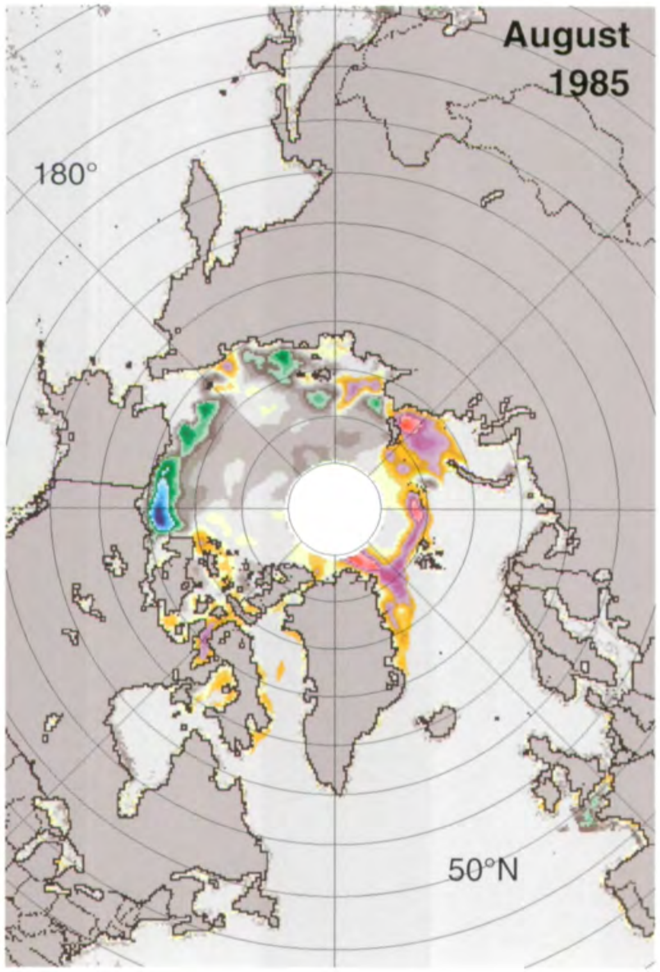
August
1985
180°
50°N

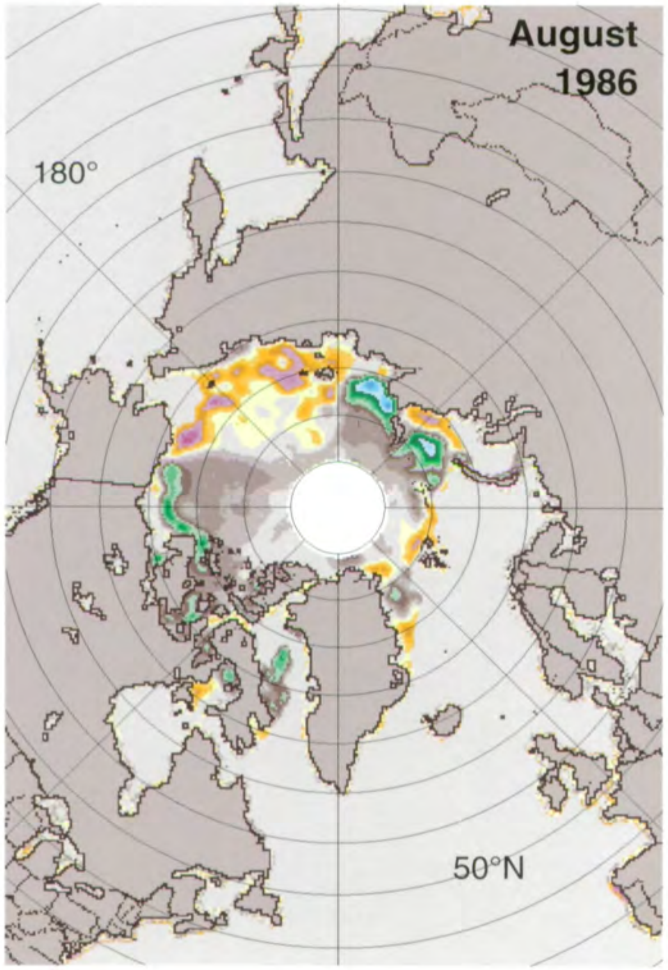
August
1986
180°
50°N

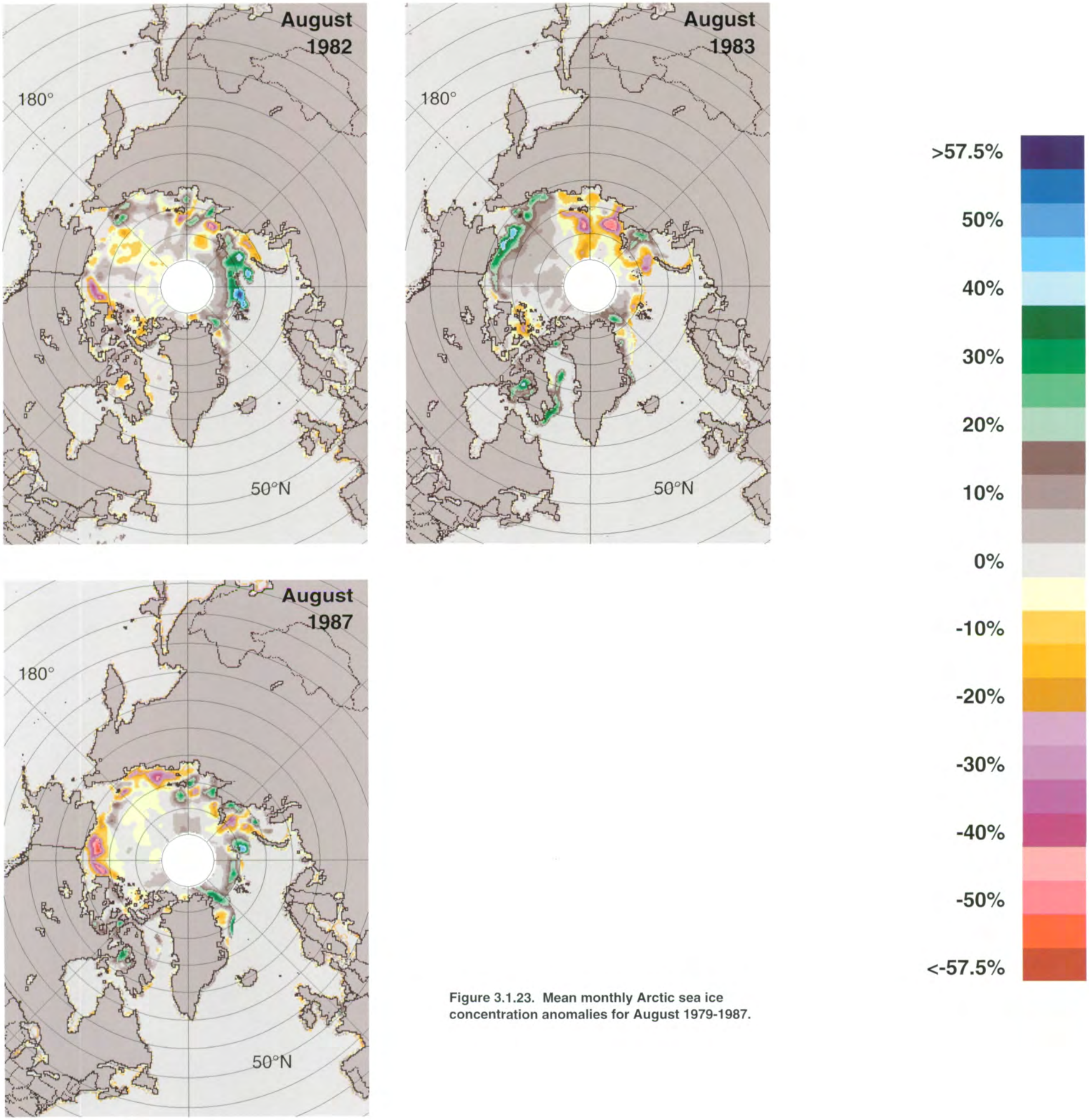

Figure 3.1.23. Mean monthly Arctic sea ice concentration anomalies for August 1979-1987.

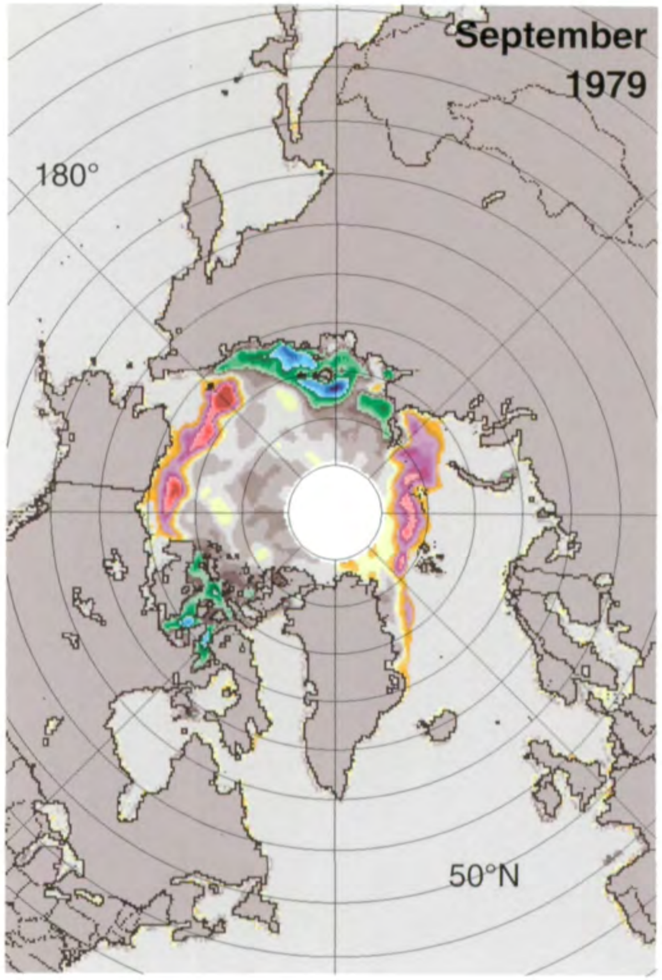
September
1979
180°
50°N

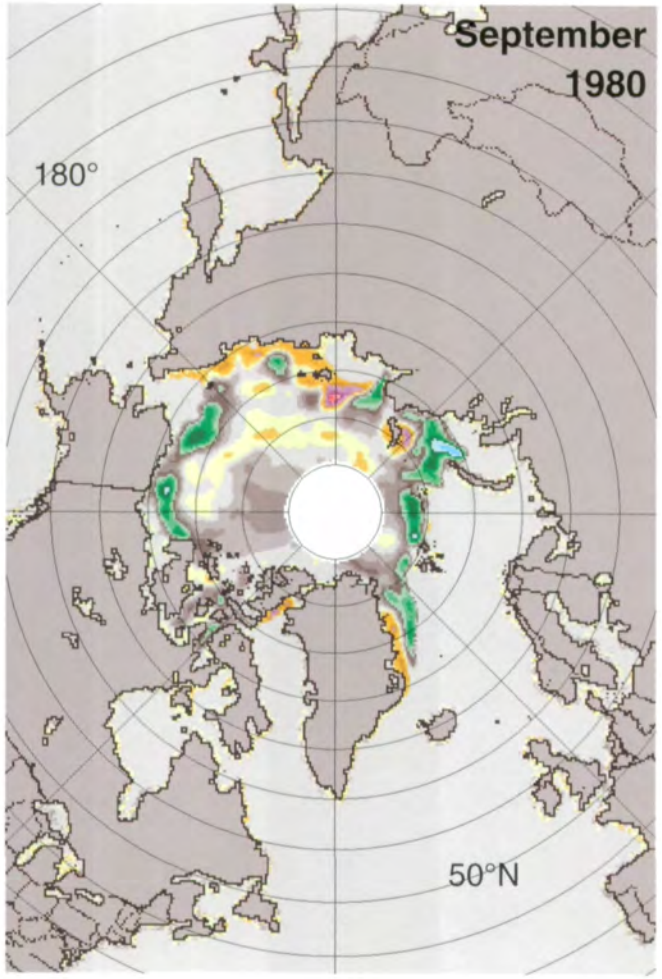
September
1980
180°
50°N

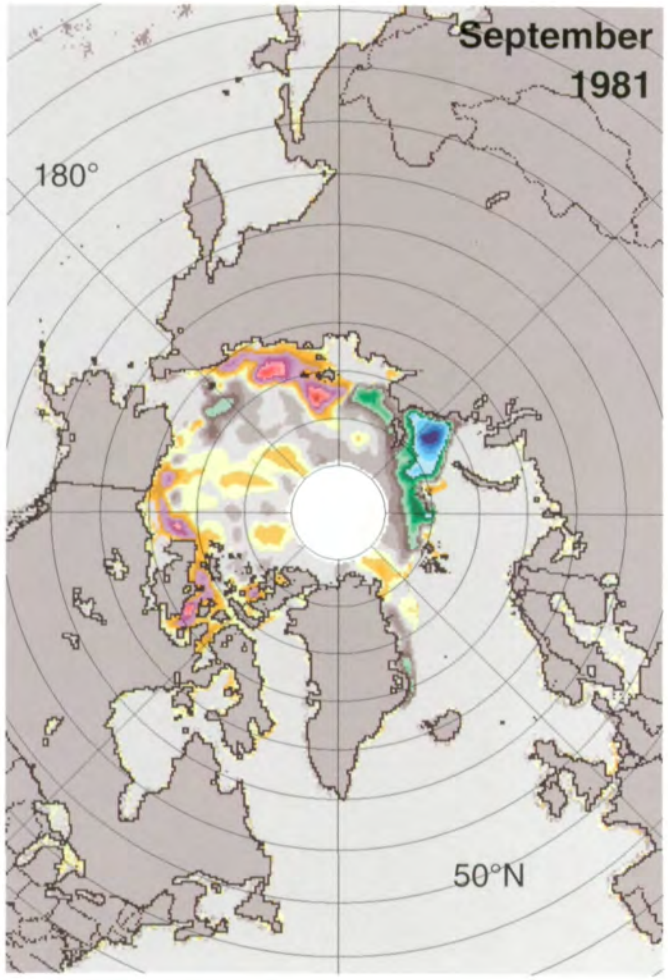
September
1981
180°
50°N

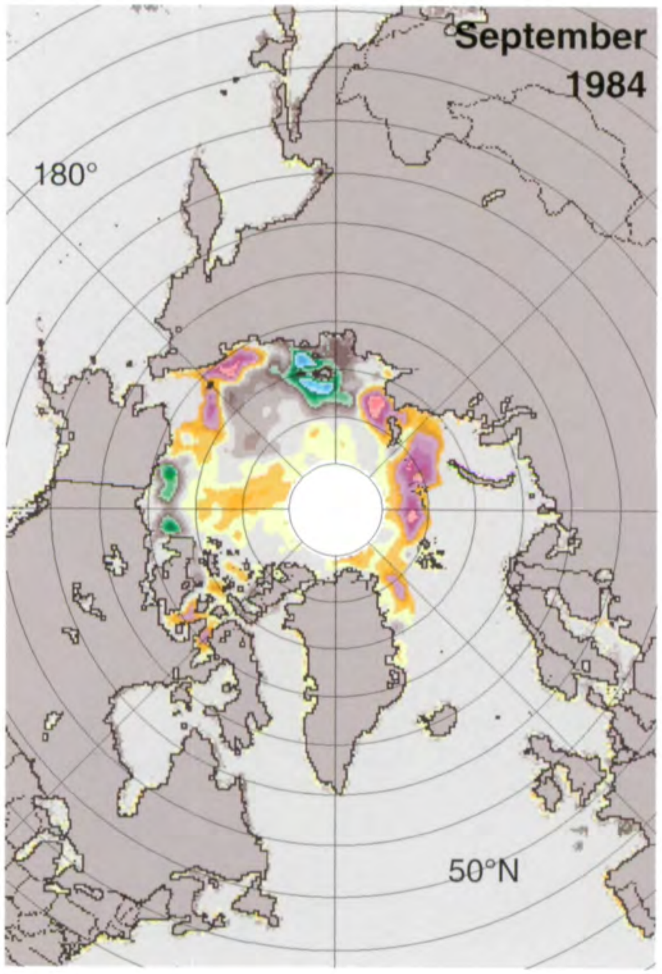
September
1984
180°
50°N

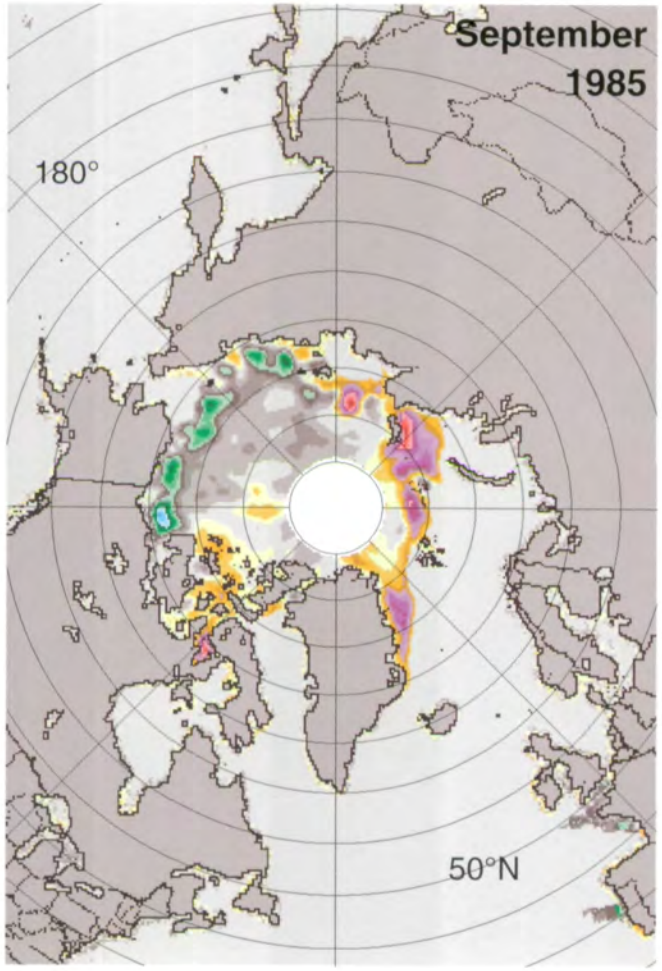
September
1985
180°
50°N

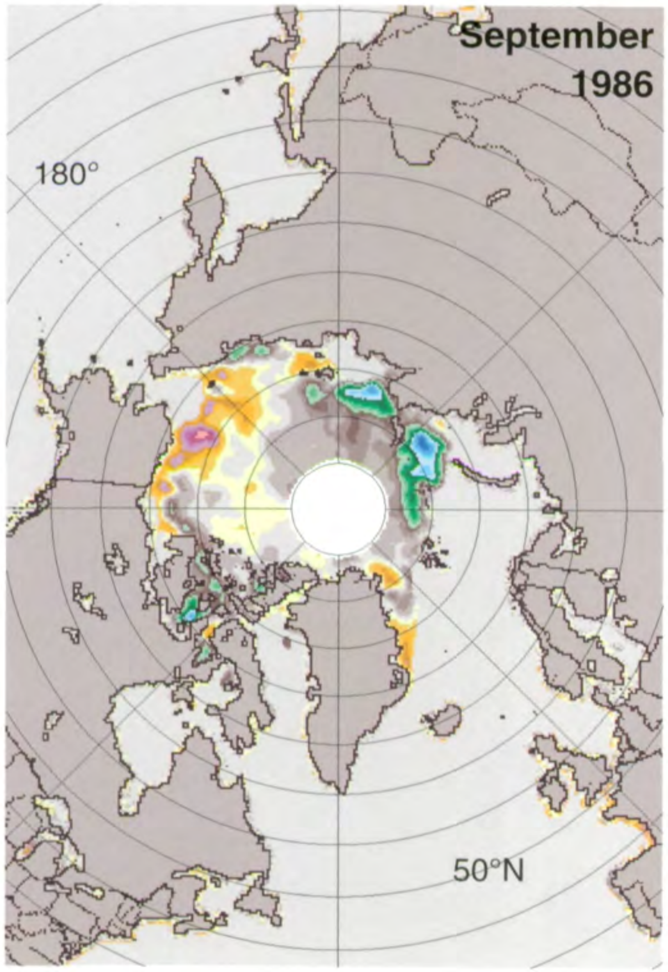
September
1986
180°
50°N

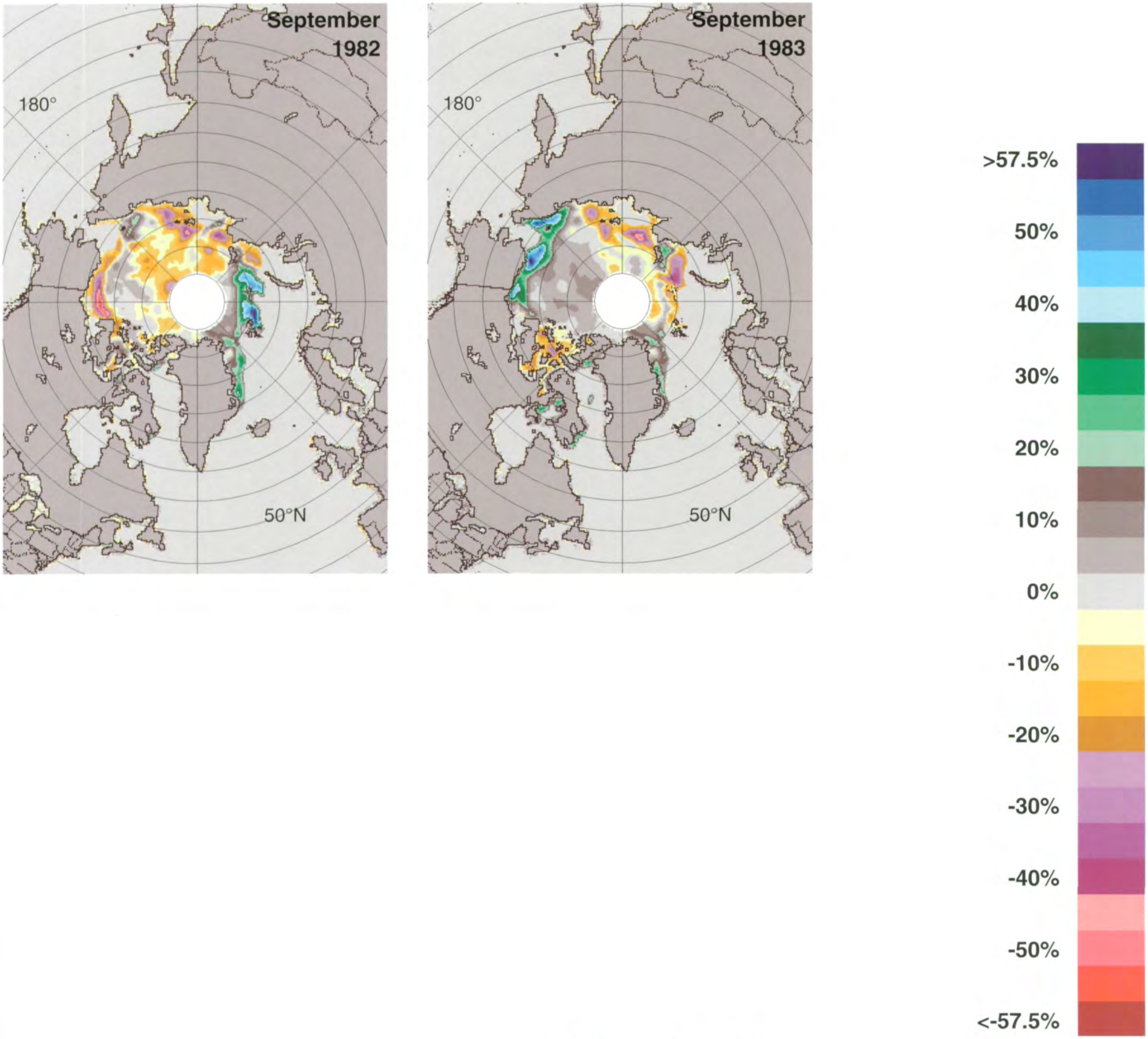

Figure 3.1.24. Mean monthly Arctic sea ice concentration anomalies for September 1979-1986.

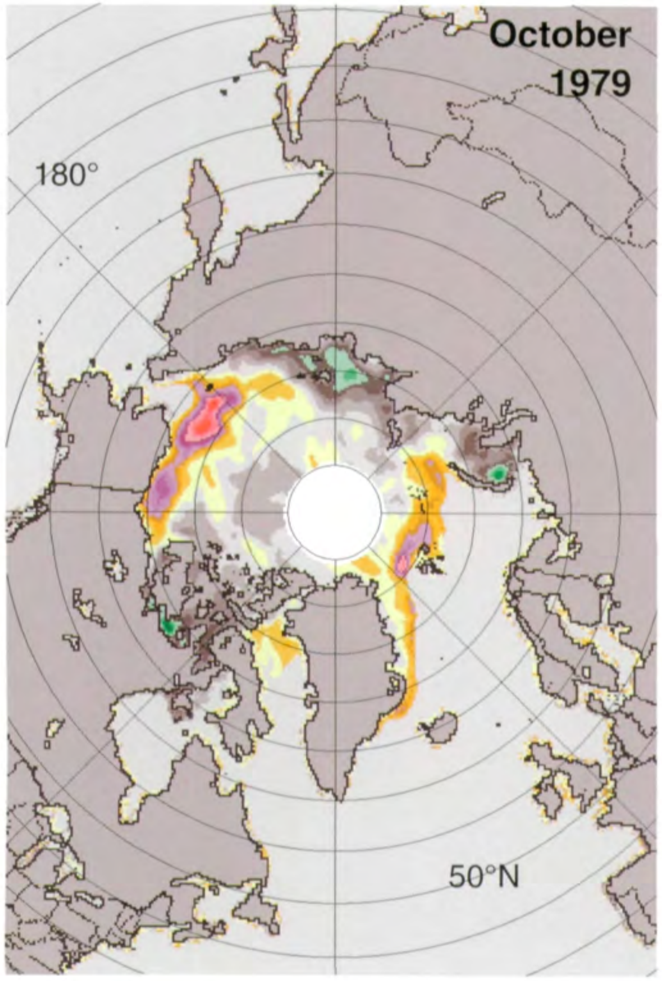
October 1979
180°
50°N

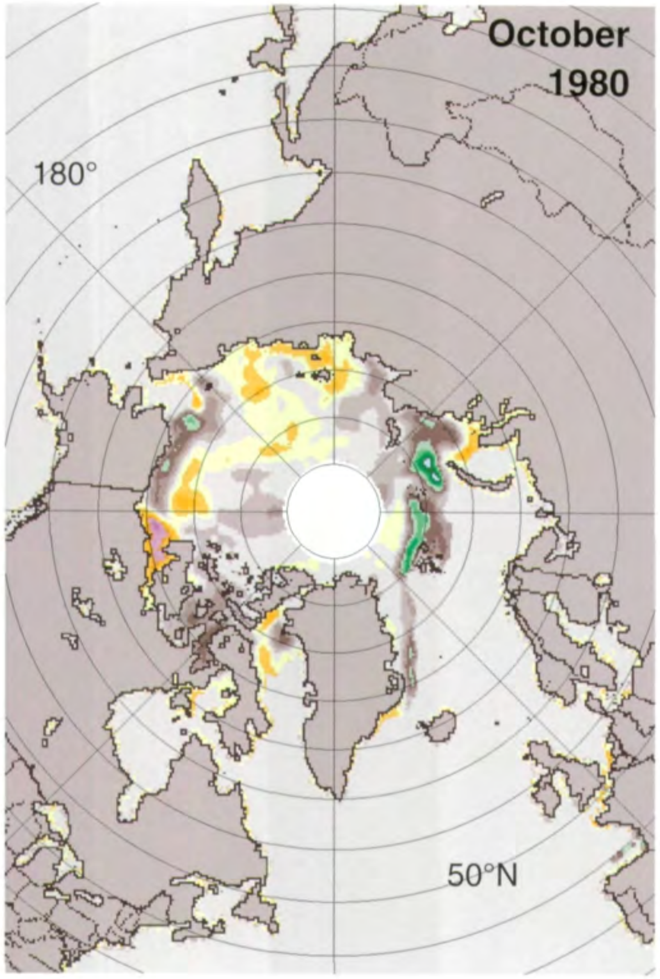
October 1980
180°
50°N

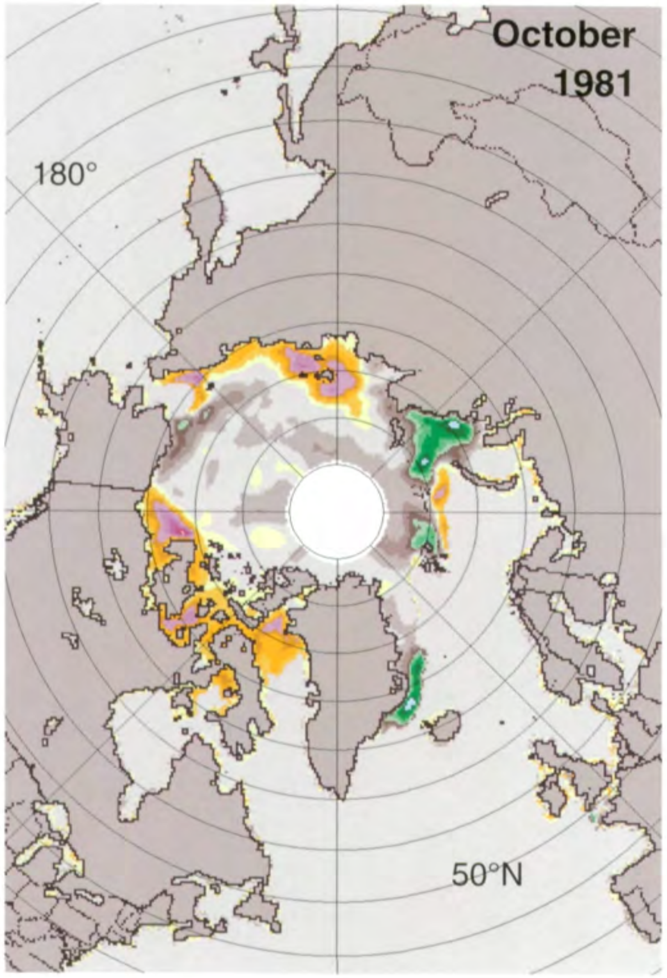
October 1981
180°
50°N

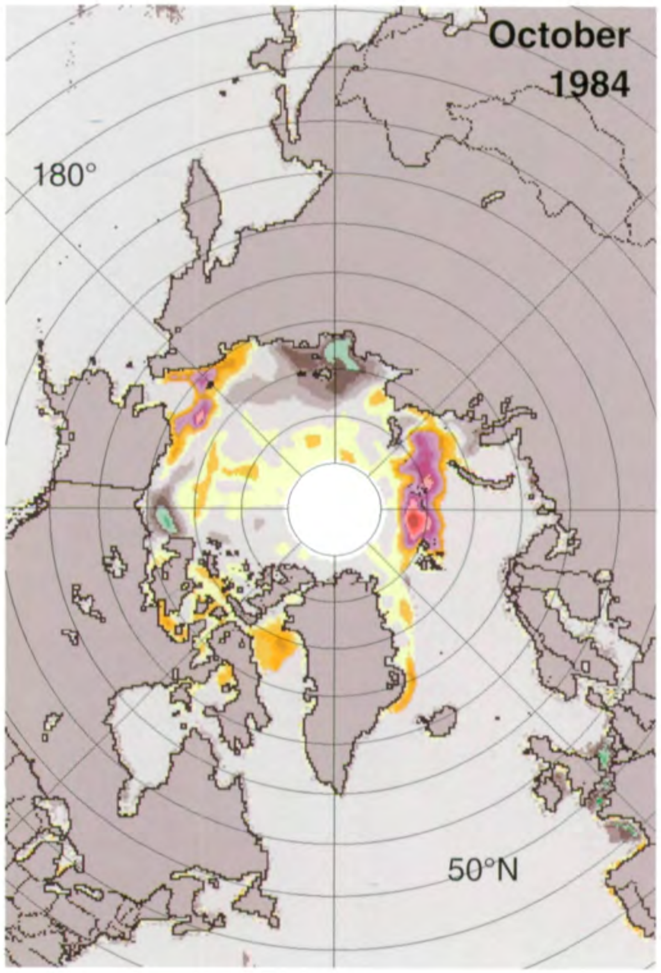
October 1984
180°
50°N

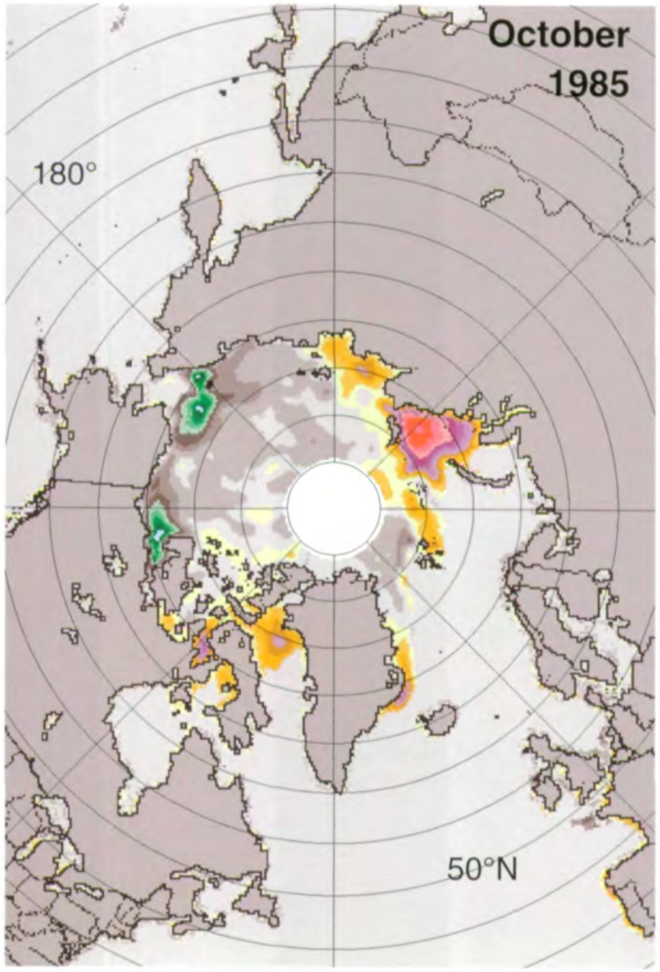
October 1985
180°
50°N

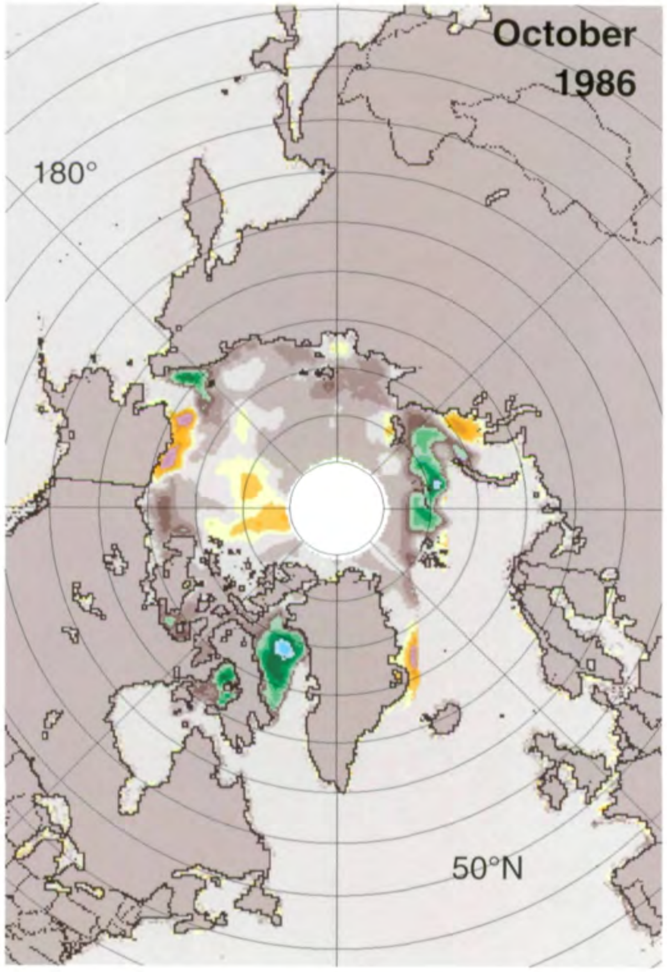
October 1986
180°
50°N

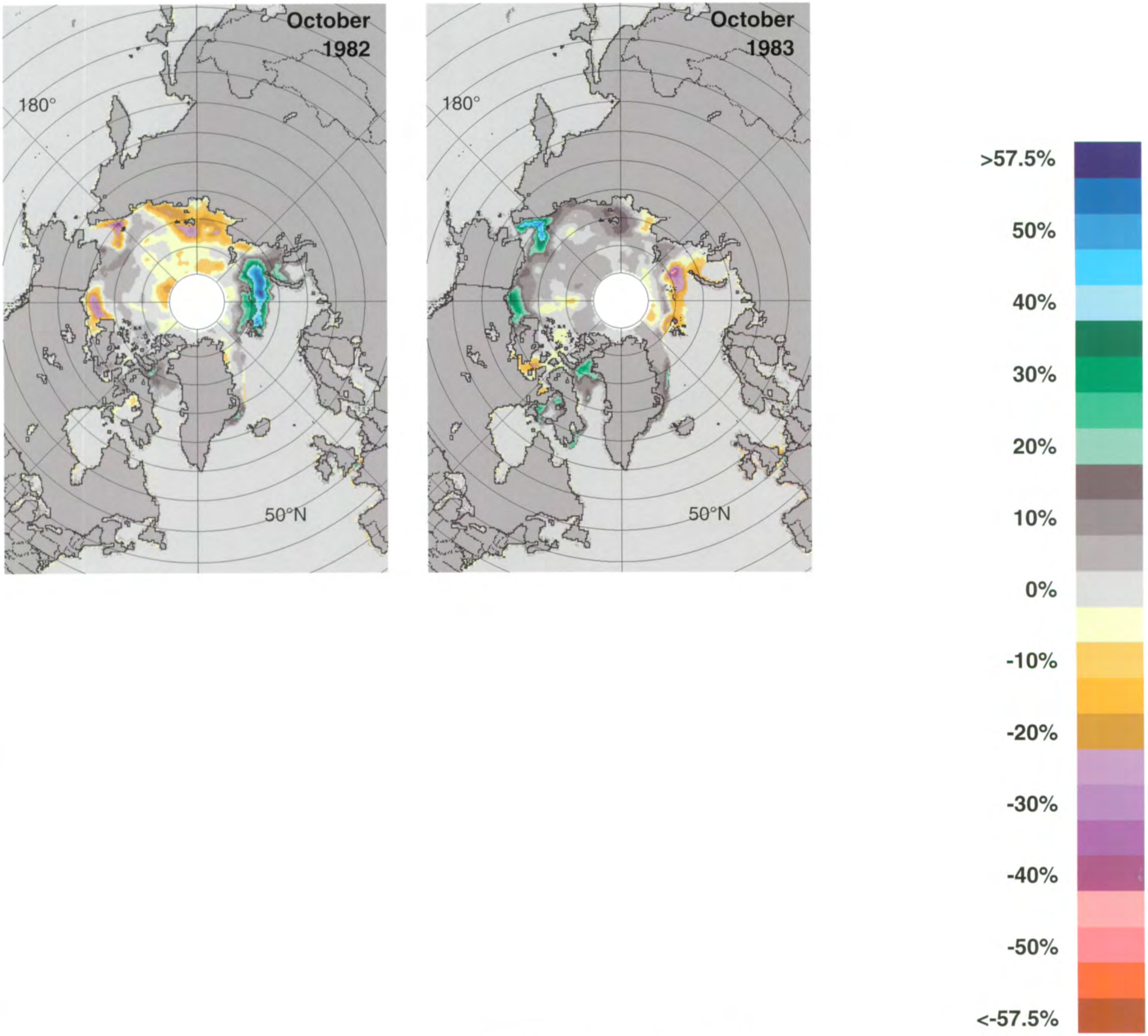

Figure 3.1.25. Mean monthly Arctic sea ice concentration anomalies for October 1979-1986.

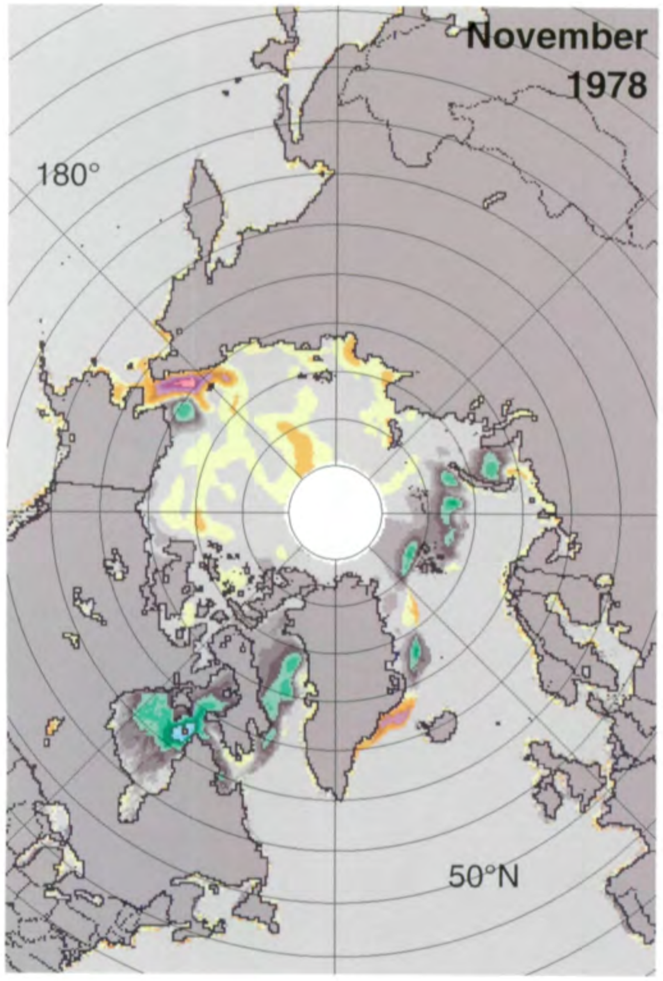
November
1978
180°
50°N

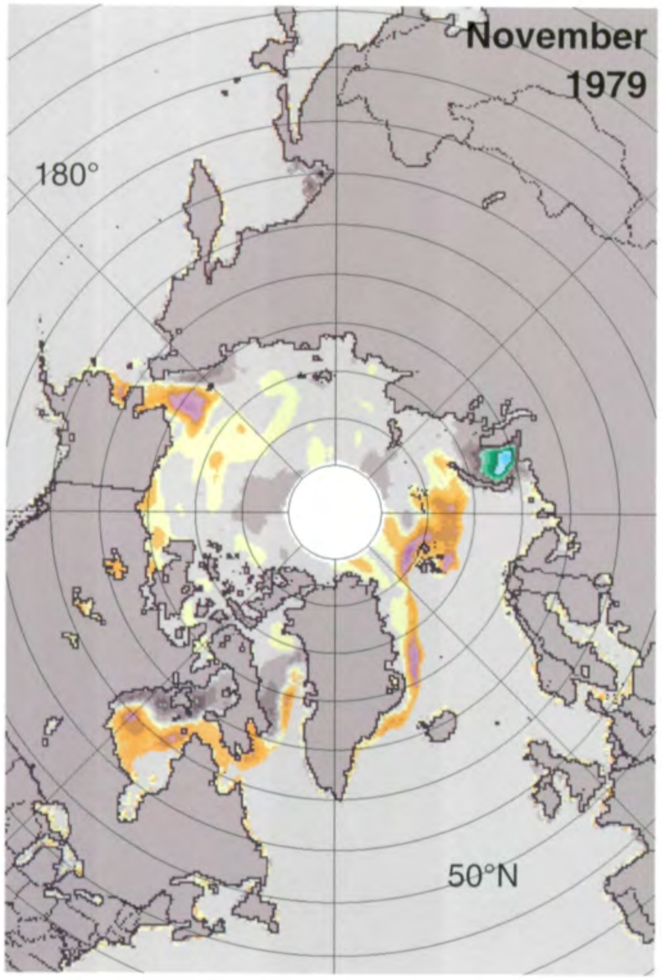
November
1979
180°
50°N

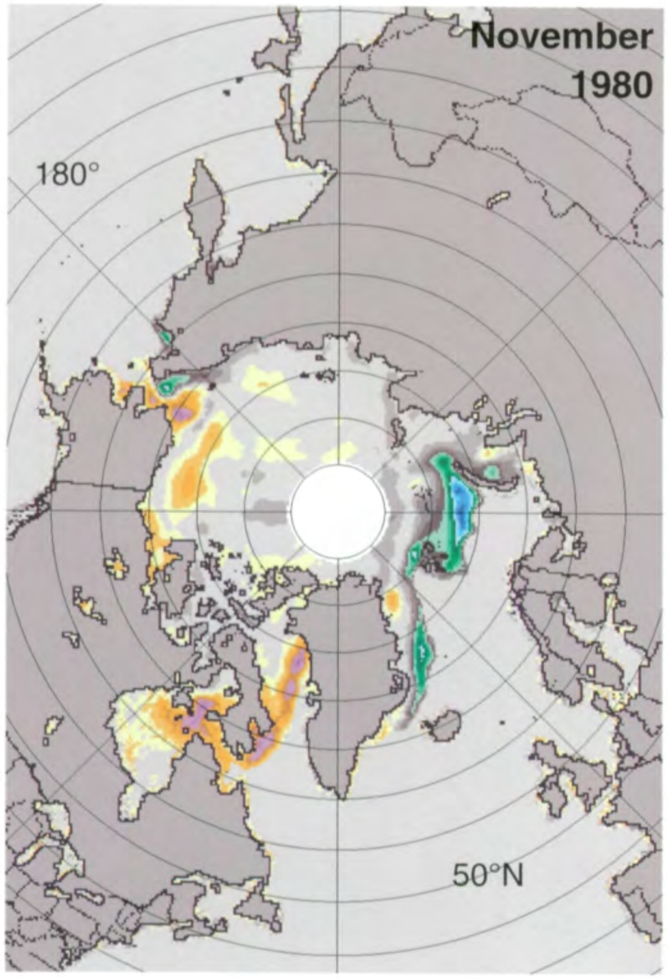
November
1980
180°
50°N

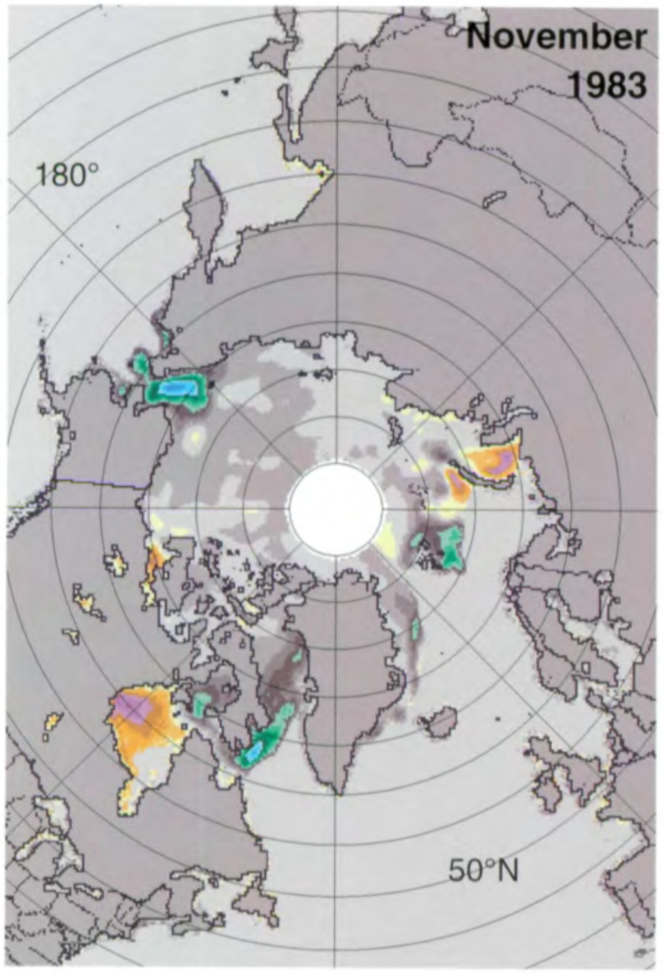
November
1983
180°
50°N

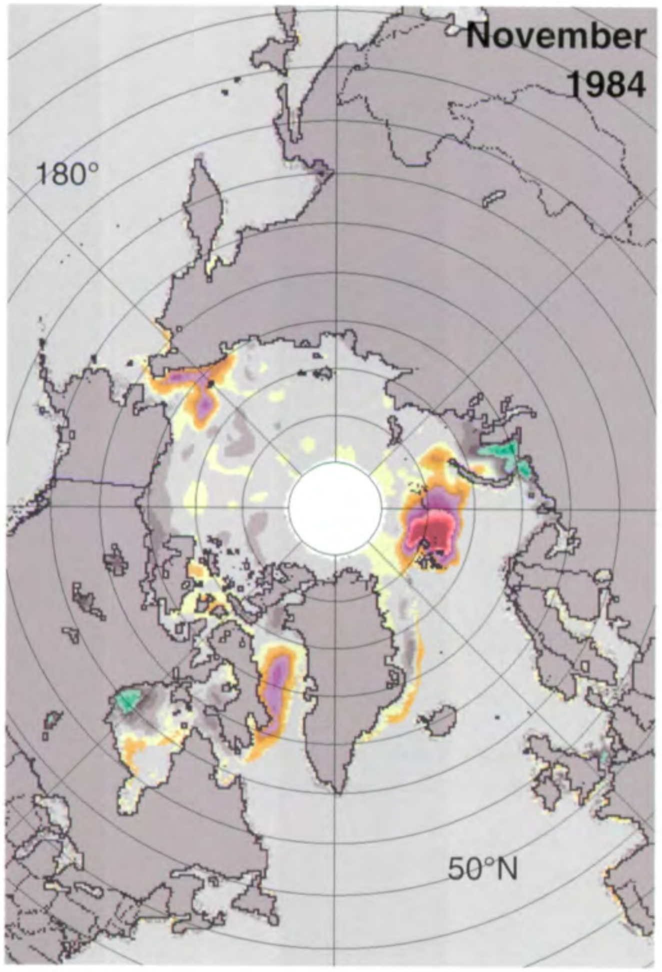
November
1984
180°
50°N

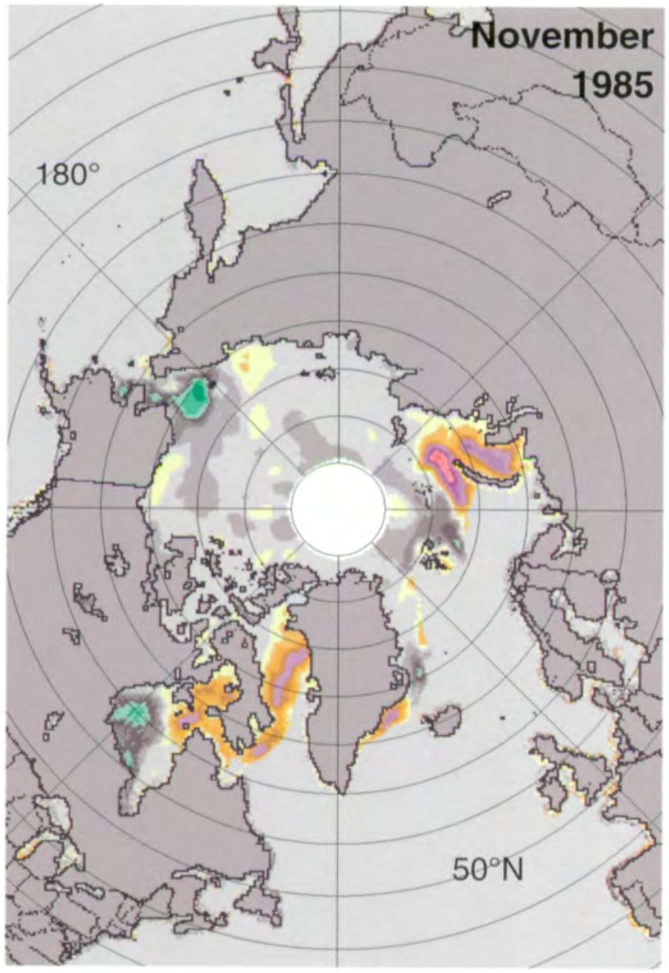
November
1985
180°
50°N

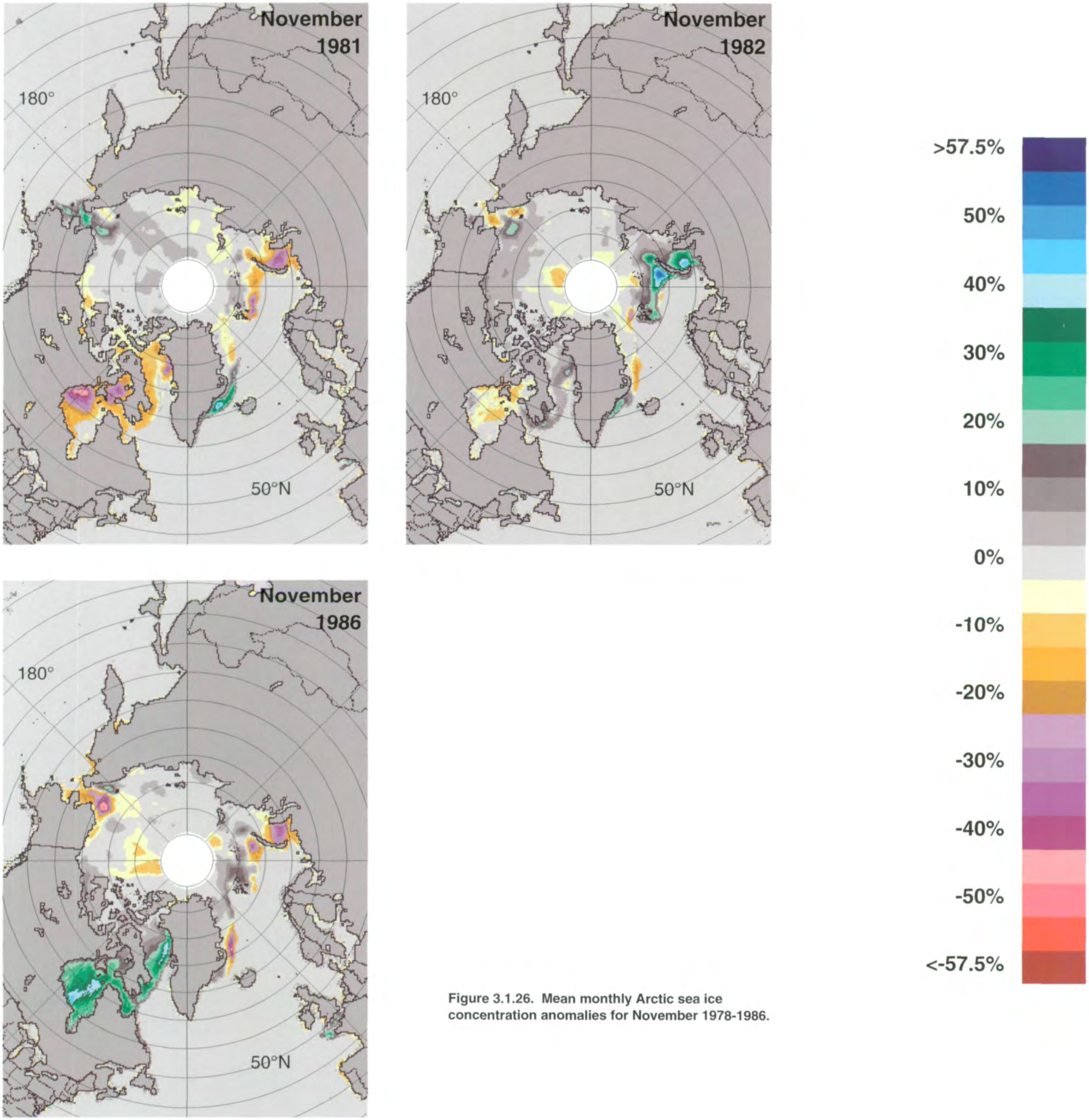

Figure 3.1.26. Mean monthly Arctic sea ice concentration anomalies for November 1978-1986.

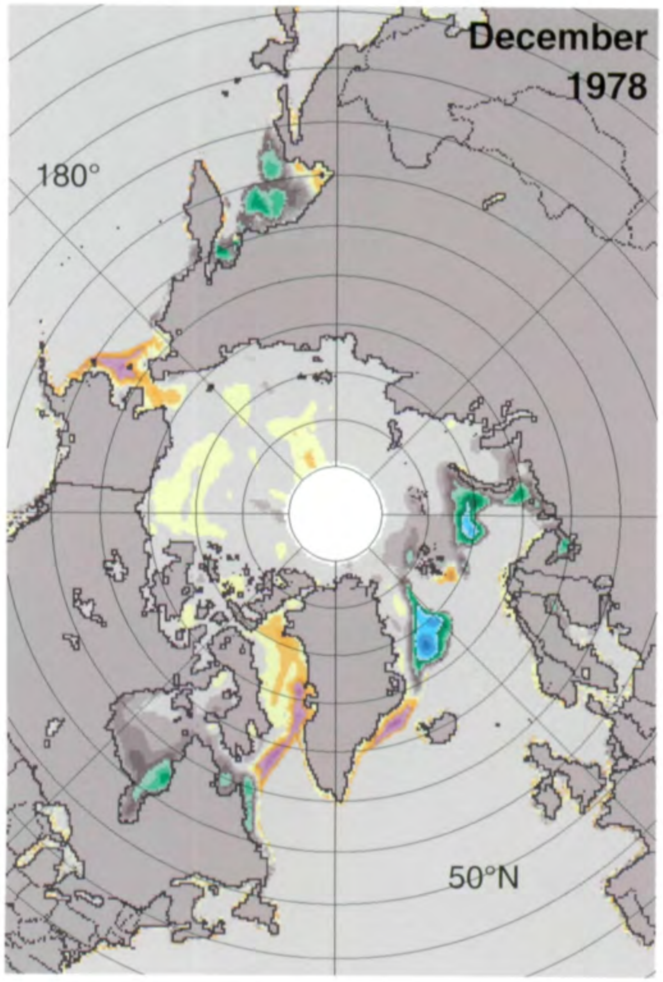
December
1978
180°
50°N

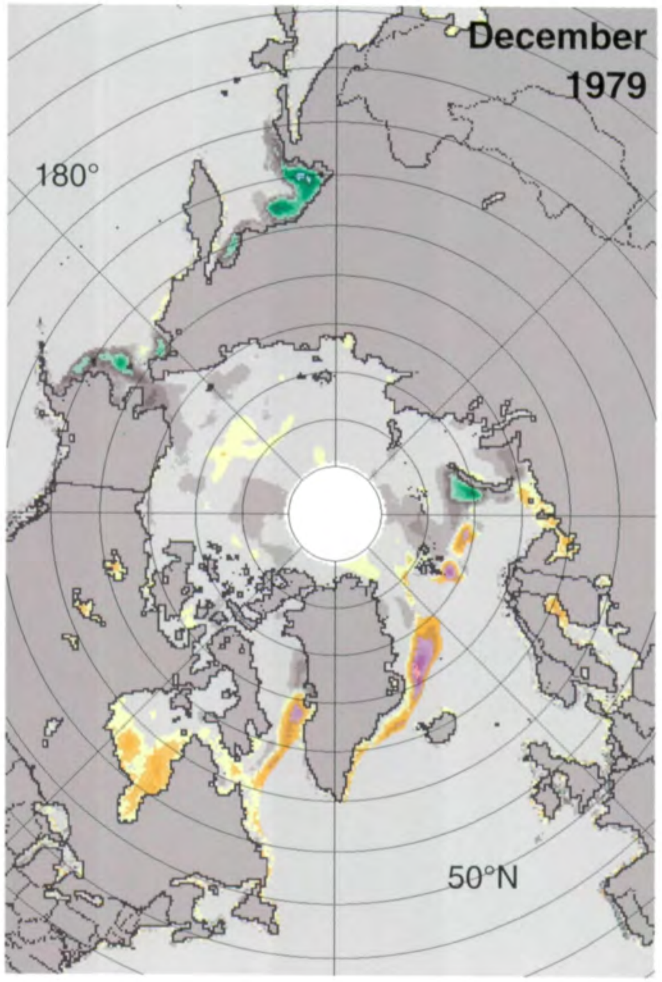
December
1979
180°
50°N

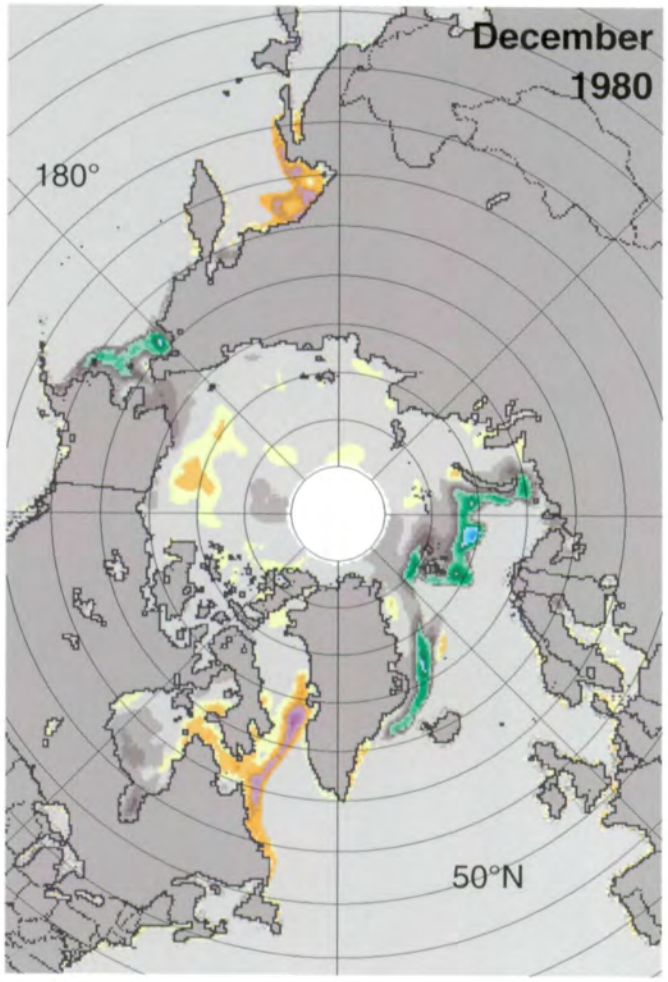
December
1980
180°
50°N

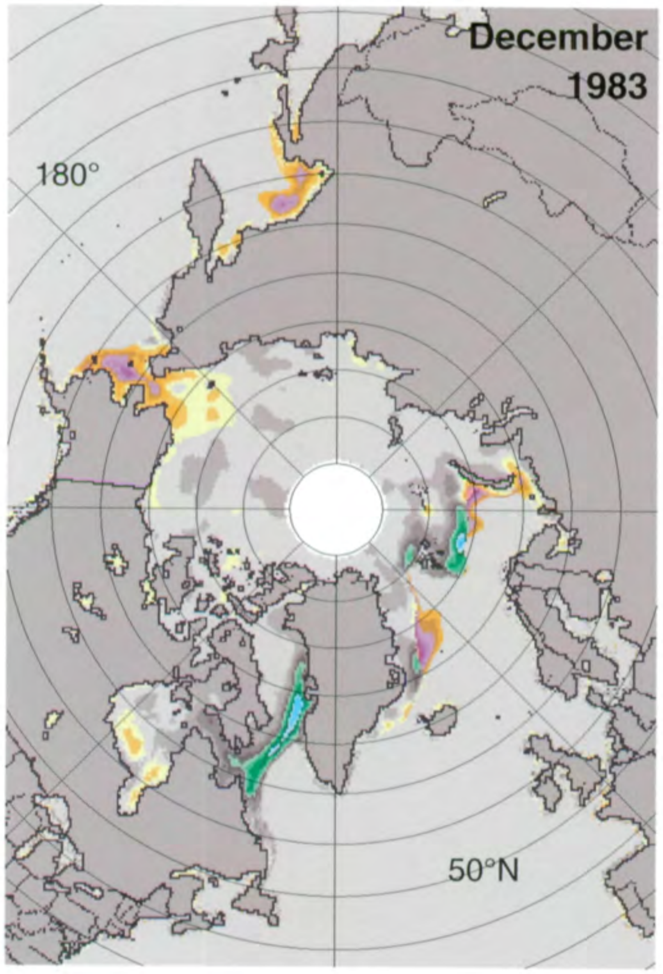
December
1983
180°
50°N

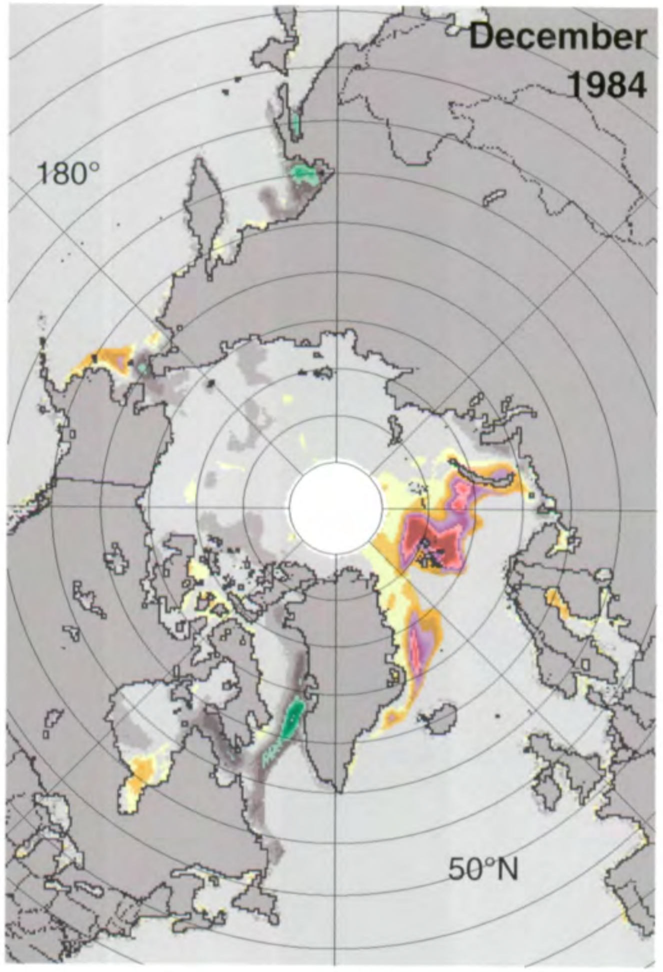
December
1984
180°
50°N

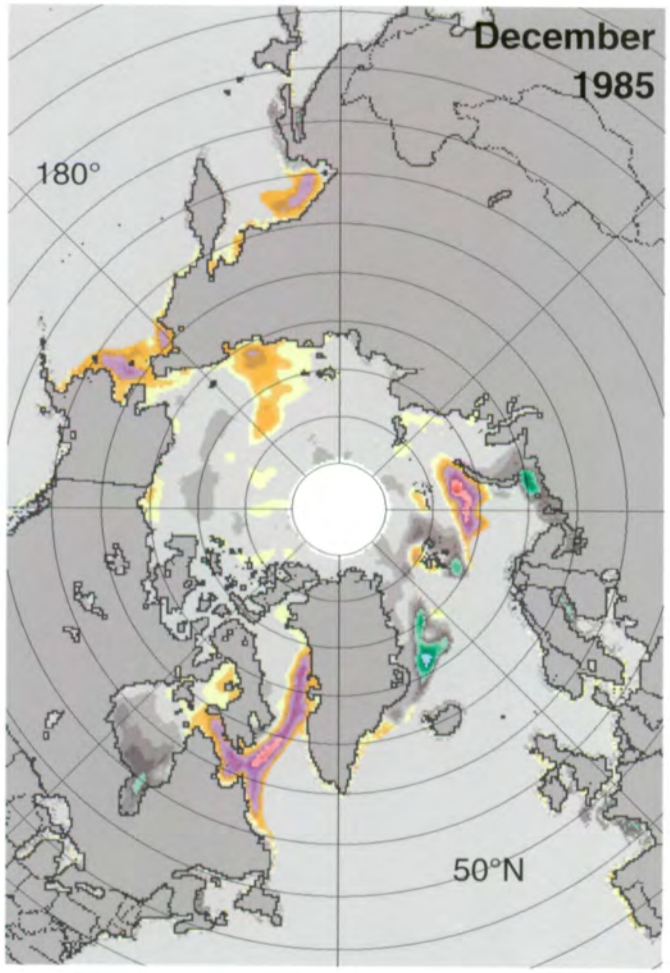
December
1985
180°
50°N

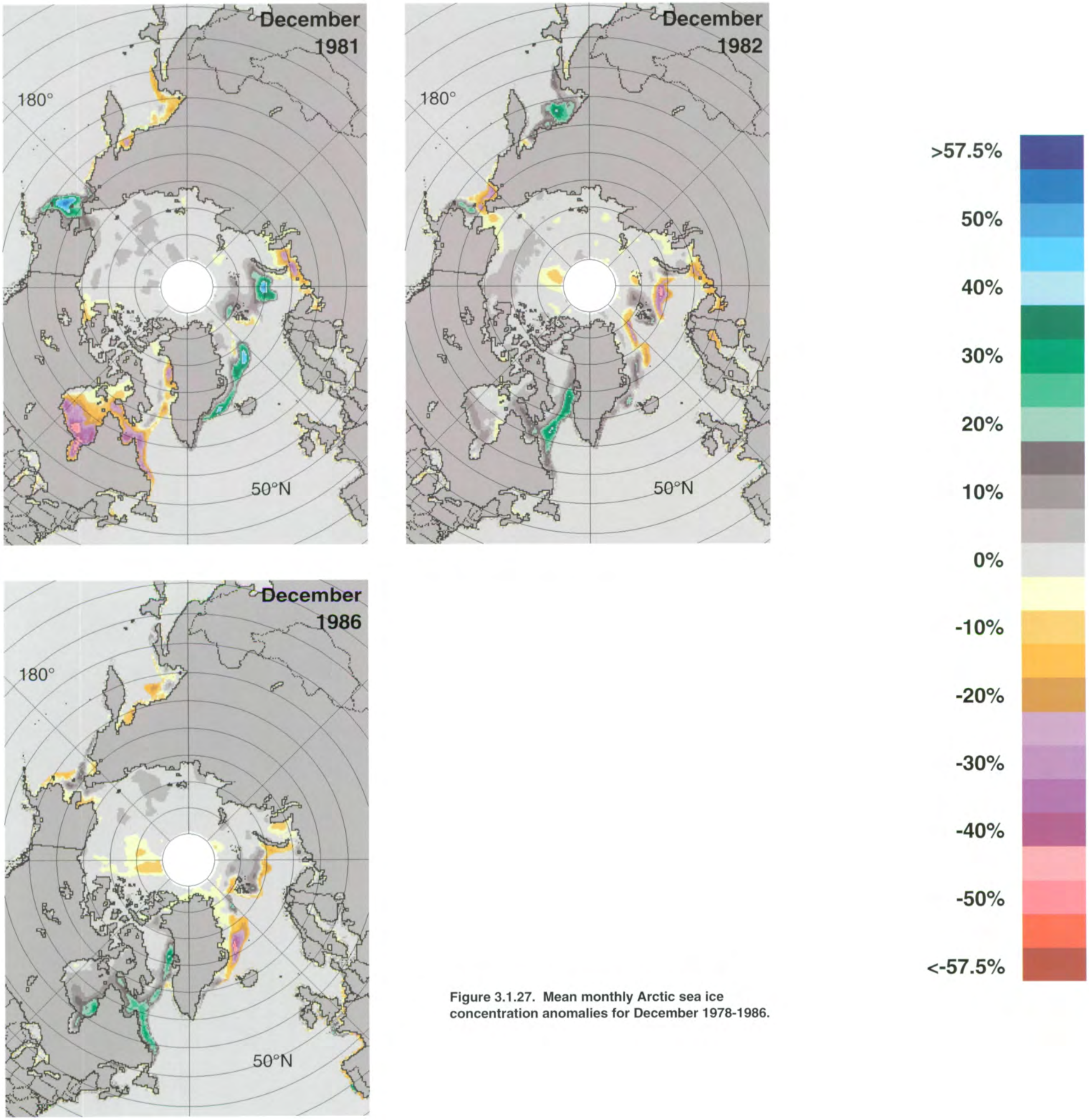

Figure 3.1.27. Mean monthly Arctic sea ice concentration anomalies for December 1978-1986.

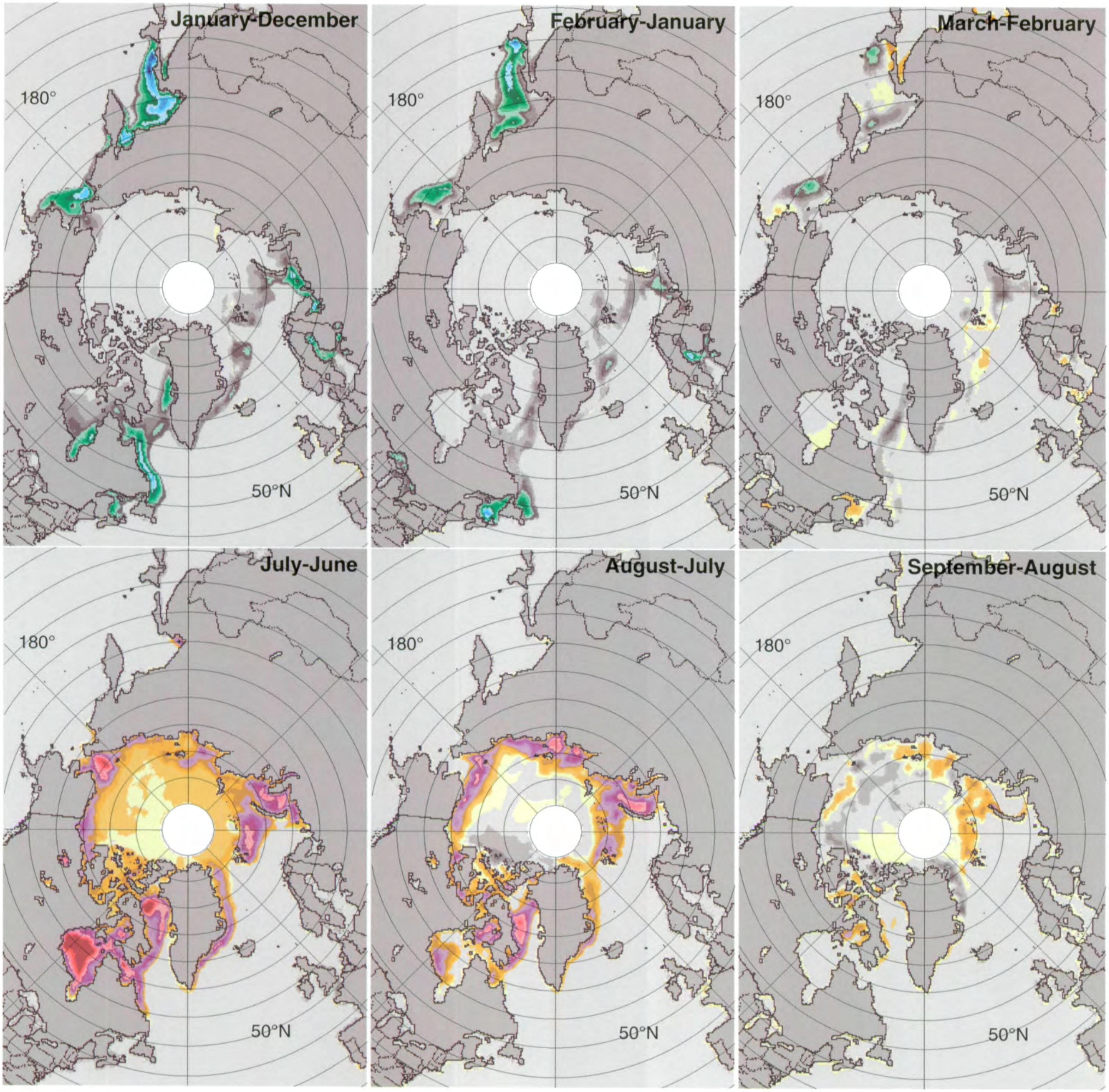
January-December
180°
50°N
February-January
180°
50°N
March-February
180°
50°N
July-June
180°
50°N
August-July
180°
50°N
September-August
180°
50°N

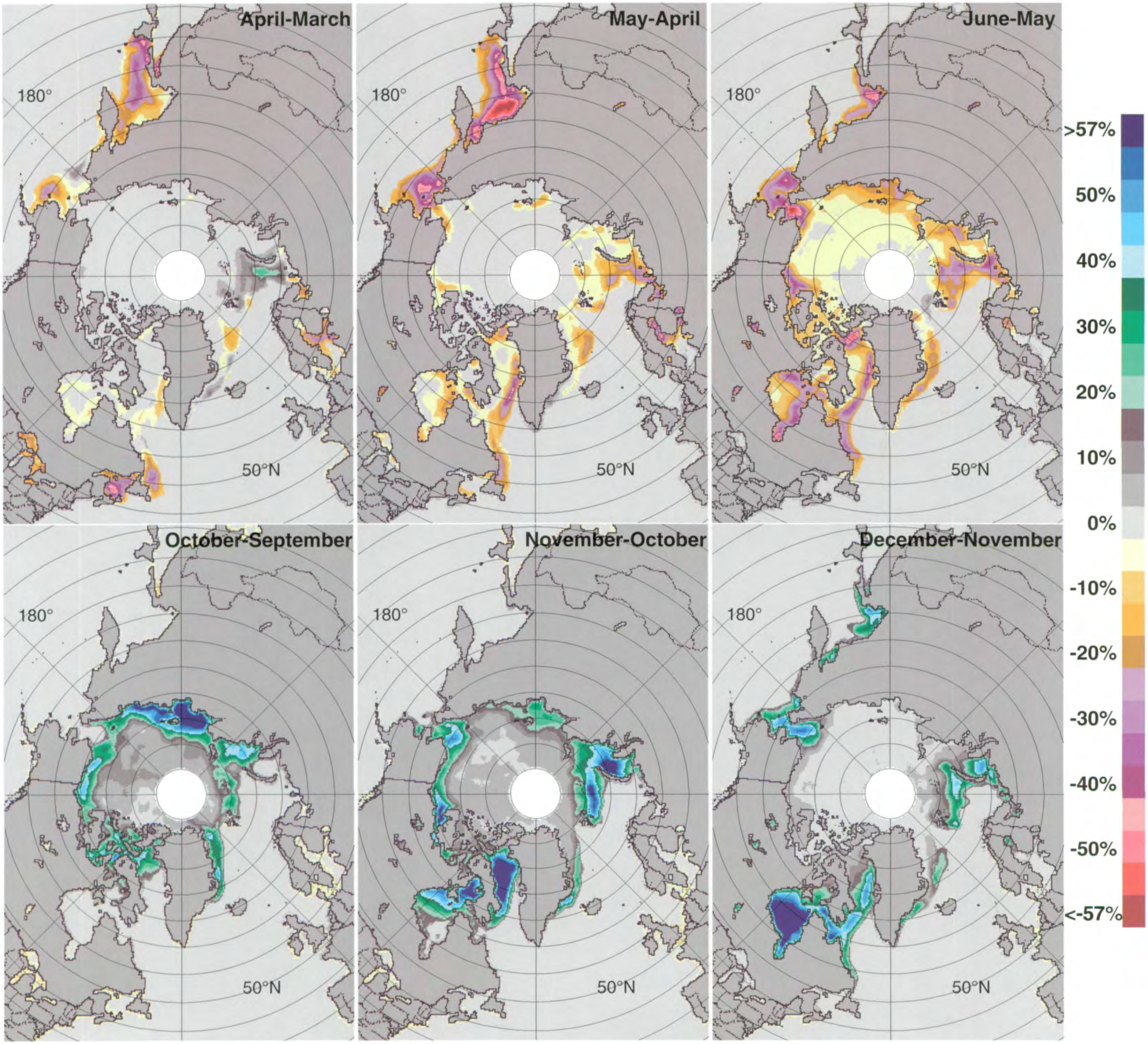

Figure 3.1.28. Average monthly change in Arctic sea ice concentrations over the SMMR lifetime.

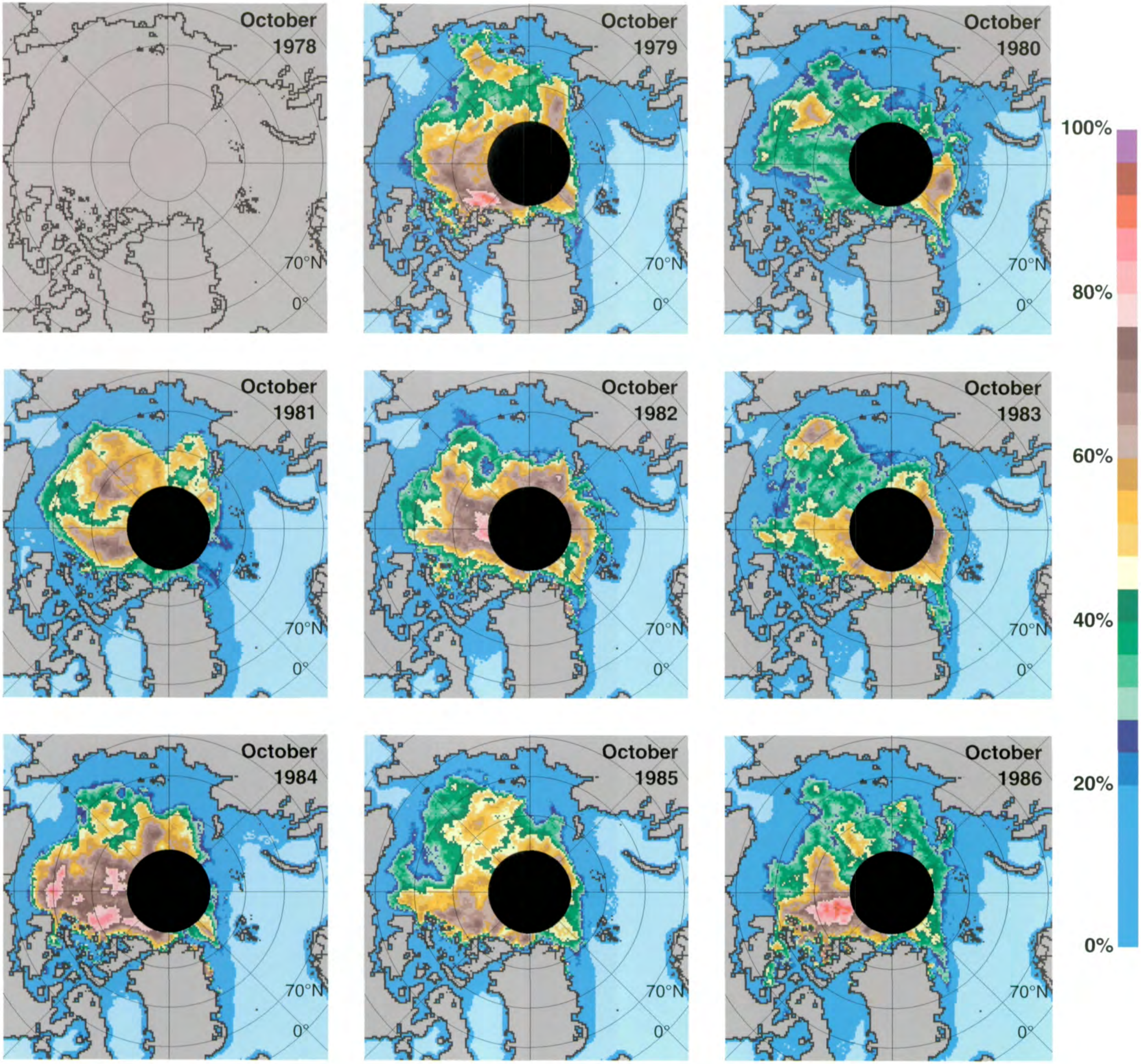

Figure 3.1.29. Mean monthly Arctic multiyear sea ice concentrations for October 1979-1986.

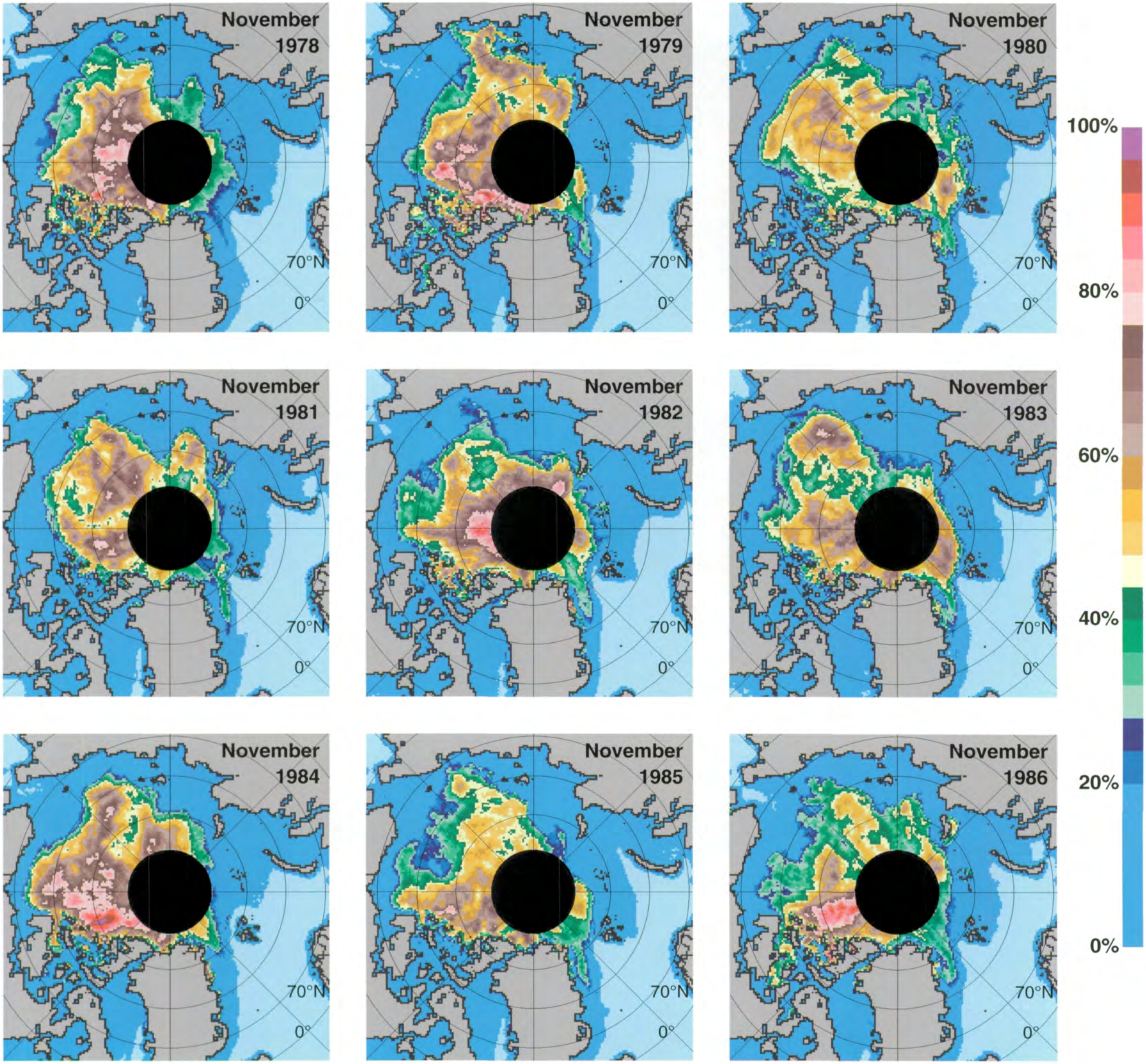

Figure 3.1.30. Mean monthly Arctic multiyear sea ice concentrations for November 1978-1986.

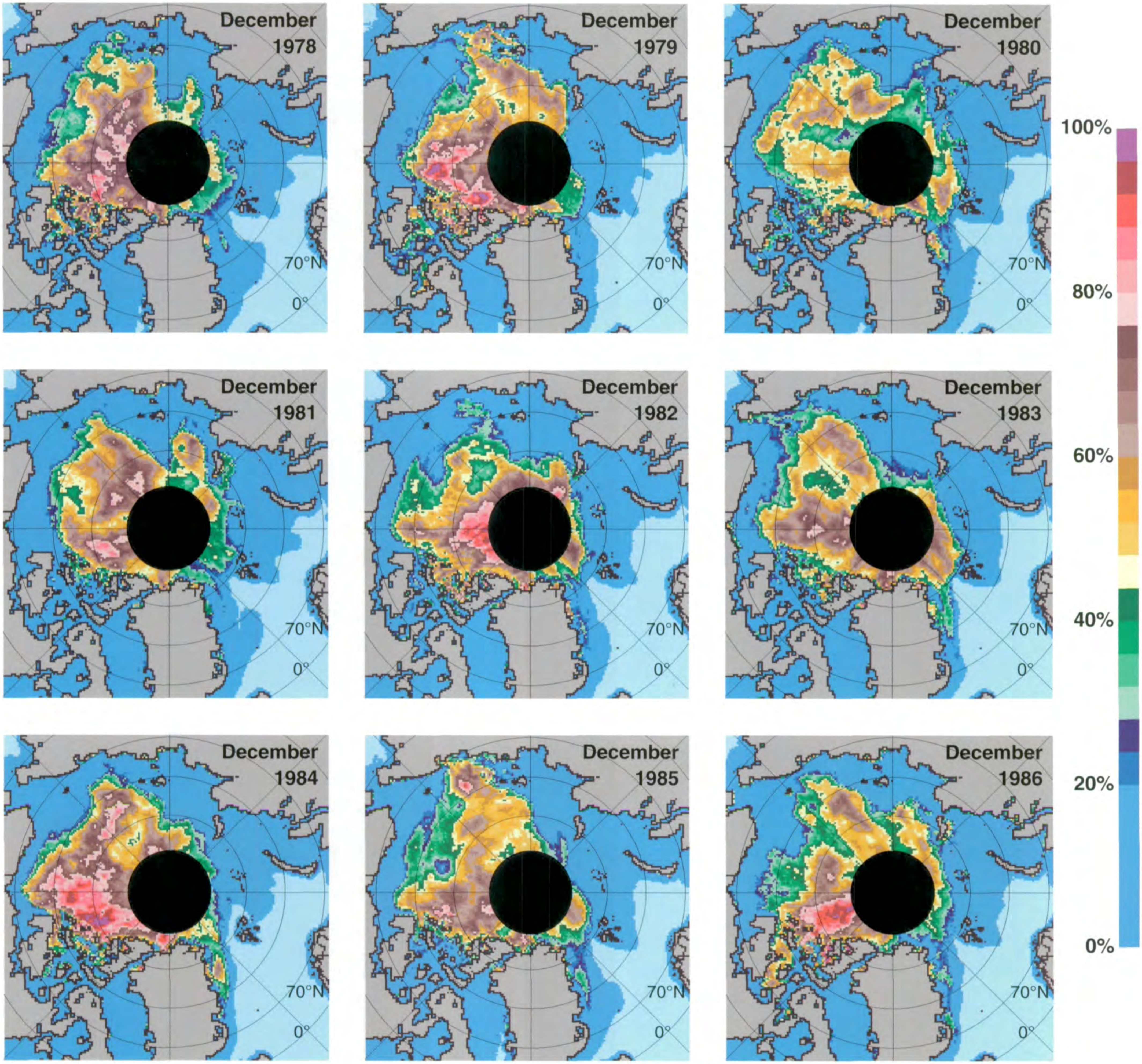

Figure 3.1.31. Mean monthly Arctic multiyear sea ice concentrations for December 1978-1986.

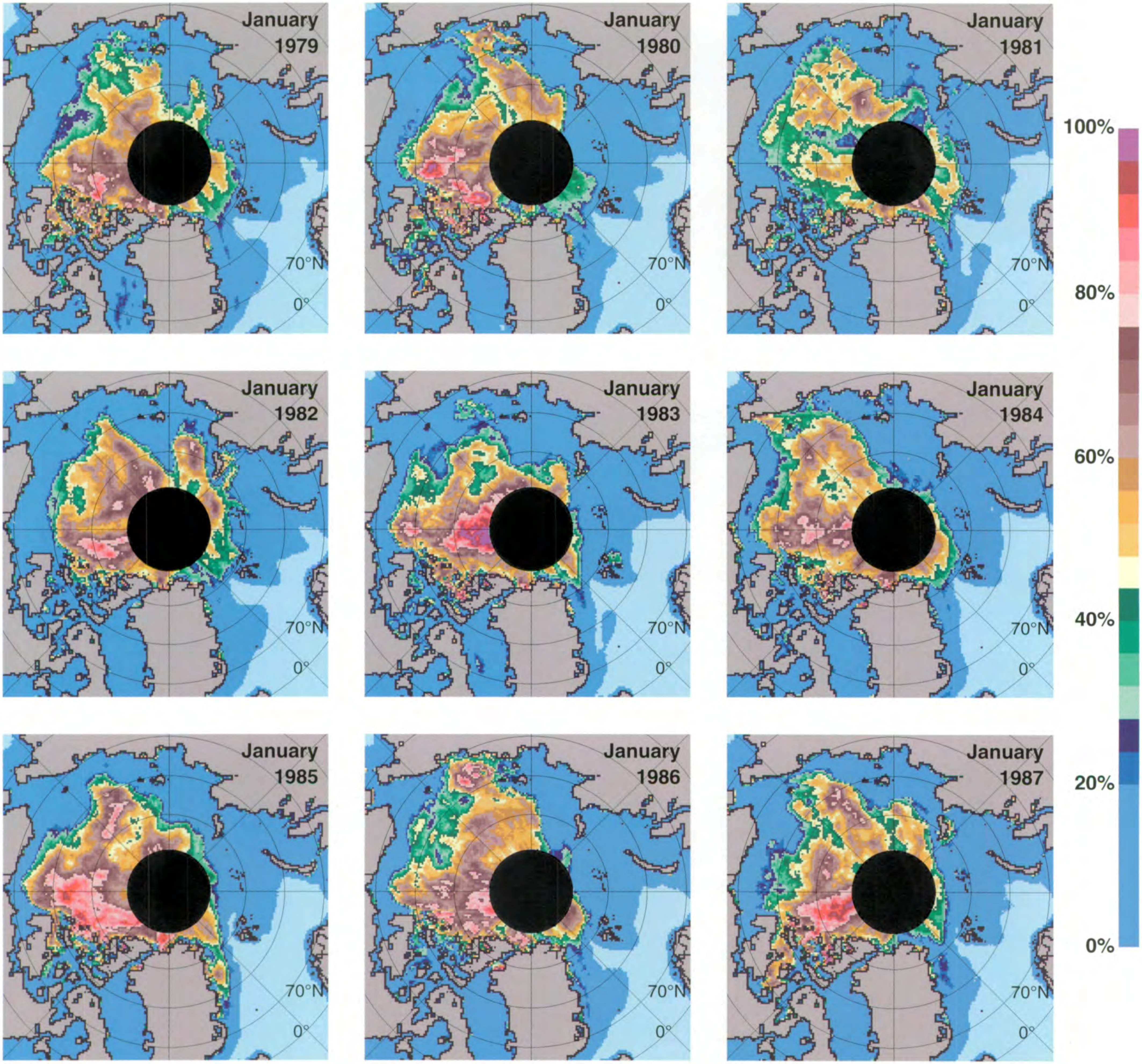

Figure 3.1.32. Mean monthly Arctic multiyear sea ice concentrations for January 1979-1987.

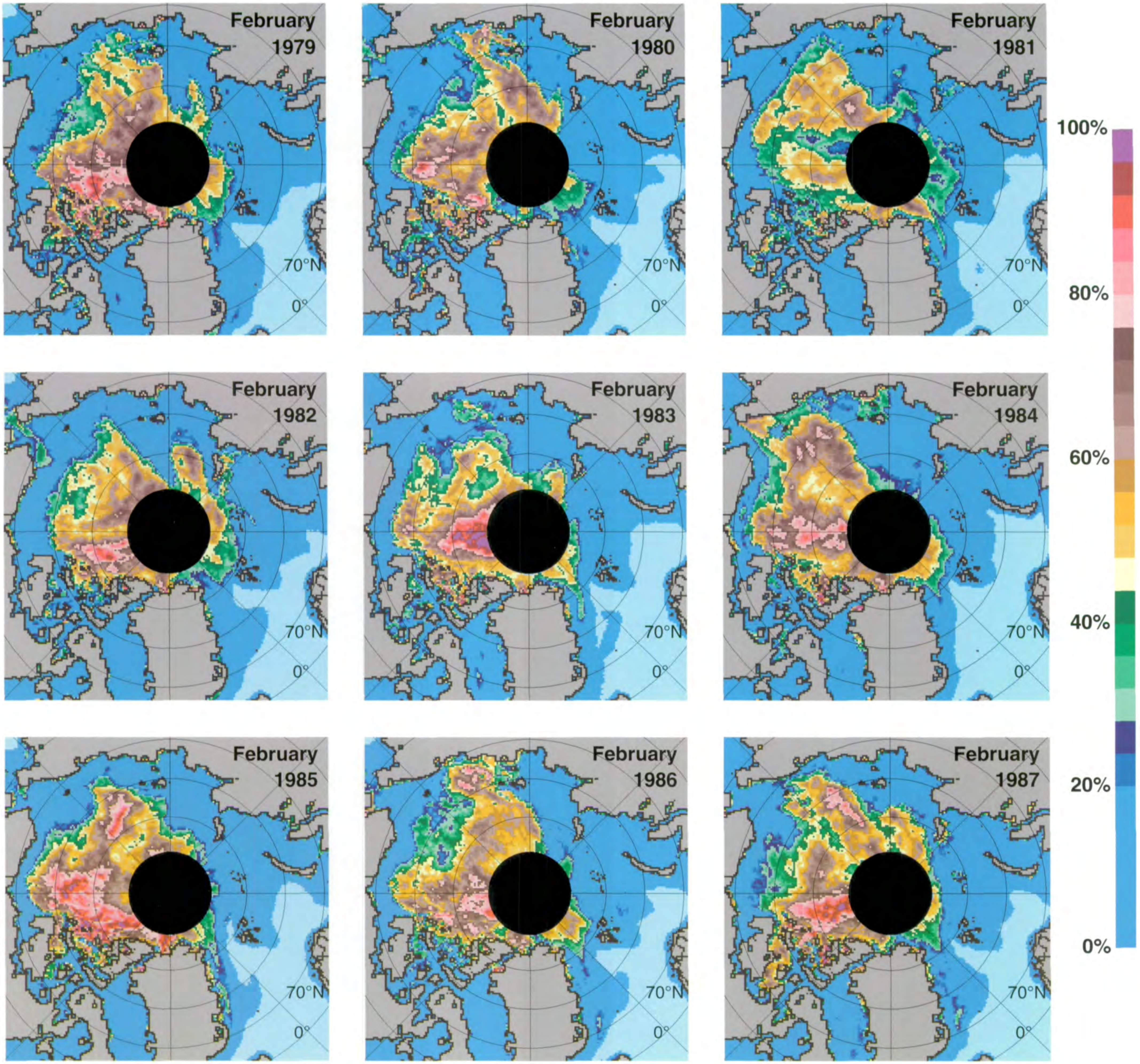

Figure 3.1.33. Mean monthly Arctic multiyear sea ice concentrations for February 1979-1987.

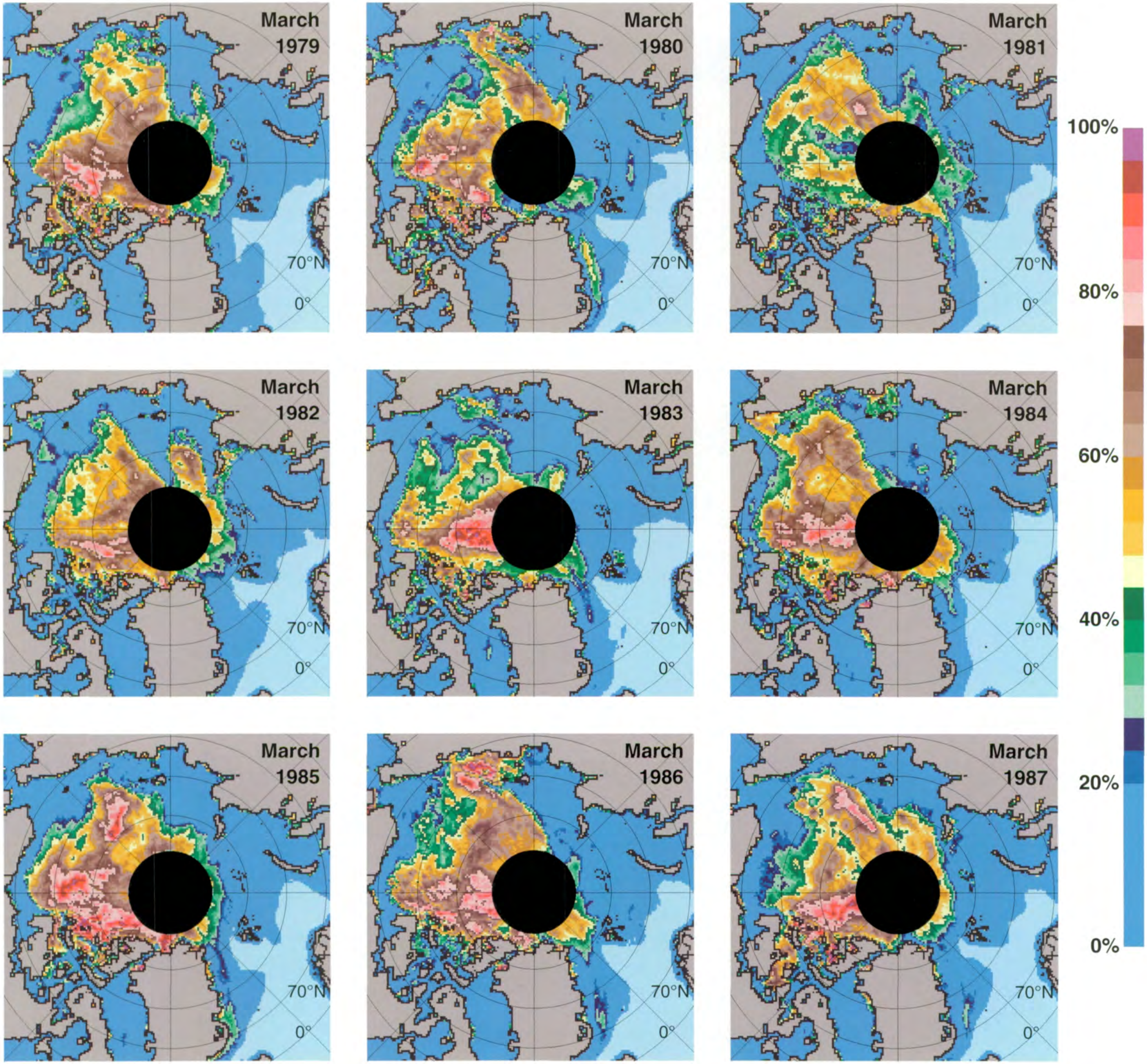

Figure 3.1.34. Mean monthly Arctic multiyear sea ice concentrations for March 1979-1987.

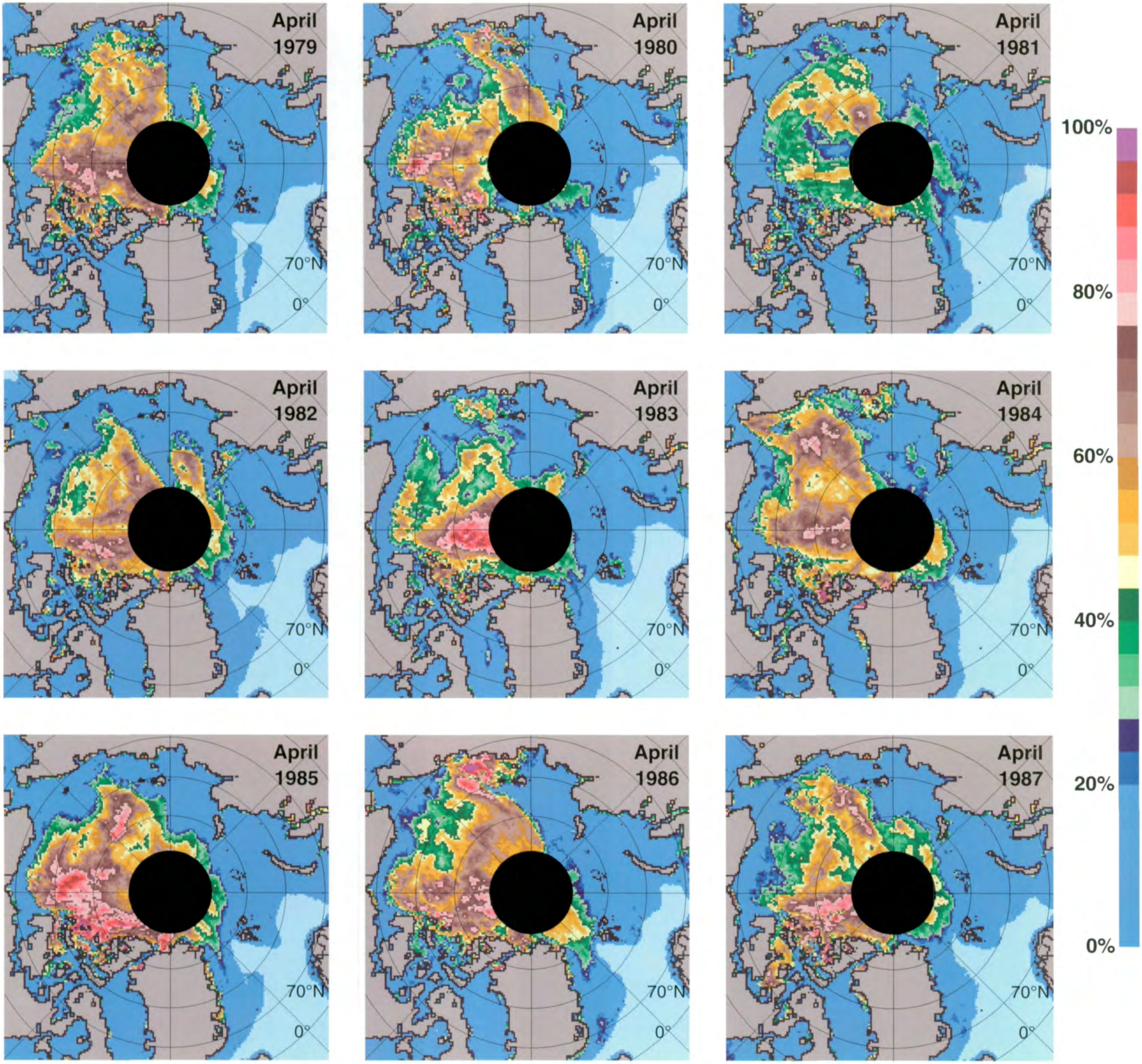

Figure 3.1.35. Mean monthly Arctic multiyear sea ice concentrations for April 1979-1987.

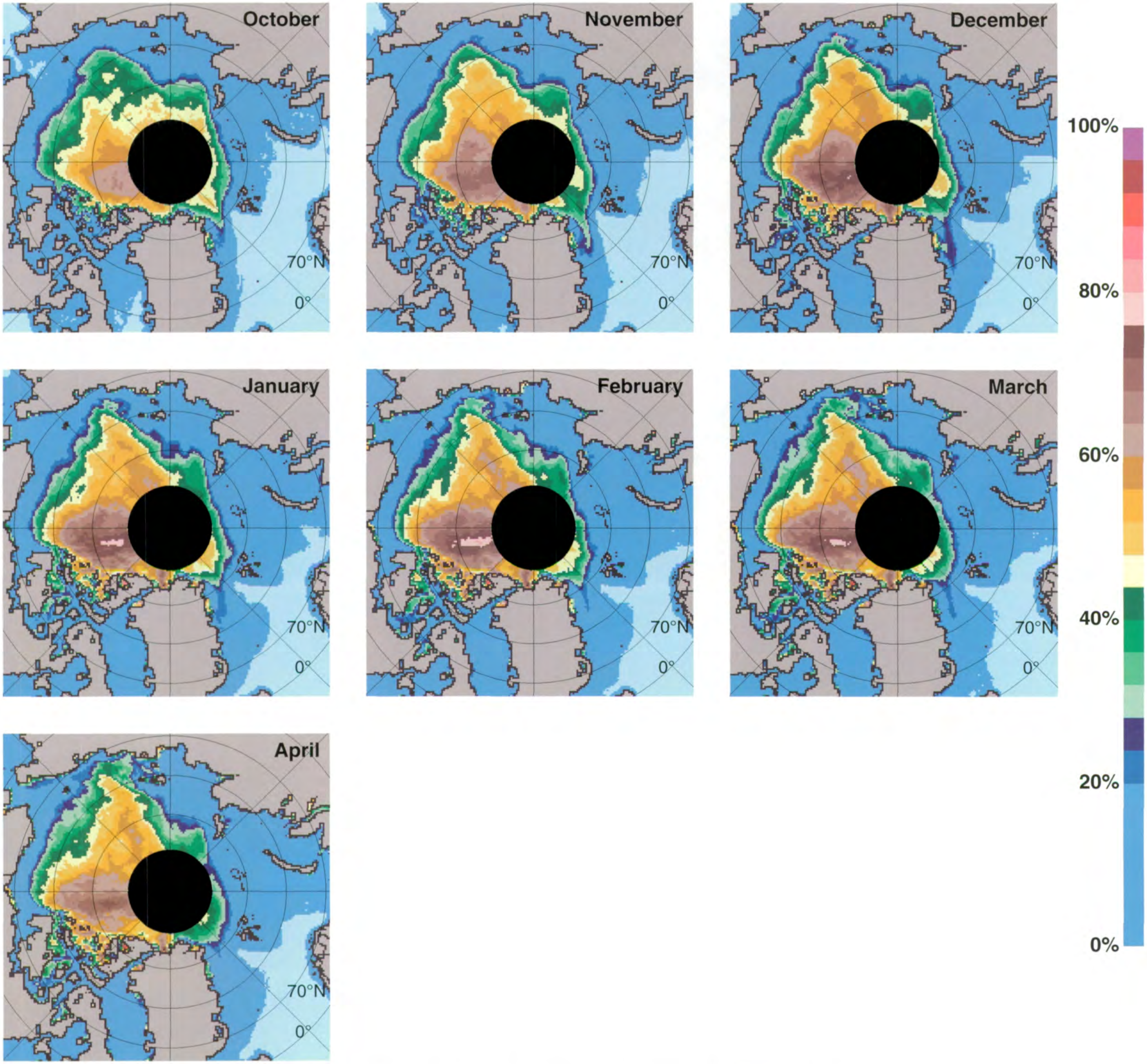

Figure 3.1.36. Monthly Arctic multiyear sea ice concentrations averaged over the SMMR lifetime.

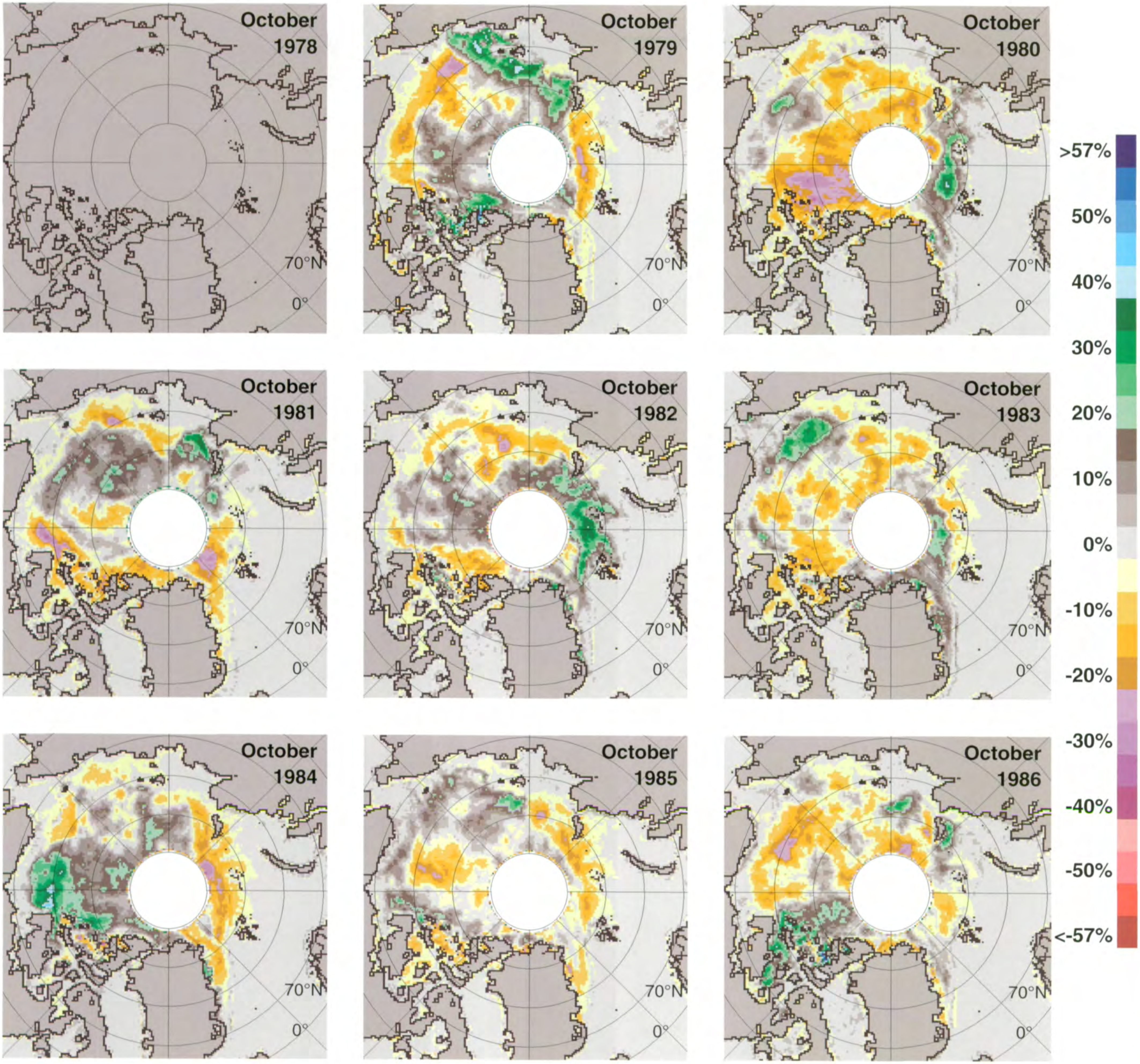

Figure 3.1.37. Mean monthly Arctic multiyear sea ice concentration anomalies for October 1979-1986.

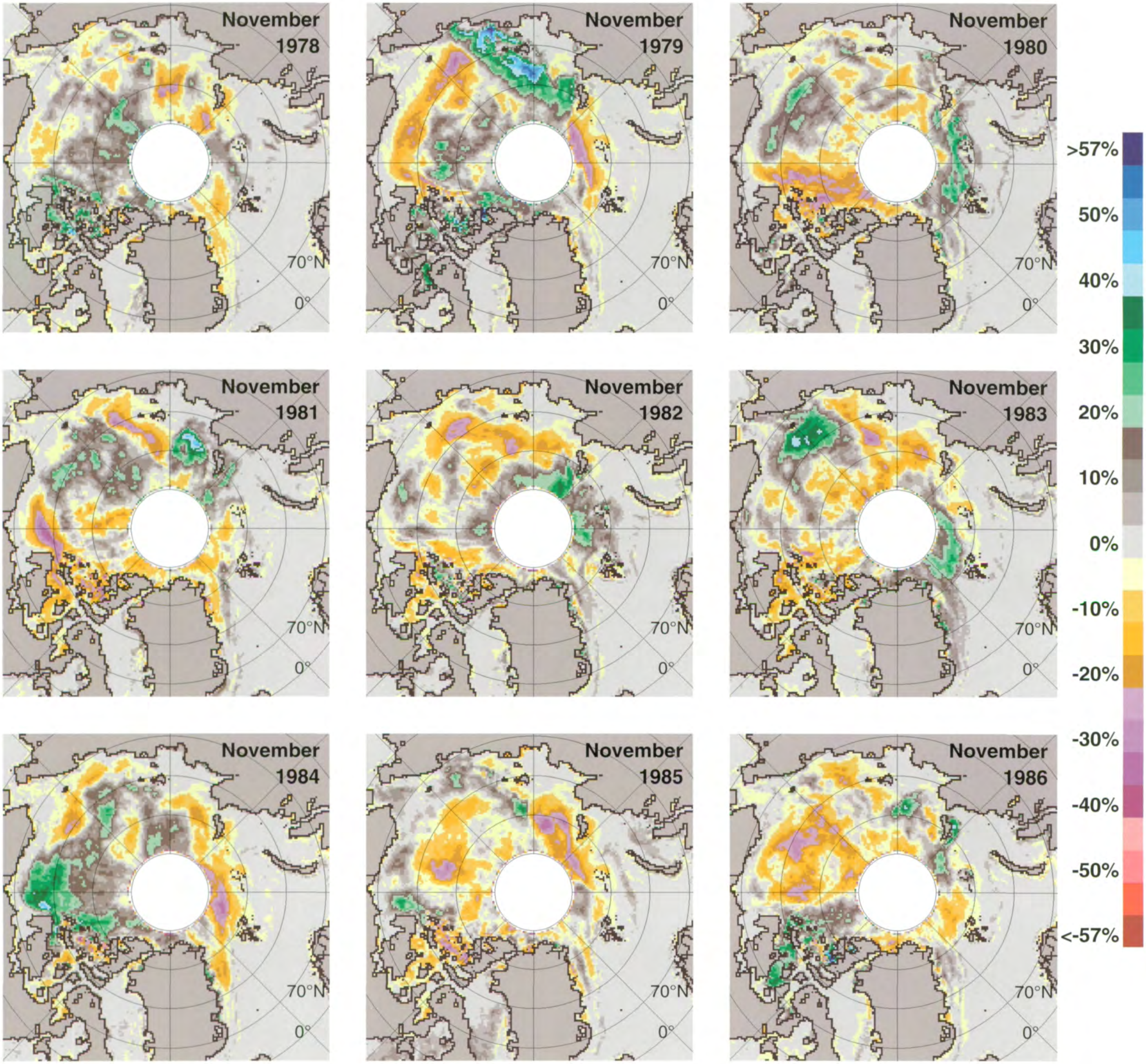

Figure 3.1.38. Mean monthly Arctic multiyear sea ice concentration anomalies for November 1978-1986.

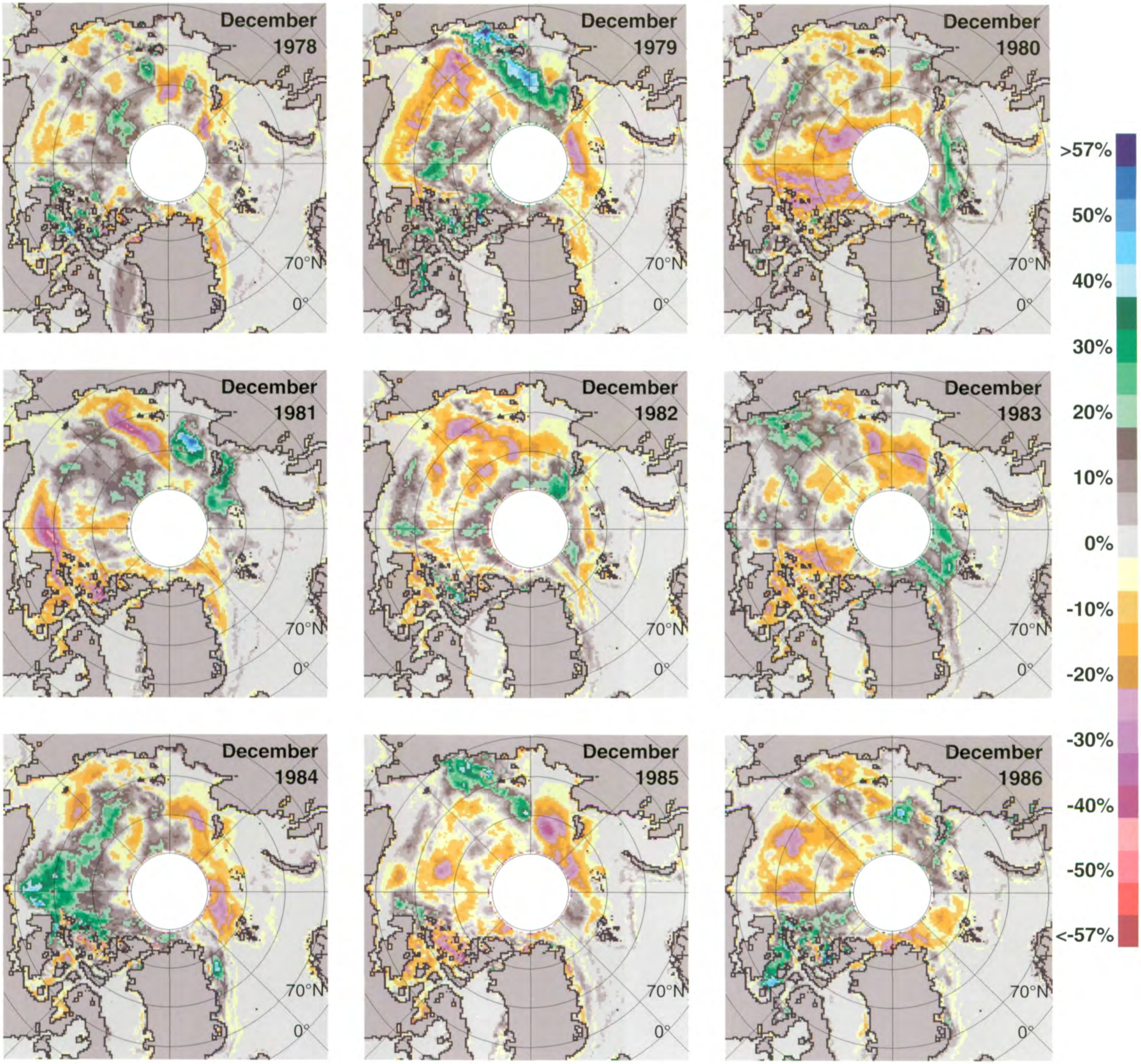

Figure 3.1.39. Mean monthly Arctic multiyear sea ice concentration anomalies for December 1978-1986.

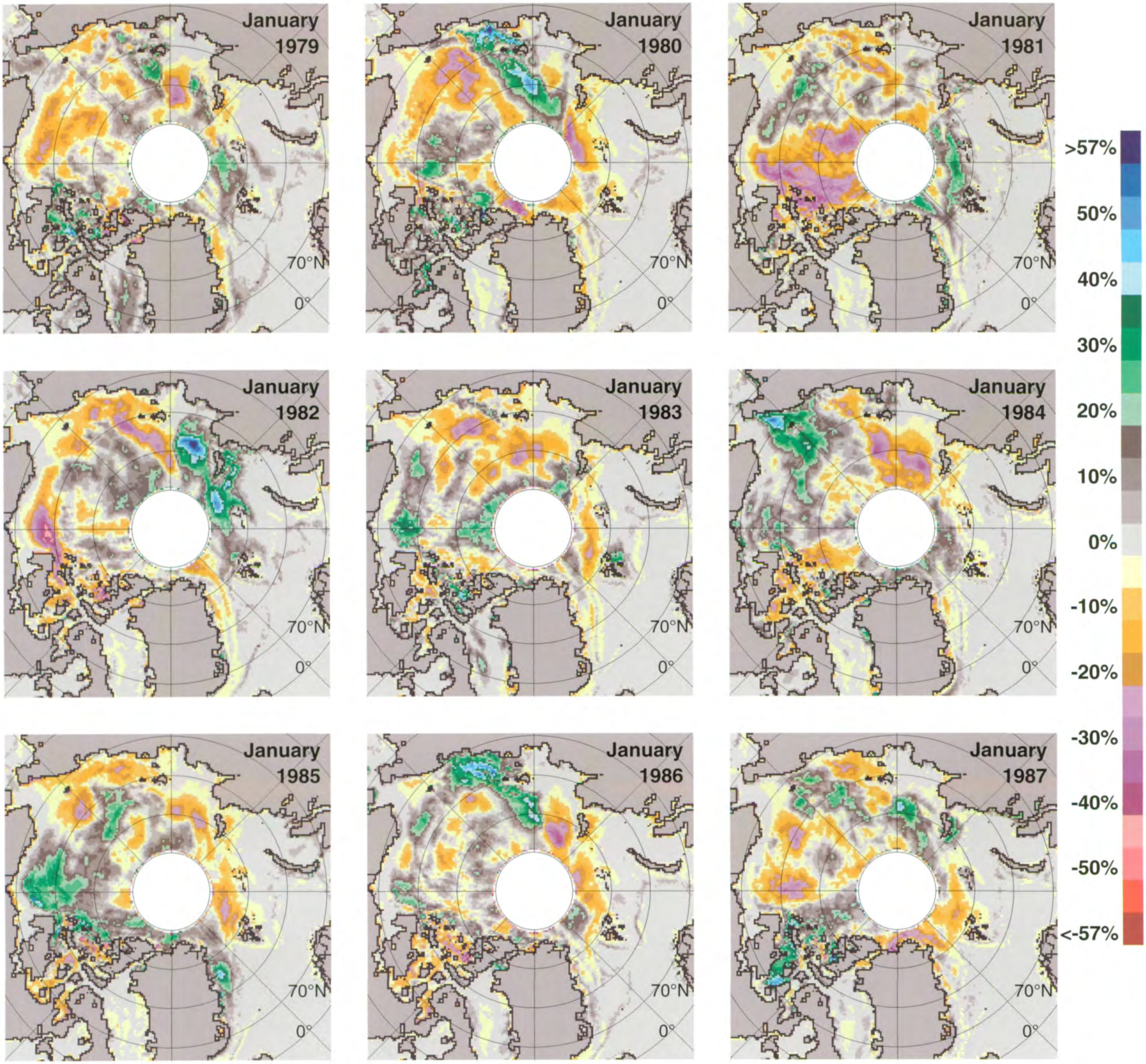

Figure 3.1.40. Mean monthly Arctic multiyear sea ice concentration anomalies for January 1979-1987.

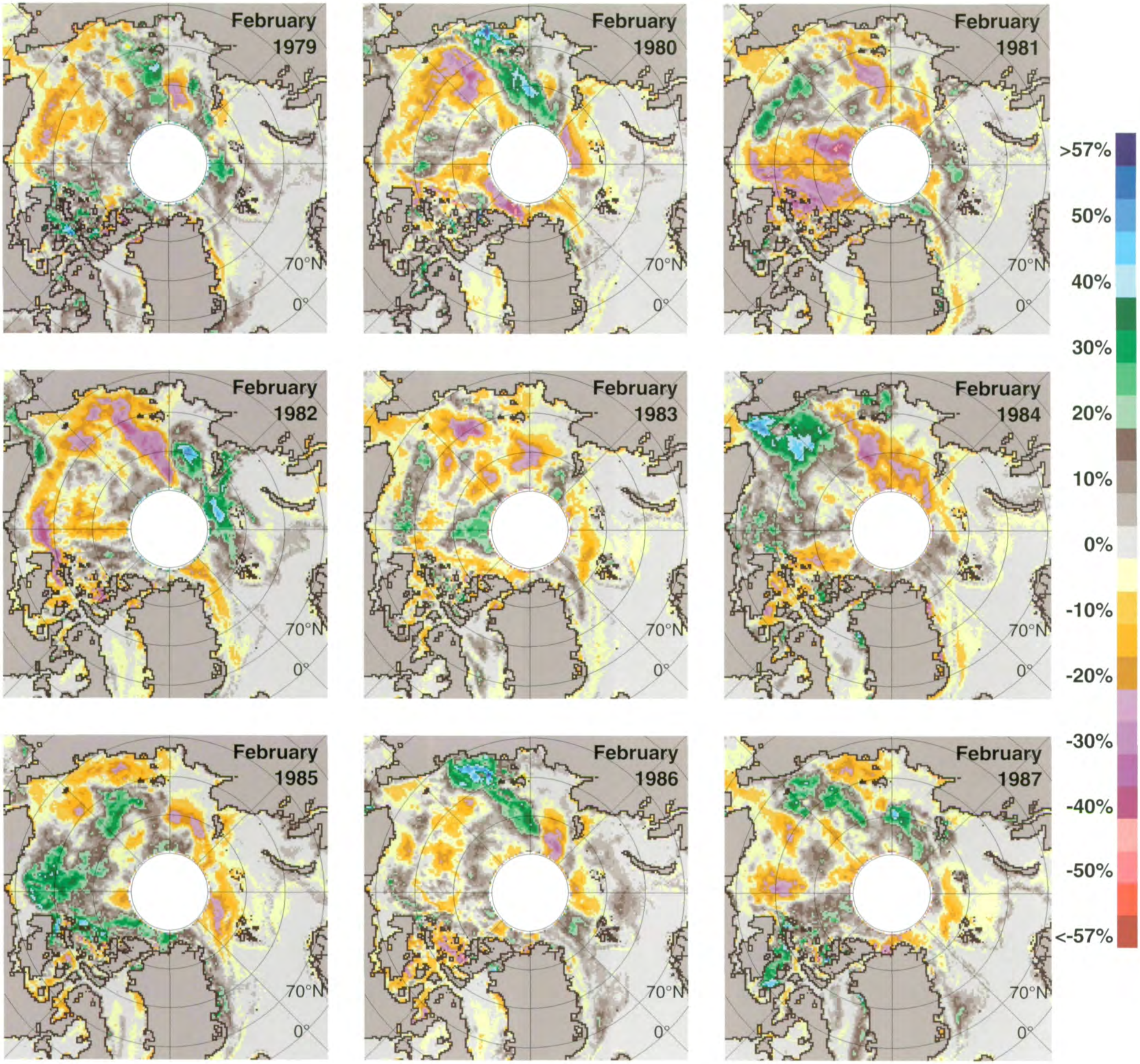

Figure 3.1.41. Mean monthly Arctic multiyear sea ice concentration anomalies for February 1979-1987.

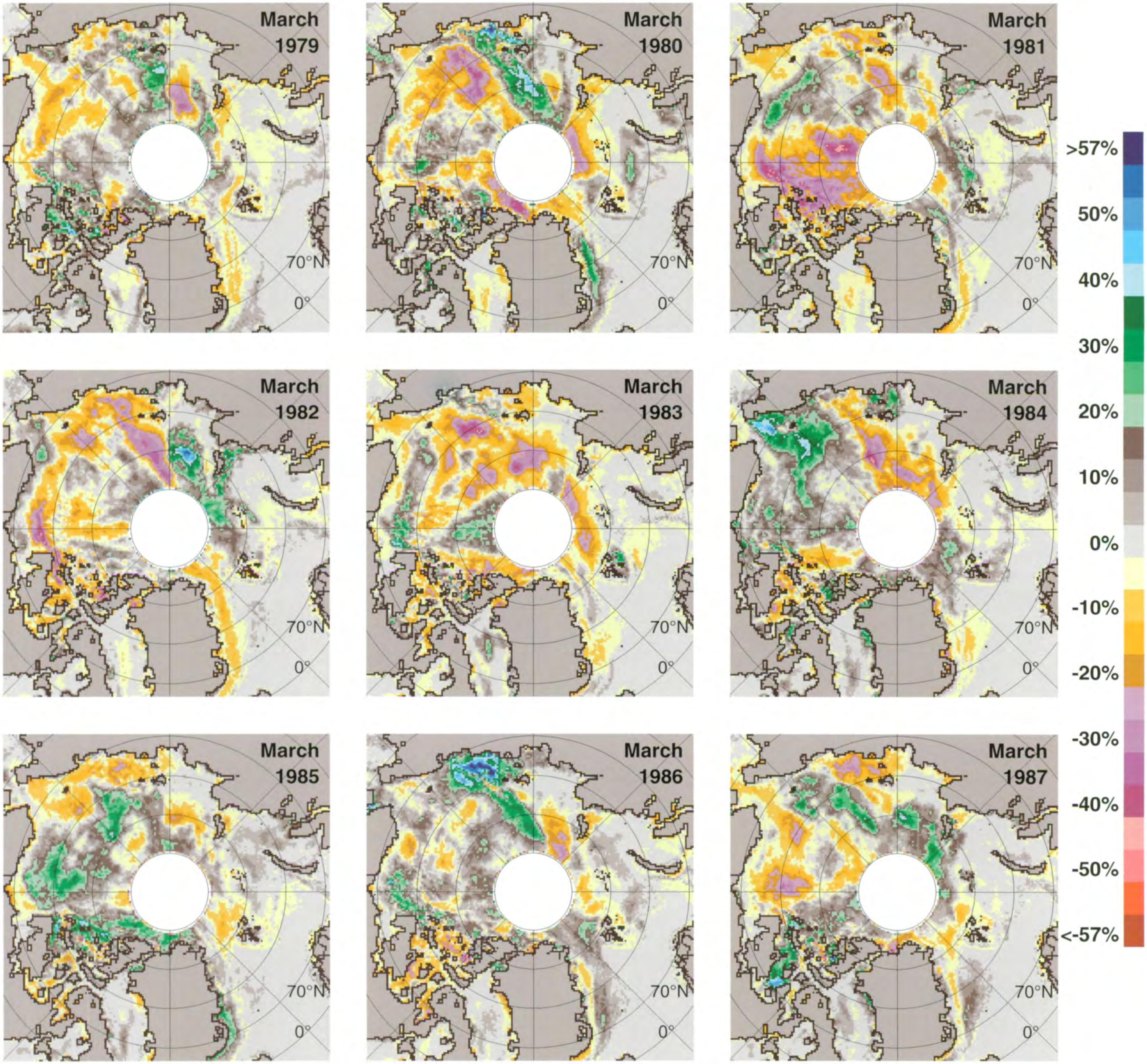

Figure 3.1.42. Mean monthly Arctic multiyear sea ice concentration anomalies for March 1979-1987.

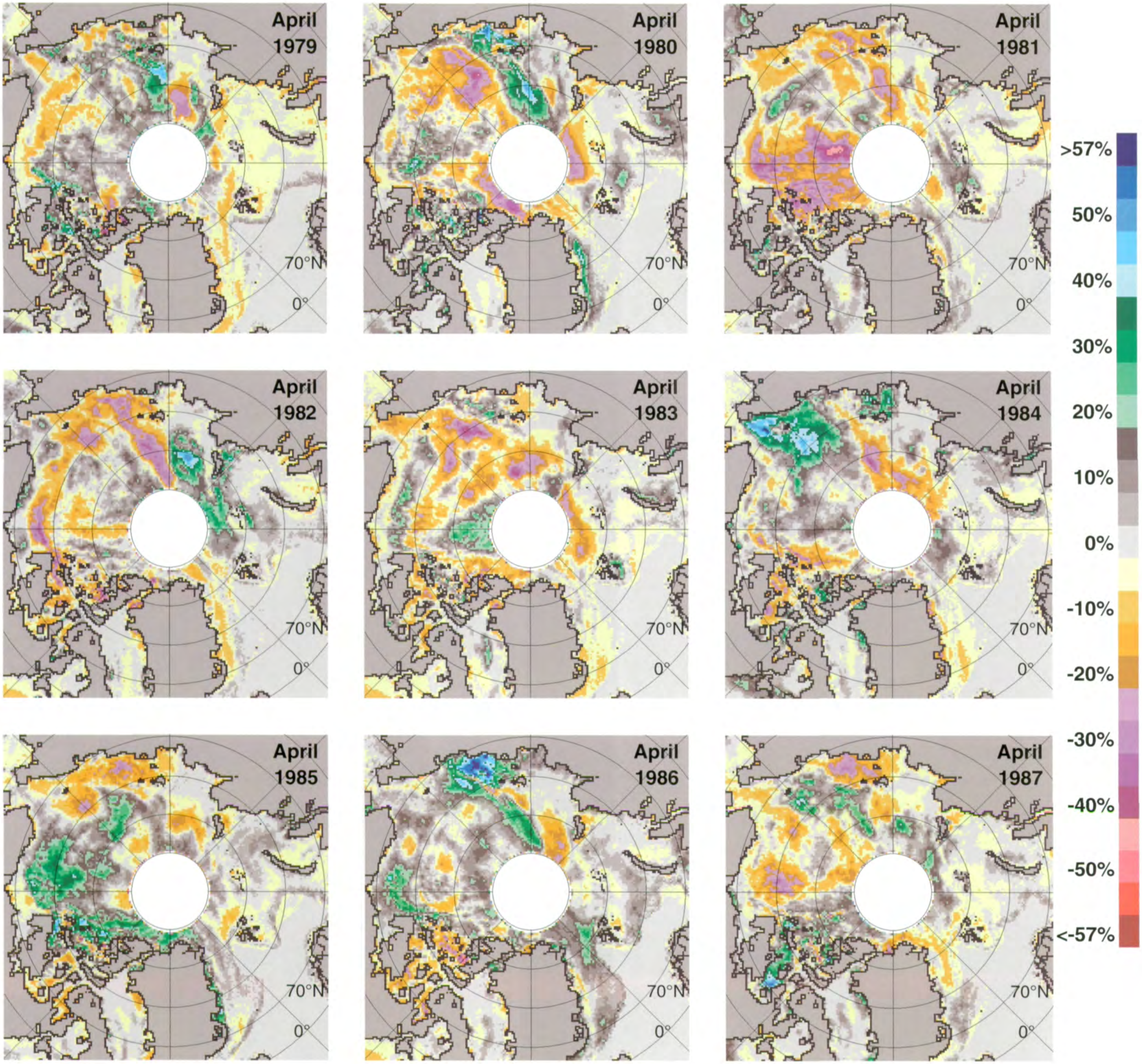

Figure 3.1.43. Mean monthly Arctic multiyear sea ice concentration anomalies for April 1979-1987.

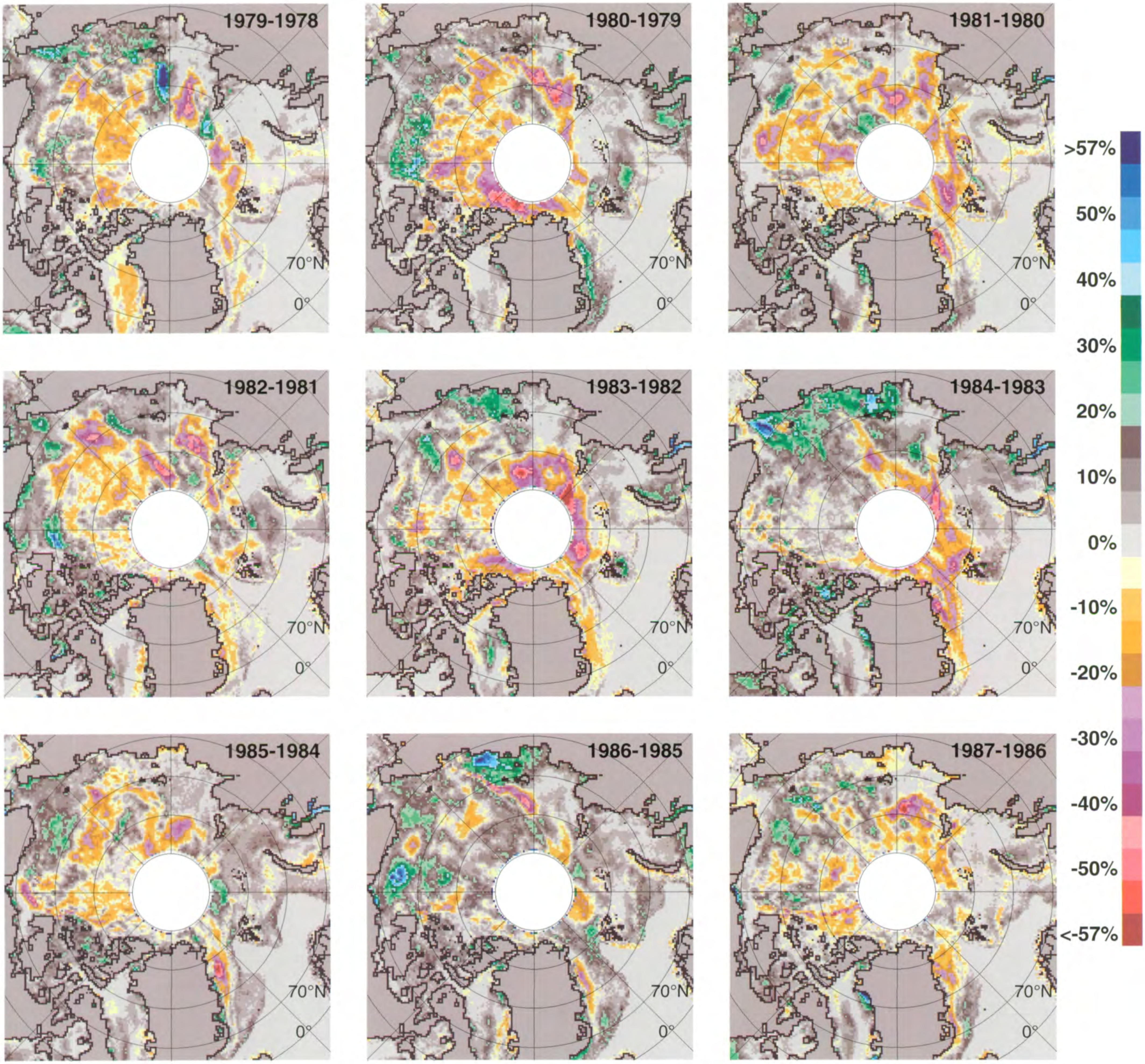

Figure 3.1.44. Changes in Arctic multiyear sea ice concentrations, April minus previous December.

in shape and phase from one year to the next. The timing of ice growth and ice decay varies by as much as 24 days during the 1978-1987 period (Gloersen and Campbell, 1988a). Further discussion of the interannual variations in ice coverage is given in Chapter 5.

The average seasonal cycle of Northern Hemisphere sea ice extent (Figures 3.1.46-3.1.47) reaches a maximum of 15.7 x 10^6 km^2 in late March, and a minimum of 9.3 x 10^6 km^2 in early September. The respective maximum and minimum values of sea ice extent for 1973-1976 from the ESMR data are 14.8 x 10^6 km^2 and 7.9 x 10^6 km^2 (Parkinson et al., 1987). For the sea ice area, the average maximum and minimum are 13.9 x 10^6 km^2 and 6.2 x 10^6 km^2 for the 1978-1987 period, and 13.0 x 10^6 km^2 and 4.7 x 10^6 km^2 for the 1973-1976 period.

The reasons for the differences in winter ice extent and area between the two periods of observation are uncertain. As discussed in Chapter 2, the spatial resolutions represented in the respective SMMR and ESMR grid maps are comparable, so the differences cannot be entirely attributed to different spatial resolutions. We lack sufficient in situ information to ascertain whether or not these differences result from geophysical changes. However, part of the difference in summer ice extent is a result of the different treatment of boundary pixels for ESMR and SMMR, as discussed in Chapter 2. For both the ice areas and extents, differences between the methods for calculating ice concentrations with the single-frequency ESMR and the multifrequency SMMR data may also contribute to the differences.

A number of interesting features are evident in the curves depicting open water and thin ice (see Chapter 2 and the following section) within the pack (Figure 3.1.45c). The open water peaks in the early summer and constitutes approximately 30% of the total ice extent at that time. Within the Northern Hemisphere sea ice, the duration of enhanced open water within the ice pack during the melt season is generally about 75 days. At the time of the winter maximum ice extent, the amount of open water within the total Arctic sea ice is about 14%, on average. However, as noted in the following sections, the concentration of open water derived from the data is only about 2.8%, on average, in the Arctic Ocean region during winter. In the peripheral seas, where the ice conditions are more comparable to the Antarctic, the open water percentage (15%-40%) is notably larger than in the Arctic Ocean, and this percentage varies significantly during the winter.

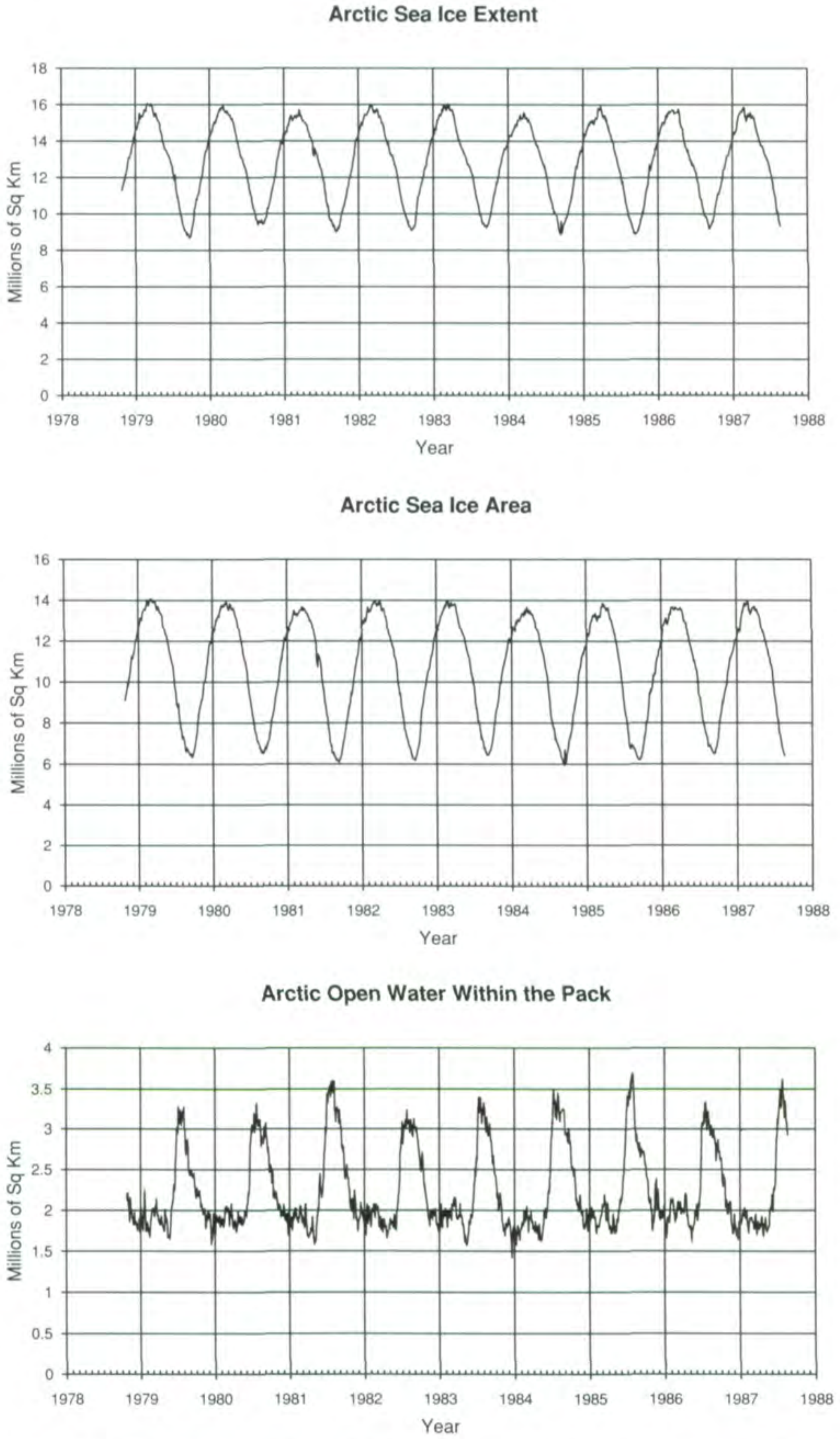

Figure 3.1.45. Sea ice extent, sea ice area, and amount of open water within the pack for the Arctic during the SMMR period.

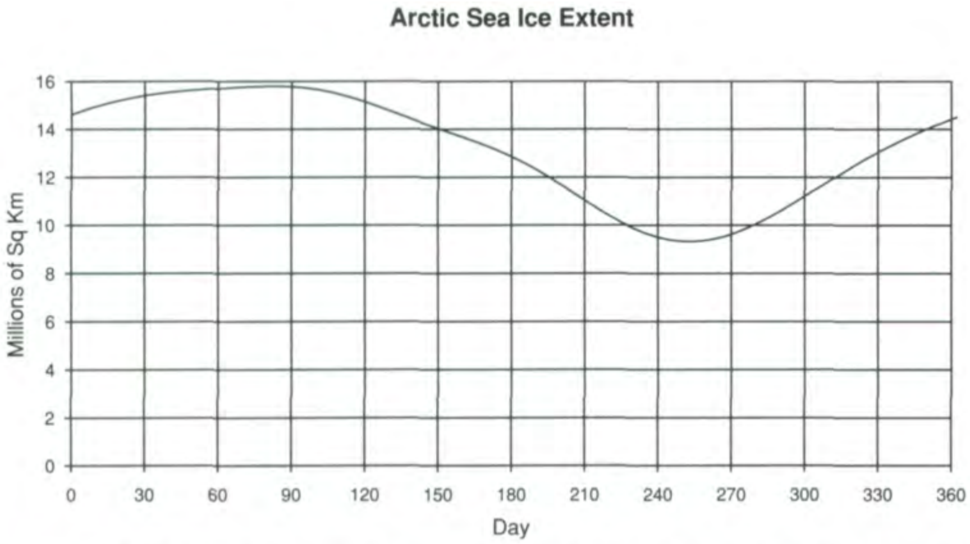

Figure 3.1.46. Modeled average seasonal cycle for the Arctic, as obtained from the SMMR data by Fourier analysis.

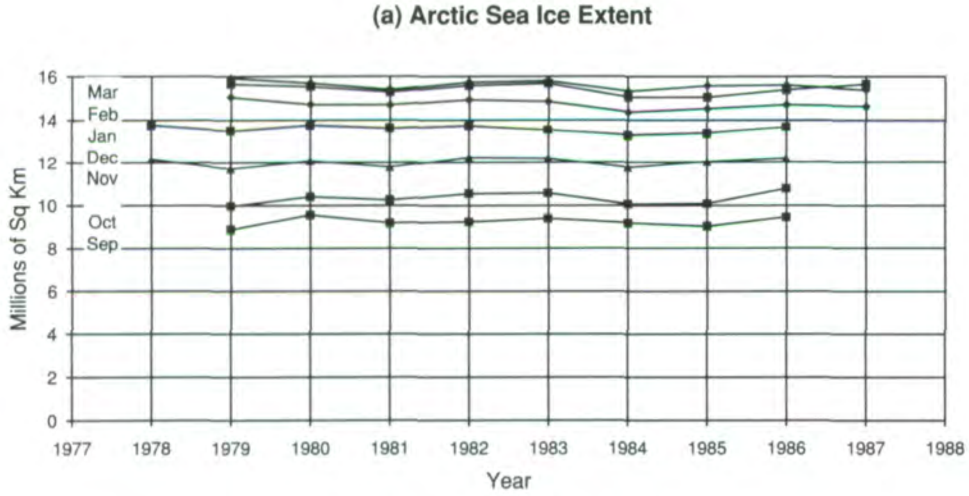

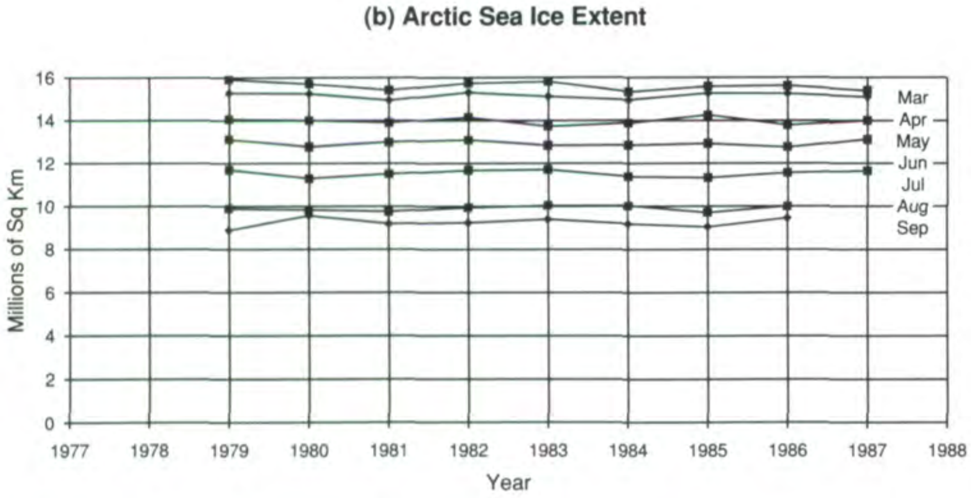

Figure 3.1.47. Month-by-month, year-to-year changes of the sea ice extents of the Arctic, (a) September to March, (b) March to September.

3.2 Arctic Ocean

During his classic 1893-1896 drift across the Arctic in the *Fram*, Fridtjof Nansen found ocean depths greater than 3,700 m (Nansen, 1897). The Arctic Ocean is now known to have an intricate bathymetry (Figure 3.2.1) with maximum depths exceeding 4,300 m. The Eurasian continental shelf extends well out into the ocean, with very shallow depths in the Laptev, East Siberian, and Chukchi Seas (Figure 3.1.1). Depths over the continental shelves are generally less than 50 m, extending as far as 600 km from the shore. The deep part of the Arctic Ocean is not a single depression, as had been thought by many 19th century scientists, but has two deep basins—the Canadian Basin and the Eurasian Basin. These basins are separated by the 2,000-km long Lomonosov Ridge, which extends across the ocean floor from the north end of Greenland to Novosibirskiye, as postulated by Mikhail Lomonosov in the 18th century (Mirsky, 1948).

The Arctic Ocean ice cover is the most complicated within the Northern Hemisphere (Figures 3.2.1-3.2.12). During the course of each year, a large variety of sea ice types exists throughout most of the Arctic Ocean, ranging from nilas and frazil to all stages of first-year ice and multiyear ice (Chapter 2). The ice pack floats on an ocean of variable currents carrying variable fluxes of heat and momentum. The ocean currents and fluxes in the Arctic are among the least well-described of the global oceans, largely because of the logistical difficulties involved in making oceanographic measurements from the continually breaking and shifting ice floes. Nevertheless, the general features of Arctic ice and ocean circulation are known. Figure 3.2.2 shows the tracks and drifts of 34 ships and ice stations, described in more detail in the ESMR Arctic atlas. Two main features of average ice drift and upper-ocean circulation patterns in the Arctic are shown by the drift arrows on the map: the Transpolar Drift Stream (extending northward from the East Siberian and Chukchi Seas across the pole and continuing southward into and through Fram Strait between Svalbard and Greenland), and the Beaufort Sea Gyre (a clockwise circulation in the Canadian Basin).

The sea ice distribution is strongly influenced by variations in the patterns of ice drift in the Arctic Ocean. Since 1979, information on the motion of the pack ice has been greatly expanded by the Arctic Ocean Buoy Network (AOBN), which consists of air-dropped drifting buoys tracked by the Argos system on NOAA satellites (Thorndike and Colony, 1980). The AOBN operated throughout the SMMR lifetime and provided data on ice drift in the Arctic Ocean, surface atmospheric pressures, and ice-air surface temperatures (as shown in Appendix A). The drift maps show that the motion of the Arctic Ocean ice pack is variable—both seasonally and interannually. The marked interannual variations in the annual drift patterns are well illustrated by the contrast between 1979 (Thorndike and Colony, 1980) and 1983 (Colony and Muñoz, 1986). For 1979, a well-established circulation in the Beaufort Sea Gyre and a clearly defined Transpolar Drift Stream are

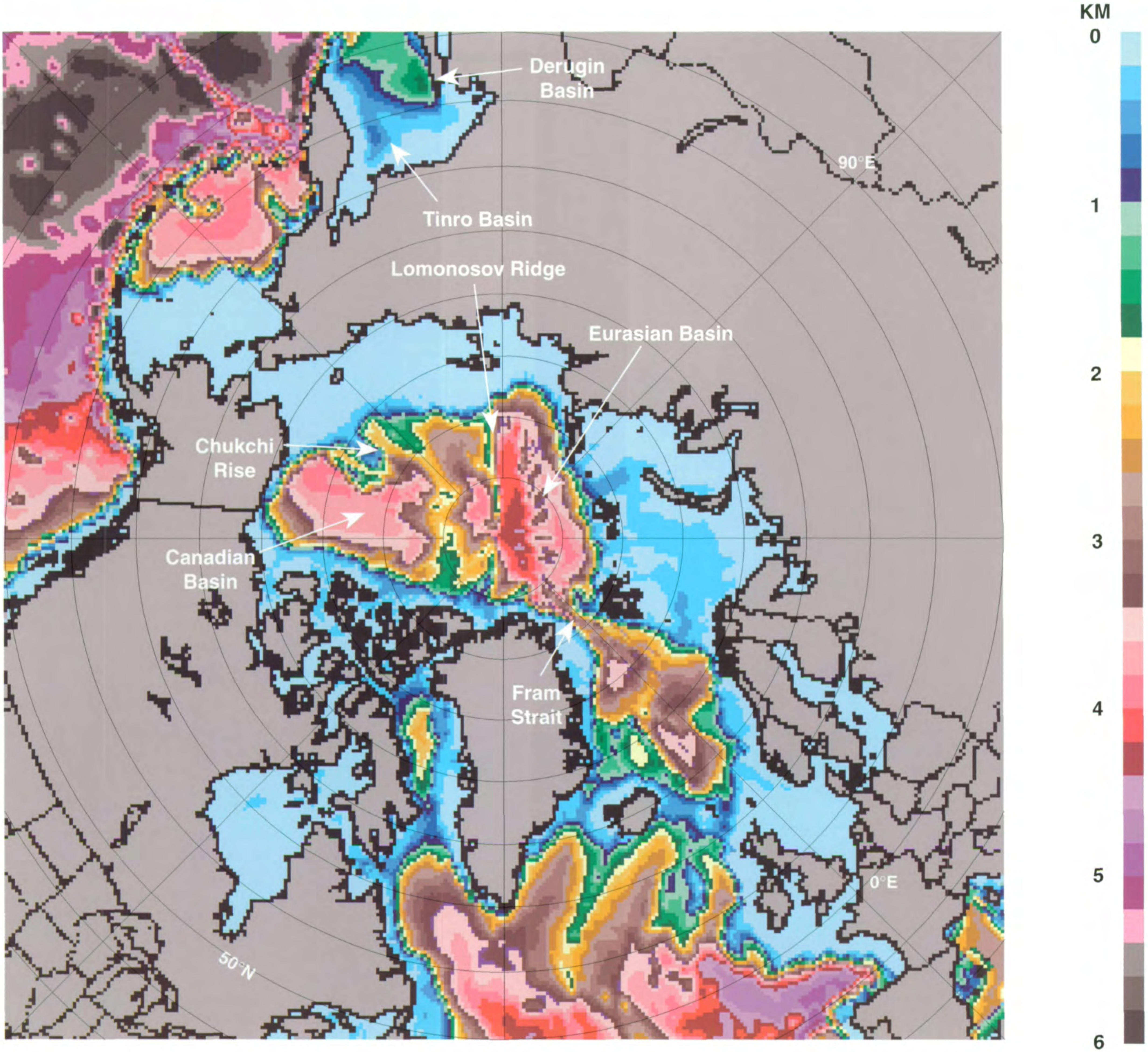

Figure 3.2.1. Bathymetry map (after Parkinson et al., 1987).

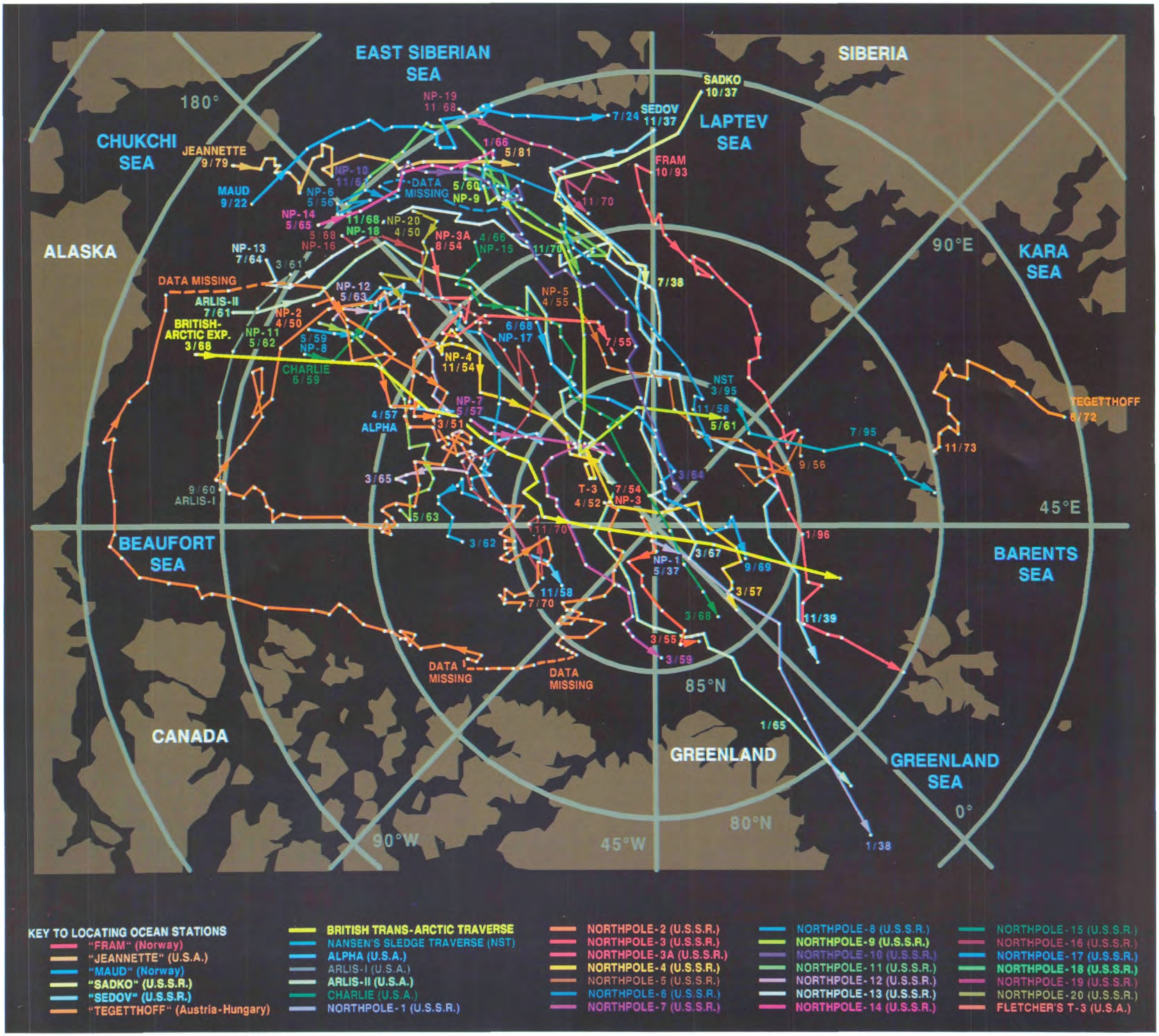

Figure 3.2.2. Drifts of ships and manned ice-floe stations in the Arctic Ocean from the 1893-1896 voyage of the Fram through North Pole 20, plus the route of the 1968 British Trans-Arctic traverse (from Parkinson et al., 1987; after Hastings, 1971).

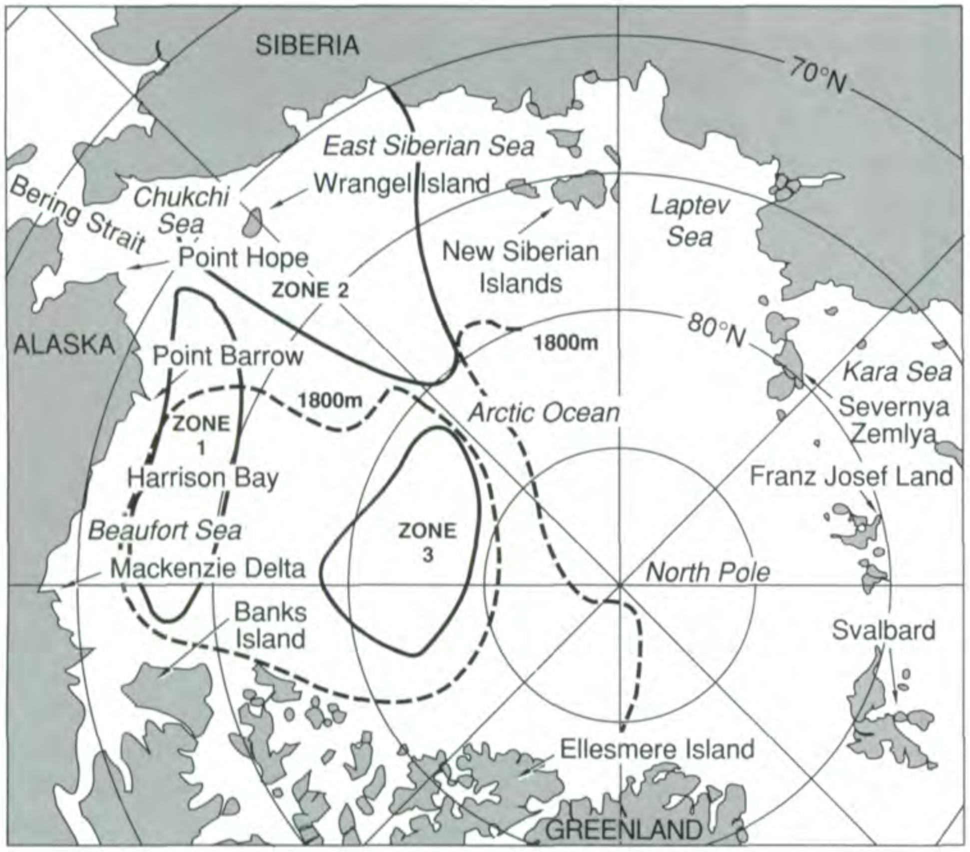

Figure 3.2.3. Location map for the Arctic Ocean showing three zones of persistent reduced ice concentrations during winter and the 1800-m depth contour.

both evident and closely resemble the long-term pattern shown in Figure 3.2.3. In contrast, the drift pattern for 1983 possesses neither of these classic features. Indeed, deviations from the mean velocity are significant on daily, as well as on seasonal and interannual, time scales. An analysis of the ice trajectory data (Thorndike and Colony, 1982; Thorndike et al., 1983) has shown that for intervals of one day, the standard deviation from the mean velocity greatly exceeds the mean value. The deviation being about 7 km per day, and the mean only about 2 km per day. The variable patterns of convergence and divergence in the ice drift patterns indicate changes in the distribution of total sea ice and multiyear ice concentrations on daily to interannual time scales, as discussed below.

3.2.1. Seasonal and interannual variations in total ice concentration

The distribution of sea ice concentration or of open water (along with its variations on daily to annual time scales) is important for polar heat budget studies. In winter, the fluxes of heat and water vapor through open water within the pack can be orders of magnitude greater than through the surrounding pack ice (Badgley, 1966). Also, the heat flux through thin ice is much greater than through thick ice (Maykut, 1978). Furthermore, in summer, open water absorbs significantly more solar radiation than sea ice does.

During November through May, sea ice covers the entire Arctic Ocean (Figures 3.1.2 and 3.2.3) with a monthly average of at least 15% concentration (Figure 3.1.15). The average ice concentration during winter is about 97% (corresponding to 3% open water) (Figure 3.2.4).

During winter, the observed open water area (Figure 3.2.4) declines from about 0.3×10^6 km^2 in the beginning of December to a minimum of about 0.15×10^6 km^2 at the end of April, corresponding to a decline in open water from 4.2% to 2.1%. Open water area decreases during the winter, since vertical ice growth increases the average ice thickness and makes the pack resistant to deformation. Earlier analyses based on thermodynamic calculations of heat balance and ice growth suggested that the open water is probably only 1% or less (Untersteiner, 1964; Maykut, 1978). The true amount of open water within the Arctic Ocean during winter remains somewhat uncertain, because the estimated accuracy of the open water amounts from SMMR is also several percent.

During winter, no interannual variation in ice extent occurs in the Arctic Ocean region, because the pack fills the entire region. Therefore, variations in ice area and open water area occur simultaneously: as open water increases, the ice area decreases. At the winter extrema, the minimal amounts of open water occur in 1980, 1984, and 1985, and the maximal, in 1979 and 1986. The respective average open water concentrations ($1-C_T$) are about 1.5% and 2.8%. However, the 1.3% difference in these values is only about three times larger than the estimated residual errors associated with the long-term brightness temperature calibration (Chapter 2), and probably not as reliable as the previously mentioned change in the open water amount during each winter season.

At the summer minimum in September, sea ice with a concentration of at least 15% still covers about 6.2×10^6 km^2, or 87% of the 7.08×10^6 km^2 of the Arctic Ocean region (Figure 3.2.4). The average ice concentration within the pack during summer is about 80%, corresponding to an open water concentration of 20%, on average, (including the open water in melt ponds on the ice). The open water area usually peaks in August, remains high until mid-September, and then declines sharply as freezing occurs throughout most of the Arctic Ocean. In contrast, the minima in both sea ice extent and area usually occur in early to mid-September, which is a few weeks later than the open water maximum in most years. One exception is 1982, when the minima in extent and area are essentially simultaneous with the maximum in open water. Occurrence of the peak in open water area prior to the minima in ice extent and ice area implies that new ice growth commences in the central parts of the pack while the ice boundary is still retreating. The timing of the commencement of new ice growth has important implications concerning the amount of multiyear ice area formed each year, as discussed in Section 3.2.3.

The interannual variation in maximum open water area during summer is about 30%. The interannual variation in the minimum ice area is 10% and in the minimum ice extent, 5%. In the 1981 summer, when the open water area within the pack is greater than in any of the other years, the ice area and

Sea Ice Extent in the Arctic Ocean

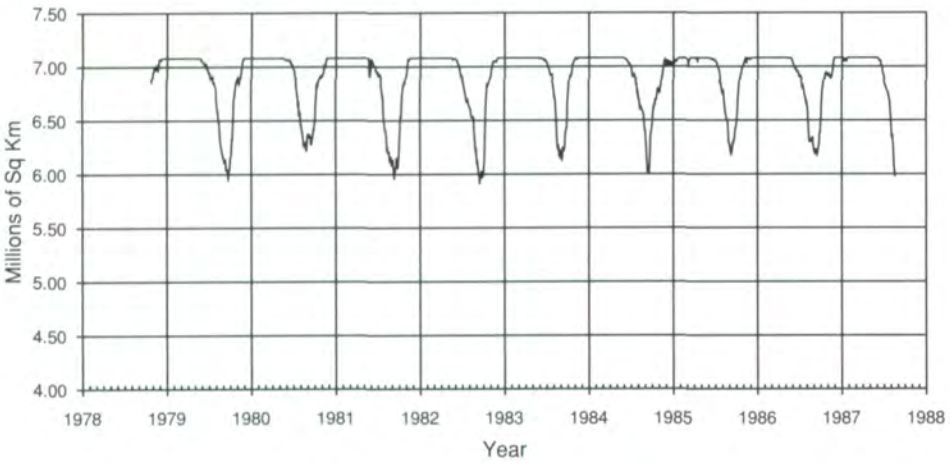

Sea Ice Area in the Arctic Ocean

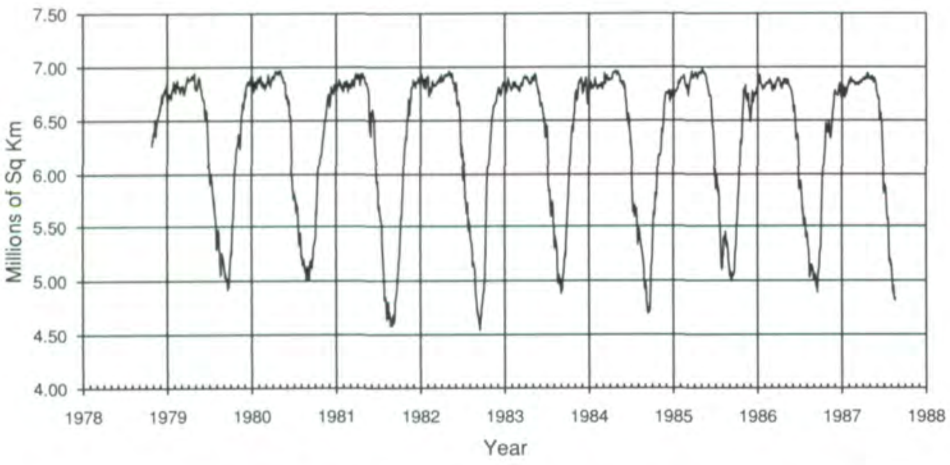

Open Water Within the Pack in the Arctic Ocean

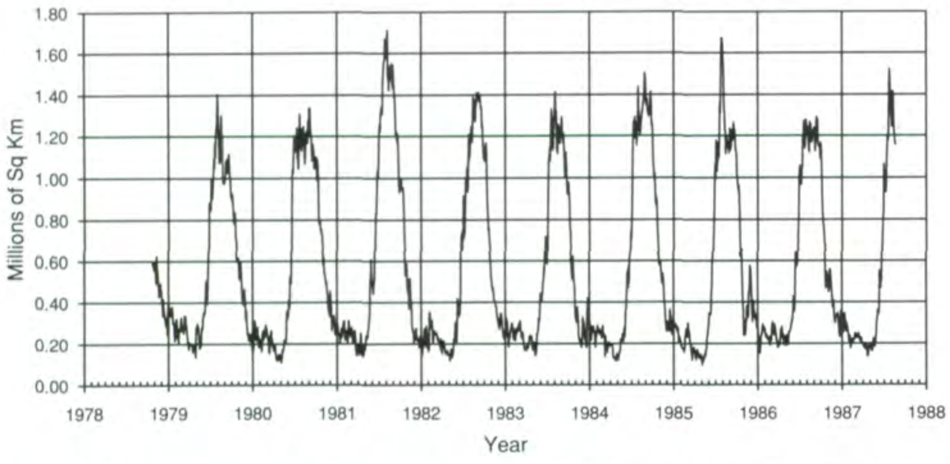

Figure 3.2.4. Sea ice extent, sea ice area, and amount of open water within the pack for the Arctic Ocean from October 26, 1978 to August 20, 1987.

Sea Ice Extent in the Arctic Ocean

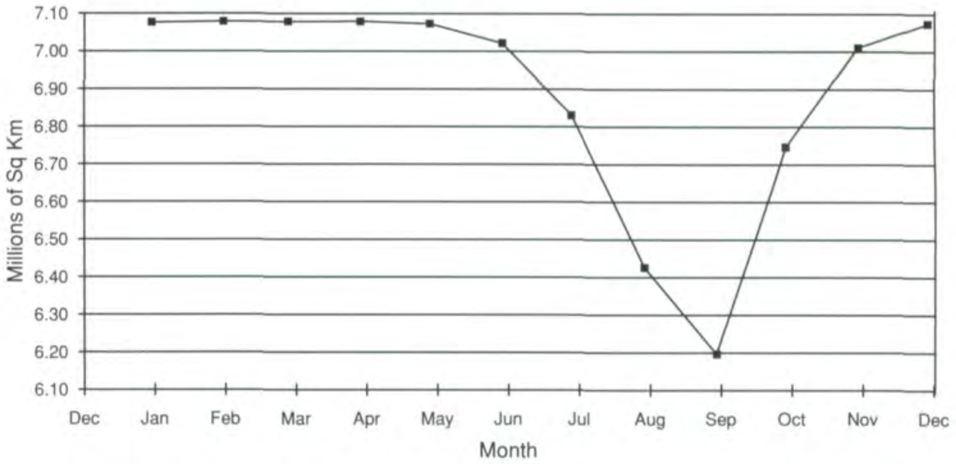

Figure 3.2.5. Average seasonal cycle of sea ice extents for the Arctic Ocean.

(a) Multiyear Sea Ice Area in the Arctic Ocean

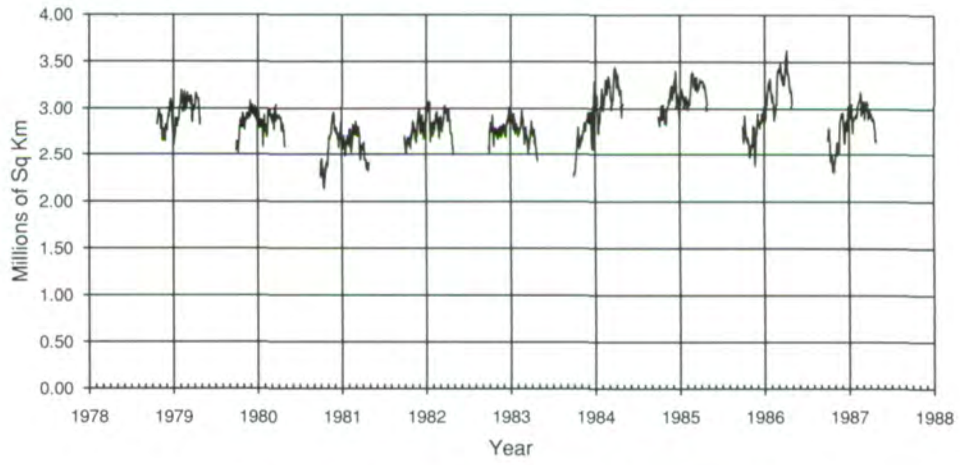

(b) Multiyear Sea Ice Extent in the Arctic Ocean

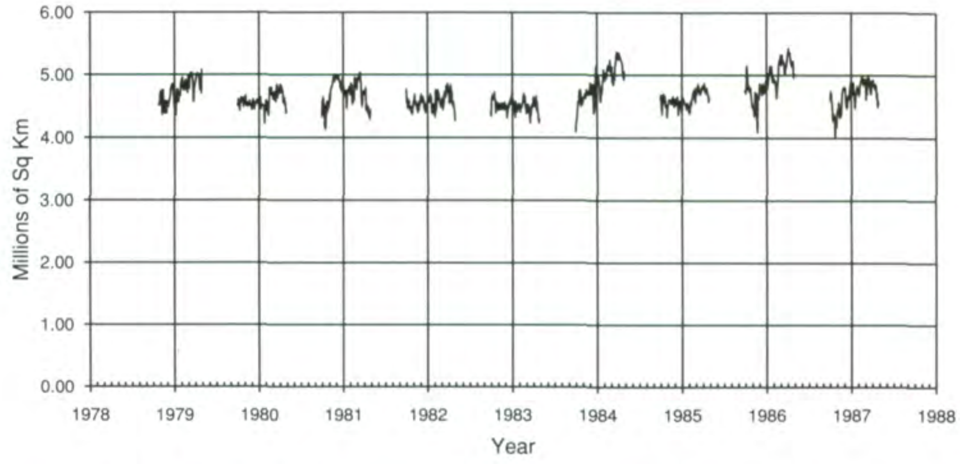

Figure 3.2.6. Time series of (a) areal coverage and (b) extent of multiyear sea ice (area enclosed by the 20% C_{MY} isopleth) in the Arctic Ocean.

the ice extent are both near the lowest of the 9 years. Specifically, the pack was both less compact (77% average concentration) and less extensive at the summer minimum in 1981 than in the other years. In contrast, 1980 and 1985 both have relatively large ice extents and relatively low amounts of open water within the pack, but the 80% average ice concentration is only 3% higher than in 1981. Although the ice pack appears to be more compact, on average, when the ice extent is greater than usual, the ice area and the ice extent tend to vary in phase, so that the variation in compactness is not as extreme, on a percentage basis, as the variation in the amount of open water within the pack.

Areas of low ice concentrations in midwinter

The interannual variations in the location of low ice concentration areas in the midwinter ice cover are described in the February maps of monthly ice concentrations (Figure 3.1.4), the 9-year average ice concentrations (Figure 3.1.15), and the ice-concentration anomalies (Figure 3.1.17). As noted previously, the estimated accuracy of the monthly-averaged ice concentrations is ±7% or better, so reduced ice concentrations of less than 93% may be considered significant. Also, the interpretations of the areas of reduced concentrations here and in the next section, are based on comparison with the concentrations in the surrounding ice pack. The persistence of the areas of reduced concentrations throughout the season suggests a geophysical cause rather than an unknown anomaly in the instrument calibration or in the microwave properties of the ice and atmosphere.

Areas of anomalously low ice concentrations, in the range of negative 5% to 15% in the monthly-averaged ice concentrations, occur in all winters during 1978-1987. The anomalies are remarkably persistent during each season, but significantly different from year to year. The reduced-concentration features are generally established by November or December, persist through March and sometimes April, but tend to diminish in strength during the season.

Most of the anomalies are located in three main zones, which are illustrated in Figure 3.2.3.

- Zone 1 is located in the Beaufort Sea between 70° N and 75° N from 125° W to 165° W and has negative anomalies during the winters of 1979, 1981, and 1982.
- Zone 2 is located in the Transpolar Drift Stream around the vicinity of the 180° meridian from 70° N near Wrangel Island and the East Siberian Sea to 80° N and has negative anomalies during 1979, 1980, 1981, 1984, and 1986. Zone 2 overlaps with a "zone of occasional polynyas" described in an analysis by Yakovlev (1977) of long-term Soviet drift station and aircraft observations.
- Zone 3 is located closer to the pole along 80° N from 100° W to 170° W, and has negative anomalies during the winters of 1983, 1986, and 1987.

In February 1979, areas of anomalously low monthly averaged ice concentrations, in the 88%-92% range, are located in the Beaufort Gyre (Zone 1) and the Transpolar Drift Stream (Zone 2). The areas of reduced concentration are in the form of wide bands running east-west along 75° N from Banks Island into the East Siberian Sea, and a wide north-south band running from east of Wrangel Island toward the pole in the Transpolar Drift Stream. This pattern of reduced ice concentrations is persistent throughout the winter, being clearly established in November 1978 and lasting through March 1979. In April, when the pack is most consolidated and the observed ice concentration is greatest throughout the Arctic Ocean, only the band closest to the coast in the Beaufort Gyre remains in the 88%-92% range.

In February 1980, anomalously low ice concentrations do not occur in the same areas as in 1979, but rather in the McKenzie Delta, Chukchi Sea, and in an extensive area north of the Chukchi Sea in the eastern part of Zone 2. Similar to the preceding year, the low concentrations north of the Chukchi Sea are long-lived, being established in December 1979 and lasting through March 1980. In contrast, the reduced concentrations in the McKenzie Delta and Chukchi Sea persist only through February and March of 1980. The following year, 1981, has reduced concentrations in Zone 1 between 70° N and 75° N, similar to 1979 but without the banding, and in an area in Zone 2 closer to the Chukchi Sea. Again, the pattern is persistent, starting in November 1980 and lasting through March 1981.

Some of the lowest midwinter ice concentrations in the Arctic Ocean occur in February and March 1982 in the Southern Beaufort Sea (Zone 1), in the McKenzie Delta, along the north coast of Alaska, and into the Chukchi Sea. Although greater in magnitude (up to 15% anomalous) than other years, the low-concentration areas are not as persistent in 1982, beginning only in February and ending by April (cf. Case 3 in the following section). In the winter of 1983, a different situation occurs, with low-concentration areas with negative anomalies of 5%-10% in Zone 2 and circling the pole into the Laptev Sea. In the following winter, 1984, all of the Arctic Ocean had normal ice concentrations with the exception of the Chukchi Sea in Zone 2, where negative anomalies of 15% persisted from December 1983 through March 1984. The winter of 1985, which has the most uniformly high concentrations across the Arctic Ocean, is the most atypical of the 1978-1987 period. Another characteristic of the 1985 distribution is the large area of reduced concentrations in the Fram Strait extending toward the pole, along with an atypical area of open water extending 200 km north of Svalbard.

The patterns of anomalously low ice concentrations are exceptionally persistent during the 1986 and 1987 winters, being established in November of each year and lasting through April. Again, however, the decreasing open water in the area during each season is consistent with the expected growth and consolidation of the pack. In 1986, the predominant area of reduced concentrations is in the western part of Zone 2, and several small areas are in Zones 1 and 3. In 1987, the predominant area of reduced concentrations is in Zone 3.

Areas of low ice concentrations in summer

The interannual variation in the location of the areas of low summertime sea ice concentrations is described, using primarily the August and September ice concentrations (Figures 3.1.10 and 3.1.11) and their anomalies (Figures 3.1.23 and 3.1.24). These maps show numerous areas on the scale of several hundred kilometers with concentrations in the range of 60% to 80%. Wittman and Schule (1966), in their analysis of aircraft visual observations of the Arctic ice pack obtained by U.S. Navy Bird's Eye aircraft, found that considerably greater amounts of open water occurred during all seasons than had previously been believed, including an estimated average for summer months of 12% in the Canadian Basin and 7% in the Eurasian Basin. Campbell et al. (1978) and Gloersen et al. (1978), in their analysis of simultaneous aircraft and satellite ESMR observations obtained during the main Arctic Ice Dynamics Joint Experiment (AIDJEX) in 1975-1976, interpreted the areas of low brightness temperatures as areas of reduced ice concentrations, with smaller areas of ice-free melt ponds. Campbell et al. (1984) found that during each of the four ESMR years, large low-concentration areas occurred during the late summer with amounts of open water equal to or greater than those observed by Wittman and Schule (1966).

The passive-microwave measurement of the low-concentration areas during summer is complicated by the occurrence of melt ponds, as discussed in Chapter 2. Ice-free melt ponds have the microwave signature of water, whereas melt ponds with a frozen surface have the signature of first-year sea ice (Campbell et al., 1978; Grenfell, 1992). In the Arctic Ocean, melt ponds grow rapidly from the onset of melt, and normally reach maximum areal coverage of about 20%-30% of the ice area in July (Campbell et al., 1978, 1984; Carsey, 1982). Passive-microwave estimates of the magnitude and timing of the melt-pond effect can be made (cf. discussion in Section 3.2.3). With regard to timing, the open water in the SMMR data peaks during August (Figure 3.2.4), and the areas of reduced concentration are most extensive in August and September, after the July maximum in melt-pond coverage. Crane et al. (1982) examined possible alternative interpretations of the late-summer low brightness temperatures, measured by ESMR in 1974, and made estimates of the possible magnitude of the melt-pond effect.

In an analysis of SMMR data for 1978-1984, Barry and Maslanik (1989) found large areas of low brightness temperatures, which imply reduced ice concentrations, during 4 of the 6 years, and found supporting evidence of reduced concentrations in their interpretation of visible-band imagery and drifting buoy temperatures. Specifically, the large region of less than 60% concentration in the Beaufort Sea, described later in Figure 3.2.7i-l, also shows low concentrations in visible imagery (Barry and Maslanik, 1989) even though the Navy/NOAA Joint Ice Center maps show 10/10 old ice coverage.

The August-September areas of reduced ice concentrations in the interior of the ice pack occurred during the 1973-1976 period in two principal patterns (Campbell et al., 1984). In the ESMR Arctic atlas, the anomalies occur along the Transpolar Drift Stream in September 1973, 1974, and 1976. In 1975, they occurred in a broad semicircular pattern within a zone between 77° N and 88° N. During September 1978-1987, these patterns are less distinct (Figure 3.1.11), with a Drift Stream orientation appearing only in 1982. Semicircular patterns of low ice concentrations appear in the Septembers of 1979 and 1980, although located farther south than in 1975. In 1984, the areas of low concentration are again farther north, perhaps forming in a semicircular pattern partly obscured by the data gap polewards of 84° N. Widespread areas of reduced concentrations are located north of the Laptev Sea in the Augusts of 1981, 1982, and 1983, and in the Canadian Basin in 1981, 1982, and 1984. A large opening occurs along the northeastern and northern coast of Greenland in August of 1985, but not in any of the other years.

Positional modes of the summer ice pack

The interannual variability in the position of the ice pack in the Arctic Ocean at the September minimum appears to be characterized by two principal modes. In one mode, the pack is displaced towards the Alaskan side of the Arctic Ocean, causing the ice to impinge on the Alaskan and McKenzie Delta coastlines and causing positive ice-concentration anomalies in the Beaufort Sea. In the second mode, the pack is displaced from the Alaskan coast towards the Siberian side, leaving a wide band of open water along the coastline of the southern Beaufort Sea and negative anomalies usually in the Beaufort Sea ice pack. Interannual variations in the position of the ice edge are as large as 300 km or about 20% of the approximate radius of the summer ice pack, whereas interannual variability in the area of ice extent is only 5%. The Alaskan mode occurs during the summers of 1980, 1983, 1984, and 1985. The Siberian mode occurs during the summers of 1979, 1981, 1982, 1986, and 1987. During the 1973-1976 summers, the Alaskan mode occurs only in 1975. In some years, the right-hand edge of the ice pack in Figure 3.1.11 is displaced more to the left than in others, forming a nearly straight line running from the Kara Sea to the eastern coast of Greenland, most clearly evident in September 1979, and also in 1983-1985. A similar pattern occurred in September 1976.

The variation in position of the summer ice pack appears to be associated with departures of the ice drift (Figure A.14) from the long-term pattern (Figure A.15). A pattern close to the long-term drift occurs during 1979, 1981, 1982, 1986, and 1987, when the Siberian mode appears. The long-term drift pattern clearly broke down in 1983, 1984, and 1985, when the Alaskan mode appears. However, the departure from the long-term drift pattern is not as clear in 1980, when the Alaskan mode also occurs. Nevertheless, the surface atmospheric pressure maps for the period of May through September 1980 indicate that the wind forcing is predominantly toward the Alaskan coast.

3.2.2. Short-term variations in areas of reduced ice concentrations

In the previous section, we discussed temporal behavior of the ice concentrations in the Arctic Ocean ice pack on time scales as short as one month. In order to focus in on shorter time scales, we have selected eight events during 1978-1987, when pronounced areas of low ice concentrations occurred in the Arctic Ocean. These are illustrated with sequences of single-day maps because the daily sequences reveal additional information on the complexity and dynamism of the ice pack, and, in particular, on the areas of persistently reduced ice concentrations discussed in the previous section. The amount of open water in the areas of reduced concentration is, of course, greater at times than is shown in the monthly average maps, and this is illustrated in the daily maps. The sequences illustrate continual fluctuations in the observed ice concentration in winter and late summer. As noted previously, some portion of thin ice area is included in the SMMR open water values. However, thin ice can only form where open water has recently occurred. Thus, the SMMR observations indicate that large and persistent areas of reduced sea ice concentration occur. Alternative causes of the spatial and temporal variations in brightness temperature that could be responsible for the derived low winter ice concentrations have been examined, but none are considered to be plausible explanations other than real variations in the area of open water. For example, the possible effects of intermittent atmospheric warming and consequent surface melting have been excluded by noting that the multiyear ice signature did not disappear during the events.

Case 1. 29 October 1980-20 March 1981 (Figure 3.2.7a-h)

Large areas of low ice concentration, as low as 70%, appear in the southern Beaufort Sea on 29 October 1980, in Zone 1 (Figure 3.2.3) of the Arctic Ocean recurrent low-concentration zones mentioned above. These include the large shore leads across the north coast of Alaska and two large polynya zones just north of them extending to 75° N. During the next 6 days, the shore leads close but the two large areas with polynyas remain open. These reduced ice concentrations persist until 16 December 1980, with ice concentrations as low as 80%. They fluctuate in size until 25 January 1981, with core-ice concentrations of 84%, continue until 28 February 1981, with similar concentrations, and are still present on 20 March 1981. By this time, a shore lead reappears between Pt. Barrow and Wainwright, with ice concentrations as low as 56%.

Case 2. 29 August 1981-4 September 1981 (Figure 3.2.7i-l)

This late-summer case illustrates the rapidity with which polynyas can form and disappear during the melt season. It also illustrates a very important relationship between the late-summer sea ice concentrations and the total and multiyear ice concentrations the following winter. On 29 August 1981, a large area of low ice concentrations (approximately 50%) covers most of the Beaufort Gyre region. Two days later, a zone of even lower ice concentrations (40%) appears at 80° N and 155° W and increases in size during the next 2 days. After only 2 more days, the ice concentrations have increased markedly throughout the region, indicating new ice growth. Furthermore, this region of low ice concentration is not followed by low concentrations in the next winter. Indeed, by October 1981, the total sea ice concentrations are anomalously high and remain so throughout the winter (Figures 3.1.24 to 3.1.27 and 3.1.16 to 3.1.19). In contrast, however, the concentrations of multiyear ice are anomalously low in this region, starting in October 1981 and continuing through April 1982 (Figures 3.1.29 to 3.1.35). Only the ice formed prior to the summer and remaining at the end of the summer (e.g., perhaps most of the ice in this region of polynyas on 2 September 1981) becomes multiyear ice, and the new ice formed during summer (e.g., between 2 and 4 September 1981) becomes first-year ice. Therefore, the observed relationship of low total ice concentration in late summer and low multiyear ice concentration in winter, with normal or higher total ice concentration in winter, is exactly as expected. Indeed, the minimum values of total ice concentration in the late-summer daily maps in this region are close to the values of multiyear concentration in December, but the total concentrations in the September average concentration map are much higher (cf. the next section).

Case 3. 3 February 1982-9 March 1982 (Figure 3.2.7m-r)

A deep-winter opening of the southern Beaufort and Chukchi Seas commences on 3 February 1982, in Zone 1 of the recurrent low ice-concentration zones. By 5 February 1982, a polynya zone extends from the McKenzie Delta along the entire Alaskan coast to the Bering Strait out to 74° N, with concentrations as low as 65%. The daily surface-pressure maps and buoy drifts (Thorndike et al., 1983) show offshore wind and buoy drifts from 28 January through 4 February 1982 that are the likely cause of the reduced concentrations. The drift reverses direction for one day on 5 February, and then fluctuates in direction through 9 March 1982. However, averaging of the daily variations of the wind-forcing inherent in the monthly average pressure map for February 1982 (Figure A.2) masks the variable wind-forcing that causes ice divergence and the low concentrations. During this period, the ice concentrations fluctuate around 80%, but the area retains its size until at least 9 March 1982. During April and May, the monthly ice concentrations in this area increased. As noted in the previous section, this situation differs from others that form in early winter and persist throughout the winter.

Case 4. 11 October 1982-10 March 1983 (Figure 3.2.8a-d)

During the winter of 1982-1983, the Canadian sector of the Arctic Ocean has anomalously high ice concentrations, with the exception of the area referred to above as Zone 3 of the recurrent low ice-concentration areas. On 11 October 1982, a polynya zone with ice concentrations as low as 75% forms in the area 81° N to 84° N and 140° W to 170° W. The area expands until 17 October 1982 and persists until 16 November 1982, when a slightly greater ice concentration appears at its core of 80%. Throughout the winter, the area varies in size, but retains its general position until 10 March 1983, when core concentrations are about 85%. This feature persists until May 1983, as can be seen in the monthly ice concentrations and concentration anomaly maps (Figures 3.1.3-3.1.14 and 3.1.16-3.1.27).

Case 5. 2 October 1983-29 October 1983 (Figure 3.2.8e-h)

Approximately a year after the winter polynya area discussed in Case 4 formed in Zone 3, it occurs again. The reduced concentration area is apparent on 2 October 1983, with a center slightly east of the center of the previous year and again with core-ice concentrations of 75%. Polynya zones also form southeastwards from this area along the Canadian coast. The size and shape are the same 10 days later on 12 October 1983, when core concentrations are 80%. The area persists with slightly greater concentrations through 20 October 1983 and 28 October 1983. It remains as a weak feature in the November 1983 average concentration and anomaly maps (Figures 3.1.12 and 3.1.25), but essentially disappears by December. However, reduced concentrations persist near the Canadian coast around 80° N throughout the winter.

Case 6. 21 December 1983-25 February 1984 (Figure 3.2.8i-l)

On 21 December 1983, a large polynya area with ice concentrations as low as 60% forms in the southern half of Zone 2, extending south into the Chukchi Sea. This feature persists through the remainder of the winter, as noted in the previous section. By 12 January 1984, the ice concentrations in the Chukchi Sea have increased significantly, with a core concentration of about 75%. On 7 February 1984, the Chukchi Sea concentration is reduced slightly, while the Zone 2 polynya area persists with about the same size and slightly higher concentrations. On 25 February 1984, the areas remain, but with slightly higher concentrations, while most of the rest of the Arctic Ocean has concentrations greater than 95%. The concentrations in Zone 2 continue to increase through May 1984, when, 5 months after its December formation, a small area with concentrations in the 94% to 96% range remains (Figures 3.1.3-3.1.7).

Case 7. 20 November 1985-26 March 1986 (Figure 3.2.8m-r)

In the winter of 1985-1986, long-lived polynya areas occur at various times in all three zones of recurrently low-ice concentrations. Large low-concentration areas (90%) occur in Zone 3 on 20 November 1985, as well as in the southern part of Zone 2 and the Chukchi Sea. The surface maps and buoy data (Colony and Muñoz, 1986) for 18 November 1985 show a strong low-pressure system (980 mbar) centered at 85° N and 120° W, with the consequent strong divergent drift of the ice pack over the polynya area in Zone 3. By 28 November 1985, the polynya area in Zone 3 continues, but the ice distributions in Zones 1 and 2 are radically transformed. In Zone 1, a shore lead with concentrations ranging from 44%-80% extends across the entire north coast of Alaska, while concentrations greater than 85% cover the northern part of this zone. Again, the buoy and pressure data indicate wind-forcing of the open water in Zone 1; strong southerly offshore winds and northward ice drift are shown from 24 to 29 November. A large polynya area with concentrations as low as 65% covers the northern half of Zone 2 and extends southwestward to the central coast of the East Siberian Sea. There is no evidence of the polynya area in Zone 2 in October (Figure 3.1.12), so it clearly must have formed during November. However, no buoys are located in Zone 2 west of about 178° E and the possible divergence of the ice pack is not easily inferred from the pressure fields. After November, reduced ice concentrations persist in all three zones, but by 12 December 1985, the ice concentrations in Zones 1 and 2 increase. Similarly low concentrations are evident in all three zones, but with increasing concentrations, through 26 March 1986. By May 1986 (Figure 3.1.8) the concentrations in these zones reach their highest values with only a small area in Zone 2 near the Siberian coast having concentrations of less than 92%. Thus, this low-concentration distribution involving all three zones persists for about 6 months.

Case 8. 9 November 1986-11 February 1987 (Figure 3.2.9a-e)

Large areas of polynyas occurred in all three zones again in the winter of 1986-1987, but those in Zone 2 lasted only through December 1986 (Figures 3.1.3-3.1.14). Zone 1 has concentrations greater than 94% by January 1987, on average, but an area in Zone 3 persisted with minimum monthly average concentrations of about 90% through May 1987. On 9 November 1986, widespread polynya zones cover much of Zones 1, 2, and 3, persisting until 17 November 1986. By 27 November 1986, Zone 1 is fully ice-covered, whereas Zones 2 and 3 have anomalously low ice concentrations with core values of 80%-88%. By 27 December 1986, Zone 2 is also essentially fully ice-covered and remains so throughout the rest of the winter. In contrast, Zone 1 opens again with a polynya just west of Point Barrow with concentrations about 70% and with concentrations about 80%-90% over much of Zone 1. At the same time, the amount of open water in Zone 3 has increased, with some concentrations less than 80%. This open-water pattern persists until 12 January 1987, with slightly increased ice concentrations.

These case studies clearly show that large areas of reduced ice concentrations (polynya areas) occur in the Arctic Ocean during all seasons. The areas tend to be persistent for several months within a season, but not necessarily from season to season, as shown by the counter-example of Case 2 (late summer in the Beaufort Sea). What forcing factors cause these low ice-concentration areas to form and be so persistent? Certainly, wind-forcing plays a role in their establishment and fluctuation by forcing divergence of the ice pack, as shown, for example, in Case 3 (midwinter 2-month opening near the coast in the southern Beaufort Sea). Case 5 in Zone 3 is another example of a 2-month-long feature, located near a longer-lived feature of the previous winter. However, many of the other areas discussed in the previous section and this section (Cases 1, 4, 6, 7, and 8) had low concentrations that persisted throughout much of the winter season. Since wind-forcing and the consequent convergence and divergence of the ice pack typically change markedly from day-to-day and month-to-month (Figures A.1-A.12), it is unlikely that localized areas of wind-forced ice divergence and open water would persist throughout a winter season. Consequently, a more persistent forcing factor is likely to be involved in maintenance of the polynya areas throughout the winter. We surmise that, at times, under these zones persistent divergence of the water-surface flow occurs. The shapes and locations of

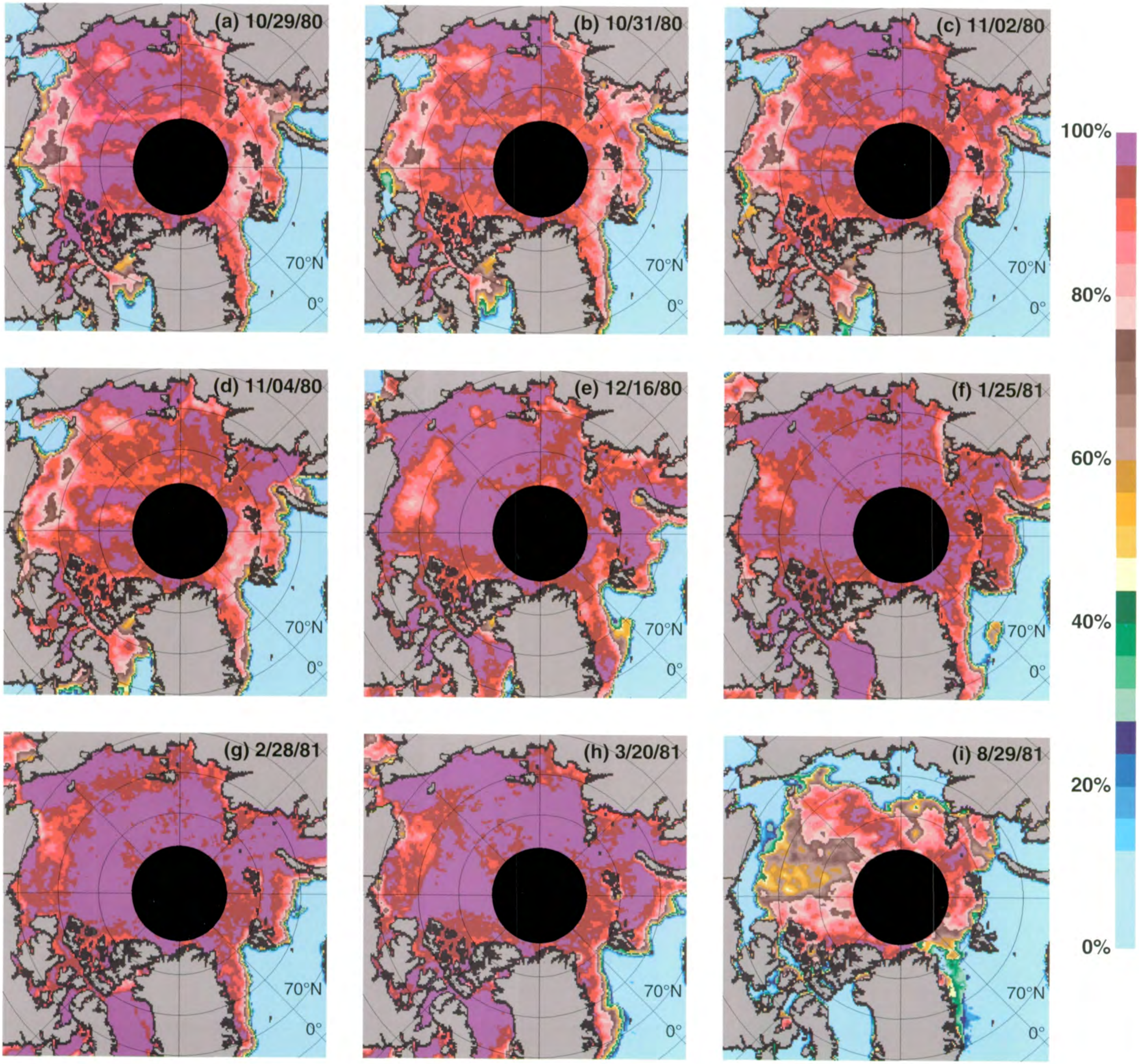
(a) 10/29/80
(b) 10/31/80
(c) 11/02/80
(d) 11/04/80
(e) 12/16/80
(f) 1/25/81
(g) 2/28/81
(h) 3/20/81
(i) 8/29/81
70°N
0°
100%
80%
60%
40%
20%
0%

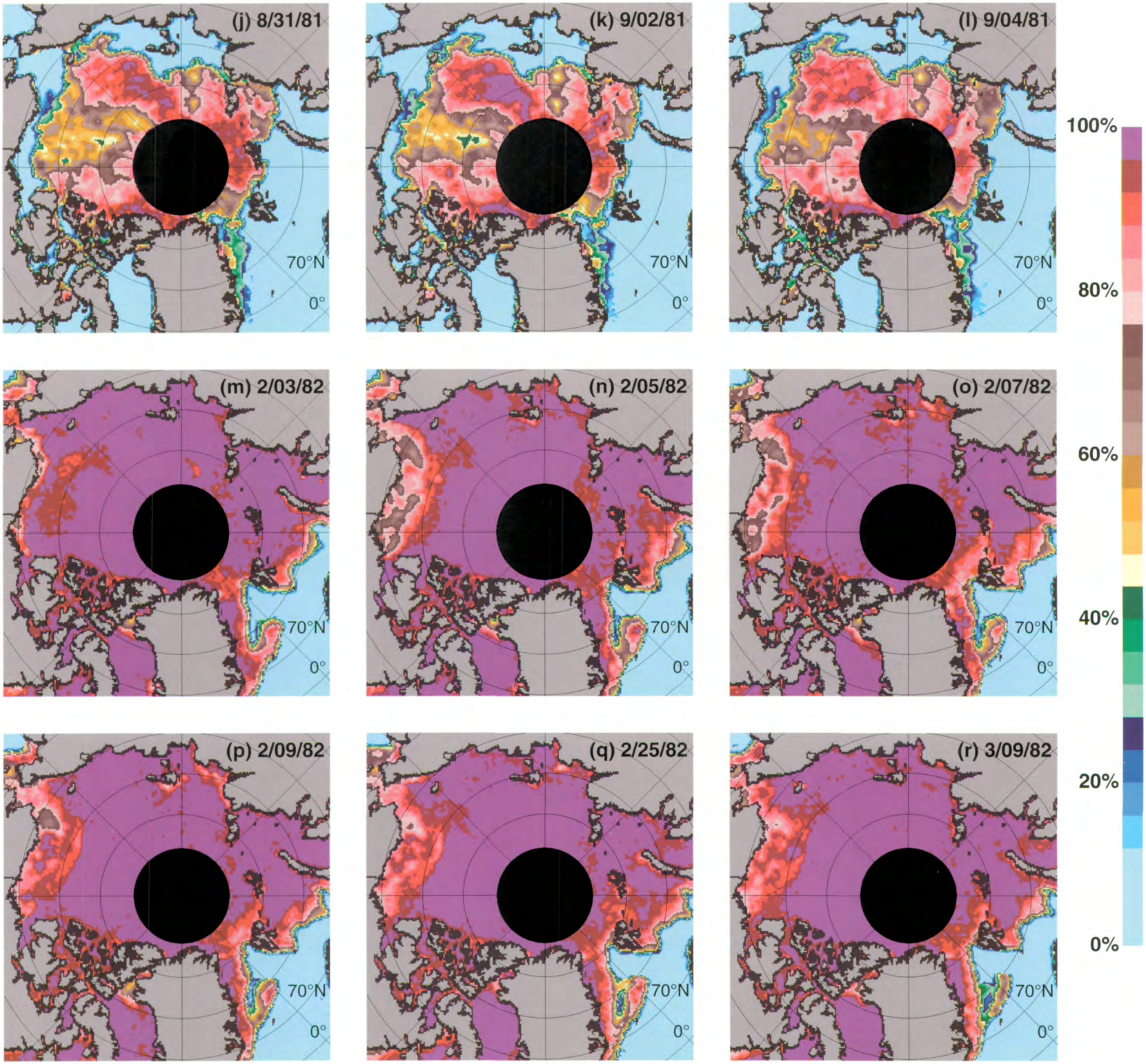

Figure 3.2.7. Selected sequences of single-day synoptic ice concentrations. Case 1: a-h. Case 2: i-l. Case 3: m-r.

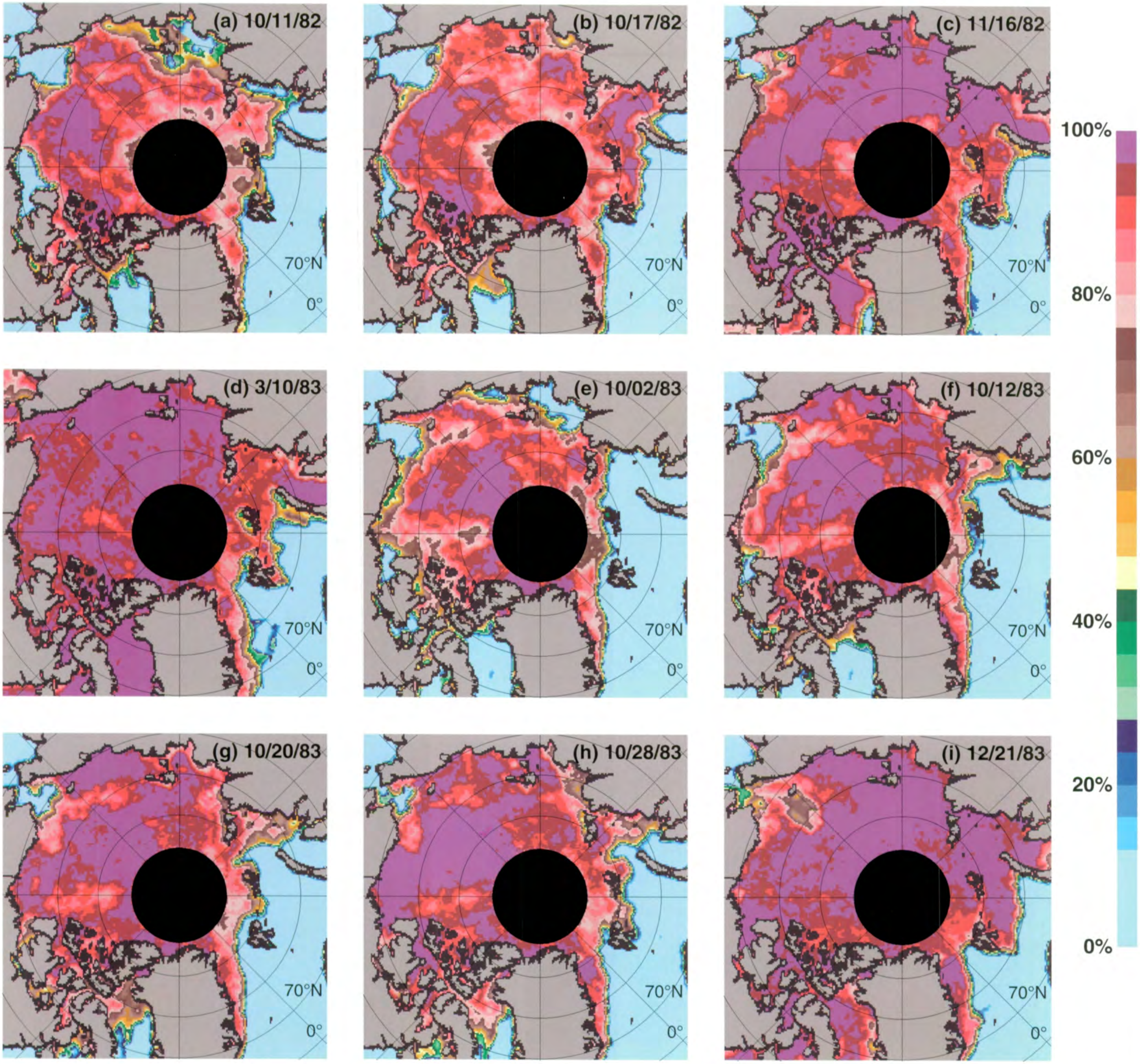
(a) 10/11/82
(b) 10/17/82
(c) 11/16/82
(d) 3/10/83
(e) 10/02/83
(f) 10/12/83
(g) 10/20/83
(h) 10/28/83
(i) 12/21/83
70°N
0°
100%
80%
60%
40%
20%
0%

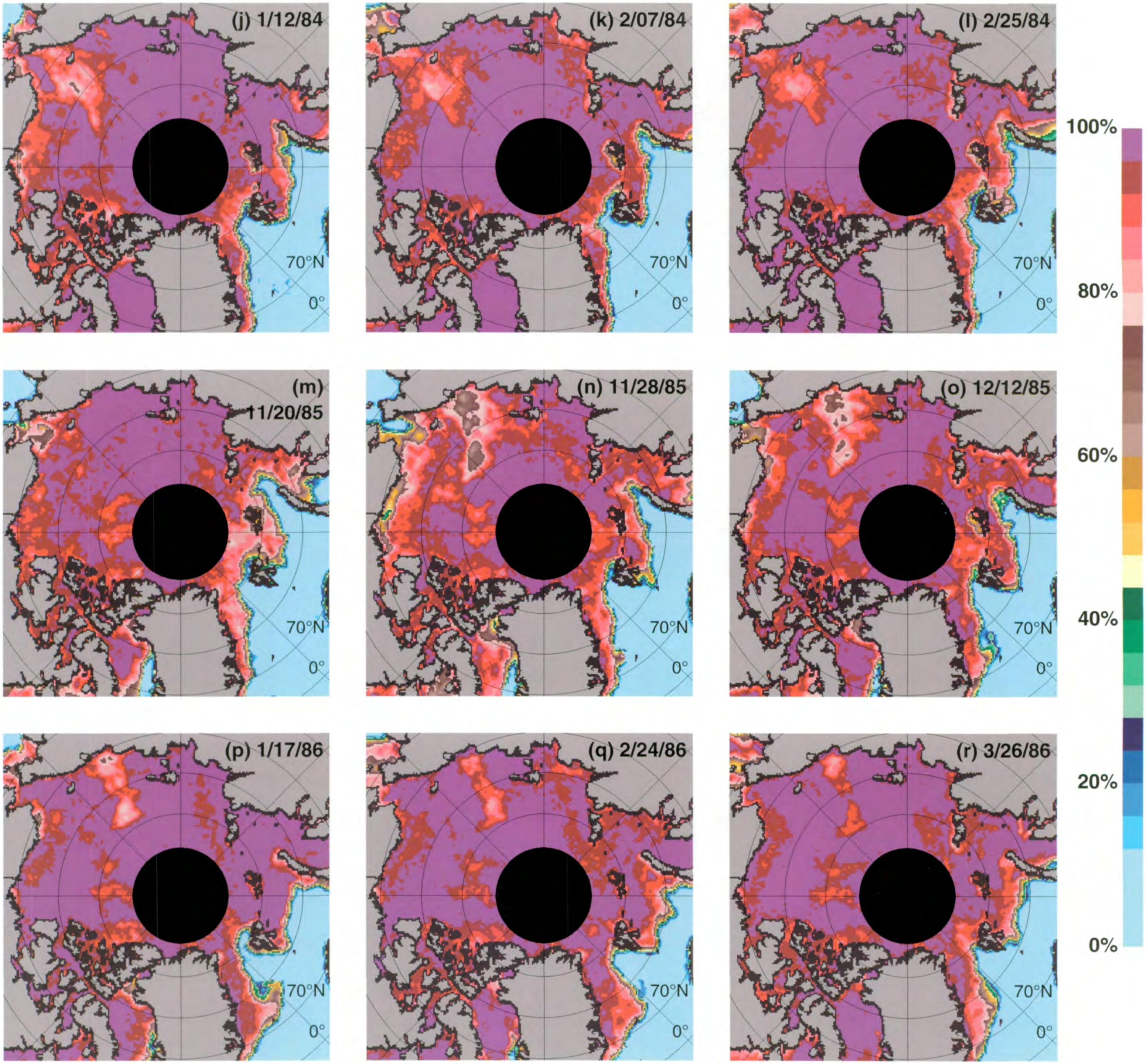

Figure 3.2.8. Selected sequences of single-day synoptic ice concentrations. Case 4: a-d. Case 5: e-h. Case 6: i-l. Case 7: m-r.

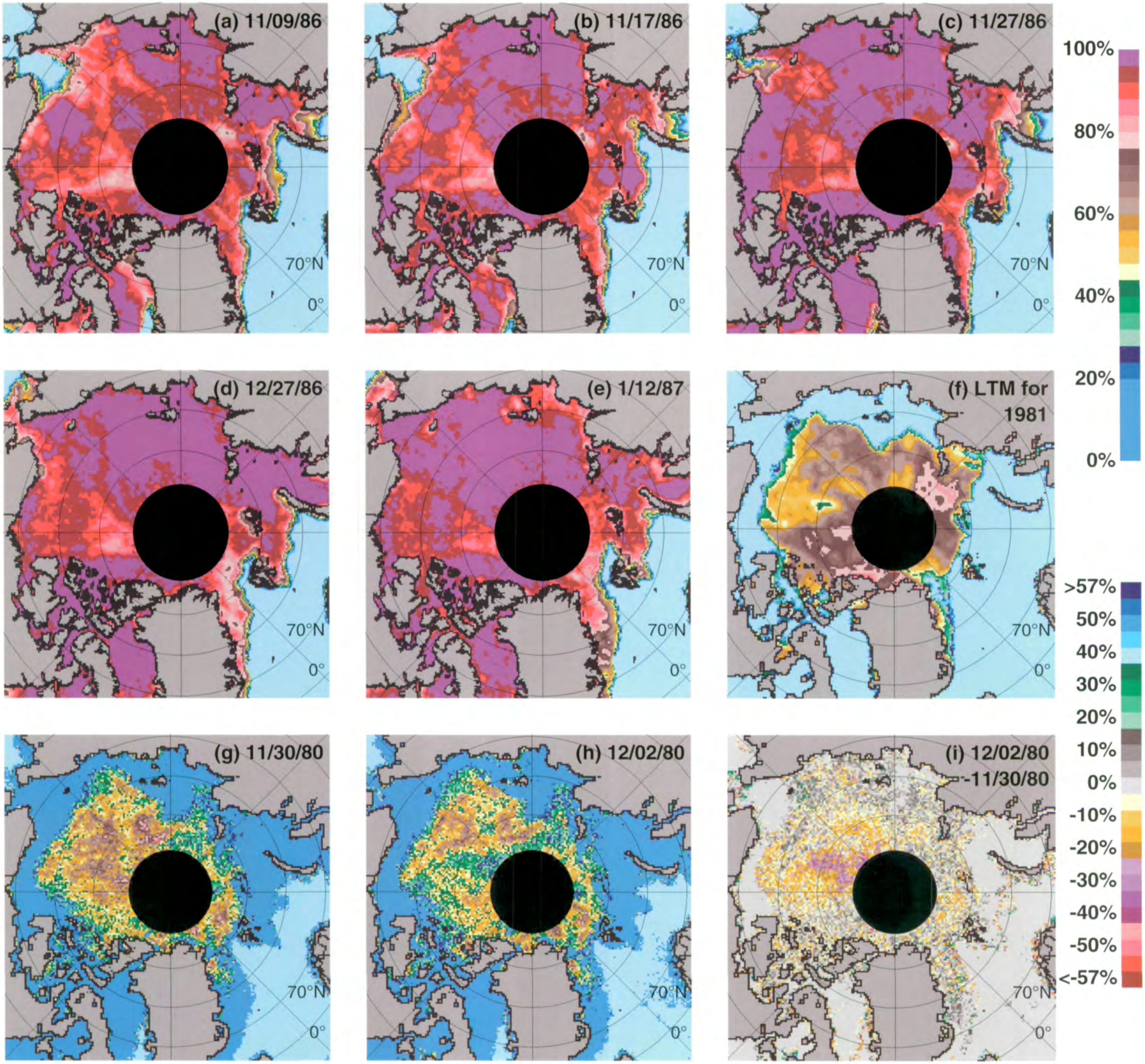

Figure 3.2.9. a-e. Single-day synoptic ice concentrations, Case 8. f. LTM for 1981 (see text). g-h. Single-day multiyear ice concentrations. i. (h) minus (g).

these zones may be determined by the patterns of surface-water divergence. In some cases, with a 1- to 2-month duration, surface divergence may be caused principally by persistent wind-forcing. In the longer-lived cases, up to 6 months, it may be that ocean forces, such as tidal currents and upwelling, play an important role in these divergences. Note in Figure 3.2.3 that Zones 1 and 3 are located near shelf breaks where surface divergence could occur, and that Zone 2 occurs upon a shallow shelf.

3.2.3. Interannual variations in multiyear ice distribution

The thickness and area of ice that survives the summer melt season are principal factors affecting the amount of ice growth the following winter which, in turn, affects the amount of ice the following summer, the average albedo, and the heat absorbed to melt ice. Distribution and variability of multiyear sea ice are of interest, because the greater thickness of multiyear ice reduces the ocean-atmosphere heat transfer compared to that through a new or young sea ice cover (Chapter 2). For these reasons, various studies have considered the possibility and consequences of decreases or disappearances of the summer ice pack under influences such as a warmer climate (Parkinson and Kellogg, 1979) or a decreased river runoff (Holt et al., 1984). Although large-scale measurement of ice thickness is not presently possible, the area of multiyear sea ice is a useful indicator of the state of the ice pack and may be combined with ice models to investigate the dynamic and thermodynamic factors affecting its long-term mass balance (Walsh and Zwally, 1990).

The ice-drift fields (Figures 3.2.3, A14, and A15) suggest that most of the ice incorporated into the Beaufort Sea Gyre remains there for at least 4 years, which is about the time required for ice to reach a thickness in equilibrium between the summer melt and winter accretion (Campbell et al., 1978; Thorndike, 1986). Similarly, ice incorporated into the Transpolar Drift Stream remains there for at least 2 years. Thus, a significant portion of the ice created in the Arctic Ocean becomes multiyear ice. When the long-term drift pattern breaks down, as in 1983, the average residence time may be even longer. The annual drift trajectories for 1983 (Colony and Muñoz, 1986) imply a reduction in the annual ice export. Only four of the AOBN buoys that started 1983 in the Greenland and Norwegian Seas advected through the Fram Strait and down the east coast of Greenland.

The total amount of multiyear ice in the Arctic Ocean, for every 2 days from October to April during 1978-1987, is shown in the time series of multiyear ice area in Figure 3.2.6a. Multiyear ice areas from May through September are not shown, because the ability of the SMMR to distinguish ice types disappears during the melt season, for the reasons explained in Chapter 2. Also shown is the total extent of the multiyear ice pack (Figure 3.2.6b), which is defined as the total area covered by multiyear ice concentrations of 20% or greater. During winter, the multiyear ice area is typically 3.0 x 10^6 km^2, which is about 42% of the area of the Arctic Ocean. The unobserved area poleward of 84° N is assumed to have 75% multiyear ice concentration, cf. Chapter 2.

The total amount (either area or volume) of multiyear ice in the Arctic has been a subject of considerable uncertainty. Because the SMMR does not provide data north of 84° N, the transport of multiyear ice into and out of this region adds to this uncertainty. Another major source of error is the difficulty inherent in distinguishing multiyear ice from other ice types in large-scale surveys. For example, wintertime operational ice maps typically classify most of the ice north of the summer-minimum ice edge as 10/10 (95%-100%) multiyear. In contrast, early airborne surveys (Wittman and Schule, 1966) characterized the winter ice pack in terms of "polar ice" (3 m average thickness), "thick winter ice" (0.3 to 2.4 m), and "new ice" (< 0.3 m). Their estimates of the polar-ice area range from 45% to 90% in the Arctic Ocean (cf. summary of the Wittman and Schule results in Cavalieri et al., 1984). Submarine-based surveys (e.g., Wadhams and Horne, 1980) characterize ice types on the basis of sonar-measured thickness distributions. However, quantitative determinations of multiyear coverage from the thickness distributions are a problem because of the overlap of the first-year ice peak at about 1 m with the multiyear distribution. In comparison, the SMMR-based values show multiyear concentrations (C_{MY}) that are greater than 90% in a limited region north of the Canadian Archipelago and that range between 40% and 80% over most of the pack. A recent comprehensive comparison of observed areal coverages of multiyear ice by several techniques (airborne SAR and high-resolution passive-microwave) shows their agreement with the SSMI-derived values using the SMMR algorithm (SSMI values minus other values) equal to +12%±11% (Chapter 2, Table 2.3.4).

Relationship between multiyear ice and summer-ice areas

The difference between the area of multiyear ice in winter (3.0 x 10^6 km^2) and the minimum area of all sea ice types in September (4.9 x 10^6 km^2) is approximately 1.9 x 10^6 km^2 (Figures 3.2.6a and 3.2.4b). If all the ice cover at the "summer minimum" in September were converted into multiyear ice, the area of multiyear ice should be 4.9 x 10^6 km^2, not 3.0 x 10^6 km^2. The difference has been attributed recently by Comiso (1990) to inadequate accounting of all the multiyear ice area in the winter measurements. However, the ice existing at the September minimum includes both ice remaining from the previous winter, which becomes multiyear ice, and new ice formed during late summer, which becomes first-year ice.

Previously, Zwally (1984) compared the position of the ice edge at the summer minimum ice extent on September 26, 1979, with the SMMR-derived multiyear ice distribution the following February. Zwally noted that the differences in position may be caused, in part, by the new ice growth prior to the minimum ice extent and, in part, by drift of the multiyear pack during winter. Because the transition from melting (ice-pack decay) to freezing (ice-pack growth) does not occur simultaneously throughout the Arctic Ocean, areas of new ice growth are necessarily included in all determinations of the "summer minimum" that measure all areas simultaneously. The ice pack in September extends over 15° of latitude and across a surface-temperature difference of about 10 K. Thus, the melt-freeze conditions have large spatial variations, as well as temporal variations. Consequently, any single-look map cannot represent the true minimum in ice cover, nor can the minima in the daily average values of the ice area (Figure 3.2.4). It follows that the monthly average maps (Figures 3.1.3 to 3.1.14) give even higher concentrations for a particular region than the regional minima.

The relevant summer total ice-concentration (C_T) values for estimating the amount of multiyear ice at the end of the summer are the localized minima in C_T, which may occur at different times at different locations. These values are defined for each map pixel as the local-temporal minima (LTM) in C_T. Prior to the LTM, the C_T within a pixel decreases as the pack melts. After the LTM, C_T increases as new ice forms. The ice formed before the summer season, and remaining at the LTM, becomes multiyear ice.

Much of the open water area at the LTM becomes covered with new first-year ice. Local transition from melting to freezing may undergo several reversals around the time of the LTM, therefore some prior-year ice may also melt after some new ice has already formed. However, such melting is likely to be very small, because new ice would be more vulnerable than old ice, and melting of the new ice would produce a new minimum. The open water area within a pixel at LTM would be decreased by convergence of the ice pack after LTM, or increased by divergence.

The effects of convergence or divergence differ before and after the LTM. Before the LTM, the primary effect of convergence and divergence is to change the area of open water, since freezing conditions do not prevail. After the LTM, the area of new ice is reduced by ridging during convergence of the ice pack, and increased by the growth of new ice following divergence, now under more prevalent freezing conditions. These processes should be less important for the thicker, older ice. Since the amount of convergence tends to balance the divergence, when averaged over some period of time after the LTM, the areas of new ice destroyed and created after LTM tend to cancel. Therefore, the sum of the ice area at individual LTM's over all locations in the Arctic Ocean should provide a good estimate of the area of ice that becomes multiyear ice at the end of the summer.

It should be noted that estimates of LTM may be affected by advection of the ice pack that could move areas of low concentration into areas for which the true LTM would be higher than observed. The spatial scale of the areas over which the LTM occurs within the same 6 days is typically several hundred kilometers, as can be seen in a map of LTM dates (not shown) associated with Figure 3.2.9f. The effect of advection on the derived LTM is likely to be small, because rates of advection are typically only a few kilometers per day.

The local C_T in late summer varies widely across the Arctic Ocean, for example, from 40% to 100% on September 2, 1981 (Figure 3.2.7k). Also, the local C_T varies significantly with time, by more than 10% in only 2 days (e.g., Figure 3.2.7(i), (k)). Figure 3.2.9f displays a map of the LTM derived from the SMMR data for the summer of 1981 by selecting, for each pixel, the minimum C_T from single-day SMMR maps. Since these maps are averages of the separate northbound and southbound maps (as stored on the 12-volume CD-ROM SMMR polar data set), the LTMs so derived will be slightly overestimated. Large areas of the Arctic Ocean regions north of the Canadian Archipelago and north of the Kara Sea have ice concentrations of no less than 70% throughout the summer season. However, large areas of the Beaufort Sea and the Transpolar Drift Stream have minimum concentrations of about 50% at some time during the summer. Therefore, C_{MY}s of >70% and ca. 50% should be expected in these respective regions in the following winter. The average value of the LTM over the ice pack shown in Figure 3.2.9f is 61%, excluding values of LTM that are less than 20%.

In contrast to the average LTM of 61%, the minimum C_T, averaged over the ice pack during any one day, is about 80% (values from Figure 3.2.4). This "summer minimum" value typically occurs on or about September 15. In 1981, the average C_T at the "summer minimum" was 78% (from Figure 3.2.4), and the difference from the calculated average LTM of 61% indicates that the area of new ice included in the "summer minimum" is about 17% of the "summer minimum" extent.

In December 1981, the spatially averaged C_{MY} within the multiyear-ice-pack extent is 62% (2.8×10^6 km^2 of multiyear ice area divided by the 4.5×10^6 km^2 extent of the multiyear pack, defined as the area within the 20% multiyear ice isopleth, Figure 3.2.6), which is nearly equal to the calculated average LTM of 61% for 1981. Therefore, within the area covered by more than 20% multiyear ice in winter, the average C_{MY} derived from SMMR is approximately equal to the average LTM, indicating that the multiyear ice area measured by SMMR is essentially equal to the area of ice that survived the summer melt, at least within the area defined by the overlap of the LTM and the subsequent MY ice extent.

In terms of area, about 3.4×10^6 km^2 of prior-year ice survived the 1981 summer melt season (integrated LTM ice area in Figure 3.2.9f). The difference between the area of multiyear ice the following winter (2.8×10^6 km^2; see Figure 3.2.6a) and the integrated LTM ice area may imply that 0.6×10^6 km^2 of multiyear ice is outside the area of the winter multiyear ice pack defined by the 20% multiyear ice isopleth. In fact, the extent of the LTM (5.6×10^6 km^2) is 1.1×10^6 km^2 greater than the extent of the multiyear ice pack. This difference in extents, multiplied by the average LTM (61%), accounts for the 0.6×10^6 km^2 difference between the LTM ice area and the multiyear ice area in the winter.

The total ice area at the 1981 summer minimum is 4.6×10^6 km^2, including 1.2×10^6 km^2 of new ice of which about 0.3×10^6 km^2 (0.4×10^6 km^2 times an average perimeter concentration of 75%) lies outside the perimeter of the LTM. The occurrence of these areas of new ice near the boundary of the total ice pack at the time of the mid-September "summer minimum" can also be inferred from the Navy/NOAA Joint Ice Center (JIC) ice maps. For example, in 1981, the minimum ice limit occurred in the 1 September map in the western Laptev Sea; in the 29 September map, in the eastern Laptev and western East Siberian Sea; in the 15 September map, in the Beaufort Sea north of Alaska; and in the 13 October map, west of Banks Island. Therefore, over a span of at least 90 days around the "summer minimum," new ice is forming along the edge of the pack in some locations as the pack is still retreating elsewhere. The typical meridional extent of such variations is about 100 km along the approximately 5000-km perimeter of the ice edge, which is consistent in area with the 0.3 x 10^6 km^2 mentioned above. These differences are also evident from comparison of the LTM map (Figure 3.2.9f) and the monthly average concentration map for September 1981 (Figure 3.1.11).

While the presence of melt ponds (predominantly in July and early August) are of concern (see Chapter 2), the late-August, early-September ice-concentration data for the central Arctic in Figure 3.2.7i-l suggest that melt ponds do not cause a significant error (i.e., >5%) in the LTM, at least where the ice concentration is 96%-100%. If the effect of melt ponds were large, on average, it would have to be selectively very small in the regions of 96%-100% ice concentration that are evident in Figure 3.2.7i-l. After late August, when surface temperatures, on the average, are below freezing, it is reasonable to presume that the area of melt ponding is about 5% or less (cf. Carsey, 1982), and this percentage would limit the melt pond effects.

A suggestion has been made that multiyear ice (as might be found in a portion of the Kara Sea where ice was present at the summer minimum) with a first-year ice signature (possibly the result of a storm passage that served to change the signature), could play a significant role in the discrepancy between the summer minimum ice area and the multiyear ice area in the following winter (Comiso, 1990). An alternative explanation (Zwally, unpublished analysis) suggests that the absence of multiyear ice occurs because the LTM map (Figure 3.2.9f) shows little ice remaining in the selected area. Furthermore, the predominant wind pattern subsequent to the LTM caused much of the remaining multiyear ice to be advected out of the area.

Similarly, north to northwestward advection of the pack north of the East Siberian and Laptev Seas in the 1981-1982 winter, followed by new ice formation, caused a first-year ice signature to appear as far north as 84°, near 135° E, in March 1982 (Figures 3.1.30 and 3.1.34; cf. Section 3.2.4). This alternative explanation suggests that multiyear ice with a first-year ice signature does not play a significant role in the difference.

Interannual variations in multiyear ice distribution

In the discussion to follow, the primary SMMR data referred to are the 9-year average C_{MY} maps (Figure 3.1.36), the monthly C_{MY} maps (Figures 3.1.29 -3.1.35), the monthly C_{MY} anomaly maps (Figures 3.1.37-3.1.43), and the December to April C_{MY} seasonal change maps (Figure 3.1.44). Interannual variations in the total extent of the multiyear ice pack ($C_{MY} > 20\%$) and the total area of multiyear ice are depicted by the time-series curves in Figure 3.2.6.

The major features of the 9-year average monthly C_{MY} distributions (Figure 3.1.36) during the SMMR period remain more or less constant throughout the winter. However, the individual years (Figures 3.1.29 to 3.1.35) show significant variations in the large-scale distribution of the multiyear pack, and changes during the season associated with the large-scale drift of the ice pack. For example, the previously described north-to-northeastward advection of the pack north of the East Siberian and Laptev Seas in the direction of the Transpolar Drift Stream is not evident in the 9-year maps because it does not occur every year. On average, the greatest amount of multiyear ice is in the northwestern sector of the Arctic Ocean adjacent to the northern Canadian Archipelago, where the 9-year average C_{MY} is 80%. The 50% C_{MY} isopleth has two lobes projecting southward: the McKenzie Delta Lobe extends to 73° N, and the East Siberian Sea Lobe extends to 72° N. Between these lobes, the isopleth swings northward to 78° N. The Southern Beaufort, Chukchi, and Laptev Seas contain less than 20% multiyear ice.

The highly variable seasonal, annual, and interannual C_{MY} distributions occurring during 1978-1987 are seen in a comparison of the monthly maps, the monthly anomaly maps, and the seasonal change maps. During February 1979, the C_{MY} distribution is similar to the 9-year February mean, but has anomalies in multiyear (MY) ice concentration in the western sector adjacent to the Canadian Archipelago (up to +25%), and in the area between two MY ice lobes in the Beaufort and Chukchi Seas (as low as -25%). Alternate positive and negative anomalies occur north of the East Siberian and Laptev Seas. During February 1980, the MY ice concentration is less than average (anomalies as low as -40%) in a band adjacent to the Canadian Archipelago, with even larger anomalies in the Transpolar Drift Stream region, ranging from +40% to -40% on the Siberian side of the Pole to -20% between the Pole and Fram Strait. The total amount of MY ice is about 6% less than in 1978-1979.

The most anomalous C_{MY} distribution during 1978-1987 occurs in the winter of 1980-1981. The February 1981 maps show no C_{MY} greater than 80%-84%. A broad north-south band with $C_{MY} = 20\%-40\%$ cuts across the Beaufort Sea toward the pole. The anomaly map also shows high negative anomalies of -15% to -45%. The origin of this feature is described in the next section. The Beaufort-Chukchi Seas had negative anomalies in the preceding year, but now contain positive anomalies of +15% to +30%. This difference in anomaly patterns for February 1980 and 1981 indicates major interannual differences in the forcing of the ice pack. The total amount of MY ice in the 1980-1981 winter is again about 6% less than the preceding year. However, the extent of the multiyear ice pack (Figure 2.3.6b) is not unusually low, indicating that a lesser amount of multiyear ice is spread over a larger area (average multiyear concentration is only about 57%).

In February 1982, most of the Beaufort Sea has negative anomalies as low as -35%, as does the region north of the East Siberian Sea. The total area of multiyear ice increased by about 6% from the previous winter. The sector north of the Laptev Sea has large positive anomalies up to +50%. A large area with anomalously low C_{MY} protrudes into the multiyear ice pack to 84° N north of Canada.

In February 1983, a strikingly different feature is the large area of anomalously low C_{MY} just east of the 180° meridian extending as far north as 82° N. Indeed the high C_{MY} lobe that normally extends towards the East Siberian Sea does not exist in 1983, so the total amount of MY ice in the region of the Transpolar Drift Stream is abnormally low. As noted earlier, the long-term ice-drift pattern broke down in 1983, when neither the Transpolar Drift Stream nor the Beaufort Sea Gyre were evident (Colony and Muñoz, 1986, Figure A.14).

In 1984, the total amount of MY ice increased by about 14% from the previous year, attaining one of the three highest MY amounts during 1978-1987. The usual lobe of the multiyear ice pack extending into the East Siberian Sea reappears, and the Transpolar Drift Stream has negative C_{MY} anomalies ranging from -10% to -40%. A large area of high C_{MY} (90%) is located between Novosibirskiye and the mainland. This feature is highly anomalous (up to +30%) and has the highest MY amount in that geographical area during 1978-1987.

The total amount of MY ice in 1985 is about the same as in 1984, but the C_{MY} distribution is quite different. The boundary of the multiyear ice pack in the East Siberian Sea has retreated again. The Canadian Basin has anomalously high multiyear concentrations (up to +35%). While the area of multiyear ice is unusually high in the 1985, the extent of the multiyear pack is slightly below average, indicating a more compact multiyear ice pack with above-average multiyear concentrations within the pack. The average multiyear concentration within the pack is about 70% in 1984-1985, compared with the previously mentioned low of about 57% in 1980-1981. Therefore, significant interannual variations in the average concentration of the multiyear ice pack occur that are not related in a simple way to interannual variations in the area of multiyear ice.

In February 1986, the multiyear distribution is dramatically changed, with negative anomalies less than -10% over much of the Beaufort Sea. The East Siberian Sea MY lobe once again is reestablished with positive C_{MY} anomalies up to +45%.

The final winter, 1986-1987, has a decrease of about 7% in the total amount of MY ice compared to the preceding three winters. The East Siberian Sea MY lobe projects almost to the Siberian coast, as it did in several previous years, and the ice pack has anomalously high C_{MY}s (80%-90%) much farther south than is the case in other years. A dramatically different C_{MY} distribution is observed on the other side of the Arctic Ocean, where the McKenzie Delta lobe is unusually diminished. Farther to the east, a very unusual separation of the multiyear pack from the northern Greenland coast occurs. This separation, not evident in the November 1986 map (Figure 3.1.30), first appears in December 1986, and remains through April 1987. This event bears some resemblance to the earlier separation of the pack from the eastern part of the northern coast of Greenland in August 1986, described earlier.

In comparing the time series of total ice areas (Figure 3.2.4b) and multiyear ice areas (Figure 3.2.6a), it is evident that there is little correlation between a summer minimum ice area and the multiyear ice area the following winter. This is exemplified by an unusually low multiyear ice area in 1980-1981, preceded by an atypically large sea ice area at the summer minimum in 1980. Additionally, the 1981-1982 winter exhibits an increase in multiyear ice area compared to the preceding winter, even though it followed a summer with an unusually low sea ice area at the summer minimum. The summer minimum areas also are not anticorrelated, as can be seen by comparing the 1983 summer minimum total ice area with the MY area in 1984. Considering the discussion earlier in this section, on the relationship between the area of winter multiyear ice and the integrated LTM area, this lack of correlation is not surprising and supports the hypothesis that the amount of multiyear ice in a given winter does not correspond to the ice area at the September ice area minimum.

Short-term variations of multiyear sea ice concentration

There is a fundamental difference between the spatial and temporal variations of multiyear ice and of total ice concentrations. Open water and new ice forms within the pack during most of the year. However, the multiyear ice area is approximately conserved as it is transported with the pack during winter. Therefore, it is also possible to use sequential SMMR images of MY distributions to track the movement of large areas of sea ice and provide information on the large-scale drift of the ice pack and the small-scale divergence (Zwally and Walsh, 1987). The variability of the total area of multiyear ice during the season is about 10% (cf. Figure 3.2.6), which is at least partially caused by advection and spreading of the multiyear ice beyond the 20% multiyear ice edge. Another cause may be ice-temperature fluctuations, cf. Chapter 2 and Figure 2.1.1 (e) and (f). During convergence, it is presumed that most of the ridging occurs in the new first-year ice, which is weaker than the multiyear ice, and reductions in multiyear ice area caused by ridging of the multiyear ice are small.

During periods of divergence in the ice pack, the multiyear ice floes increase their separation, and C_{MY} decreases. Following divergence, C_{MY} remains at a lower value until the pack converges again. Typically, periods of decreasing C_{MY} lasting for several days are followed by several-day periods of increasing C_{MY}, as the wind-forcing of the pack changes with the synoptic weather conditions. A particularly intense divergent event occurred on December 2, 1980, in the vicinity of 80° N and 165° W (Figure 3.2.9h). This event was shown (Zwally and Walsh, 1987) to be caused by the passage of an unusually strong cyclone (Figure 3.2.10), resulting in 20%-40% changes of C_{MY} over the course of 2 days (Figure 3.2.9i). Strong ice divergence, which was forced by the observed atmospheric pressure field during this event, was indicated by both the Arctic buoy data and an ice dynamics model of the ice pack. The scar of this divergence event persists in the C_{MY} maps until the following spring, after which it disappears during the course of the summer. Although the total concentration C_T also decreases during this divergence, the effect of the divergence on the C_T maps does not persist. Here, as is the general case during winter, decreases in C_T are short-lived (several hours in duration), as new ice rapidly forms in the open water within the pack created during divergence. (See Section 3.2.2 for a discussion of localized areas of persistently lower total ice concentrations.)

Part of the year-to-year variation in April-December differences in C_{MY} is caused by interannual variability in the ice drift. To illustrate this, we note that a

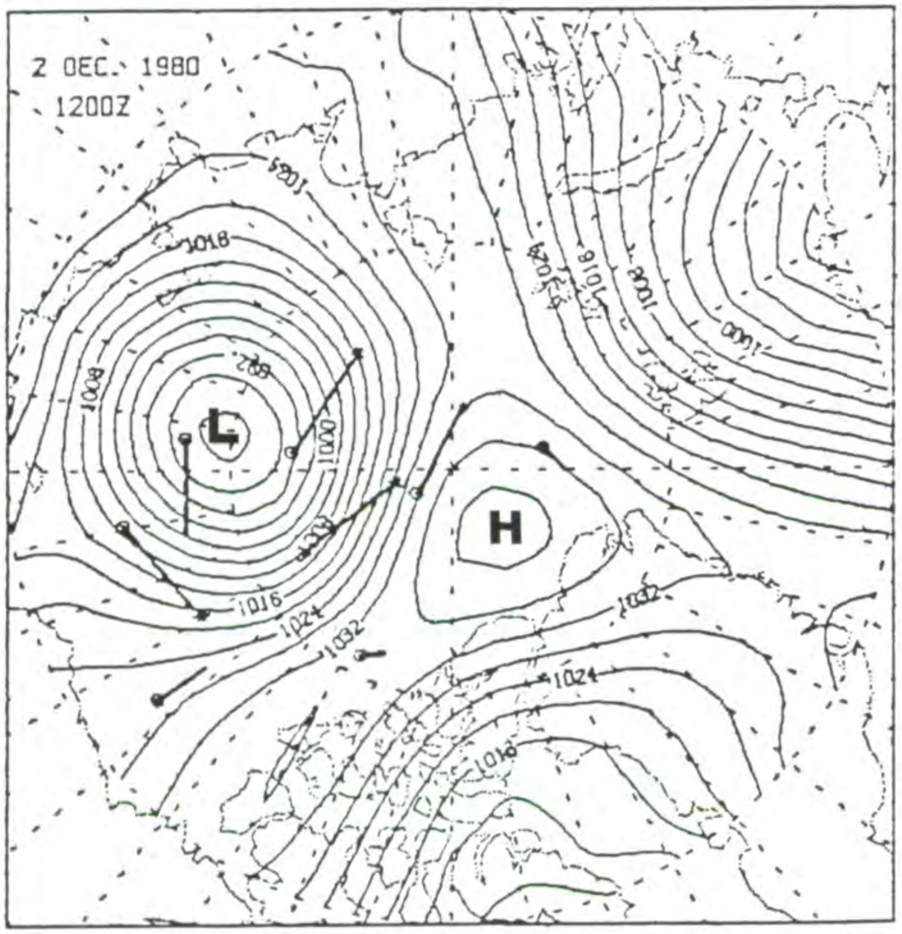

SURFACE PRESSURE/BUOY DRIFT

Figure 3.2.10. Sea-level pressure analysis for 12:00 Z, December 2, 1980. Positions of Arctic buoys are shown by open circles, direction of buoy drift by linear segments (from Thorndike and Colony, 1981).

simulation of the 1978-1979 average drift from November 25 to January 28 shows that the drift was predominantly transpolar (Figure 3.2.11). In addition, the atmospheric pressure system usually forcing the Beaufort Gyre was positioned over Northern Canada, southeast of its normal position. These two factors probably caused the region of strong positive April-December difference in C_{MY} just east of the 135° W meridian for 1978-1979 (Figure 3.1.44). This difference is interpreted as a southward advance of the ice pack in that region (Zwally and Walsh, 1987). The circulation pattern also varies on shorter time scales, as shown for November and December 1978 (Figure 3.2.11), where a 28-day period of strong transpolar drift was followed by a 28-day period of strong drift toward the Siberian coast. The change in shape of the multiyear ice boundary along the 135° W meridian from November to December 1978 (Figures 3.1.29-3.1.31) may be interpreted in terms of the changes in the circulation patterns (Figure 3.2.11). The winter of 1979-1980 had a more typical pattern of simulated ice drift (Figure 3.2.11), with a stronger Beaufort Gyre, and the positive difference that occurred in 1978-1979 does not appear in the following year.

The region of strong positive April-December difference in C_{MY} near the 135° W meridian for 1980-1981 and the strong negative one farther to the west (Figure 3.1.44.) imply a net eastward drift of more than 200 km from December to April. Examination of the pattern of changes in the vicinity of 80° N and 135° E can be used to suggest the prevailing direction of the winter ice drift in each year (Figures 3.1.30, 3.1.35, and 3.1.44): northwestward in 1978-1979, northeastward in 1979-1980 and 1980-1981, northward in 1981-1982, northward by about 300 km in 1982-1983, northeastward in 1983-1984, northward in 1984-1985, eastward south of 80° N and westward north of 80° N in 1985-1986, and northward in 1986-1987. Another example is in the Beaufort Sea in 1985-1986, where alternate advance and retreat of the multiyear ice pack and net divergence off the coast of Prince Patrick Island are consistent with the typical ice motion in the Beaufort Gyre.

Another part of the year-to-year variation in these April-December differences results from regional convergence and divergence in the multiyear-ice pack. Generally within the ice pack, there are alternate regions of net April-December divergence or convergence, as indicated by the alternate regions of net decreases or increases in C_{MY} from December to April in Figure 3.1.44. In some years, such as 1979-1980, the pack appears to be generally more divergent and in others, more convergent. Net decreases of C_{MY} within the central part of the ice pack, as shown, for example, in the 1979-1980 and 1980-1981 winters, imply a corresponding increase in the area of first-year ice and provide a measure of the new ice production during this period. Finally, part of the year-to-year variation in April-December differences in C_{MY} is caused by interannual variability in the September ice minima (Figures 3.2.4 and 3.2.12), or, more correctly, the LTM (not shown).

3.3 Seas of Okhotsk and Japan

Located predominantly between 50° and 60° N and bounded largely by the Kamchatka Peninsula, Siberia, Sakhalin Island, and the Kuril Island chain, the Sea of Okhotsk (Figure 3.3.1) is a relatively isolated sea. Lying at lower latitudes than most of the globe's regions covered by sea ice, the Sea of Okhotsk is typically free of ice for 4 months of the year. The winter ice cover begins to form in a few locations in November, then expands to cover most of the sea by March and retreats over the next 3 months until only lingering remnants remain by the beginning of June. The Sea of Japan, located to the southwest of the Sea of Okhotsk, has very little ice at any time. In most years, sea ice covers only a very small area at the northernmost tip of the Sea of Japan, and that only during the months December to March.

Averaged over the nine SMMR years, the ice extent of the Seas of Okhotsk and Japan peaks at 1.2 x 10^6 km^2 in March (Figures 3.3.2 and 3.3.3). The calculated area is 0.2-0.3 x 10^6 km^2 for the months of June through November, but most of this is caused by radiometric contamination from land (see Chapter 2), as the Seas of Okhotsk and Japan are essentially ice-free in summer.

1978-1979 (NOV.25-JAN.28)

1979-1980 (NOV.25-JAN.28)

1980-1981 (NOV.25-JAN.28)

SIMULATED DRIFT VECTORS

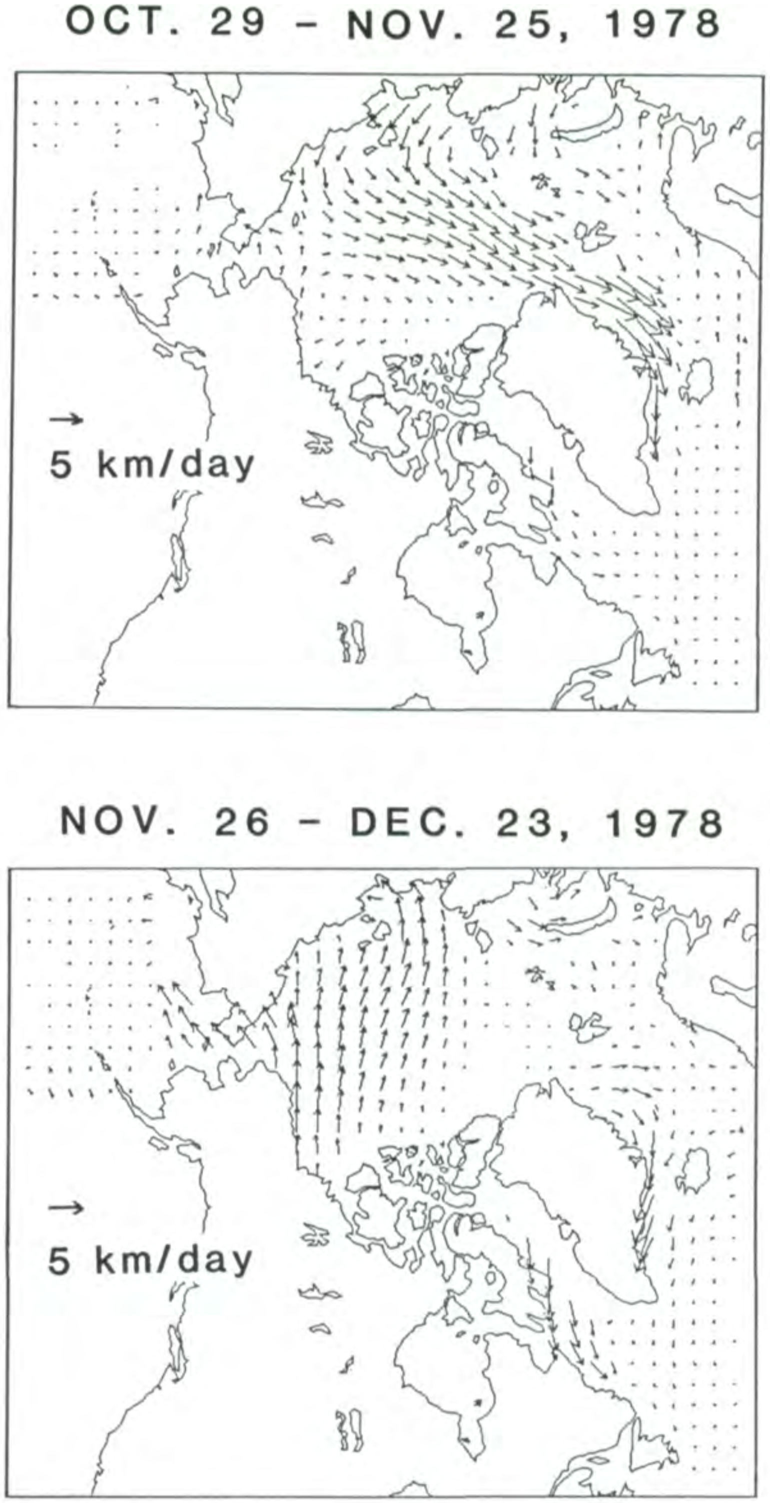

OCT. 29 - NOV. 25, 1978

NOV. 26 - DEC. 23, 1978

SIMULATED DRIFT VECTORS

Figure 3.2.11. Simulated drift vectors for November 25 to January 30 of 1978-1979, 1979-1980, and 1980-1981; also, for October 29 to November 25 and November 26 to December 23, 1978 (from Zwally and Walsh, 1987).

(a) Sea Ice Extent in the Arctic Ocean

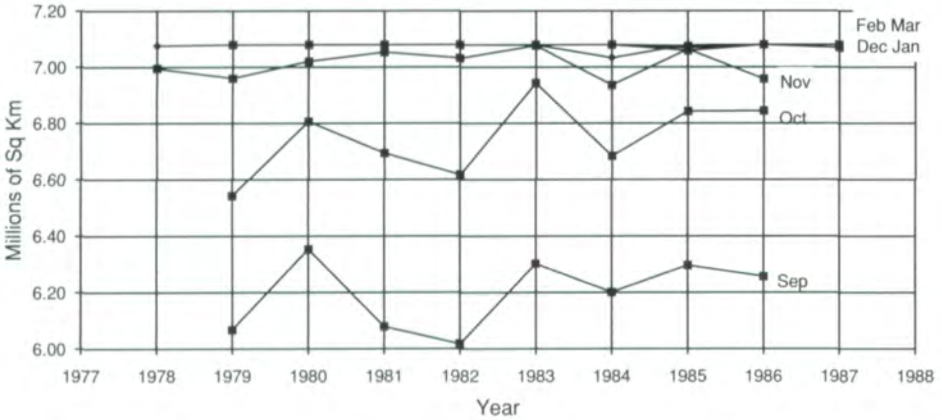

(b) Sea Ice Extent in the Arctic Ocean

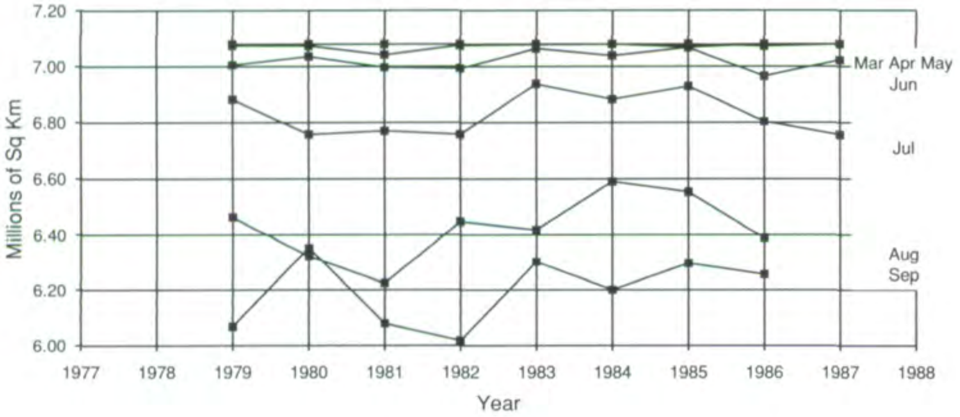

Figure 3.2.12. Month-by-month, year-to-year changes of the sea ice extents of the Arctic Ocean, (a) September to March, (b) March to September.

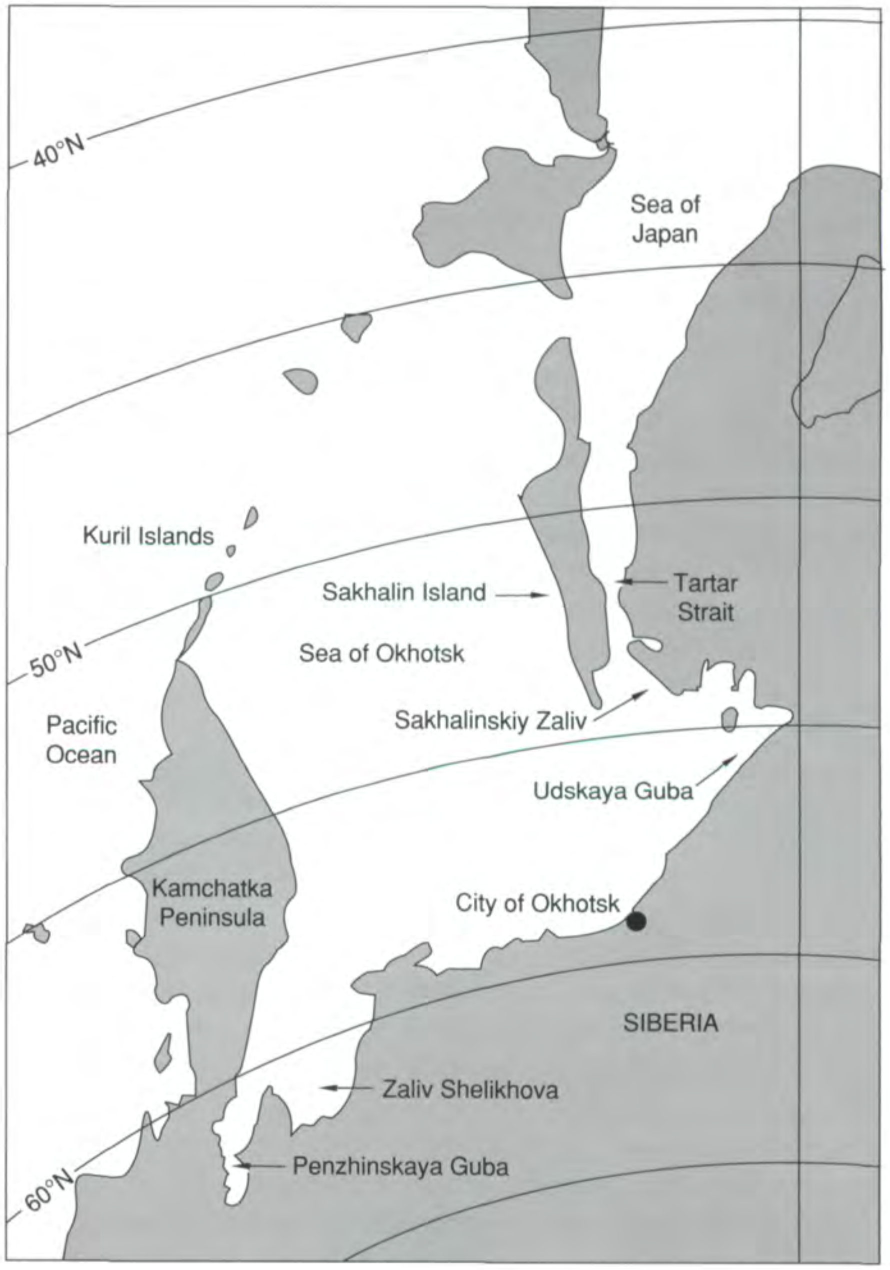

Figure 3.3.1. Location map for the Seas of Okhotsk and Japan.

Considering the individual years, the monthly averaged ice extent maximum occurs in March in each year except 1987, when it occurs in February (Figure 3.3.4). In the 3 ESMR years that have both February and March data, the maximum ice extent in the Sea of Okhotsk (on the truncated ESMR grid) occurs in March in each year (Parkinson et al., 1987). All years from both data sets indicate near ice-free conditions from June through November.

At the start of the growth season in late November, the regional sea ice cover begins to form in a few confined coastal locations, predominantly in the northeastern and northwestern corners of the Sea of Okhotsk. The ice cover then expands in the north and forms along Sakhalin Island in December, along the remainder of the northern and western boundaries and part of Kamchatka Peninsula in January, and along much of the rest of the western Kamchatka coastline in February. The ice advances inward toward the center of the Sea of Okhotsk from all coastlines, so that by mid-February most of the sea is typically covered with ice of at least 30% concentration. This coverage continues through mid-March, with the maximum ice extent being reached sometime between mid-February and mid-March. The ice along the west coast of Sakhalin Island, in the Sea of Japan, begins to retreat in March and completes its retreat in April. In the Sea of Okhotsk, the ice begins to retreat first in the center of the basin and along the east coast in March, followed by retreat along the north and west coasts. By June, the only remaining ice tends to lie in coastal areas, predominantly in the northwest corner of the sea (Figure 3.1.15). The strong east/west asymmetry in the ice cover is caused largely by the warm saline water moving northward along the Kamchatka Peninsula in the West Kamchatka Current. The warm water flow delays ice formation in the autumn and winter, and speeds ice decay in the spring.

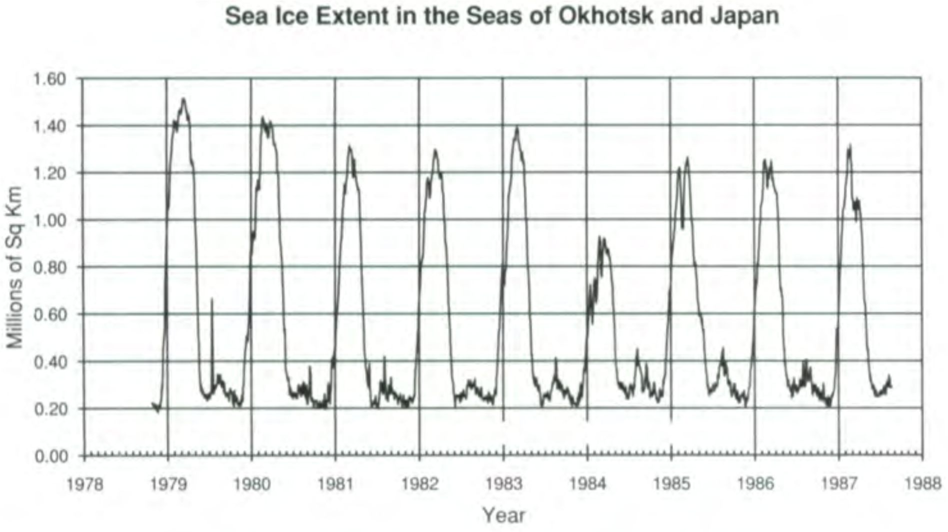
Sea Ice Extent in the Seas of Okhotsk and Japan

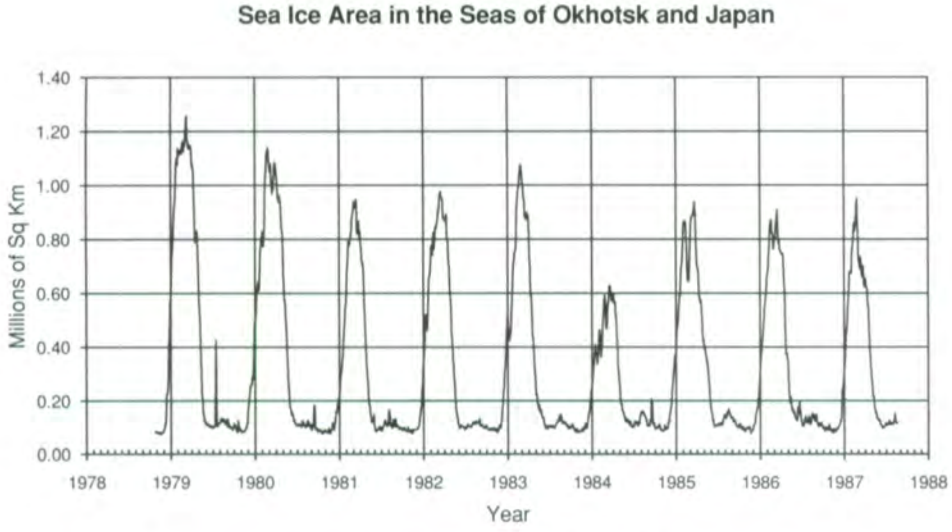
Sea Ice Area in the Seas of Okhotsk and Japan

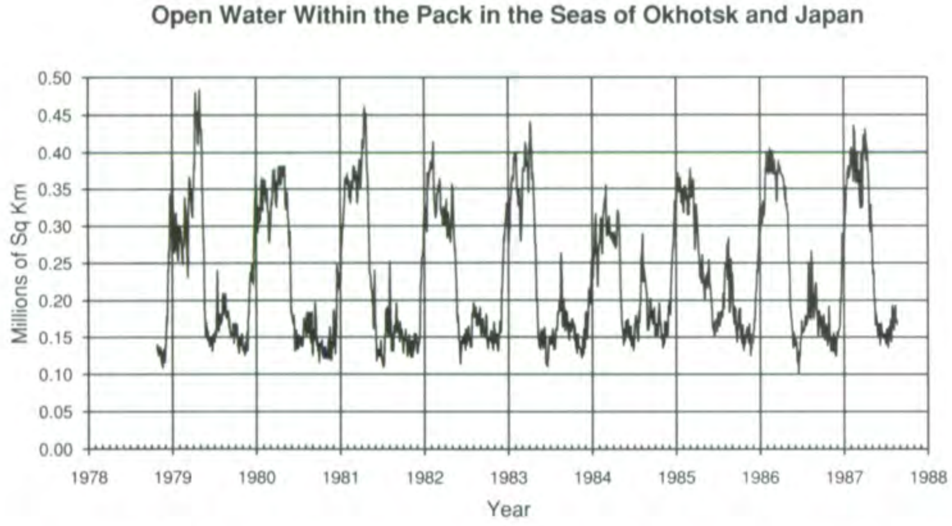
Open Water Within the Pack in the Seas of Okhotsk and Japan

Figure 3.3.2. Sea ice extent, sea ice area, and amount of open water within the pack for the Seas of Okhotsk and Japan from October 26, 1978 to August 20, 1987. The misleading indication of ice during the summer months is the result of a temperature-dependent land effect.

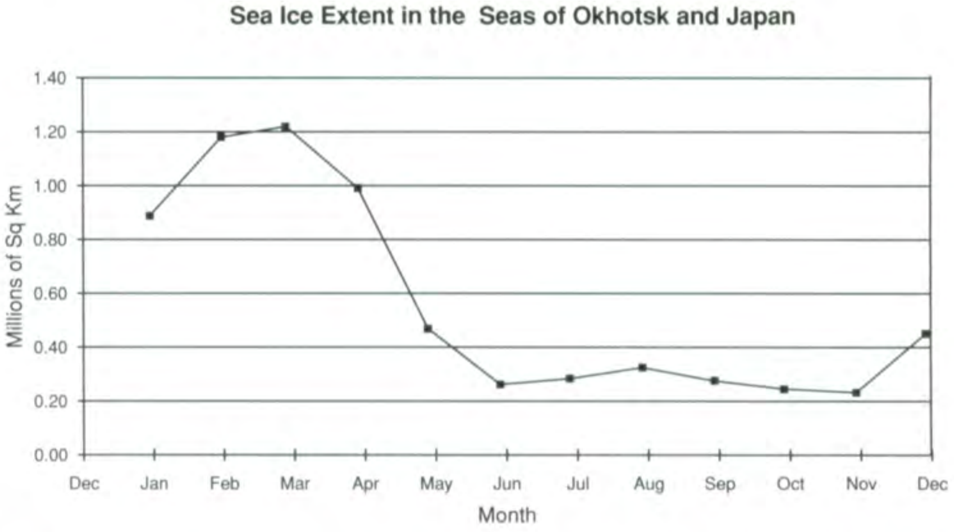
Sea Ice Extent in the Seas of Okhotsk and Japan

Figure 3.3.3. Average seasonal cycle of sea ice extents for the Seas of Okhotsk and Japan.

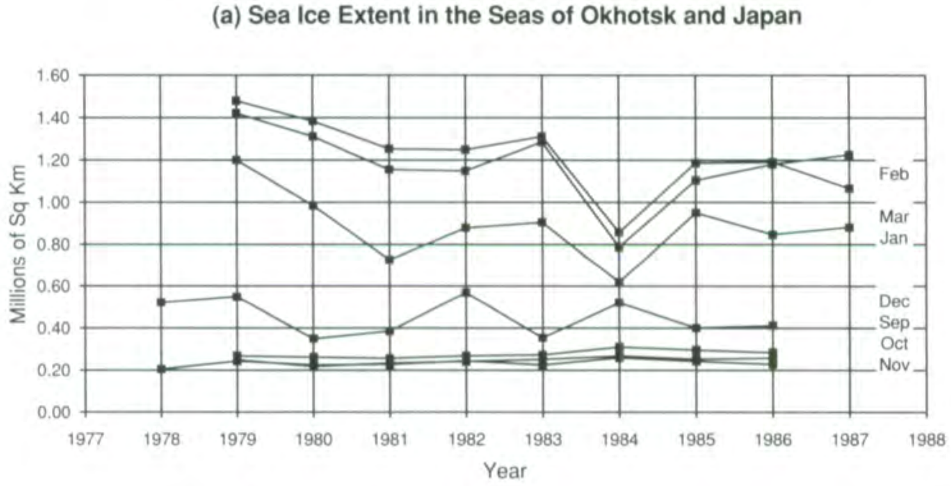
(a) Sea Ice Extent in the Seas of Okhotsk and Japan

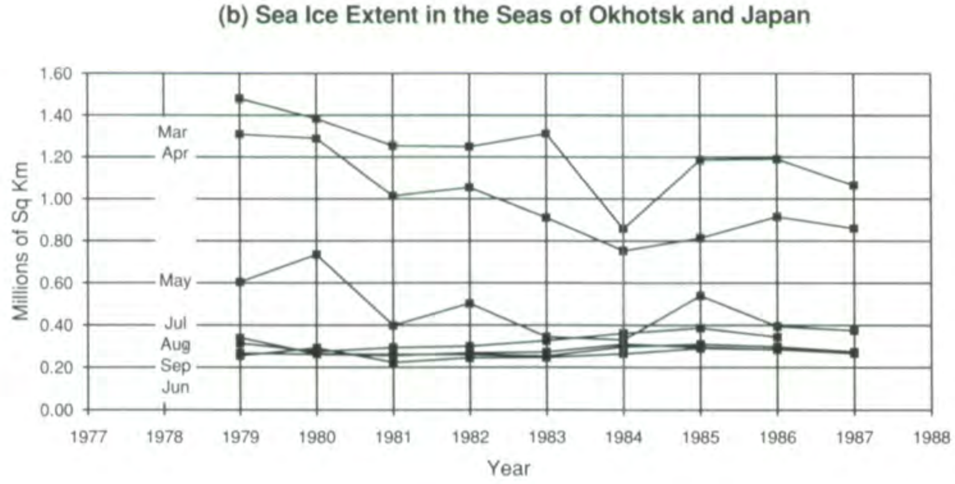
(b) Sea Ice Extent in the Seas of Okhotsk and Japan

Figure 3.3.4. Month-by-month, year-to-year changes of the sea ice extents of the Seas of Okhotsk and Japan, (a) September to March, (b) March to September.

The most pronounced interannual contrast in the sea ice extent of the Seas of Okhotsk and Japan is the anomalously low wintertime ice extent in 1984 (Figures 3.3.2-3.3.3). In contrast to the situation in the other years, most of the central portion of the Sea of Okhotsk remains ice free throughout the 1983-1984 winter (Figures 3.1.3-3.1.14). The anomalously low ice coverage for 1984 is particularly apparent in January, February, and March.

The winter with the most ice in the Seas of Okhotsk and Japan is 1978-79, when the monthly average ice extent exceeds 1.2 x 10^6 km^2 in each of the months January, February, and March (Figure 3.3.4). The other months when the ice extent exceeds this amount are February and March of 1980 and 1983, March of 1981 and 1982, and February of 1987. Although the overall trend for the sea ice extent in this region is downward over the 1978-87 period, the decrease is clearly not uniform, since the last three years all exhibit considerably greater ice extents than the 1984 year of minimal coverage (Figures 3.3.2 and 3.3.4).

Many of the interannual differences, the unusually heavy wintertime ice cover in the Sea of Okhotsk in 1979 and the relatively light ice cover in 1984, are highlighted in the anomaly maps (Figures 3.1.16 to 3.1.27). Both temporal and spatial variations in the anomalies are quite apparent. For instance, in February 1987, about equal-sized areas had contrasting relatively heavy and light ice covers, but in the following two months, almost the entire sea had an anomalously light ice cover, with the exception of the southernmost portion. Two examples of spatial differences are the heavy ice cover in the west and relatively light ice cover in the east during March 1983 (Figure 3.1.18) and the heavy ice cover in the north and relatively light ice cover in the south during April 1985 (Figure 3.1.19).

The ice concentration monthly change maps (Figure 3.1.28) further clarify the spatial patterns in the growth/decay cycle. On average, most of the Sea of Okhotsk is undergoing ice growth from November to February, with no major regions of ice decay, whereas from February to March, there is a mixture of growth in some portions of the sea and decay in other portions. By March to April, most of the sea is experiencing decay, which continues through June until little ice remains.

The relationships of the Sea of Okhotsk ice cover to oceanic and atmospheric processes have been examined by several authors using the passive-microwave data. Parkinson and Gratz (1983) compare the general features of the annual cycle of sea ice distribution with basic oceanographic factors, showing that ice forms first in cold, shallow, low-salinity waters and then drifts in a direction approximating the basically counterclockwise current patterns of the Okhotsk Gyre. Alfultis and Martin (1987) analyze the recurring Kashevarova polynya in the center of the Sea of Okhotsk and its apparent maintenance by the upwelling of warm water. They also analyze another polynya over the northwest continental shelf, using its SMMR-derived area in conjunction with weather station data to calculate production rates of ice, salt, and dense shelf water. Parkinson (1990) compares interannual differences in the Sea of Okhotsk ice extents with interannual differences in the Siberian High and Aleutian Low pressure systems, finding a far weaker correspondence over the years 1978-86 than had earlier been noted by Parkinson and Gratz (1983) for 1973-76. Earlier discussions of interannual differences in the Sea of Okhotsk are given by Akagawa (1973), who stresses the influence of atmospheric circulation, and by Watanabe (1967), who summarizes ice drift characteristics.

3.4 Bering Sea

The Bering Sea is bounded by the Bering Strait on the north, by the Aleutian Island chain on the south, by the Siberian coast on the west, and by the Alaskan coast on the east (Figure 3.4.1). Approximately half of the 2.2 x 10^6 km^2 area of the Bering Sea overlies a shallow continental shelf

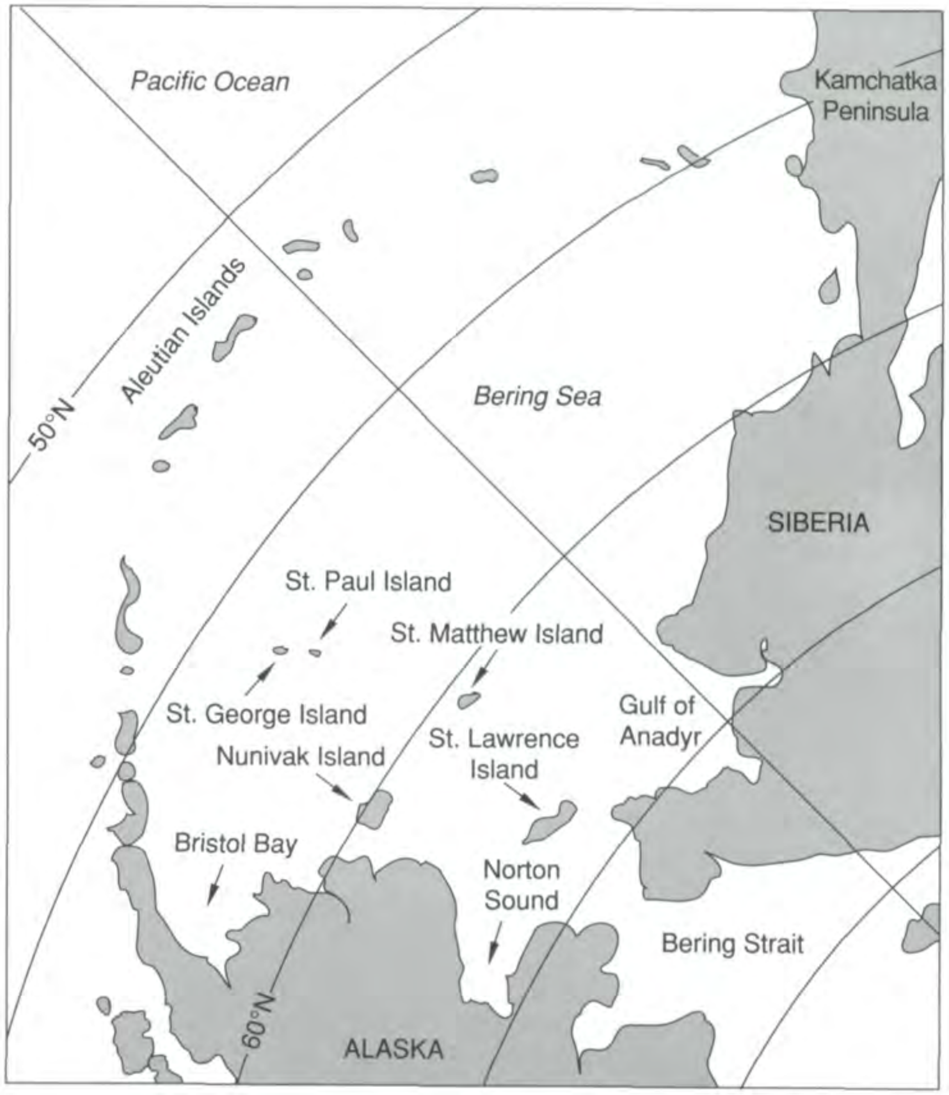

Figure 3.4.1. Location map for the Bering Sea.

Sea Ice Extent in the Bering Sea

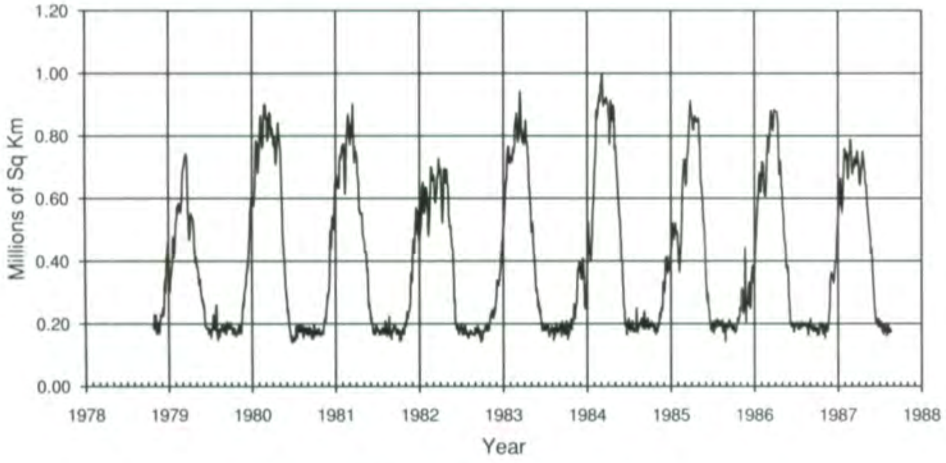

Sea Ice Area in the Bering Sea

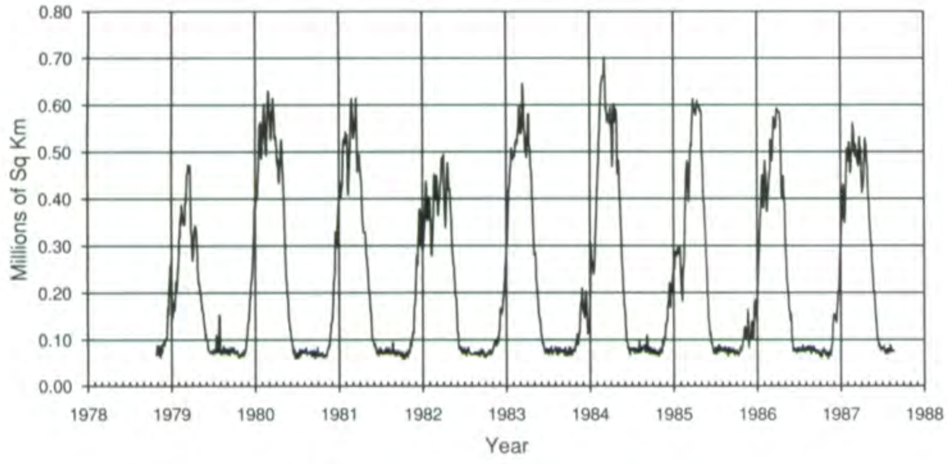

Open Water Within the Pack in the Bering Sea

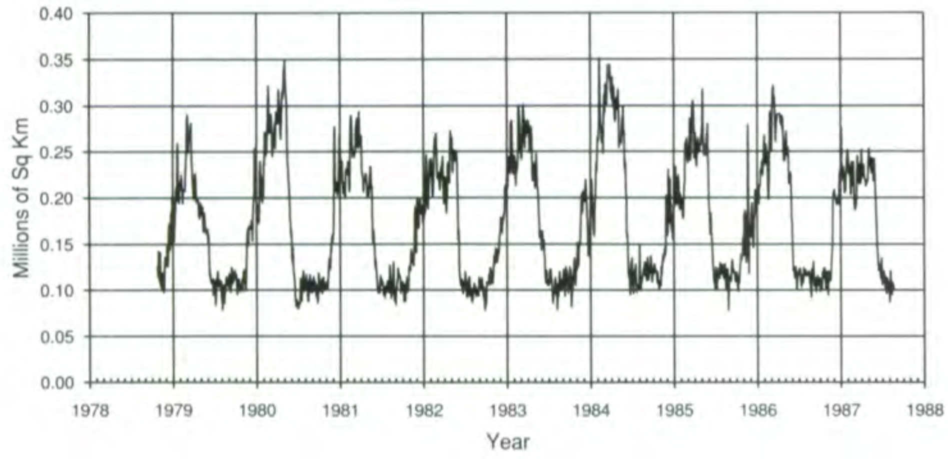

Figure 3.4.2. Sea ice extent, sea ice area, and amount of open water within the pack for the Bering Sea from October 26, 1978 to August 20, 1987.

Sea Ice Extent in the Bering Sea

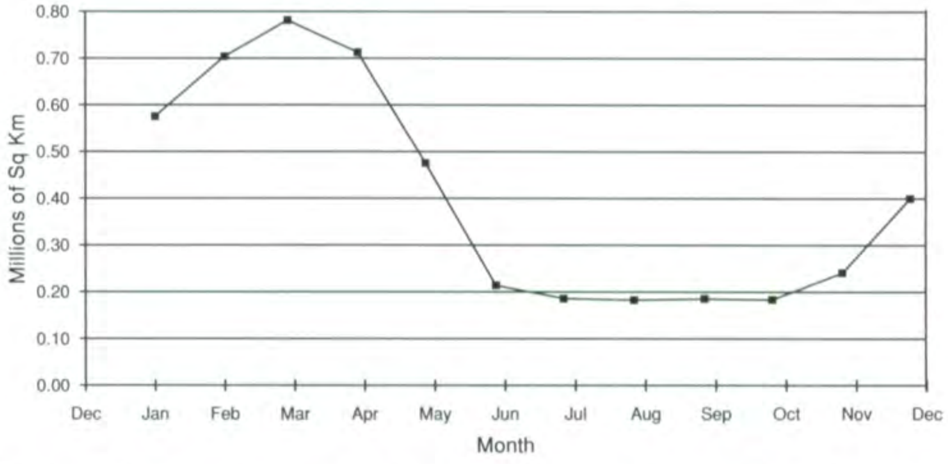

Figure 3.4.3. Average seasonal cycle of sea ice extents for the Bering Sea. The misleading indication of ice during the summer months is the result of a temperature-dependent land effect.

(a) Sea Ice Extent in the Bering Sea

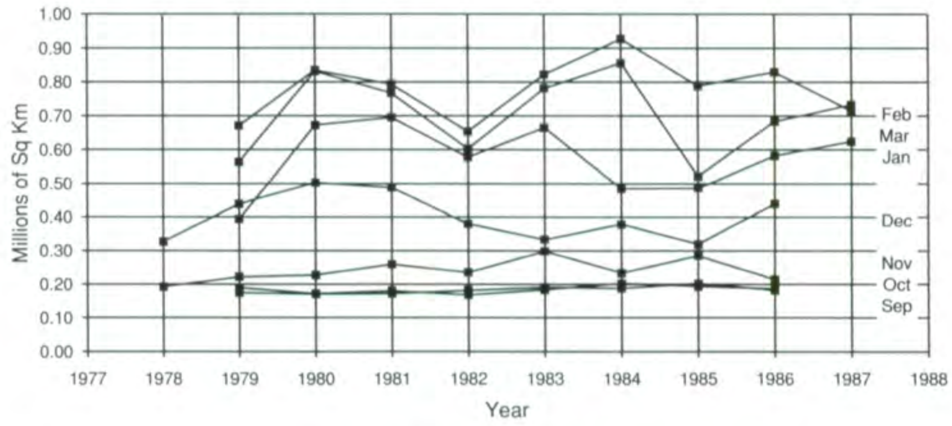

(b) Sea Ice Extent in the Bering Sea

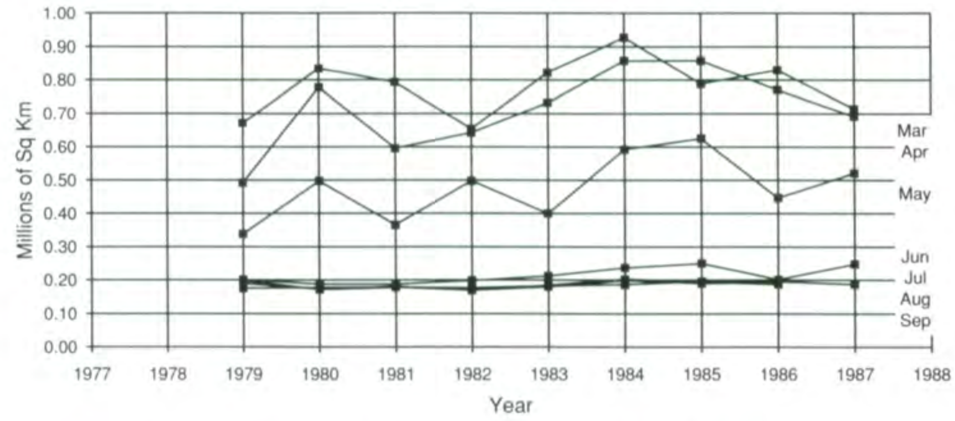

Figure 3.4.4. Month-by-month, year-to-year changes of the sea ice extents of the Bering Sea, (a) September to March, (b) March to September.

where depths are typically less than 200 m. The other half overlies the Aleutian Basin, where maximum depths exceed 4,000 meters. Oceanographic currents associated with the continental shelf break, which runs in a northwest-southeast direction across the sea, serve to limit the Bering Sea wintertime ice extent.

The seasonal cycle of Bering Sea ice growth and decay is illustrated in the 9-year record of sea ice extents (Figure 3.4.2) and its 9-year average (Figure 3.4.3). Ice growth begins in early autumn with a significant ice cover apparent as early as November in Norton Sound and along the coastlines in the northern part of the sea (Figures 3.1.13 and 3.1.15). The ice cover expands rapidly in the eastern Bering Sea as a result of southward ice advection and in situ ice growth, usually reaching Nunivak Island by December. The ice edge generally extends across the Bering Sea in a northwest-southeast direction and advances intermittently until the average maximum ice extent of about 0.8×10^6 km^2 is reached in March. Rapid ice retreat and decay occur from April to June (Figures 3.4.2 and 3.4.3), beginning first in the southeastern and central portions of the sea. The last vestiges of ice along the northern coastal areas usually disappear by June (Figure 3.1.15), although some ice remains in Norton Sound in some years (Figure 3.1.8). The Bering Sea remains ice-free during the summer months (the calculated ice extent of 0.2×10^6 km^2 is attributed to radiometric contamination from the land; see Chapter 2).

The seasonal cycles of sea ice extents for the 9 years reveal a considerable interannual variability (Figure 3.4.2). Over this period, the greatest ice-extent maximum occurred in March 1984, whereas the smallest occurred in March 1982. The spatial distribution of the ice-extent anomalies for these two Marches is illustrated in Figure 3.1.18. The map for March 1982 shows a large wedge-shaped negative anomaly centered in the southwest Bering Sea, with maximum value of about 50%, while a small region in Bristol Bay had concentrations greater than the 9-year mean. During March 1984, a large positive anomaly lies along most of the southern sea ice margin, while negative anomalies lie South of Nunivak Island in Bristol Bay, in the Gulf of Anadyr, and south of St. Lawrence Island. The anomaly maps for January, February, and April also show large spatial variability (Figures 3.1.16, 3.1.17, and 3.1.19).

Interestingly, comparison with the corresponding data for the Sea of Okhotsk (Figure 3.3.2) reveals some out-of-phase relationships in the maximum sea ice extents of the two seas. For example, the year with the smallest ice-extent maximum in the Sea of Okhotsk, 1984, had the heaviest ice cover in the Bering Sea, and the year with the largest ice-extent maximum in the Sea of Okhotsk, 1979, had a light ice cover in the Bering Sea (Figure 3.4.2). This out-of-phase variability is apparent in the anomaly maps, which also indicate its spatial extent. During January through April, 1979, the Sea of Okhotsk has strong positive anomalies in the eastern portion of the sea, resulting in an anomaly gradient extending from the coastal region to the edge of the pack, whereas the Bering Sea generally has smaller and weaker anomalies with strong negative anomalies only along a relatively narrow portion of outer Bering Sea ice pack (Figure 3.1.17). In contrast, the negative anomaly for March 1984 is centrally located in the Sea of Okhotsk, and the positive anomaly in the Bering Sea again lies along a band near the outer pack. Evidence of similar, but weaker, out-of-phase variability is also present in other years (Figures 3.1.16-3.1.19).

The interannual variability in the monthly mean ice extents is illustrated in Figure 3.4.4 . The months of maximum extent are April in 1985, February in 1980 and 1987, and March in the remaining years (1979, 1981 to 1984, and 1986). Changes in the seasonality of the Bering Sea ice cover are also apparent in the figure. For the early years, 1978 to 1981, a large part of the seasonal ice growth took place from November to December, but from 1981 to 1983 there was a sharp decrease in the early winter ice growth. In 1983, because of the relatively large growth in November of that year, there was very little change in ice extent from November to December. From 1982 until 1985, most of the growth occurred between December and February, while in 1985, there was larger-than-normal growth from February to March. This interannual variability in the seasonal growth of the Bering Sea ice cover is associated with interannual changes in the position of the Aleutian Low (Cavalieri and Parkinson, 1987). More general studies relating the variability in ice extents to meteorological and/or oceanographic influences have been described previously (e.g., Walsh and Johnson, 1979; Overland and Pease, 1983; Crane, 1983; Parkinson and Gratz, 1983; Cavalieri and Parkinson, 1987; Niebauer, 1988; Parkinson and Cavalieri, 1989).

One of the more interesting and important features observed in the Bering Sea is the recurrence of coastal polynyas. The persistent nature of these polynyas arises from the predominantly northeasterly winds that blow across the east-west trending coastlines of Alaska and Siberia, the Chukchi peninsula, and the St. Lawrence, St. Matthew, and Nunivak islands, and force the ice away from the land. The coastal polynyas, forced by the synoptic wind fields, have characteristic periods of from 1 to 3 weeks. An example of the opening and closing of the St. Lawrence Island polynya is illustrated in Figure 3.4.5 for the period March 13 through March 29, 1985. The March 13 image shows a small reduction in ice concentration, which signaled the opening of a polynya off the southwest coast of the island. From March 13, the polynya continues to grow in a southwestward direction, reaching its maximum extent on March 23. Other prominent coastal polynyas apparent during this time are located off the southern coast of the Chukchi Peninsula and off the coast of Seward Peninsula between Nome and Cape Prince of Wales. On March 25, the areal extents of both the Siberian coast and St. Lawrence Island polynyas decrease dramatically. By March 29, a smaller, but still clearly defined polynya, occurs south of St. Lawrence Island. The importance of polynya processes to the regional oceanography and climatology is well-recognized and has been the subject of intense study during recent decades (cf. overview by Smith et al., 1990).

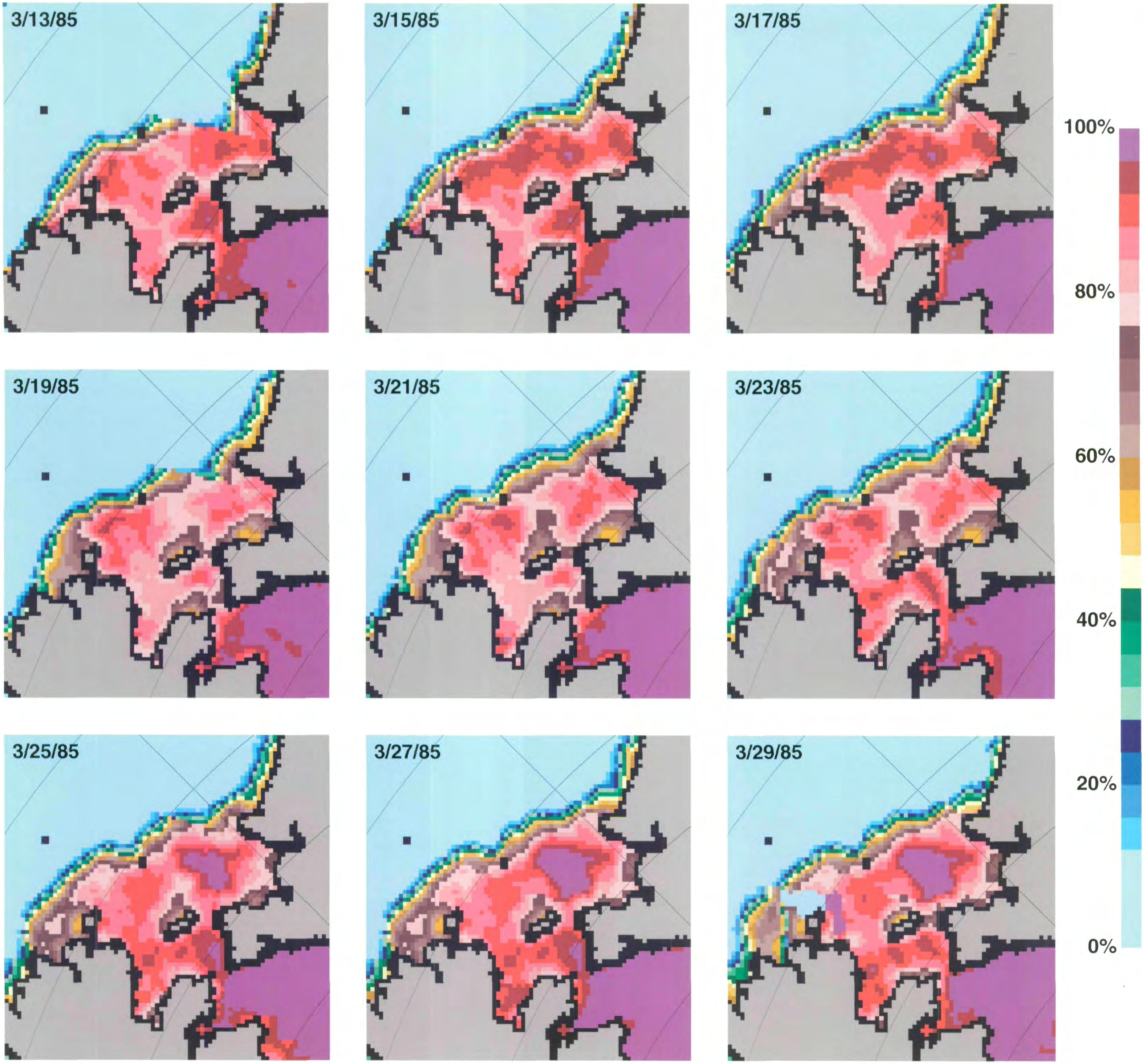

Figure 3.4.5. Examples showing the variation of sea ice concentration in the location of the St. Lawrence Island polynya during March 1985.

3.5 Hudson Bay

Located in northeastern Canada, Hudson Bay (Figure 3.5.1) is largely landlocked, with its links to the rest of the world's oceans coming through the passage to the Atlantic Ocean provided by Hudson Strait in the northeast and the circuitous passage to the Arctic Ocean through the narrow straits of the Canadian Archipelago. Being an essentially inland sea under the influence of a continental climate, Hudson Bay experiences a far different seasonal cycle of sea ice conditions than does either the Sea of Okhotsk or the Bering Sea, in spite of being located in the same general latitude range.

Hudson Bay is almost totally ice-covered for 6 months of the year, from December through May, with only a slight breakup of the ice in June (Figure 3.1.15). The summer ice decay is very rapid, proceeding from a nearly complete ice cover in June to nearly ice-free conditions in August, and the autumn growth is equally rapid from October to December (Figures 3.5.2-3.5.3). Some ice remains in Foxe Basin, defined here as part of the Hudson Bay region (Figure 3.5.1), for almost the entire year. These basic aspects of the seasonal cycle are consistent through each of the SMMR years (Figures 3.1.3-3.1.14 and 3.5.4). On average, monthly ice extents increase from a minimum of 0.28 x 10^6 km^2 in September to a maximum of 1.16 x 10^6 km^2 in each of the months January through April (Figure 3.5.3).

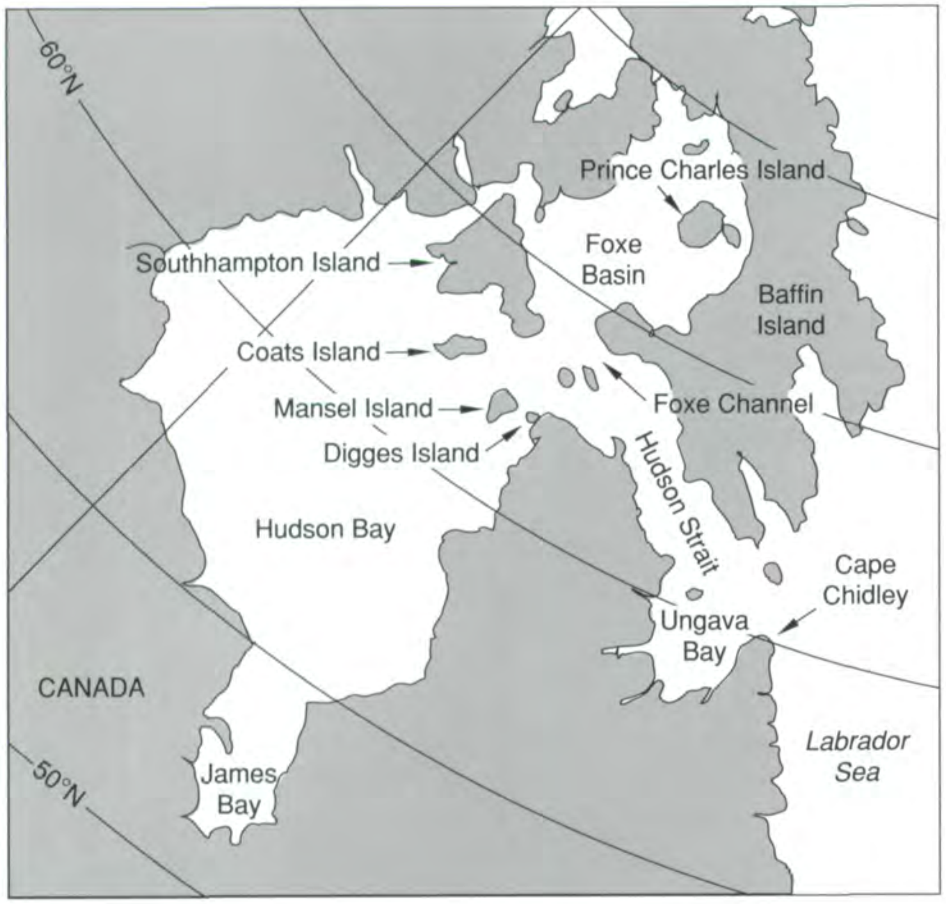

Figure 3.5.1. Location map for Hudson Bay.

In contrast to the situation in several of the other regions, the basic ice-decay sequence in Hudson Bay does not approximate a reversal of the ice-growth sequence, which would have the decay proceeding basically from south to north. Instead, the decay, on average, (Figure 3.1.15) proceeds generally from northeast to southwest, presumably because the major opening to the warmer waters of the Atlantic is in the northeast. However, distinct interannual differences occur in the pattern of decay, as well as in the timing and speed. In all years, Hudson Bay remains largely ice-covered in June, but the distributions of the emerging openings vary. In 1979, 1980, 1982, 1983, and 1985, the openings occur along the east coast, whereas in 1981, 1986, and 1987, they occur along the northwest coast, and in 1984, they occur along the north and east coasts (Figure 3.1.8).

Interannual differences in the Hudson Bay ice distributions occur predominantly in the June, July, October, and November transition months, especially July and November (Figures 3.1.3-3.1.14), although lesser differences also occur in the other months and are readily identifiable in the anomaly maps (Figures 3.1.16-3.1.27). The interannual differences in the July ice covers are considerable in each of the three main geographical portions of the Hudson Bay region--Foxe Basin, Hudson Strait, and Hudson Bay proper. The July extremes for Foxe Basin occur in 1981, when there is considerable open water, and in 1983, when most of the basin still has highly concentrated ice (Figures 3.1.9 and 3.1.22). Hudson Strait is open in July in several of the years (1980, 1981, and 1986) but retains considerable ice in other years (1983 and 1984). The July ice coverage in Hudson Bay proper varies from the situation in 1979 and 1980, when very little ice remains (mostly in the southwest corner of the bay and with concentrations under 40%) to the situation in 1985 and 1986, when much higher concentrations exist in the southwest corner, and the ice cover extends over a larger portion of the bay (Figure 3.1.9). The anomaly maps of Figure 3.1.22 cannot reveal where ice existed and where it did not exist, but they do provide quantitative indications of the amount of interannual contrast.

In October of each year, Hudson Bay south of the Coats Island/Mansel Island boundary is essentially ice-free, as is most of Hudson Strait. Therefore, interannual differences for October occur mostly in the northernmost portion of the Hudson Bay region, namely Foxe Basin. Foxe Basin is about two-thirds ice-covered in October 1986, about one-third ice-covered in October 1983, and predominantly ice-free in the other six Octobers (Figure 3.1.12). The interannual differences in Foxe Basin during October are followed by at least as strong interannual differences in Hudson Bay proper during November. The extremes in the November southward extent of the ice occur in 1981, when the ice does not extend much beyond Coats and Mansel Islands, and in 1986, when the ice cover extends throughout most of the bay (Figure 3.1.13). The respective negative and positive anomalies for Novembers of 1981 and 1986 are evident in the anomaly maps (Figure 3.1.26).

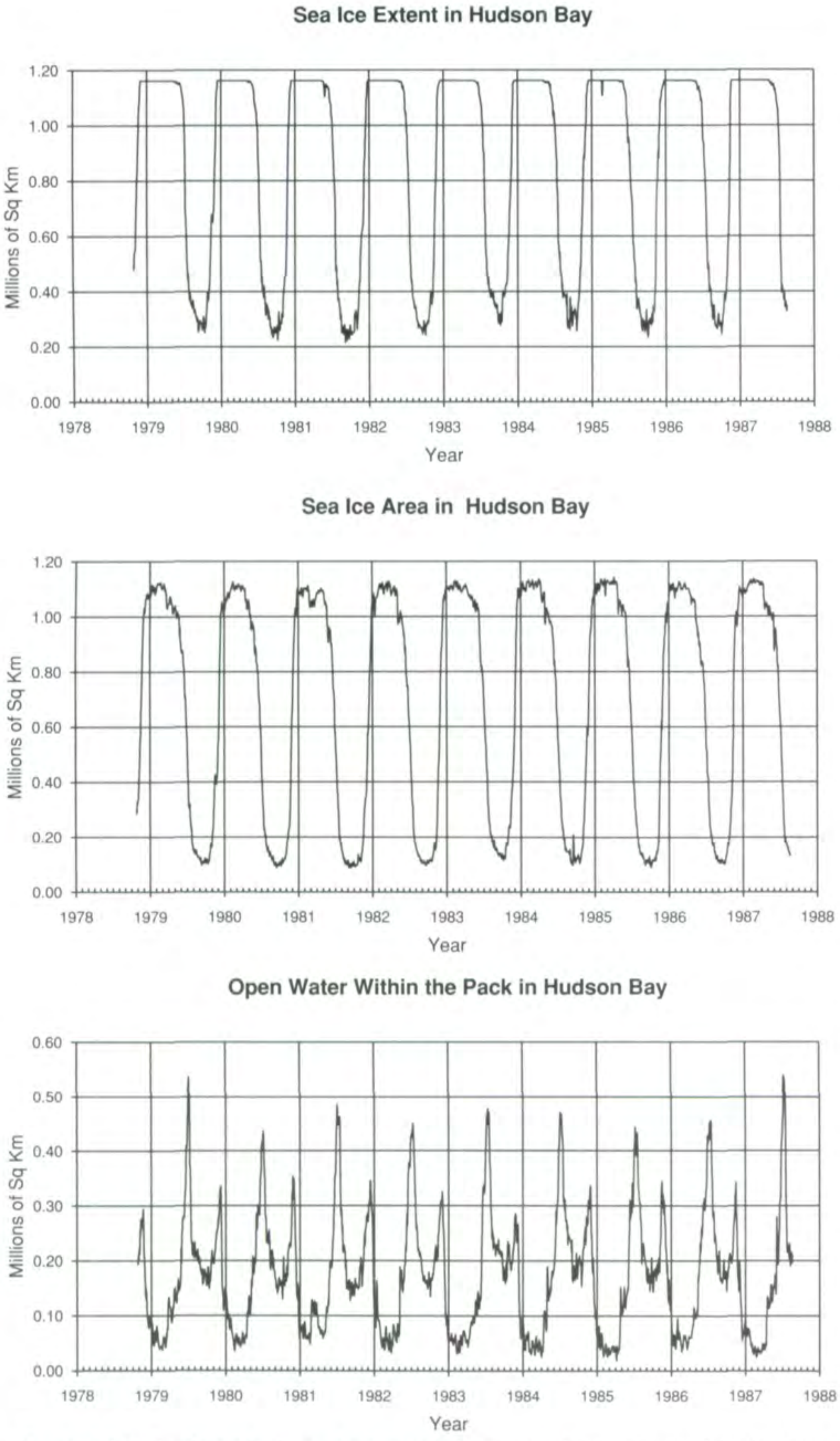

Figure 3.5.2. Sea ice extent, sea ice area, and amount of open water within the pack for Hudson Bay from October 26, 1978 to August 20, 1987.

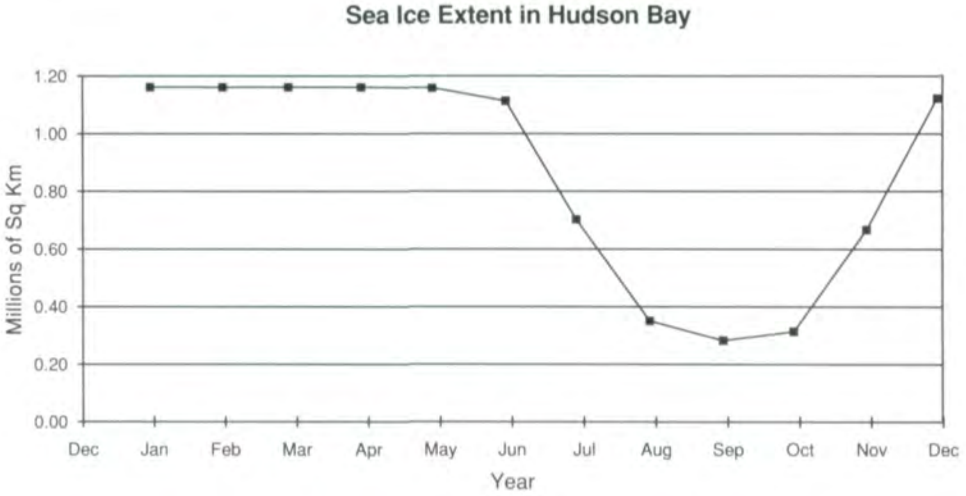

Figure 3.5.3. Average seasonal cycle of sea ice extents for Hudson Bay. The misleading indication of ice during the summer months is largely the result of a temperature-dependent land effect.

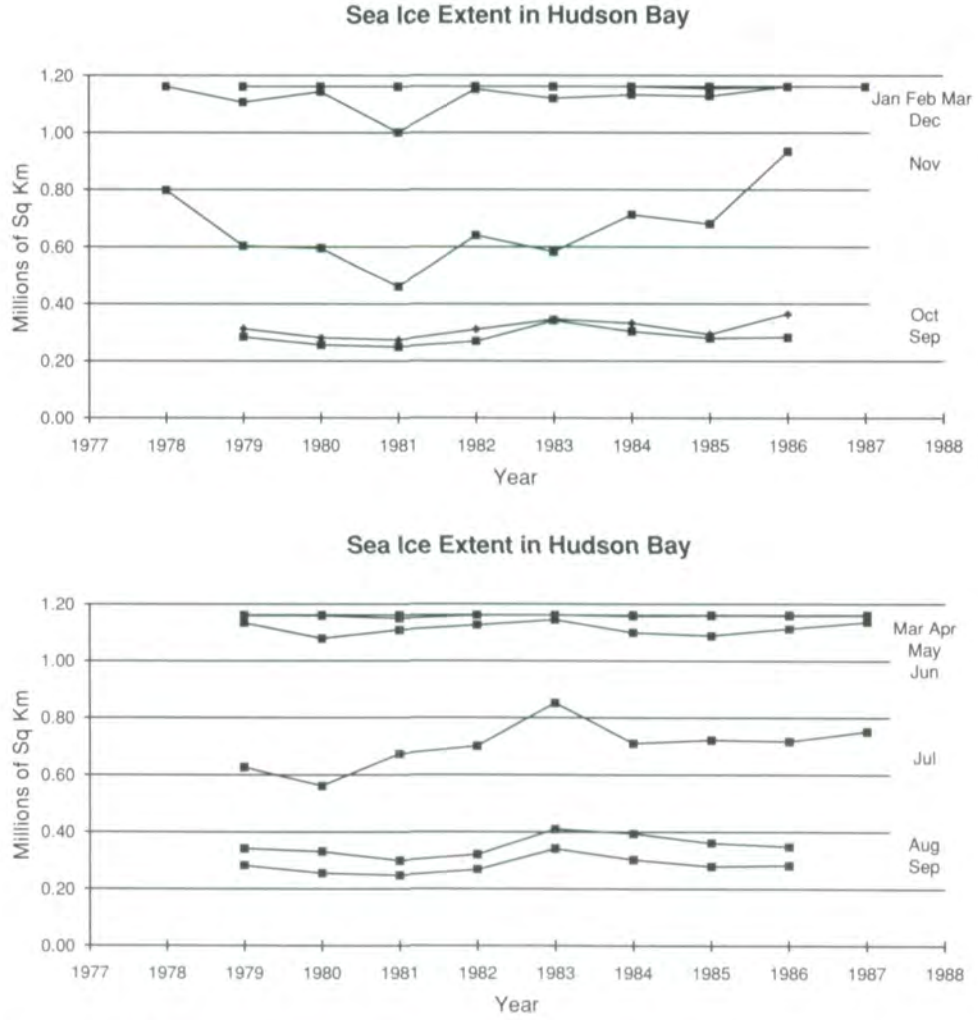

Figure 3.5.4. Month-by-month, year-to-year changes of the sea ice extents of Hudson Bay, (a) September to March, (b) March to September.

Although the fact that the Hudson Bay region fills with ice during each winter prevents an easy estimation of the 9-year trends in the ice cover from the time series of Figure 3.5.2, some indication of trends can be gathered from the transition months. The June ice cover remains almost complete in each year; however, the July ice cover shows an upward trend (Figure 3.5.4), and the November results show minima in the middle of the SMMR time period. When the ice extents are combined to yearly averages and a linear least-squares fit is calculated, as done by Parkinson and Cavalieri (1989), a slight upward trend is found for the 1979-1986 period with SMMR yearly averages (see also Figure 5.1.1e). This suggests that the region experienced a slight cooling, at least of surface-water temperatures, rather than an anticipated warming. The cooling could be an extension of the cooling found by others in the North Atlantic (e.g., Wigley, 1989; Houghton et al., 1990).

3.6 Baffin Bay, Davis Strait, and the Labrador Sea

The combined Baffin Bay, Davis Strait, and Labrador Sea region (Figure 3.6.1) is bounded on the northeast and northwest by Greenland and Baffin Island, respectively, and on the southwest by Newfoundland. The region opens to the Atlantic Ocean to the southeast and, through several narrow passages, to the Arctic Ocean to the north. Baffin Bay retains some ice cover throughout the year, so that in this respect, the Baffin Bay, Davis Strait, and Labrador Sea region differs from the regions of the Sea of Okhotsk and Bering Sea. In addition, it differs from Hudson Bay in that it exhibits far greater interannual variability in its seasonal sea ice cycle (Figure 3.6.2).

Averaged over the 9 SMMR years, the annual cycle of monthly ice extents in the Baffin Bay, Davis Strait, and Labrador Sea region has a minimum of 0.33 x 10^6 km^2 in September and a maximum of 1.45 x 10^6 km^2 in March (Figure 3.6.3). The ice at the summer minimum is confined largely to Kane Basin at the far north of the region (Figures 3.6.1 and 3.1.15), a fact that is valid for August, as well as September. In October, low-concentration ice extends over much of northwestern Baffin Bay. In November, these areas have much higher ice concentrations, and ice also covers the western portion of the bay. There is a prominent east-west asymmetry in the spatial distribution of ice in November, with the ice lying to the west of a nearly north-south ice edge. This unusual ice-edge orientation arises from the influence of the relatively warm, north-flowing West Greenland Current, which prevents the eastern portion of the region from freezing until later in the year, similar to the effect of the Kamchatka Current in the Sea of Okhotsk. In December, Baffin Bay is almost completely ice-covered, while the eastern portion of Davis Strait and almost the entire Labrador Sea remain ice-free. The ice cover advances somewhat farther southward over the next 3 months, especially along the Canadian coast. However, it never completely covers the region (Figure 3.1.15), since the warm Atlantic waters and the West Greenland Current prevent ice formation in the region's southeast portion.

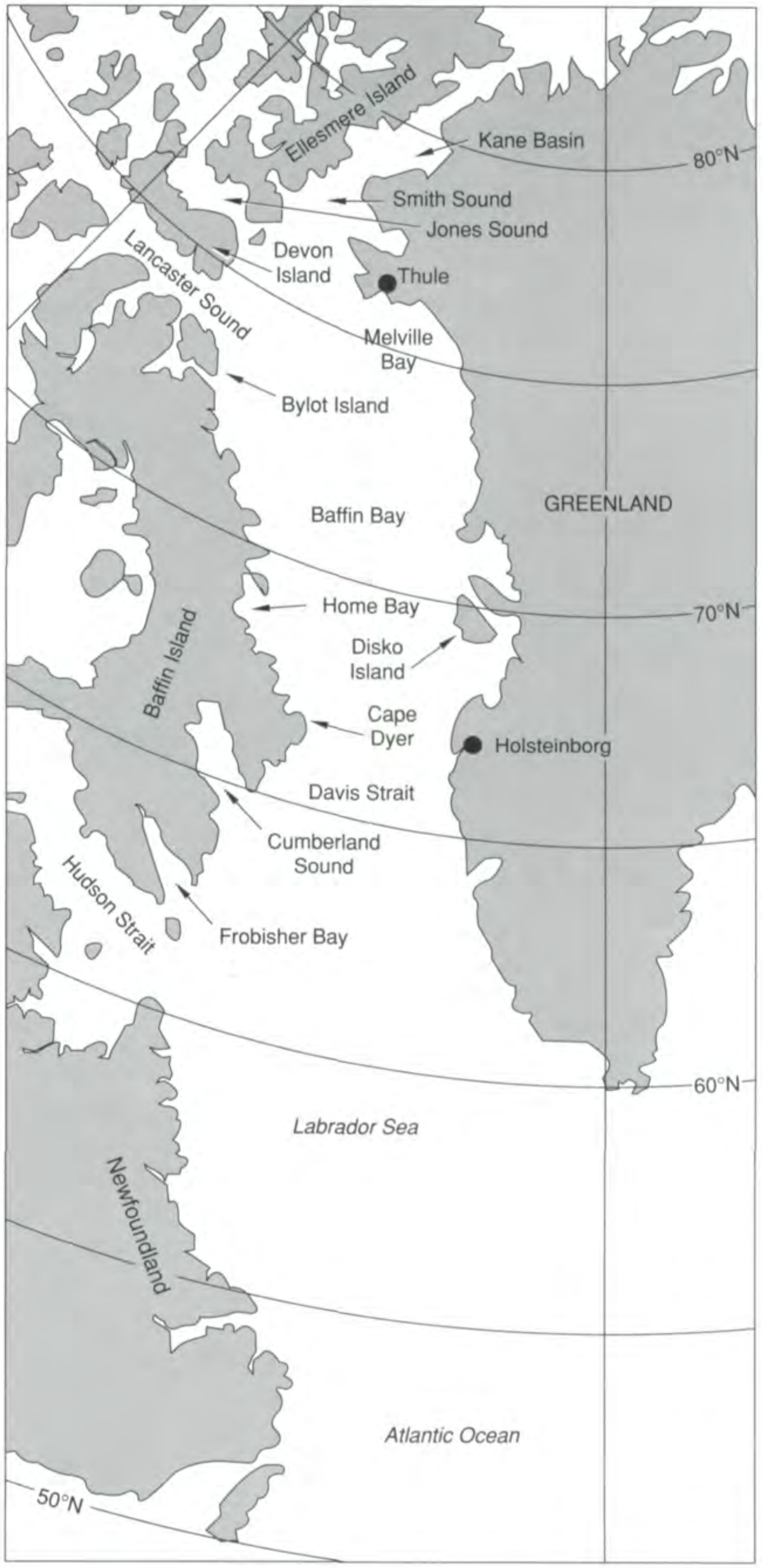

Figure 3.6.1. Location map for Baffin Bay, Davis Strait, and Labrador Sea.

Sea Ice Extent in Baffin Bay, Davis Strait, and Labrador Sea

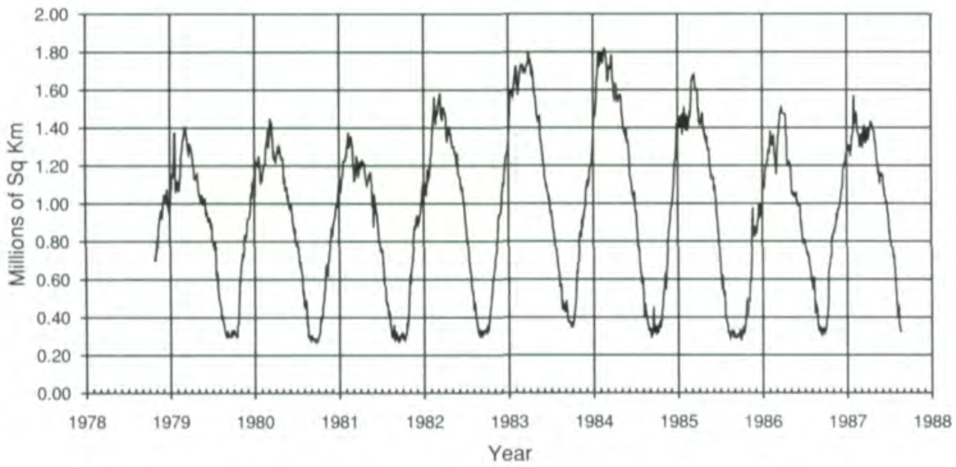

Sea Ice Area in Baffin Bay, Davis Strait, and Labrador Sea

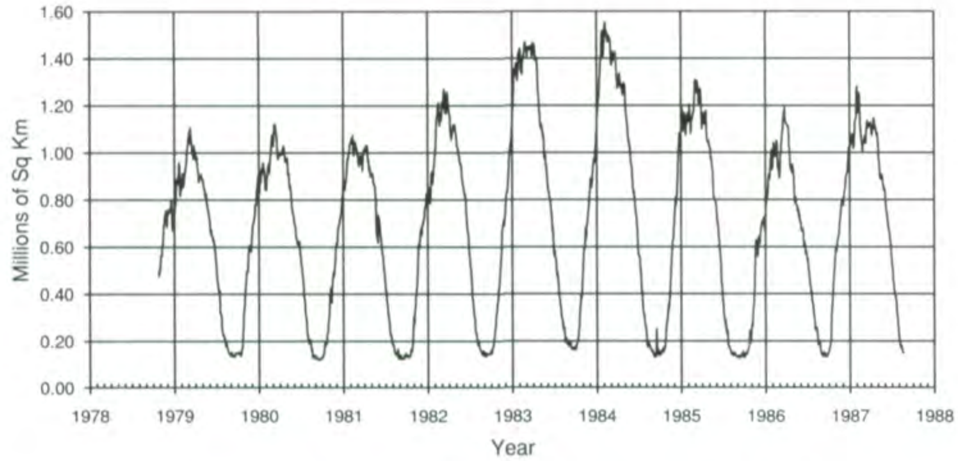

Open Water Within the Pack in Baffin Bay, Davis Strait, and Labrador Sea

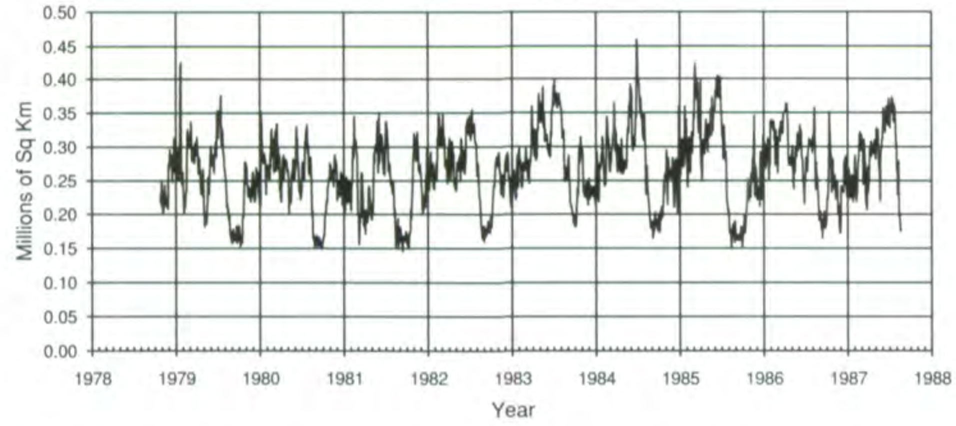

Figure 3.6.2. Sea ice extent, sea ice area, and amount of open water within the pack for Baffin Bay, Davis Strait, and the Labrador Sea, from October 26, 1978 to August 20, 1987.

Sea Ice Extent in Baffin Bay, Davis Strait, and Labrador Sea

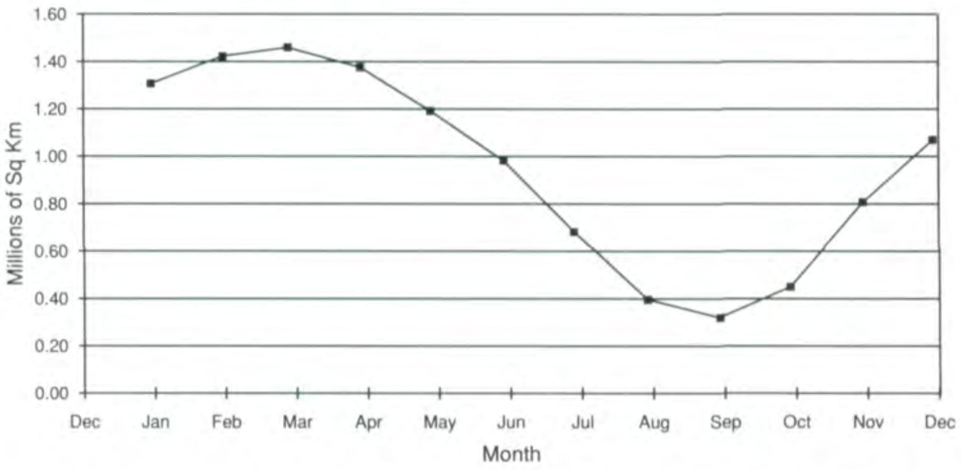

Figure 3.6.3. Average seasonal cycle of sea ice extents for Baffin Bay, Davis Strait, and the Labrador Sea. The misleading indication of ice during the summer months is largely the result of a temperature-dependent land effect.

(a) Sea Ice Extent in Baffin Bay, Davis Strait, and Labrador Sea

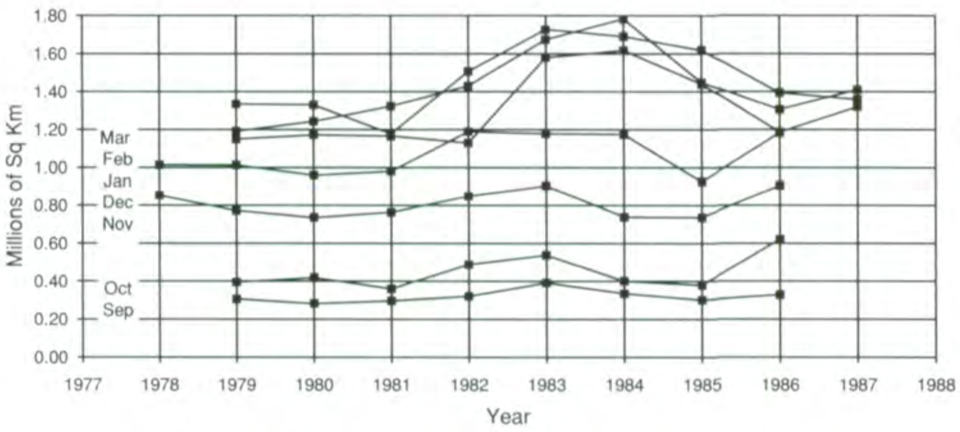

(b) Sea Ice Extent in Baffin Bay, Davis Strait, and Labrador Sea

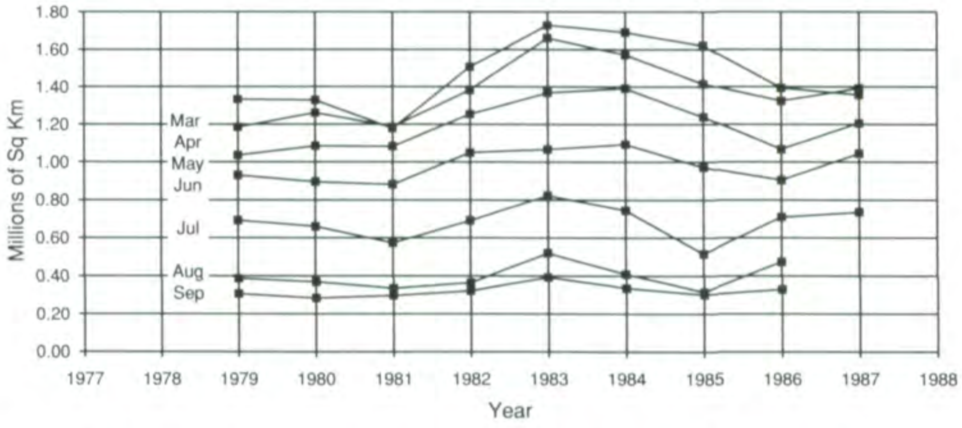

Figure 3.6.4. Month-by-month, year-to-year changes of the sea ice extents Baffin Bay, Davis Strait, and the Labrador Sea (a) September to March, (b) March to September.

Furthermore, in Smith Sound, just to the north of Baffin Bay proper, there is an area of relatively low ice concentration even at the March ice-extent maximum (Figure 3.1.15). This latter area is the region of the North Water polynya, discussed further at the end of this section.

Ice decay in the Baffin Bay, Davis Strait, and Labrador Sea region proceeds with a slow northward retreat of the ice edge from March to May, accompanied by decreasing ice concentrations. By June, the reduced ice concentrations in Smith Sound have evolved into a sizable opening, and the Baffin Bay ice-edge retreat during June and July proceeds both from the north (starting from Smith Sound) and from the south. By August, very little ice remains except in Kane Basin (Figure 3.1.15).

Interannual differences are strong in the Baffin Bay, Davis Strait, and Labrador Sea region. Maximum wintertime ice extents range from just under 1.4 x 10^6 km^2 in 1981 to just over 1.8 x 10^6 km^2 in 1984, with the ice-extent time series suggesting a cycle more than a trend. Wintertime ice extents during the final SMMR year are larger than, but close to, those during the initial year and much smaller than those in the intermediate years 1983 and 1984 (Figure 3.6.2). The 1981/1984 contrast is quite apparent from the January, February, and March images (Figures 3.1.3-3.1.5 and 3.1.16-3.1.18) and can be summarized by noting that the open water area to the southwest of Greenland was greater in 1981, in both its northward and its westward extent, and that (perhaps as a result) the weakened ice conditions in Smith Sound are more in evidence in 1981. In January of 1984, the ice along the west coast of Greenland reaches to 62° N, over 4° farther south than in January 1981 (Figure 3.1.3). The winter season contrast is also well-developed in the preceding 3 months (Figures 3.1.12 -3.1.14). These interannual differences could be oceanographically induced, with the effect of the West Greenland Current being greater and extending farther north in 1981 than in 1984, or they could result from interannual differences in the positioning and strength of the Icelandic low-pressure system, or both.

Another aspect of the interannual variability is the timing of maximum and minimum ice extents. The timing of minimum ice extent (on a monthly average basis) is consistent (Figure 3.6.4), occurring in September every year. Maximum ice extent occurs in March in 6 years (1979, 1980, 1982, 1983, 1985, and 1986), and in February in the remaining 3 years (1981, 1984, and 1987).

The October-April multiyear ice images show almost no multiyear ice of concentration greater than 20% anywhere in the Baffin Bay, Davis Strait, and Labrador Sea region, with the exception of an occasional small amount evident in Kane Basin (Figures 3.1.29-3.1.35). Although almost all the ice formed in the region is first-year ice, some multiyear ice is advected into the region from the central Arctic, Lancaster Sound, and Jones Sound.

The feature of the Baffin Bay ice cover that has received the most research attention over the years is the North Water polynya, which occurs frequently in Smith Sound. The North Water polynya is the largest recurring polynya in the Northern Hemisphere, and it was studied extensively with in situ observations prior to the availability of satellite passive-microwave observations (e.g., Dunbar, 1969; Muench, 1971; Dunbar and Dunbar, 1972; Muench and Sadler, 1973). Satellite data, including the ESMR and SMMR passive-microwave data, have allowed a more temporally complete data set since 1972 and have contributed to further research results on the polynya (e.g., Crawford and Parkinson, 1981; Ito, 1982; Steffen, 1985; Steffen, 1986). A particularly inclusive study was the North Water Project carried out over the years 1972-1981 by a team of Canadian and Swiss scientists and involving both field studies and modeling studies of the local ice cover and oceanic and meteorological conditions (e.g., Muller et al., 1977; Ito, 1982).

The North Water is generally bounded to the north by fast ice connecting Ellesmere Island and Greenland and to the south by a less distinct and more variable edge. It opens and closes throughout the course of the winter and spring seasons, and generally contains a considerable amount of ice, even when open, though of low concentrations relative to the surrounding ice cover. By May, open water becomes apparent on individual days at the 30- x 30-km resolution of the passive-microwave images. The polynya expands considerably in June and July, with the expanding polynya providing the southward retreat of the northern Baffin Bay ice edge, referred to above in the context of the ice edge retreating from both the north and the south. The polynya generally loses its identity sometime near the end of July, at which time it is joined with the open water to the south.

Figure 3.6.5 illustrates the fluctuating sea ice concentrations within the North Water region (Figure 3.6.6) throughout the yearly cycle by presenting a time series of average ice concentrations for October 1, 1985, through September 30, 1986. Both the size and the duration of the polynya openings vary throughout the winter season, with a particularly large midwinter opening occurring in February. The evolution of this opening and its subsequent closing are highlighted in Figure 3.6.7, which shows ice-concentration maps of the North Water region every 4 days from

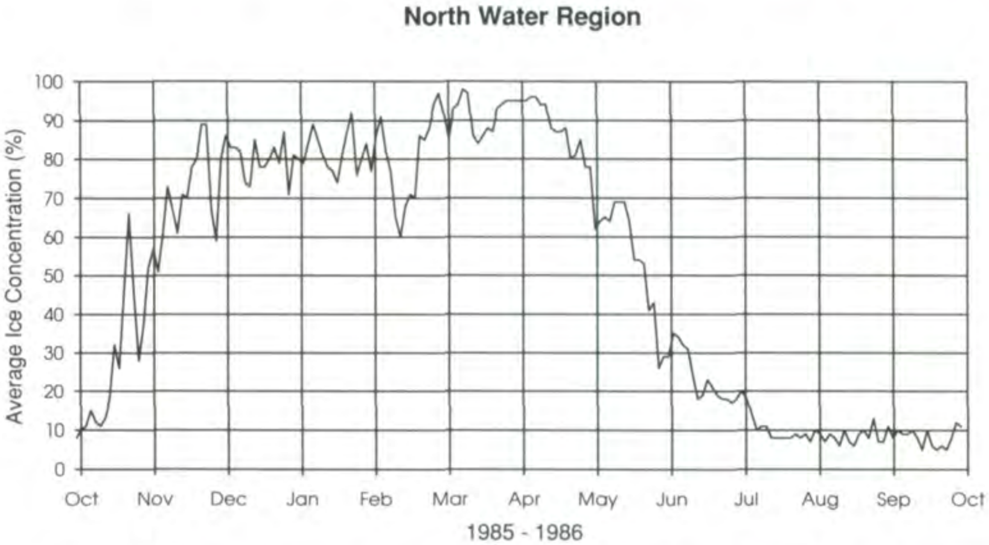

Figure 3.6.5. Average ice concentrations in the North Water region for the period October 1, 1985 through September 30, 1986. The averaging is over the smaller region depicted in Figure 3.6.6.

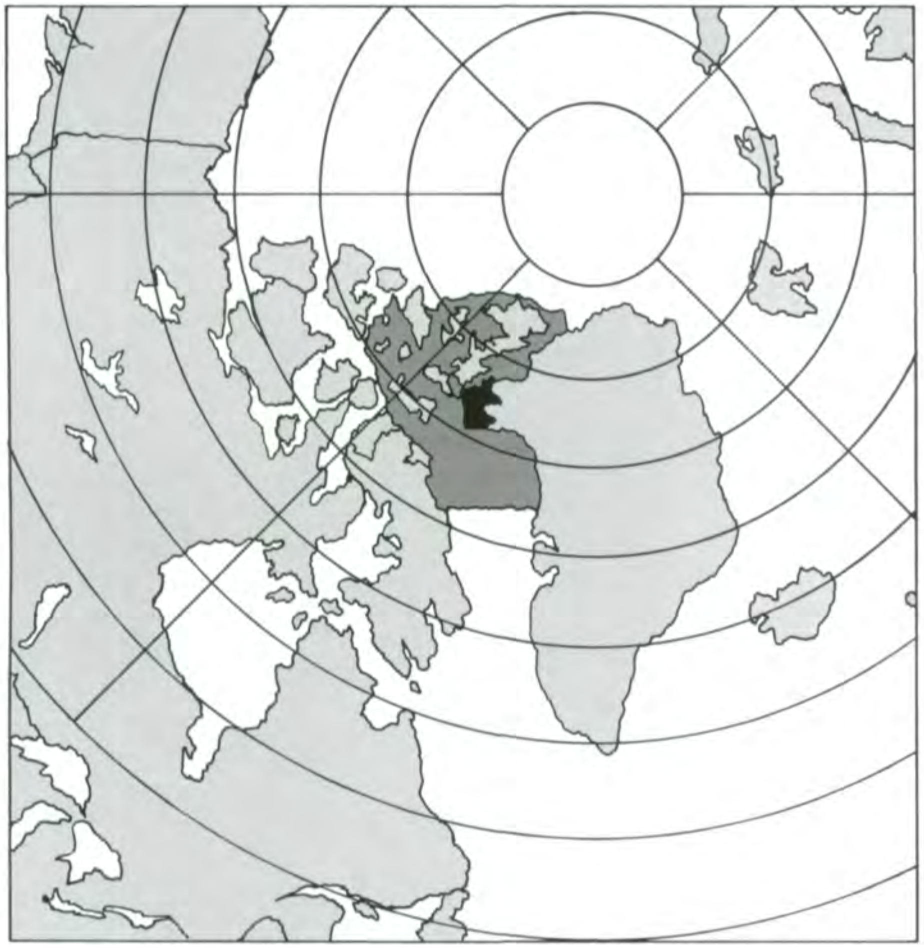

Figure 3.6.6. The North Water region (light gray) and the region (dark gray) of the maps in Figure 3.6.7.

February 4, 1986, through March 8, 1986. Although the North Water region has ice concentrations considerably below those of the surrounding ice on February 4, the ice concentrations still exceed 76% in all pixels. The polynya expands and deepens over the next 8 days, with some pixels having concentrations as low as 40% by February 12, at which time this particular polynya opening is near its height. Ice concentrations within the region proceed to increase fairly steadily over the next 2 weeks, so that by February 28, almost the entire North Water area has ice concentrations in excess of 88%. These high concentrations remain only briefly, however, since by March 4, the polynya has reopened, although to a lesser extent than in mid-February. This subsequent opening does not persist as long as in February, since substantial closing is apparent by March 8 (Figure 3.6.7).

3.7 Gulf of St. Lawrence

The Gulf of St. Lawrence, the smallest of the nine Arctic regions, covers an area of 0.64×10^6 km^2 (Table 3.1.1). The Gulf of St. Lawrence is bounded by the following Canadian Provinces: Quebec to the north, Newfoundland to the east, New Brunswick to the west, and Nova Scotia to the south (Figure 3.7.1). The St. Lawrence River empties into the Gulf at the northwest corner of the region. The Gulf is connected to the Labrador Sea by the Strait of Belle Isle in the northeast corner. Cabot Strait between Newfoundland and Nova Scotia connects the Gulf of St. Lawrence to the Atlantic Ocean. This region, as defined in Figure 3.1.2, extends farther from Newfoundland and Nova Scotia southward to the edge of the map.

The seasonal cycle of the regional ice growth and decay is illustrated in Figure 3.7.2 and in the 9-year-average cycle of sea ice extents (Figure 3.7.3). In both figures, there are false indications of sea ice in summer as a result of temperature-dependent land effects that are discussed in Chapter 2. Large ocean-land temperature differences in summer result in the secondary maxima in August, that are comparable to the ice-extent maxima. This effect is enhanced by the relatively large ratio of land perimeter to the area of the region and the absence of sea ice.

Ice growth begins in December along the northern and western coastal regions (Figure 3.1.14) and generally progresses eastward from the western part of the region and from the Strait of Belle Isle. The period of most rapid ice growth is from January to February or March (Figure 3.7.4), with maximum ice cover occurring either in February or March. The rapid rate of ice growth is caused, in part, by the influx of relatively fresh water from river runoff. The maximum ice extent of over 0.25×10^6 km^2 was reached in March 1986. Extremely rapid ice retreat and decay occur from March to April (Figure 3.7.4), first in the northern and northwestern portions of the region. The last vestiges of ice are often found in the southwestern portion of the Gulf where Prince Edward Island serves as an anchor for the ice and in the northeastern corner where ice clogs the Strait of Belle Isle. The Gulf of St. Lawrence region remains ice-free during the summer months.

The interannual variability in the monthly mean ice extents is illustrated in Figure 3.7.4. The years for which the maximum extent clearly occurs in February are 1981 and 1983, whereas in 1979, 1982, and 1986, the maximum extent clearly occurs in March. In other years, the maximum appears to straddle both months. The year that exhibits an anomalously low March ice extent is 1981. The March anomaly maps (Figure 3.1.18) show that, for March 1981, negative anomalies cover the entire region, with anomalies ranging from over 50% in the western region to 40% in the eastern portion of the Gulf. For March 1986, the month of greatest ice-extent maximum, positive anomalies cover the entire Gulf, ranging from about 25% in the west to 40% in the east.

In contrast to March 1981 and 1986, March 1983, the month with the second lowest ice-extent maximum, has a strong negative anomaly covering the eastern portion of the region, while a small positive anomaly covers the extreme

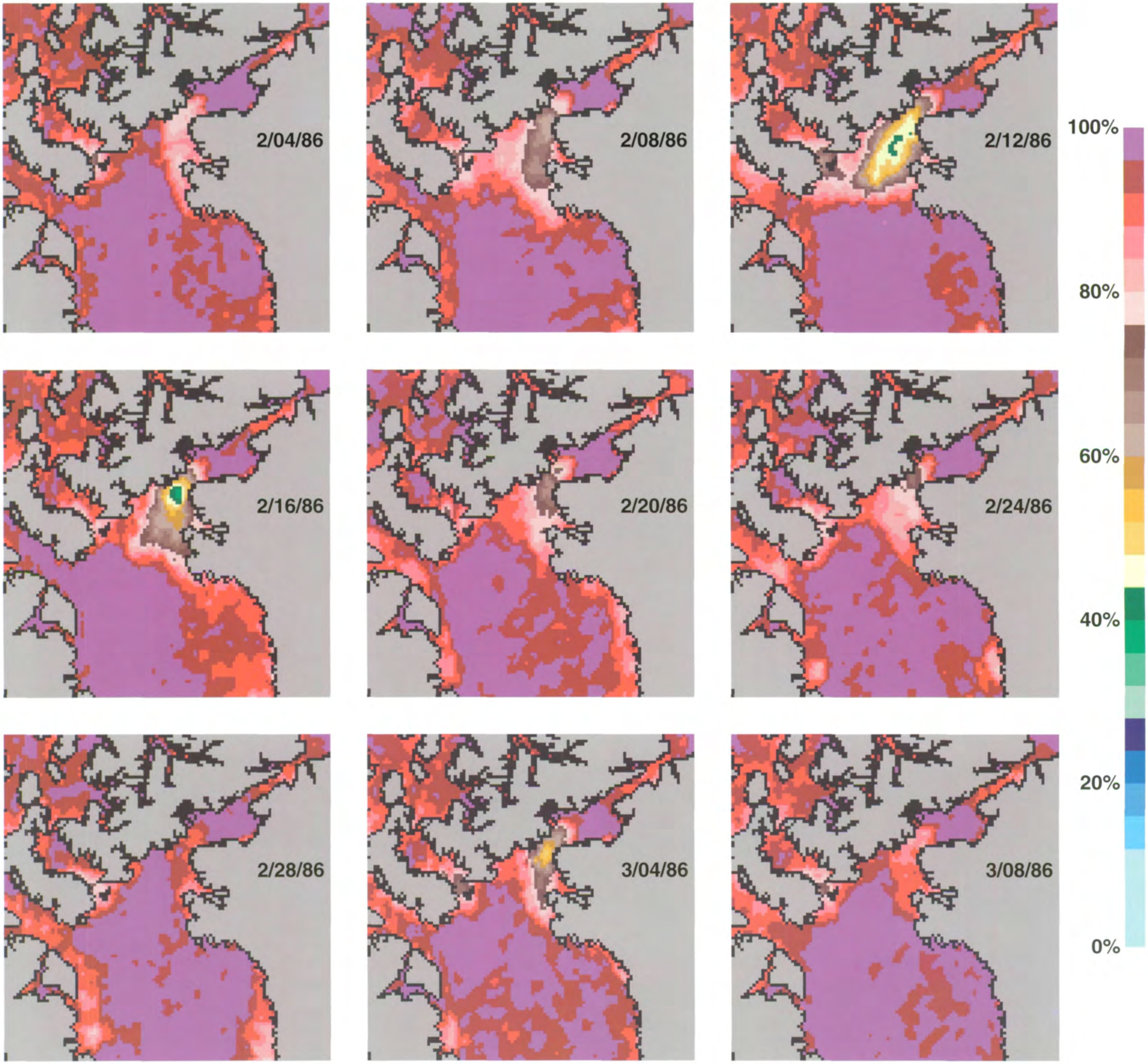

Figure 3.6.7. Single-day images of ice concentrations in the North Water region and surroundings on 4-day intervals from February 4 through March 8, 1986.

Figure 3.7.1. Location map for the Gulf of St. Lawrence.

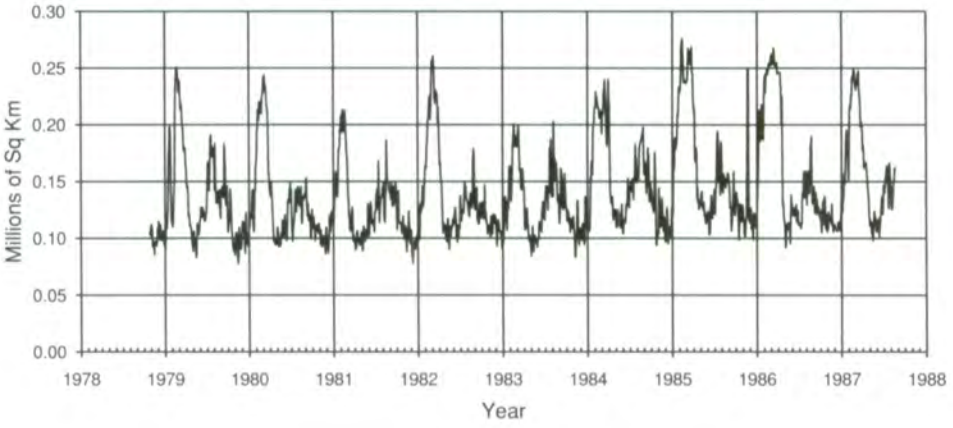
Sea Ice Extent in the Gulf of St. Lawrence

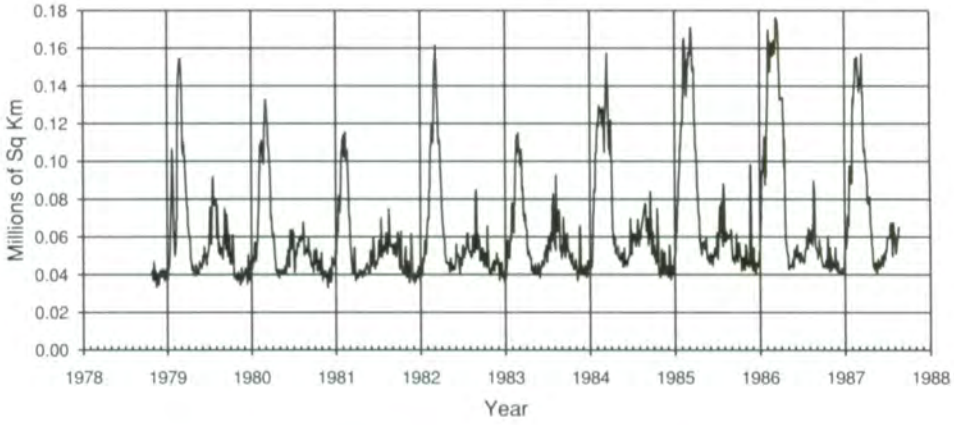
Sea Ice Area in the Gulf of St. Lawrence

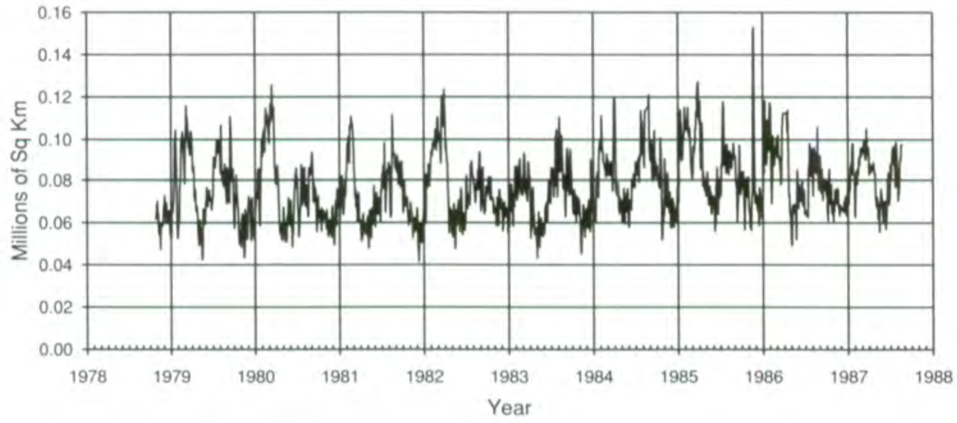
Open Water Within the Pack in the Gulf of St. Lawrence

Figure 3.7.2. Sea ice extent, sea ice area, and amount of open water within the pack for the Gulf of St. Lawrence from October 26, 1978 to August 20, 1987. The misleading indication of ice during the summer months is the result of a temperature-dependent land effect.

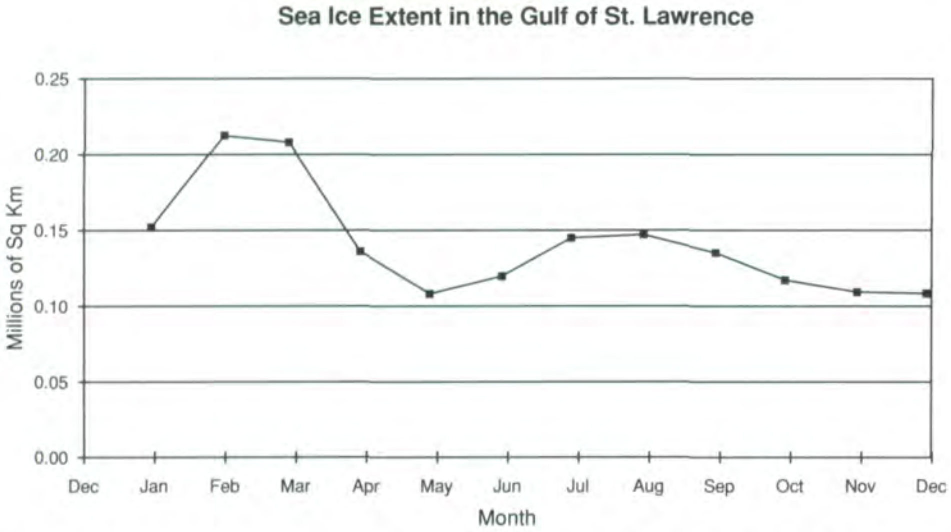

Figure 3.7.3. Average seasonal cycle of sea ice extents for the Gulf of St. Lawrence. The misleading indication of ice during the summer months is the result of a temperature-dependent land effect.

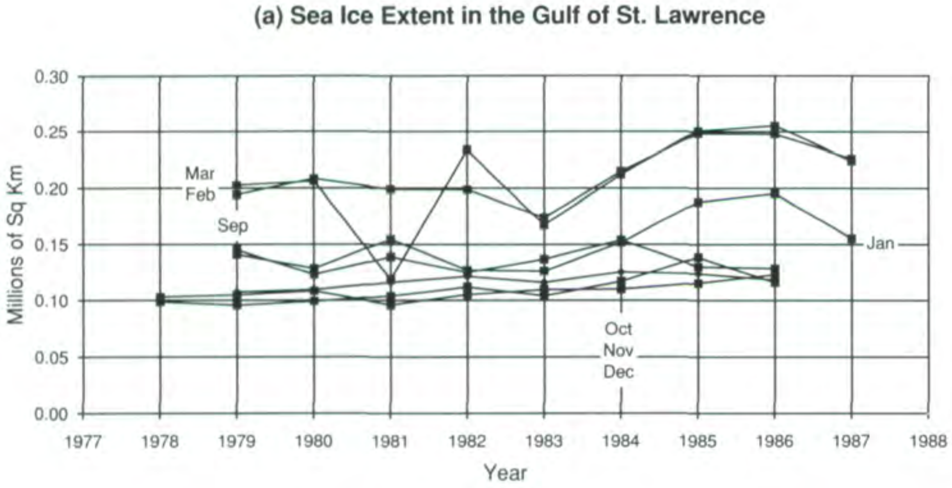

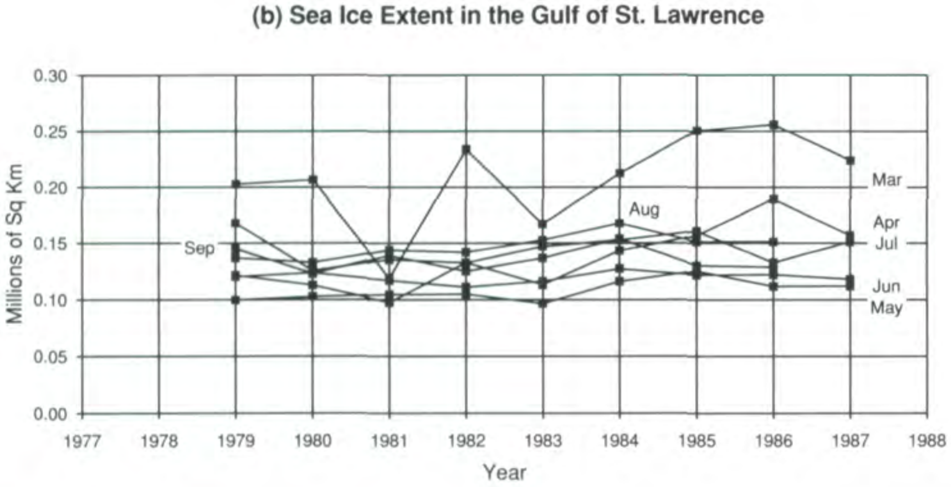

Figure 3.7.4. Month-by-month, year-to-year changes of the sea ice extents of the Gulf of St. Lawrence, (a) September to March, (b) March to September.

western portion. For March 1985, the month with the second highest ice-extent maximum, the spatial anomaly patterns are reversed. Other anomaly maps for January to March also show large spatial variability (Figures 3.1.16 -3.1.18).

For the winter months, December through March, the ice extents from 1984 through 1987 are generally greater than their corresponding values for the earlier SMMR years. As with the Hudson Bay results, the cooling trend associated with the greater ice extents could be connected to a cooling in the North Atlantic (e.g., Wigley, 1989; Houghton et al., 1990).

3.8 Greenland Sea

The region consisting of Fram Strait and the Greenland Sea (Figure 3.8.1) has been the locale for a number of field experiments that took place before and during the lifetime of SMMR, as mentioned in Chapter 2. In addition to providing data for developing and testing the SMMR sea ice algorithm, these experiments provided detailed information about air-ice-ocean processes. The first expeditions were the Norwegian Remote Sensing Experiment (NORSEX Group, 1983), which took place in the Fram Strait region in 1977 and 1978 (Svendsen et al., 1983), which revealed eddy formations near the ice edge that are important in energy-exchange processes. These were followed by a series of experiments in 1983, 1984, and 1987 called the Marginal Ice Zone Experiments (MIZEX) (Johannessen, 1984a, 1984b; Shuchman et al., 1984.) These three experiments used SMMR sea ice-ocean observations in a near-real-time mode to aid in their execution. The sequential mesoscale aircraft microwave and in situ oceanographic observations provided detailed information on the structure and dynamics of ice-ocean eddies (Johannessen, O.M., et al., 1987; Johannessen, J.A., et al., 1987; Campbell et al., 1987; Shuchman et al., 1987).

Another result from these field studies has been the realization that certain features along the ice edge in this area occur with regularity. One of these features is a small ice protrusion that appears under low wind conditions (Campbell et al., 1987; Gloersen and Campbell, 1988b) over the Malloy Deep at 79°8' N and 2°50' E, resulting from a gyre that regularly forms there and that transports ice outwards from the edge. Since this feature disappears under high wind conditions (ibid.), it is difficult to see in the monthly averages (Figures 3.1.3-3.1.14), but can be seen in the enlargements of single-day images in Figure 3.8.2, obtained during the MIZEX in 1987. Indeed, the wavy nature of the ice edge, in general, under low wind conditions is thought to result from similar eddies that occur elsewhere (Campbell et al., 1987). These single-day images depict significant variations in the spatial distribution of sea ice over short time scales.

As can be seen in the single-day images obtained near the maximum extents for each year during 1979-1987 (Figure 3.8.3), the interannual variations in the spatial distribution of sea ice, as well as the time of its

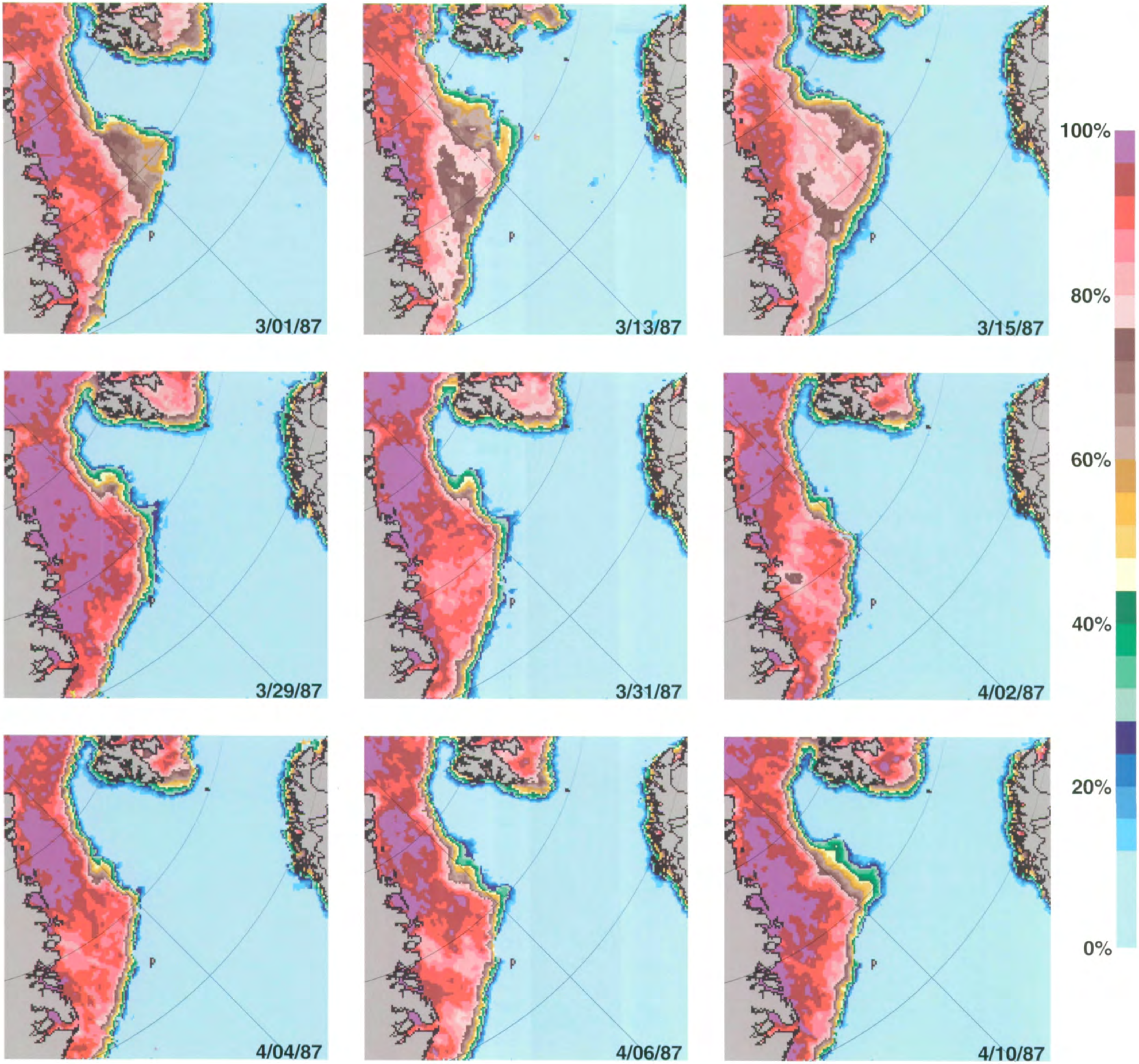

Figure 3.8.2. Single-day images of ice concentrations during MIZEX 87.

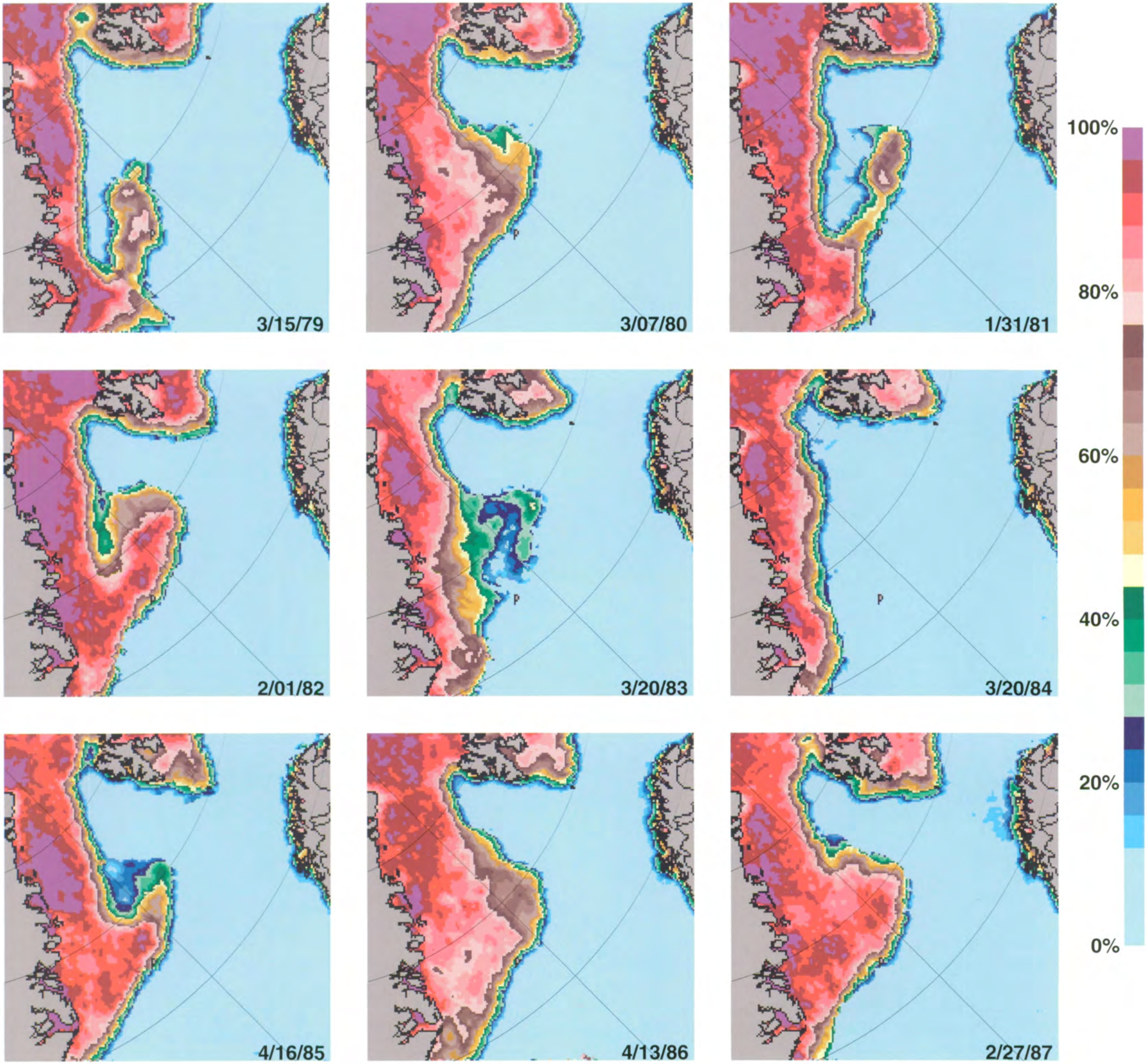

Figure 3.8.3. Single-day images of ice concentrations near the sea ice extent maxima, 1979-1987.

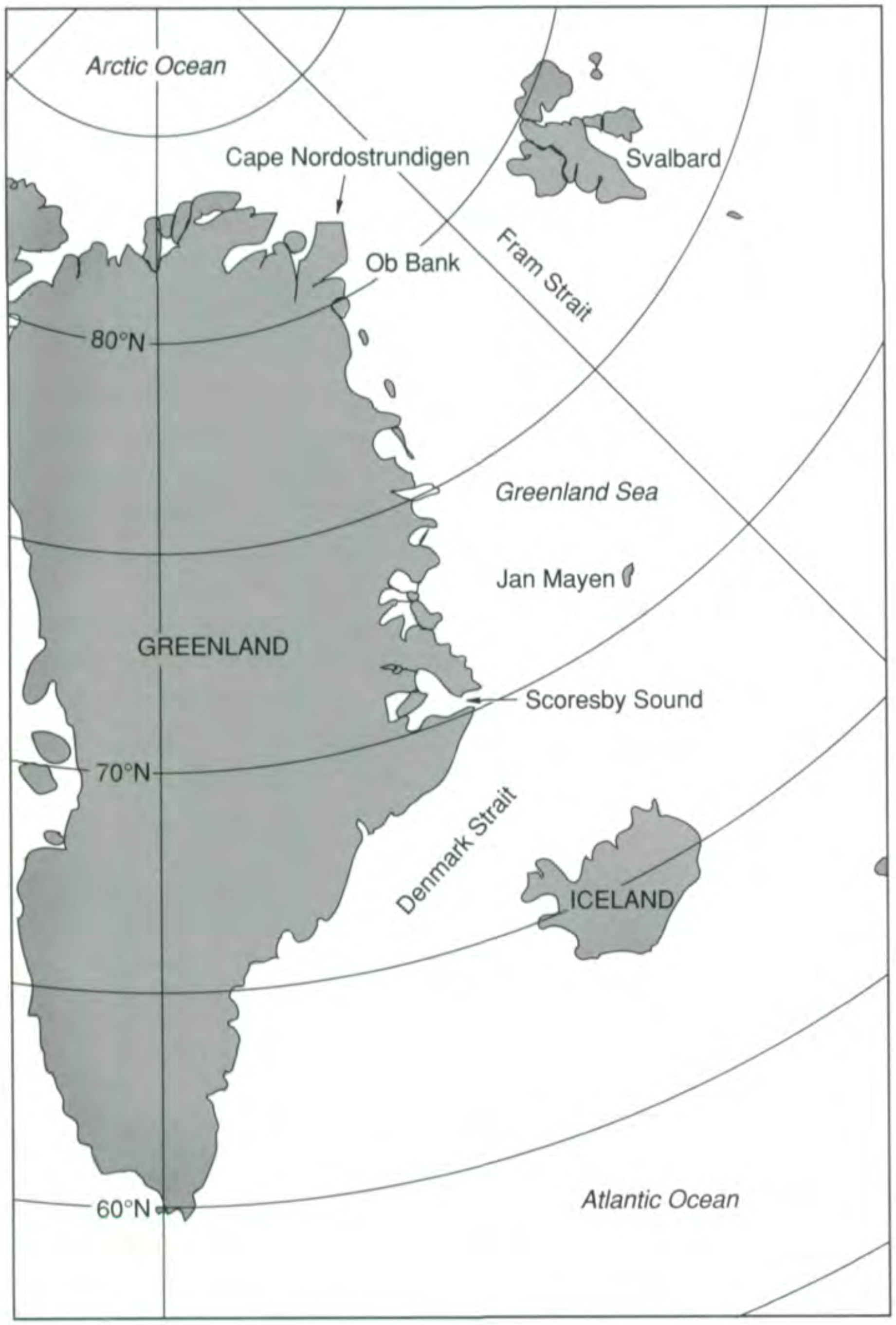

Figure 3.8.1. Location map for the Greenland Sea.

maximum extent in the Greenland Sea, vary considerably. The "Odden," so named by ancient Norse mariners, is a protuberance of sea ice in the East Greenland Current that extends several hundred kilometers into the Greenland Sea, sometimes to the east of the Greenwich Meridian. The rapid 2-4-day changes of this zonal ice-edge extent centered at 74° N appear to be an annual event normally encountered toward the end of the winter season (Figure 3.8.3). Under the appropriate atmospheric conditions, the Odden appears in the cold waters transported away from Greenland in an oceanic feature

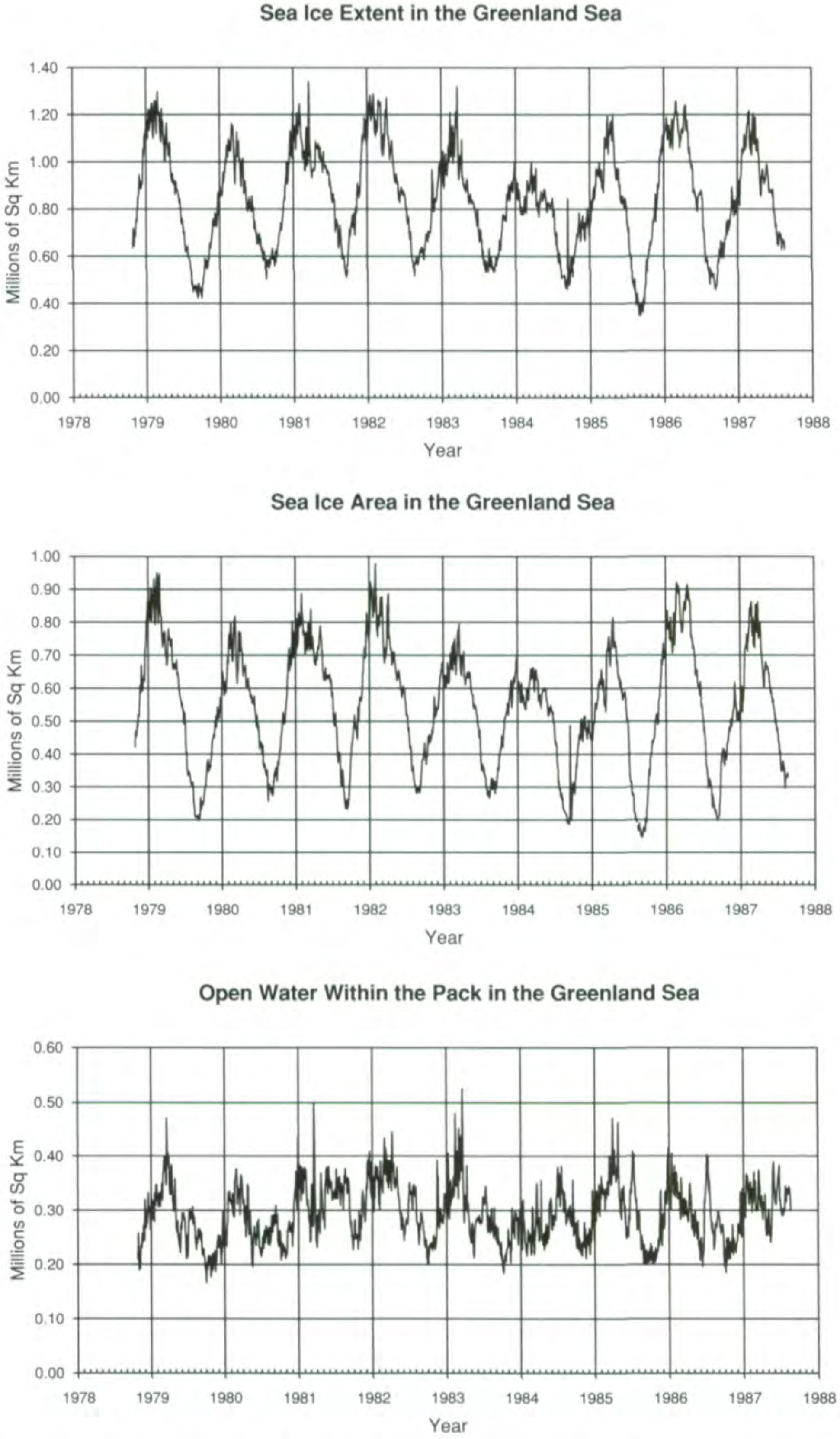
Sea Ice Extent in the Greenland Sea

Sea Ice Area in the Greenland Sea

Open Water Within the Pack in the Greenland Sea

Figure 3.8.4. Sea ice extent, sea ice area, and amount of open water within the pack for the Greenland Sea from October 26, 1978 to August 20, 1987.

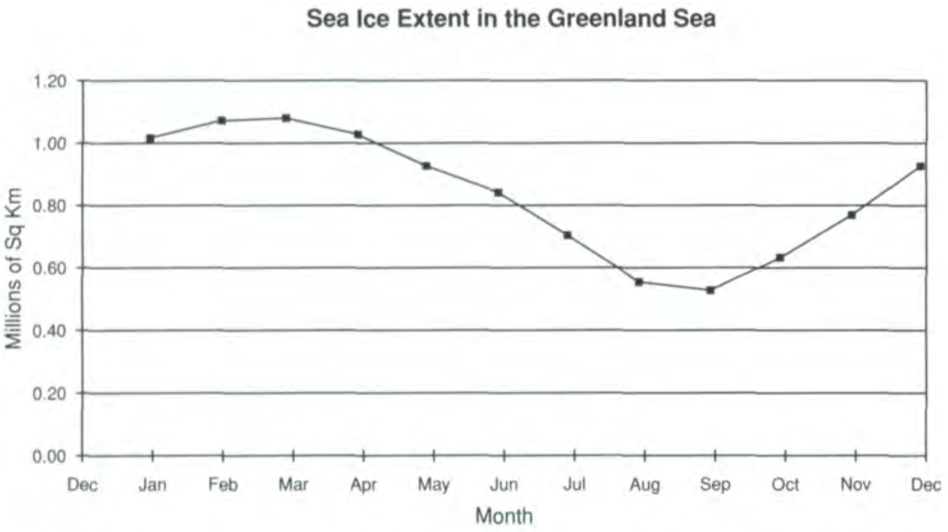

Figure 3.8.5. Average seasonal cycle of sea ice extents for the Greenland Sea.

(a) Sea Ice Extent in the Greenland Sea

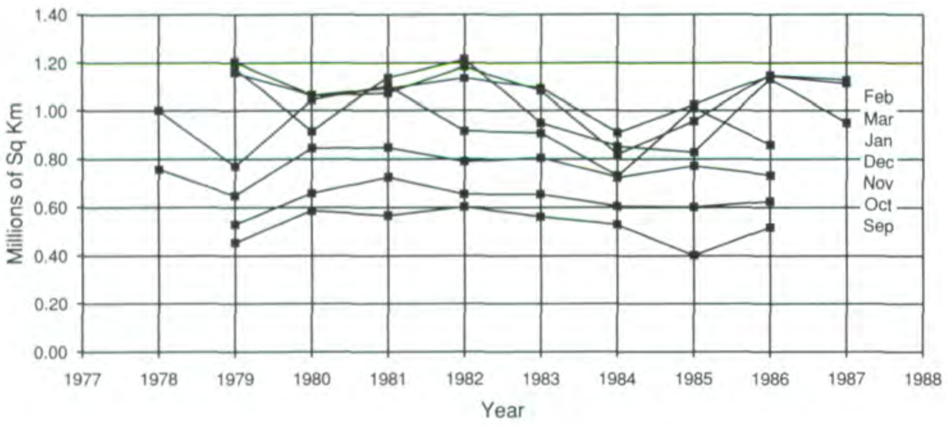

(b) Sea Ice Extent in the Greenland Sea

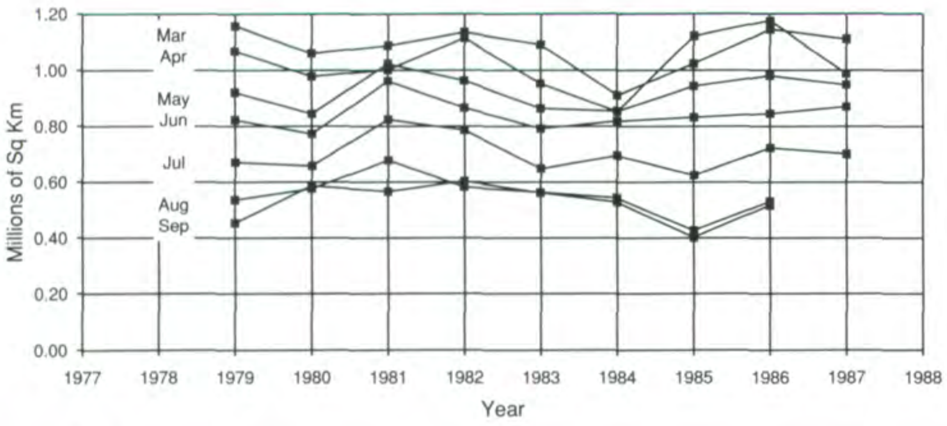

Figure 3.8.6. Month-by-month, year-to-year changes of the sea ice extents of the Greenland Sea, (a) September to March, (b) March to September.

known as the Jan Mayen Gyre. The sudden occurrence of the Odden has been reported for centuries by Scandinavian fisherman and sealers.

As can be seen in Figures 3.1.3-3.1.14, the Odden appears in all of the years of SMMR operations except for 1984 . Its absence in 1984 is probably a result of unusually warm local weather conditions during that year, but this conjecture remains to be substantiated by closer scrutiny of the weather records for the 8-year period, a task in progress. On average, the Odden begins its appearance in December, reaching its maximum extent and total area in February and disappearing by May. In the winters of 1978-1979, 1981-1982, and 1985-1986, the Odden appeared earlier in December and was greater in area in February than the average. During the winter of 1979-1980, the February maximum was not as great as the years just cited, but it was again above average in areal coverage, after a later-than-usual start in its formation. In 1981, again after a later-than-usual start the previous December, the Odden was at its peak in January rather than the usual February.

During a given winter, rapid oscillations in extent of the Odden, as well as in its areal coverage by sea ice is evident. Sometimes the Odden separates from the main Greenland Sea ice pack and persists for a week or so in the open sea as a separate raft of ice. At other times, it forms as a disconnected raft of ice, later to grow into the main pack. The detailed shape of the Odden varies from year to year, but it generally forms in the east-to-northward-flowing portion of the Jan Mayen Gyre. Associated with the Odden is an area of warmer water just to its north, sometimes ice-free, which was called the "Nordbukta," or northern bay, by the early Norse fishermen.

Time series of sea ice extent and the area covered by sea ice in the Greenland Sea region for the nearly 9-year operation period of the SMMR are shown in Figures 3.8.4.-3.8.6. There are a number of noteworthy features in the oscillatory record of the sea ice in these figures. The amplitude of the annual cycle varies by as much as 60% during the 9-year period, with the smallest peak occurring in 1984, the only year in which the Odden was absent. There appears to be a slow oscillation in the amplitude of the peaks, with a period of about 4 years.

On a shorter time scale, there appear to be oscillations with a period of about a month superimposed on the annual cycle. This phenomenon is currently under investigation, but it appears to correspond to an aliasing of the time interval between SMMR observations at a given location (about 48.6 hours) and the M_2 (Principal Lunar) tidal period (12.421 hours), which results in an alias period of about 24 days. The working hypothesis for this investigation is that the ice-edge relaxation has the period associated with the horizontal M_2 tidal currents, which is recorded by the SMMR at different phases of the tide at each observation.

On still shorter time scales, the spikes are not instrument noise, but are attributable to sudden changes in the ice distribution related to the passage of weather systems. The 8.8-year record of open water within the pack in the Greenland Sea (Figure 3.8.4) shows a remarkable lack of seasonal signal, the areas of open water generally being in the range of 2-4 x 10^5 km^2.

The location of the ice perimeter near its maximum extent varies both spatially and temporally, as illustrated in Figure 3.8.3. Most of the interannual variation in the spatial distribution of growth and decay of sea ice in the Greenland Sea (Figure 3.8.4) near its maximum extent takes place in the general vicinity of the Odden and Nordbukta.

Multiyear sea ice has been observed in the Greenland Sea from airborne and surface platforms, presumably as a result of advection from the Arctic Basin (Parkinson et al., 1987). The SMMR record shows less multiyear ice than is actually present principally because of the conservative 20% lower limit we have placed on the sea ice algorithm outputs in order to reduce the occurrences of false indications of multiyear ice. Furthermore, a limited number of field measurements have indicated that the multiyear ice in this region is not as thick as in the Arctic Basin, which also would tend to cause the SMMR to give indications of less multiyear ice than is actually present (see Chapter 2). On the other hand, multiyear ice does appear and disappear in limited regions on time scales shorter than the season in the monthly averages during most winters, suggestive of transport from the north. Indeed, in viewing a sequence of single-day images (not shown), a southward flow of the multiyear patterns is indicated. However, one must be cautious in interpreting the calculations of multiyear sea ice concentration here. Since the Greenland Sea is a perimeter sea, it is subject to heavy snow accumulation and metamorphosis, which could lead to false indications of multiyear ice. On the other hand, this area is subject to strong storms that can result in waves washing over the sea ice and an accompanying decrease in the calculated multiyear sea ice concentrations.

3.9 Kara and Barents Seas

The Kara and Barents Seas (Figure 3.9.1), separated by the island of Novaya Zemlya, are located to the north of Scandinavia and western Russia. They contrast sharply in their oceanographic properties, with Novaya Zemlya providing an effective barrier between the cold Arctic waters in the Kara Sea and the much warmer waters in the Barents Sea, the latter being influenced significantly by the relatively warm inflow from the Norwegian Current. The temperature difference is matched by a corresponding difference in the sea ice coverage, with the Kara Sea exhibiting a high-concentration sea ice cover for much of the year and the Barents Sea often remaining predominantly ice-free even in the midst of winter.

The typical yearly sea ice cycle for the Kara Sea during the SMMR period 1978-1987 shows the minimum ice coverage to occur in September, when the sea is free of ice except in its northernmost portion (Figure 3.1.15). During the autumn growth period, the ice edge moves southward to about 75° N in October and to 70° N in November. By December, ice covers almost the entire sea, with concentrations predominantly above 90%. Near-total ice coverage remains through May, after which small openings appear along the coast in June. These openings expand considerably in July, with ice concentrations in the rest of the sea generally reduced to 44%-76%. By August, the Kara Sea is largely free of ice south of 75° N, and by September, the ice edge has retreated northward another 1°-2° latitude.

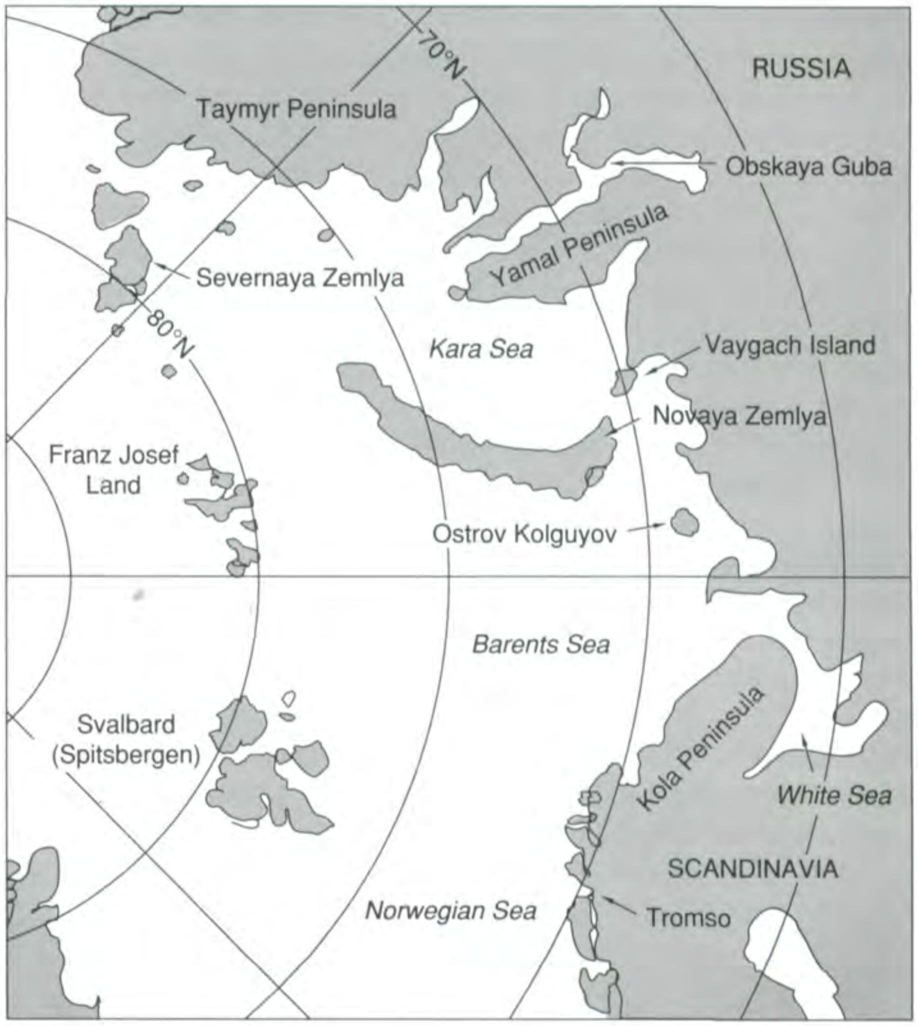

Figure 3.9.1. Location map for the Kara and Barents Seas.

The Barents Sea is almost entirely free of ice in August and September, after which the ice edge progresses southward to about 78° N in October, 77° N in November, 75° N in December, and 74° N in January, February, and March. Beginning in December, ice growth also proceeds westward from Novaya Zemlya, so that by March, most of the sea east of 45° E is ice-covered. A slight amount of growth continues from both the north and east in April, when the maximum ice extent is reached. Ice decay begins with a lessening of ice concentrations throughout most of the sea in May, followed by an eastward ice-edge retreat to the coast of Novaya Zemlya in June and a northward retreat to about 77° N in July and 79° N in August (Figure 3.1.15).

Considering the combined Kara and Barents Seas, the total sea ice extent shows an average seasonal sea ice cover (Figure 3.9.3) expanding from a

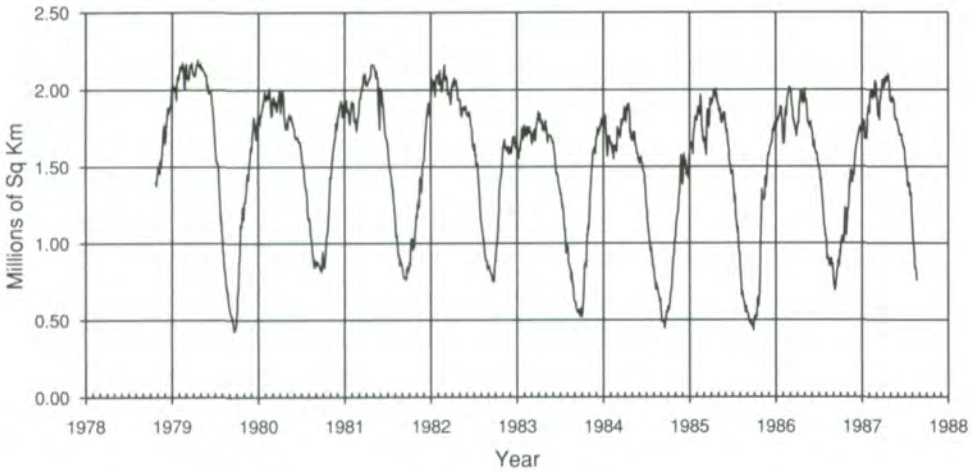
Sea Ice Extent in the Kara and Barents Seas

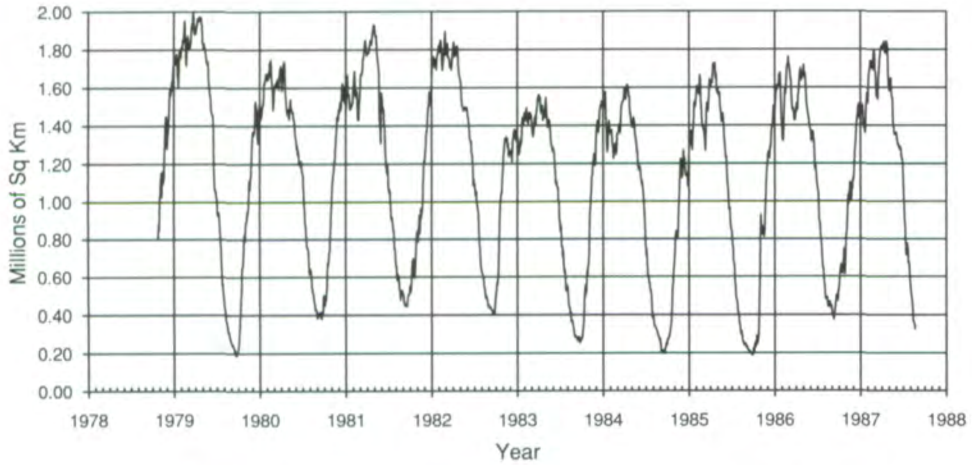
Sea Ice Area in the Kara and Barents Seas

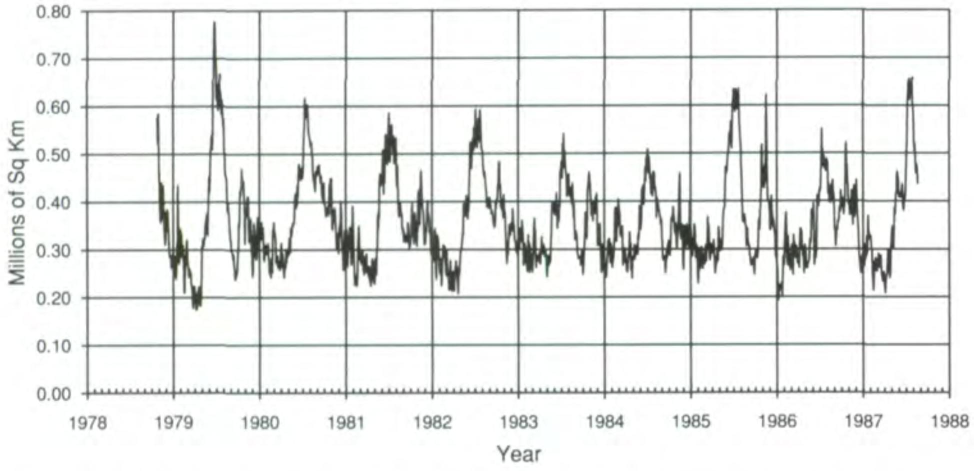
Open Water Within the Pack in the Kara and Barents Seas

Figure 3.9.2. Sea ice extent, sea ice area, and amount of open water within the pack for the Kara and Barents Seas from October 26, 1978 to August 20, 1987.

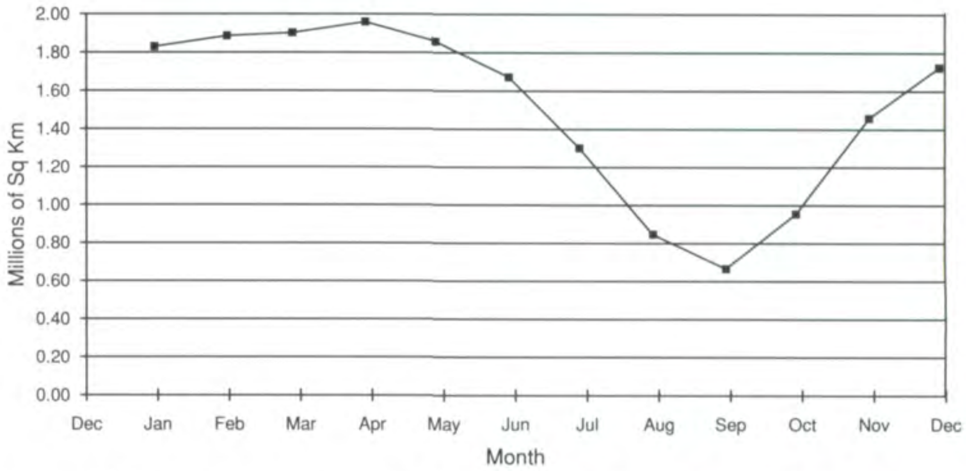
Sea Ice Extent in the Kara and Barents Seas

Figure 3.9.3. Average seasonal cycle of sea ice extents for the Kara and Barents Seas.

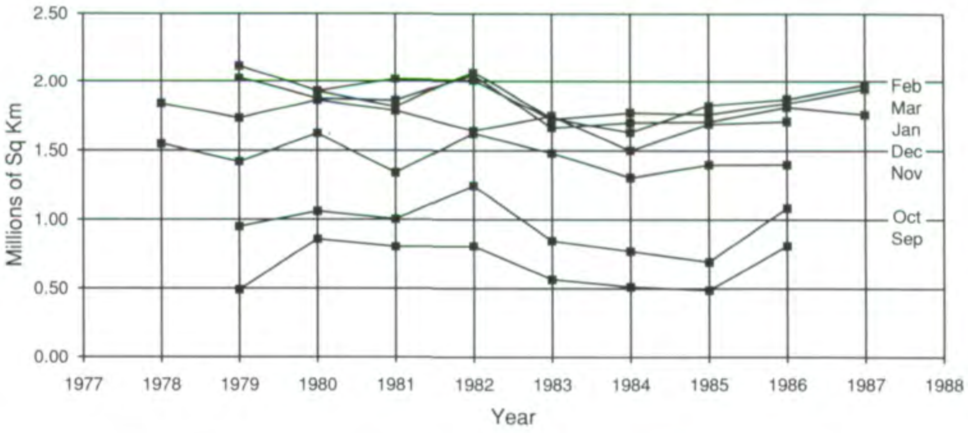
(a) Sea Ice Extent in the Kara and Barents Seas

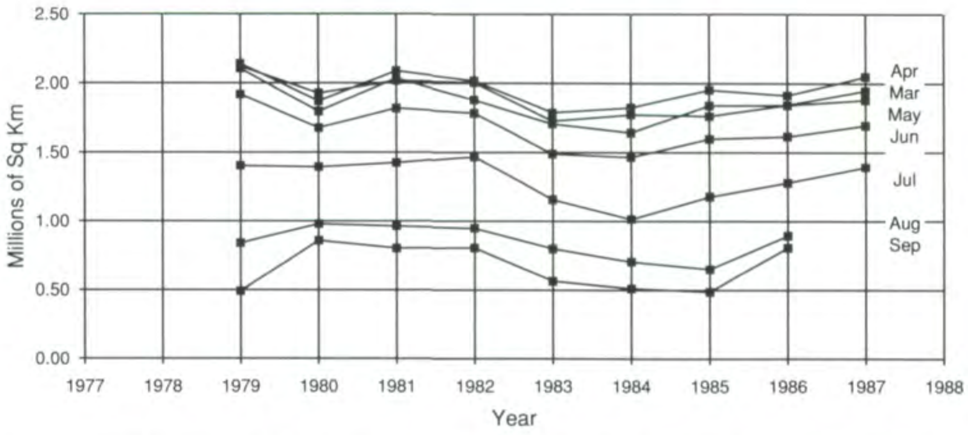
(b) Sea Ice Extent in the Kara and Barents Seas

Figure 3.9.4. Month-by-month, year-to-year changes of the sea ice extents of the Kara and Barents Seas, (a) September to March, (b) March to September.

minimum of 0.7 x 10^6 km^2 in September to a maximum of 1.9 x 10^6 km^2 in April. Although some multiyear ice is transported into the Kara and Barents Seas from the central Arctic, and some is formed in situ, the 9-year-average monthly maps do not show multiyear ice concentration exceeding 20% in the region (Figure 3.1.36).

Similarly to the Greenland Sea, the Kara and Barents Seas region exhibits strong interannual differences in both the summer and the winter months (Figures 3.1.3-3.1.14, 3.9.2, and 3.9.4). Although monthly average minimum ice extent consistently occurs in September, the magnitude of the minimum ranges from a low of 0.5 x 10^6 km^2 in September 1979 and 1985 to a high of 0.9 x 10^6 km^2 in September 1980 (Figure 3.9.4). The September differences are quite noticeable in the ice-concentration maps (Figure 3.1.11) and occur predominantly in the northern Kara Sea between 75° and 80° N. This zone is almost entirely ice-covered in September 1980 but almost entirely ice-free in September 1979 and 1985, with the ice covers in the remaining Septembers being intermediate between these extremes (Figure 3.1.11).

Maximum ice extent in the Kara and Barents Seas exhibits sharp interannual variations in timing, as well as magnitude. The month of maximum ice extent is February in 1980 and 1982, and April in 1979, 1981, and 1983-1987 (Figure 3.9.4). During the ESMR years, it was January in 1976, March in 1975, and April in 1974 (Parkinson et al., 1987). The magnitude of maximum ice extent over the SMMR years varies from a minimum of 1.8 x 10^6 km^2 in April 1983 to a maximum of 2.2 x 10^6 km^2 in April 1979. Since 1983, the maximum ice extent has generally been increasing (Figure 3.9.2).

Spatial variations in maximum ice coverage in the Kara and Barents Seas region occur predominantly in the Barents Sea. In April 1983, most of the Barents Sea is free of ice except in the area north of 76° N and in the area east of 45° E. Where there is ice in the Barents Sea in April 1983, it is generally of concentrations under 90%. By contrast, in April 1979, a large area of the Barents Sea has ice with concentrations exceeding 96%, and ice covers almost all of the sea north of 75° N and almost all of the sea east of 40° E (Figure 3.1.6). In the Kara Sea, the ice cover is complete at maximum ice coverage in each year, and with very high ice concentrations. For instance, in April 1983, most of the Kara Sea has ice concentrations exceeding 96%, and the rest of the sea, along its southern and eastern boundaries, has concentrations between 88% and 96%. In April 1979, ice concentrations exceed 96% throughout the Kara Sea (Figure 3.1.6).

3.10 Canadian Archipelago

Undoubtedly the most geographically complex part of the Arctic in which sea ice exists is the Canadian Archipelago, a vast labyrinth of generally shallow straits, bays, sounds, islands, channels, and peninsulas (Figure 3.10.1), throughout which all types of sea ice flow. The morphology and dynamics of the sea ice in the archipelago are as complex as its geography, and the existence of significant amounts of grounded ice further complicates the sea ice picture. The ESMR observations (Parkinson et al., 1987) show that significant interannual variabilities in ice types occur throughout the archipelago. An analysis of sequential Landsat imagery acquired early in the ESMR period during March through November 1973 (Ramseier et al., 1975) found that, although the ice motion within the archipelago was complex, a general pattern existed, similar to that observed earlier by ships and aircraft: an advection of ice southward through the many channels and straits between the northern islands of the archipelago into the large east-west Parry Channel, made up of M'Clure and Barrow Straits and Viscount Melville and Lancaster Sounds, with an eastward flux through Lancaster Sound into Baffin Bay, and a westward flux out of Amundsen Gulf into the Beaufort Sea. Ramseier et al. (1975) observed ice velocities as great as 58 km per day in Lady Ann Strait and between 20 and 30 km per day in Amundsen Gulf. The advection of ice southward through the channels of the northern islands in the eastern sector of the archipelago and then eastward through Jones and Lancaster Sounds into Baffin Bay has also been found by Dunbar (1973), Dey (1981), and Ito (1982) from analyses of aircraft, NOAA (visible and infrared), and Landsat observations. Dunbar (1973) estimates this flux in the early 1970s to be as great as 225 km^3 per year, and Dey (1981) estimates that for the period 1974 through 1978, it averaged 201 km^3 per year.

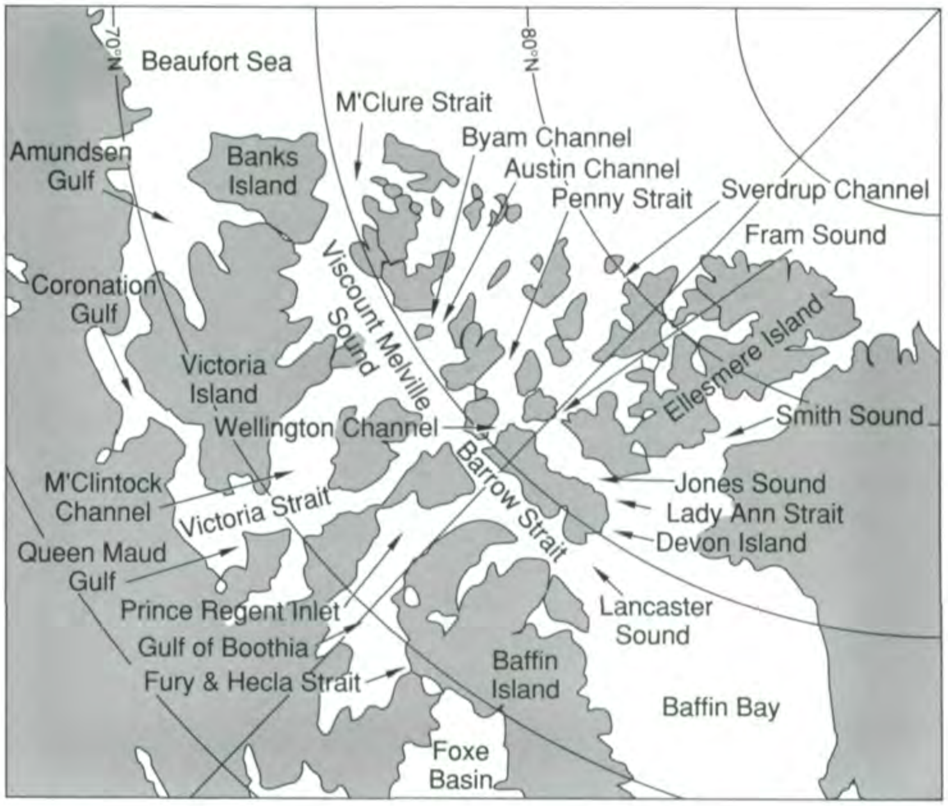

Figure 3.10.1 . Location map for the Canadian Archipelago.

The Canadian Archipelago region has by far the highest ratio of coastline length to maximum ice area of all the regions. Therefore, it is

Sea Ice Extent in the Canadian Archipelago

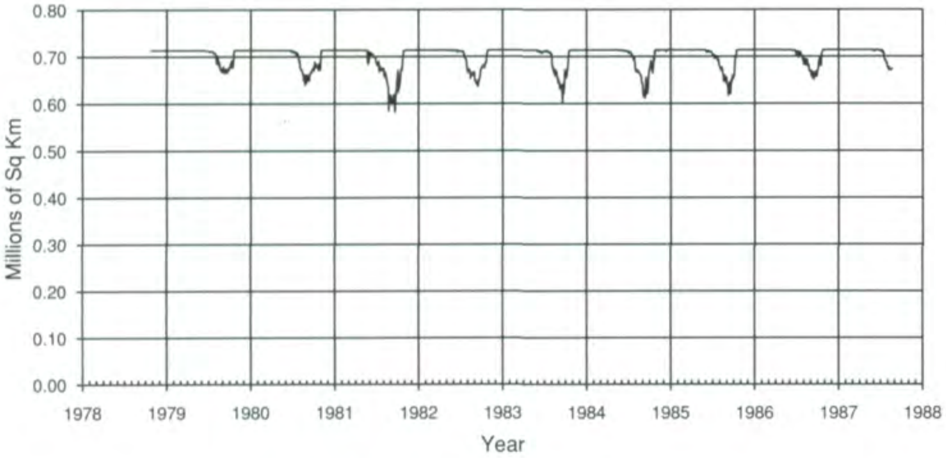

Sea Ice Area in the Canadian Archipelago

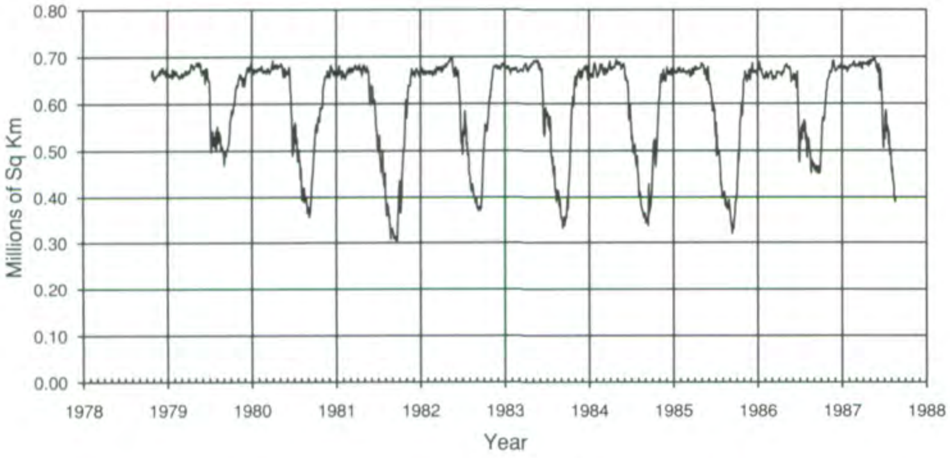

Open Water Within the Pack in the Canadian Archipelago

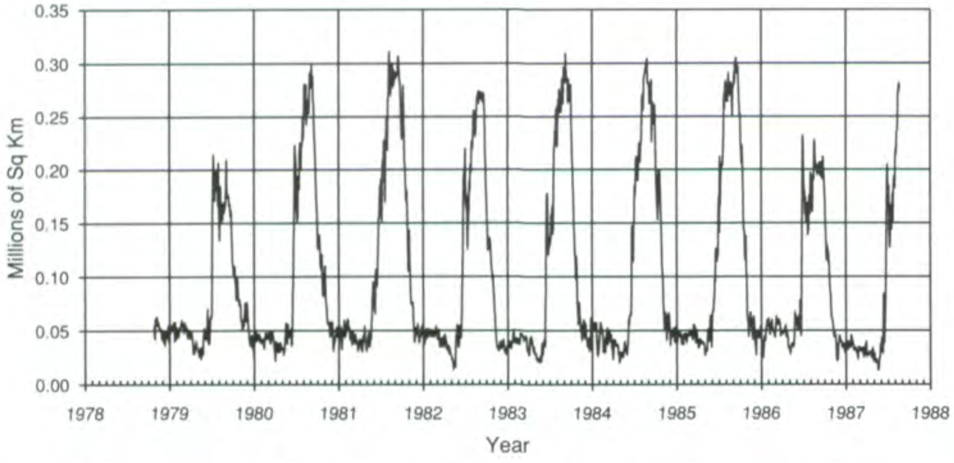

Figure 3.10.2. Sea ice extent, sea ice area, and amount of open water within the pack for the Canadian Archipelago from October 26, 1978 to August 20, 1987.

Sea Ice Extent in the Canadian Archipelago

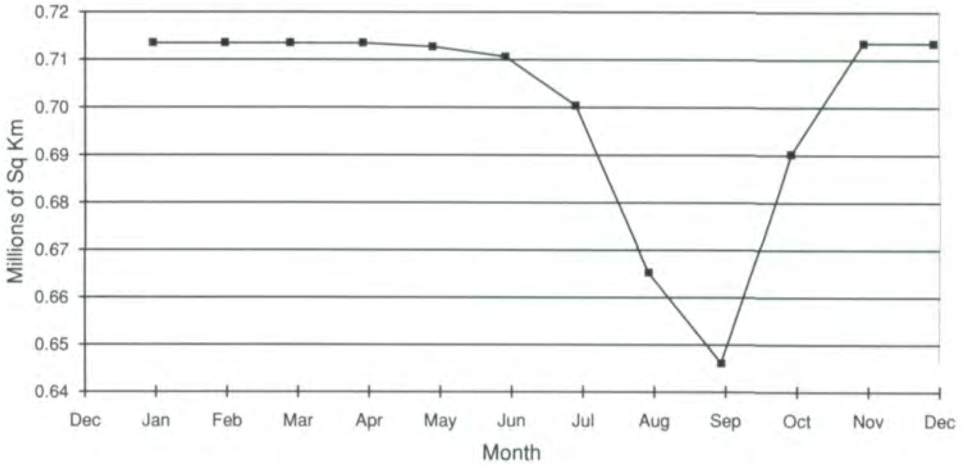

Figure 3.10.3. Average seasonal cycle of sea ice extents for the Canadian Archipelago.

(a) Sea Ice Extent in the Canadian Archipelago

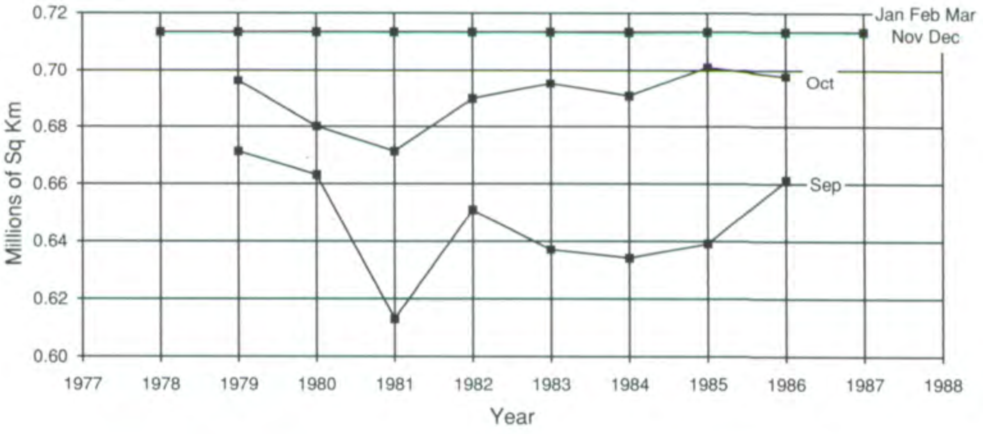

(b) Sea Ice Extent in the Canadian Archipelago

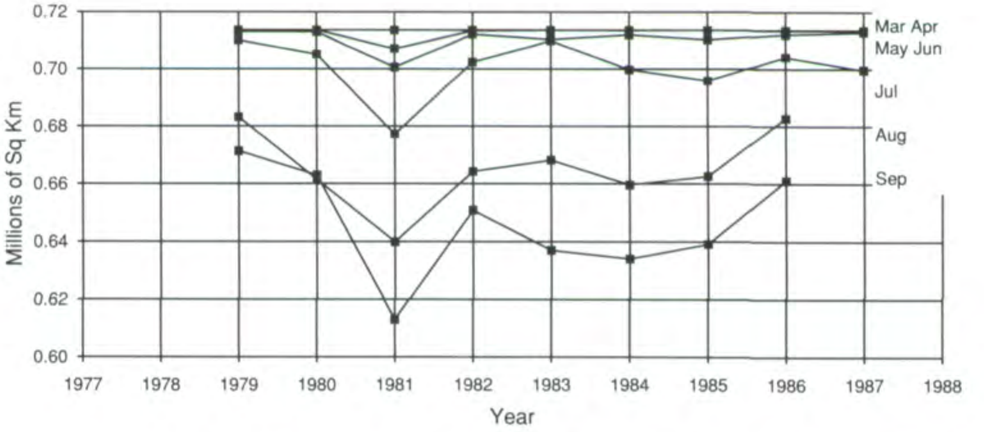

Figure 3.10.4. Month-by-month, year-to-year changes of the sea ice extents of the Canadian Archipelago, (a) September to March, (b) March to September.

particularly important to keep in mind the land spillover effects described in Section 2.2.3 when considering the ice minima described in the following paragraph.

Averaged over the 8.8-year SMMR period, the ice extents range from 0.65×10^6 km^2 during the summer minimum to the fully extended winter maximum of 0.71×10^6 km^2, which persists for about 8 months each year (Figures 3.10.2-3.10.4). Within the range, significant interannual variabilities occur (Figure 3.10.2), with a summer low extent of 0.60×10^6 km^2 in 1981 and a summer high of 0.68×10^6 km^2 in 1979. The archipelago is never completely ice-covered during 1978-1987. The area of open water within the pack during each winter averages 0.05×10^6 km^2 (Figure 3.10.2), with only minor interannual variations. However, this is not the case for the summer, when the amount of open water ranges from a low of 0.17×10^6 km^2 in 1979 to a high of 0.29×10^6 km^2 in 1981 (Figure 3.10.2). On the average, 36% of the archipelago is ice-free during the August-September period of maximum summer melt.

The average spatial variations of ice concentrations in the archipelago occurring during 1978-1987 are shown in the 9-year average monthly ice-concentration maps (Figure 3.1.15). The open water maximum occurs in September, when Amundsen Gulf is ice-free, the Queen Maud Gulf, the Gulf of Boothia, and Lancaster Sound have ice concentrations in the range 24%-40%, the central channels have ice concentrations in the range 40%-72%, and the northern channels are in the 80%-92% range. At the start of freeze-up in October, all of the central and northern channels are almost fully ice-covered, with the exception of Lancaster Sound (C_T = 56%-68%), whereas many southern areas still have reduced ice concentrations—28%-36% in Amundsen Gulf, 40%-48% in Coronation Gulf, and 56%-72% in Queen Maud Gulf. By November, the entire archipelago is covered with ice concentrations in the high range 84%-100%, and by midwinter in January, all ice is above 88% ice concentration. This universally high ice concentration persists until the start of breakup in May, when Lancaster Sound and Amundsen Gulf experience ice concentrations reduced to the 80%-92% range. The breakup occurs first primarily in the southern channels. By July, Amundsen and Coronation Gulfs are half ice-free, and Queen Maud Gulf and the Gulf of Boothia are 16%-28% ice-free. As the summer proceeds, the zone of reduced ice concentrations proceeds northward, and in the eastern sector, Jones Sound and Prince Regent Inlet have ice concentrations as low as 30%.

The previous discussion indicates the average behavior of sea ice within the archipelago during 1978-1987. Observations during the last century have shown that great interannual variations occur, especially during freeze-up and breakup. Dey et al. (1979) used a combination of NOAA and Landsat imagery to map the breakup and freeze-up pattern in the archipelago during 1975 through 1977, and these patterns closely match the corresponding ESMR patterns for the years 1975 and 1976 (Parkinson et al., 1987). The variations that occur during 1978-1987 are shown in the monthly ice-concentration maps (Figures 3.1.3-3.1.14) and the monthly ice-concentration-anomaly maps (Figures 3.1.16-3.1.27).

In discussing the freeze-up patterns observed with SMMR, we shall focus on the October averages and anomalies for each year. Data are not available for most of October 1978, and by November all the waterways are ice-covered with high ice concentrations, 88%-100%, corresponding to the average state of freeze-up in November. The freeze-up pattern in October 1979 (Figure 3.1.25) is about average, but with higher than average concentrations in Queen Maud Gulf and the Gulf of Boothia. In October 1980, the pattern shows a less complete freeze-up than average. The least complete October freeze-up during 1978-1987, and also during 1972-1976, occurs in October 1981. Figure 3.1.25 shows that October 1981 has the most negative ice-concentration anomalies (generally, 5%-25%) of all the Octobers over the entire archipelago.

The freeze-up in October 1982 is about average in most of the archipelago, but with Amundsen Gulf ice-free, and, in the southeast, the Gulf of Boothia and Queen Maud Gulf have concentration anomalies of 5%-15%. The following year is a reverse of 1982 in the southern sector where the western waterways are anomalously high and the eastern ones are low in concentration.

October 1984 has a freeze-up pattern similar to 1981, but more complete. All of the southern and central waterways have negative concentration anomalies (-5% to -20%) but the northern ones are only slightly below the average. The October 1985 freeze-up pattern is similar to the one in 1983, with the southwestern waterways having positive ice-concentration anomalies from 10% to 40%, and the southeastern ones low, -10% to -25%. November 1986 is close to average in terms of freeze-up observed with SMMR.

The interannual variations in ice breakup within the archipelago are as great as those for freeze-up. What is invariant about the breakup pattern during 1978-1987, as was also the case during 1972-1976, is that it always starts in the southern waterways of Amundsen, Coronation, and Queen Maud Gulfs and in the eastern central waterways of Lancaster and Jones Sounds. It is the timing of the start and how the breakup commences that vary.

In 1979, all the southern waterways have positive ice-concentration anomalies of 5%-40% during August-September. The only southern waterway that is ice-free during July-September is Amundsen Gulf. This pattern is reversed for breakups in the following 2 years, when all southern waterways have negative ice-concentration anomalies of 5%-15% by July, and the central ones have negative anomalies of 5%-25% in August. In 1981, all of the southern waterways were ice-free in September, as was most of Lancaster Sound. The start of the breakups of 1982 and 1983 is about average in the southern waterways but the pattern differs in the central waterways. In 1982, Lancaster Sound has anomalously low concentrations in July and anomalously high ones in the rest of Parry Channel. In July 1983, Lancaster Sound and Barrow Strait have unusually high concentrations with positive anomalies of 25%, while the western part of Parry Channel is close to average, -5% to +5%.

By July of both 1984 and 1985, essentially all of the southern and central waterways have negative concentration anomalies in the range of 5%-15%, representing the earliest breakups observed with SMMR. The amounts of open water in the southern and central waterways during August of both years are comparable to those in 1981, and together are the greatest observed by SMMR. The situation is reversed in the two following breakups in 1986 and 1987. The breakups are late, with anomalously high ice concentrations during July in the southern and central waterways and higher in August.

The average spatial variations of the multiyear ice concentrations in the archipelago during 1978-1987 are shown in the 9-year average monthly multiyear ice concentration maps (Figure 3.1.36). These maps clearly show that multiyear ice is advected from the Arctic Ocean through the northern channels and into the central archipelago. As explained in Chapter 2, the SMMR-derived C_{MY}s are not accurate until winter conditions exist, and by November, this is the case throughout the archipelago. The average C_{MY} November map shows that at the start of winter, multiyear ice occurs only in the far north of the archipelago, with several channels in the Queen Elizabeth Islands having C_{MY} = 50%-60%. As the winter proceeds, the multiyear ice moves southward through the labyrinthine channels and straits into the central region, such as Viscount Melville Sound and Barrow Strait. This is clearly illustrated in the November through March maps of 9-year monthly multiyear ice concentrations (Figure 3.1.36).

How can we say that this multiyear ice was advected southward rather than created within the central region? Simply, because any multiyear ice that is formed in the archipelago appears by November when the winter conditions are established. Snow accumulation and metamorphosis on the sea ice can adversely affect the accuracies of the SMMR total and multiyear ice concentration calculations, especially for deep and wet snowpacks, as discussed in Chapter 2. We believe that the C_{MY} results given in the November to March maps for the archipelago are close to the actual ones for the same reasons cited in Chapter 2 for the ice in the Arctic Ocean. During the winter, the range of surface air temperatures is sufficiently low, so that no free water can exist in the snow cover (Chang et al., 1976). Also, during this period, the total ice concentration in the channels is above 95% (Figure 3.1.10). Thus, the flux of moisture through the leads to form snow or hoarfrost is low. Snow depths throughout the archipelago are shallow, with depths of typically 10 cm to 30 cm (Findlay and Goodison, 1979), slightly greater than in the Arctic Ocean. As in the Arctic Ocean, the snow cover on the ice in the archipelago is subjected to frequent strong winds, which cause the crystals to blow about and their size to remain small.

Another source of error in C_{MY} that must be considered is its dependence on T_{ice} under freezing conditions, as illustrated for the central Arctic during 1984 in Figure 2.1.1 (e) and (f) from Julian days 300 to 350, and also in Figure 3.2.6 (a). These temperature-dependent changes are, however, proportionately small compared to the changes shown in Figure 3.10.5, which, then, are construed to represent real increases in the amount of multiyear sea ice.

The maximum amount of multiyear ice in the archipelago observed with SMMR (Figure 3.10.5) occurs in March (there may be more in the late spring, but by April the surface warming diminishes the SMMR accuracy in the C_{MY} determination). The amount of multiyear sea ice at its peak varies from 0.26 x 10^6 km^2 in 1979 to 0.14 x 10^6 km^2 in 1986. By March, the southern waterways are predominantly full of first-year ice, with C_{MY} less than 20%, but M'Clintock Channel has C_{MY} = 28%-52%. The central waterway of Parry Channel has C_{MY} = 0%-56%, with 36% in M'Clure Strait, 56% in western Viscount Melville Sound, and 20% or less in Barrow Strait and Lancaster Sound. The northern channels all have C_{MY} = 52%-60%.

The interannual variations of the multiyear ice concentrations in the archipelago are great in the central and northern waterways and minor in the southern waterways, where the total amount is essentially always below 20%. The variations in the central and northern waterways are both in and out of phase, as are those between the eastern and western sectors of the central waterways. In February 1979, these areas had uniformly positive C_{MY} anomalies, from 20% to 45%. In 1980, most areas were about average except for Fram Sound and part of Melville Sound, where anomalies of 25% were reached. The ice concentrations were about average again in 1981, except for anomalies of down to -30% in M'Clure Strait and part of Melville Sound and up to 25% in M'Clintock Channel. Generally negative anomalies were present in the central and northern channels in 1982, 1983, and 1986. In 1983, the anomalies ranged up to 25% in the northern and down to -20% in the central channels. In 1984, the anomalies were generally negative, except for the eastern part of Fram Sound, where the anomaly was as high as 30%. An east-west asymmetry characterizes the anomalies in 1985 and 1987, with anomalies as high as 40% in the west and as low as -25% in the east.

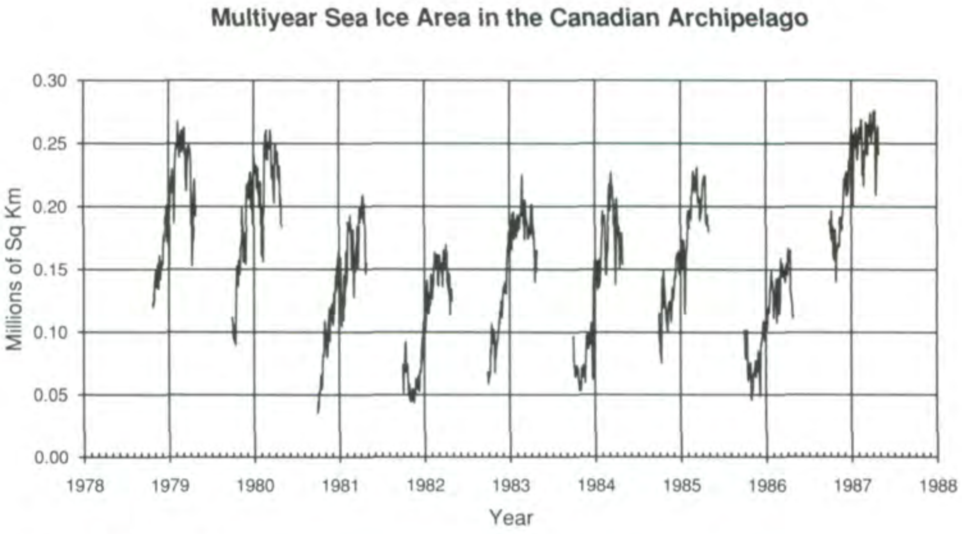

Figure 3.10.5. Time series of areal coverage of multiyear sea ice in the Canadian Archipelago.

Page Intentionally Left Blank

4
ANTARCTIC SEA ICE

4.1 Introduction

The distribution of sea ice around the Antarctic continent is influenced by the atmospheric and oceanic circulations and temperatures in the south polar region, as described in the ESMR Antarctic atlas (Zwally et al., 1983a). An Antarctic location map is shown in Figure 4.1.1. The large-scale circulation of the southern ocean (Figure 4.1.2) is dominated by the eastward-flowing Antarctic Circumpolar Current, which has a total flow estimated to be 127±24 Sverdrups (Fandry and Pillsbury, 1979). The Antarctic convergence, an oceanic polar front characterized by large meridional gradients of temperature, salinity, and density, nominally lies between 50° S and 65° S. Near the polar front, ocean surface temperatures approach 6 °C in summer and 4 °C in winter (Gordon and Molinelli, 1982). The edge of the ice pack, where surface temperatures are near freezing, extends northward in winter to within about 50 to 1000 km of the polar front. Closer to the continent lies the Antarctic divergence, which is generally a region of oceanic upwelling driven by strong prevailing westerlies to the north and prevailing easterly winds near the continent. Another important oceanographic phenomenon is the vertical circulation of the ocean and the associated production of Antarctic bottom water. Freezing of the ocean surface during winter results in the formation of cold, highly saline sea water. The continual production of ice in coastal polynyas, and its northward transport from the continental shelves, is a particularly important

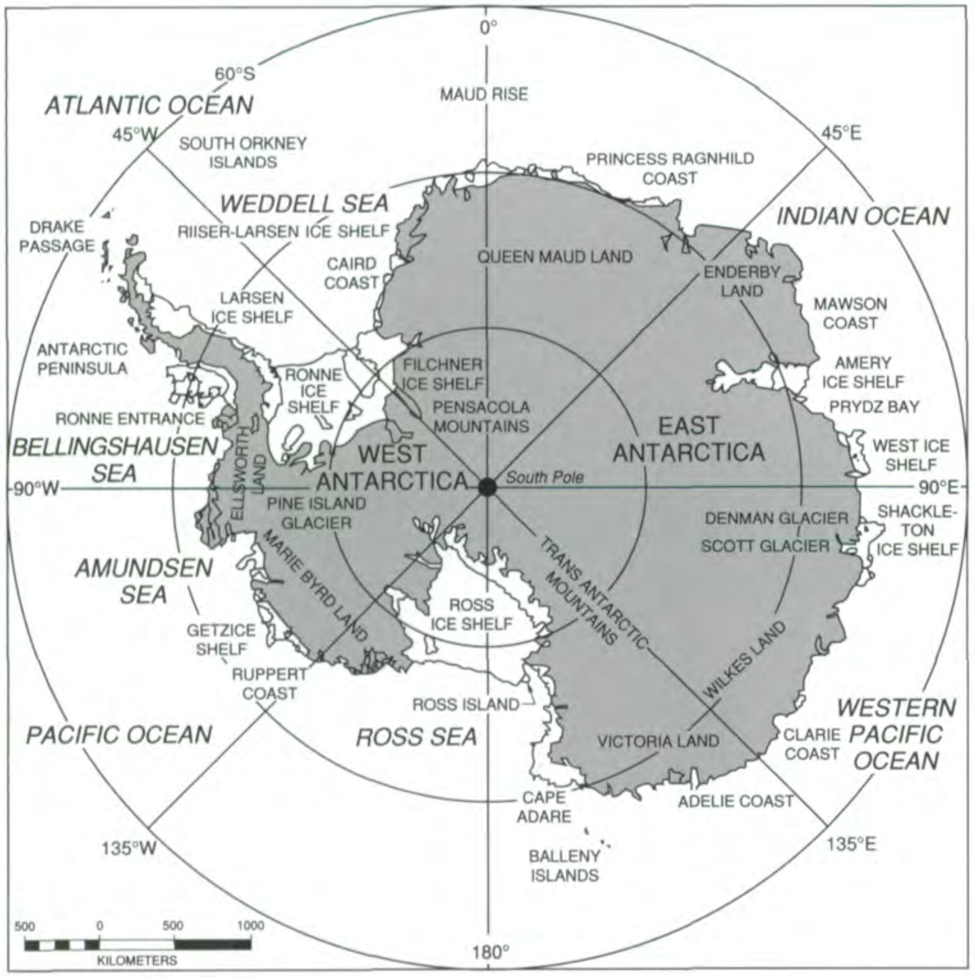

Figure 4.1.1. Antarctic location map.

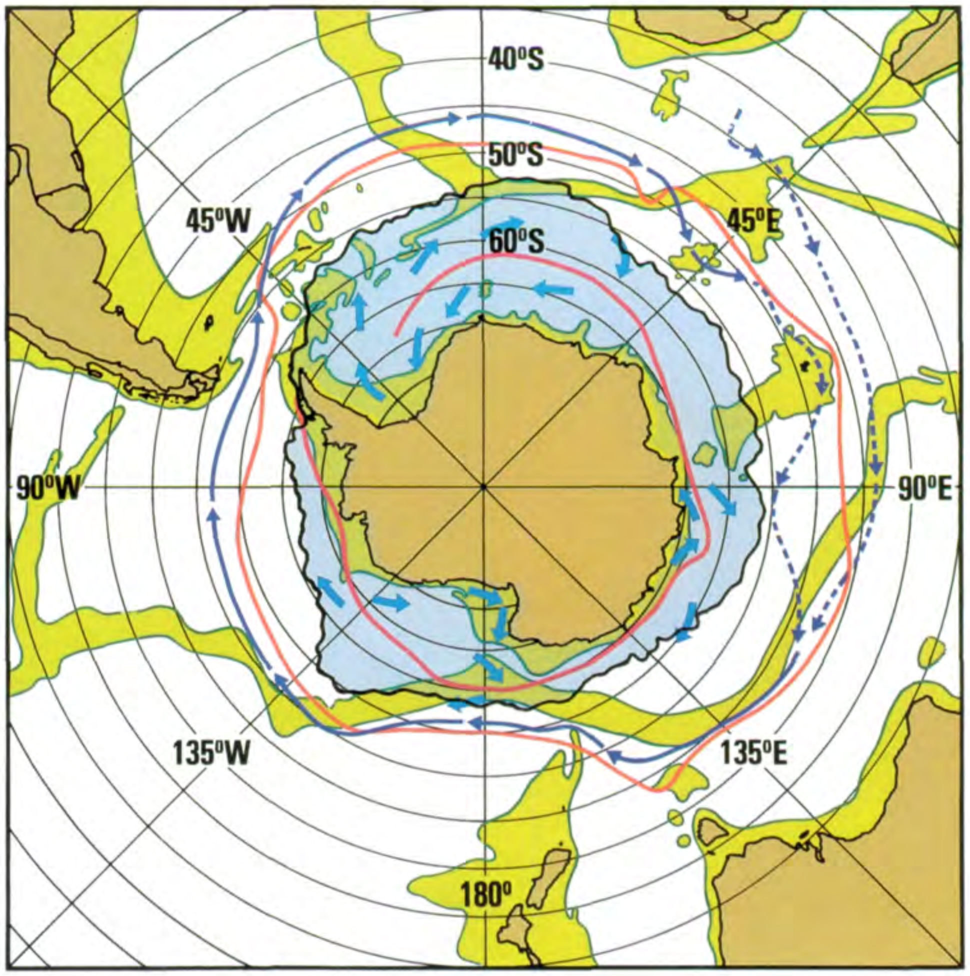

Figure 4.1.2. Antarctic bathymetry and southern ocean circulation.

mechanism for producing dense sea water (Zwally et al., 1985; Cavalieri and Martin, 1985). This dense water flows off the shelves between 70° to 75° S, mixes with circumpolar deep water, and sinks to the bottom as Antarctic bottom water (Gordon, 1974).

Dominant features of the atmospheric circulation are a high-pressure system centered over the East Antarctic plateau and a ring of low-pressure cells between 60° S and 70° S. Particularly intense, semipermanent low-pressure systems are found in winter over the Weddell and Ross Seas and off the east Antarctic coast, forming the so-called Circumpolar Trough. During the summer months, this trough weakens and the semipermanent features are not as well defined (see the climatological sea level pressure maps in the ESMR Antarctic atlas).

Many of the large-scale features of the sea ice distribution and its seasonal cycle have known relationships to the atmospheric and oceanic circulations and temperatures. For example, north-south extensions in the outer edge of the ice pack are related to deflections in the circumpolar current as it crosses submarine ridges in the deep ocean (e.g., at 135° W in Figure 4.1.2). Also, during the autumn months, the 271.2-K isotherm in surface-air temperature moves equatorward ahead of the sea ice edge. After the maximum ice extent occurs during September and October, the freezing isotherm and ice edge are nearly coincident as the ice retreats. Relationships between large-scale atmospheric flow and variations in sea ice extent have been studied (Ackley, 1981; Cavalieri and Parkinson, 1981; Parkinson and Cavalieri, 1982; Sturman and Anderson, 1985; Carleton, 1989). An association has also been observed between the location of the Weddell Polynya of the mid-1970s (Zwally et al., 1976, 1983a; Zwally and Gloersen, 1977; Gordon, 1978; Carsey, 1980) and upwelling of warmer deep water around 0° E (Martinson et al., 1981; Parkinson, 1983), a region of persistent atmospheric low pressure and oceanic divergence.

The relatively large amount of open water (averaging about 21%) and thin ice within the ice pack, unknown before the advent of satellite passive-microwave observations in late 1972 (Gloersen et al., 1974a), implies large fluxes of heat, salt, and moisture between ocean and atmosphere. Many of the quantitative aspects of these implications are only beginning to be explored. For example, recent modeling of the general circulation of the atmosphere (Simmonds and Budd, 1990) included Arctic and Antarctic sea ice concentrations that reflected observed polar differences in the open water measurements using ESMR data. As a consequence of this and similar model studies, Simmonds and Budd successfully simulated the strong southern mid-latitude westerlies and the ring of low-pressure systems around Antarctica near 60° S (Budd, priv. comm., 1990).

Of particular interest is the determination of long-term changes in the extent of the sea ice pack and their relationship to large-scale changes in atmospheric and oceanic temperature and circulation. It was suggested at one point that an overall decline in the ice extent from 1973 to 1980 may be related to a CO_2-induced greenhouse warming of the atmosphere (Kukla and Gavin, 1981). However, the sea ice extent had increased from the 1960s until 1973 (Kukla, 1978), preceding the mid-1970s decline, which was, in turn, followed by an increase. Consequently, several studies (Chiu, 1983; Zwally et al., 1983b; Gloersen and Campbell, 1988a and 1991b) concluded that these variations are characteristic of the large interannual variability of the Antarctic ice pack, and a long-term trend is not detectable in the SMMR data set. Analysis of the sea ice data available through 1981 provides a number of conclusions on the variability of Antarctic sea ice (Zwally et al., 1983b). The observed trends in the sea ice data through 1981 are essentially the same for each of the four seasons and the same in each sector of the southern ocean. For intervals of several years, larger-than-average winter maximum ice extents appear to be associated with smaller-than-average summer minimum ice extents.

In the following sections, the characteristics of the seasonal cycle and interannual variations of the Antarctic ice cover are described for the southern ocean region as a whole and for each of the five sectors (Figure 4.1.3) over the 8.8-year SMMR period. As in Chapter 3 for the Arctic, mean-monthly ice-concentration maps are presented (Figures 4.1.4-4.1.15), as are mean-monthly maps averaged over the SMMR period (Figure 4.1.16). The anomalies in the ice-concentration distribution for each month (Figures

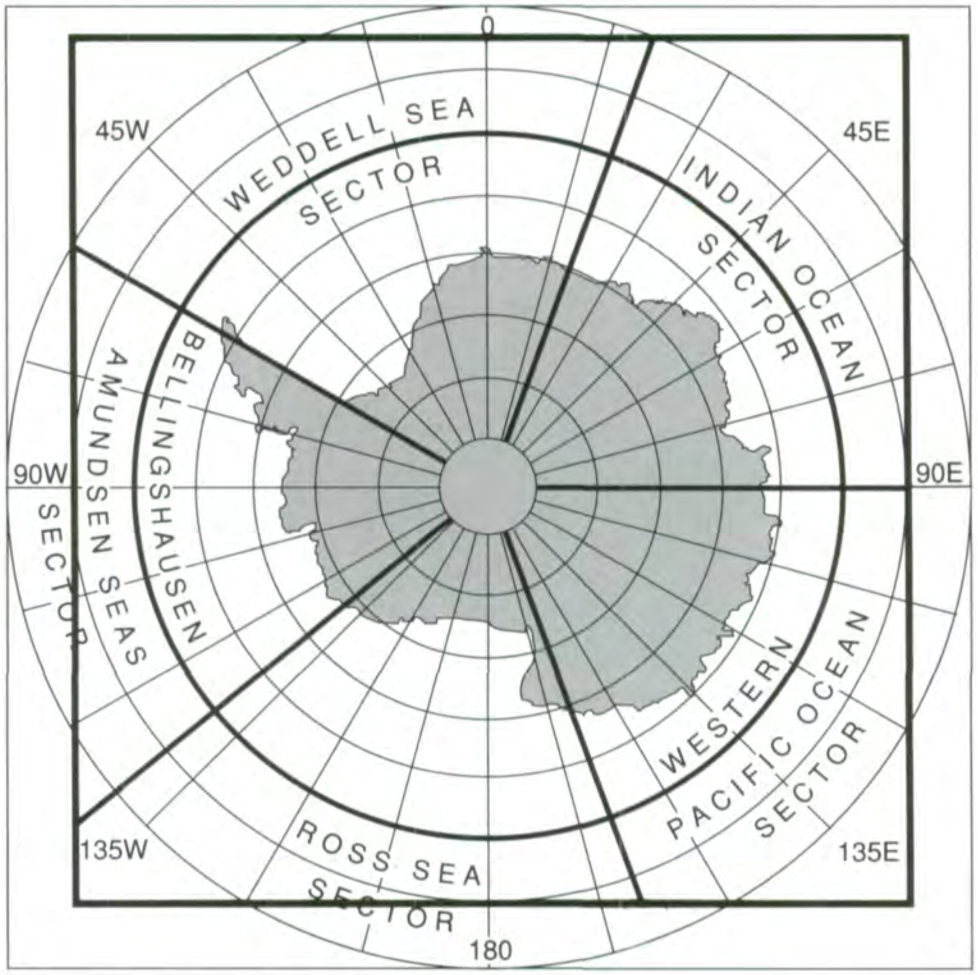

Figure 4.1.3. Antarctic sector map.

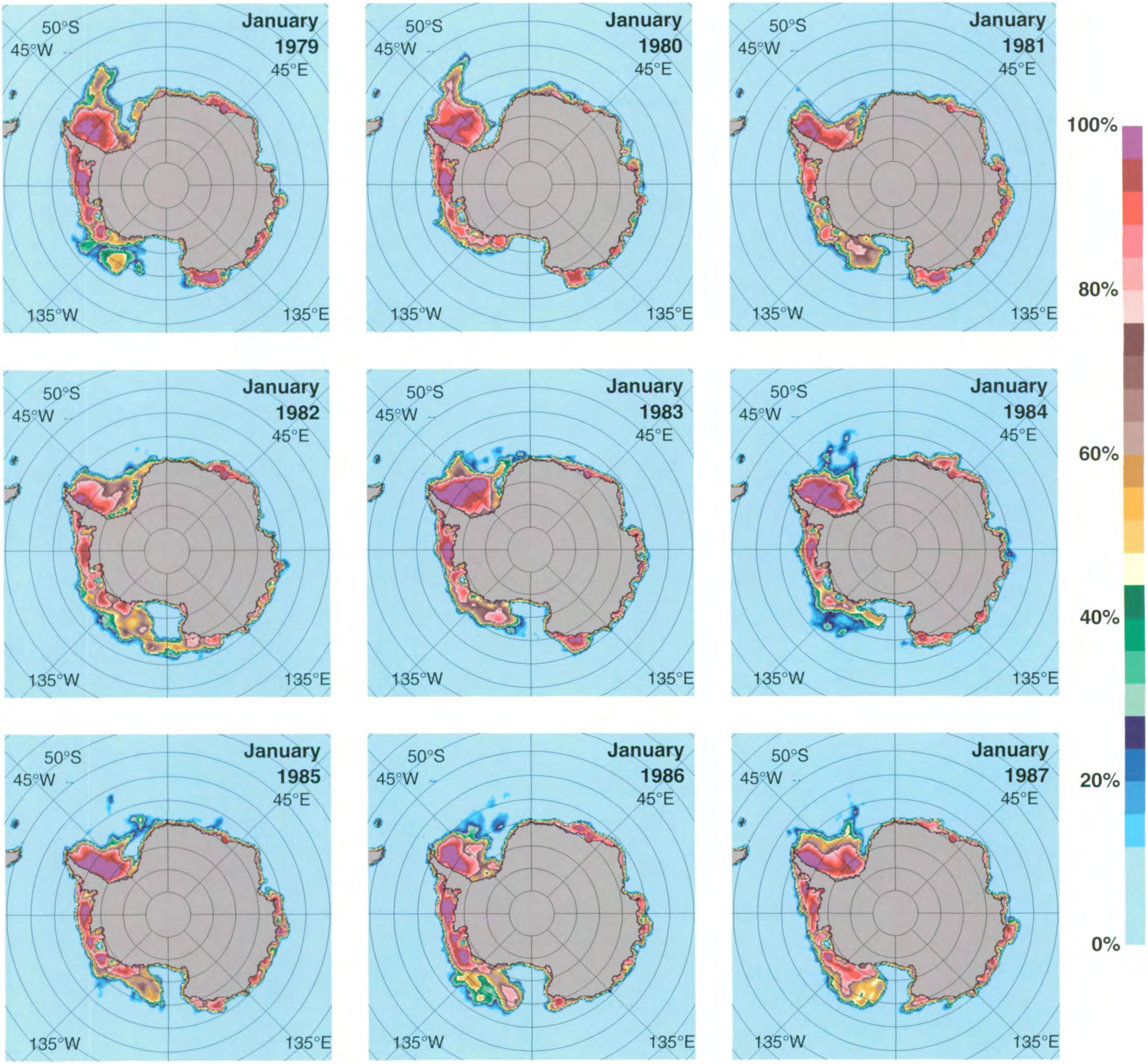

Figure 4.1.4. Mean monthly Antarctic sea ice concentrations for January 1979-1987.

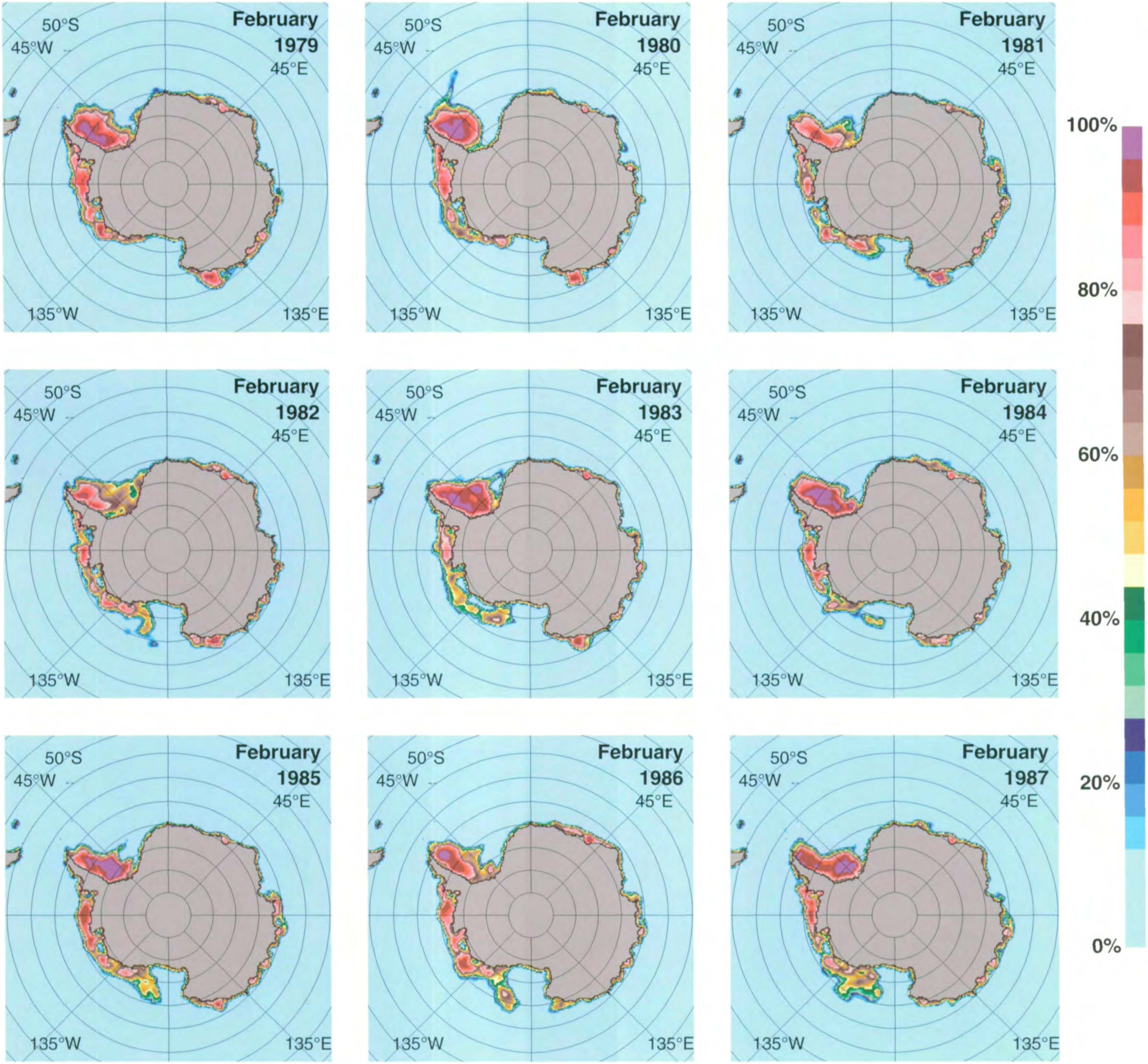

Figure 4.1.5. Mean monthly Antarctic sea ice concentrations for February 1979-1987.

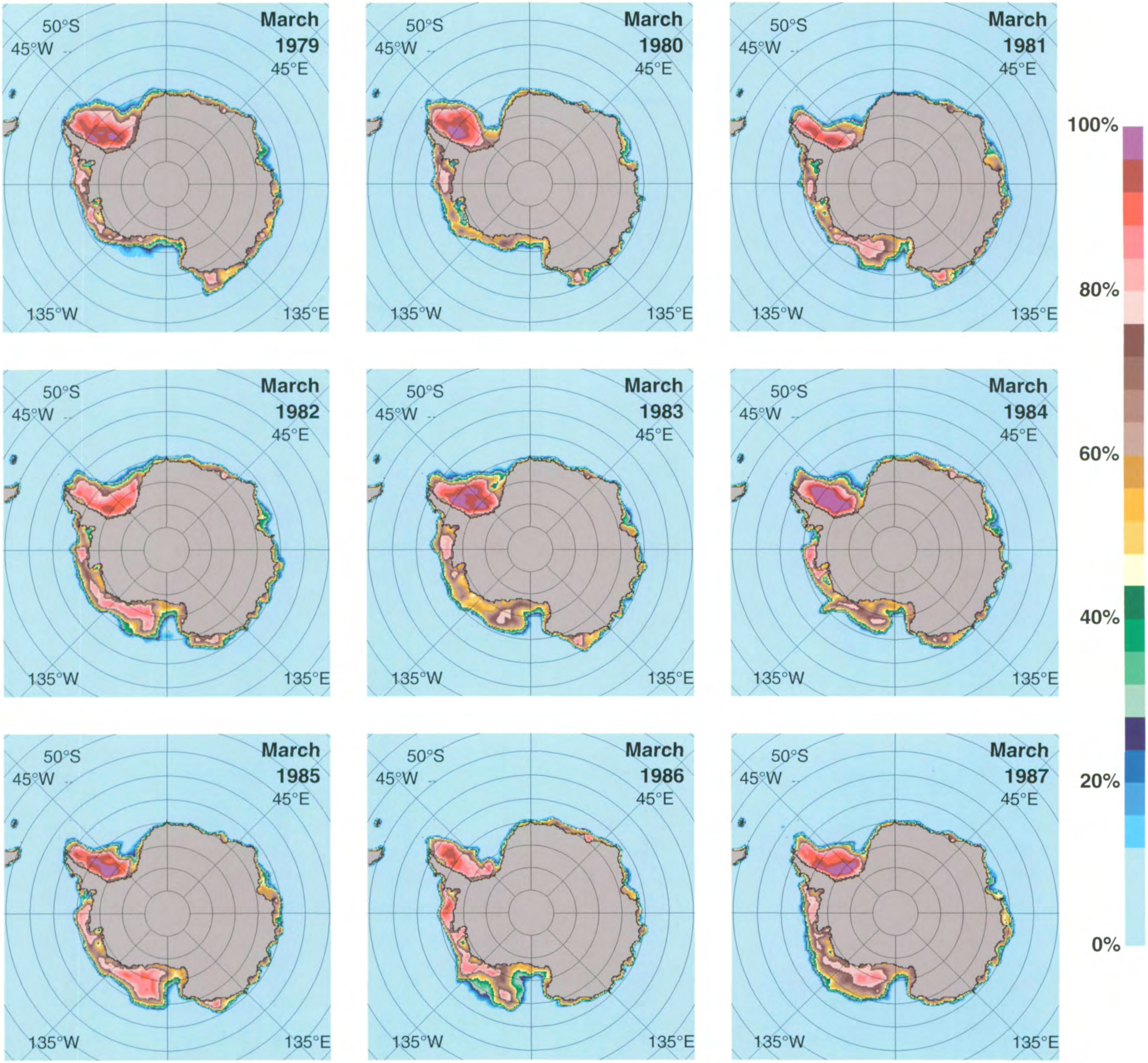

Figure 4.1.6. Mean monthly Antarctic sea ice concentrations for March 1979-1987.

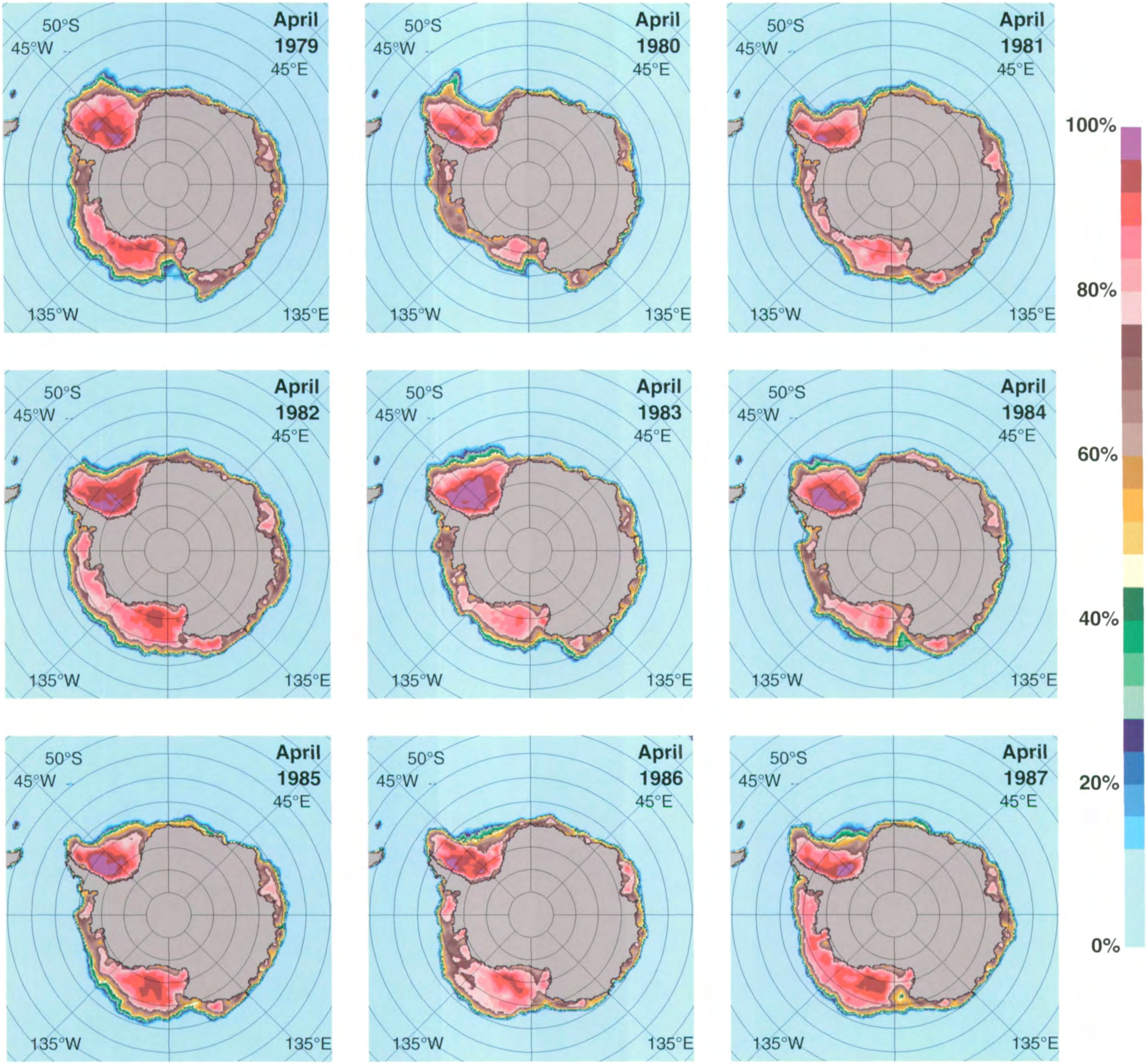

Figure 4.1.7. Mean monthly Antarctic sea ice concentrations for April 1979-1987.

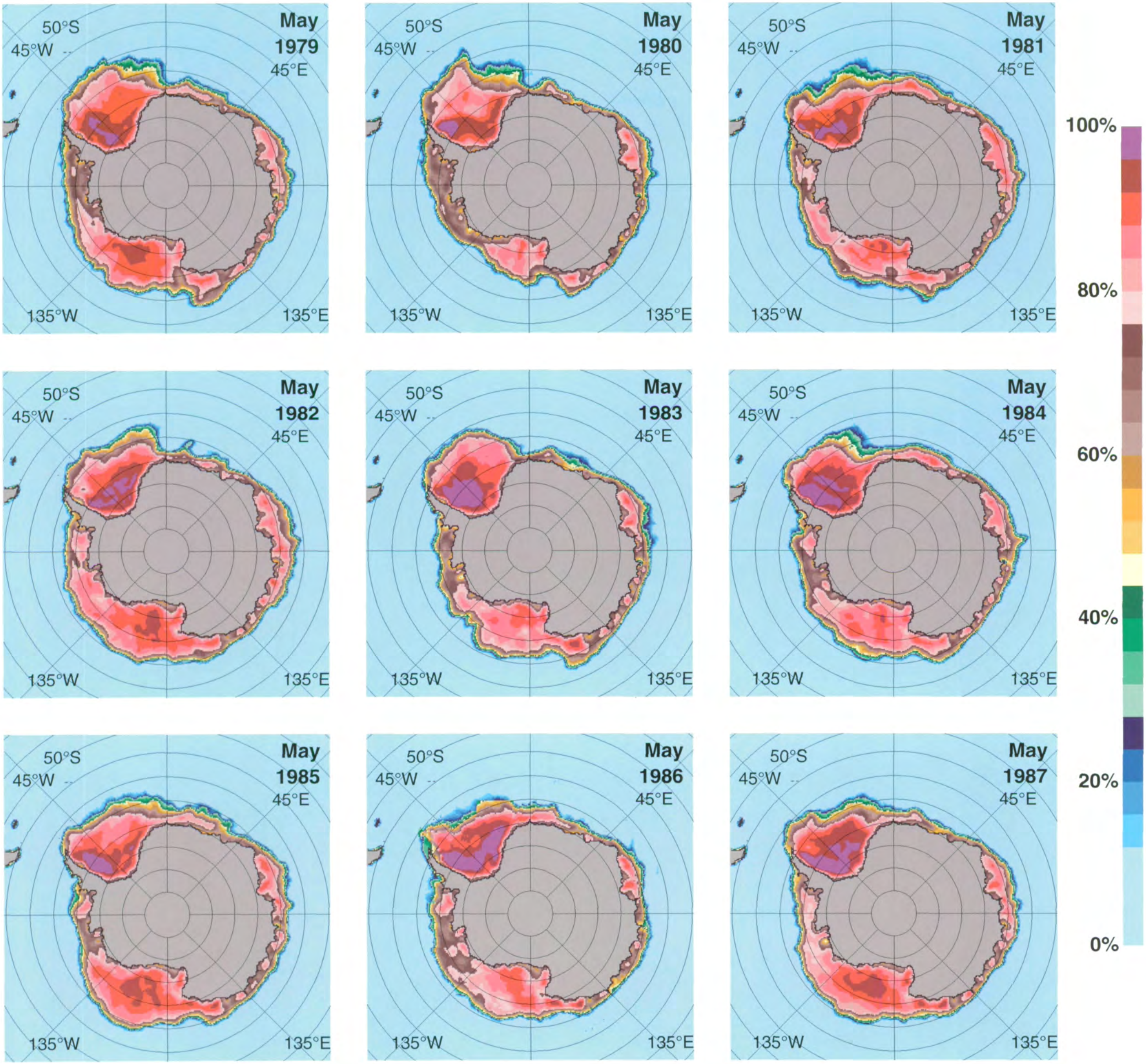

Figure 4.1.8. Mean monthly Antarctic sea ice concentrations for May 1979-1987.

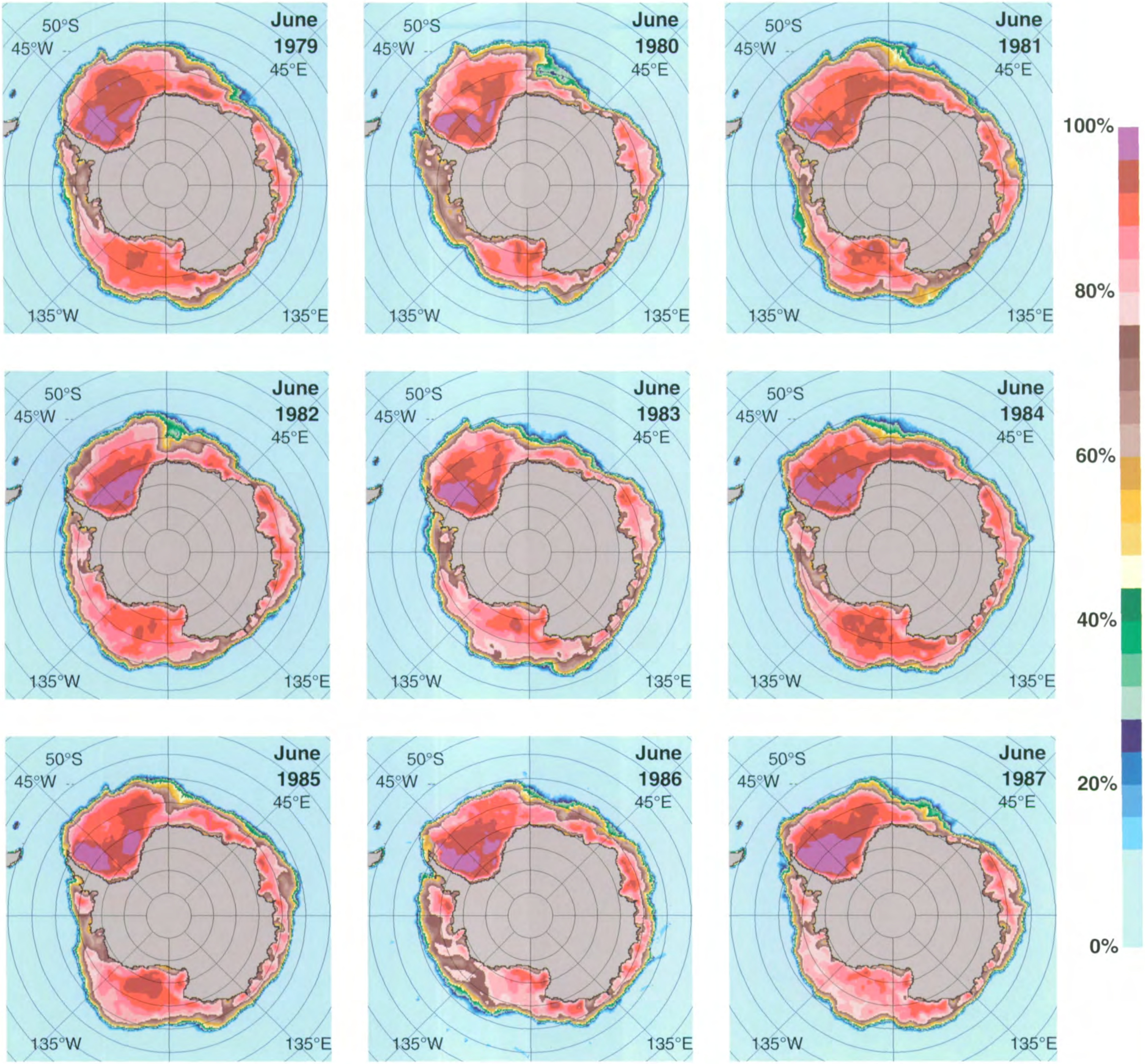

Figure 4.1.9. Mean monthly Antarctic sea ice concentrations for June 1979-1987.

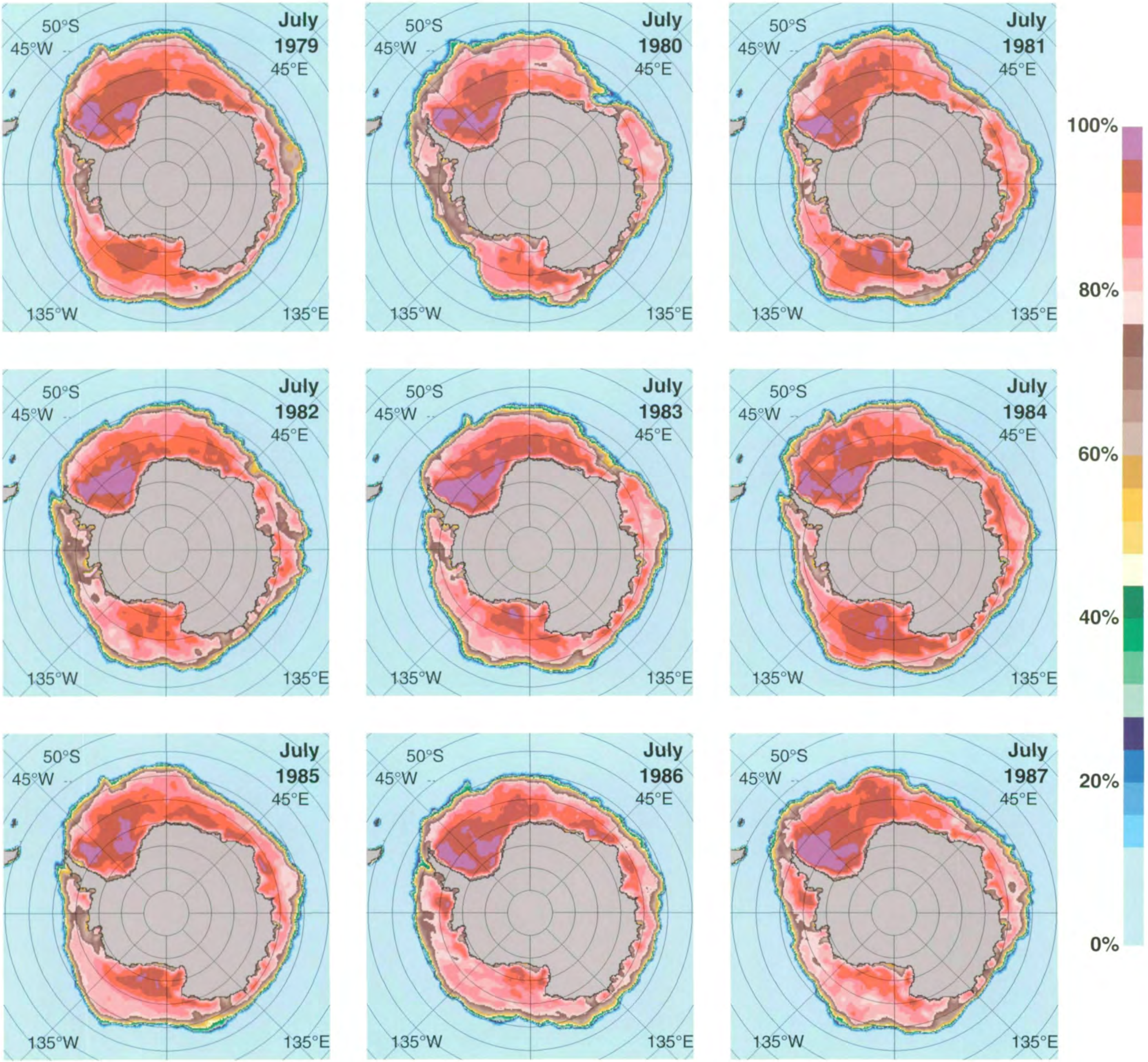

Figure 4.1.10. Mean monthly Antarctic sea ice concentrations for July 1979-1987.

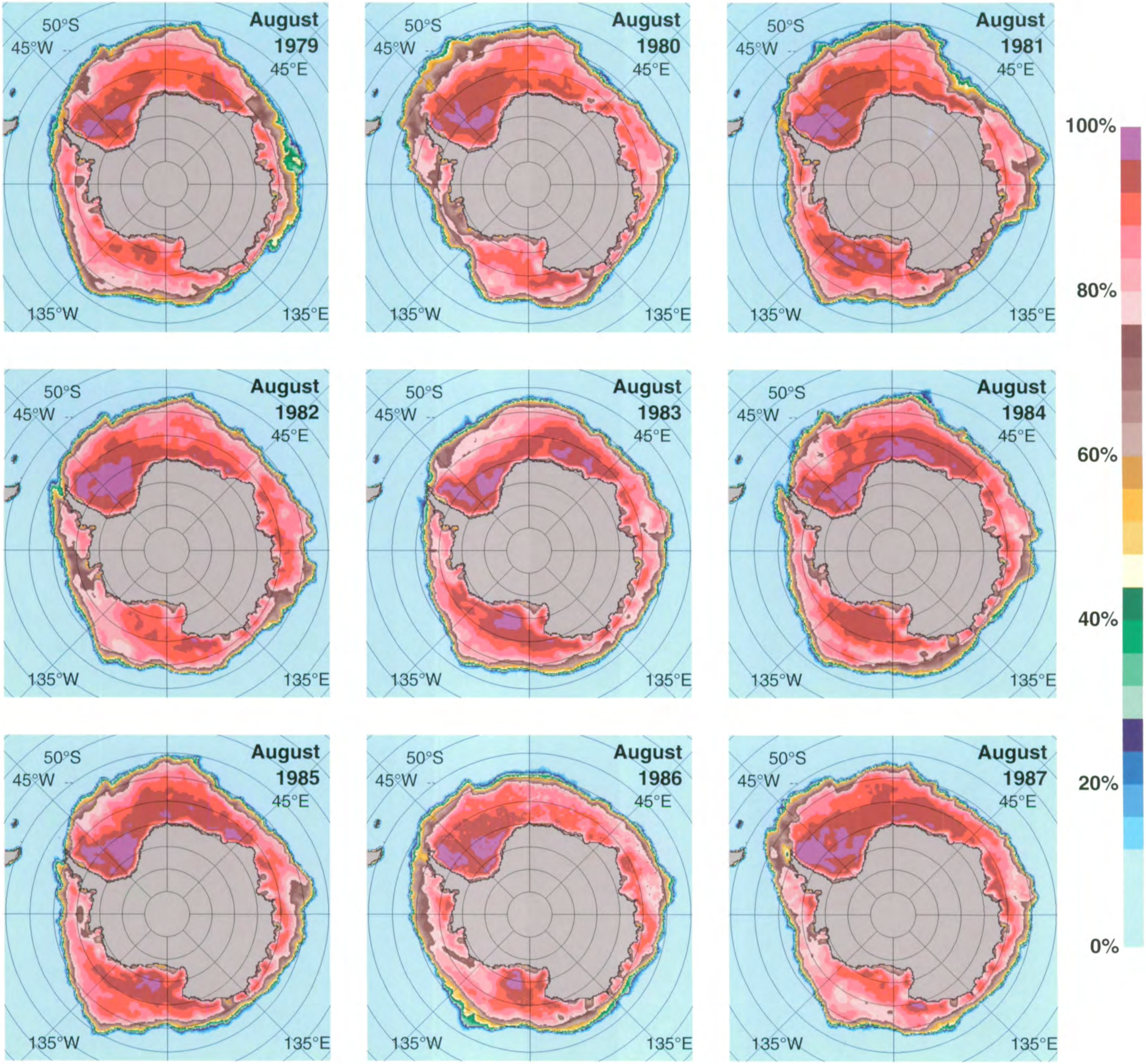

Figure 4.1.11. Mean monthly Antarctic sea ice concentrations for August 1979-1987.

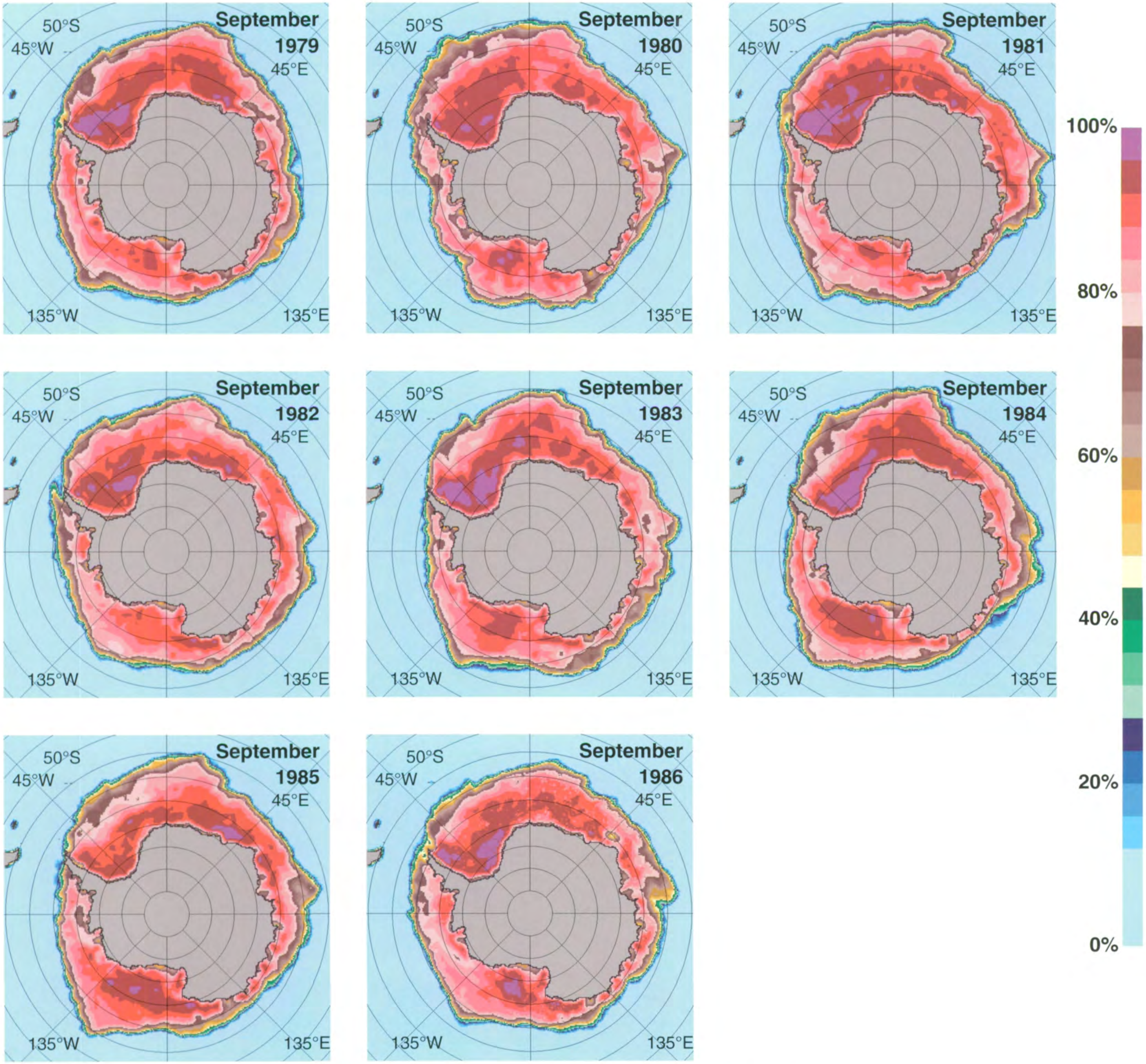

Figure 4.1.12. Mean monthly Antarctic sea ice concentrations for September 1979-1986.

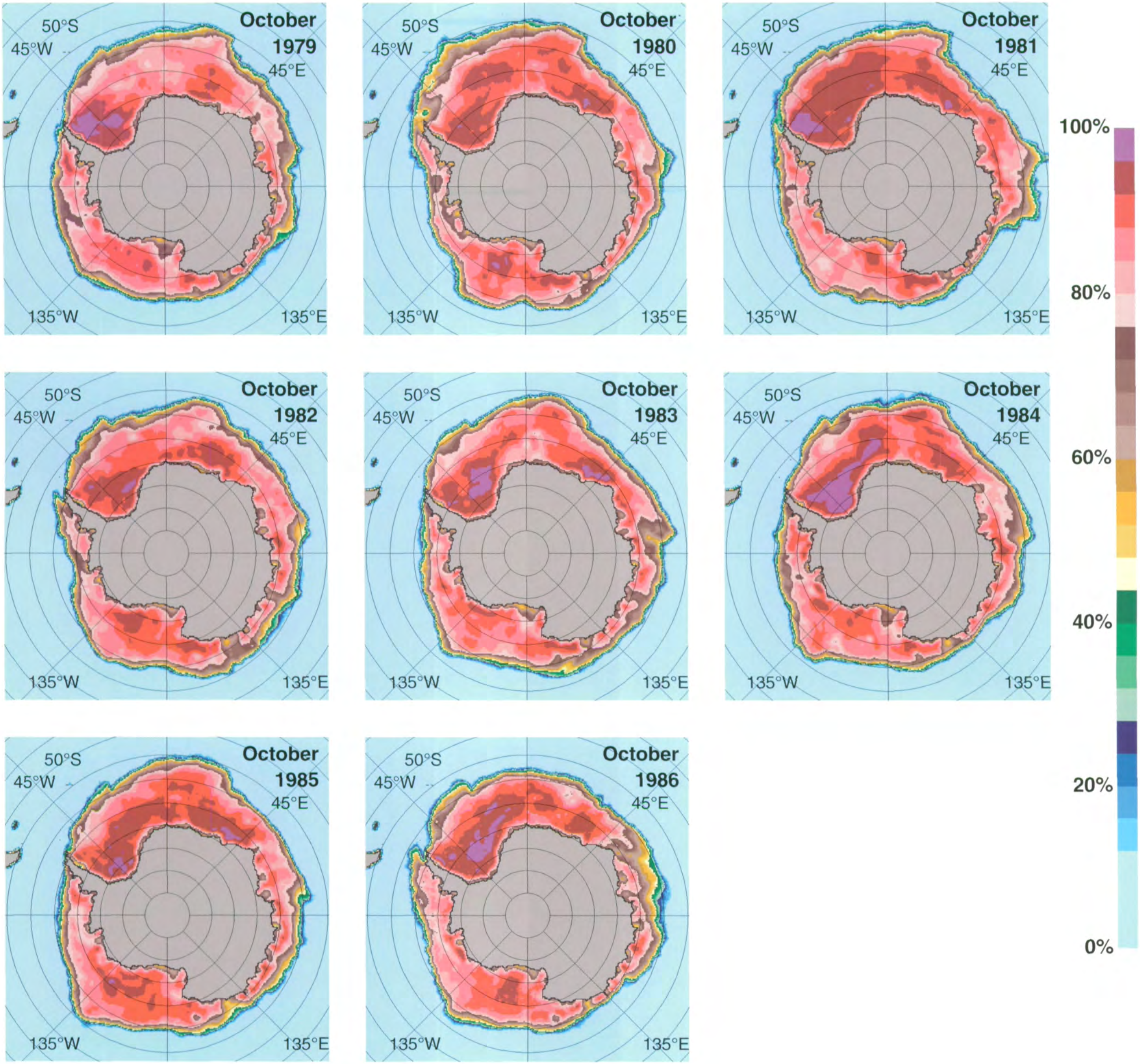

Figure 4.1.13. Mean monthly Antarctic sea ice concentrations for October 1979-1986.

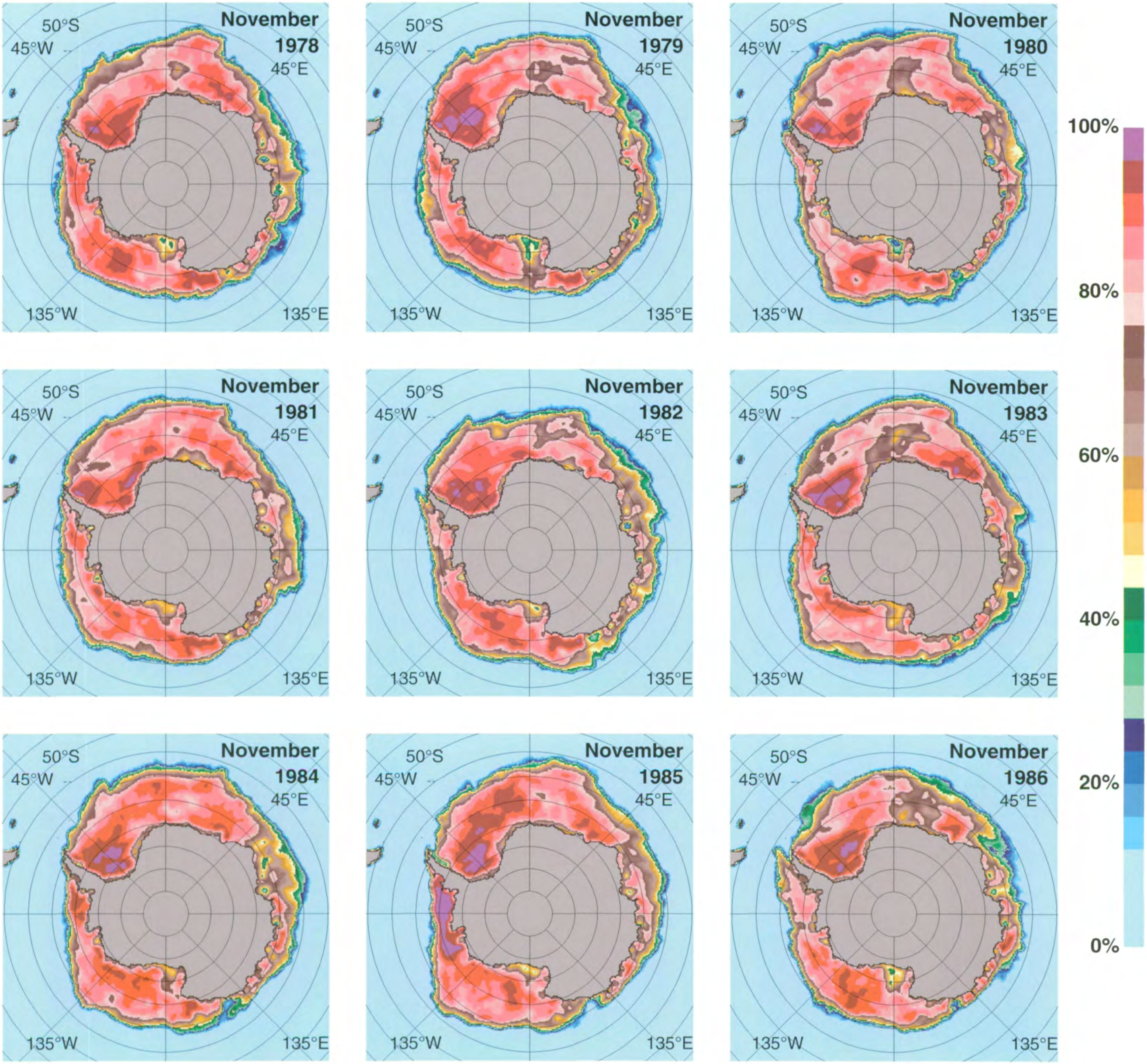

Figure 4.1.14. Mean monthly Antarctic sea ice concentrations for November 1978-1986.

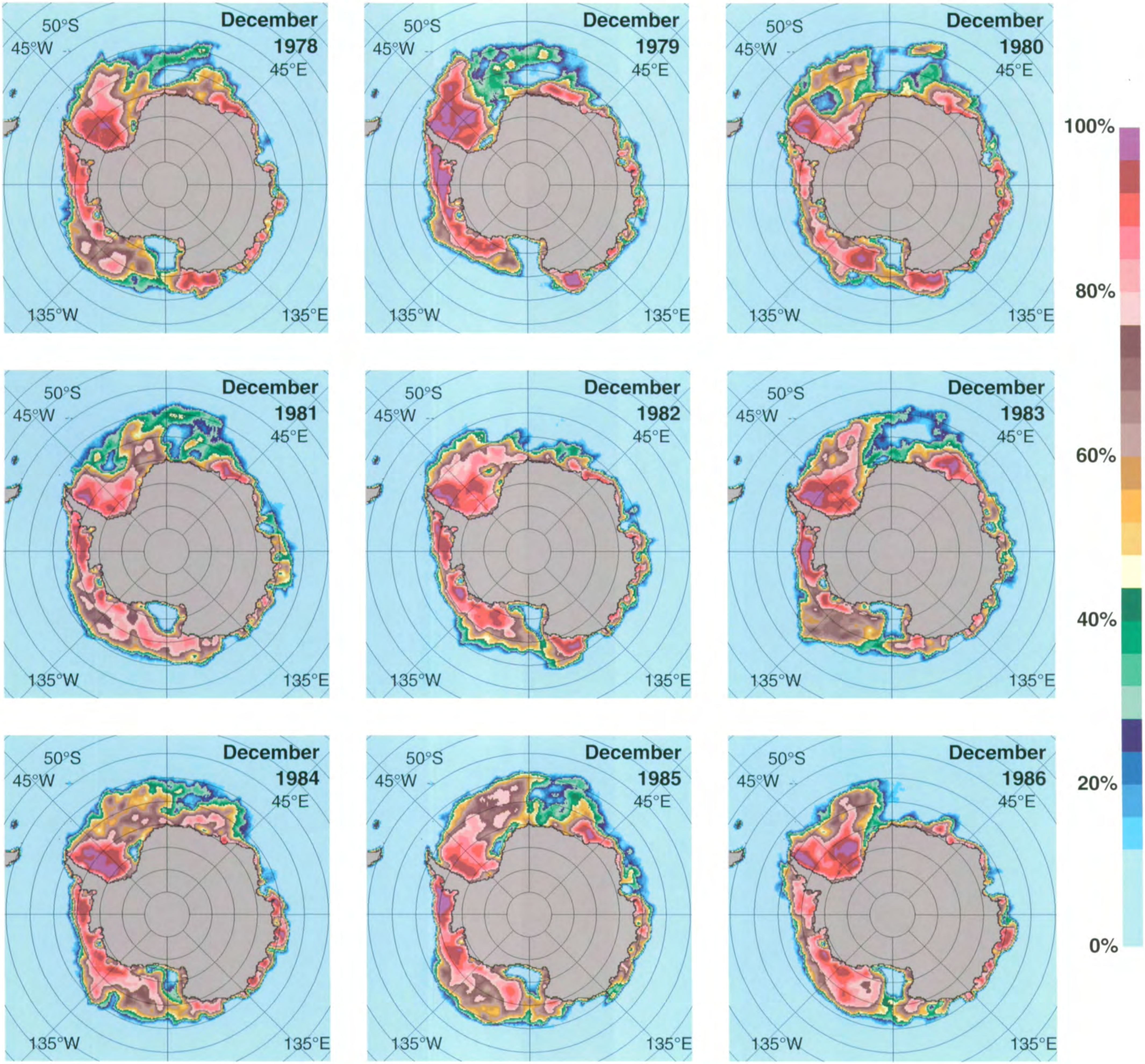

Figure 4.1.15. Mean monthly Antarctic sea ice concentrations for December 1978-1986.

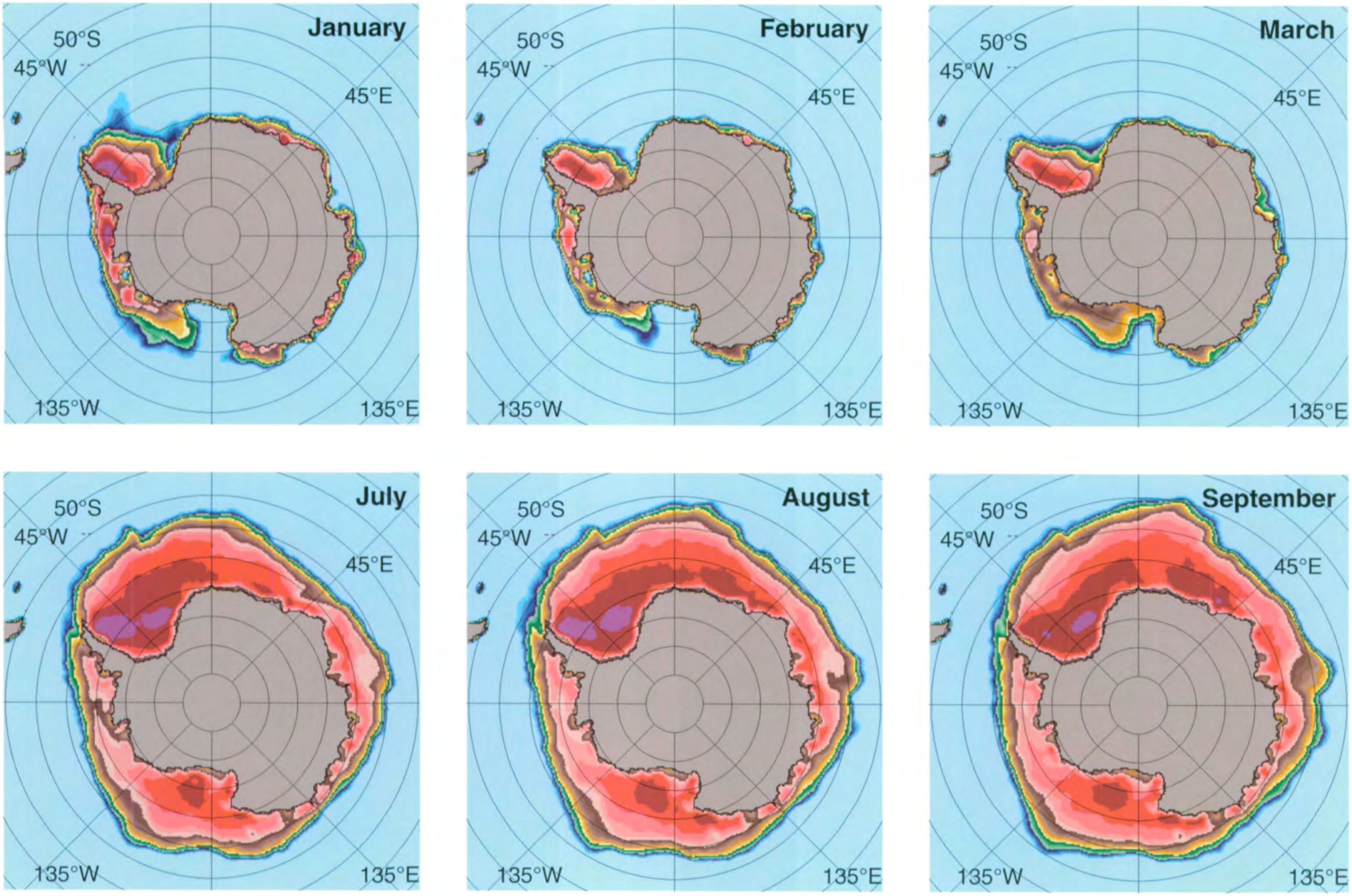
January
February
March
July
August
September
50°S
45°W
45°E
135°W
135°E

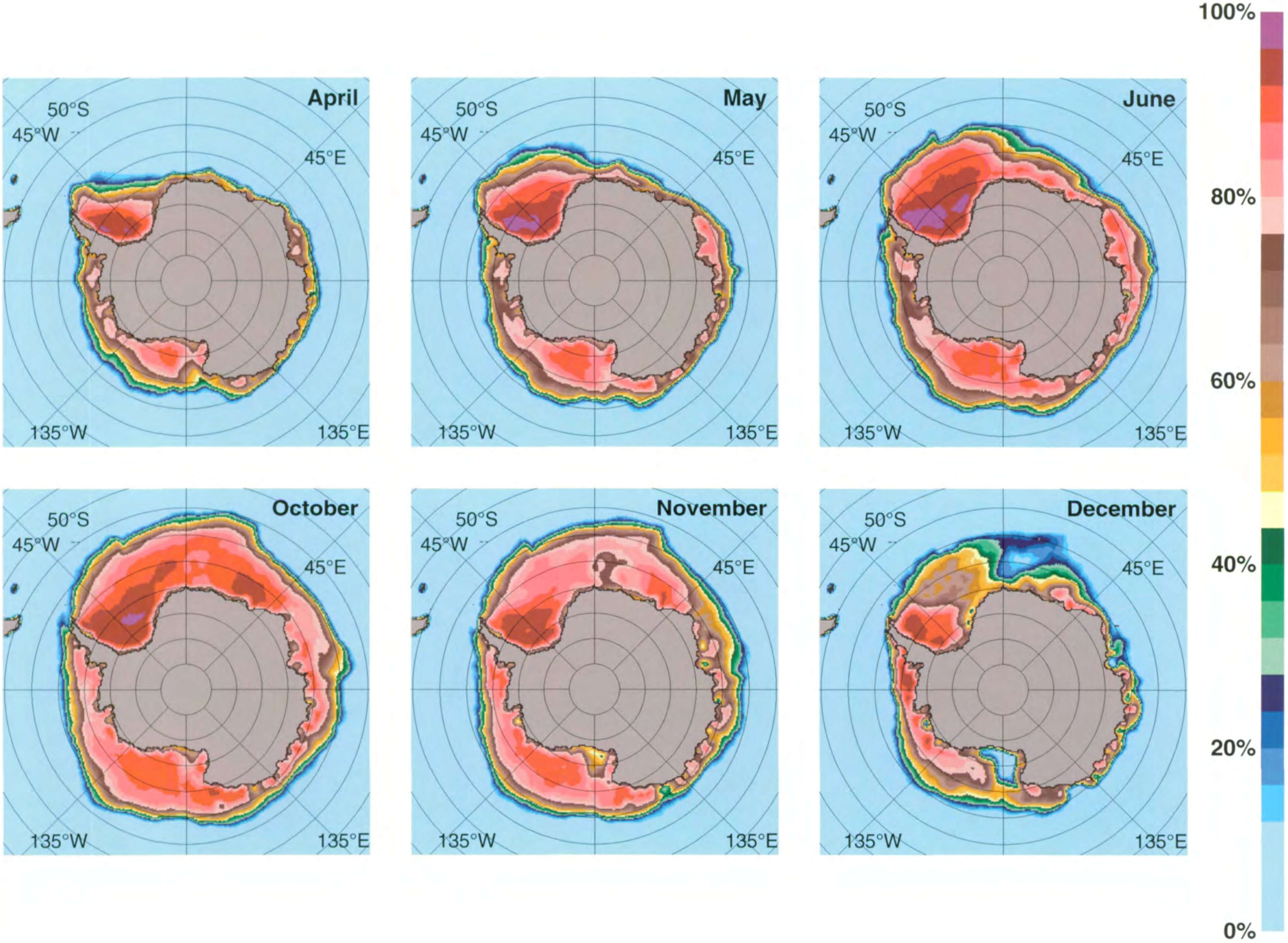

Figure 4.1.16. Mean monthly Antarctic sea ice concentrations averaged over the SMMR lifetime.

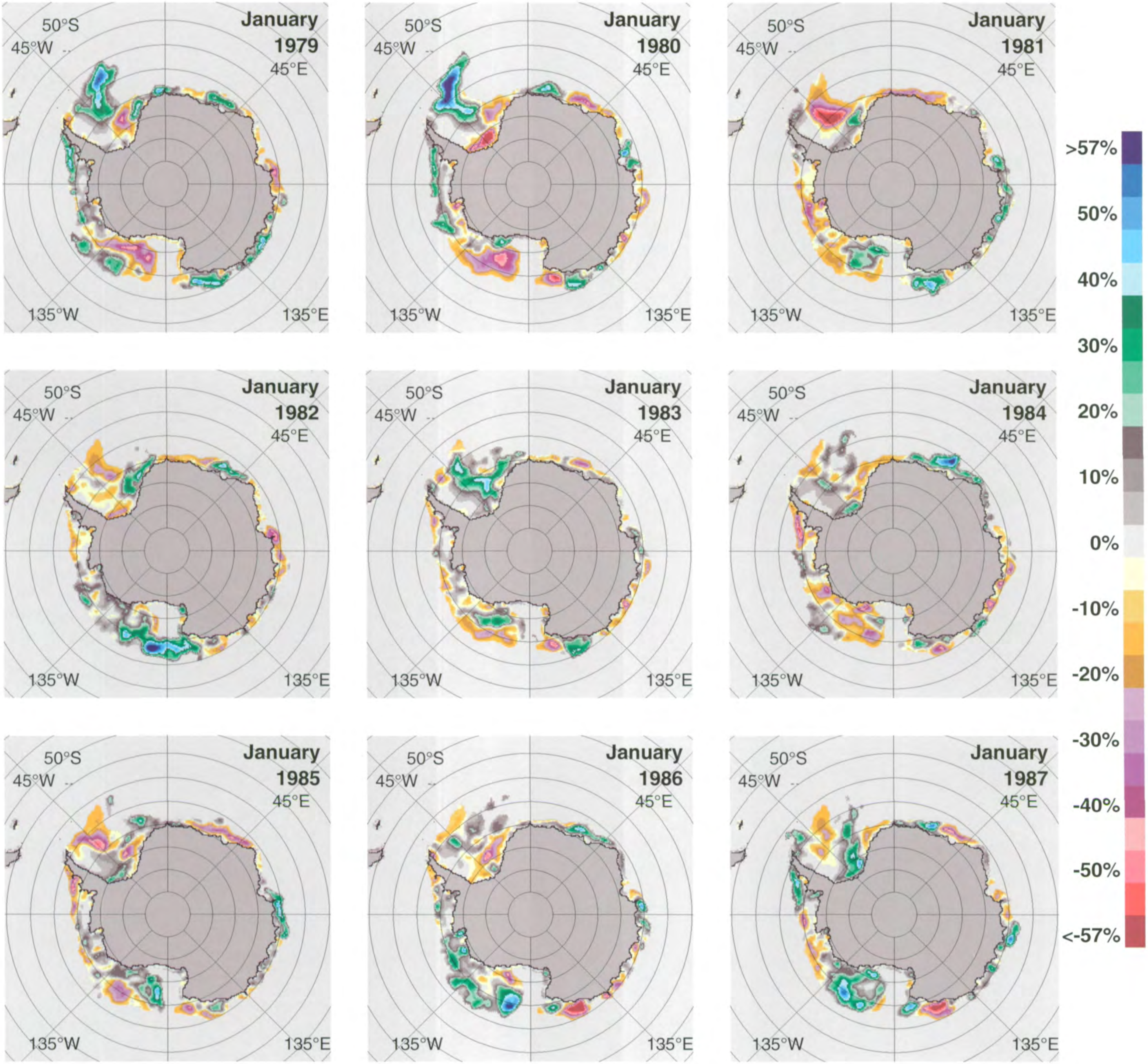

Figure 4.1.17. Mean monthly Antarctic sea ice concentration anomalies for January 1979-1987.

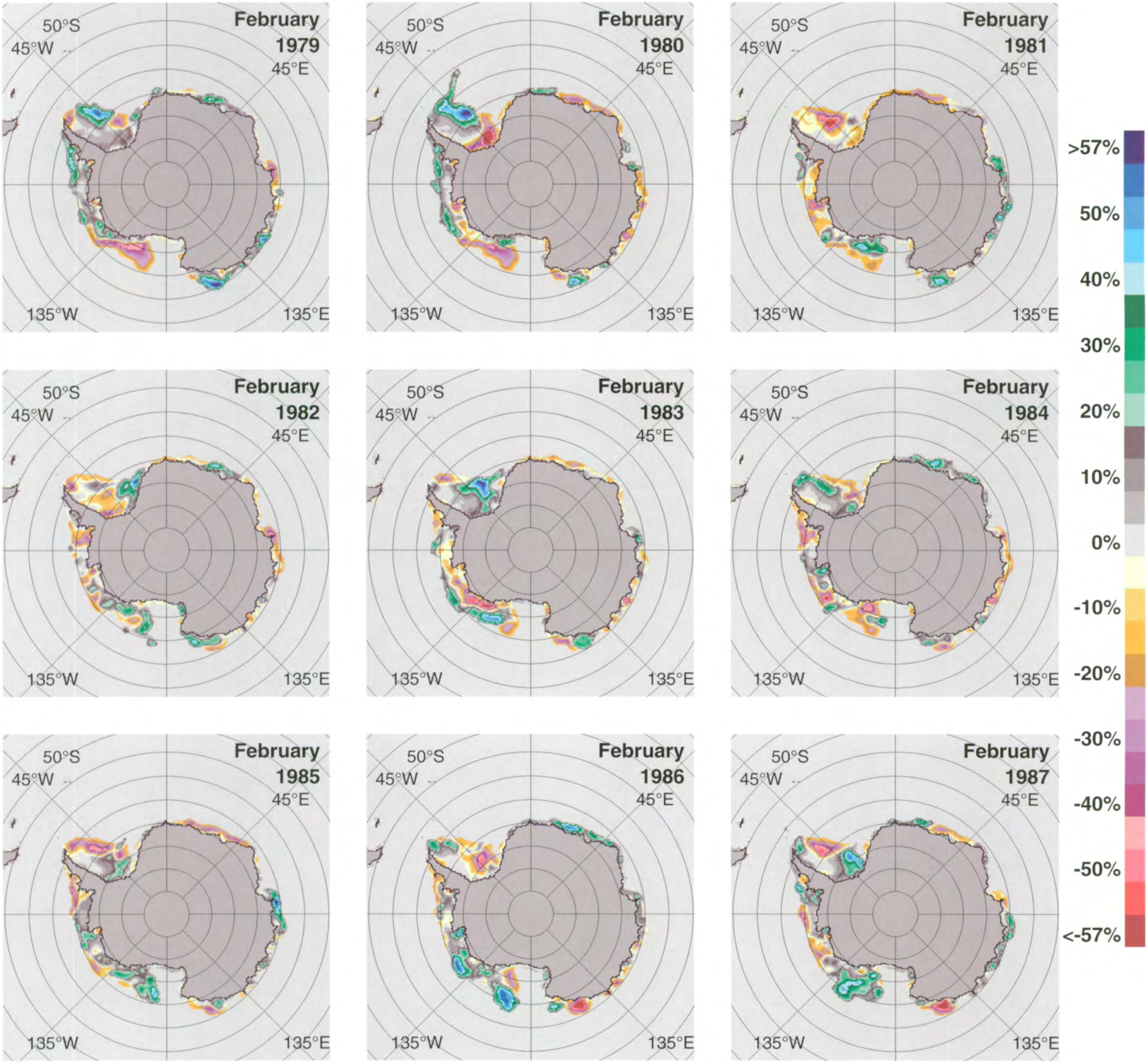

Figure 4.1.18. Mean monthly Antarctic sea ice concentration anomalies for February 1979-1987.

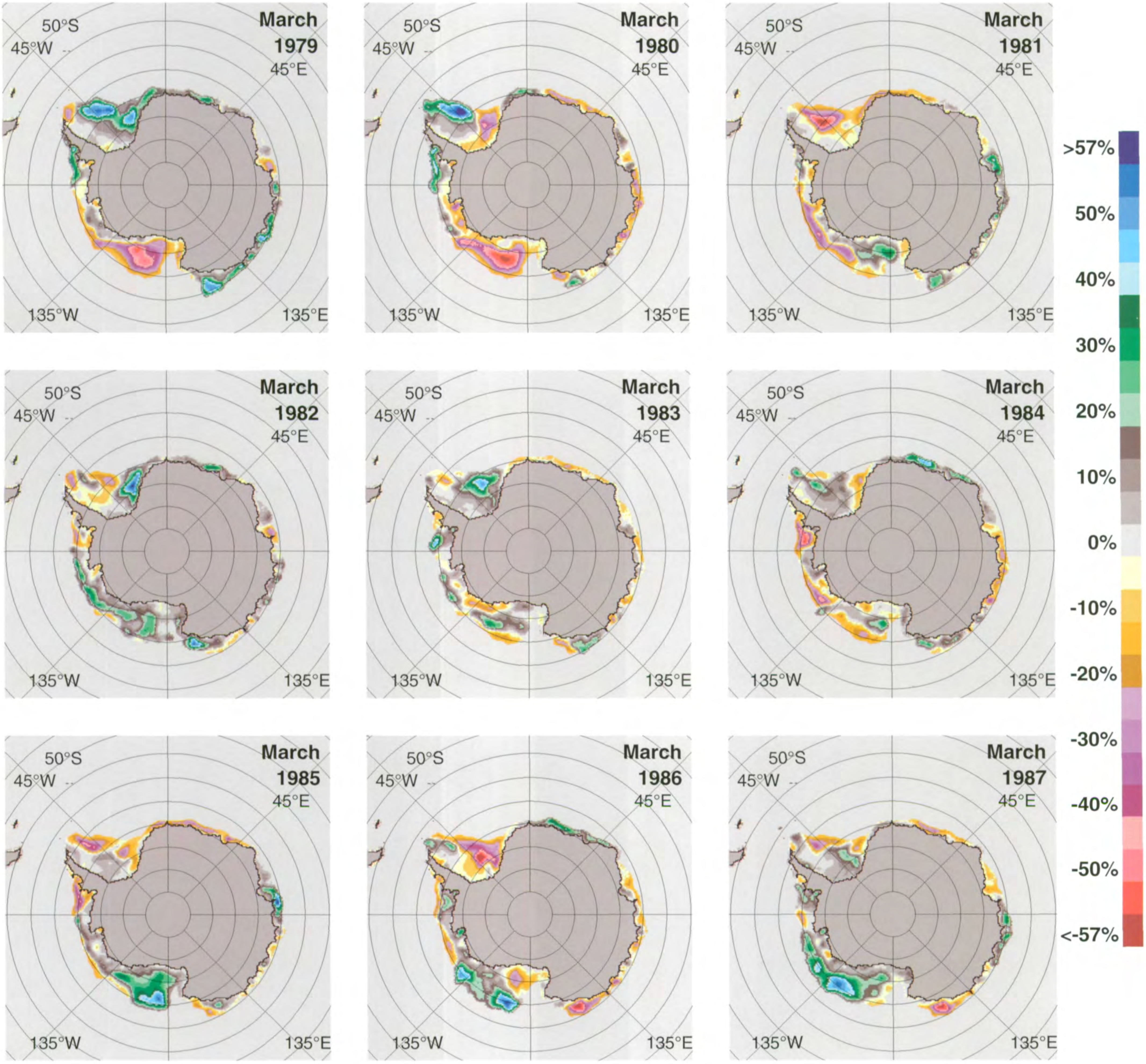

Figure 4.1.19. Mean monthly Antarctic sea ice concentration anomalies for March 1979-1987.

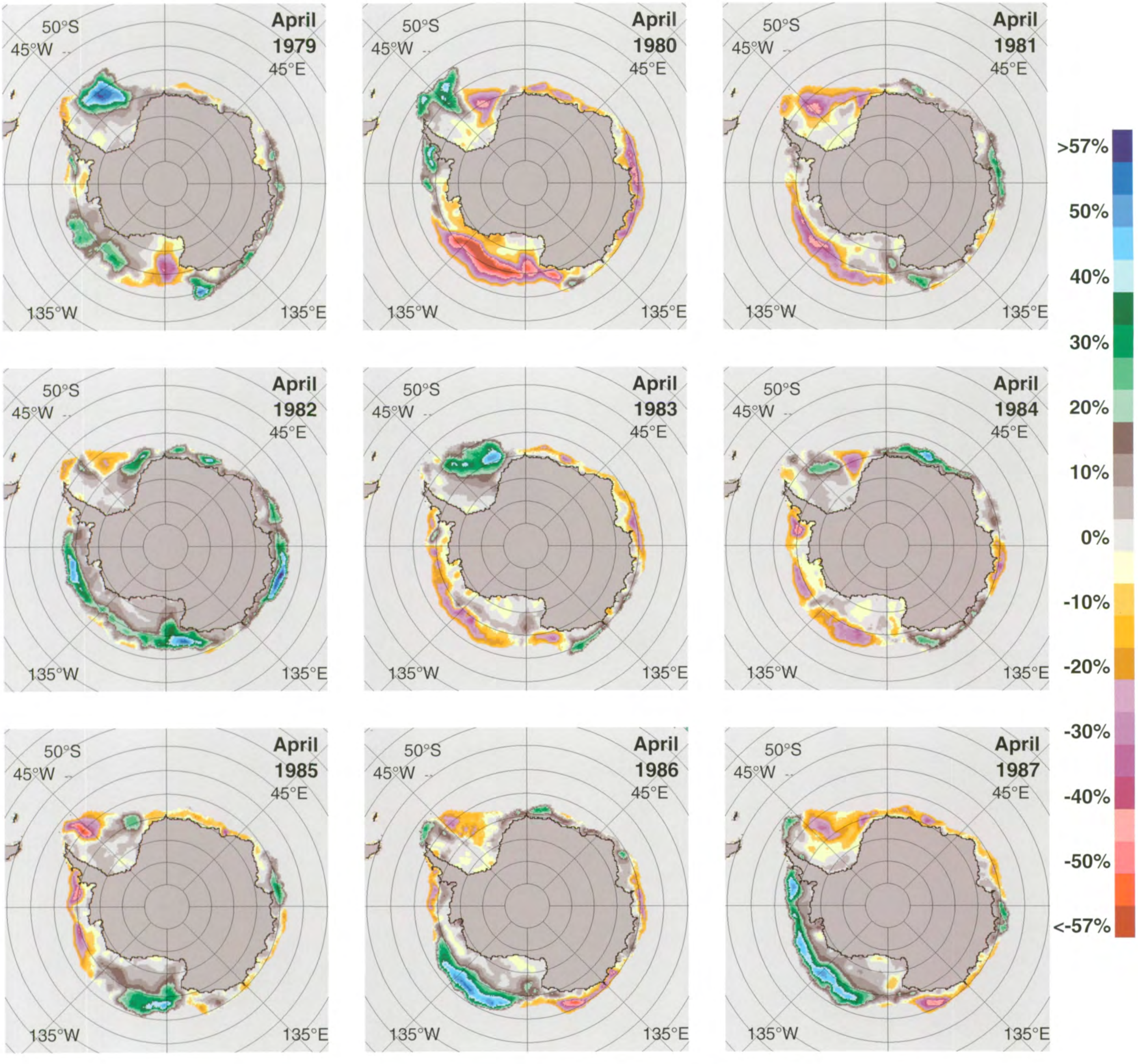

Figure 4.1.20. Mean monthly Antarctic sea ice concentration anomalies for April 1979-1987.

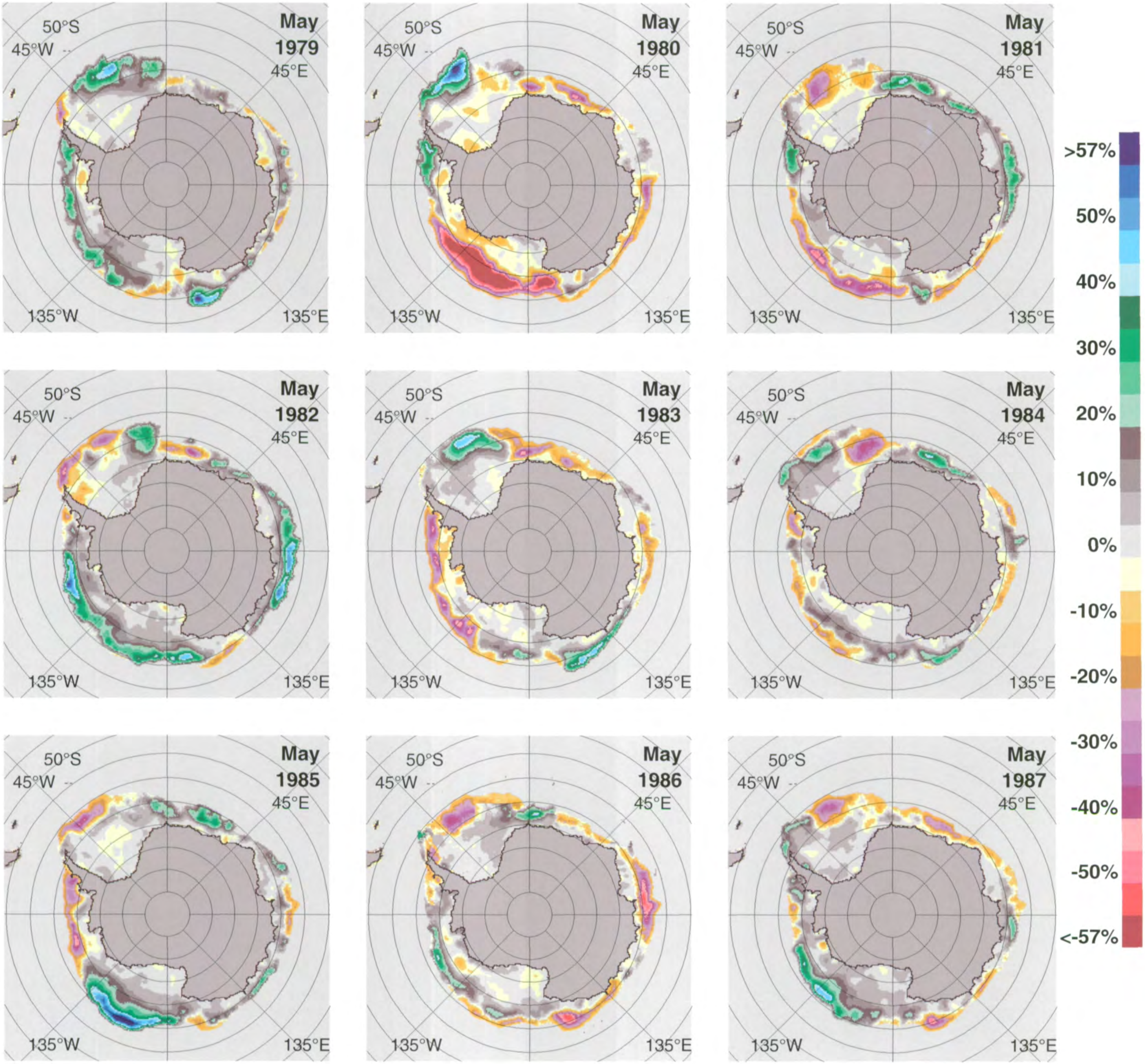

Figure 4.1.21. Mean monthly Antarctic sea ice concentration anomalies for May 1979-1987.

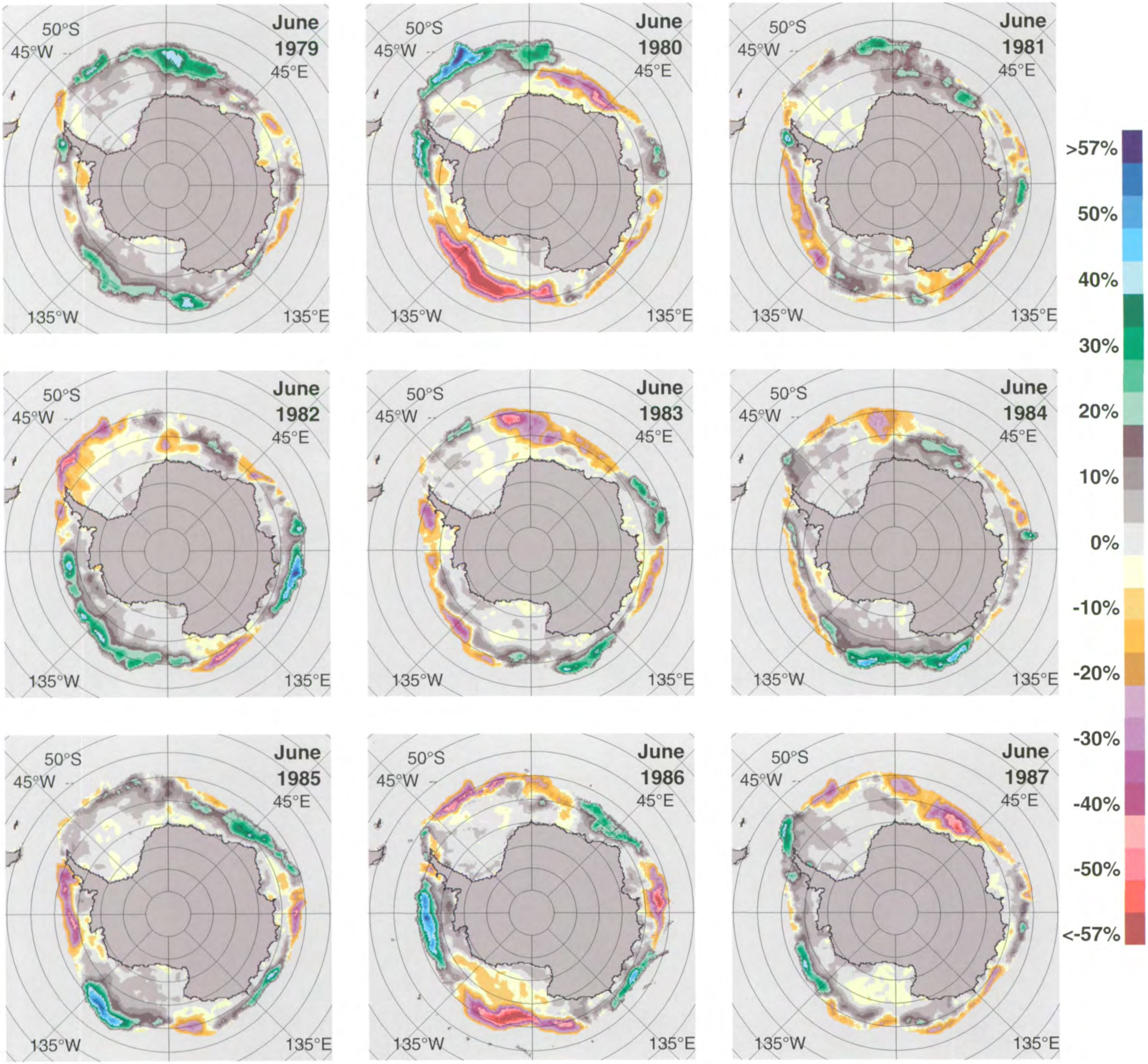

Figure 4.1.22. Mean monthly Antarctic sea ice concentration anomalies for June 1979-1987.

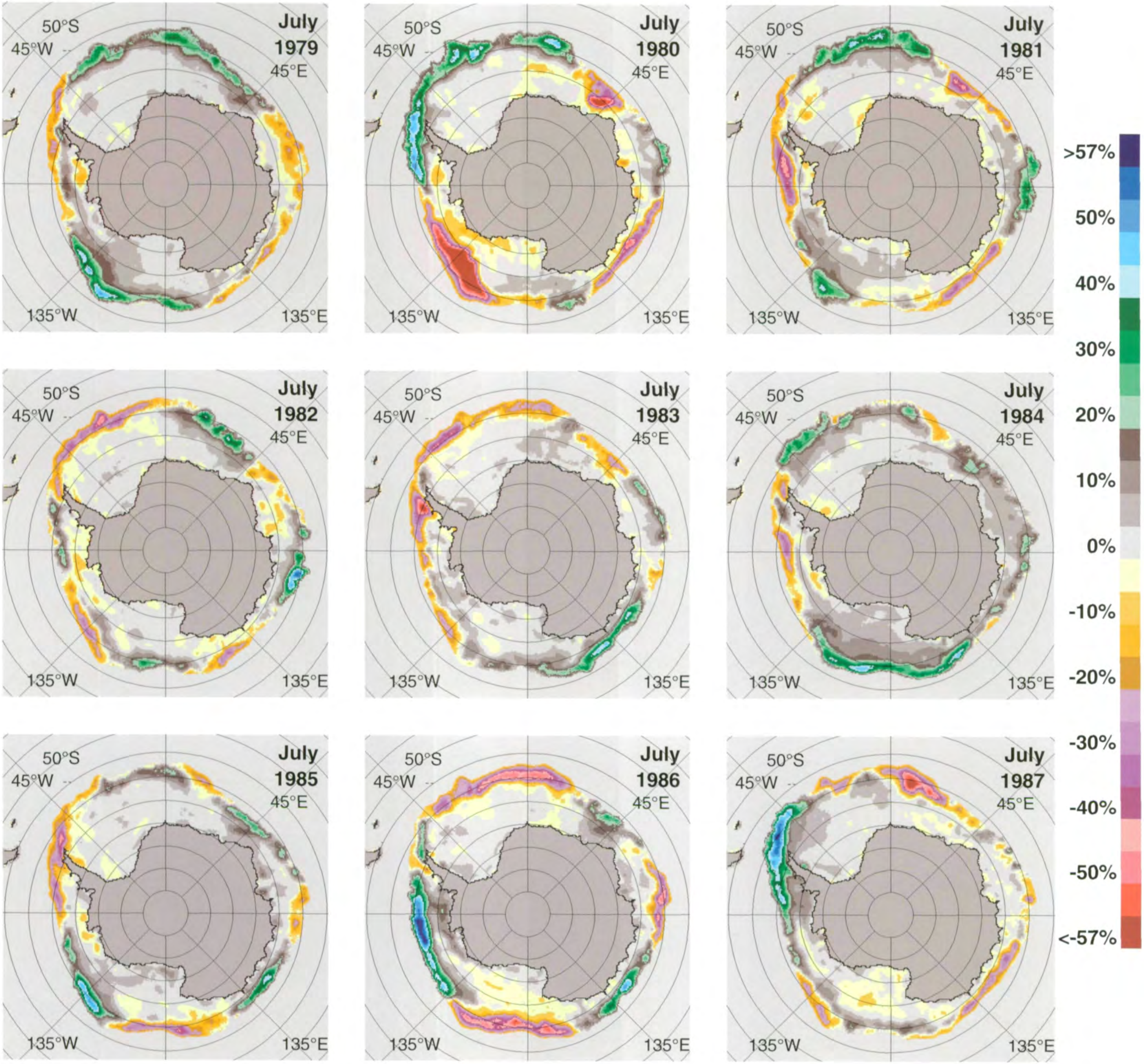

Figure 4.1.23. Mean monthly Antarctic sea ice concentration anomalies for July 1979-1987.

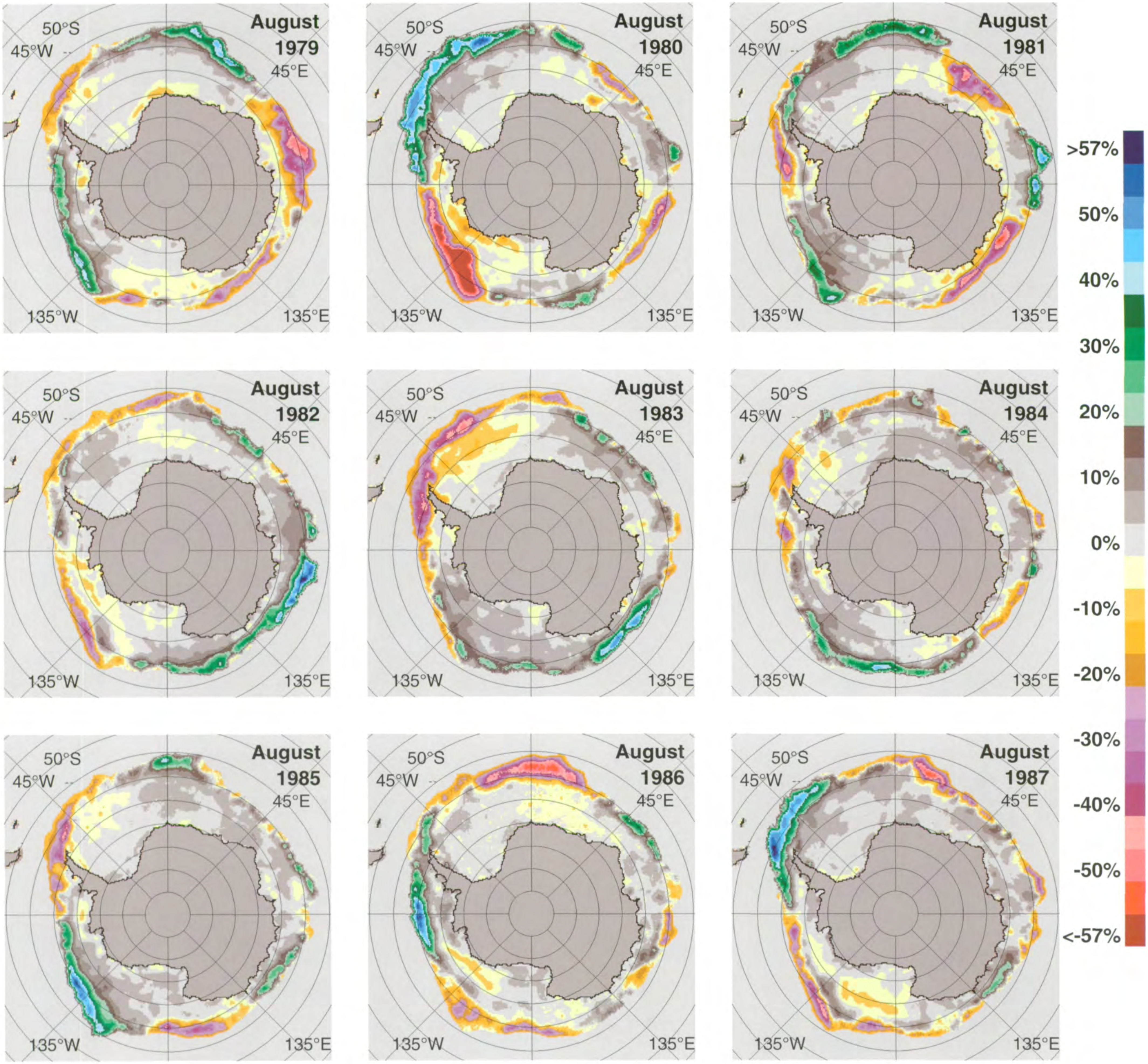

Figure 4.1.24. Mean monthly Antarctic sea ice concentration anomalies for August 1979-1987.

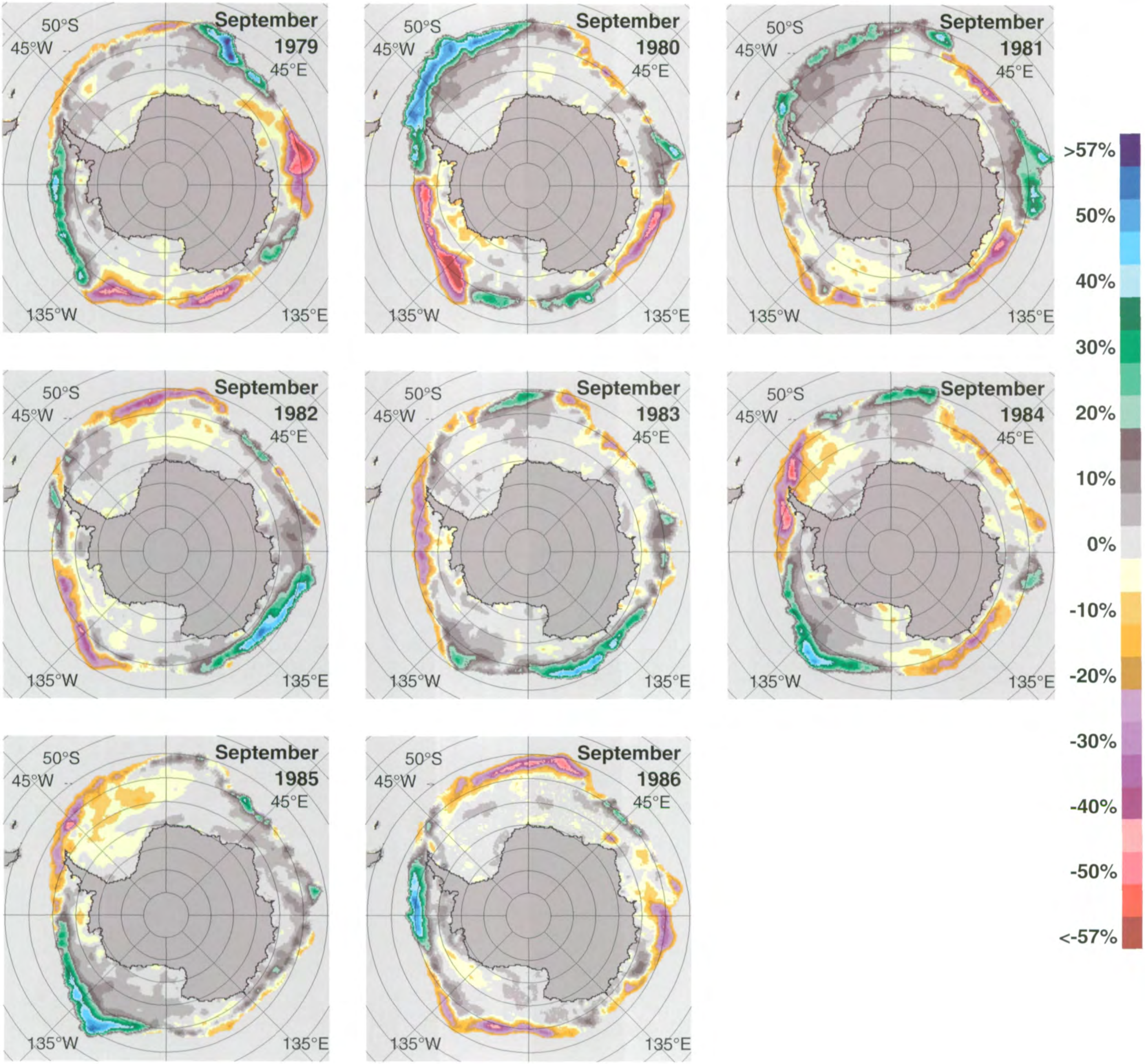

Figure 4.1.25. Mean monthly Antarctic sea ice concentration anomalies for September 1979-1986.

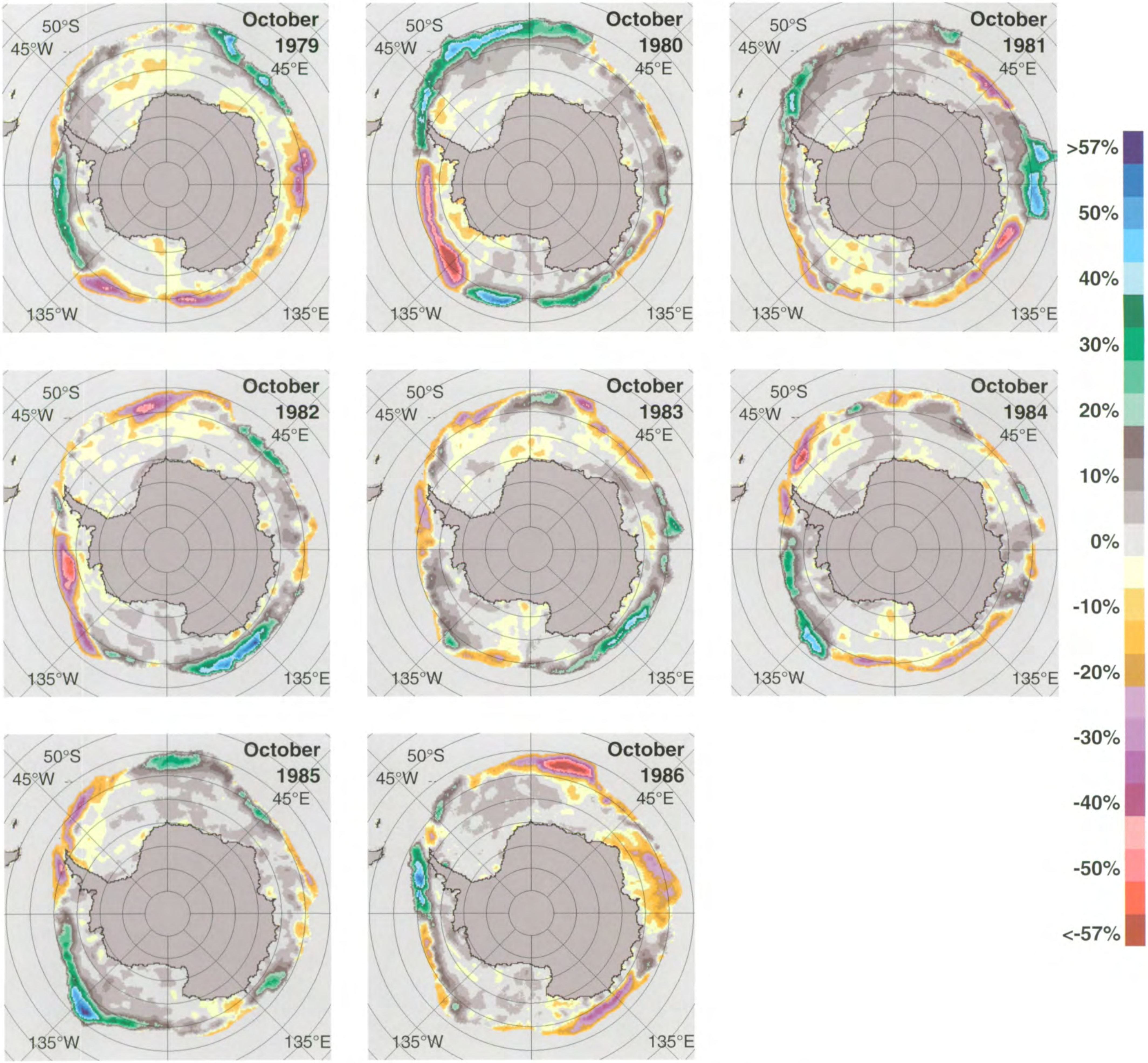

Figure 4.1.26. Mean monthly Antarctic sea ice concentration anomalies for October 1979-1986.

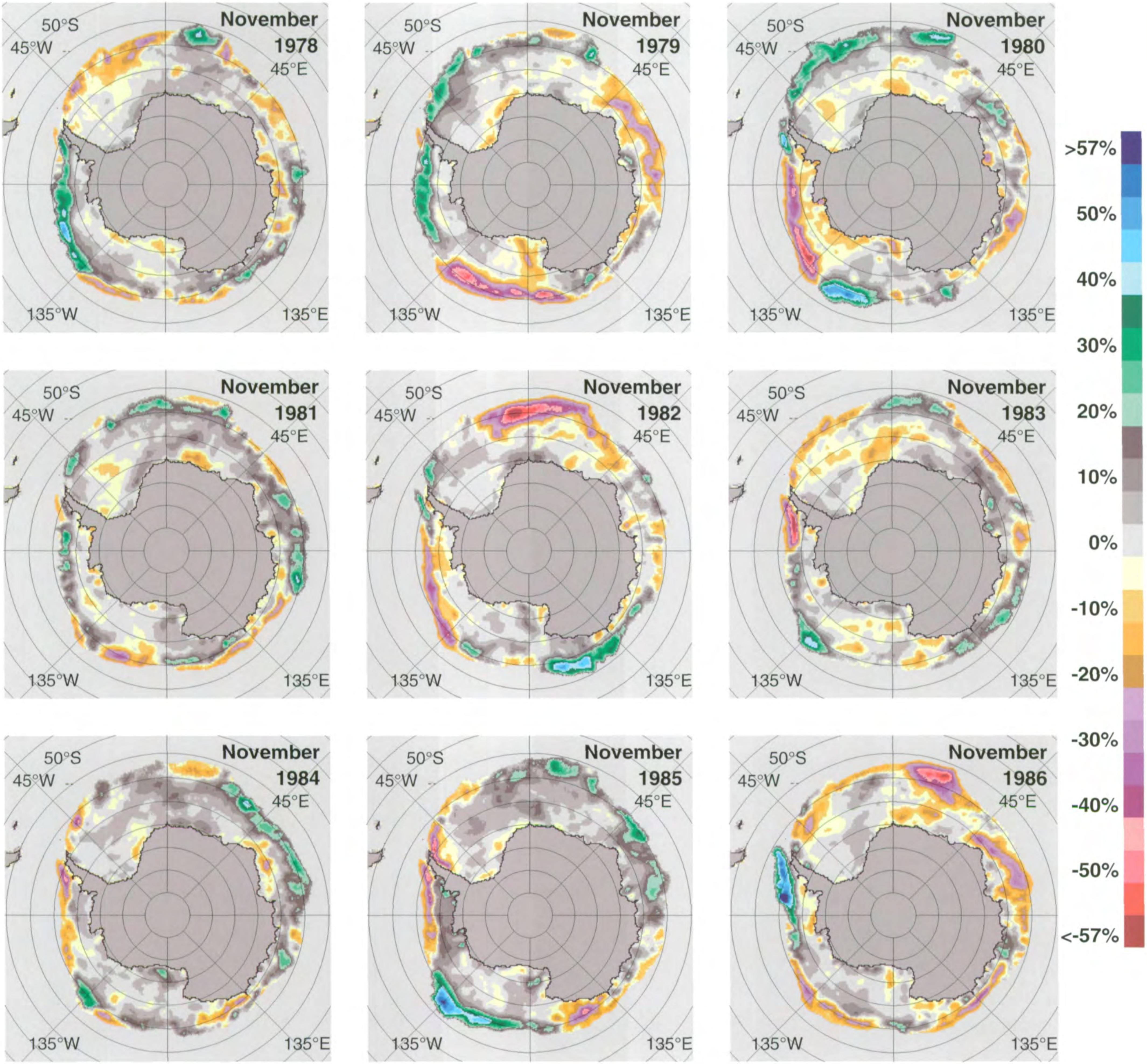

Figure 4.1.27. Mean monthly Antarctic sea ice concentration anomalies for November 1978-1986.

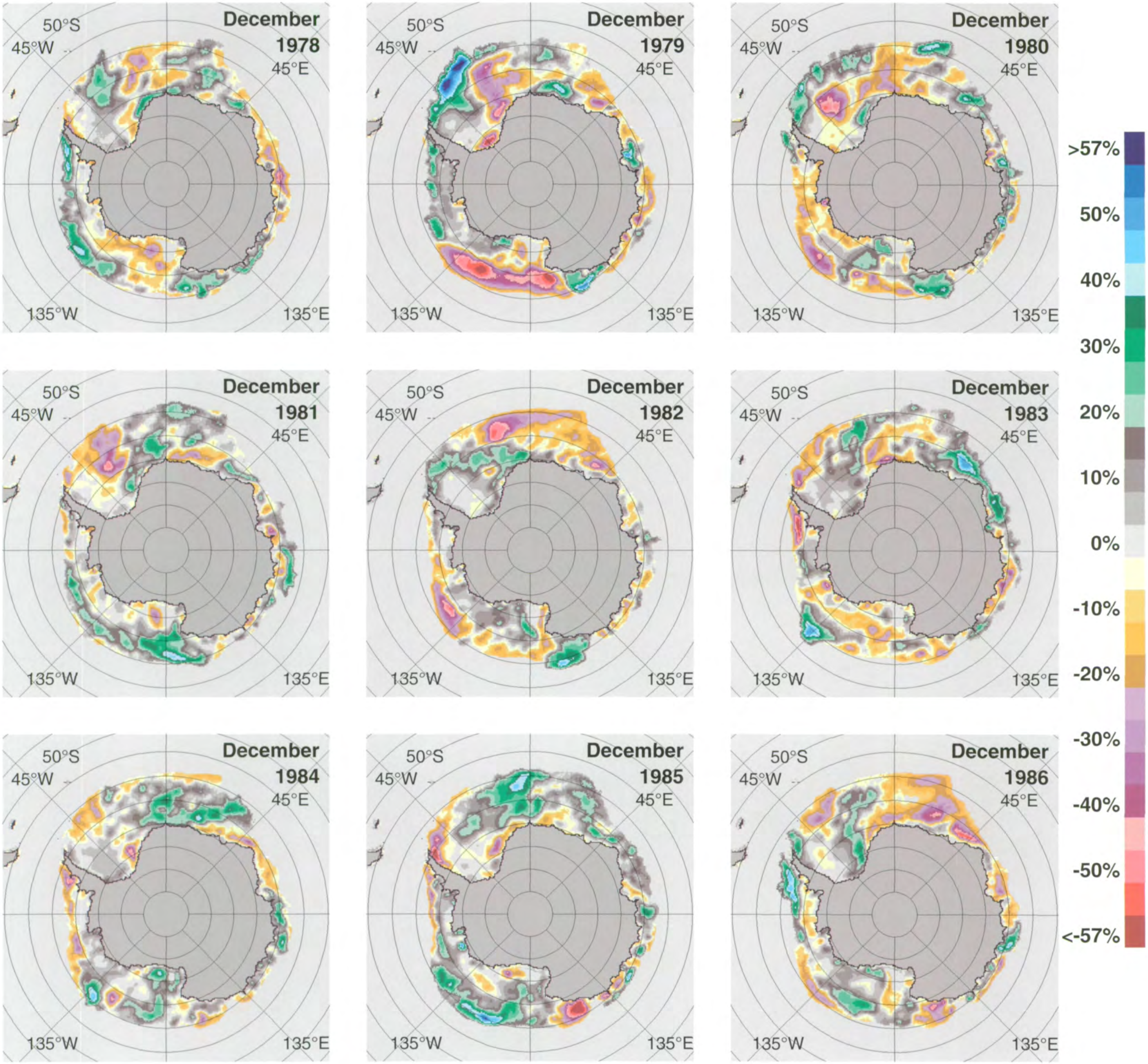

Figure 4.1.28. Mean monthly Antarctic sea ice concentration anomalies for December 1978-1986.

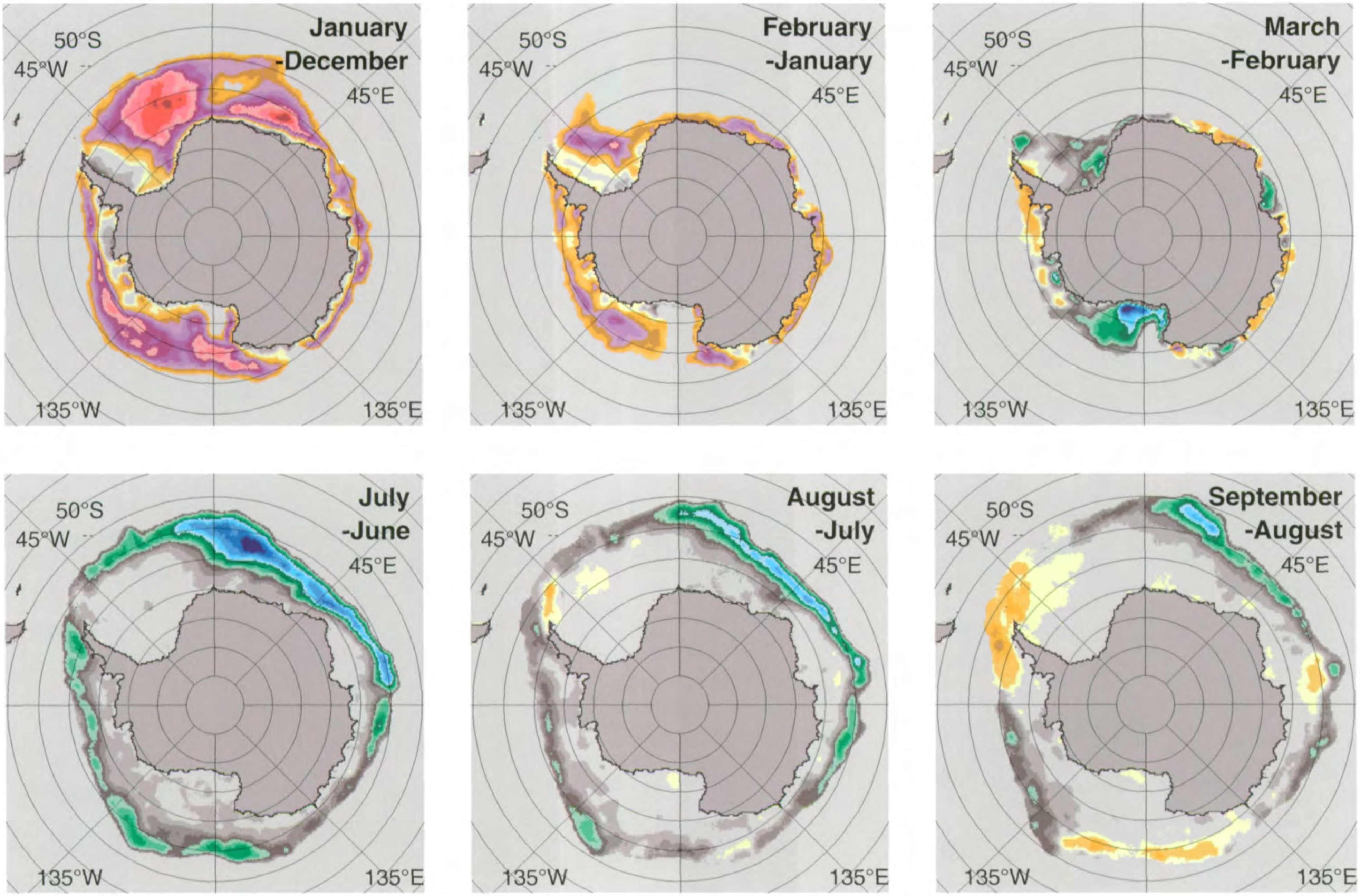
January
-December
February
-January
March
-February
July
-June
August
-July
September
-August
50°S
45°W
45°E
135°W
135°E

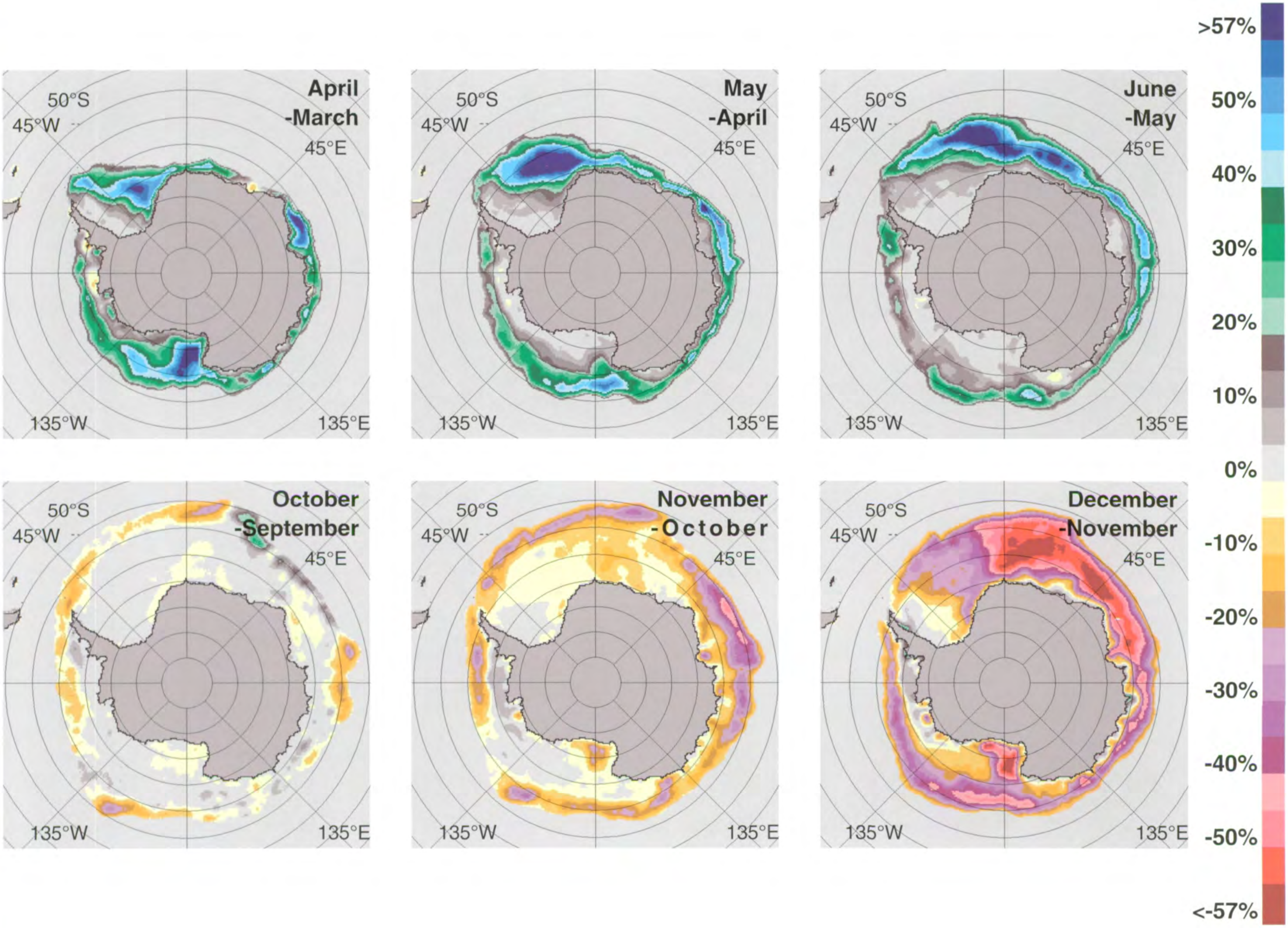

Figure 4.1.29. Monthly change in Antarctic sea ice concentrations averaged over the SMMR lifetime.

4.1.17-4.1.28) are obtained by subtracting the monthly concentrations averaged over the 1978-1987 period from the monthly maps. The anomaly maps are useful for describing the interannual variability of the sea ice distribution. The regional variability of the seasonal cycle is depicted in the monthly change maps (Figure 4.1.29), which are created by differencing pairs of consecutive monthly concentration maps to obtain growth and decay rates in units of concentration change per month and then averaging over the SMMR lifetime. Time series of daily (usually obtained every other day) sea ice extents, sea ice areas, and their differences (open water within the ice boundary) are given for the southern ocean region as a whole in Figure 4.2.1. The 9-year annual cycle and the month-by-month variability for all years are shown in Figures 4.2.2 and 4.2.3.

For the purpose of analyzing the regional characteristics of the sea ice distribution, the southern ocean is divided into five sectors (Figure 4.1.3) similar to those in the ESMR Antarctic atlas, although the original "Pacific Ocean" sector is renamed the "Western Pacific Ocean" sector. The areas of the sectors are given in Table 4.1.1. Time series similar to Figures 4.2.1 through 4.2.3 for the southern ocean region as a whole are also provided for each of the five sectors individually in Figures 4.3.1 through 4.7.3.

Table 4.1.1. Areas of the Southern Ocean Sectors

(in 10^6 km^2)

Weddell Sea	12.36
Ross Sea	9.64
Bellingshausen/Amundsen Seas	7.94
Indian Ocean	9.00
Western Pacific Ocean	7.76
Total sector area	46.70
(Antarctica, not included above	13.70)

The Weddell Sea sector (60° W to 20° E) contains relatively cold ocean waters influenced by a persistent large-scale cyclone in the Weddell Sea and the topographic barrier of the Antarctic Peninsula (Figure 4.1.3). The large area of compact sea ice remaining each summer and the occasional occurrence of the Weddell Polynya are partial consequences of these features. In the Indian Ocean sector (20° E to 90° E) and the Western Pacific Ocean sector (90° E to 160° E), where the continent extends farther from the pole, the sea ice edge retreats to the coast in many locations during the summer. The Ross Sea sector (160° E to 130° W), like the Weddell Sea sector, contains relatively cold water and a cyclonic circulation that influences the formation of open water near the front of the Ross Ice Shelf. The Bellingshausen-Amundsen Seas sector (130° W to 60° W) is characterized by strong stratification in the upper ocean (Gordon, 1967) that contributes to the retention of a large summer ice cover.

4.2 Southern Ocean

In winter, sea ice extends as far as 2,200 km from the Antarctic continent, covering approximately 19 x 10^6 km^2 of the southern ocean (Figure 4.2.1). In contrast to much of the Arctic sea ice pack, the Antarctic pack has an outer boundary unconstrained by land. Further, the Antarctic sea ice pack is subject to strong circumpolar winds that produce, on average, an outward stress component on the sea ice. Consequently, the Antarctic sea ice cover, surrounded by open ocean and acted on by circumpolar winds, is generally more divergent than much of the Arctic ice cover. Greater divergence of the ice pack produces a larger amount of open water and thin ice. Within the winter Antarctic ice pack, open water covers about 21% of the total area at maximum ice extent (Figure 4.2.1). The lowest ice concentrations are located in the outer margin of the ice pack and in numerous coastal polynyas around the continent (Kurtz and Bromwich, 1985; Cavalieri and Martin, 1985; and Zwally et al., 1985; Jacobs and Comiso, 1989), where drainage winds from the ice sheet force frequent changes in the ice concentration (Figures 4.1.11- 4.1.14). In the Weddell Sea, a very large (0.25 x 10^6 km^2) polynya, called the Weddell Polynya, persisted during the winters of 1974, 1975, and 1976 (Zwally et al., 1976, 1983a; Zwally and Gloersen, 1977), but did not reappear during the SMMR period.

In summer, the Antarctic ice pack retreats to the coast along approximately 50% of the Antarctic coastline. The largest areas of summer sea ice cover the eastern Ross Sea, much of the Bellingshausen and Amundsen Seas, and the western Weddell Sea, where the ice extends up to 1000 km from the coast (Figure 4.1.5). The total extent of the minimum summer ice pack is approximately 4 x 10^6 km^2 (Figure 4.2.1). The pattern of coastal polynyas changes from winter to spring, with the formation of numerous mesoscale coastal polynyas and open embayments in spring (see Figures 4.1.4 and 4.1.15). Some near-shore areas actually have more ice in summer than in winter because of the changes in wind-forcing of the ice pack (Zwally et al., 1985).

The seasonal cycle of southern ocean sea ice (see Figures 4.1.4 through 4.1.15 and 4.2.1) is characterized by a minimum in the sea ice cover during February. This is followed by an expansion of the ice cover until the maximum coverage during August to October, and then by a rapid decay from November through December. The average monthly ice-concentration difference maps in Figure 4.1.29 are useful for illustrating the spatially dependent ice growth and decay over an annual cycle. During February to March, growth of ice extent and area occur mainly in the Ross and Weddell Seas, while their decay continues near the outer margin of much of the ice pack, especially in the Bellingshausen-Amundsen Seas and Indian Ocean sectors. The most rapid expansion of the ice cover occurs during the period from March to June. The ice growth from February to March is more rapid in the Ross Sea than in the other four sectors. In the Weddell Sea, expansion of the ice cover during autumn is predominantly eastward, compared to a predominantly northward expansion elsewhere. During July to August, while ice growth is occurring throughout most of the ice pack, some decreases in ice concentration occur, mainly in the Weddell Sea and the inner Ross Sea.

Interannual variations in the growth rates for a given month can be inferred from the anomaly maps (Figures 4.1.17-4.1.28). A characteristic feature of the variations in ice coverage, which is apparent as early as March and April, is the pattern of alternate regions of anomalous growth or decay, each of which extends for several thousand kilometers along the outer perimeter of the ice pack (Figures 4.1.17-4.1.28). During the winter months of August, September, and October, the anomalies exhibit a zonal wave-number 3 pattern, on average, suggesting a close relationship to the large-scale atmospheric circulation noted previously by Cavalieri and Parkinson (1981), wherein a month-to-month shift in the circulation pattern influences the expansion and contraction of the ice cover in different regions. The September-August monthly difference map over the SMMR lifetime (Figure 4.1.29) also suggests a wave 3 pattern in the alternating regions of ice growth and decay. From October to February (Figure 4.1.29), decreases in ice concentration are evident throughout the ice pack.

While the SMMR day-to-day ice extent, ice area, and open water area within the pack presented in Figure 4.2.1 and the sea ice extent averaged over the SMMR lifetime given in Figure 4.2.2 are useful for examining the seasonal cycles, the month-by-month changes in ice extent given in Figure 4.2.3 facilitate a comparison with the month-by-month changes observed previously using the 4-year ESMR data set presented in the ESMR Antarctic atlas. The timing of the minimum or maximum ice extent in this figure may differ from the times obtained from Figure 4.2.1, which shows the SMMR day-to-day values, because the values shown in Figure 4.2.3 are monthly averages.

The month of minimum ice extent for all years during the SMMR period is February (Figure 4.2.3). The minimum February ice extent (3.2 x 10^6 km^2) observed in Figure 4.2.1 occurs in 1980 and 1984. The monthly averaged ice-extent values in Figure 4.2.3 clearly show the minimum (3.5 x 10^6 km^2) to occur in 1981. The minimum ice area (2.0 x 10^6 km^2) also occurs in 1981 and is accompanied by a predominance of negative values in the February 1981 anomaly map (Figure 4.1.18). For comparison with earlier measurements, the 4-year minimum in monthly averaged ice extent for 1973-1976 is 3.4 x 10^6 km^2 during February 1975 and the 4-year monthly averaged minimum in ice area is 2.2 x 10^6 km^2 during February 1974.

The greatest ice extent for February, the month of minimum ice cover, during 1978-1987 occurred in 1987 in both the day-to-day (4.0 x 10^6 km^2) and monthly averaged (4.2 x 10^6 km^2) values (Figures 4.2.1 and 4.2.3). However, the greatest ice area for February (2.3 x 10^6 km^2) occurs in 1979 and is accompanied by a predominance of positive values in the February 1979 anomaly map (Figure 4.1.18). For comparison, the greatest monthly averaged ice extent minimum for 1973-1976 is 4.3 x 10^6 km^2, occurring in February 1973, and the greatest ice area is 2.7 x 10^6 km^2, also in February 1973. Therefore, over the combined ESMR/SMMR observation periods, the monthly averaged ice extent during February varies between 3.4 and 4.3 x 10^6 km^2, and the ice area varies between 2.0 and 2.7 x 10^6 km^2. These values indicate an interannual variability of ±11% and ±16%, respectively, during these years. It is also interesting to note that the range in maximum-minimum ice extent and ice area was greater during the ESMR years than during the SMMR years, partly because of larger uncertainty in the ESMR data, as discussed in Chapter 2.

Also of interest is the interannual variability of the sea ice cover maxima. The smallest maximum monthly averaged ice extent is 18.0 x 10^6 km^2, which occurs in September 1986. The smallest ice-area maximum is 14.2 x 10^6 km^2 (Figure 4.2.1), which also occurs in September 1986. The September 1986 anomaly map of Figure 4.1.25 shows that the abnormally low ice extent and ice area are both caused by decreases in sea cover near the outer margin of the pack in all except the Bellingshausen-Amundsen Seas sector, with very small net changes within the ice pack. For comparison with earlier measurements, the 4-year winter minimum in monthly averaged ice-extent maxima for 1973-1976 is 19.0 x 10^6 km^2 during September 1976, and the 4-year winter minimum in ice area maxima is 14.7 x 10^6 km^2 during September 1974.

The largest monthly averaged ice-extent maximum during 1978-1987 is 19.1 x 10^6 km^2, which occurs in September 1985 (Figure 4.2.3). The largest ice-area maximum is 15.5 x 10^6 km^2, which occurs in September 1980 when the ice extent is only 0.01 x 10^6 km^2 less than in 1985 (Figure 4.2.1). In general, the winter anomaly maps exhibit a large degree of regional variability, with positive anomalies in some regions and negative anomalies in other regions. In September 1980, the time of the largest ice-area maximum, a large positive anomaly in the Weddell Sea sector is only partially compensated for by negative anomalies in the Bellingshausen-Amundsen Seas and Western Pacific sectors (Figure 4.1.25). In September 1985, a large positive anomaly in the eastern part of the Ross Sea sector is only partially compensated for by negative anomalies principally in the Weddell Sea sector. For comparison with earlier measurements, the 4-year winter maximum monthly averaged ice extent for 1973-1976 is 20.2 x 10^6 km^2, and the 4-year winter maximum monthly averaged ice area is 15.9 x 10^6 km^2, both during September 1973.

Over the combined observation period, the ice extent during September varies between 18.0 and 20.2 x 10^6 km^2, and the ice area varies between 14.2 and 15.9 x 10^6 km^2. These values indicate an interannual variability in the winter ice cover of ±5% in both ice extent and ice area during these years. The difference of these two, the open water within the pack, varies from about 3.8 x 10^6 km^2 to about 4.6 x 10^6 km^2 (Figure 4.2.1). The maxima persist from September to December and represent about 21% of the area enclosed by the 15% margin, the ice extent, during that period. The years of largest winter ice coverage (1973, 1980, and 1985) span most of the observation period, and both 1973 and 1985 are followed by one or more years with anomalously low winter ice cover. Characterization of the magnitude of the interannual variability in this manner provides a basis for the assessment of possible longer term trends in the ice cover.

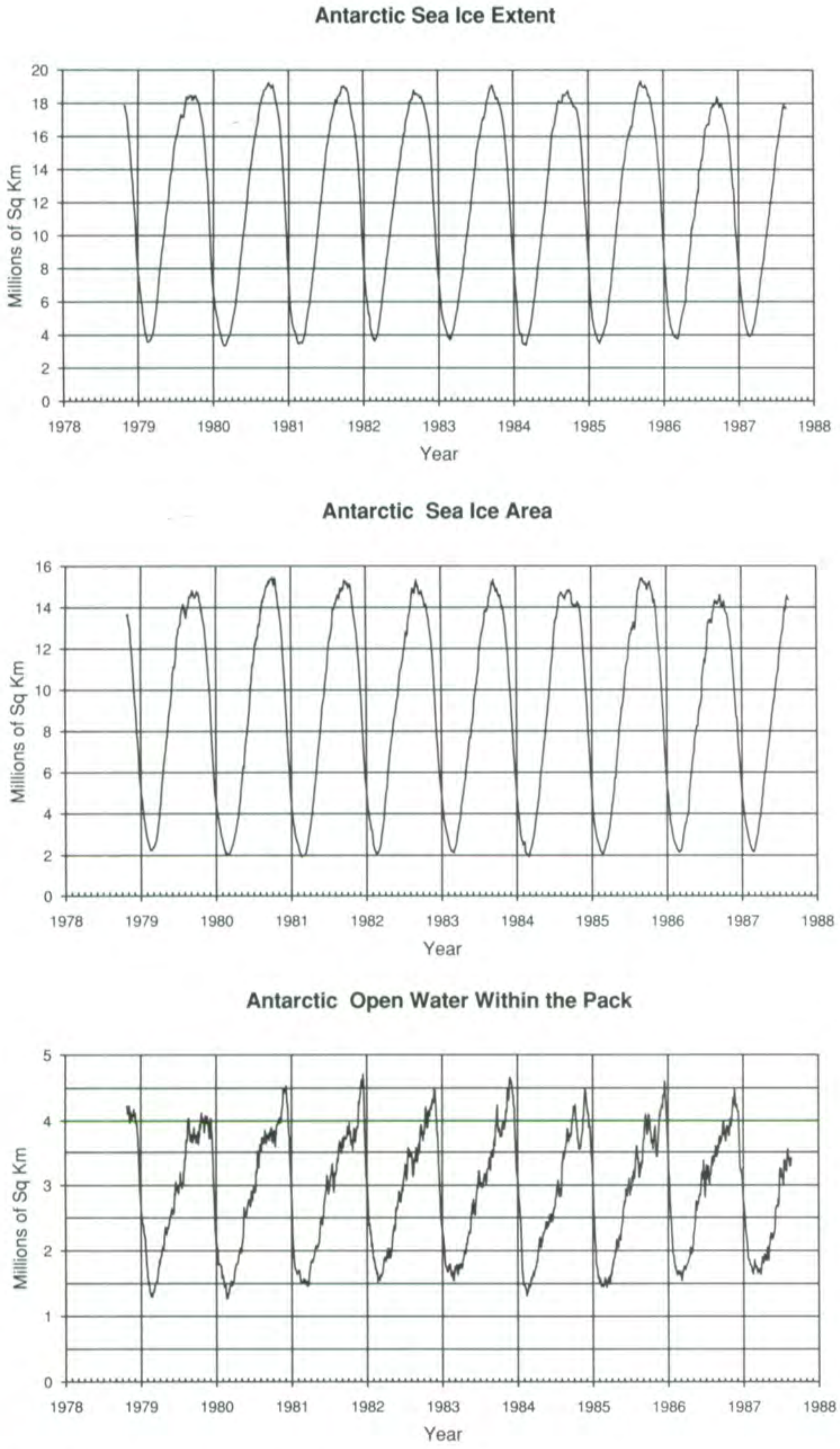

Figure 4.2.1. Sea ice extent, sea ice area, and amount of open water within the pack for the Antarctic from October 26, 1978 to August 20, 1987.

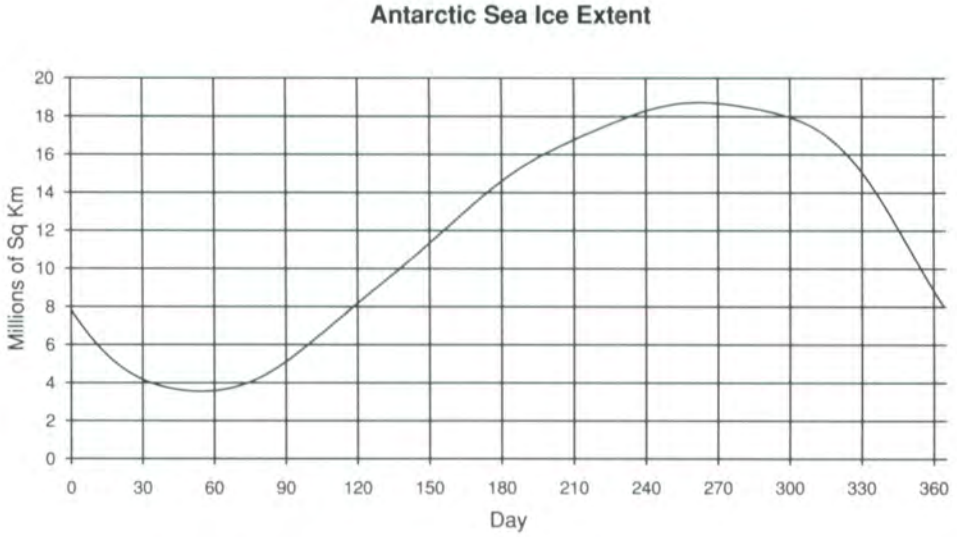

Figure 4.2.2. Average seasonal cycle of sea ice extent in the Antarctic as obtained by Fourier analysis.

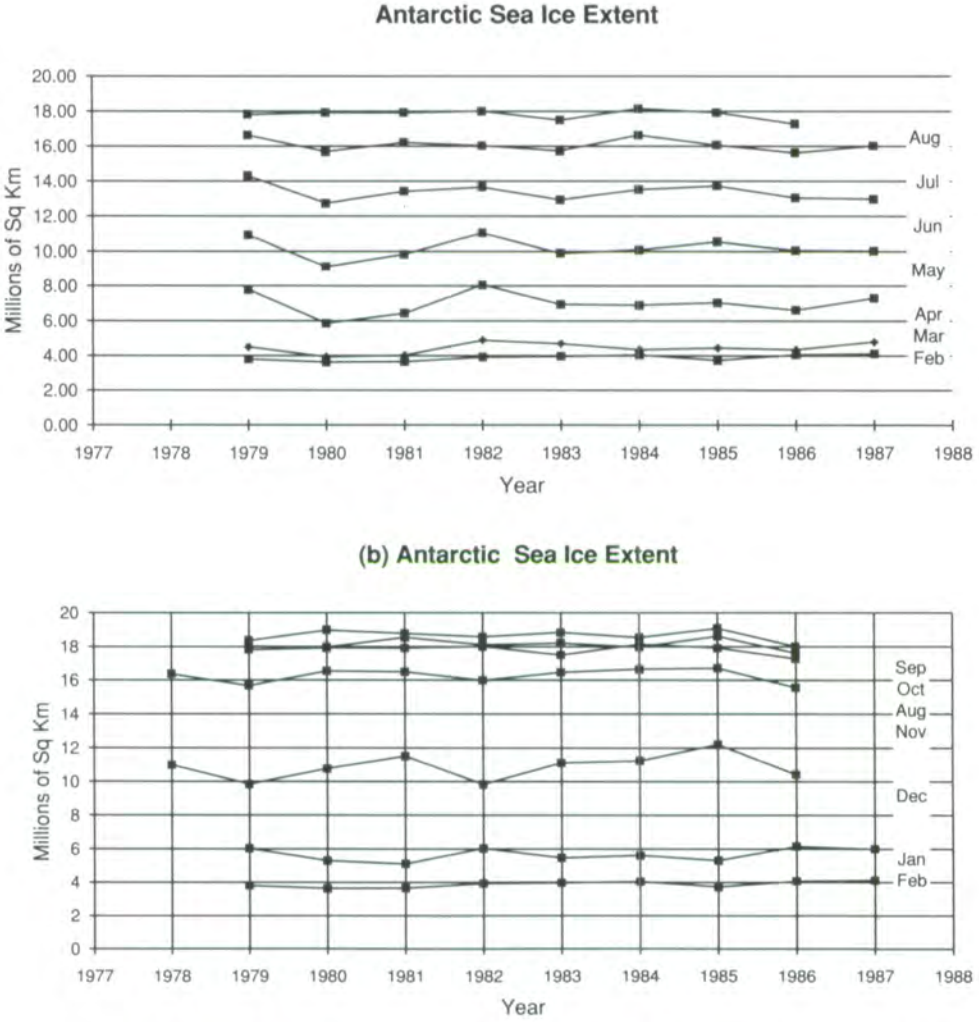

Figure 4.2.3. Month-by-month, year-to-year changes of the sea ice extent in the Antarctic, (a) February to August, (b) August to February.

The pattern of the interannual anomalies also provides some insight into the atmospheric and oceanic processes that may be causing these anomalies. It is evident that the winter anomalies occur largely in the outer zone of the ice pack and are, therefore, likely to be related to interannual variations in the atmospheric circulation, with northerly or southerly extensions of the pack being driven by variations in the wind forcing. In many cases, the winter sea ice anomaly pattern can be described by a wave number (e.g., four in 1985, three in 1986, and two in 1979), which tends to persist throughout each winter season from June through October, and which is characteristic of large-scale variations in the atmospheric circulation (Parkinson and Cavalieri, 1982).

Interannual anomalies during February have a pattern indicative of mesoscale processes. Also, the pattern of summer anomalies tends to appear only in January and disappear within a couple of months after the February summer minimum. Although the pattern of summer anomalies does not persist in the sea ice cover from month to month, there is a year-to-year persistence. For example, the anomalously low summer-ice cover in the eastern Ross Sea from 1979 to 1981 is followed first by a mixture of positive and negative anomaly patterns, and then by positive anomalies in 1985 and 1986. These summer anomalies are more likely to be associated with oceanic and radiative processes, whereby the year-to-year persistence is maintained by factors such as oceanic heat storage (Badgley, 1966; Jacobs and Comiso, 1989).

4.3 Weddell Sea

The Weddell Sea has been identified as the major source of Antarctic bottom water and one of the few oceanic regions with deep vertical mixing. Details are still unknown, but it has been postulated that the bottom-water formation process is greatly influenced by the large variability of the ice production in the region (Gordon, 1974, 1982; Foster and Carmack, 1976). The ice extent, ice area, and open water area within the ice pack in the Weddell Sea sector over the 8.8-year SMMR period are shown in Figure 4.3.1 Sea ice extent in the Weddell Sea varies from about 0.9×10^6 km^2 in austral summer of 1981 to about 7.6×10^6 km^2 in austral winter of 1980. The winter ice-extent maximum varies by about 1.7×10^6 km^2 from a minimum in 1986 to its maximum in 1980 during the SMMR period. It is interesting to note that the winter of 1980, when the ice extent and area are the greatest, is followed by the summer with the least ice extent and area. This sequence is suggestive of a greater retention of oceanic heat during the winter, which may enhance the melting of the summer ice (Fletcher, 1969).

A comparison of ice-concentration maps for each month shows considerable variability over several years (Figures 4.1.4-4.1.15; see also Parkinson, 1992). The times of most rapid change in the Weddell Sea are from November to January and from April to June (Figure 4.3.1 and 4.1.29), when the coastal area usually becomes free of ice except along the Antarctic Peninsula, where ice survives the summer (Figures 4.1.4-4.1.5). Interannual variations in the rate of decay vary substantially, with 1980 having the least amount of ice along the coast. In February, the ice cover is reduced to its minimum extent. The coastline from the Greenwich meridian to the Ronne Ice Shelf was largely free of ice during most SMMR years. In March, the advance of ice is slow but obvious, with the rate of advance varying considerably from one year to the next and with the rates slowest and fastest in 1981 and 1979, respectively (Figure 4.1.19). By April, the ice cover has advanced to the farthest north at some meridional locations (e.g., 40° W to 50° W). The influence of the Weddell Gyre (Figure 4.1.2) on the ice cover, i.e., the longitudinal protrusion east of the tip of the Antarctic Peninsula, can be seen most clearly in January 1979 and in January, February, and April 1980.

In May, ice advance continues, basically north-eastward, with the eastern edge close to the Greenwich meridian. During some years (e.g., 1982) a sharp north-south boundary is observed near the Greenwich Meridian, while in other years (e.g., 1985), it is not as obvious. Part of the reason might be oceanographic, since this sharp edge coincides approximately with the location of Maud Rise, which was the site of the large Weddell Polynyas in the 1970s (Zwally et al., 1976, 1983a; Gordon, 1978) and which is now known to be an area where the deep water is significantly warmer than adjacent regions (Bagriantsev et al., 1989; Gordon and Huber, 1990). This is also an area where the ice is generally thinner (Wadhams et al., 1987). By June, the portion of the sector south of 60° S is almost completely covered with sea ice. From June through September, a significant eastward advance of the ice cover is apparent, with the most obvious being in 1984 (Figure 4.1.9 through 4.1.12). The maximum extent occurs in September (Figure 4.3.2), with the ice margin extending as far north as 54° S near 10° E (Figure 4.1.16).

The seasonal breakup of ice in the Weddell Sea generally begins in November, usually starting inside the ice pack near Maud Rise (Figure 4.1.16) as a result of oceanographic factors (Martinson et al., 1981, Comiso and Gordon, 1987). Extensive breakup also occurs along the coastal regions, especially near the Riiser-Larsen Ice Shelf (about 73° S, 15° W). The overall character of the ice pack changes dramatically in December, when a large fraction of the ice cover east of 45° W melts at almost the same time. The most rapid retreat of the Weddell Sea ice cover occurs over the 2-month period December through January (see Figure 4.3.2).

Both the spatial and temporal change in ice cover can be evaluated with the aid of the monthly difference maps shown in Figure 4.1.29. In the Weddell Sea sector, ice growth is greatest during the months of March through July, with the ice edge advancing very rapidly from west to east or from south to north. In August and September, ice cover advance is observed in the eastern Weddell Sea, but at the same time, a loss in ice cover is apparent in the western Weddell Sea. Maximum extent occurs either in September or October, followed by a rapid decay in November, December, and January.

An interesting interannual difference in the Weddell Sea ice distribution is provided by the years 1980 and 1983. In September 1980, the ice cover was at its 8.8-year maximum, and the ice edge at about 35° W was farther north

Sea Ice Extent in the Weddell Sea

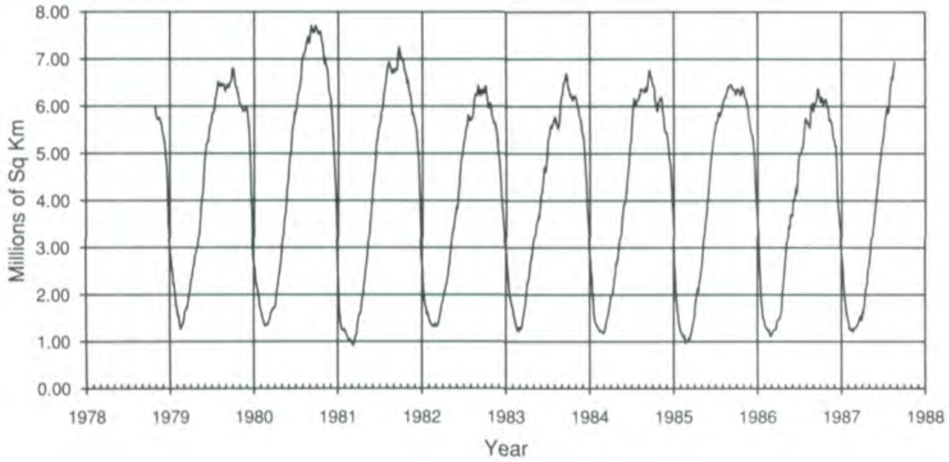

Sea Ice Area in the Weddell Sea

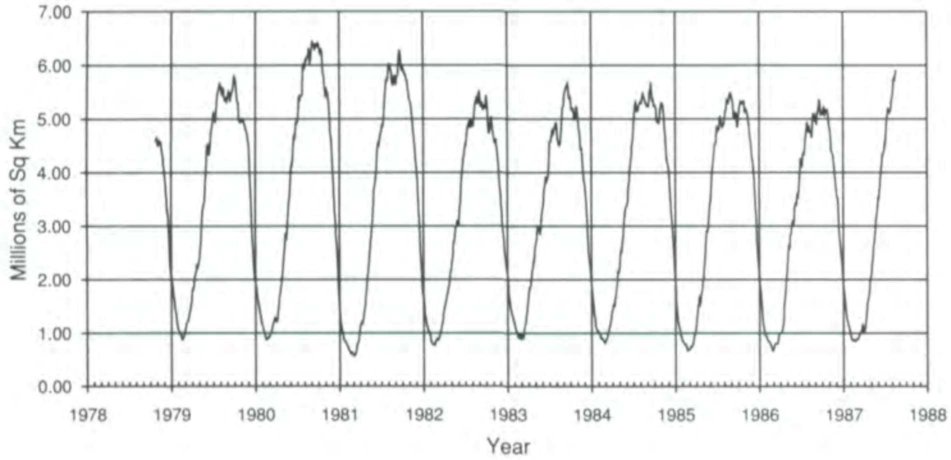

Open Water Within the Pack in the Weddell Sea

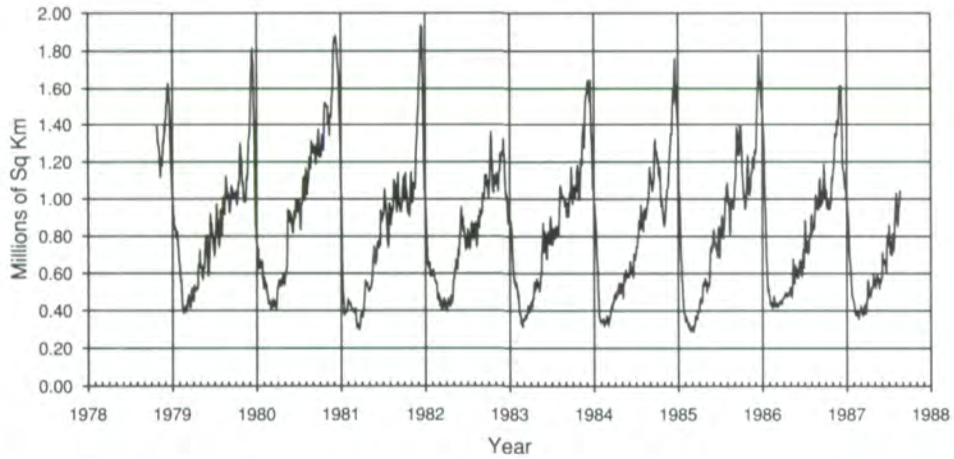

Figure 4.3.1. Sea ice extent, sea ice area, and amount of open water within the pack for the Weddell Sea from October 26, 1978 to August 20, 1987.

Sea Ice Extent in the Weddell Sea

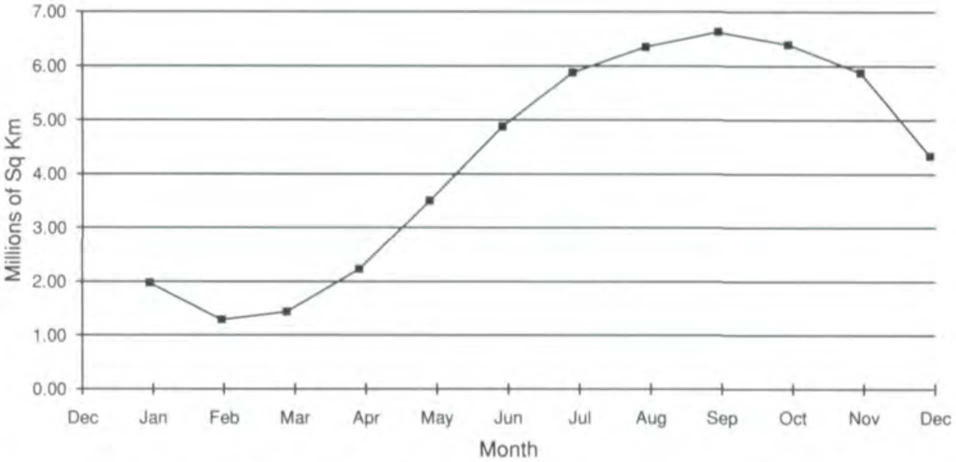

Figure 4.3.2. Average seasonal cycle of sea ice extent for the Weddell Sea.

Sea Ice Extent in the Weddell Sea

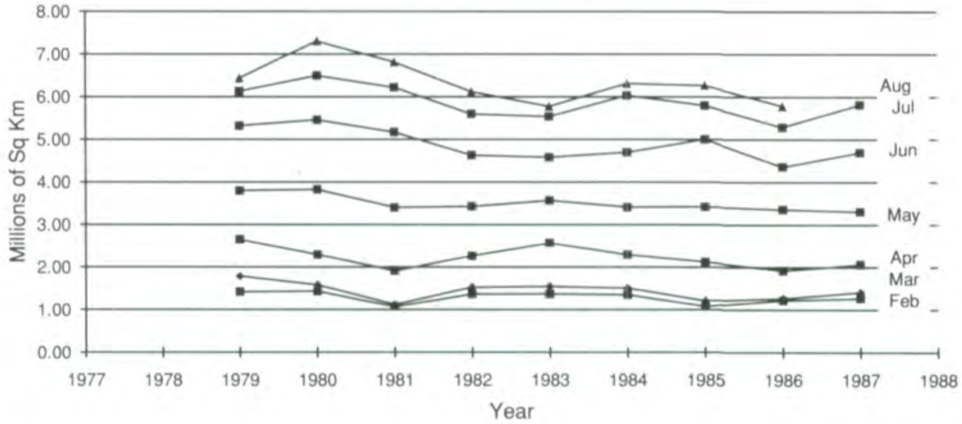

(b) Sea Ice Extent in the Weddell Sea

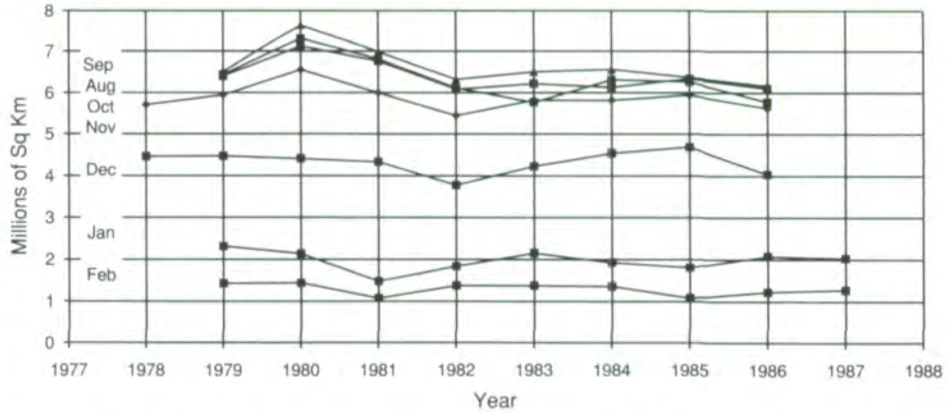

Figure 4.3.3. Month-by-month, year-to-year changes of the sea ice extent in the Weddell Sea, (a) February to August, (b) August to February.

than in any other SMMR year, while 1983 had a relatively small September ice maximum (Figure 4.3.3). The sequence of both the monthly ice-concentration maps (Figures 4.1.4 to 4.1.8) and the anomaly maps (Figures 4.1.17 to 4.1.21) for January through May shows a strikingly different spatial distribution for the two years, apparently the result of strong interannual differences in atmospheric and oceanographic forcing.

4.4 Ross Sea

The Ross Sea sector (from 160° E to 130° W, Figure 4.1.3) extends farther south than any of the other sectors. In the southwest, the sea ice is bounded by the Ross Ice Shelf and the northernmost extension of the Transantarctic Mountains, from which small outlet glaciers emerge. In the southeast, it is bounded by small ice shelves and outlet glaciers from the West Antarctic Ice Sheet.

The shape of the edge of the ice pack in the Ross Sea sector is influenced by the Antarctic Circumpolar Current and deflections of the current by the submarine topography (Figure 4.1.2) (Zwally et al., 1985). In particular, the persistent northward extension of the pack around 145° W in September (Figure 4.1.12) is a manifestation of this relationship. The cyclonic ocean circulation in the Ross Sea influences the formation of open water near the front of the Ross Ice Shelf, where periodic areas of reduced concentration are observed during winter and a mesoscale polynya forms in the spring as the pack ice opens to the north (Figures 4.1.14-4.1.15).

The seasonal cycle of the sea ice extent and the area of sea ice in the Ross Sea (Figures 4.4.1-4.4.3) differs from the seasonal cycle in the other sectors. The growth of the ice cover occurs most rapidly in the 3-month period from March to June (Figure 4.4.2), followed by a slower expansion until September. It is noteworthy that the peaks of the ice areas and extents (Figure 4.4.1) tend to be broader in the Ross Sea than in the Weddell Sea (Figure 4.3.1). Rapid decay of the ice cover occurs from November to February, not unlike that for the Weddell Sea. In January and February, the western portion is mostly ice-free, including most of the area along the Ross Ice Shelf edge (Figures 4.1.4, 4.1.5 and 4.1.16). (At least some of the ice concentration observed along the coast is probably caused by the sensor's 55-km integrated FOV smearing the land-ocean boundary, see Section 2.2.3.) In contrast, the eastern portion retains a sea ice cover that extends over 700 km, on average, from the coast (Figure 4.1.5). In 1979 and 1980, the eastern portion of the Ross Sea sector has considerably less ice than in other years (Figure 4.4.1).

The year-to-year monthly averaged variations of the ice extent in the Ross Sea are shown in Figure 4.4.3. The austral summers of 1979 and 1980 are marked by anomalously low sea ice extents in the Ross Sea of only 0.3-0.4 x 10^6 km^2, resulting from the unusually small ice cover in the eastern portion of this sector. This is followed by an increase of the summer-ice extent to 1.1 x 10^6 km^2 in 1987 (see also Figure 4.4.1). For four of the SMMR years, the month of sea ice extent maximum is September with the maximum extent occurring in August for three of the years, and only in 1986 is October the month of maximum extent (Figure 4.4.3). In contrast to the Weddell Sea sector, the ice extent is greater in the later SMMR years than in the earlier years. Only in 1986 do both sectors show a relatively low ice cover (Figures 4.3.3 and 4.4.3). Interestingly, for the Ross Sea sector there is a positive trend in sea ice extent for the summer months November through February over the SMMR years.

The anomaly maps (Figures 4.1.17 through 4.1.28) illustrate the considerable spatial variability in sea ice concentration from one year to the next, particularly in the central and eastern portions of the sector during January and February. During the months of maximum ice extent, most, but not all, of the variability occurs at the ice-pack perimeter. There is generally a transition from a positive anomaly zone to a negative zone as a result of the semipermanent low-pressure system located in this region.

During the winter, the amount of open water within a few hundred kilometers of the Ross Ice Shelf is strongly influenced by the synoptic weather systems that force the sea ice away from the ice shelf (Zwally et al., 1985). During these events, the normal drift of ice away from the shelf with the cyclonic ocean circulation (Figure 4.1.3) is greatly enhanced. The amount of open water over approximately a 121,000-km^2 area (centered at 77.5° S, 178.7° E) in front of the ice shelf averaged 22% during the winter of 1974 (Zwally et al., 1985). Similar open water values can be inferred from Figures 4.1.8-4.1.13. In other regions along the coast, the open water area during winter is predominantly associated with outlet glaciers, where the channeling of katabatic winds from the ice sheet causes frequent openings and closings of near-shore polynyas, e.g., Terra Nova Bay at 75° S, 165° E (Kurtz and Bromwich, 1985). Two areas of polynyas were also identified (Jacobs and Comiso, 1989) near the continental shelf break that occur primarily during spring and autumn, but have reduced ice concentrations during winter. One polynya area northeast of the Pennell Bank (75° S, 175° W) and the other northeast of Victoria Land appear to be maintained by divergence above a submarine bank and by upwelling of warmer water near the slope front.

Sea Ice Extent in the Ross Sea

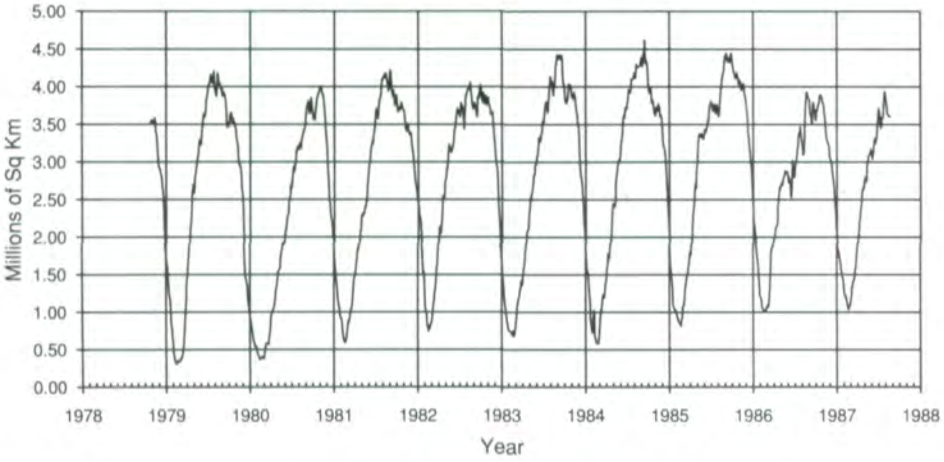

Sea Ice Area in the Ross Sea

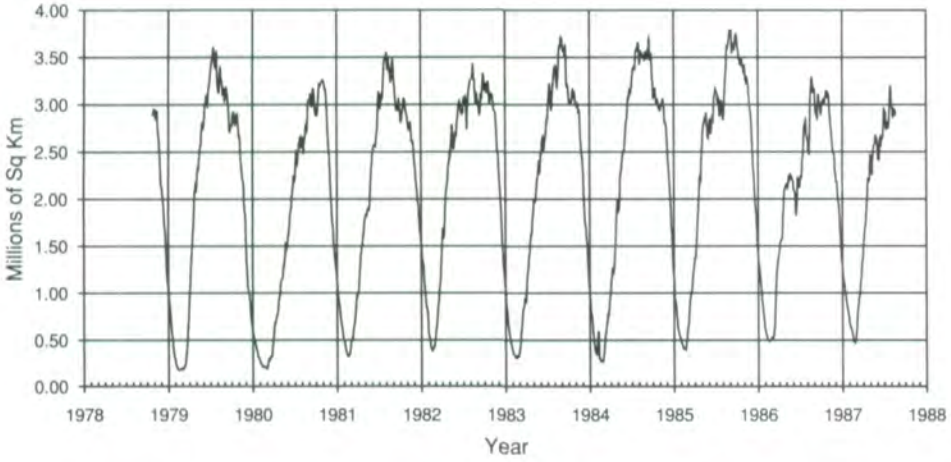

Open Water Within the Pack in the Ross Sea

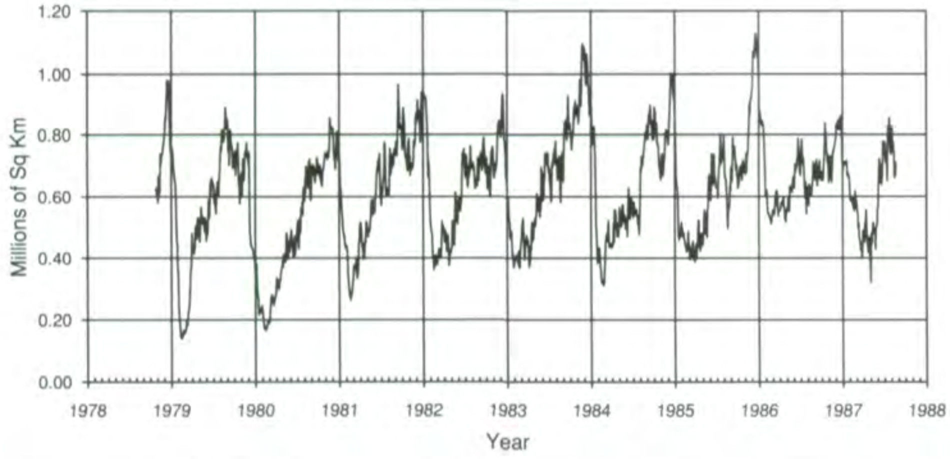

Figure 4.4.1. Sea ice extent, sea ice area, and amount of open water within the pack for the Ross Sea from October 26, 1978 to August 20, 1987.

Sea Ice Extent in the Ross Sea

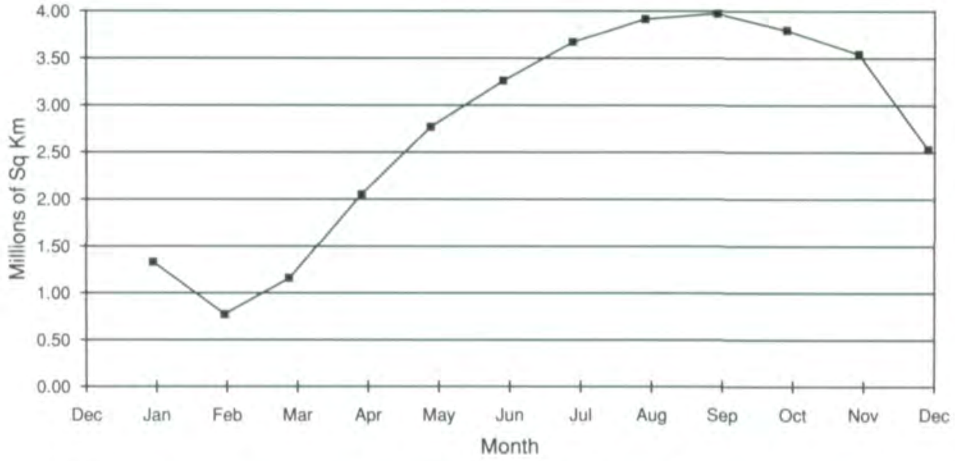

Figure 4.4.2. Average seasonal cycle of sea ice extent for the Ross Sea.

(a) Sea Ice Extent in the Ross Sea

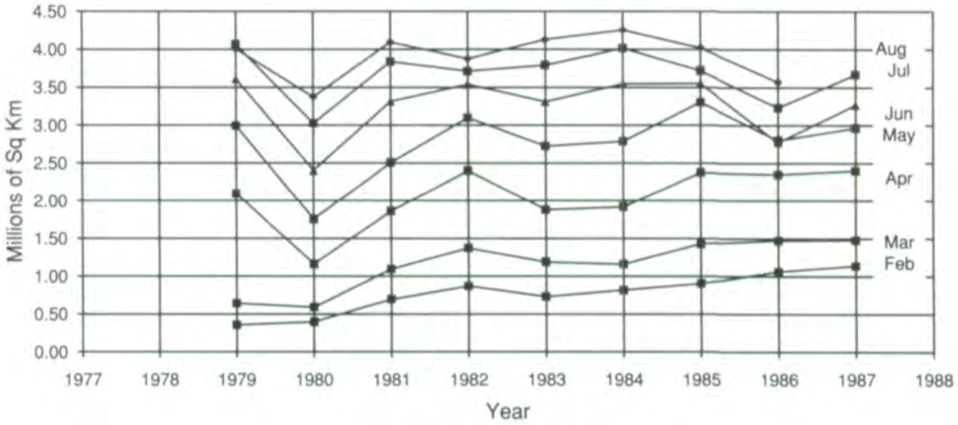

(b) Sea Ice Extent in the Ross Sea

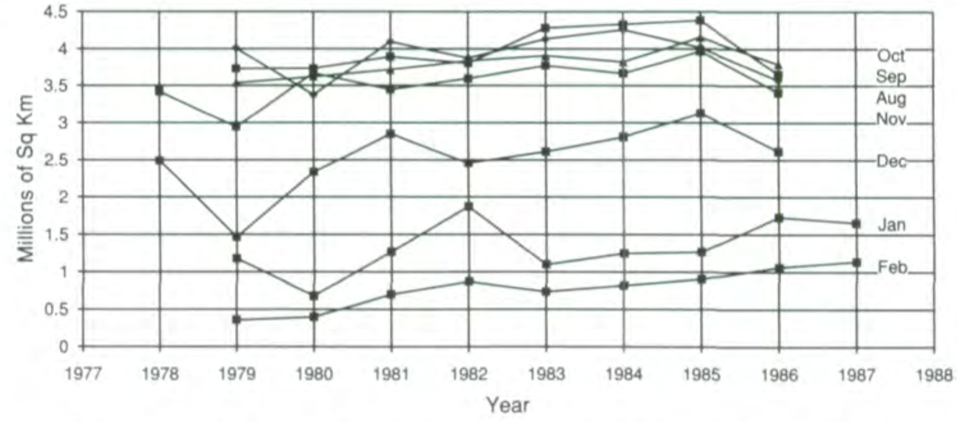

Figure 4.4.3. Month-by-month, year-to-year changes of the sea ice extent in the Ross Sea, (a) February to August, (b) August to February.

4.5 Bellingshausen and Amundsen Seas

The Bellingshausen and Amundsen Seas sector (Figure 4.1.3) has the second largest (second only to the Weddell Sea sector) ice cover during the summer. The ice cover in this region also has the least seasonal variation among the southern ocean sectors. The reason for this is unknown, but it may be caused partly by below-freezing surface temperatures throughout most of the year and partly by the north-south coastline of the Antarctic Peninsula, which diverts the Circumpolar Current.

The ice area in the Bellingshausen and Amundsen Seas sector has a summer-to-winter ice-cover ratio of about 1 to 4 (Figure 4.5.1). The ice extent varies from about 0.7 x 10^6 km^2 in austral summer of 1984 to about 2.8 x 10^6 km^2 in austral winter of 1986. Within the ice pack, the area covered by open water is about 0.3 x 10^6 km^2 in summer and about 0.7 x 10^6 km^2 in winter. The open water area is largest in 1986 and smallest in 1983.

The average seasonal cycle for sea ice extent for this sector (Figure 4.5.2) reveals a number of interesting differences. Unlike the Ross and Weddell sea sectors, the minimum sea ice extent occurs in March rather than in February, although the February extent is only slightly higher than the March minimum. The monthly average sea ice extents for each of the years (Figure 4.5.3) show a large interannual variability. This is in contrast to either the Weddell or Ross sea sectors that show less interannual variability for these months of ice growth. Unlike the year-to-year, monthly averaged ice extents for the Ross Sea sector (Figure 4.4.3), the Bellingshausen and Amundsen Seas sector (Figure 4.5.3) shows no overall trend. The sea ice extents during August, September, and October decrease from 1979 to 1983 and increase from 1983 to 1986, in contrast to the Ross Sea sector that shows relatively higher winter ice extents from 1981 through 1986. This suggests that the interannual fluctuations in sea ice extent between the Ross and Bellingshausen and Amundsen Seas result largely from large-scale atmospheric influences. The monthly images of ice concentration (Figures 4.1.4-4.1.15) provide information about the spatial distribution of the ice cover in the region. In winter, large areas of low ice concentration (70%-80%) can be observed in approximately the same region where ice survived in the summer. While the ice cover reaches its minimum in the Bellingshausen and Amundsen Seas sector during March, significant ice growth is already evident in the adjacent Ross Sea sector. The advance of sea ice is evident in the autumn, but the concentration within the ice pack is significantly lower than in the other sectors. Early winter coverage can be very different during different years. For example, during July 1980, ice exists west of the tip of the Antarctic Peninsula, but during July 1983, the same region is ice-free. In spring, the ice margin retreats gradually toward the south, and breakup within the pack is minimal, except in some coastal polynya areas, the most prominent of which is along the coast in the Amundsen Sea (Figure 4.1.15).

The anomaly maps (Figures 4.1.17-4.1.28) delineate the spatial distribution of the large interannual ice-cover variations in the Bellingshausen and Amundsen Seas. The large positive sea ice-extent anomalies in April, May, and June 1982, observed in Figure 4.5.3, result from an advance of the ice edge along almost the entire perimeter of the ice pack (Figures 4.1.20 to 4.1.22). Only in the region west of the Antarctic Peninsula is there a reduction in ice extent for these three months. These anomaly maps also show that this positive anomaly extends throughout the Ross Sea sector and includes positive increases in ice concentration over most of the ice-covered seas in these two sectors. The anomaly map (Figure 4.1.25) for September, the month of maximum ice extent, indicates that the year-to-year spatial variability observed in this sector is generally part of large-scale hemispheric changes probably associated with large-scale atmospheric variability noted earlier in this chapter.

Sea Ice Extent in the Bellingshausen and Amundsen Seas

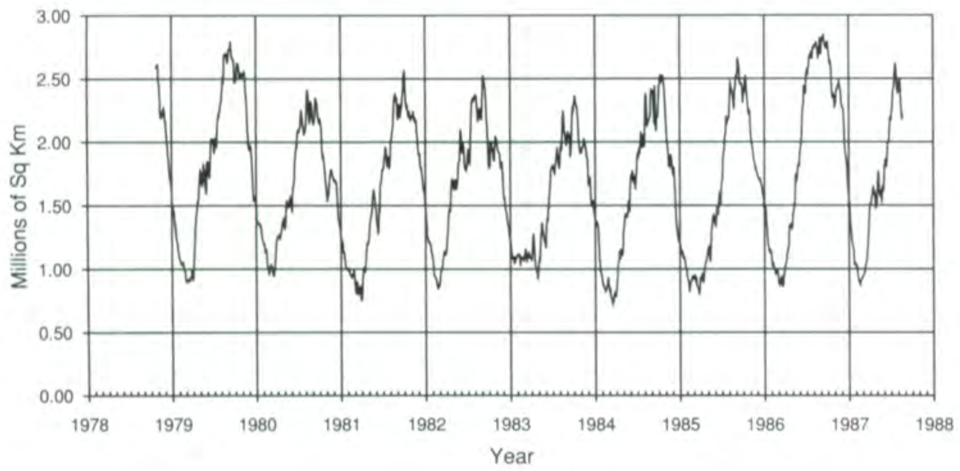

Sea Ice Area in the Bellingshausen and Amundsen Seas

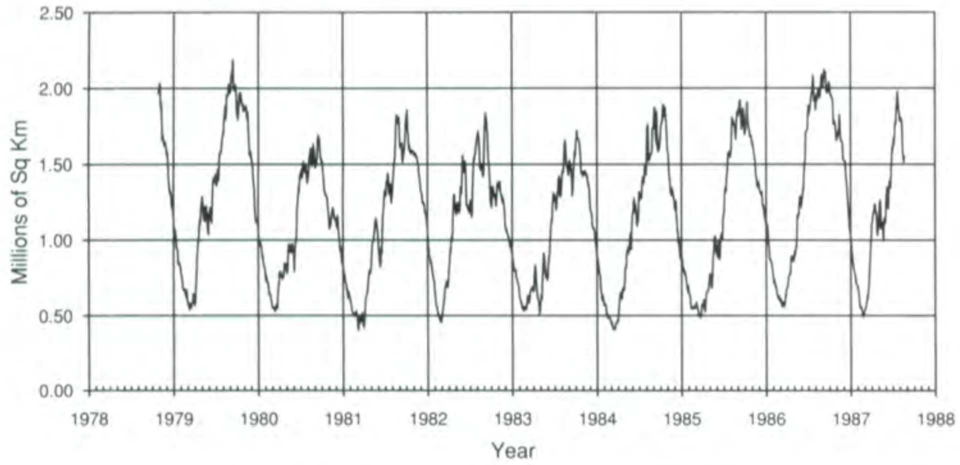

Open Water Within the Pack in the Bellingshausen and Amundsen Seas

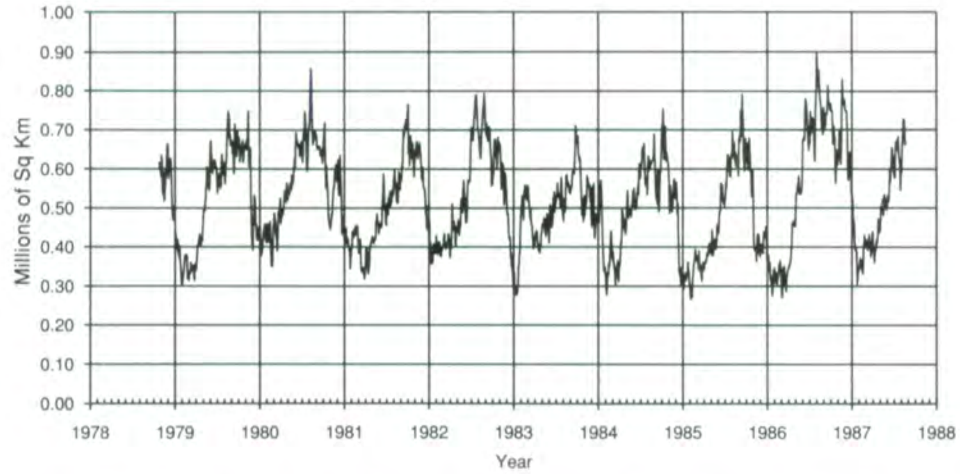

Figure 4.5.1. Sea ice extent, sea ice area, and amount of open water within the pack for the Bellingshausen and Amundsen Seas from October 26, 1978 to August 20, 1987.

Sea Ice Extent in the Bellingshausen and Amundsen Seas

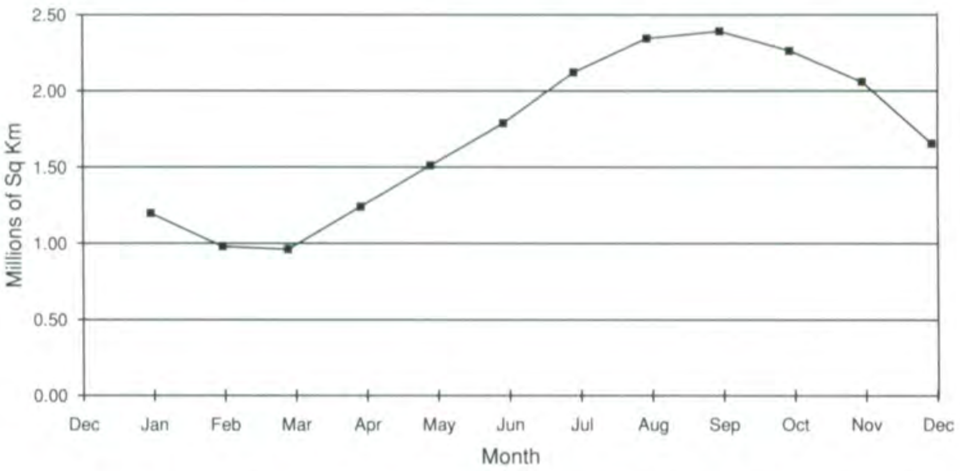

Figure 4.5.2. Average seasonal cycle of sea ice extent for the Bellingshausen and Amundsen Seas.

(a) Sea Ice Extent in the Bellingshausen and Amundsen Seas

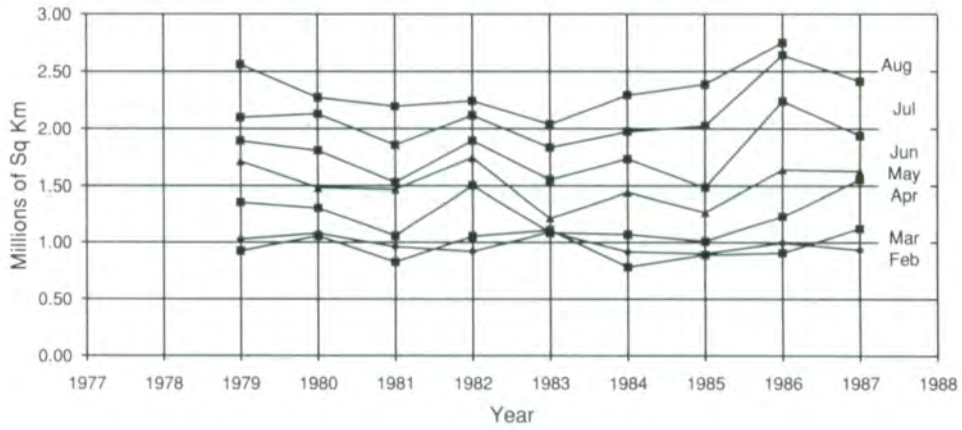

(b) Sea Ice Extent in the Bellingshausen and Amundsen Seas

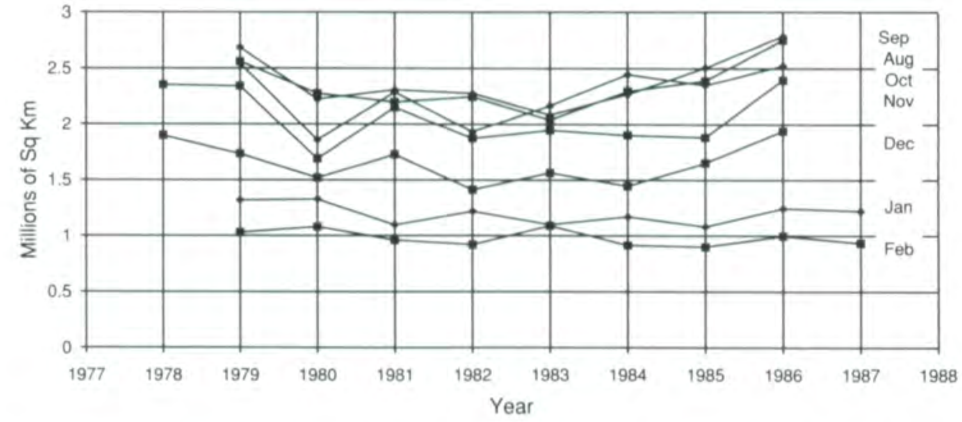

Figure 4.5.3. Month-by-month, year-to-year changes of the sea ice extent in the Bellingshausen and Amundsen Seas, (a) February to August, (b) August to February.

4.6 Indian Ocean

The Indian Ocean sector (Figure 4.1.3) is located at the eastern edge of the Weddell Gyre. It is also the site of some isolated and relatively shallow pycnoclines near the coastal regions (Jacobs et al., 1980; Gordon and Molinelli, 1982). In the Cosmonaut Sea, at about 45° E, a recurring deep-ocean polynya has been observed (Comiso and Gordon, 1987), which in many ways has the same formation characteristics as the large Weddell Polynya in the mid-1970s as seen in the ESMR Antarctic atlas. Similar to the Weddell Polynya, this polynya is usually preceded by an embayment and is located near a topographic rise. However, unlike the Weddell Sea polynya, it usually lasts for less than a month, because it is damped out by sea ice inflow as a result of its relatively small size. Polynyas must reach a certain critical size before they can persist throughout the winter (Comiso and Gordon, 1987). Although the area of open water is not as large as in the Weddell Polynya, the Cosmonaut Sea polynya occurs more frequently and the integrated effect on the oceanography may be comparable. The area is also the site of relatively large coastal polynyas along the Indian Ocean (e.g., Prydz Bay).

The areal extent, ice area, and open water area within the pack for the Indian Ocean sector are shown in Figure 4.6.1. The average seasonal cycle and seasonal cycles by month are shown in Figures 4.6.2 and 4.6.3. The ice cover in this sector is primarily seasonal, decreasing in extent from about 3.6 x 10^6 km^2 in winter to about 0.4 x 10^6 km^2 in summer (Figure 4.6.2). The ice area decreases from about 3 x 10^6 km^2 in winter to about 0.2 x 10^6 km^2 in summer (Figure 4.6.1b). The winter extent is at its 8.8-year maximum in 1981 and at its minimum in 1986 for the period 1978-1987 (Figure 4.6.1a).

While the year-to-year monthly sea ice-extent data (Figure 4.6.3) show that the minimum ice extent for this sector occurs in February or March, the monthly ice-concentration maps (Figure 4.1.5 and 4.1.6) and the monthly maps averaged over the SMMR lifetime (Figure 4.1.16) show some spatial differences during these months. The ice extent is at its minimum in the eastern part of the Indian Ocean sector near Prydz Bay in February, and is at its minimum in the western part along the Princess Ragnhild Coast in March. This spatial contrast is unusual because the continental boundary is farther north in the eastern than in the western part. This may be caused partly by higher surface-air temperatures in the eastern regions than in the western region in February, as suggested by climatological temperature data mapped in the ESMR Antarctic atlas. Prydz Bay in the eastern portion of this sector is the site of a large coastal polynya, which serves as an area of high ice production (Zwally et al., 1985). Thus, in autumn, the ice cover is more extensive in the eastern region of the sector than in the west. However, by midwinter, the reverse is true, partly because of west-to-east advance or advection of sea ice in the Weddell Sea. Although it seldom lasts for more than a few weeks, the Cosmonaut Sea polynya (Comiso and Gordon, 1987) is visible in some of the monthly images. For example, it appears as a low-concentration area near 45° E in September 1979, July and August 1980, and September 1986 (Figures 4.1.10 to 4.1.12). This region is also an area of rapid melting during spring that is particularly evident in the averaged seasonal cycle (Figure 4.6.2), with early decay located near the site of the Cosmonaut Sea polynya.

The difference maps (Figure 4.1.29) show continuous growth in the Indian Ocean sector from March through September. Ice growth is usually inhibited during April through May (e.g., 1980) near 45° E where the Cosmonaut Sea polynya usually appears, while the most rapid ice area growth rate usually occurs in July. In October, the ice cover in this region is at its maximum and is usually most stable. However, in some years (1979, 1982, and 1984), the ice cover is still in the process of advancing during this month, while in other years (1986) the ice is already receding as indicated in the anomaly maps (Figures 4.1.17 to 4.1.28). The decay process occurs very fast during November and December in the region, reducing the area of the ice cover to less than 0.1 x 10^6 km^2 during the summer.

Sea Ice Extent in the Indian Ocean

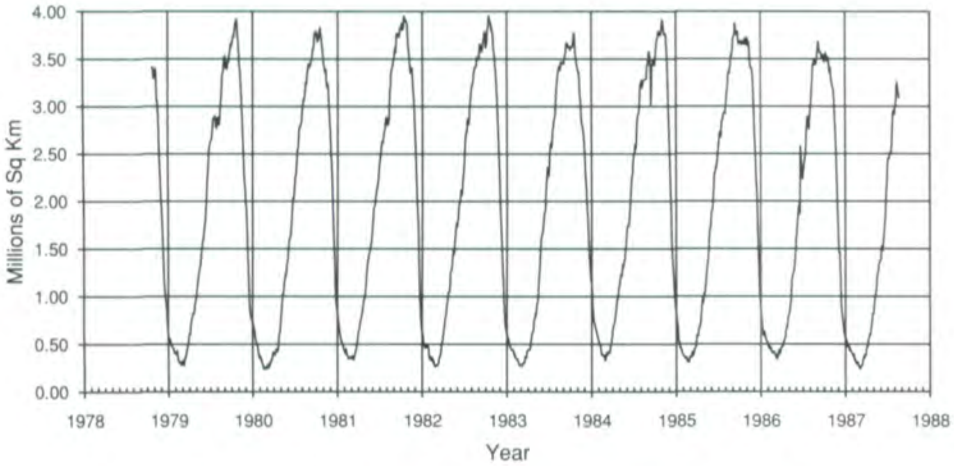

Sea Ice Area in the Indian Ocean

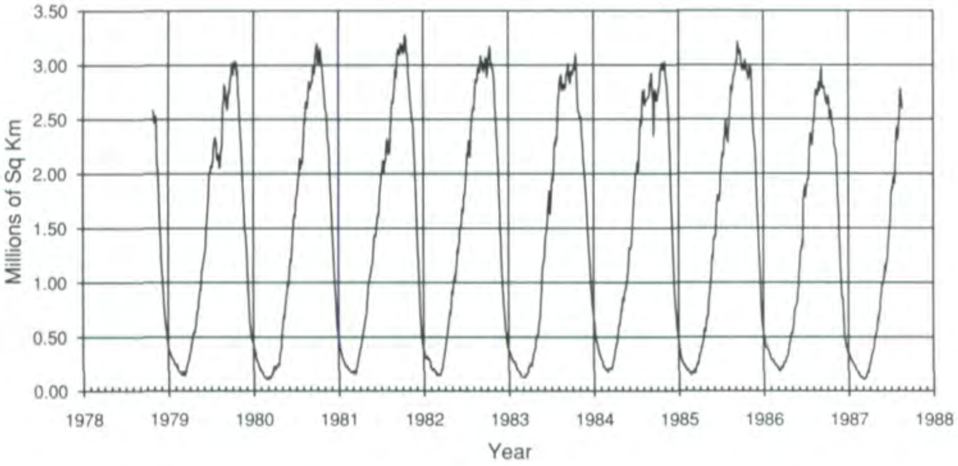

Open Water Within the Pack in the Indian Ocean

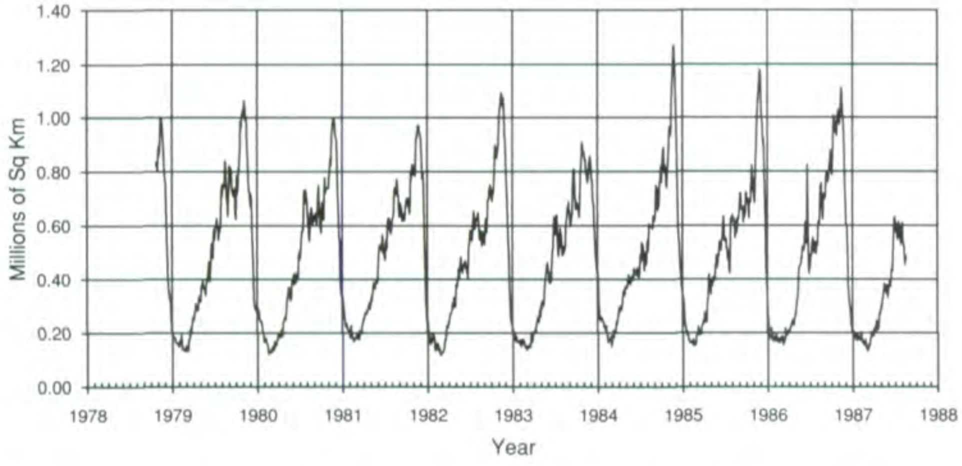

Figure 4.6.1. Sea ice extent, sea ice area, and amount of open water within the pack for the Indian Ocean from October 26, 1978 to August 20, 1987.

Sea Ice Extent in the Indian Ocean

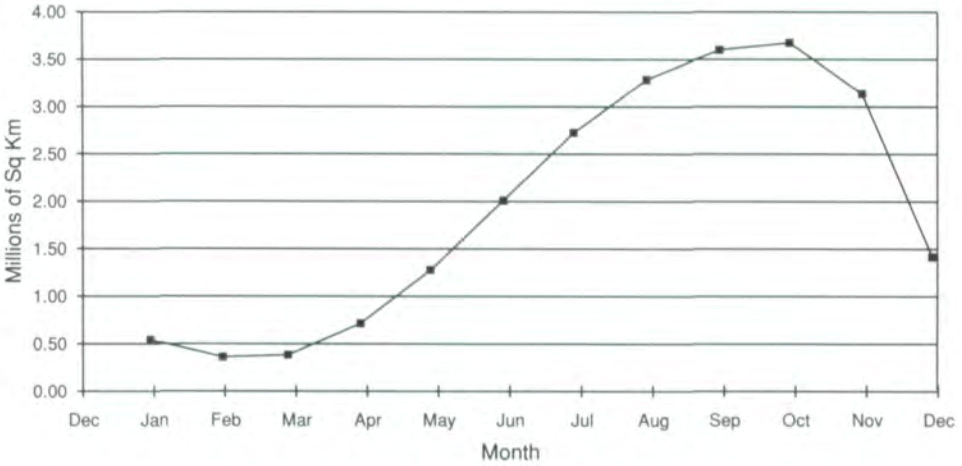

Figure 4.6.2. Average seasonal cycle of sea ice extent for the Indian Ocean.

(a) Sea Ice Extent in the Indian Ocean

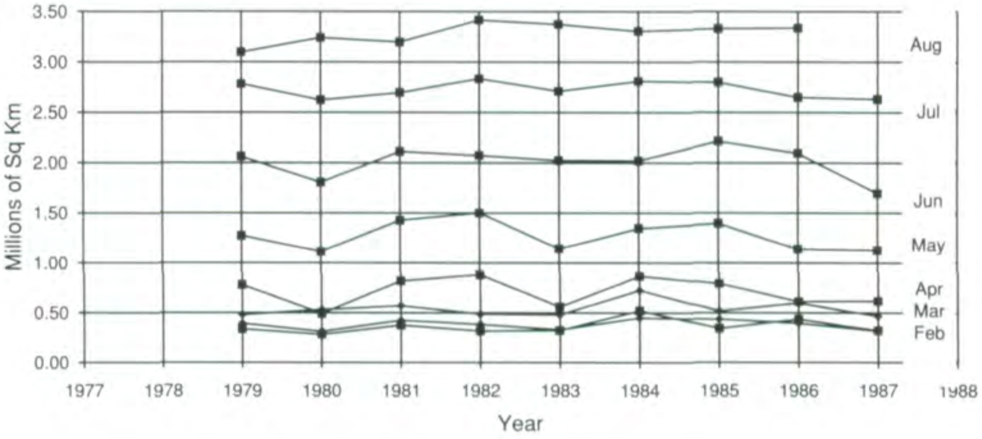

(b) Sea Ice Extent in the Indian Ocean

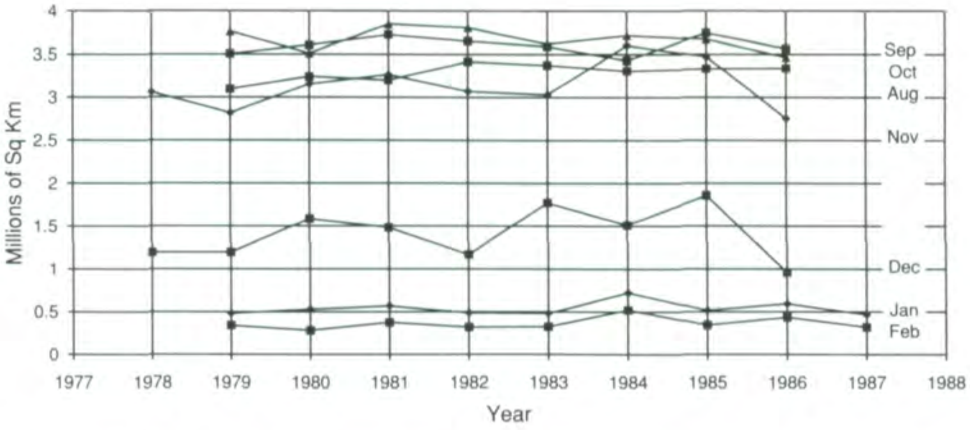

Figure 4.6.3. Month-by-month, year-to-year changes of the sea ice extent in the Indian Ocean, (a) February to August, (b) August to February.

4.7 Western Pacific Ocean

The Western Pacific Ocean sector (Figure 4.1.3) is the region south of Australia and New Zealand and is the region that is farthest from the pole. Climatological temperatures also indicate that it is the warmest southern ocean sector, and the ice cover is the least extensive throughout the year. Seasonal changes are also not as pronounced as those in other sectors because the ice edge advances to only about 500 km from the coast, whereas the ice edge may extend as far as 1500 km elsewhere. The monthly images of ice concentration (Figures 4.1.4-4.1.15) show that this sector is almost free of ice for the months of February and March. The winter months show a characteristic depletion of the ice cover in the central region (about 135° E). The width of the ice pack in the central section is about 300 km, which is comparable to the size of some marginal ice zones in other regions. At the western boundary, it can be as wide as 1000 km.

As in the other sectors, the Western Pacific sector is the site of many coastal polynyas, primarily initiated by katabatic winds from adjacent mountains and glaciers. Some of the more persistent polynyas identified are found along the Wilkes Land Coast from Cape Adare to the Shackleton Ice Shelf. These polynyas serve not only as sites of intense oceanic ventilation during winter, but are also sources of new ice and cold, saline shelf water. The production of this dense shelf water by the coastal polynyas is believed to be an important source of Antarctic bottom water (Gordon, 1974). Studies of these polynyas using ESMR and SMMR data support this hypothesis (Cavalieri and Martin, 1985; Zwally et al., 1985).

The areal extent, ice area, and open water area within the ice pack for this sector are shown in Figure 4.7.1. Ice extent in the Western Pacific Ocean sector ranges from about 0.3×10^6 km^2 in austral summer, 1986, to a maximum of about 2.6×10^6 km^2 in austral winter, 1982. The ice area, on the other hand, changes from 0.2×10^6 km^2 in summer, 1986, to as much as 2.1×10^6 km^2 in winter, 1982. As in some of the other sectors, the peaks and troughs of the open water in the ice pack are not coincident with the extrema in the area and extent, and range from about 0.15×10^6 km^2 in summer, 1986 to about 0.8×10^6 km^2 in winter, 1982. The ice cover was unusually large in 1982 and 1983, about 25% greater than average. The average seasonal cycle of the sea ice extent is shown in Figure 4.7.2.

The year-to-year monthly averaged ice concentrations (Figure 4.7.3) show that while there was an increase in ice extent from 1980 to 1982 for the months of April, May, June, and July, by far the greatest increase in ice extent occurred from July to August in 1982 and, to a lesser extent, in 1983. The August monthly ice-concentration map (Figure 4.1.11) and the August anomaly map (Figure 4.1.24) indicate that most of the ice growth occurred in the western portion of this sector (about 100° E). The August anomaly map also shows that the Indian, Western Pacific and Ross Sea sectors have above-average ice extents and concentrations, while the Weddell and Bellingshausen-Amundsen Sea sectors have below-average ice covers.

Sea Ice Extent in the Western Pacific Ocean

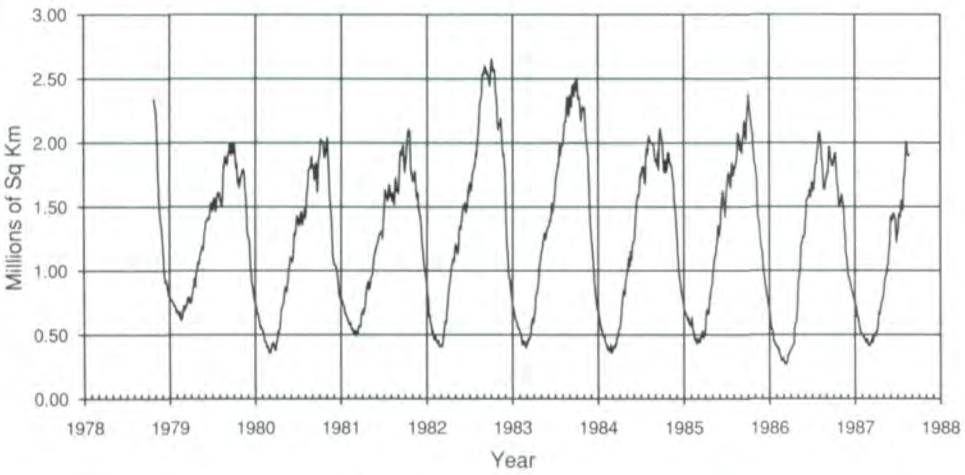

Sea Ice Area in the Western Pacific Ocean

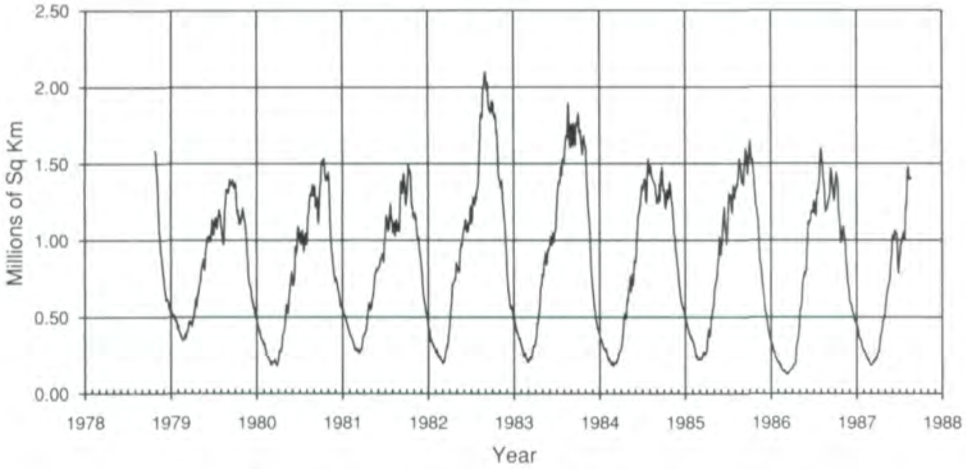

Open Water Within the Pack in the Western Pacific Ocean

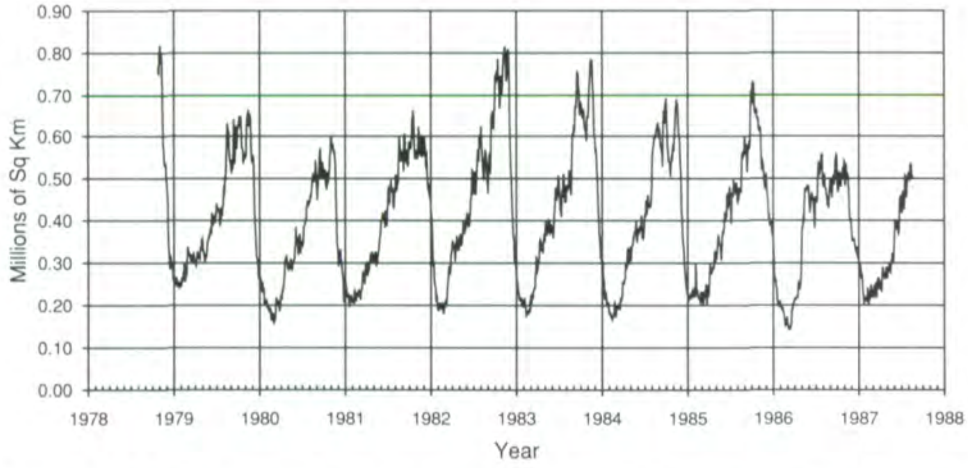

Figure 4.7.1. Sea ice extent, sea ice area, and amount of open water within the pack for the western Pacific Ocean from October 26, 1978 to August 20, 1987.

Sea Ice Extent in the Western Pacific

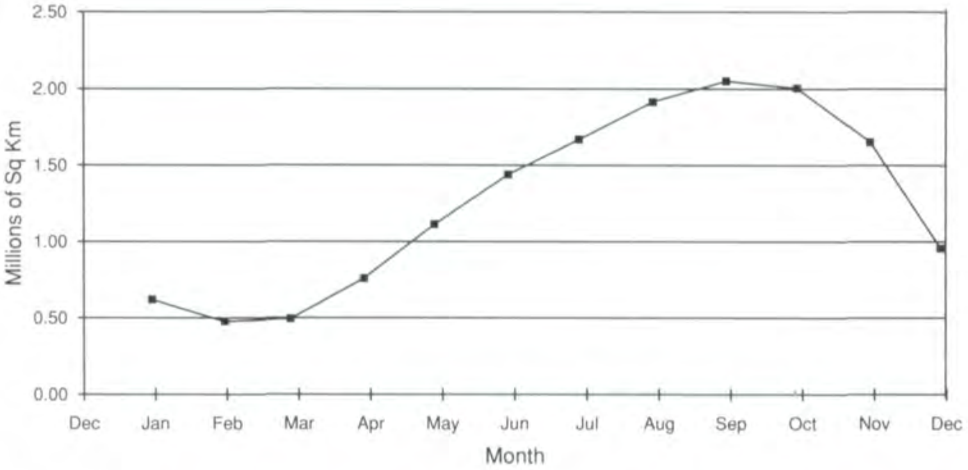

Figure 4.7.2. Average seasonal cycle of sea ice extent for the western Pacific Ocean.

(a) Sea Ice Extent in the Western Pacific

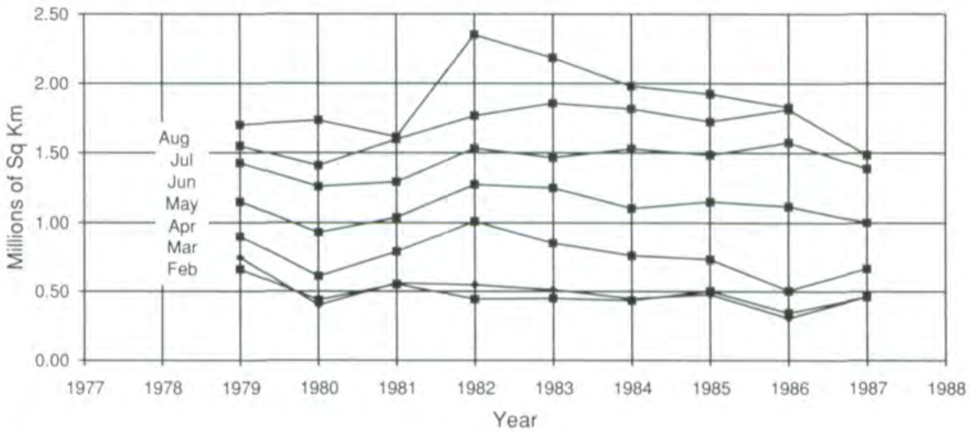

(b) Sea Ice Extent in the Western Pacific

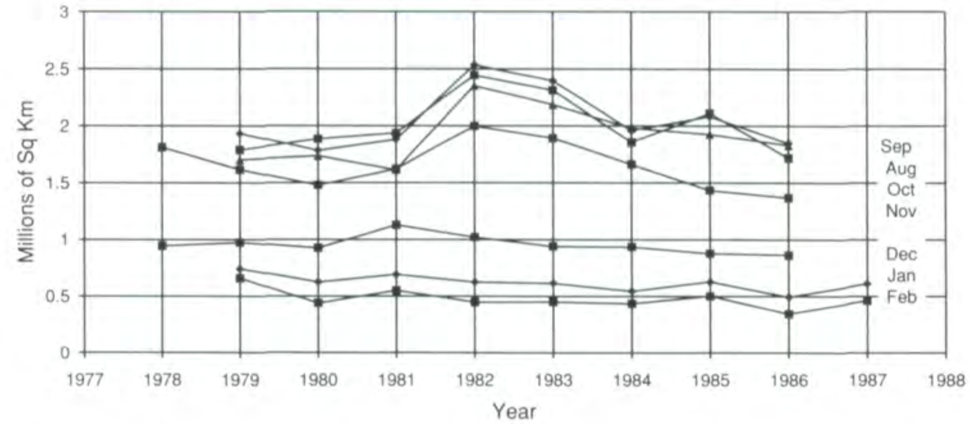

Figure 4.7.3. Month-by-month, year-to-year changes of the sea ice extent in the western Pacific Ocean, (a) February to August, (b) August to February.

5

REGIONAL, INTERANNUAL, AND GLOBAL VARIATIONS OF SEA ICE

The realization that sea ice variations can be indicators of climatic change has long been cited as a reason for monitoring the ice canopy of the Earth with satellite observations. While the satellite record is still too short to provide evidence of change on climatic time scales, the existing satellite record has been examined for changes in the sea ice areas and extents in both the Antarctic (Sissala et al., 1972; Streten, 1973; Budd, 1975; Kukla and Gavin, 1981; Zwally et al., 1983a) and the Arctic (Carsey, 1982; Campbell et al., 1984; Parkinson et al., 1987; Gloersen and Campbell, 1988a; Parkinson and Cavalieri, 1989). Sea ice extent extrema were first studied on a global scale by Gloersen and Campbell (1988a) using both the ESMR and SMMR data sets, but at that time still uncorrected for instrument drift and orbital errors. More recently, Gloersen and Campbell (1991a,b) have extended the SMMR analysis using the corrected data set. In this chapter, we update the interregional Arctic comparisons of Parkinson and Cavalieri (1989) with corrected annually averaged SMMR data, present a similar comparison for the Antarctic, and summarize the global analyses of Gloersen and Campbell (1991a,b). Finally, we present some comparisons of SMMR and SSMI sea ice data during the 2-month period of sensor overlap. These results provide a measure of the degree of consistency in sea ice concentrations obtained from the two sensors.

5.1 Interannual Variations of Annual Mean Ice Extents

Two dominant characteristics of both the Arctic and Antarctic sea ice covers as revealed by the SMMR record in Chapters 3 and 4 are the large seasonal cycle and the large regional variability in each hemisphere. Another characteristic is the surprisingly low interannual variability for each hemisphere as a whole, given the large regional variability of ice extents, areas, and open water amounts from year to year. Those regions and sectors showing the largest interannual variability are located in seasonal sea ice zones, areas particularly susceptible to large-scale atmospheric forcing. Previous studies have demonstrated that much of the interannual variability observed on a regional scale can be explained by large-scale atmospheric or oceanic forcing (Walsh and Johnson, 1979; Overland and Pease, 1983; Crane, 1983; Parkinson and Gratz, 1983; Cavalieri and Parkinson, 1987; Niebauer, 1988; Enomoto and Ohmura, 1990).

For the purpose of examining the annual contribution of each region to the overall interannual variability observed for each hemisphere, annual averages of sea ice extents were calculated for each Arctic and Antarctic region. These are plotted in Figures 5.1.1 and 5.1.2, together with trend lines. Following Parkinson and Cavalieri (1989), the trend lines were calculated by employing a linear-least-squares analysis for these annual averages, in order to determine which regions are positive contributors and which regions are negative contributors to the overall hemispheric ice-cover trends over the 8.8-year SMMR record. The total and regional trends are summarized for both the Arctic and the Antarctic in Table 5.1.1. These trends are generally not statistically significant because of the very small number of data points and their large standard deviation from the trend.

Table 5.1.1. Total and Regional Linear-Least-Squares Trends for the Annually Averaged Arctic and Antarctic Sea Ice Extents

REGION	SLOPE *($X10^6$ km^2/yr)*	AVERAGE ABSOLUTE DEVIATION FROM TREND *($X10^6$ km^2)*
Arctic		
Arctic Ocean	0.005	0.022
Okhotsk/Japan	-0.015	0.037
Bering Sea	0.006	0.024
Hudson Bay	0.006	0.012
Baffin Bay/Davis Str./ Labrador Sea	0.019	0.068
Gulf of St. Lawrence	0.004	0.006
Greenland Sea	-0.005	0.045
Kara/Barents	-0.028	0.065
Canadian Archipelago	0.000	0.003
Total	-0.008	0.091
Antarctic		
Weddell Sea	-0.064	0.12
Ross Sea	0.056	0.14
Bellingshausen/ Amundsen Seas	0.004	0.10
Indian Ocean	0.008	0.07
Western Pacific Ocean	-0.001	0.08
Total	0.003	0.17

(a) Total Arctic

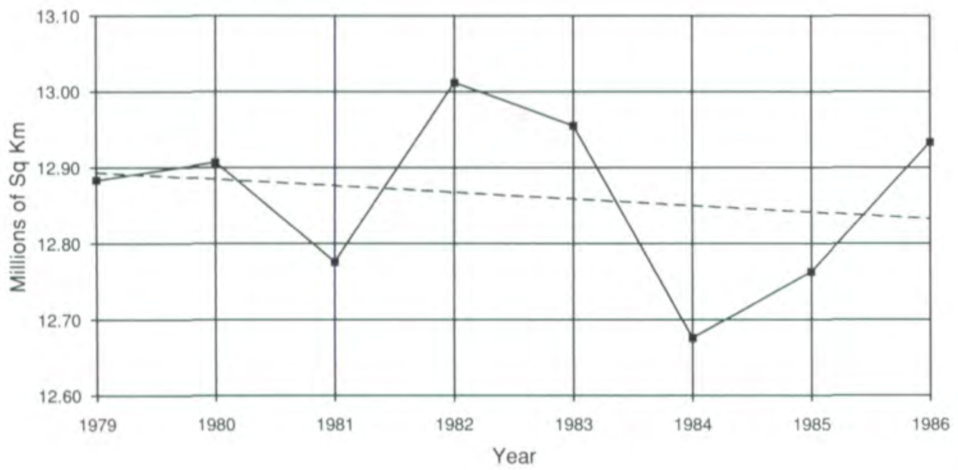

(b) Arctic Ocean

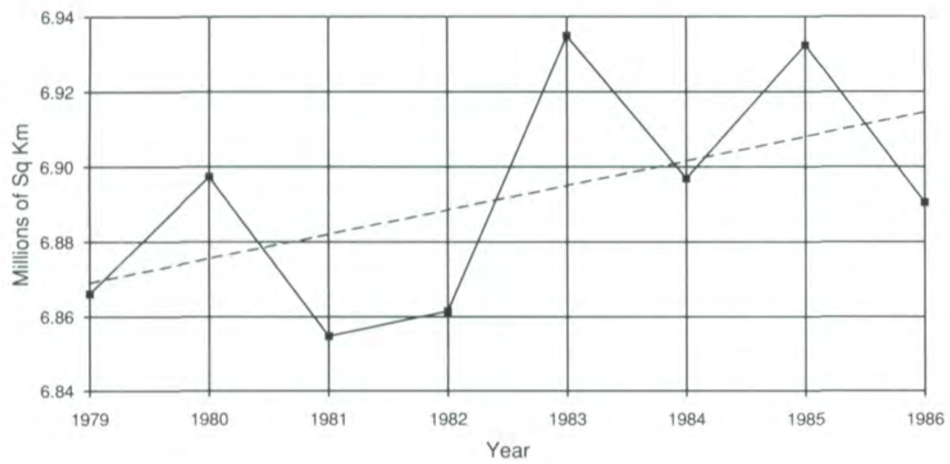

(c) Seas of Okhotsk and Japan

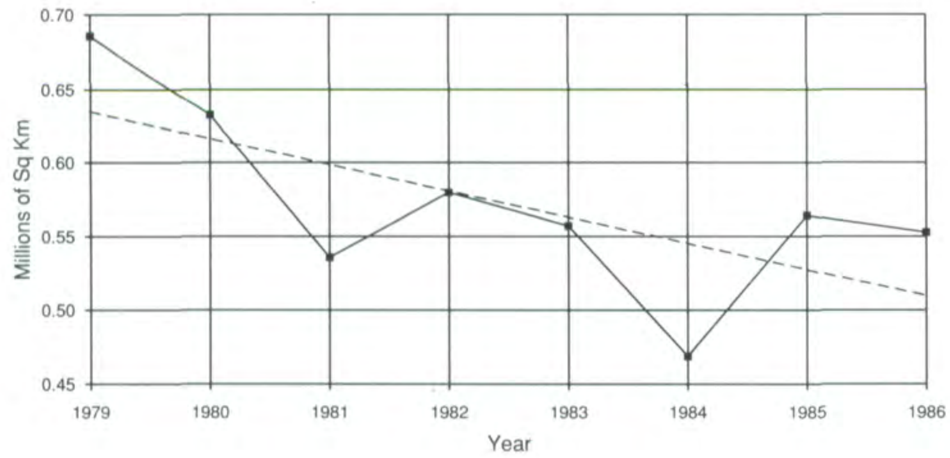

(d) Bering Sea

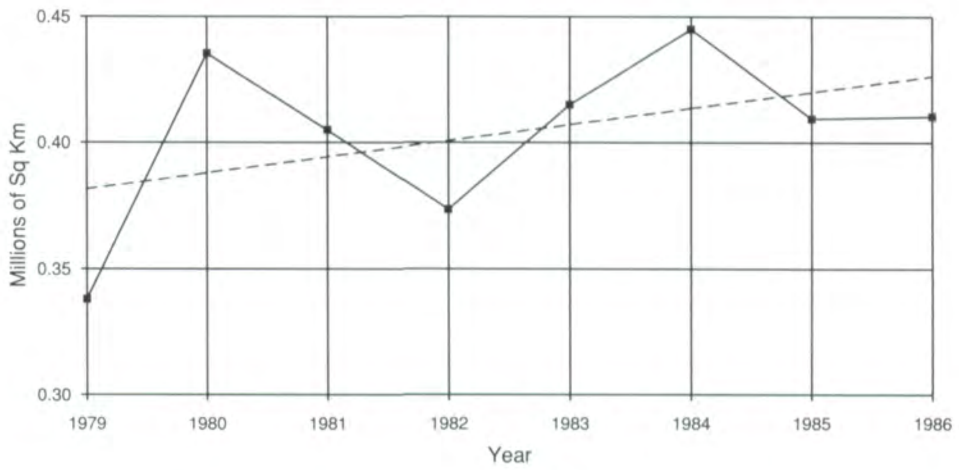

(e) Hudson Bay

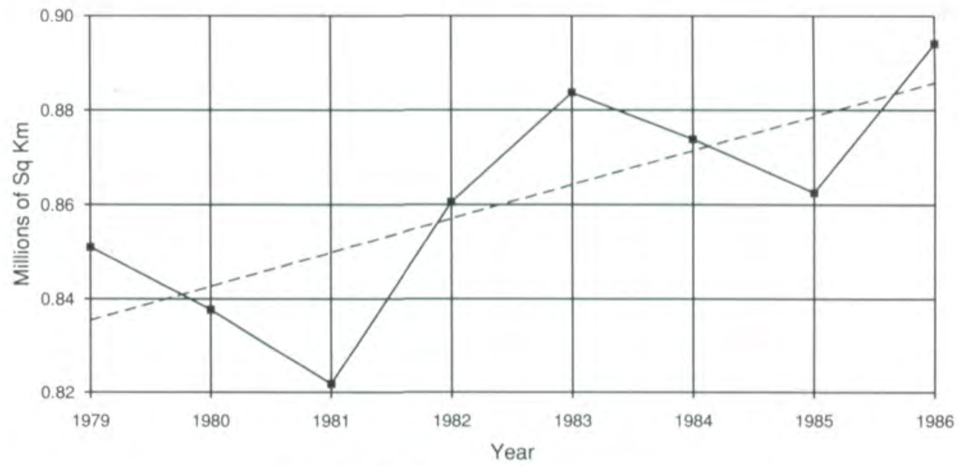

(f) Baffin Bay, Davis Strait, and Labrador Sea

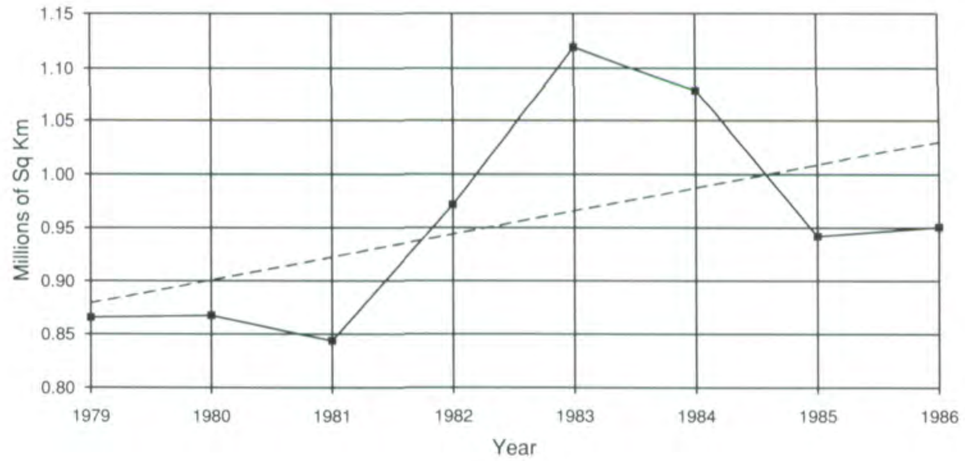

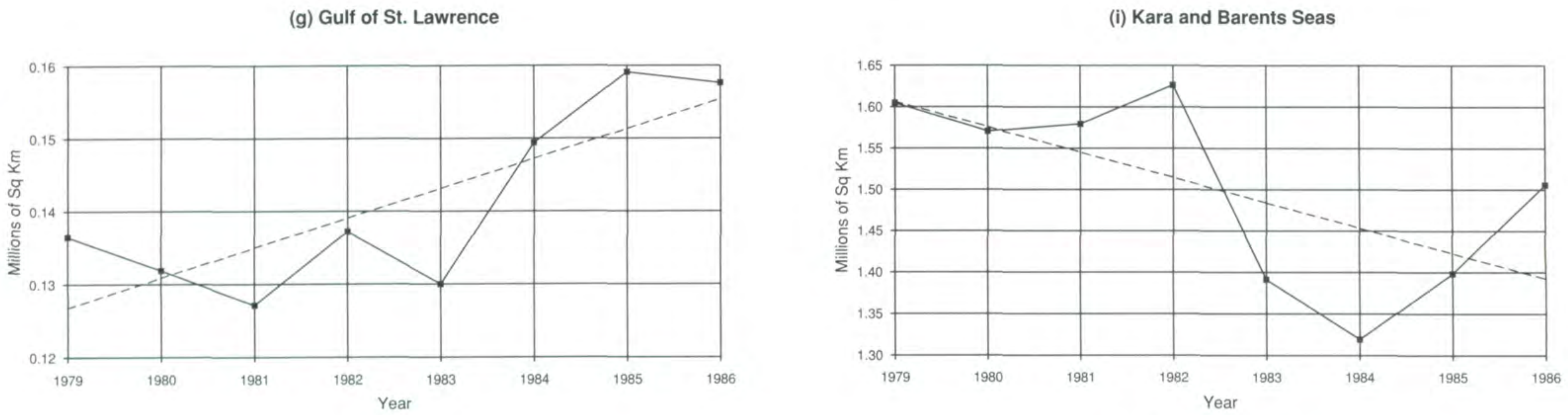

(g) Gulf of St. Lawrence

(i) Kara and Barents Seas

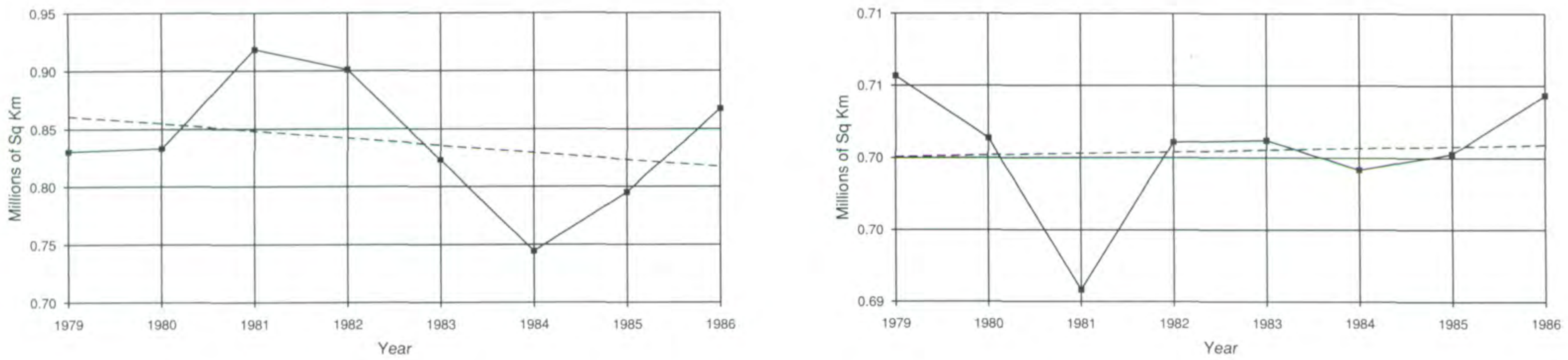

(h) Greenland Sea

(j) Canadian Archipelago

Figure 5.1.1. Annually averaged sea ice extents for the Arctic and its 9 regions.

For the entire Arctic, the slope of the linear-least-squares fit is -0.008 x 10^6 km^2/yr (Table 5.1.1). The largest positive deviation (0.14 x 10^6 km^2) from the trend line for the Arctic as a whole occurs in 1982, while the largest negative deviation (-0.17 x 10^6 km^2) occurs just 2 years later in 1984 (Figure 5.1.1). Regionally, negative trends occur in the Seas of Okhotsk and Japan, the Greenland Sea, and the Kara and Barents Seas. Positive trends occur in the Arctic Ocean, Bering Sea, Hudson Bay, Baffin Bay/Davis Strait, and the Gulf of St. Lawrence regions, but these are not sufficient to offset the overall negative trend. The largest positive trend (0.019 x 10^6 km^2/yr) occurs in the Baffin Bay/Davis Strait/Labrador Sea region, the region with the largest mean absolute deviation about its trend line. The largest negative trend (-0.028 x 10^6 km^2) occurs in the Kara and Barents seas, the region second only to Baffin Bay in the magnitude of its deviations about the trend line.

In the Antarctic (Figure 5.1.2), the trend lines are negative in the Weddell Sea and Western Pacific sectors, and positive in the Ross Sea, Indian Ocean, and Bellingshausen and Amundsen Seas sectors, with a net result of a slightly positive (but statistically insignificant) slope. The sector with the largest negative slope (-0.064 x 10^6 km^2/yr) is the Weddell Sea, while the Ross Sea sector has the largest positive slope (0.056 x 10^6 km^2/yr; see Table 5.1.1). As in the Arctic, the sectors with the largest positive and negative trends have the largest deviations about their respective trend lines. This is consistent with the anomaly maps presented in Chapters 3 and 4. Large positive anomalies are often observed to cancel correspondingly large negative anomalies, resulting in little net change in the overall hemispheric ice cover. This suggests that year-to-year variability in large-scale atmospheric and oceanic forcing is the likely cause of these trends. Whether or not there is an underlying climatological cause must await a longer data record and more thorough data analysis.

(a) Total Antarctic

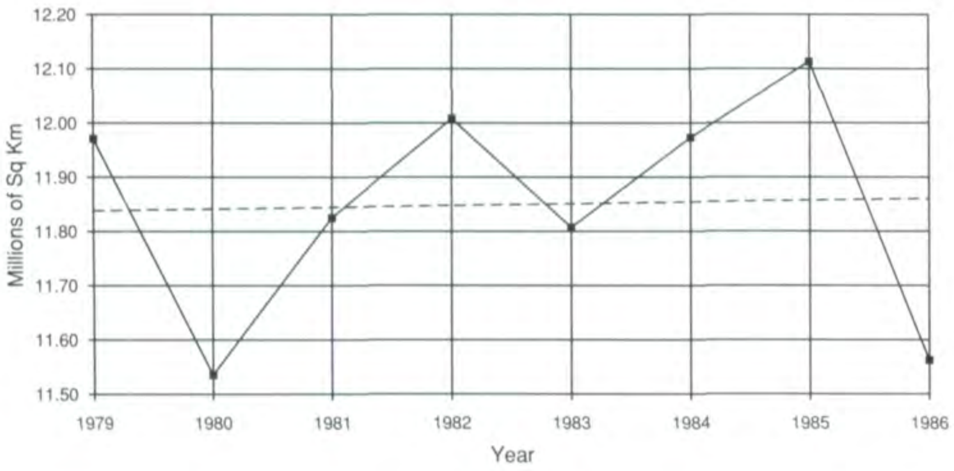

(b) Weddell Sea

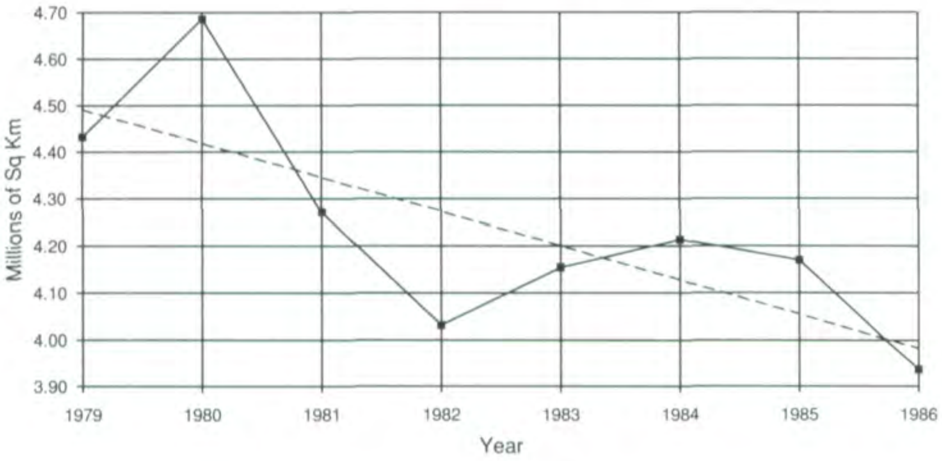

(c) Ross Sea

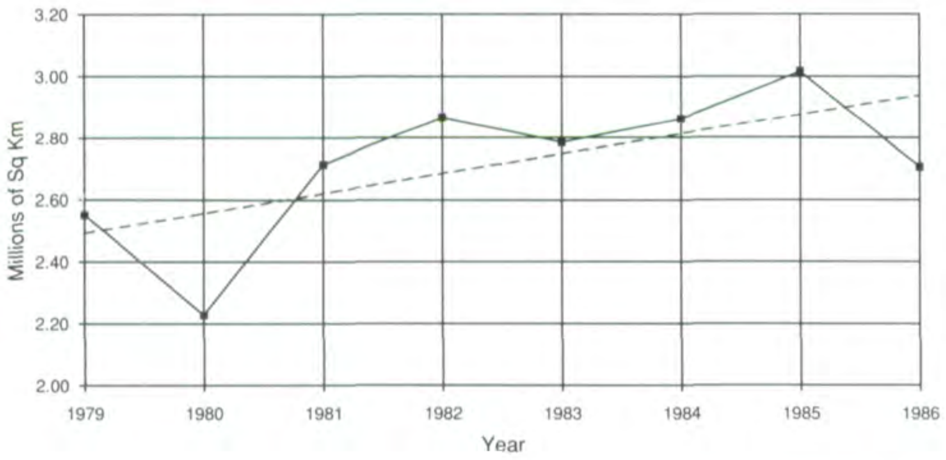

(d) Bellingshausen and Amundsen Seas

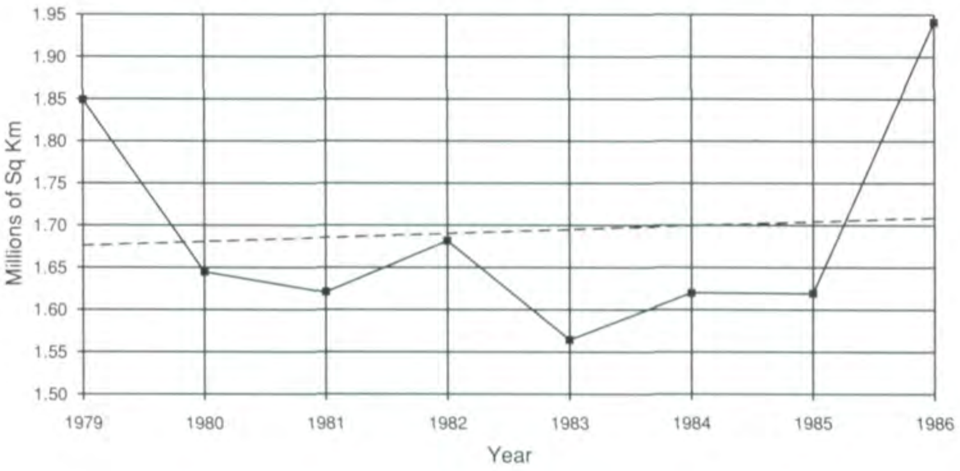

(e) Indian Ocean

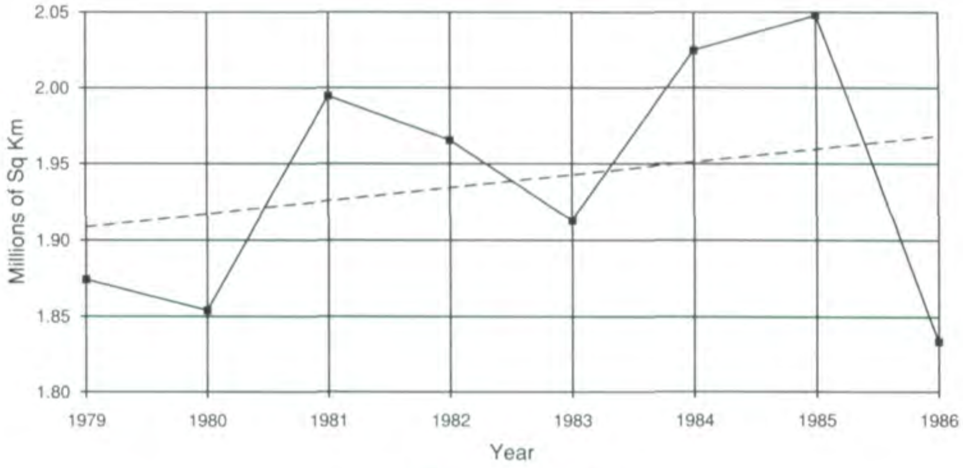

(f) Western Pacific

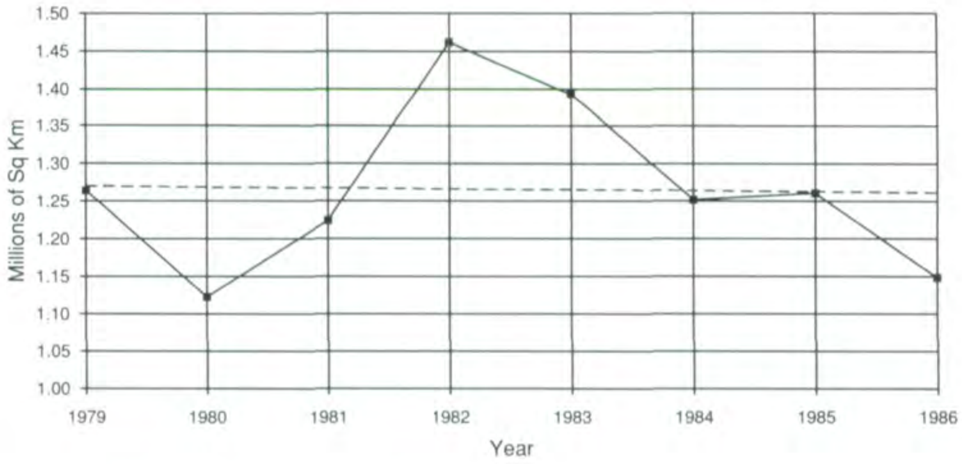

Figure 5.1.2. Annually averaged sea ice extents for the Antarctic and its 5 regions.

5.2 Seasonal Cycles on a Global Scale

We now examine the sea ice parameters for the globe as a whole. Variations in the Arctic and Antarctic sea ice extents, sea ice areas, and open water areas shown in Figures 3.1.45 and 4.2.1 for the 8.8-year SMMR record have been summed to provide the global curves in Figure 5.2.1 and have been reproduced in Figures 5.2.2 through 5.2.4 with the addition of trend lines that are discussed in the following section. For the first two variables, the timing of the minimum of the global seasonal oscillations (Figure 5.2.1) coincides closely with that of the minimum in the Antarctic sea ice extent and area (Figures 5.2.2 and 5.2.3), which falls within a few days of February 25 every year. The timing of the Arctic minima (Figures 5.2.2 and 5.2.3) is not quite as regular as that for the Antarctic. Furthermore, the length of time between consecutive winter ice-extent maxima in the Arctic varies by as much as 24 days. The global extent maxima are broader than those of the individual hemispheres and have double peaks, with the valley between them occurring at approximately the same time as the Arctic minima.

Variations in the relative phases of oscillations in the Arctic and Antarctic ice-pack areas are reflected in the year-to-year changes in the shape of the oscillations shown in Figure 5.2.1. The double-peaked maxima in the global ice-area oscillations are more or less symmetrical for the years 1979 and 1984, when the southern maximum and northern minimum nearly coincide, resulting in a dip near the center of the crest. However, in other years, this dip appears earlier in the crest. These interannual variations in the shape of the global ice-cover oscillations (Gloersen and Campbell, 1988a, 1991a) may be explained by the large regional interannual variabilities that occur in the ice extents of each hemisphere (Parkinson and Cavalieri, 1982, 1989; Zwally et al., 1983a; Parkinson et al., 1987), with the amount of sea ice decreasing in some regions while increasing in others, because of corresponding shifts in the average weather patterns in the area.

The global ice area varies seasonally by as much as 40% of the mean (Figure 5.2.1; also Gloersen and Campbell, 1988a) and represents an annual change of about 10^{21} J in the amount of latent heat stored in the global sea ice, assuming a constant average ice thickness in the seasonal ice zones of 0.5 m. The seasonal variation in the areas of open water within the pack on the global scale (Figure 5.2.1) is about 80% of their mean. The shape of the open water crests (Figure 5.2.1) is largely determined by variations in the areas of the Antarctic open water within the pack, but the rise to maximum values is noticeably modified by the Arctic open water variations (Figure 5.2.4). Maximum open water (approximately 6.8×10^6 km^2) occurs from July through December, which, when divided by the maximum global sea ice extent (approximately 28×10^6 km^2), represents 24% of the area enclosed by the ice boundaries. Since there can be a 2- to 3-order-of-magnitude difference in the rate of sensible heat exchange between the atmosphere and the ocean surface in the winter depending on whether ice exists on the surface or not (Badgley, 1966; Maykut, 1978), annual fluctuations in the global sea ice area can play a significant role in atmospheric circulation (Budd, 1975; Simmons and Budd, 1990).

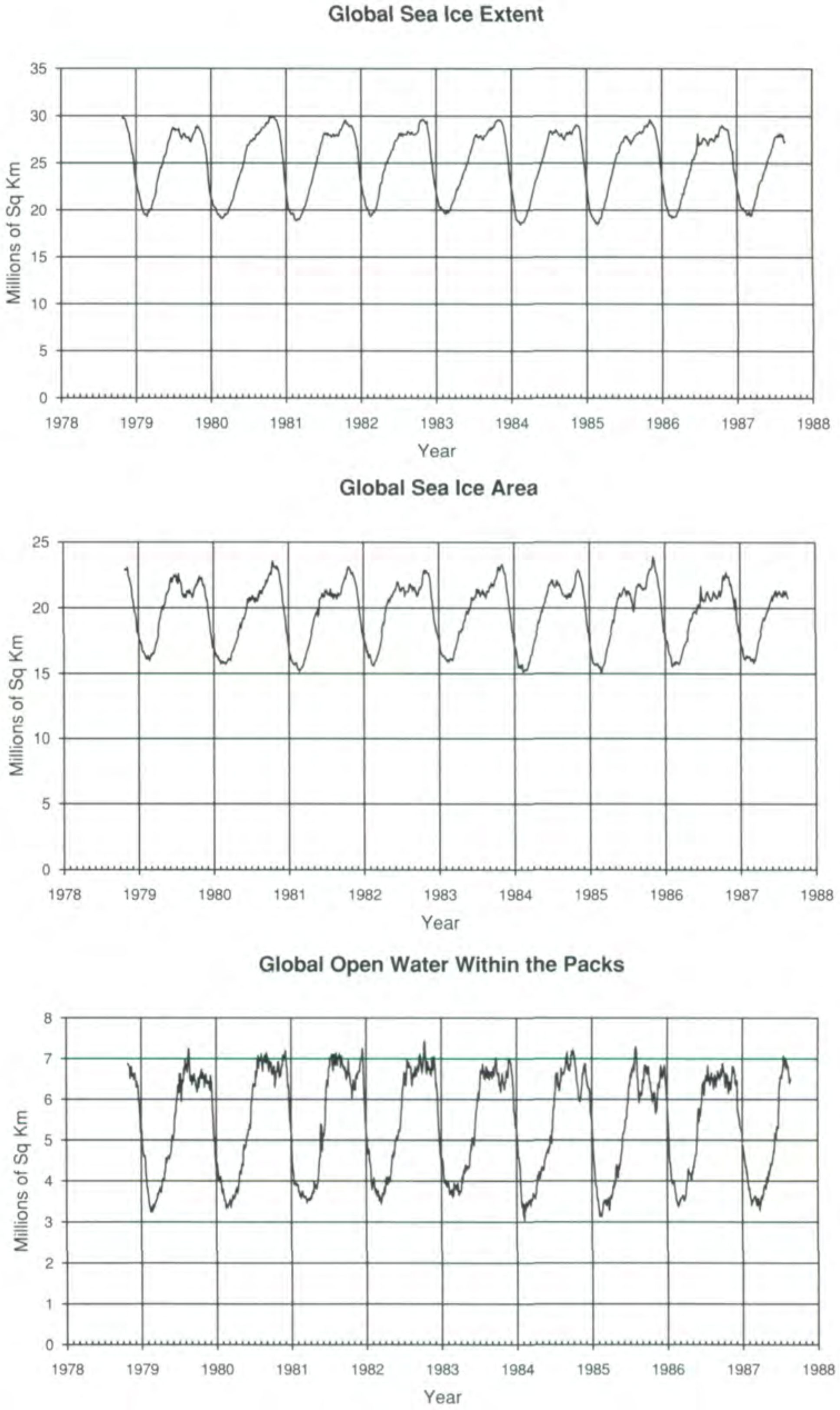
Global Sea Ice Extent

Global Sea Ice Area

Global Open Water Within the Packs

Figure 5.2.1. Global sea ice extent, sea ice area, and amount of open water within the pack from October 26, 1978 to August 20, 1987.

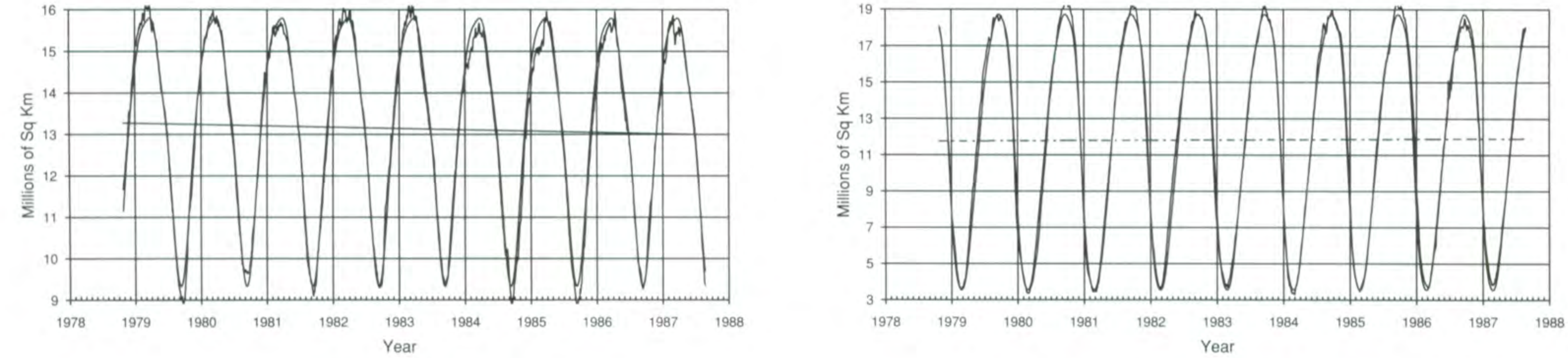

Arctic Sea Ice Extent

Antarctic Sea Ice Extent

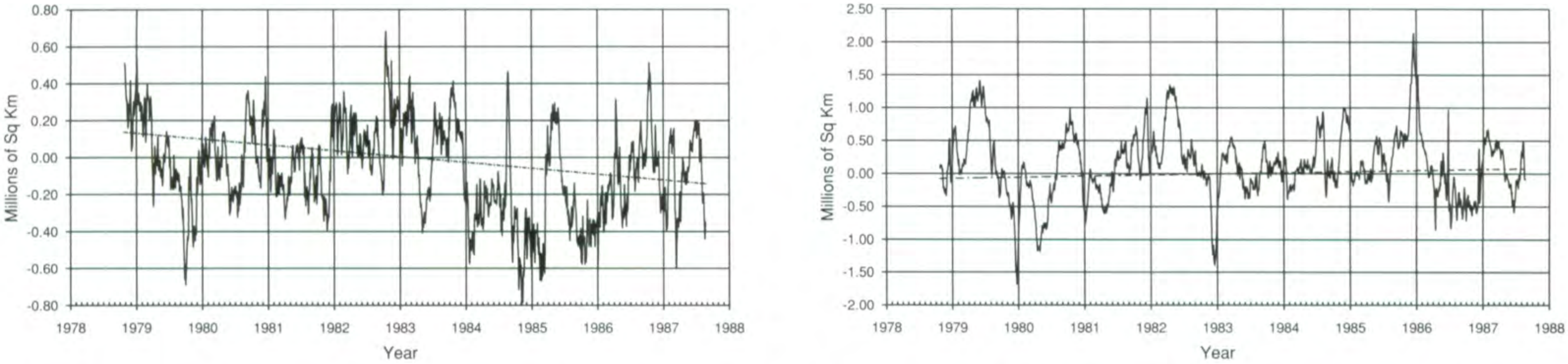

Arctic Sea Ice Extent Residual

Antarctic Sea Ice Extent Residual

Figure 5.2.2. Arctic and Antarctic sea ice extents, residuals, and trends from October 26, 1978 to August 20, 1987. In the left-hand column are shown the time series of ice extent (solid curve), model seasonal cycles (dashed curve, see text), and trends. On the right, the trends are shown on an expanded scale, with the residuals corresponding to the curves to the left, obtained by subtracting the model seasonal cycles from the data.

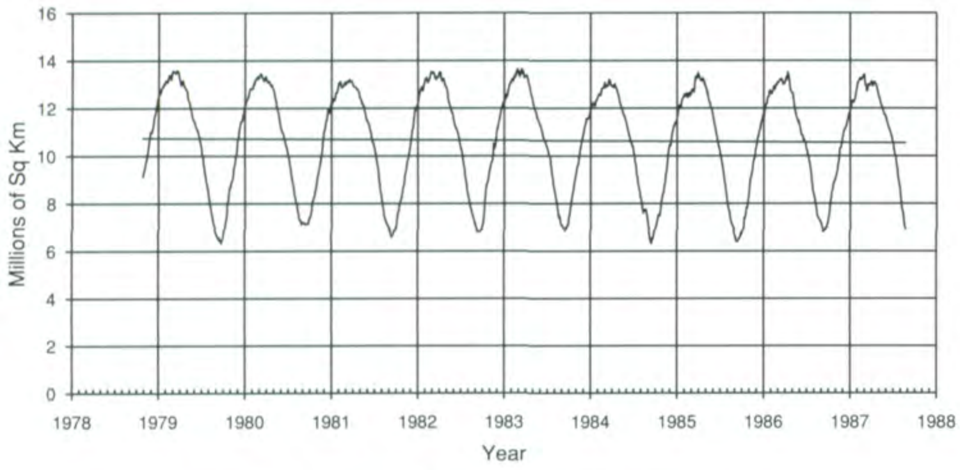

Arctic Sea Ice Area and Trend

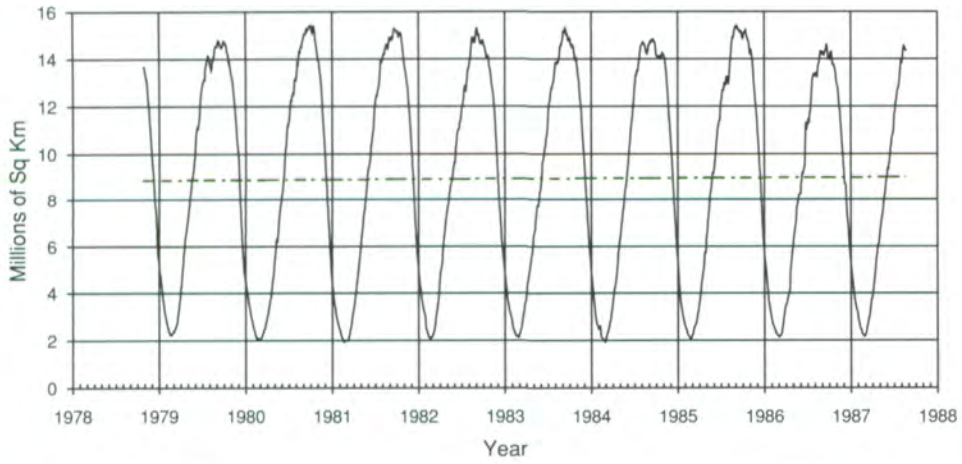

Antarctic Sea Ice Area and Trend

Figure 5.2.3. Arctic and Antarctic sea ice areas and their trends from October 26, 1978 to August 20, 1987.

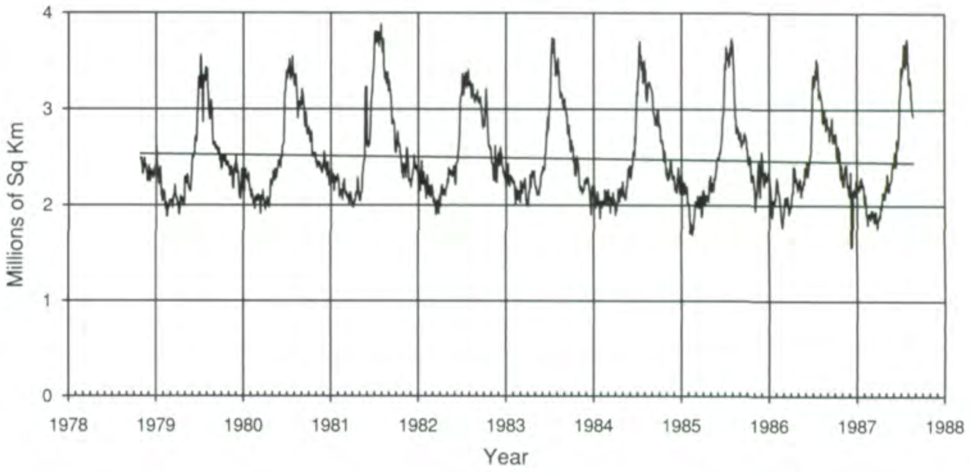

Open Water Within the Arctic Ice Pack and Trend

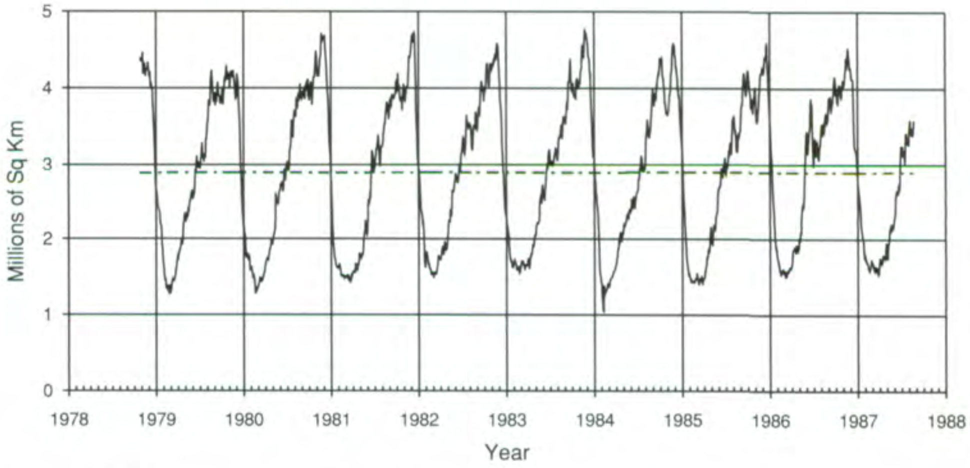

Open Water Within the Antarctic Ice Pack and Trend

Figure 5.2.4. Open water within the Arctic and Antarctic ice packs and their trends from October 26, 1978 to August 20, 1987.

5.3 Global Sea Ice Trends

Previous studies of the individual records of Arctic and Antarctic sea ice-extent extrema or annual averages of the extents (Zwally et al., 1983a, b; Parkinson et al., 1987; Gloersen and Campbell, 1988a; Parkinson and Cavalieri, 1989) found no evidence of significant trends. In contrast, the maxima in the global sea ice extent (the sum of the Arctic and Antarctic sea ice extents) were found to have a more significant trend, in the statistical sense (Gloersen and Campbell, 1988a). More recently, Gloersen and Campbell (1991a,b) have looked for trends in the unaveraged SMMR sea ice extent and area data sets (Figures 5.2.2 to 5.2.4). Since these unaveraged data sets are serially correlated and not normally distributed, a linear-least-squares approach is inappropriate for trend analysis. Gloersen and Campbell (1991a) analyzed the data after removing the average seasonal cycle, but found that some serial correlation persisted, so they (1991b) applied a band-limited regression (BLR) technique (Lindberg, 1991) to the Arctic and Antarctic sea ice data. A summary of their results is presented in Table 5.3.1. The trends given in Table 5.3.1 are superimposed on the data shown in Figures 5.2.2 to 5.2.4. For the Arctic sea ice extent, they obtained a trend of -2.1%±0.9% over the 8.8-year time span, at a confidence level of 96.5%. The confidence level ascribed to the Arctic sea ice area trend is less, at 88.5% For the Arctic open water area within the ice cover, the BLR technique yields a trend of -3.5%±2.0%, at a confidence level of 93.5%. The results for the Antarctic are statistically insignificant, since the standard deviations of the trends are greater than the trends themselves.

Table 5.3.1. Band-limited Regression Analysis of Polar Sea Ice Covers

	SLOPE *$(10^6\ km^2/yr)$*	STANDARD DEVIATION *$(10^6\ km^2/yr)$*	8.8-YR TREND *(% of mean)*	CONFIDENCE LEVEL *(%)*
Arctic Sea Ice Extent	-0.0315	0.0143	-2.1±0.9	96.5
Antarctic Sea Ice Extent	+0.0177	0.0188	**	**
Arctic Sea Ice Area	-0.0214	0.0151	-1.8±1.2	88.5
Antarctic Sea Ice Area	+0.0157	0.0175	**	**
Arctic Open Water Area	-0.0102	0.0058	-3.5±2.0	93.5
Antarctic Open Water Area	+0.0020	0.0044	**	**

** Statistically insignificant

5.4 A Look to the Future

The launch of the Nimbus 7 SMMR in 1978 extended and improved the global measurement of polar sea ice begun in 1972 with the single-channel Nimbus 5 ESMR. Subsequent multichannel sensors such as the DMSP SSMI will continue to provide the continuity needed to obtain even longer records of sea ice data. As new sensors replace old ones, there is a critical need for periods of data overlap between a given sensor and its successor. A prime example of the kinds of problems encountered by the lack of overlap is the case of the ESMR and SMMR data records. Comparisons made between ESMR and SMMR sea ice data (Gloersen and Campbell, 1988a; Parkinson and Cavalieri, 1989) would have benefited greatly if overlap data had been available. An overlap period would have allowed determination of the extent to which the difference in ice areas resulted from differences in sensor antenna patterns, instrument calibration, and processing algorithms.

Fortunately, there was an overlap period between the Nimbus 7 SMMR and the first DMSP SSMI sensor launched in June 1987. The available SMMR-SSMI overlap data covered the period July 9 through August 20, 1987, and was used to advantage in fine-tuning the sea ice algorithm coefficients (see Section 2.3.2) for both instruments. The resultant total ice-concentration differences (SMMR minus SSMI) for the period August 1-20, 1987, had a bias in the means of 0.2% and a standard deviation of 2.5% in the Antarctic (austral winter) and 0.5% and 5%, respectively, in the Arctic (boreal summer). Presumably, the Arctic differences would have been comparable to the Antarctic ones had the comparison been possible during the boreal winter. These agreements are close in spite of the 8- to 16-hour time difference in the SMMR and SSMI overpasses and the dynamic nature of the ice covers. These results provide a measure of consistency between the SMMR and SSMI sea ice concentrations and should encourage further analyses of a combination of the data sets. It is hoped that there also will be overlap periods between the present and later SSMI sensors, as well as between SSMI and the EOS series of passive-microwave imagers.

REFERENCES

Aagaard, K., and E.C. Carmack, The role of sea ice and other fresh water in the Arctic circulation, *J. Geophys. Res.* **94,** 14,485-14,498, 1989.

Ackley, S.F., Mass balance aspects of Weddell Sea pack ice, *J. Glaciol.* **24**, 391-406, 1979.

Ackley, S.F., A review of sea ice weather relationships in the Southern Hemisphere, in *Sea Level, Ice and Climatic Change*, I. Allison, ed., International Association of Hydrological Sciences, Guildford, Great Britain, pp. 127-159, 1981.

Ackley, S.F. , A. J. Gow, K. R. Buck, and K.M. Golden, Sea ice studies in the Weddell Sea aboard USCGC Polar Sea, *Antarctic J. U. S.* **15**, 84-86, 1980.

Akagawa, M., The characteristics of atmospheric circulation in the years with abnormal sea ice conditions along the Okhotsk coast of Hokkaido, Japan, *Oceanogr. Mag.* **24**, 81-100, 1973.

Alfultis, M.A., and S. Martin, Satellite passive-microwave studies of the Sea of Okhotsk ice cover and its relation to oceanic processes, 1978-1982, *J. Geophys. Res.* **92**, 13,013-13,028, 1987.

Anderson, M.R., The onset of spring melt in first-year ice regions of the Arctic as determined from Scanning Multichannel Microwave Radiometer data for 1979 and 1980, *J. Geophys. Res.* **92**, 13,153-13,163, 1987.

Anderson, M.R., R.G. Crane, and R.G. Barry, Characteristics of Arctic Ocean ice determined from SMMR data for 1979: Case studies in the seasonal sea ice zone, *Adv. Space Res.* **5**, 257-261, 1985.

Badgley, F.I., Heat budget at the surface of the Arctic Ocean, in *Proceedings of the Symposium on the Arctic Heat Budget and Atmospheric Circulation*, J. O. Fletcher, ed., pp. 267-277, 1966.

Bagriantsev, N.V., A.L. Gordon, and B.A. Huber, Weddell Gyre: Temperature maximum stratum, *J. Geophys. Res.* **94**, 8331-8334, 1989.

Barry, R.G., Arctic Ocean ice and climate: Perspective on a century of polar research, *Ann. Am. Geographers* **74** (4), 485-501, 1983.

Barry, R.G., and J. Maslanik, Arctic sea ice characteristics and associated atmosphere-ice interactions in summer inferred from SMMR data and drifting buoys: 1979-1984, *GeoJournal* **18**, 36-44, 1989.

Bryan, K., S. Manabe, and R.C. Pacanowski, A global ocean-atmosphere climate model. Part II. The ocean circulation, *J. Phys. Oceanography* **5**, 30-46, 1975.

Budd, W.F., Antarctic sea ice variations from satellite sensing in relation to climate, *J. Glaciol.* **15**, 417-426, 1975.

Burns, B.A., D.J. Cavalieri, M.R. Keller, W.J. Campbell, T.C. Grenfell, G.A. Maykut, and P. Gloersen, Multisensor comparison of ice concentration estimates in the marginal ice zone, *J. Geophys. Res.* **92**, 6843-6856, 1987.

Businger, S., and R.J. Reed, Polar lows, in *Polar and Arctic Lows*, Twitchell, P.F., E.A. Rasmussen, and K.L. Davidson, eds., A. Deepak, Hampton, VA, pp. 3-45, 1989.

Cahalan, R.F., and L.S. Chiu, Large-scale short-period sea ice-atmosphere interaction, *J. Geophys. Res.* **91**, 10709-10717, 1986.

Campbell, W.J., NASA remote sensing of sea ice in AIDJEX, *Proceedings of the World Meteorological Organization Technical Conference*, Tokyo, Japan, **WMO No. 350**, pp. 55-66, 1973.

Campbell, W.J., P. Gloersen, W. Nordberg, and T.T. Wilheit, Dynamics and morphology of Beaufort Sea ice determined from satellite, aircraft, and drifting stations, in *Proceedings of the Symposium on Approaches to Earth Survey Problems Through Use of Space Techniques*, Akademie-Verlag, Berlin, pp. 311-327, 1974.

Campbell, W.J., P. Gloersen, and R.O. Ramseier, Synoptic ice dynamics and atmospheric circulation during the Bering Sea Experiment, in *Proceedings of the Final Symposium on the Results of the Joint Soviet-American Expedition,* K. Ya. Kondratyev, Yu. I. Rabinovich, and W. Nordberg, eds., Gidrometeoizdat, Leningrad, 196-218, 1975a. (Republished as USSR/USA Bering Sea Experiment by A. A. Balkema, Rotterdam, 307 pp., 1982.)

Campbell, W.J., W.F. Weeks, R.O. Ramseier, and P. Gloersen, Geophysical studies of floating ice by remote sensing, *J. Glaciol.* **15**, 305-328, 1975b.

Campbell, W.J., P. Gloersen, W.J. Webster, T.T. Wilheit, and R.O. Ramseier, Beaufort Sea ice zones as delineated by microwave imagery, *J. Geophys. Res.* **81**, 1103-1110, 1976a.

Campbell, W.J., R.O. Ramseier, W.F. Weeks, and P. Gloersen, An integrated approach to the remote sensing of floating ice, *Proceedings of the XXVI International Astronautical Congress,* Lisbon, Portugal, L.G. Napolitano, ed., pp. 445-487, 1976b.

Campbell, W.J., R.O. Ramseier, and W.F. Weeks, Skylab Floating Ice Experiment, Canadian Department of Fisheries and the Environment, Ottawa, *Miscellaneous Special Publication No. 34,* 23 pp., 1977a.

Campbell, W.J., R.O. Ramseier, W.F. Weeks, and J.A. Wayenberg, Visual observations of floating ice from Skylab, in *Skylab Explores the Earth, NASA SP-380,* National Aeronautics and Space Administration, Washington, D.C., pp. 353-379, 1977b.

Campbell, W.J., J. Wayenberg, J.B. Ramseyer, R.O. Ramseier, M.R. Vant, R. Weaver, A. Redmond, L. Arsenault, P. Gloersen, H.J. Zwally, T.T. Wilheit, T.C. Chang, D. Hall, L. Gray, D.C. Meeks, M.L. Bryan, F.T. Barath, C. Elachi, F. Leberl, and T. Farr, Microwave remote sensing of sea ice in the AIDJEX main experiment, *Boundary-Layer Meteorology* **13**, 309-337, 1978.

Campbell, W.J., P. Gloersen, R.O. Ramseier, and H.J. Zwally, Arctic sea ice variations from time-lapse microwave imagery, *Boundary-Layer Meteorology* **18**, 99-106, 1980a.

Campbell, W.J., P. Gloersen, H.J. Zwally, R.O. Ramseier, and C. Elachi, Simultaneous passive and active microwave observations of near-shore Beaufort Sea ice, *J. Petroleum Technology* **21**, 1105-1112, 1980b.

Campbell, W.J., R.O. Ramseier, H.J. Zwally, and P. Gloersen, Structure and variability of Bering and Okhotsk sea ice cover by satellite microwave imagery, in *Energy Resources of the Pacific,* M.T. Halbouty, ed., American Association of Petroleum Geologists, Tulsa, Oklahoma, pp. 343-354, 1981.

Campbell, W.J., P. Gloersen, and H.J. Zwally, Aspects of Arctic sea ice observable by sequential passive-microwave observations from the Nimbus 5 satellite, in *Arctic Technology and Policy,* I. Dyer and C. Chryssostomidis, eds., Hemisphere Publishing, New York, pp. 197-222, 1984.

Campbell, W.J., P. Gloersen, E.G. Josberger, O.M. Johannessen, P.S. Guest, N. Mognard, R. Shuchman, B.A. Burns, N. Lannelongue, and K. L. Davidson, Variations of mesoscale and large-scale sea ice morphology in the 1984 Marginal Ice Zone Experiment as observed by microwave remote sensing, *J. Geophys. Res.* **92**, 6805-6824, 1987.

Carleton, A.M., Monthly variability of satellite-derived cyclonic activity for the Southern Hemisphere winter, *J. Climatology* **1**, 21-38, 1981.

Carleton, A.M., Synoptic sea ice-atmosphere interactions in the Chukchi and Beaufort Seas from Nimbus 5 ESMR data, *J. Geophys. Res.* **89**, 7245-7258, 1984.

Carleton, A.M., Satellite climatological aspects of the "polar low" and "instant occlusion," *Tellus* **37A**, 433-450, 1985.

Carleton, A. M., Antarctic sea ice relationships with indices of atmospheric circulation of the Southern Hemisphere, *Climate Dynamics* **3**, 207-220, 1989.

Carsey, F.D., Microwave observation of the Weddell Polynya, *Mon. Weather Rev.* **108**, 2032-2044, 1980.

Carsey, F.D., Arctic sea ice distribution at end of summer 1973-1976 from satellite microwave data, *J. Geophys. Res.* **87**, 5809-5835, 1982.

Carsey, F.D., Summer Arctic sea ice character from satellite microwave data, *J. Geophys. Res.* **90**, 5015-5034, 1985.

Cavalieri, D.J., and C.L. Parkinson, Large-scale variations in observed Antarctic sea ice extent and associated atmospheric circulation, *Mon. Weather Rev.* **109**, 2323-2336, 1981.

Cavalieri, D.J., S. Martin, and P. Gloersen, Nimbus 7 SMMR observations of the Bering Sea ice cover during March 1979, *J. Geophys. Res.* **88**, 2743-2754, 1983.

Cavalieri, D.J., P. Gloersen, and W.J. Campbell, Determination of sea ice parameters with the Nimbus 7 SMMR, *J. Geophys. Res.* **89**, 5355-5369, 1984.

Cavalieri, D.J., and S. Martin, A passive-microwave study of polynyas along the Antarctic Wilkes Land coast, in *Oceanology of the Antarctic Continental Shelf,* S.S. Jacobs, ed., Antarctic Research Series vol. 43, American Geophysical Union, Washington, D.C., pp. 227-252, 1985.

Cavalieri, D.J., and H.J. Zwally, Satellite observations of sea ice, *Adv. Space Res.* **5**, 247-255, 1985.

Cavalieri, D.J., P. Gloersen, and T.T. Wilheit, Aircraft and satellite passive-microwave observations of the Bering Sea ice cover during MIZEX West, *IEEE Trans. Geoscience and Remote Sensing* **GE-24**, 368-377, 1986.

Cavalieri, D.J., and C.L. Parkinson, On the relationship between atmospheric circulation and the fluctuations in the sea ice extents of the Bering and Okhotsk Seas, *J. Geophys. Res.* **92**, 7141-7162, 1987.

Cavalieri, D.J., B.A. Burns, and R.G. Onstott, Investigation of the effects of summer melt on the calculation of sea ice concentration using active and passive-microwave data, *J. Geophys. Res.* **95**, 5359-5369, 1990.

Cavalieri, D.J., J.P. Crawford, M.R. Drinkwater, D.T. Eppler, L.D. Farmer, R.R. Jentz, and C.C. Wackerman, Aircraft active and passive-microwave validation of sea ice concentration from the DMSP SSMI, *J. Geophys. Res.* **96**, 21,989-22,008, 1991.

Chang, T.C., P. Gloersen, T. Schmugge, T.T. Wilheit, and H.J. Zwally, Microwave emission from snow and glacier ice, *J. Glaciol.* **16**, 23-39, 1976.

Chiu, L.S., Variation of Antarctic sea ice: An update, *Mon. Weather Rev.* **111**, 578-580, 1983.

Colony, R., and E.A. Muñoz, *Arctic Ocean Buoy Program Data Report, 1 January 1983-31 December 1984*, University of Washington Polar Science Center, Seattle, 1985.

Colony, R., and E.A. Muñoz, *Arctic Ocean Buoy Program Data Report,* 1 January 1984-31 December 1985, University of Washington Polar Science Center, Seattle, 1986.

Comiso, J.C., and H.J. Zwally, Antarctic sea ice concentrations inferred from Nimbus 5 ESMR and Landsat imagery, *J. Geophys. Res.* **87**, 5836-5844, 1982.

Comiso, J.C., Sea ice effective microwave emissivities from satellite passive-microwave and infrared observations, *J. Geophys. Res.* **88**, 7686-7704, 1983.

Comiso, J.C., S.F. Ackley, and A.L. Gordon, Antarctic sea ice microwave signatures and their correlation with in situ ice observations, *J. Geophys Res.* **89**, 662-672, 1984.

Comiso, J.C., and H.J. Zwally, Concentration gradients and growth/decay characteristics of the seasonal sea ice cover, *J. Geophys Res.* **89**, 8081-8103, 1984.

Comiso, J.C., Characteristics of Arctic winter sea ice from satellite multispectral microwave observations, *J. Geophys. Res.* **91**, 975-994, 1986.

Comiso, J.C., and A.L. Gordon, Recurring polynyas over the Cosmonaut Sea and the Maud Rise, *J. Geophys. Res.* **92**, 2819-2833, 1987.

Comiso, J.C., T.C. Grenfell, D.L. Bell, M.A. Lange, and S.F. Ackley, Passive-microwave observations of winter Weddell sea ice, *J. Geophys. Res.* **94**, 10,891-10,905, 1989.

Comiso, J.C., and H.J. Zwally, Polar microwave brightness temperatures from Nimbus 7 SMMR, *NASA RP-1223,* 82 pp., 1989.

Comiso, J.C., Arctic multiyear ice classification and summer ice cover using passive-microwave satellite data, *J. Geophys. Res.* **95**, 13,411-13,422, 1990.

Comiso, J.C., N.G. Maynard, W.O. Smith, Jr., and C.W. Sullivan, Satellite ocean color studies of Antarctic ice edges in summer and autumn, *J. Geophys. Res.* **95**, 9481-9496, 1990.

Comiso, J.C., P. Wadhams, W.B. Krabill, R.N. Swift, J.P. Crawford, and W.B. Tucker III, Top/bottom multisensor remote sensing of Arctic sea ice, *J. Geophys. Res.* **96**, 2693-2709, 1991.

Crane, R.G., Atmosphere-sea ice interactions in the Beaufort/Chukchi Seas and in the European sector of the Arctic, *J. Geophys. Res.* **88**, 4505-4523, 1983.

Crane, R.G., R.G. Barry, and H.J. Zwally, Analysis of atmosphere-sea ice interactions in the Arctic Basin using ESMR microwave data, *Int. J. Remote Sensing,* **3**, 259-276, 1982.

Crawford, J.P., and C.L. Parkinson, Wintertime microwave observations of the North Water polynya, in *Oceanography from Space,* J.F.R. Gower, ed., Plenum Press, New York, pp. 839-844, 1981.

Davis, J.C., *Statistics and Data Analysis in Geology,* John Wiley & Sons, New York, N.Y., 1973.

Dey, B., H. Moore, and A.F. Gregory, Monitoring and mapping sea ice breakup and freezeup of Arctic Canada from satellite imagery, *Arctic and Alpine Res.* **11**, 229-242, 1979.

Dey, B., Monitoring winter sea ice dynamics in the Canadian Arctic with NOAA-TIR images, *J. Geophys. Res.* **86**, 3223-3235, 1981.

Dunbar, M.J., The geophysical position of the North Water, *Arctic* **22**, 438-441, 1969.

Dunbar, M., and M.J. Dunbar, The history of the North Water, *Proc. of the Royal Society of Edinburgh, Ser. B* **72**, 231-241, 1972.

Dunbar, M., Ice regime and ice transport in Nares Strait, *Arctic* **26**, 282-291, 1973.

Edgerton. A.T., A. Stogryn, and G. Poe, Microwave radiometric investigation of snow pack, *Final Report No. 14-08-001-11828*, Aerojet General Corp., 1971.

Enomoto, H., and A. Ohmura, The influences of atmospheric half-yearly cycle on the sea ice extent in the Antarctic, *J. Geophys. Res.* **95**, 9497-9511, 1990.

Fandry, C.J., and R.D. Pillsbury, On the estimation of absolute geostrophic volume transport applied to the Antarctic Circumpolar Current, *J. Phys. Oceanogr.* **9**, 449-455, 1979.

Findlay, B.F., and B.E. Goodison, Archiving and mapping of Canadian snow cover data, in *Proc. of the Workshop on Snow Cover and Sea Ice Data* **Report GD-5**, World Data Center A for Glaciology [Snow and Ice], Boulder, Colorado, pp. 71-87, 1979.

Fletcher, J.O., Ice extent on the southern ocean and its relation to world climate, *Memorandum RM-5792-NSF*, 108 pp., Rand Corp., Santa Monica, Calif., 1969.

Foster, T.D., and E.C. Carmack, Frontal zone mixing and Antarctic bottom water formation in the southern Weddell Sea, *Deep-Sea Res.* **23**, 301-317, 1976.

Francis, E.A., Calibration of the Nimbus 7 Scanning Multichannel Microwave Radiometer (SMMR), 1979-1984, *M.S. Thesis*, Oregon State U., 248 pp., 1987.

Fung, A.K., and M.F. Chen, Emission from an inhomogeneous layer with irregular interfaces, *Radio Science* **16**, 289-298, 1981.

Gaut, N.E., Studies of atmospheric water vapor by means of passive-microwave techniques, *Tech. Report 467*, M.I.T. Res. Lab. Electronics, Cambridge, MA., 1968.

Gaut, N.E., and E.C. Reifenstein III, Interaction of microwave energy with the atmosphere, *AIAA Earth Resources Observations and Information Systems Conference*, Paper No. 70-197, Annapolis, MD, 1970.

Gloersen, P., W. Nordberg, T.J. Schmugge, T.T. Wilheit, and W.J. Campbell, Microwave signatures of first-year and multiyear sea ice, *J. Geophys. Res.* **78**, 3564-3572, 1973.

Gloersen, P., T.T. Wilheit, T.C. Chang, W. Nordberg, and W.J. Campbell, Microwave maps of the polar ice of the Earth, *Bull. Am. Meteorol. Soc.* **55**, 1442-1448, 1974a.

Gloersen, P., T.C. Chang, T.T. Wilheit, and W.J. Campbell, Polar sea ice observations by means of microwave radiometry, in *Advanced Concepts and Techniques in the Study of Snow and Ice*, H. S. Santeford and J.L. Smith, eds., Nat. Acad. Sci, pp. 541-550, 1974b.

Gloersen, P., R.O. Ramseier, W.J. Campbell, T.C. Chang, and T.T. Wilheit, Variations of ice morphology of selected mesoscale test areas during the Bering Sea Experiment, in *Proceedings of the Final Symposium on the Results of the Joint Soviet-American Expedition*, K.Ya. Kondratyev, Yu.I. Rabinovich, and W. Nordberg, eds., Gidrometeoizdat, Leningrad, pp. 196-218, 1975a. (Republished as USSR/USA Bering Sea Experiment by A. A. Balkema, Rotterdam, 307 pp., 1982.)

Gloersen, P., R. Ramseier, W.J. Campbell, P.M. Kuhn, and W.J. Webster, Jr., Ice thickness distribution as inferred from infrared and microwave remote sensing during the Bering Sea Experiment, in *Proceedings of the Final Symposium on the Results of the Joint Soviet-American Expedition*, K. Ya. Kondratyev, Yu. I. Rabinovich, and W. Nordberg, eds., Gidrometeoizdat, Leningrad, pp. 282-293, 1975b. (Republished as USSR/USA Bering Sea Experiment by A. A. Balkema, Rotterdam, 307 pp., 1982.)

Gloersen, P., and F.T. Barath, A scanning multichannel microwave radiometer for Nimbus G and Seasat A, *IEEE J. Oceanic Eng.* **OE-2**, 172-178, 1977.

Gloersen, P., H.J. Zwally, A.T.C. Chang, D.K. Hall, W.J. Campbell, and R.O. Ramseier, Time-dependence of sea ice concentration and multiyear ice fraction in the Arctic basin, *Boundary-Layer Meteorology* **13**, 339-359, 1978.

Gloersen, P., J. Crawford, and L. Hardis, Overseas trip report, CV 990 Underflight Mission, *NASA Tech. Memorandum 80662,* 92 pp., 1980a.

Gloersen, P., D.J. Cavalieri, and H.V. Soule, An alternative algorithm for correction of the Scanning Multichannel Microwave Radiometer polarization radiances using Nimbus 7 observed data, *NASA Tech. Memorandum 80672*, 14 pp., 1980b.

Gloersen, P., and J.K. Larabee, An optical model for the microwave properties of sea ice, *NASA Tech. Memorandum 83865*, 25 pp., 1981.

Gloersen, P., Calibration of the Nimbus 7 SMMR: II Polarization mixing corrections, *NASA Tech. Memorandum 84976,* 1983.

Gloersen, P., D.J. Cavalieri, A.T.C. Chang, T.T. Wilheit, W.J. Campbell, O.M. Johannessen, K.B. Katsaros, K.F. Kunzi, D.B. Ross, D. Staelin, E.P.L. Windsor, F.T. Barath, P. Gudmandsen, E. Langham, and R.O. Ramseier, A summary of results from the first Nimbus 7 SMMR observations, *J. Geophys. Res.* **89**, 5335-5344, 1984.

Gloersen, P., and D.J. Cavalieri, Reduction of weather effects in the calculation of sea ice concentration from microwave radiances, *J. Geophys. Res.* **91**, 3913-3919, 1986.

Gloersen, P., In-orbit calibration adjustment of the Nimbus 7 SMMR, *NASA Tech. Memorandum 100678,* 39 pp., 1987.

Gloersen, P., and W.J. Campbell, Variations in the Arctic, Antarctic, and global sea ice covers during 1978-1987 as observed with the Nimbus 7 Scanning Multichannel Microwave Radiometer, *J. Geophys. Res.* **93**, 10,666-10,674, 1988a.

Gloersen, P., and W.J. Campbell, Satellite and aircraft passive-microwave observations during the Marginal Ice Zone Experiment in 1984, *J. Geophys. Res.* **93**, 6837-6846, 1988b.

Gloersen, P., E. Mollo-Christensen, and P. Hubanks, Observations of Arctic polar lows with the Nimbus 7 Scanning Multichannel Microwave Radiometer, in *Polar and Arctic Lows*, P.F. Twitchell, E.A. Rasmussen, and K.L. Davidson, eds., A. Deepak, Hampton, Virginia, pp. 359-371, 1989.

Gloersen, P., and W.J. Campbell, Variations of extent, area, and open water of the polar sea ice covers: 1978-1987, *Proceedings of the International Conference on the Role of the Polar Regions in Global Change,* G. Weller, C.L. Wilson, and B.A.B. Severin, eds., Geophysical Institute, University of Fairbanks, Alaska, 778 pp., 1991a.

Gloersen, P., and W.J. Campbell, Recent variations in Arctic and Antarctic sea ice covers, *Nature* **352**, 33-36, 1991b.

Gordon, A.L., Structure of Antarctic waters between 20° W and 170° W, in V. Bushnell, ed., *Antarctic Map Folio Series, No. 6.,* Am. Geographical Soc., Broadway, New York, 10 pp., 1967.

Gordon, A.L., Varieties and variability of Antarctic Bottom Water, in *Processus de Formation des eaux oceaniques Profondes en particulier en Mediterranée Occidentale,* Colloques Internationaux du C.N.R.S. No. 215, Éditions du Centre National de la Récherche Scientifique, pp. 33-47, 1974.

Gordon, A.L., Deep Antarctic convection west of Maud Rise, *J. Phys. Oceanogr.* **8**, 600-612, 1978.

Gordon, A.L., Weddell deep water variability, *J. Marine. Res.* **40**, 199-217, 1982.

Gordon, A.L., and E.M. Molinelli, *Southern Ocean Atlas: Thermohaline Chemical Distributions and the Atlas Data Set,* 233 plates, Columbia University Press, New York, 1982.

Gordon, A.L., and J.C. Comiso, Polynyas in the southern ocean, *Scientific American* **256**, 90-97, 1988.

Gordon, A.L., and B.A. Huber, Southern Ocean winter mixed layer, *J. Geophys. Res.* **95**, 11,655-11,672, 1990.

Grenfell, T.C., and G.A. Maykut, The optical properties of ice and snow in the Arctic Basin, *J. Glaciol.* **18**, 445-463, 1977.

Grenfell, T.C., A theoretical model of the optical properties of sea ice in the visible and near infrared, *J. Geophys. Res.* **88**, 9723-9735, 1983.

Grenfell, T.C., and A.W. Lohanick, Temporal variations of the microwave signatures of sea ice during the late spring and early summer near Mould Bay, NWT., *J. Geophys. Res.* **90**, 5063-5074, 1985.

Grenfell, T.C., and J.C. Comiso, Multifrequency passive-microwave observations of first-year sea ice grown in a tank, *IEEE Trans. Geoscience and Remote Sensing* **GE-24**, 826-831, 1986.

Grenfell, T.C., Surface based passive-microwave studies of multiyear sea ice, *J. Geophys. Rev.* **97**, 3485-3501, 1992.

Hansen, J., and S. Lebedeff, Global surface air temperatures: Update through 1987, *Geophys. Res. Lett.* **15**, 323-326, 1988.

Hastings, A. D. , Jr., Surface climate of the Arctic Basin: *Report ETL TR-71-3*, Earth Sciences Division, Geographic Sciences Laboratory, U. S. Army Topographic Laboratories, Fort Belvoir, Virginia, 1971.

Hollinger, J.P., Passive-microwave measurements of the surface, *J. Geophys. Res.* **75**, 5200-5213, 1971.

Hollinger, J.P., and R.C. Lo, SSMI Project summary report, *NRL Memorandum Report 5055,* 106 pp., 1983.

Holt, T., P.M. Kelly, and B.S.G. Cherry, Cryospheric impacts of Soviet river diversion schemes, *Ann. Glaciol.* **5**, 61-68, 1984.

Houghton, J. T., G. J. Jenkins, and J. J. Ephraums, eds., *Climate Change: The IPCC Scientific Assessment*, Cambridge University Press, Cambridge, 365 pp., 1990.

Huntford, R., *The Last Place on Earth,* Atheneum, New York, 565 pp., 1986.

Ito, H., *Sea Ice Atlas of Northern Baffin Bay,* Department of Geography, Swiss Federal Institute of Technology, Zurich, 142 pp., 1982.

Jacobs, S.D., D. Georgi, and S. Patla, Technical report, Conrad 17 hydrographic station in the southwest-Indian Antarctic Ocean, *Tech. Rep. CU-1-80-TRI*, Lamont-Doherty Geol. Observ., Palisades, N.Y., 1980.

Jacobs, S.S., and J.C. Comiso, Sea ice and oceanic processes on the Ross Sea continental shelf, *J. Geophys. Res.* **94**, 18,195-18,211, 1989.

Johannessen, J.A., O.M. Johannessen, E. Svendsen, R. Shuchman, T. Manley, W. J. Campbell, E. Josberger, S. Sandven, J.C. Gascard, T. Olaussen, K. Davidson, and J. VanLeer, Mesoscale eddies in the Fram Strait marginal ice zone during the 1983 and 1984 Marginal Ice Zone Experiments, *J. Geophys. Res.* **92**, 6754-6772, 1987.

Johannessen, O.M., W.D. Hibler III, P. Wadhams, W.J. Campbell, K. Hasselmann, I. Dyer, and M. Dunbar, MIZEX, a program for mesoscale air-ice-ocean interaction experiments in Arctic marginal ice zones: II. A science plan for a summer marginal ice zone experiment in the Fram Strait/Greenland Sea, *CRREL Special Report 83-12,* 47 pp., 1984a.

Johannessen, O.M., W.D. Hibler III, P. Wadhams, W.J. Campbell, K. Hasselmann, and I. Dyer, Marginal ice zones: A description of air-ice-ocean interactive processes, models, and planned experiments, in *Arctic Technology and Policy: Proceedings of the Second Annual MIT Sea Grant College Program Lecture and Seminar,* ISBN 0-89116-361-1, pp.133-146, 1984b.

Johannessen, O.M., J.A. Johannessen, E. Svendsen, R. A. Shuchman, W. J. Campbell, and E. Josberger, Ice edge eddies in the Fram Strait marginal ice zone, *Science* **236**, 427-429, 1987.

Jones, P.D., Hemispheric surface air temperature variations: Recent trends and an update to 1987, *J. Climate* **1**, 654-660, 1988.

Jones, P.D., T.M.L. Wigley, C.K. Folland, D.E. Parker, J.K. Angell, S. Lebedeff, and J.E. Hansen, Evidence for global warming in the past decade, *Nature* **332**, 790, 1988.

Jones, W.L., P.G. Black, V.E. Delnore, and C.T. Swift, Airborne microwave remote-sensing measurement of Hurricane Allen, *Science* **214**, 274-280, 1981.

Kellogg, W.W., Climatic feedback mechanisms involving the polar regions, in *Climate of the Arctic,* G. Weller and S.A. Bowling, eds., Geophysical Institute, University of Alaska, pp. 111-116, 1975.

Kellogg, W.W., and P.F. Twitchell, Summary of the workshop on Arctic lows 9-10 May 1985, *Bull. Am. Meteorol. Soc.* **67**, 186-193, 1986.

Killworth, P.D., Deep convection in the world ocean, *Rev. Geophys. and Space Phys.* **21**, 1-26, 1983.

Kondratyev, K.Ya., Yu.I. Rabinovich, and W. Nordberg, eds., *Proceedings of the Final Symposium on the Results of the Joint Soviet-American Expedition, Leningrad,* May 12-17, 1974, Gidrometeoizdat, Leningrad, 316 pp., 1975. (Republished as USSR/USA Bering Sea Experiment by A.A. Balkema, Rotterdam, 307 pp., 1982.)

Kukla, G.J., Recent changes in snow and ice, in *Climate Change,* John Gribbi, ed., Cambridge University Press, pp. 114-129, 1978.

Kukla, G., and J. Gavin, Summer ice and carbon dioxide, *Science* **215**, 497-503, 1981.

Kunzi, K.F., S. Patil, and H. Rott, Snow-cover parameters retrieved from Nimbus 7 Scanning Multichannel Microwave Radiometer (SMMR) data, *IEEE Trans. Geoscience and Remote Sensing* **GE-20**, 452-467, 1982.

Kurtz, D.D., and D.H. Bromwich, A recurring, atmospherically forced polynya in Terra Nova Bay, in *Oceanology of the Antarctic Continental Shelf,* S. S. Jacobs, ed., Antarctic Research Series vol. 43, American Geophysical Union, Washington, D. C., pp. 177-201, 1985.

Lachenbruch, A.H., and B.V. Marshall, Changing climate: geothermal evidence from permafrost in the Alaskan Arctic, *Science* **234**, 689-696, 1986.

Lachenbruch, A.H., T.T. Cladouhos, and R.W. Saltuls, Permafrost temperature and the changing climate, *Permafrost* **3**, 9-17 (K. Senneset, ed., Tapir Publ., Trondheim, Norway), 1988.

Lamb, H.H., *Climate: Present, Past, and Future,* Methuen and Co., London, 613 pp., 1972.

Lamb, H.H., The climate environment of the Arctic Ocean, in *The Arctic Ocean,* L. Rey, ed., John Wiley & Sons, New York, 135-161, 1982.

Lane, J.A., and J.A. Saxton, Dielectric dispersion in pure polar liquids at very high radio frequencies, *Proc. Roy. Soc. London* **A213**, 400-408, 1952.

Ledley, T.S., A coupled energy balance climate-sea ice model: Impact of sea ice and leads on climate, *J. Geophys. Res.* **93**, 15,919-15,932, 1988.

Lindberg, C.R., Band limited regression. Part I: Simple linear models, *J. Roy. Statistical Soc.,* Part B, submitted, 1991.

Livingstone, C.E., R.K. Hawkins, A.L. Gray, L. D. Arsenault, K. Okamoto, T.L. Wilkinson, and D. Pearson, The CCRS/SURSAT active-passive experiment: 1978-1980, *The Microwave Signatures of Sea Ice,* report, Data Acquisition Div., Canada Centre for Rem. Sens, Dept. of Energy, Mines, and Res., Ottawa, 1983.

Manabe, S., K. Bryan, and M.J. Spelman, Transient response of a global ocean-atmosphere model to a doubling of atmospheric carbon dioxide, *J. Phys. Oceanogr.* **20**, 722-749, 1990.

Martin, P.C., and M. Clarke, A test of barometric pressure and temperature measurements from ADRAMS buoys, *AIDJEX Bull. 40,* pp. 61-82, University of Washington, Seattle, 1978.

Martin, S., B. Holt, D.J. Cavalieri, and V. Squire, Shuttle Imaging Radar B (SIR-B) Weddell Sea ice observations: A comparison of SIR-B and Scanning Multichannel Microwave Radiometer ice concentrations, *J. Geophys. Res.* **92**, 7173-7179, 1987.

Martin, S., and D.J. Cavalieri, Contributions of the Siberian Shelf polynyas to the Arctic Ocean intermediate and deep water, *J. Geophys. Res.* **94**, 12,725-12,738, 1989.

Martinson, D.G., P.D. Killworth, and A. L. Gordon, A convective model for the Weddell Polynya, *J. Phys. Oceanogr.* **11**, 466-488, 1981.

Maslanik, J.A., and R.G. Barry, Short-term interactions between atmospheric synoptic conditions and sea ice behavior in the Arctic, *Ann. Glaciol.* **12**, 113-117, 1989.

Mätzler, C., R.O. Ramseier, and E. Svendsen, Polarization effects in sea ice signatures, *IEEE J. Oceanic Engr.* **OE-9**, 333-338. 1984.

Maykut, G.A., and N. Untersteiner, Some results from a time-dependent thermodynamic model of sea ice, *J. Geophys. Res.* **76**, 1550-1575, 1971.

Maykut, G.A., Energy exchange over young sea ice in the central Arctic, *J. Geophys. Res.* **83**, 3646-3658, 1978.

Meeks, D.C., R.O. Ramseier, and W.J. Campbell, A study of microwave emission properties of sea ice-AIDJEX 1972, *Proceedings of the Ninth International Symposium on Remote Sensing,* Willow Run Laboratories of the Institute of Science and Technology, The University of Michigan, Ann Arbor, Michigan, pp. 307-322, 1974.

Meese, D.A., J.W. Govoni, V. Churun, B. Ivanov, V. Komarovskiy, V. Shilnikov, and A. Zachek, Sea ice observations from the Winter Weddell Gyre Study -'89, *CRREL Special Report 91-2,* 1991.

Mirsky, J., *The Story of Northern Exploration from Earliest Times to the Present,* Alfred A Knopf, Inc., New York, 344 pp., 1948.

Mitchell, B.G., E. Brody, E.N. Yeh, C. McClain, J.C. Comiso, and N.C. Maynard, Meridional zonation of the Barents Sea ecosystem inferred from satellite remote sensing and in-situ bio-optical observations, *Polar Res.,* **10**, 147-162, 1991.

MIZEX Group, O.M. Johannessen, D.A. Horn, E.Augstein, A. Baggeroer, B.A. Burns, W.J . Campbell, K.L. Davidson, G.L. Duckworth, I. Dyer, B.A. Farrelly, T. Grenfell, A. Heiberg, W.D. Hibler, J.A. Johannessen, E. G. Josberger, N. Lannelongue, T.A. Manley, G.A. Maykut, M. McPhee, J. Morisson, R.D. Muench, T. Olaussen, R.G. Onstott, S. Sandven, R.A. Shuchman, S.L. Smith, W.O. Smith, V.A. Squire, E. Svendsen, G. Symonds, W. Tucker, J.C. VanLeer, and P. Wadhams, MIZEX East 83/84: The summer marginal ice zone program in the Fram Strait/Greenland Sea, *EOS* **67**, 513-517, 1986.

Muench, R.D., The physical oceanography of the northern Baffin Bay region, in *The Baffin Bay-North Water Project*, Rep. No. 1, 150 pp., Arctic Institute of North America, Montreal, 1971.

Muench, R.D., and H.E. Sadler, Physical oceanographic observations in Baffin Bay and Davis Strait, *Arctic* **26**, 73-76, 1973.

Muller, F., A. Ohmura, and R. Braithwaite, The North Water Project (Canadian Greenland Arctic), *Geogr. Helv. (Polar Geogr.)* **2**, 111-117, 1977.

Nansen, F., *Farthest North, Vols. I & II*, Archibald Constable and Co., Westminster, England, 1181 pp., 1897.

Niebauer, H.J., Effects of El Niño-Southern Oscillation and north Pacific weather patterns on interannual variability in the subarctic Bering Sea, *J. Geophys. Res.* **93**, 5051-5068, 1988.

Njoku, E.G., J.M. Stacey, and F.T. Barath, The Seasat Scanning Multichannel Microwave Radiometer (SMMR): Instrument description and performance, *IEEE J. Oceanic Eng.* **OE-5**, 100-115, 1980.

Nordberg, W., J. Conaway, and P. Thaddeus, Microwave observation of sea state from aircraft, *Quart. J. Roy. Meteorol. Soc.* **95**, 408-413, 1969.

Nordberg, W., J. Conaway, D.B. Ross, and T. Wilheit, Measurements of microwave emission from a foam-covered, wind-driven sea, *J. Atmos. Sci.* **28**, 429-435, 1971.

NORSEX Group, Norwegian remote sensing experiment in a marginal ice zone, *Science* **220**, 781-787, 1983.

Onstott, R.G., T.C. Grenfell, C. Mätzler, C.A. Luther, and E.A. Svendsen, Evolution of microwave sea ice signatures during early summer and midsummer in the marginal ice zone, *J. Geophys. Res.* **92**, 6825-6835, 1987.

Overland, J.E., and C.H. Pease, Cyclone climatology of the Bering Sea and its relation to sea ice extent, *Mon. Weather Rev.* **110**, 5-13, 1983.

Parkinson, C.L., and W.W. Kellogg, Arctic sea ice decay simulated for a CO_2-induced temperature rise, *Climatic Change* **2**, 149-162, 1979.

Parkinson, C.L., and D.J. Cavalieri, Interannual sea ice variations and sea ice/atmosphere interactions in the Southern Ocean, 1973-1975, *Ann. Glaciol.* **3**, 249-254, 1982.

Parkinson, C.L., On the development and cause of the Weddell Polynya in a sea ice simulation, *J. Phys. Oceanogr.* **13**, 501-511, 1983.

Parkinson, C.L., and A.J. Gratz, On the seasonal sea ice cover of the Sea of Okhotsk, *J. Geophys. Res.* **88**, 2793-2802, 1983.

Parkinson, C.L., and R.A. Bindschadler, Response of Antarctic sea ice to uniform atmospheric temperature increases, in *Climate Processes and Climate Sensitivity*, J.E. Hansen and T. Takahashi, eds., Maurice Ewing Series, Vol. 5, American Geophysical Union, Washington, D.C., pp. 254-264, 1984.

Parkinson, C.L., J.C. Comiso, H.J. Zwally, D.J. Cavalieri, P. Gloersen, and W.J. Campbell, *Arctic Sea Ice, 1973-1976: Satellite Passive-Microwave Observations*, NASA SP-489, National Aeronautics and Space Administration, Washington, D.C., 296 pp., 1987.

Parkinson, C.L., and D.J. Cavalieri, Arctic sea ice, 1973-1987: Seasonal, regional, and interannual variability, *J. Geophys. Res.* **94**, 14,499-14,523, 1989.

Parkinson, C.L., The impact of the Siberian High and Aleutian Low on the sea ice cover of the Sea of Okhotsk, *Ann. Glaciol.* **14**, 226-229, 1990.

Parkinson, C.L., Interannual variability of the spatial distribution of sea ice in the north polar region, *J. Geophys. Res.* **96**, 4791-4801, 1991.

Parkinson, C.L., Interannual variability of monthly Southern Ocean sea ice distributions, *J. Geophys. Res.* **97**, 5349-5363, 1992.

Ramseier, R.O., P. Gloersen, and W.J. Campbell, Variation in the microwave emissivity of sea ice in the Beaufort and Bering Seas, in *Specialist Meeting on Microwave Scattering and Emission from the Earth: Proceedings of the URSI Commission II*, E. Schanda, ed., Inst. of Applied Physics, University of Bern, 23 pp., 1974.

Ramseier, R.O., P. Gloersen, W.J. Campbell, and T.C. Chang, Mesoscale description for the principal Bering Sea Experiment, in *Proceedings of the Final Symposium on the Results of the Joint Soviet-American Expedition*, Leningrad, May 12-17, 1974, K.Ya. Kondratyev, Yu.I. Rabinovich, and W. Nordberg, eds., Gidrometeoizdat, Leningrad, 234-269, 1975. (Republished as USSR/USA Bering Sea Experiment by A. A. Balkema, Rotterdam, 307 pp., 1982.)

Ramseier, R.O., W.J. Campbell, W.F. Weeks, L. Drapier-Arsenault, and K.L. Wilson, Ice dynamics in the Canadian Archipelago and adjacent Arctic Basin as determined by ERTS-1 observations, in *Canada's Continental Margins and Offshore Exploration*, Canadian Society of Petroleum Geologists, Calgary, Alberta, pp. 853-877, 1975.

Reed, R.J., and W.J. Campbell, The equilibrium drift of Ice Station Alpha, *J. Geophys. Res.* **67**, 281-297, 1962.

Reynolds, W.R., C.K. Folland, and D.E. Parker, Biases in satellite-derived sea surface temperature data, *Nature* **341**, 728-731, 1989.

Rothrock, D.A., D.R. Thomas, and A.S. Thorndike, Principal component analysis of satellite passive-microwave data over sea ice, *J. Geophys. Res.* **93**, 2321-2332, 1988.

Shuchman, R.A., W.J. Campbell, B. Burns, E. Ellingsen, B. Farrelly, P. Gloersen, T. Grenfell, J. Hollinger, D. Horn, J. Johannessen, O. Johannessen, E. Josberger, C. Livingstone, C. Luther, T. Manley, R. Markson, C. Mätzler, E. Mollo-Christensen, R. Onstott, D. Ross, S. Sandven, C. Schgoun, A. Stiffey, E. Svendsen, G. Simmonds, and Z. Top, Remote sensing of the Marginal Ice Zone Experiment, in *Proceedings of the IGARSS'84 Symposium*, Strasbourg, France, European Space Agency, ESA SP-215, pp. 404-409, 1984.

Shuchman, R.A., B. Burns, O.M. Johannessen, E.G. Josberger, W.J. Campbell, T. Manley, and N. Lannelongue, Remote sensing of the Fram Strait marginal ice zone, *Science* **236**, 429-431, 1987.

Simmonds, I., and W.F. Budd, A simple parameterization of ice leads in a general circulation model, and the sensitivity of climate to change in Antarctic ice concentration, *Ann. Glaciol.* **14**, 266-269, 1990.

Sissala, J.F., R.R. Sabatini, and H.J. Ackerman, Nimbus satellite data for polar ice survey, *Polar Rec.* **16**, 367-373, 1972.

Smith, S.D., R.D. Muench, and C.H. Pease, Polynyas and leads: An overview of physical processes and environment, *J. Geophys. Res.* **95**, 9461-9479, 1990.

Steffen, K., *Surface Temperature and Sea Ice of an Arctic Polynya: North Water in Winter*, Geographisches Institut der Eidgenossische Technische Hochschule, Zurich, 193 pp., 1985.

Steffen, K., Ice conditions of an Arctic polynya: North Water in winter, *J. Glaciol.* **32**, 383-390, 1986.

Steffen, K., and J.A. Maslanik, Comparison of Nimbus 7 Scanning Multichannel Microwave Radiometer radiance and derived sea ice concentrations with Landsat imagery for the North Water area of Baffin Bay, *J. Geophys. Res.* **93**, 10,769-10,781, 1988.

Steffen, K., and A. Schweiger, DMSP-SSMI NASA team algorithm for sea ice concentration retrieval: Comparison with Landsat satellite imagery, *J. Geophys. Res.* **96**, 21,971-21,987, 1991.

Stiles, W.H., and F.T. Ulaby, The active and passive-microwave response to snow parameters, *J. Geophys. Res.* **85**, 1037-1044, 1980.

Stommel, H., On the smallness of sinking regions in the ocean, *Proc. Nat. Acad. Sc., USA* **48**, 766-772, 1962.

Stouffer, R.J., S. Manabe, and K. Bryan, Interhemispheric asymmetry in climate response to a gradual increase of atmospheric CO_2, *Nature* **342**, 660-662, 1989.

Streten, N.A., Satellite observations of the summer decay of the Antarctic sea ice, *Arch. Meteorol. Geophys. Bioklimatol. Ser. A.* **22**, 129-134, 1973.

Sturman, A.P., and M.R. Anderson, A comparison of Antarctic sea ice data sets and inferred trends in ice area, *J. Appl. Climate and Appl. Met.* **24**, 275-280, 1985.

Sullivan, C.W., C.R. McClain, J.C. Comiso, and W.O. Smith, Jr., Phytoplankton standing crops within an Antarctic ice edge assessed by satellite remote sensing, *J. Geophys. Res.* **93**, 12,487-12,498, 1988.

Svendsen, E., K. Kloster, B. Farrelly, O.M. Johannessen, J.A. Johannessen, W.J. Campbell, P. Gloersen, D. Cavalieri, and C. Mätzler, Norwegian Remote Sensing Experiment: Evaluation of the Nimbus 7 Scanning Multichannel Microwave Radiometer for sea ice research, *J. Geophys. Res.* **88**, 2781-2791, 1983.

Swift, C.T., Passive-microwave remote sensing of ocean-A review, *Boundary-Layer Meteorol.* **18**, 25-54, 1980.

Swift, C.T., and D.J. Cavalieri, Passive-microwave remote sensing for sea ice research, *EOS* **66**, 1210-1212, 1985.

Swift, C.T., L.S. Fedor, and R.O. Ramseier, An algorithm to measure sea ice concentration with microwave radiometers, *J. Geophys. Res.* **90**, 1087-1099, 1985.

Thorndike, A.S., Kinematics of sea ice, Chapter 7 in *The Geophysics of Sea Ice,* N. Untersteiner, ed., pp. 485-549, NATO ASI Series, Plenum Press, New York, 1986.

Thorndike, A.S., and R. Colony, *Arctic Ocean Buoy Program Data Report, 19 January 1979-31 December 1979,* University of Washington Polar Science Center, Seattle, 1980.

Thorndike, A.S., and R. Colony, *Arctic Ocean Buoy Program Data Report, 1 January 1980-31 December 1980,* University of Washington Polar Science Center, Seattle, 1981.

Thorndike, A.S., and R. Colony, Sea ice motion in response to geostrophic winds, *J. Geophys. Res.* **87**, 5845-5852, 1982.

Thorndike, A.S., R. Colony, and E.A. Muñoz, *Arctic Ocean Buoy Program Data Report, 1 January 1981-31 December 1981,* University of Washington Polar Science Center, Seattle, 1982.

Thorndike, A.S., R. Colony, and E.A. Muñoz, *Arctic Ocean Buoy Program Data Report, 1 January 1982-31 December 1982,* University of Washington Polar Science Center, Seattle, 1983.

Tooma, S.G., R.A. Menella, J.P. Hollinger, and R.D. Ketchum, Comparison of sea ice type identification between airborne dual-frequency passive-microwave radiometry and standard laser/infrared techniques, *J. Glaciol.* **15**, 225-239, 1975.

Tucker, W.B., III, A.J. Gow, and W.F. Weeks, Physical properties of summer sea ice in the Fram Strait, *J. Geophys. Res.* **92**, 6787-6803, 1987.

Tucker, W.B., III, T.C. Grenfell, R.G. Onstott, D.K. Perovich, A.J. Gow, R.A. Shuchman, and L.L. Sutherland, Microwave and physical properties of sea ice in the winter marginal ice zone, *J. Geophys. Res.* **96**, 4573-4587, 1991.

Twitchell, P.F., E.A. Rasmussen, and K.L. Davidson, eds., *Polar and Arctic Lows,* 421 pp., A. Deepak, Hampton, VA, 1989.

Untersteiner, N., Calculations of temperature regime and heat budget of sea ice in the Central Arctic, *J. Geophys. Rev.* **69**, 4755-4766, 1964.

U.S. Navy Climatic Atlas of the World, NAVAIR 50-1C-54, 1969.

van Loon, H., Meteorology of the Southern Hemisphere, *Meteorol. Monographs* **13**, 87-100, 1972.

Vowinckel, E., and S. Orvig, *The climate in the north polar basin,* in *Climate of the Polar Regions,* Vol.14, *World Survey of Climatology,* Elsevier, Amsterdam, pp. 129-252, 1970.

Wadhams, P., and R.J. Horne, An analysis of ice profiles obtained by submarine sonar in the Beaufort Sea, *J. Geophys. Res.* **25**, 401-424, 1980.

Wadhams, P., M.A. Lange, and S.F. Ackley, The ice thickness distribution across the Atlantic sector of the Antarctic Ocean in midwinter, *J. Geophys. Res.* **92**, 14,535-14,552, 1987.

Walsh, J.E., and C.M. Johnson, Interannual atmospheric variability and associated fluctuations in Arctic sea ice extent, *J. Geophys. Res.* **84**, 6915-6928, 1979.

Walsh, J.E., and H.J. Zwally, Multiyear sea ice in the Arctic: model- and satellite-derived, *J. Geophys. Res.* **95**, 11,613-11,628, 1990.

Walsh, J.E., The Arctic as bellwether, *Nature* **352**, 19-20, 1991.

Washington, W.M., and G.A. Meehl, Climate sensitivity due to increased CO_2: Experiments with a coupled atmospheric and ocean general circulation model, *Climate Dynamics* **4**, 1-38, 1989.

Watanabe, K., Summary of drift ice in the Okhotsk Sea, in *Physics of Snow and Ice,* Vol. 1, Part 1, H. Oura, ed., Institute of Low Temperature Science, Hokkaido University, pp. 667-686, 1967.

Webster, W.J., T.T. Wilheit, D.B. Ross, and P. Gloersen, Analysis of the CV-990 passive-microwave observations of the sea states during BESEX, in *Proceedings of the Final Symposium on the Results of the Joint Soviet-American Expedition,* K.Ya. Kondratyev, Yu.I. Rabinovich, and W. Nordberg, eds., Gidrometeoizdat, Leningrad, 149-162, 1975. (Republished as USSR/USA Bering Sea Experiment by A. A. Balkema, Rotterdam, 307 pp., 1982.)

Webster, W.J., T.T. Wilheit, D.B. Ross, and P. Gloersen, Spectral characteristics of the microwave emission from a wind-driven foam-covered sea, *J. Geophys. Res.* **81**, 3095-3099, 1976.

Wigley, T.M.L., Climate variability on the 10-100-year time scale: Observations and possible causes, in *Global Changes of the Past,* R. S. Bradley, ed., University Corporation for Atmospheric Research, Boulder, Colorado, pp. 83-101, 1989.

Wilheit, T.T., W. Nordberg, J. Blinn, W. Campbell, and A. Edgerton, Aircraft measurements of microwave emission from Arctic sea ice, *Remote Sensing of Environment* **2**, 129-139, 1972.

Wittman, W.I., and J.J. Schule, Comments on the mass budget of Arctic ice pack, in *Proceedings of the Symposium on the Arctic Heat Budget and Atmospheric Circulation,* J.O. Fletcher, ed., pp. 215-246, Memo, RM-5233-NSAF, RAND Corp., Santa Monica, CA, 1966.

WMO (World Meteorological Organization), *WMO Sea Ice Nomenclature, Terminology, Codes, and Illustrated Glossary,* WMO/OMM/BMO No. 259, TP 145, Secretariat of the World Meteorological Organization, 1970.

Yakovlev, G.N., *Ice Routes of the Arctic,* translated from Russian by the Canadian Department of National Defense, Ottawa, 342 pp., 1977.

Zwally, H.J., T.T. Wilheit, P. Gloersen, and J.L. Mueller, Characteristics of Antarctic sea ice as determined by satellite-borne microwave imagers, in *Proceedings of the Symposium on Meteorological Observations from Space: Their Contribution to the First GARP Global Experiment,* Committee on Space Research of the International Council of Scientific Unions, Philadelphia, pp. 94-97, 1976.

Zwally, H.J., and P. Gloersen, Passive-microwave images of the polar regions and research applications, *Polar Rec.* **18**, 431-450, 1977.

Zwally, H.J., J.C. Comiso, C.L. Parkinson, W.J. Campbell, F.D. Carsey, and P. Gloersen, *Antarctic Sea Ice, 1973-1976: Satellite Passive-Microwave Observations,* NASA SP-459, National Aeronautics and Space Administration, Washington, D.C., 206 pp., 1983a.

Zwally, H.J., C.L. Parkinson, and J.C. Comiso, Variability of Antarctic sea ice and changes in carbon dioxide, *Science* **220**, 1005-1012, 1983b.

Zwally, H.J., Observing polar-ice variability, *Ann. Glaciol.* **5**, 191-198, 1984.

Zwally, H.J., J.C. Comiso, and A.L. Gordon, Antarctic offshore open water within the pack and oceanographic effects, in *Oceanology of the Antarctic Continental Shelf,* S.S. Jacobs, ed., Antarctic Research Series vol. 43, American Geophysical Union, Washington, D.C., pp. 203-226, 1985.

Zwally, H.J., and J.E. Walsh, Comparison of observed and modeled ice motion in the Arctic Ocean, *Ann. Glaciol.* **9**, 136-144, 1987.

Page Intentionally Left Blank

Appendix A

ARCTIC OCEAN BUOY PROGRAM DATA AND ICE TEMPERATURES FROM SMMR

Through the courtesy of Roger Colony of the University of Washington Polar Science Center, we present here monthly averages of Arctic surface atmospheric pressures (Figures A.1-A.12), 8-year averages of monthly averaged buoy temperatures (Figure A.13), annual records of the buoy tracks (Figure A.14), 8-year averages of the seasonal buoy drifts (Figure A.15), and 8-year averages of the monthly surface-wind vectors (Figure A.16), all gathered during the SMMR lifetime. Since there were so few buoys in individual years, it requires a composite of 8 years of data for a given month to produce satisfactory surface temperature and wind vector contour maps. A description of the Arctic Ocean Buoy Program (AOBP) is given in a series of data reports (Thorndike and Colony, 1980, 1981; Thorndike et al., 1982, 1983; Colony and Muñoz, 1986). These data are presented to aid in subsequent analyses of the SMMR data, particularly in regard to ice dynamics studies. An element of caution is required in using the buoy temperature data, particularly in the seasons in which solar heating of the buoys causes the interior of the buoys (where the temperature sensors are located) to become appreciably warmer than the outside air temperatures. The temperature data contoured in Figure A.13 were filtered to remove those buoys having either an exceedingly large standard deviation or a standard deviation of zero, these criteria being taken as indicators of faulty buoy operation.

Ice temperatures, as a product derived from both the SMMR radiances and the calculated sea ice concentrations (discussed in Chapter 2), are presented in this appendix also. Monthly averaged ice temperatures for the Arctic, and their 8- or 9-year averages by month, are given in Figures A.17-A.29, and for the Antarctic, in Figures A.30-A.42. The sea ice temperatures represent subsurface temperatures, i.e., the snow-ice interface temperature in the case of first-year sea ice and the ice temperature near sea level in the case of multiyear ice. Hence, they generally will be warmer than air temperatures. A comparison of the SMMR ice temperatures with monthly averages of climatological air temperatures (Parkinson et al., 1987) shows the SMMR wintertime ice temperature to be warmer, on average, by about 5°-15°. The isotherm patterns of the SMMR data set bear little resemblance to the climatological isotherms; however, the latter are based largely on data from meteorological stations on the perimeter of the Arctic Basin. In Section 2.3.4, we have also compared the wintertime (7-month) ice temperatures from SMMR and the AOBP. Although the accuracies of the SMMR ice temperatures are uncertain, we feel that the relative changes observed in the SMMR ice-temperature maps may provide useful information.

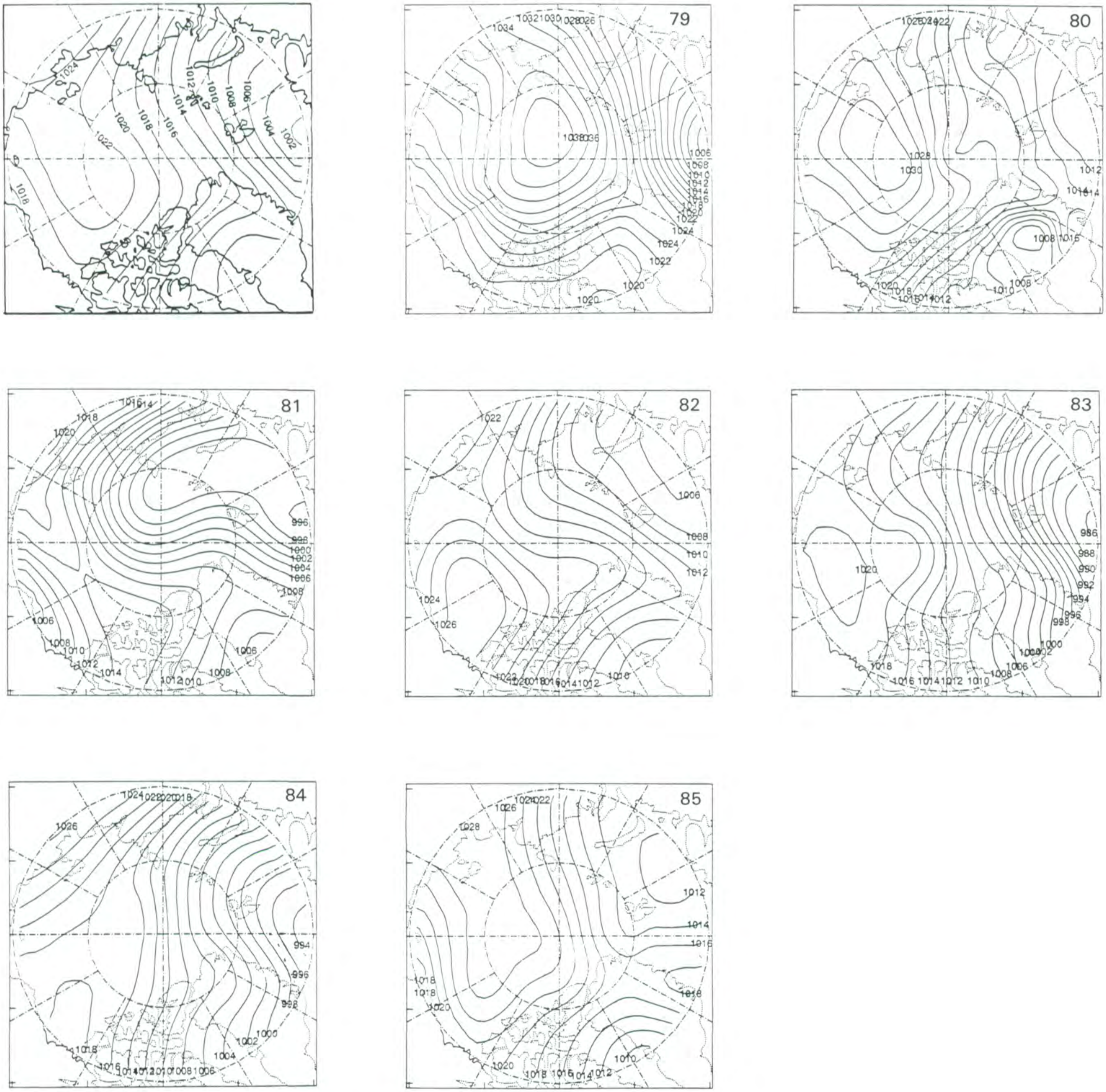

Figure A.1. Monthly average surface pressures for January 1979-1985; 7-year average, and the individual years.

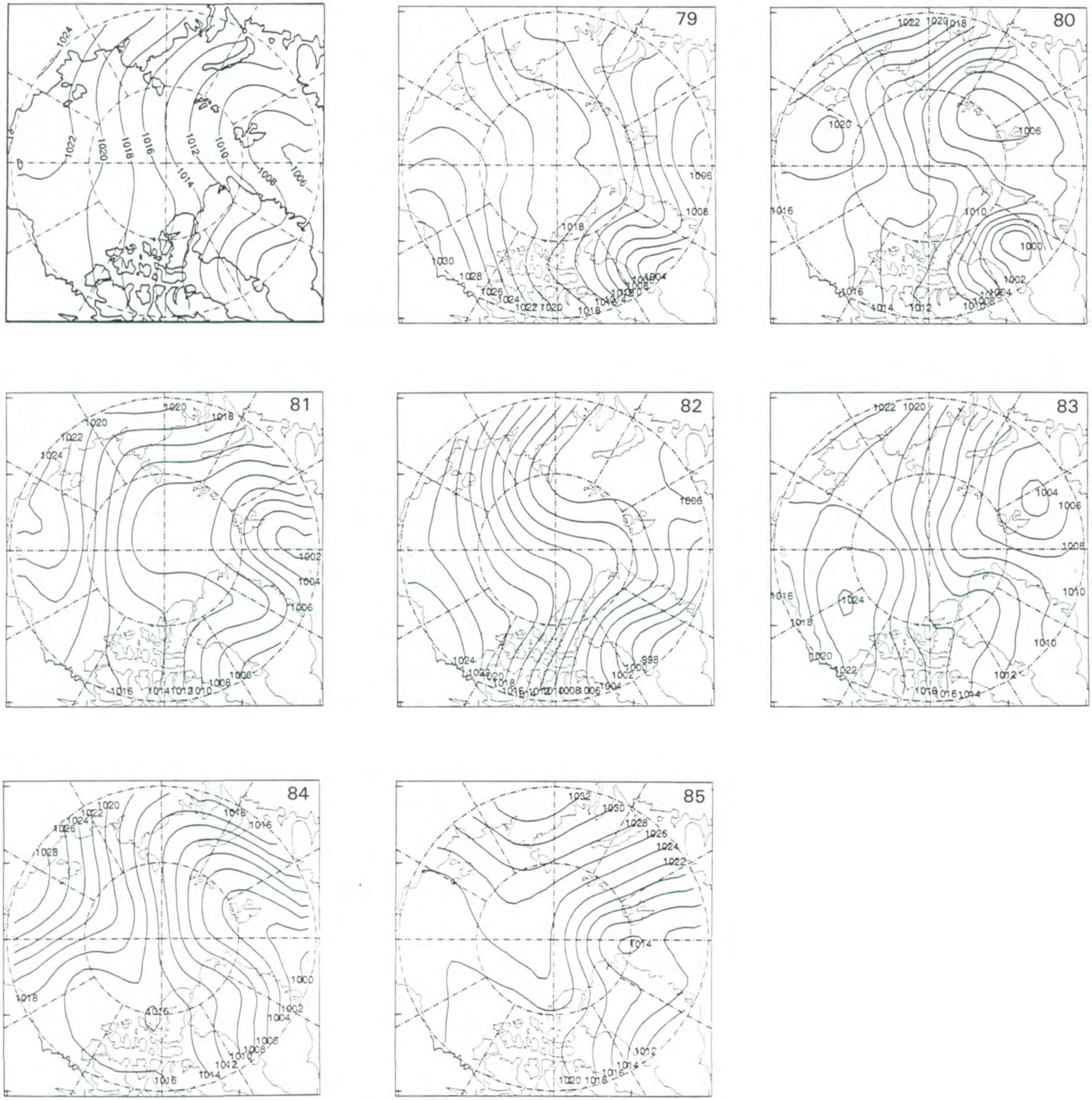

Figure A.2. Monthly average surface pressures for February 1979-1985; 7-year average, and the individual years.

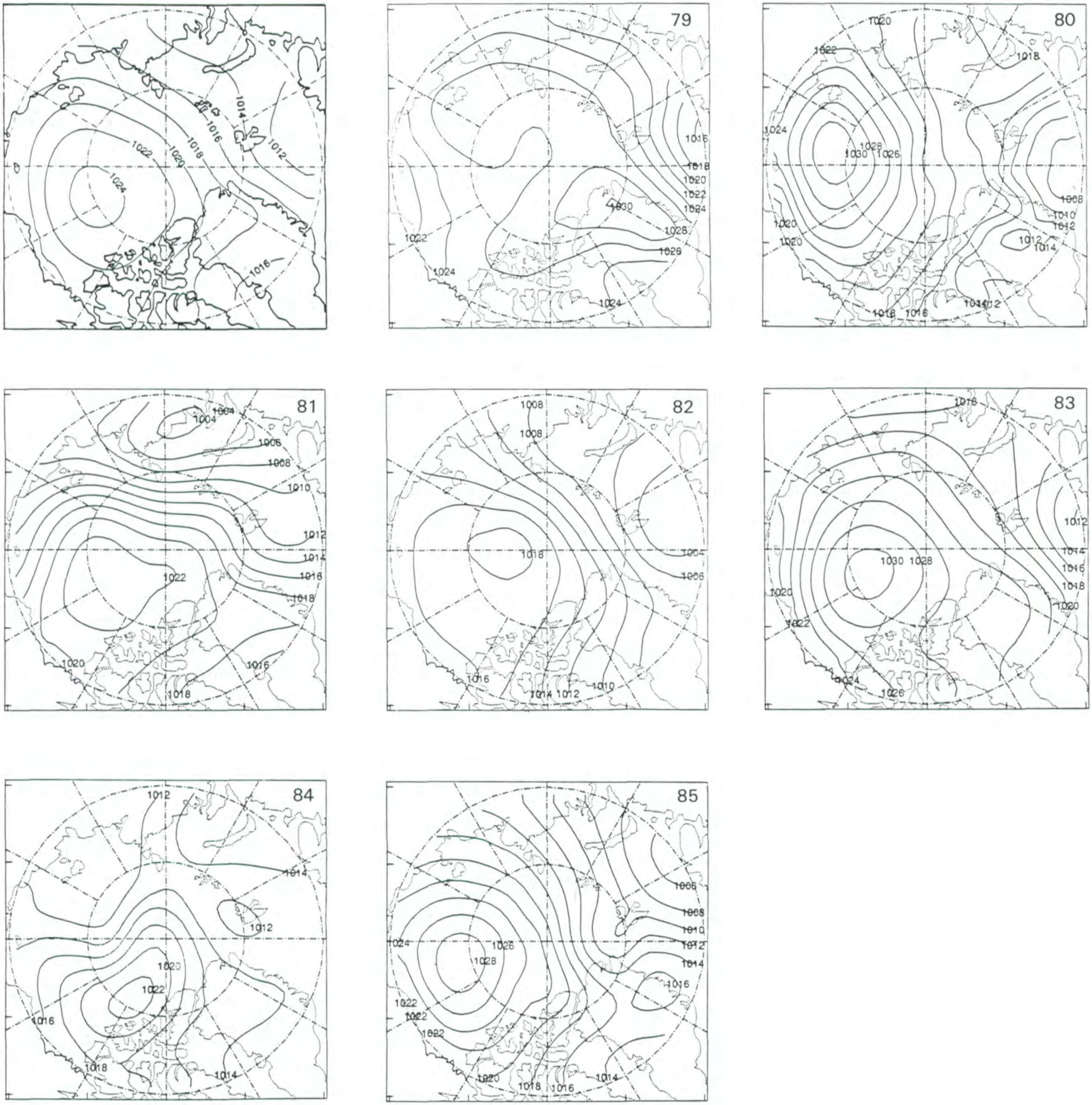

Figure A.3. Monthly average surface pressures for March 1979-1985; 7-year average, and the individual years.

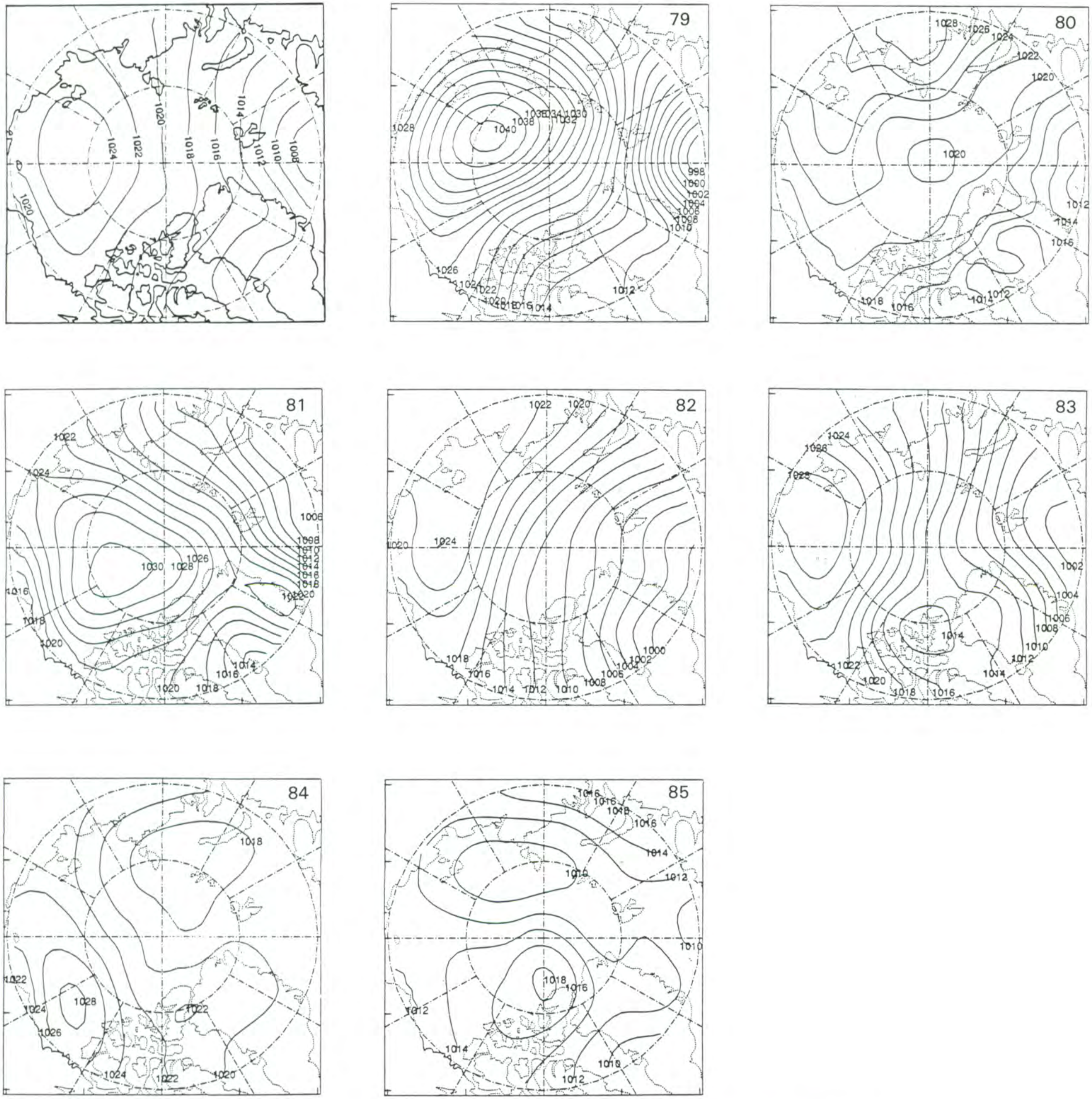

Figure A.4. Monthly average surface pressures for April 1979-1985; 7-year average, and the individual years.

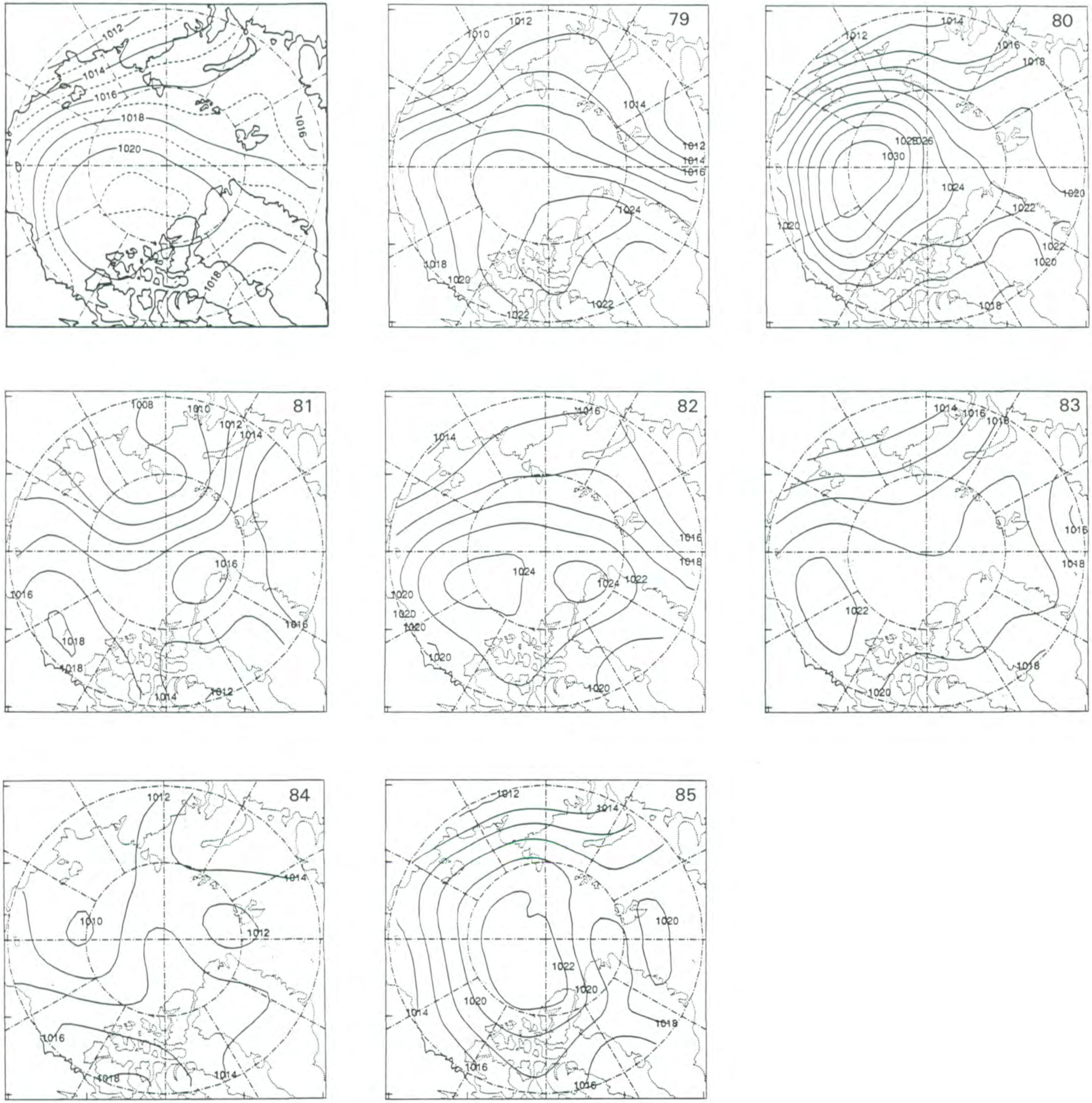

Figure A.5. Surface pressures for May 1979-1985; 7-year average, and the individual years.

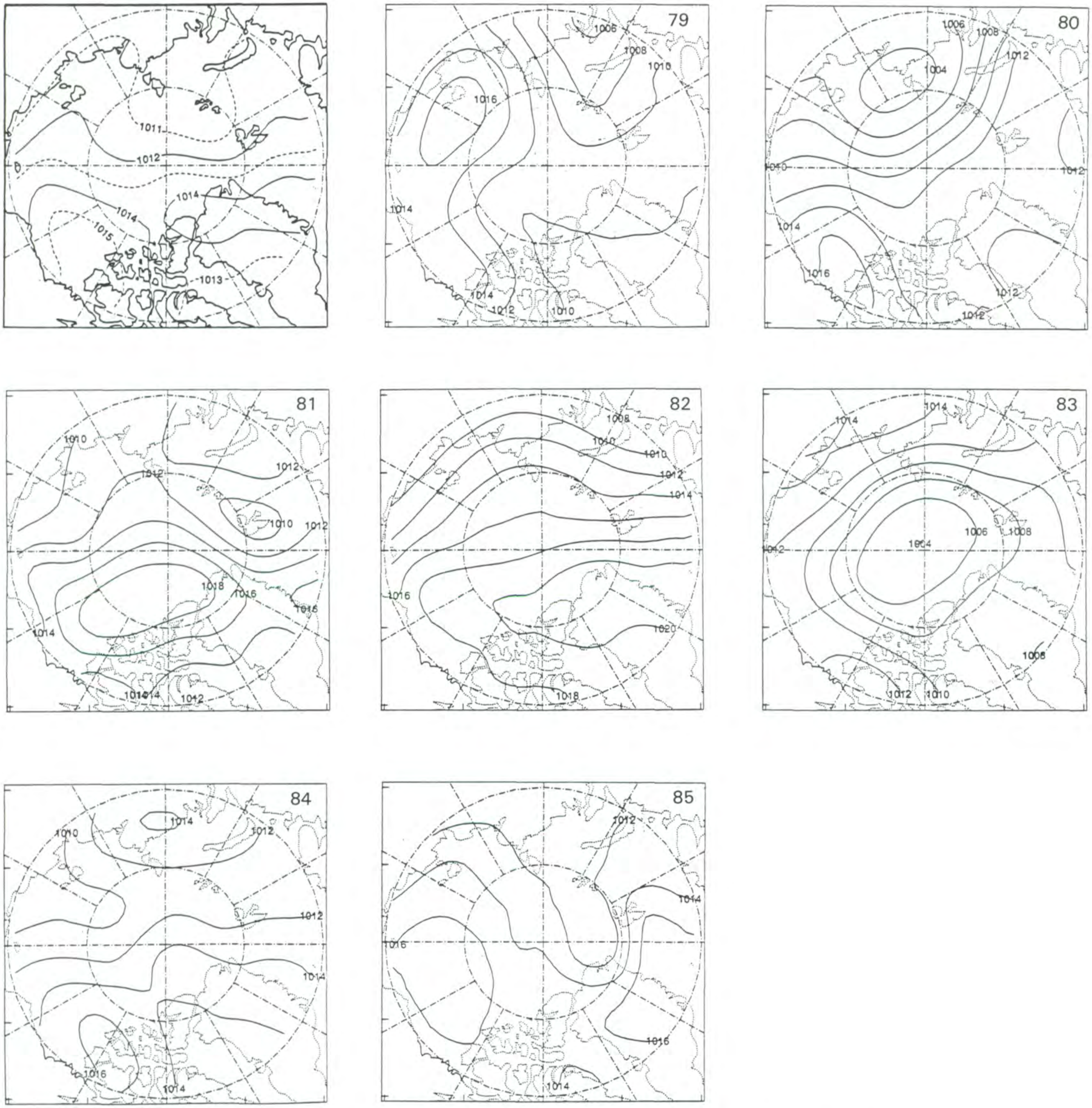

Figure A.6. Monthly average surface pressures for June 1979-1985; 7-year average, and the individual years.

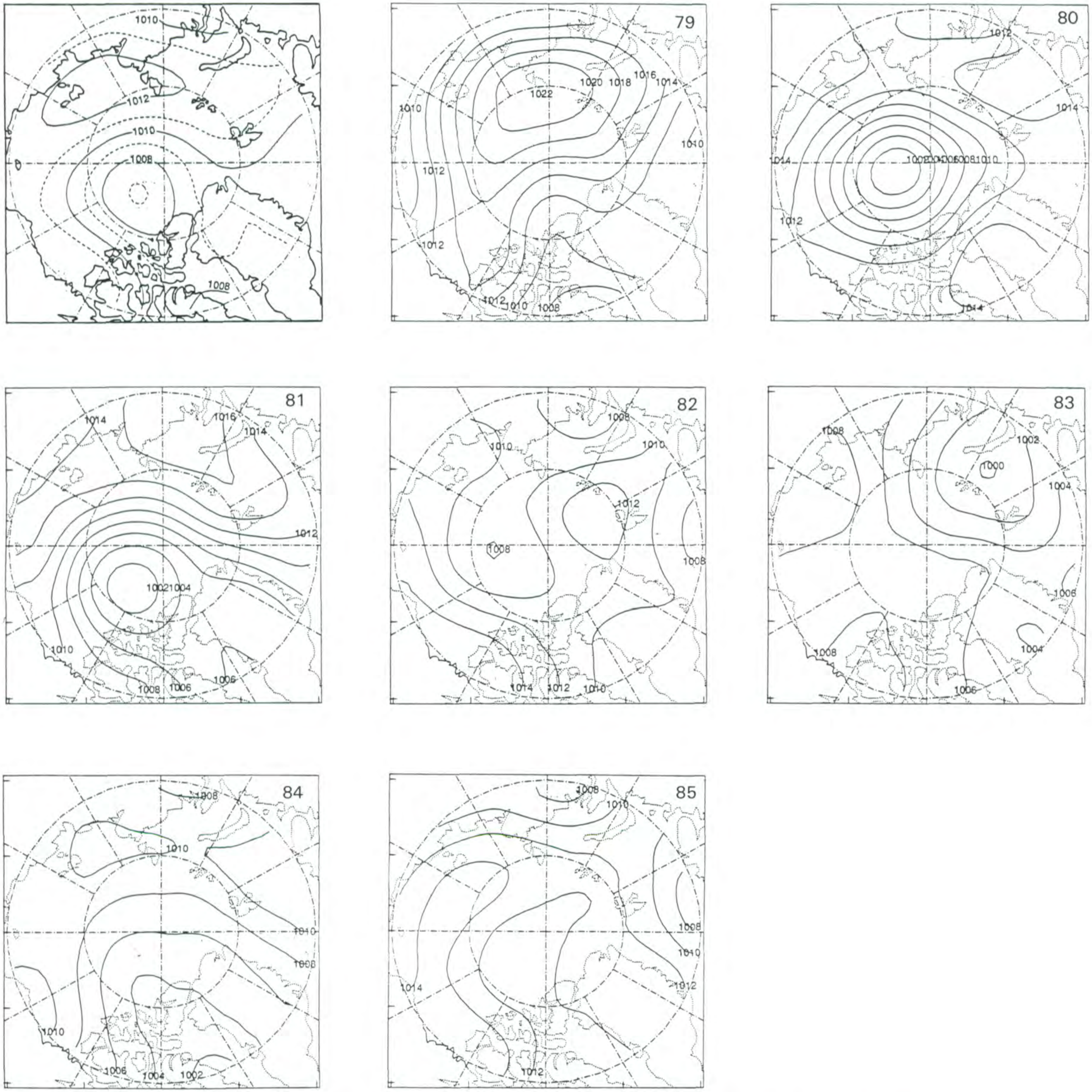

Figure A.7. Monthly average surface pressures for July 1979-1985; 7-year average, and the individual years.

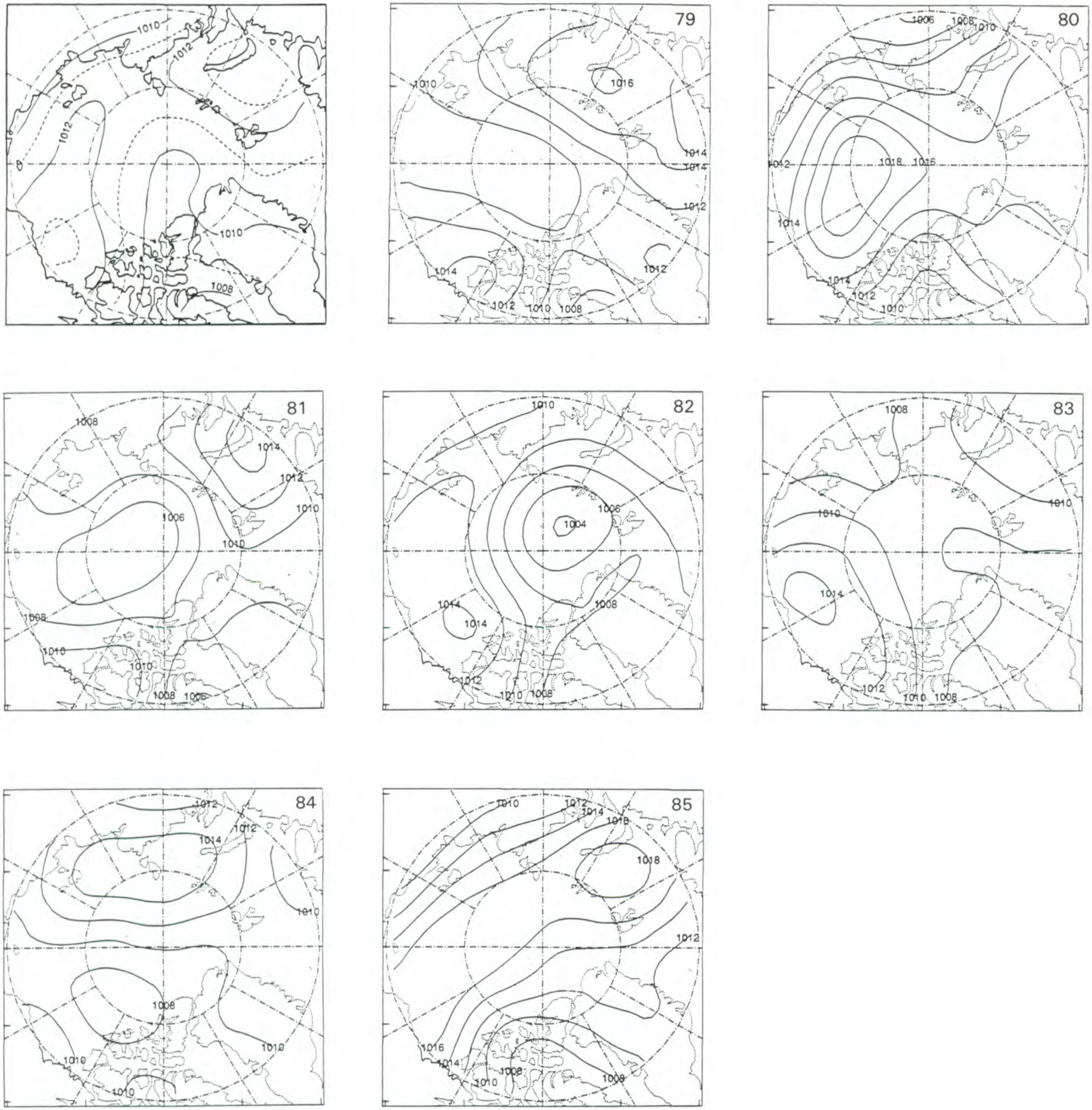

Figure A.8. Monthly average surface pressures for August 1979-1985; 7-year average, and the individual years.

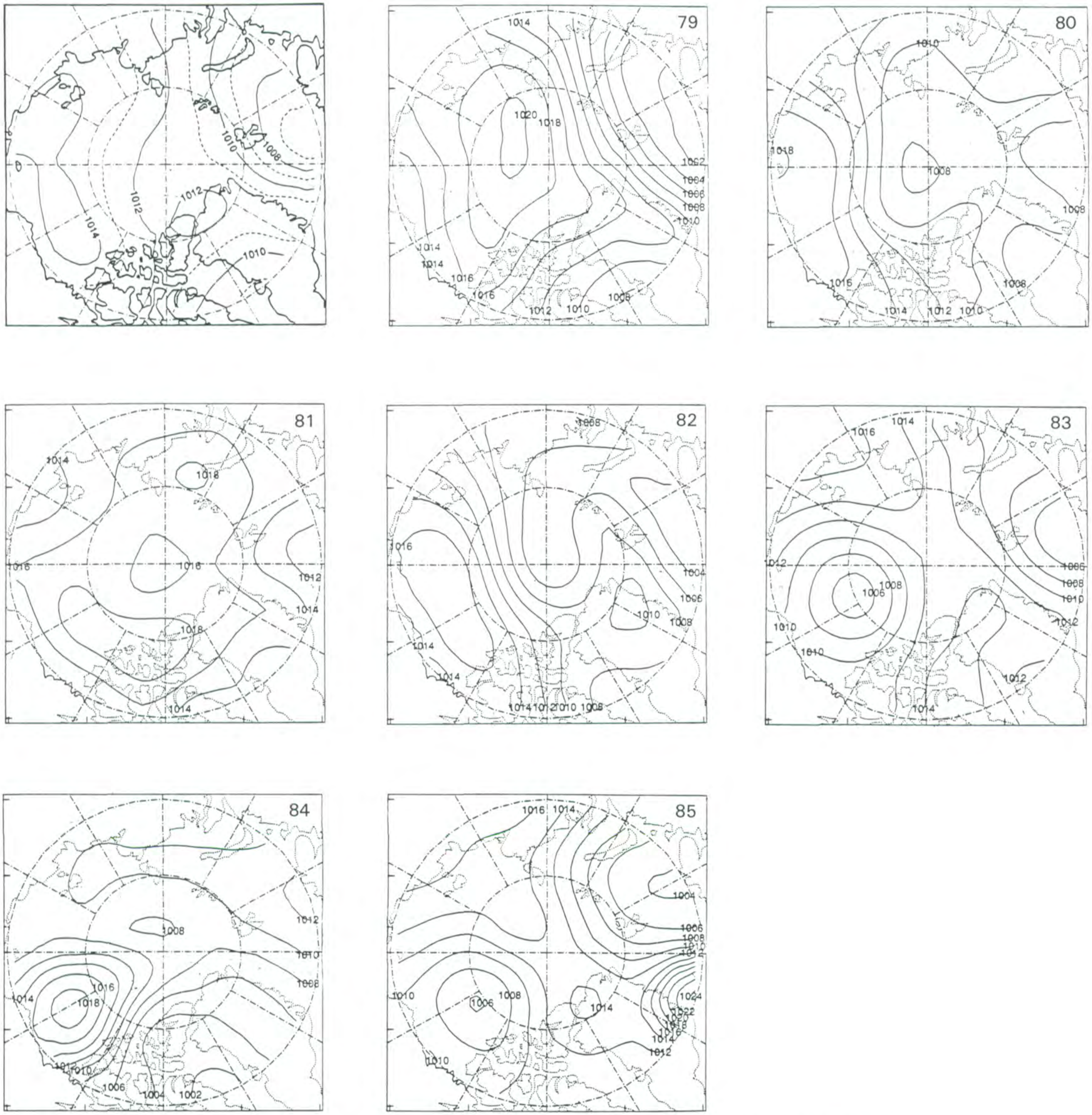

Figure A.9. Monthly average surface pressures for September 1979-1985; 7-year average, and the individual years.

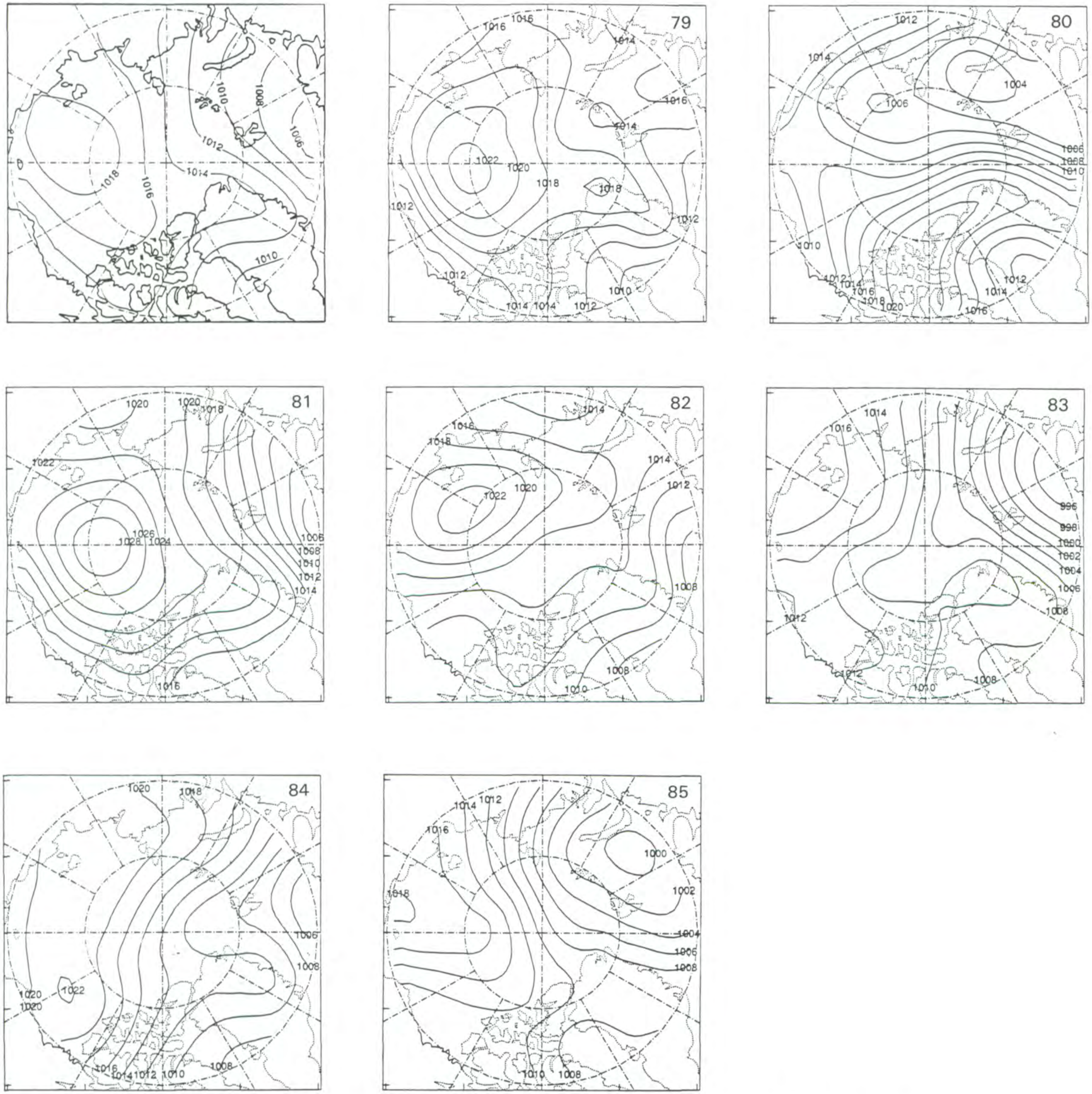

Figure A.10. Monthly average surface pressures for October 1979-1985; 7-year average, and the individual years.

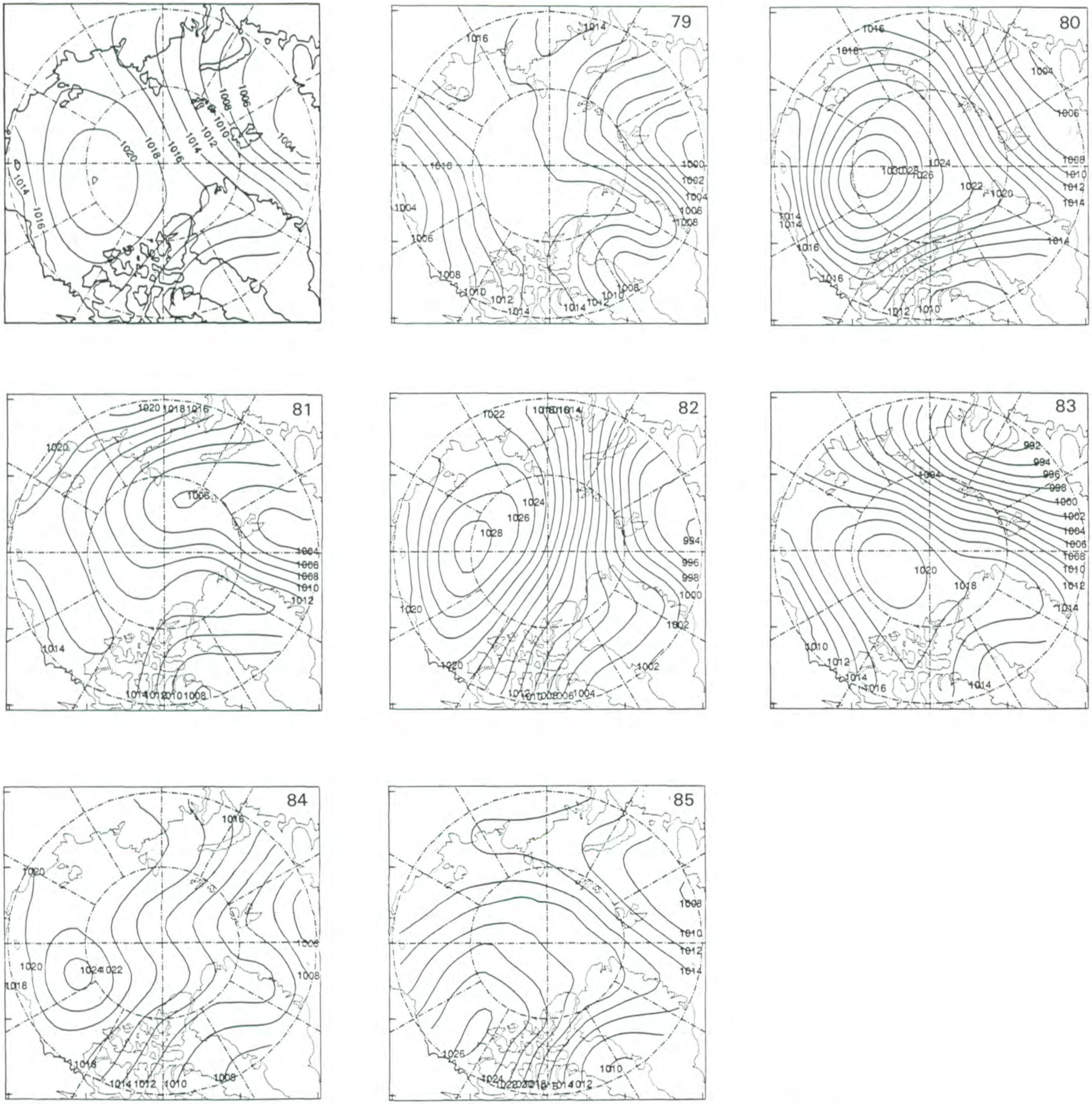

Figure A.11. Monthly average surface pressures for November 1979-1985; 7-year average, and the individual years.

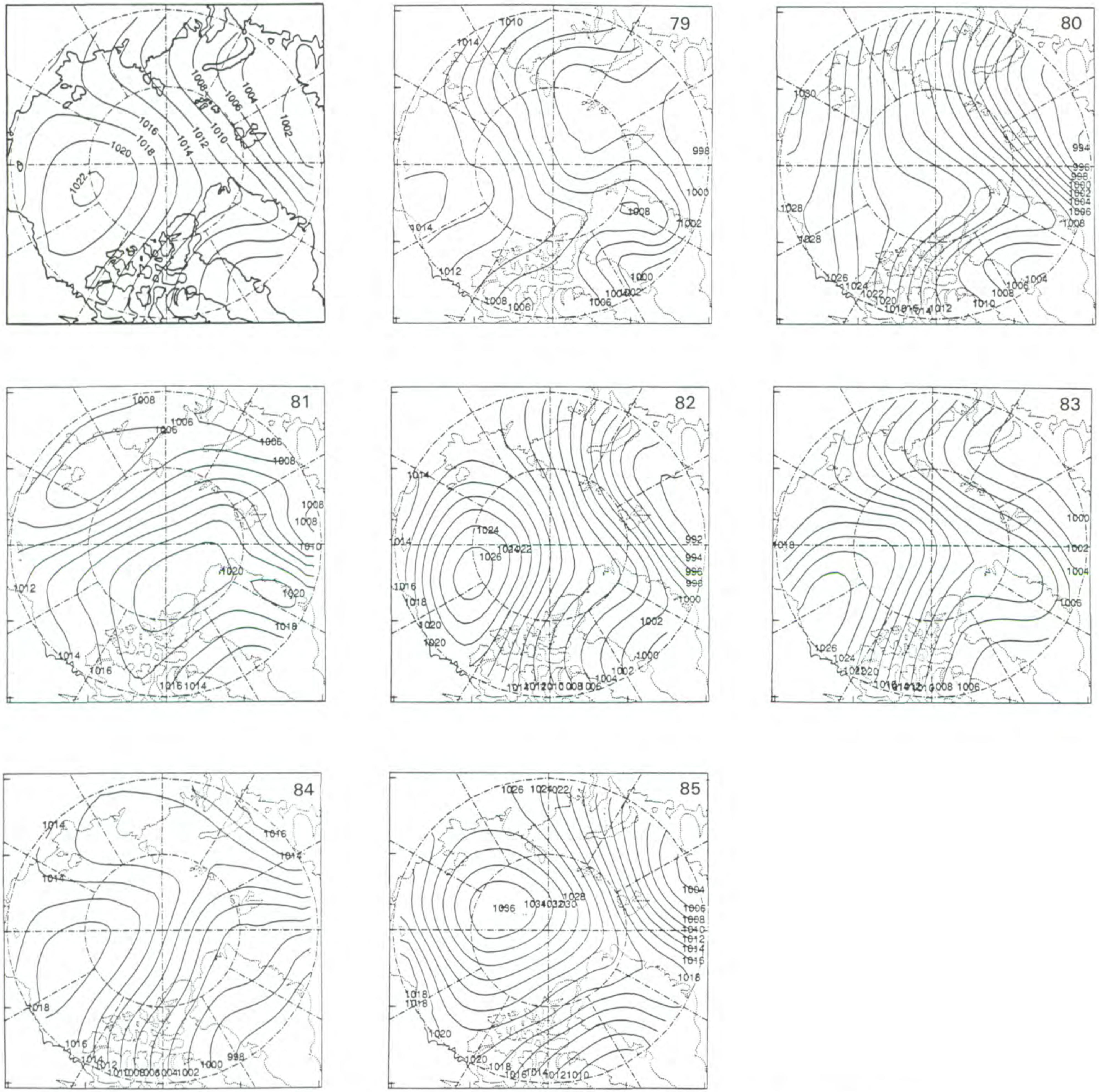

Figure A.12. Monthly average surface pressures for December 1979-1985; 7-year average, and the individual years.

JANUARY

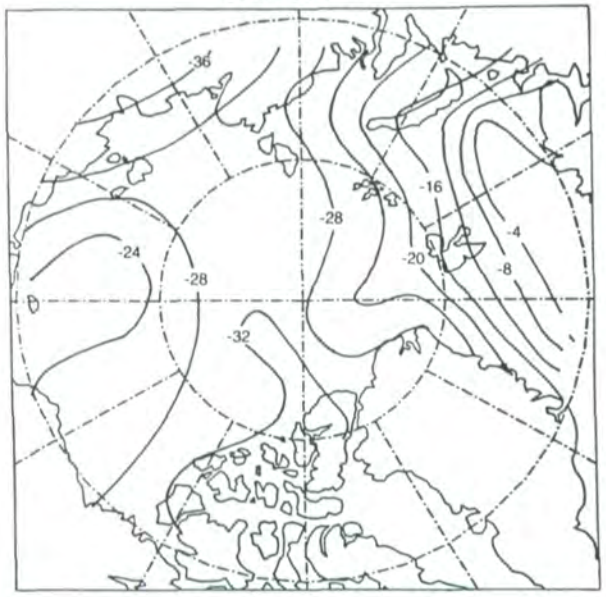

FEBRUARY

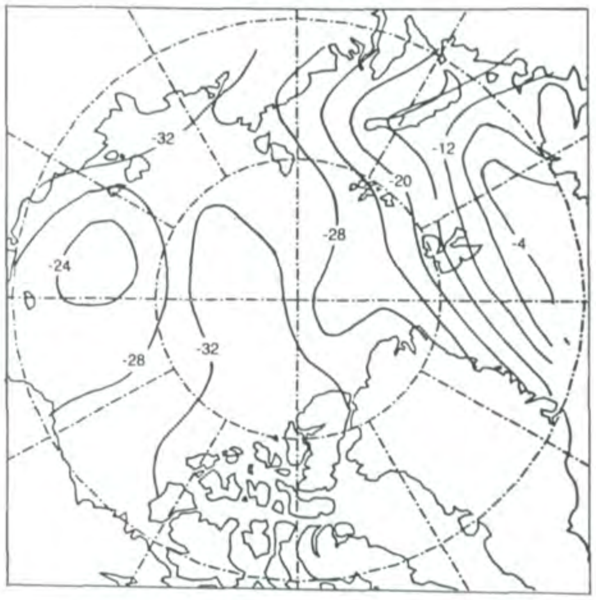

MARCH

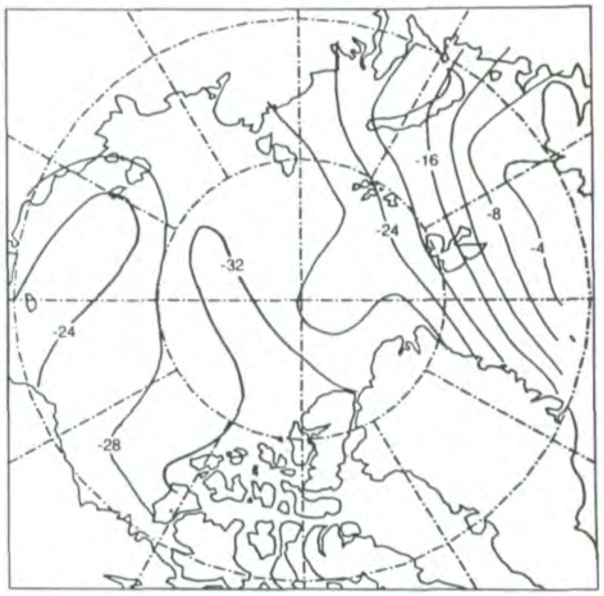

JULY

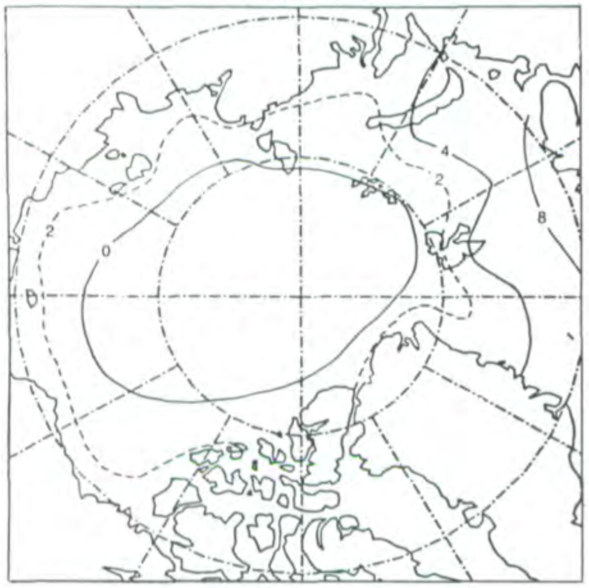

AUGUST

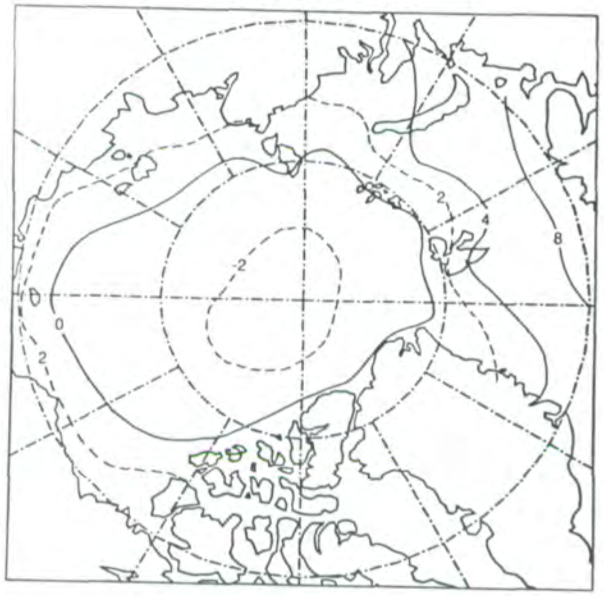

SEPTEMBER

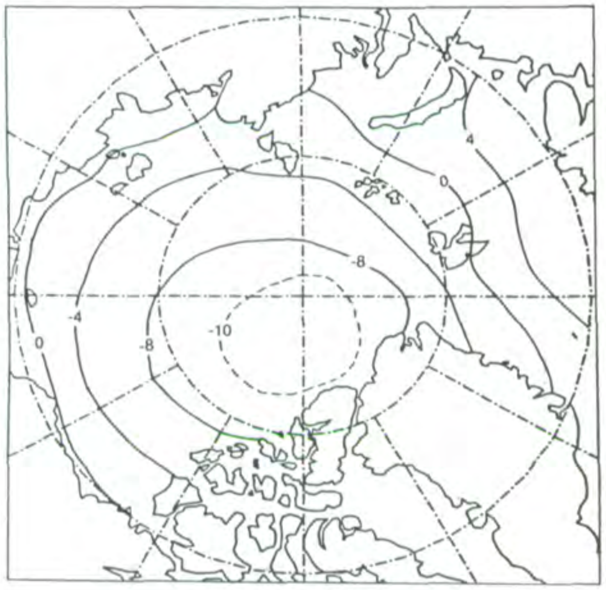

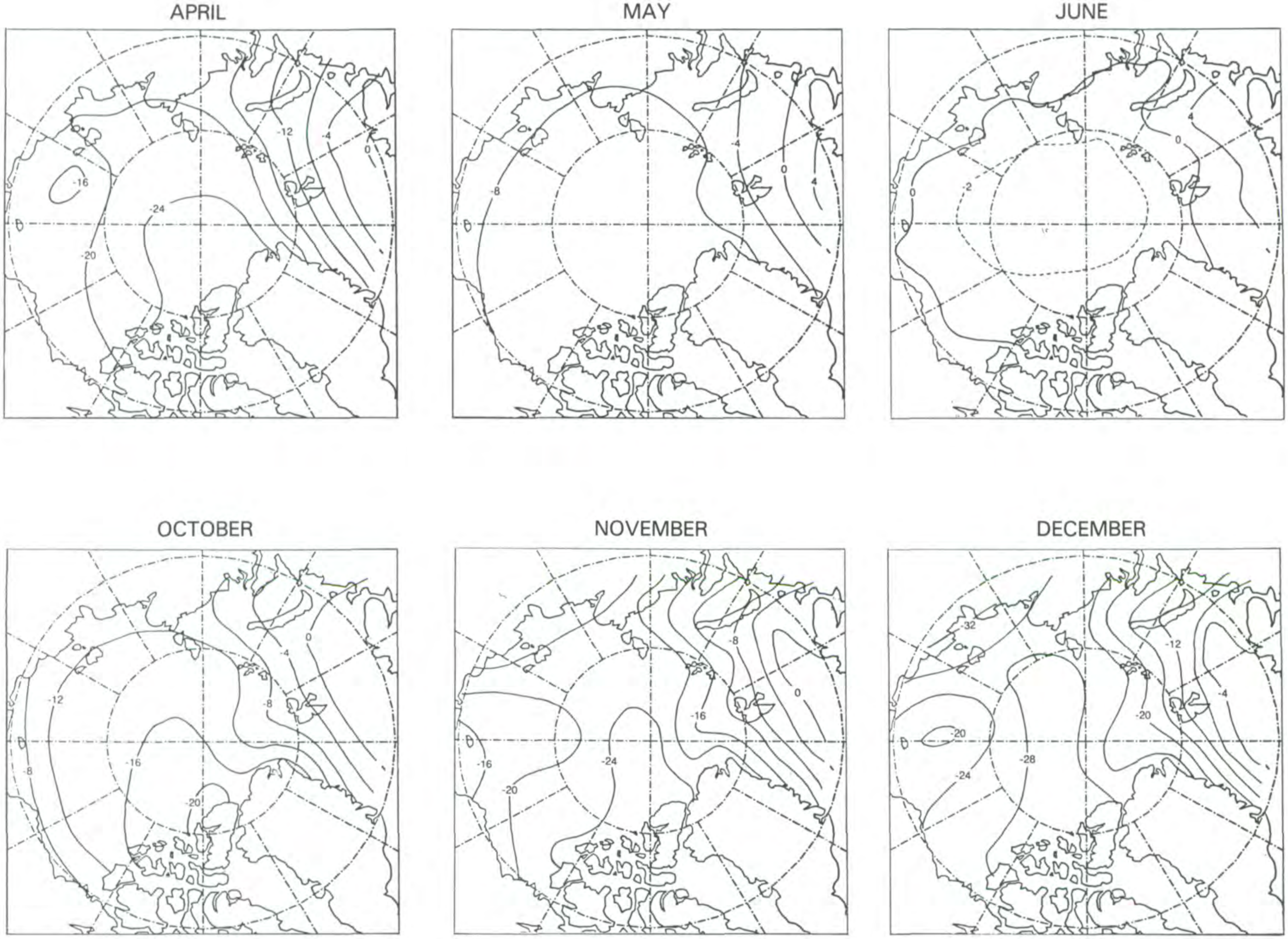
APRIL

MAY

JUNE

OCTOBER

NOVEMBER

DECEMBER

Figure A.13. 8-year averages of monthly-averaged buoy temperatures, 1979-1986.

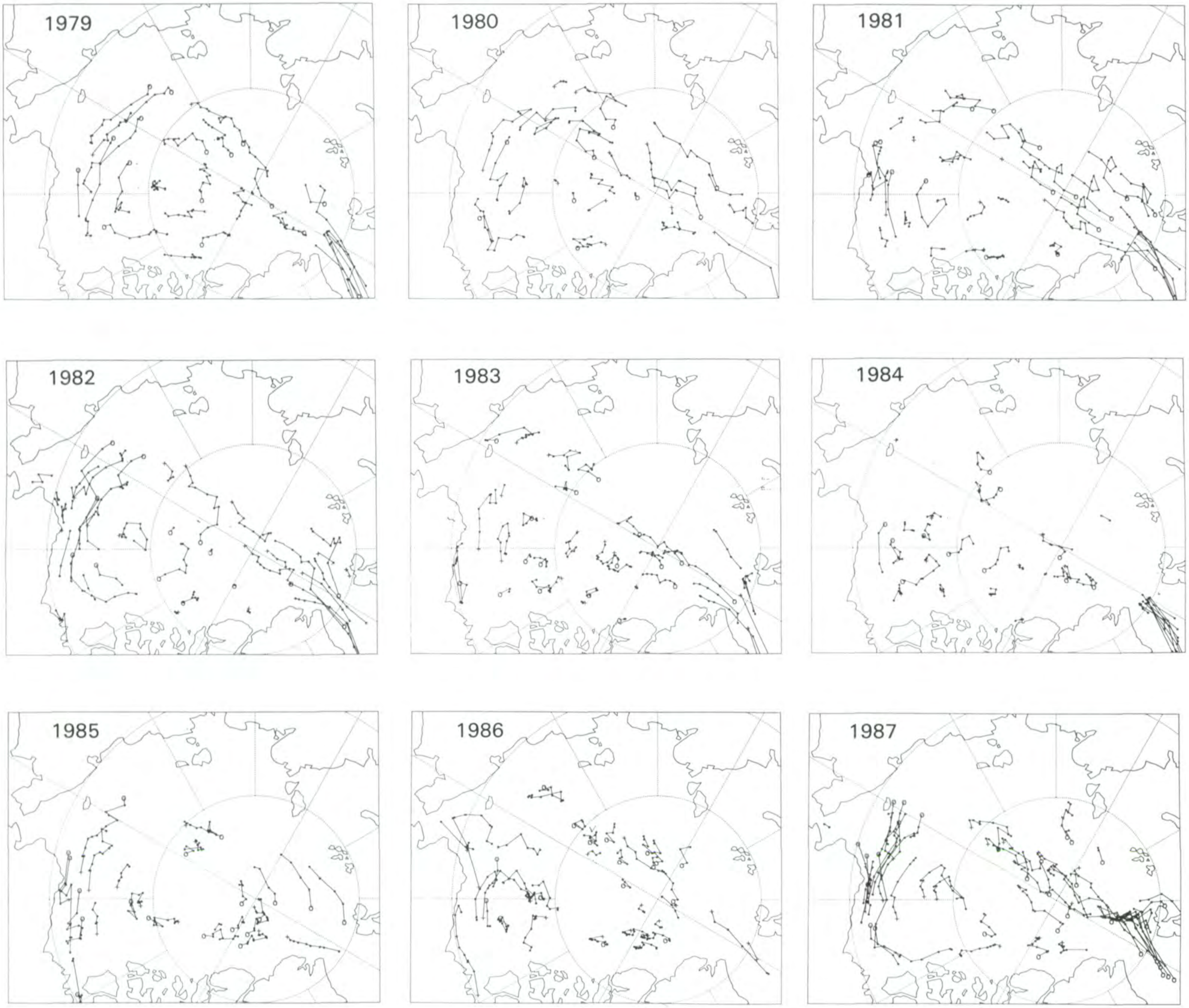

Figure A.14. Annual records of the Arctic buoy tracks, 1979-1987. The open circles denote the beginnings of the tracks.

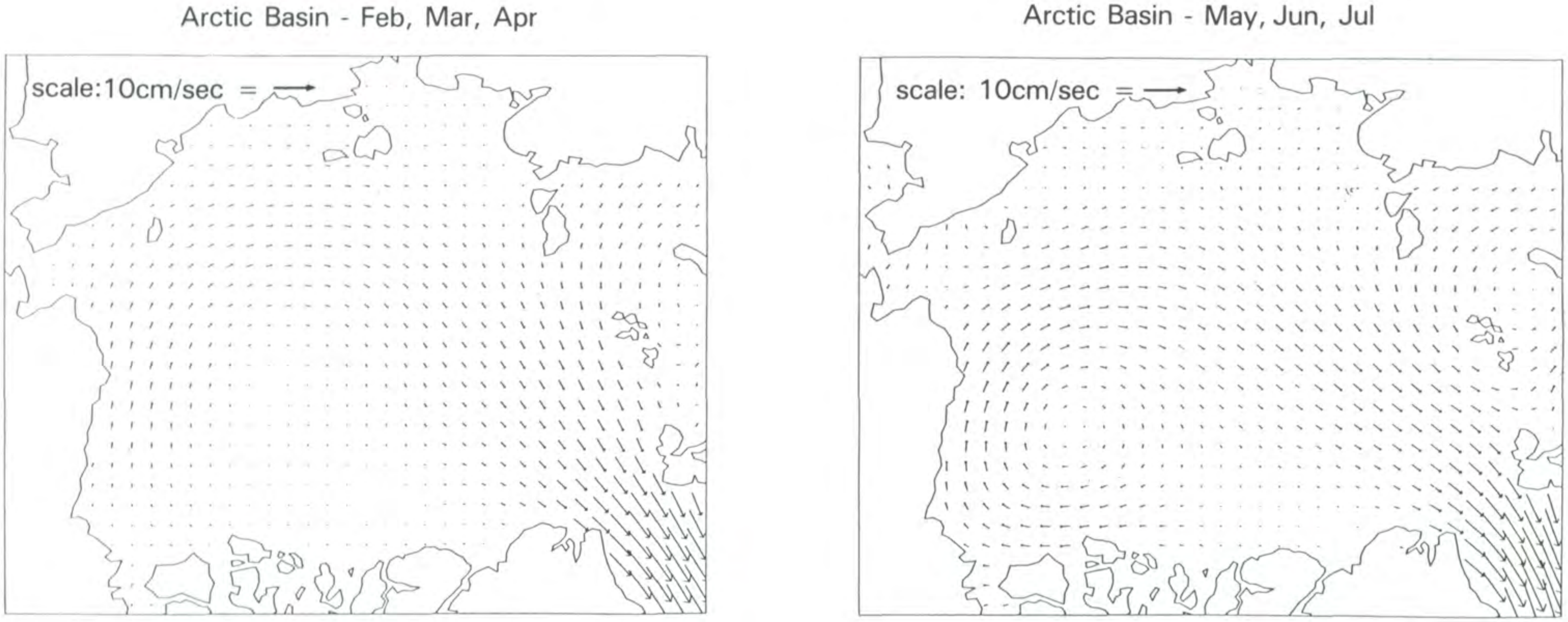

Arctic Basin - Feb, Mar, Apr

Arctic Basin - May, Jun, Jul

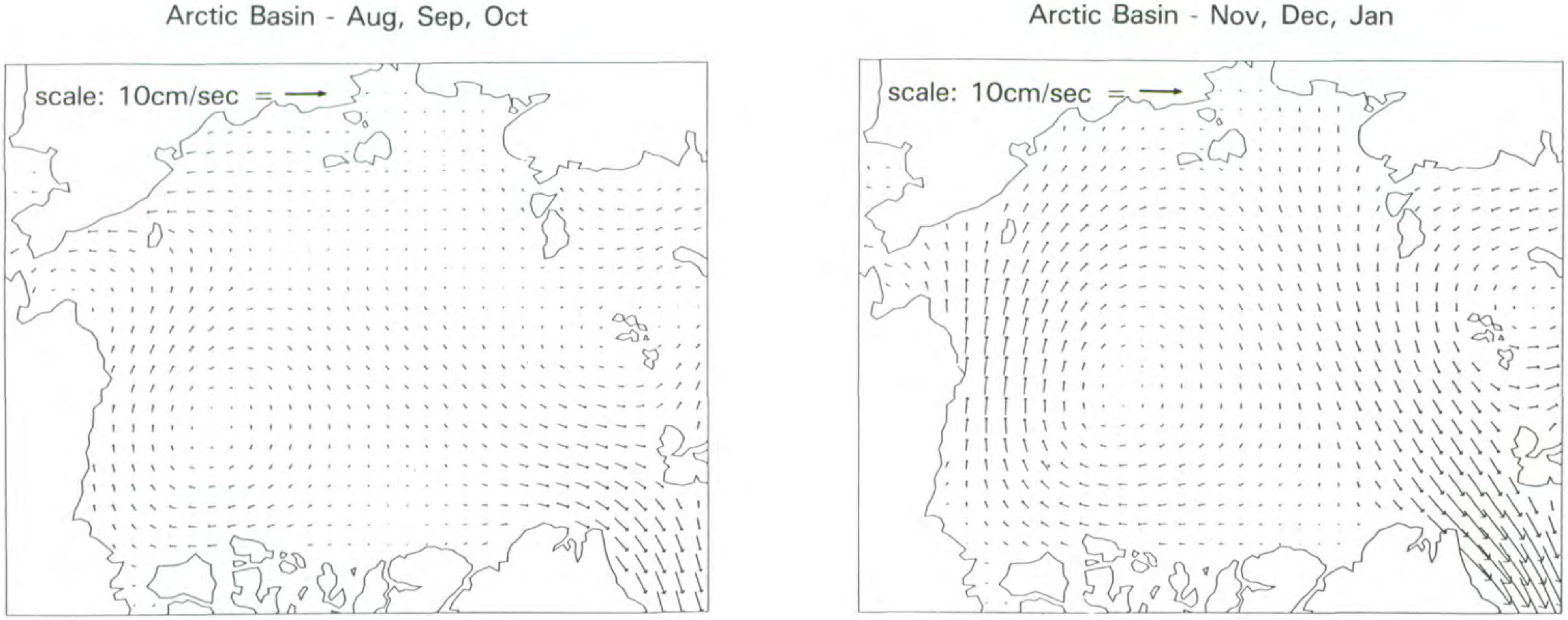

Arctic Basin - Aug, Sep, Oct

Arctic Basin - Nov, Dec, Jan

Figure A.15. 8-year averages of the seasonal drifts.

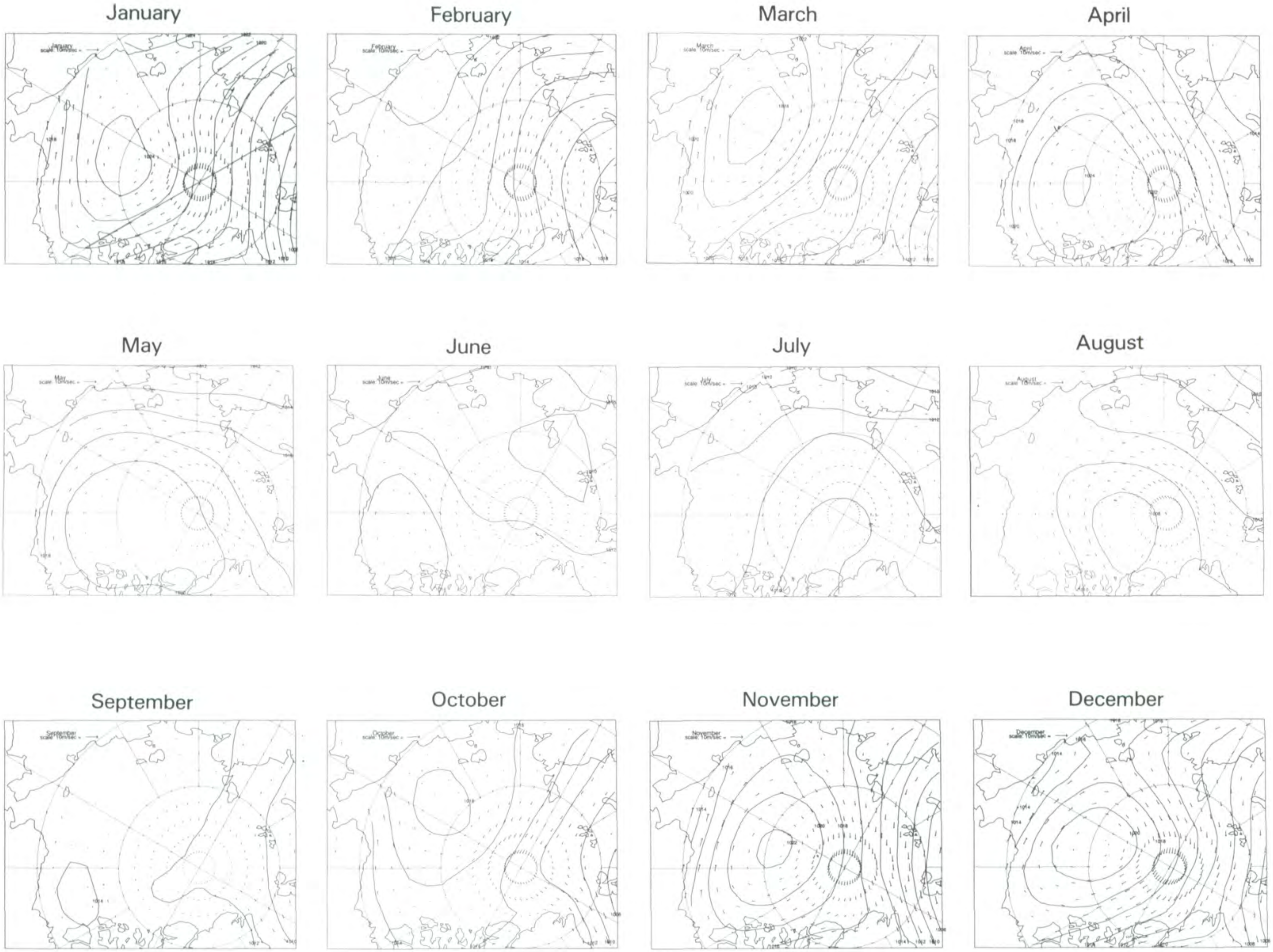

January

February

March

April

May

June

July

August

September

October

November

December

Figure A.16. 8-year averages of the Arctic buoy wind vectors.

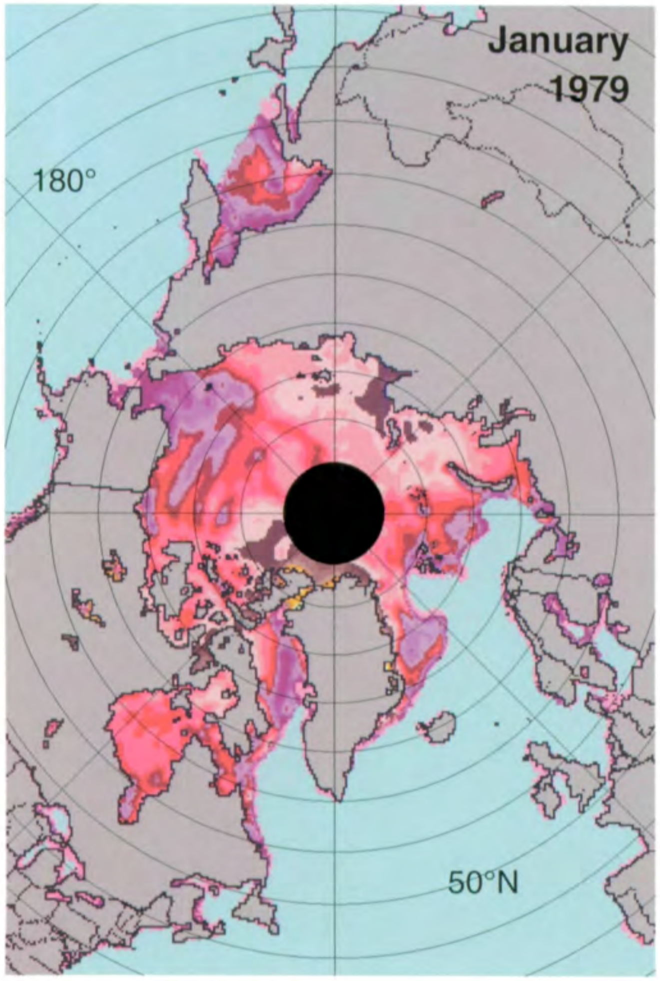
January
1979
180°
50°N

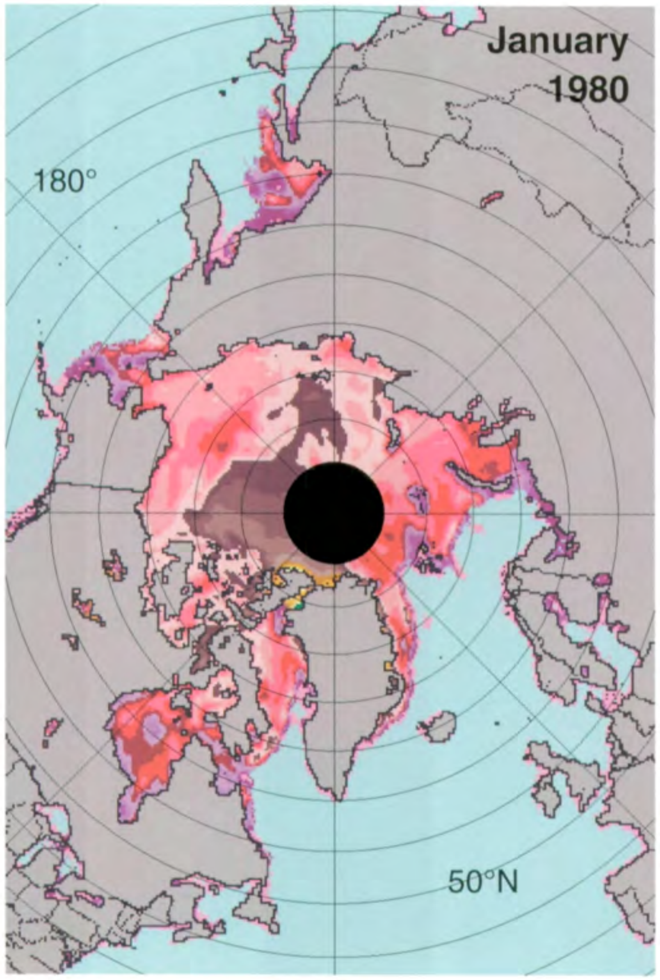
January
1980
180°
50°N

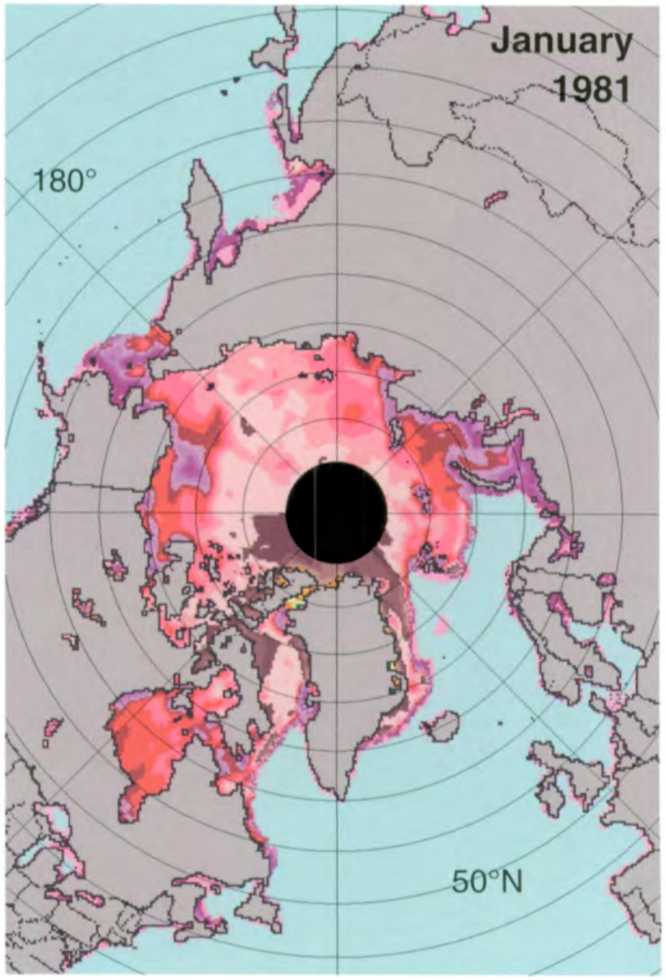
January
1981
180°
50°N

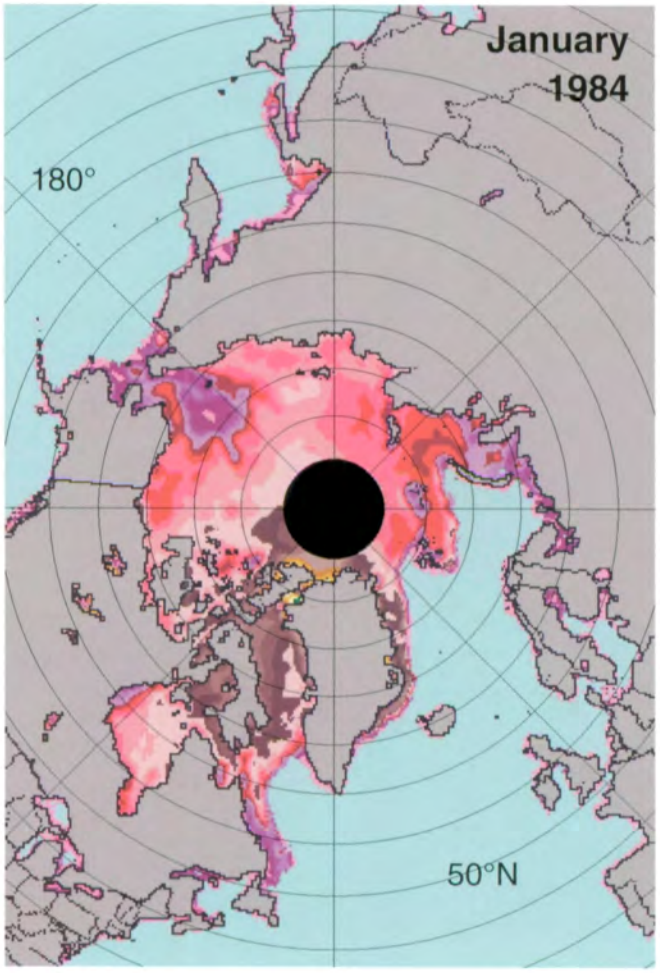
January
1984
180°
50°N

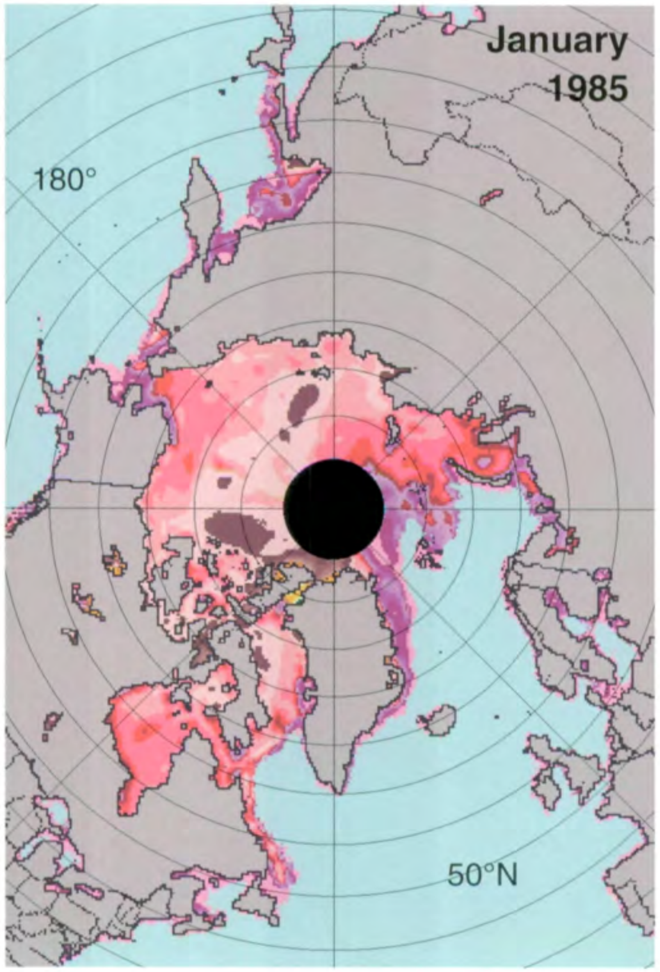
January
1985
180°
50°N

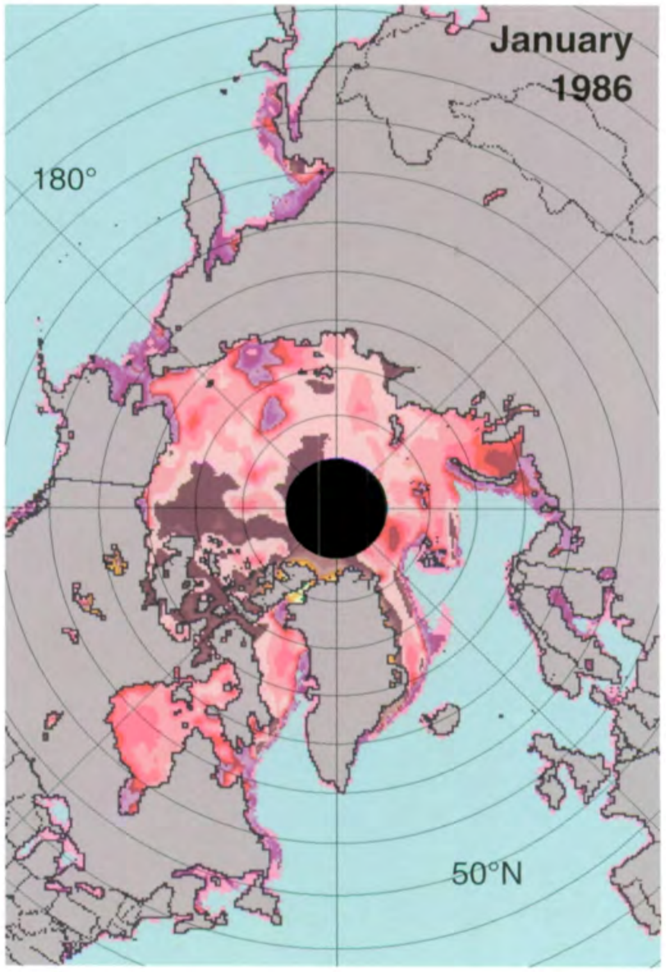
January
1986
180°
50°N

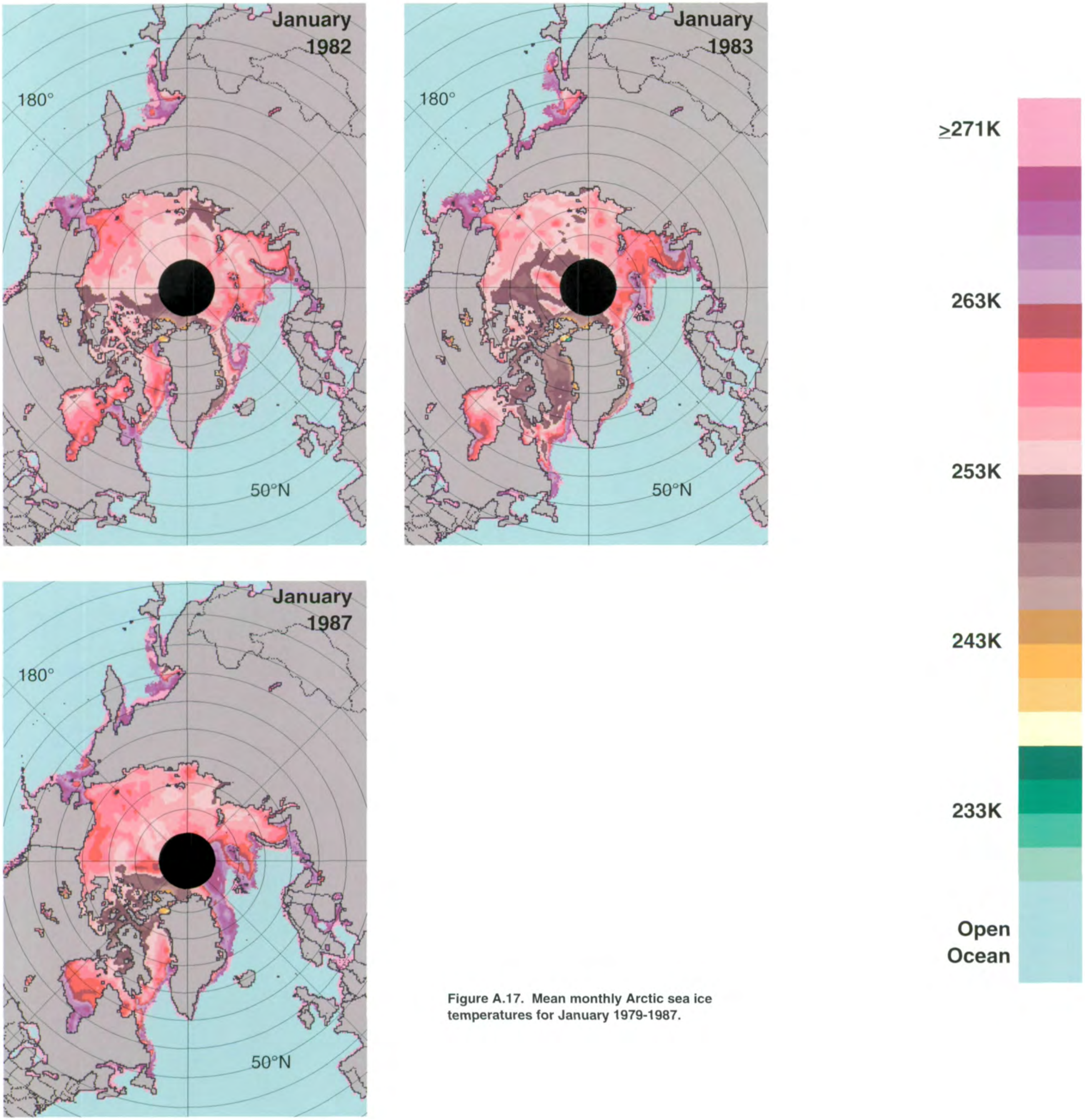

Figure A.17. Mean monthly Arctic sea ice temperatures for January 1979-1987.

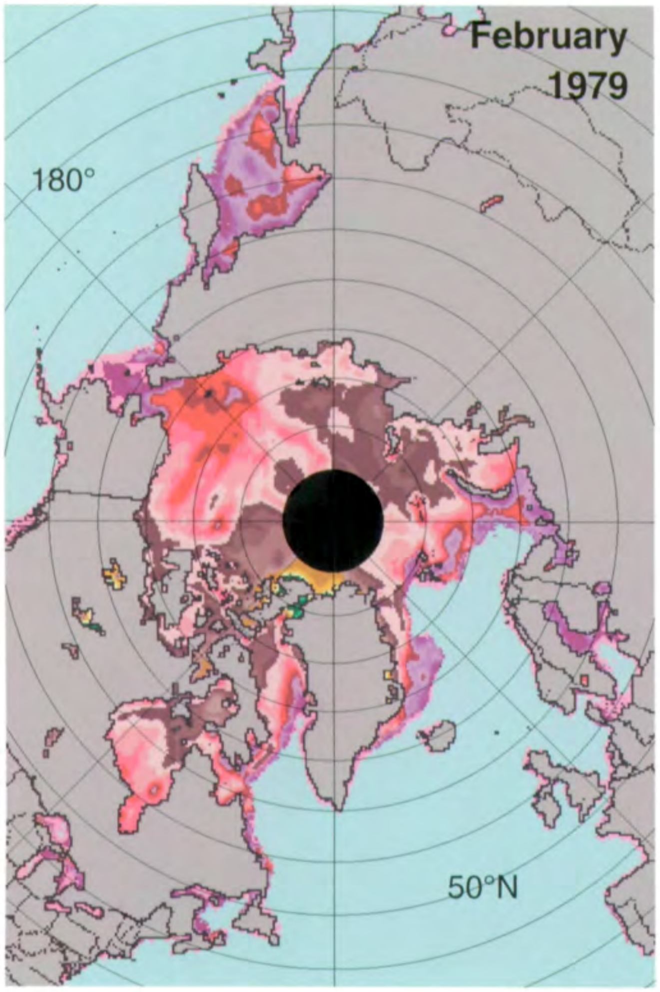
February
1979
180°
50°N

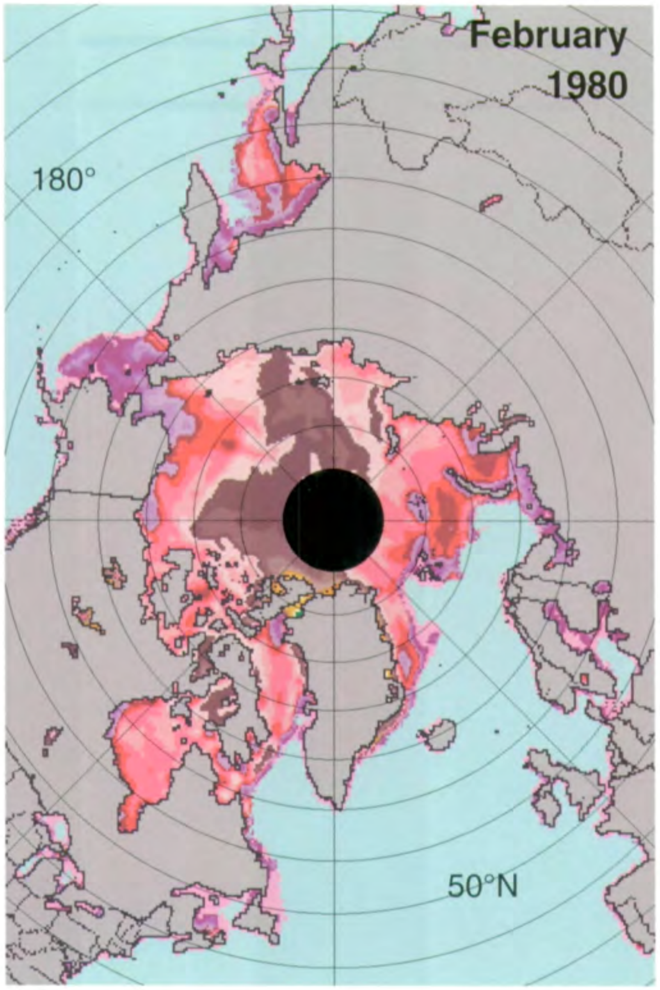
February
1980
180°
50°N

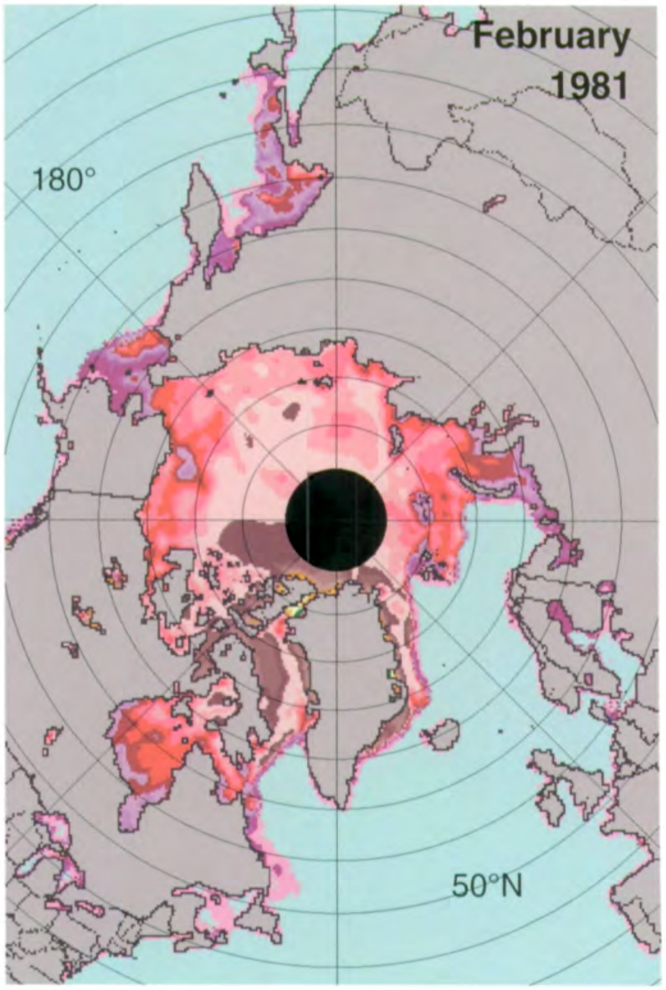
February
1981
180°
50°N

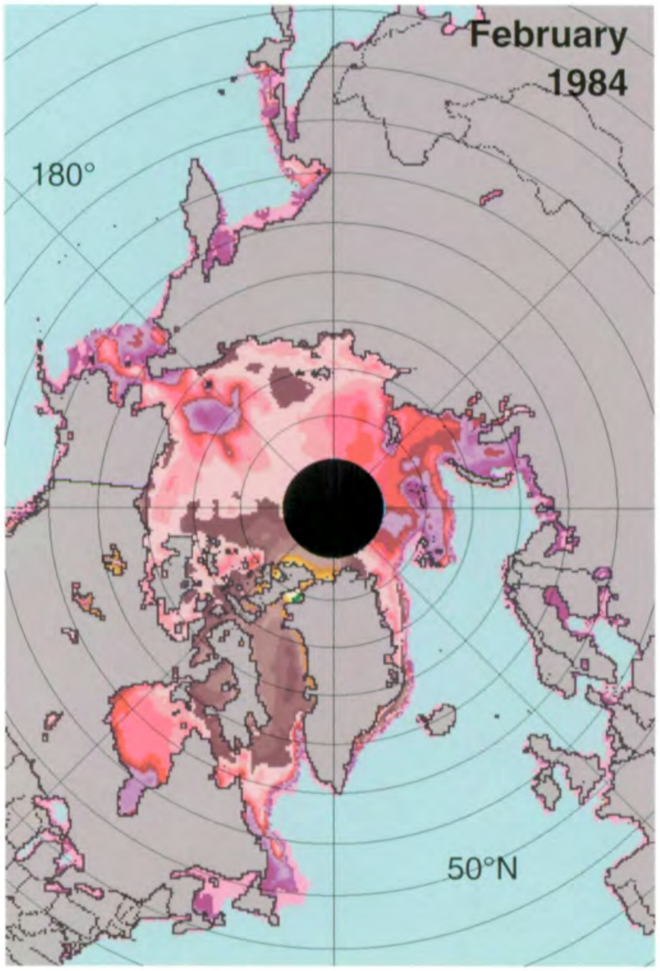
February
1984
180°
50°N

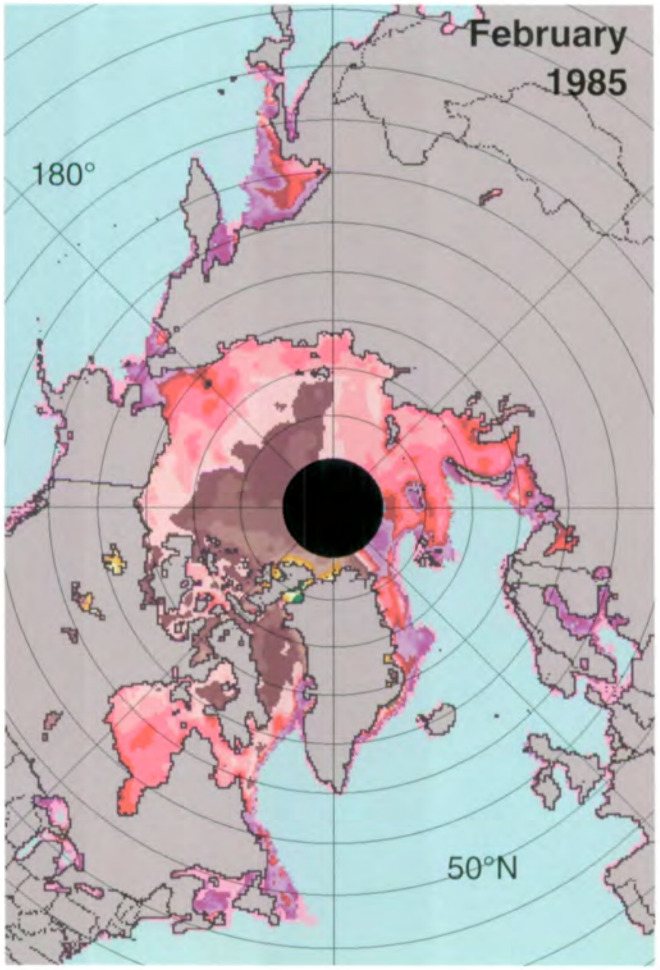
February
1985
180°
50°N

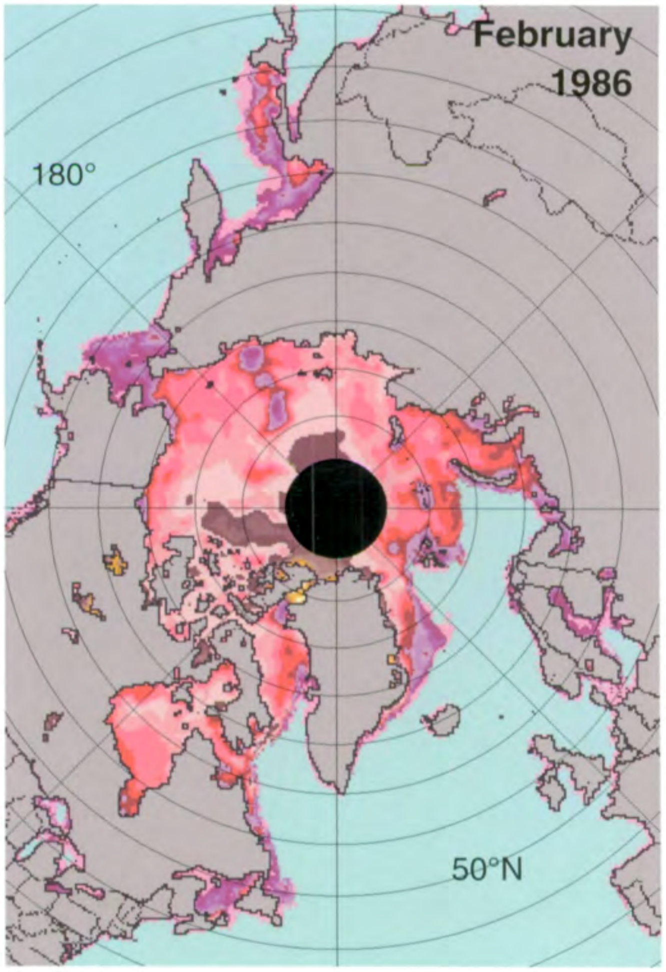
February
1986
180°
50°N

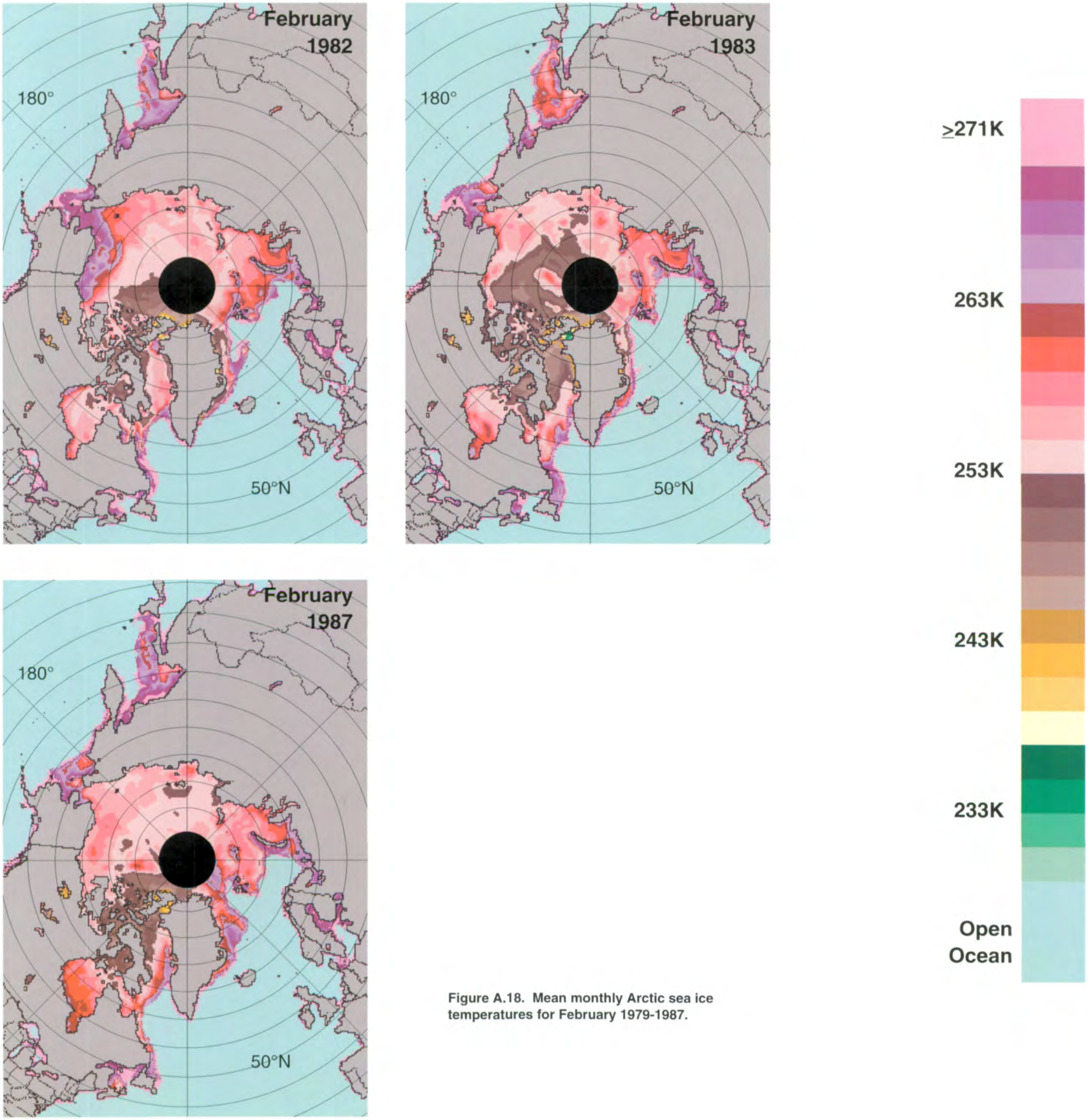

Figure A.18. Mean monthly Arctic sea ice temperatures for February 1979-1987.

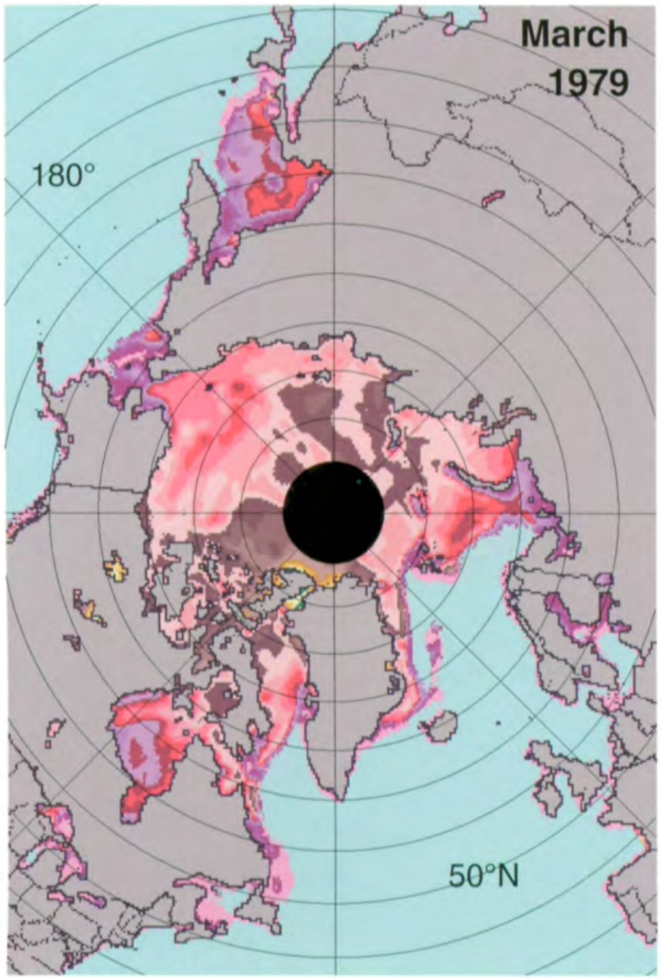
March
1979
180°
50°N

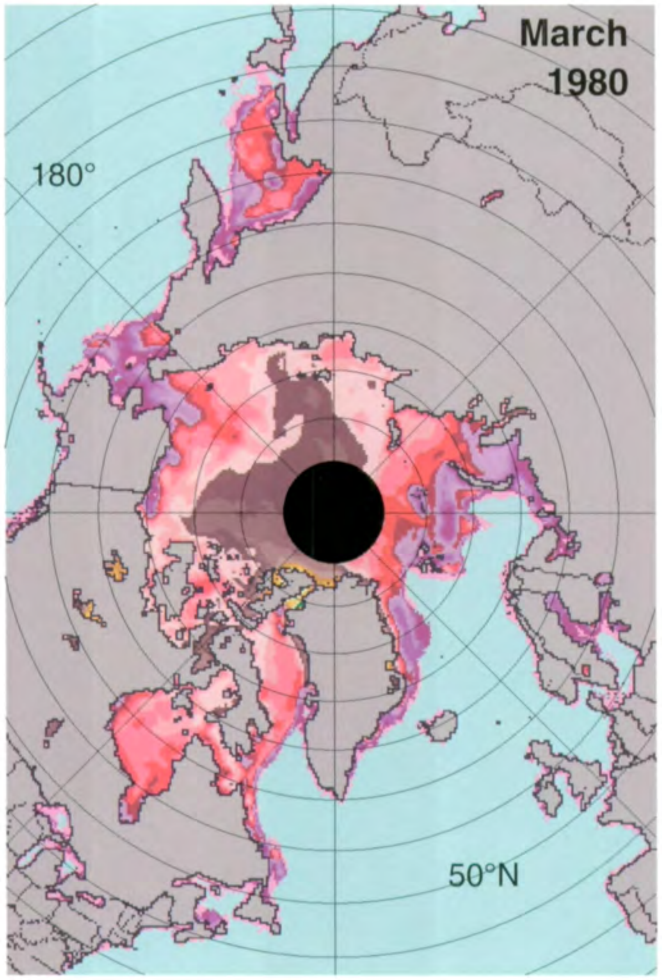
March
1980
180°
50°N

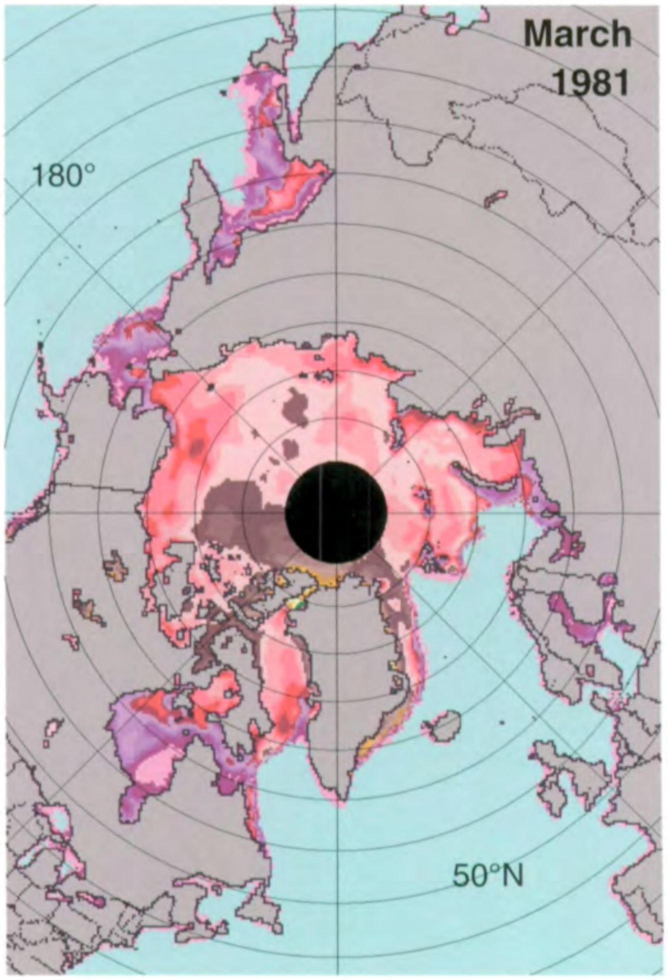
March
1981
180°
50°N

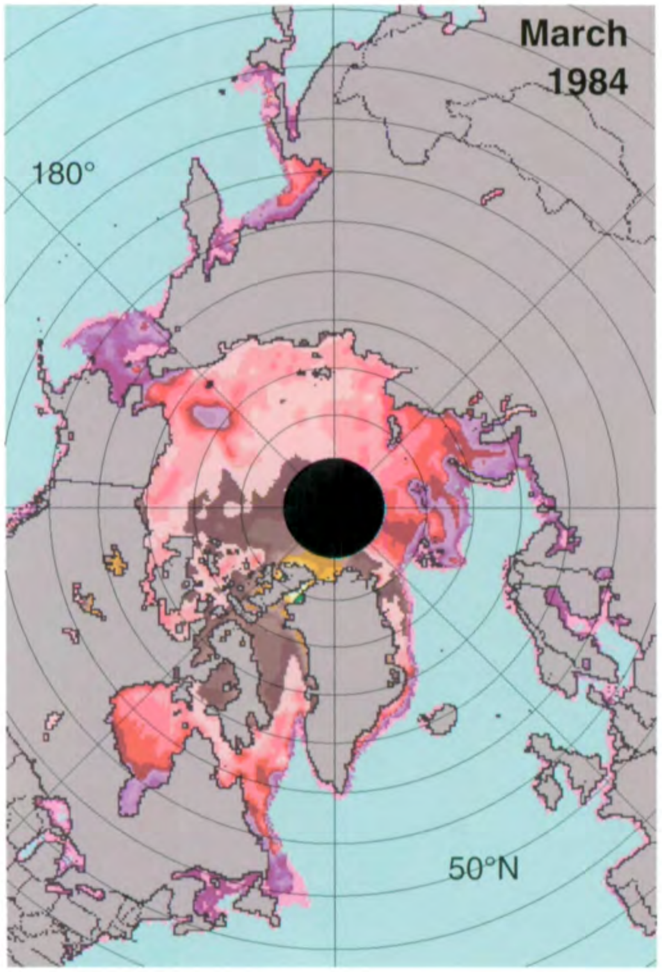
March
1984
180°
50°N

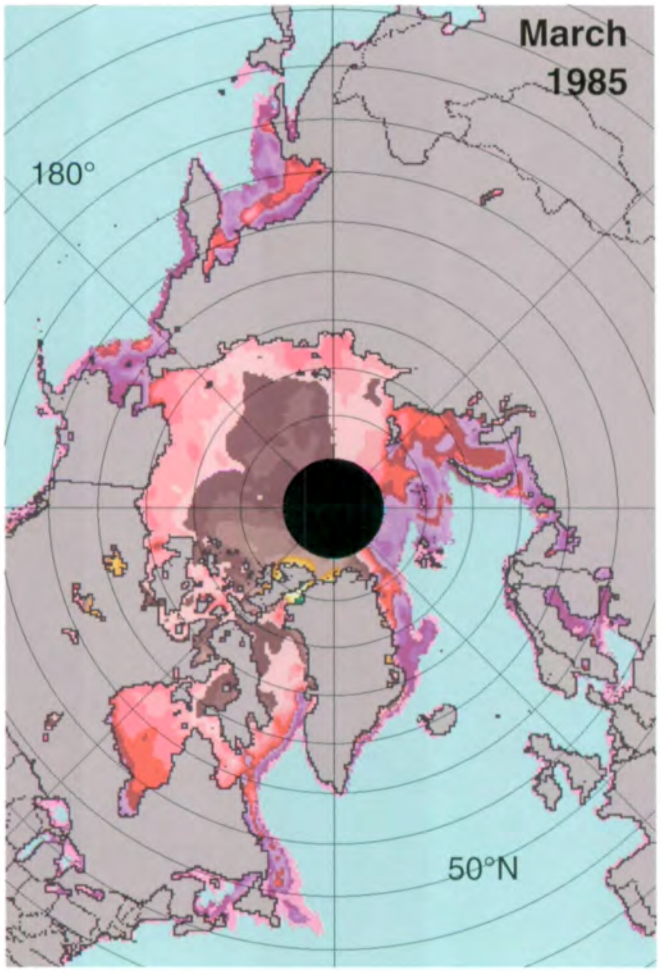
March
1985
180°
50°N

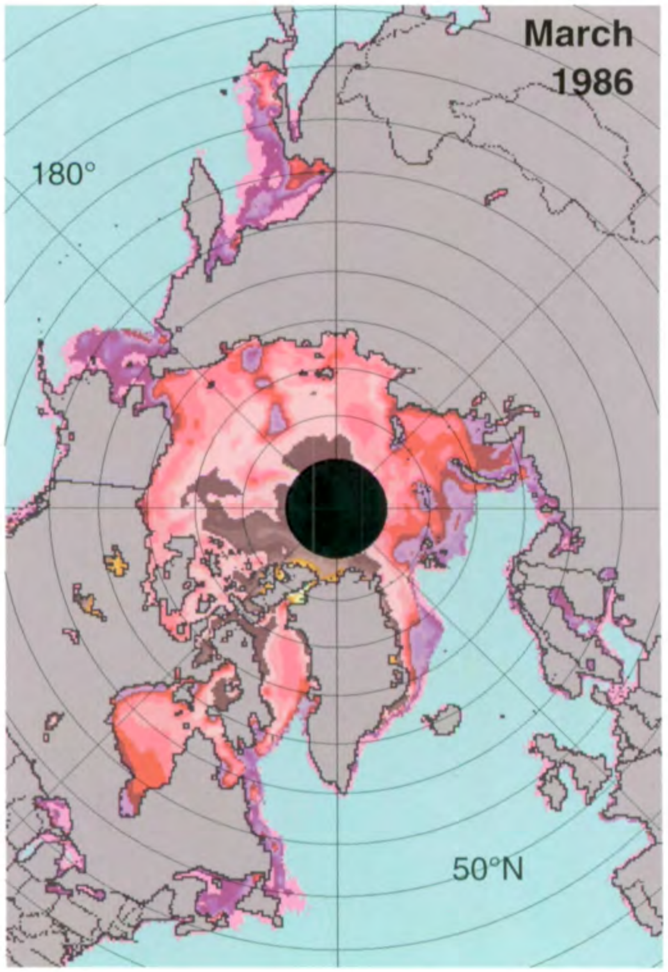
March
1986
180°
50°N

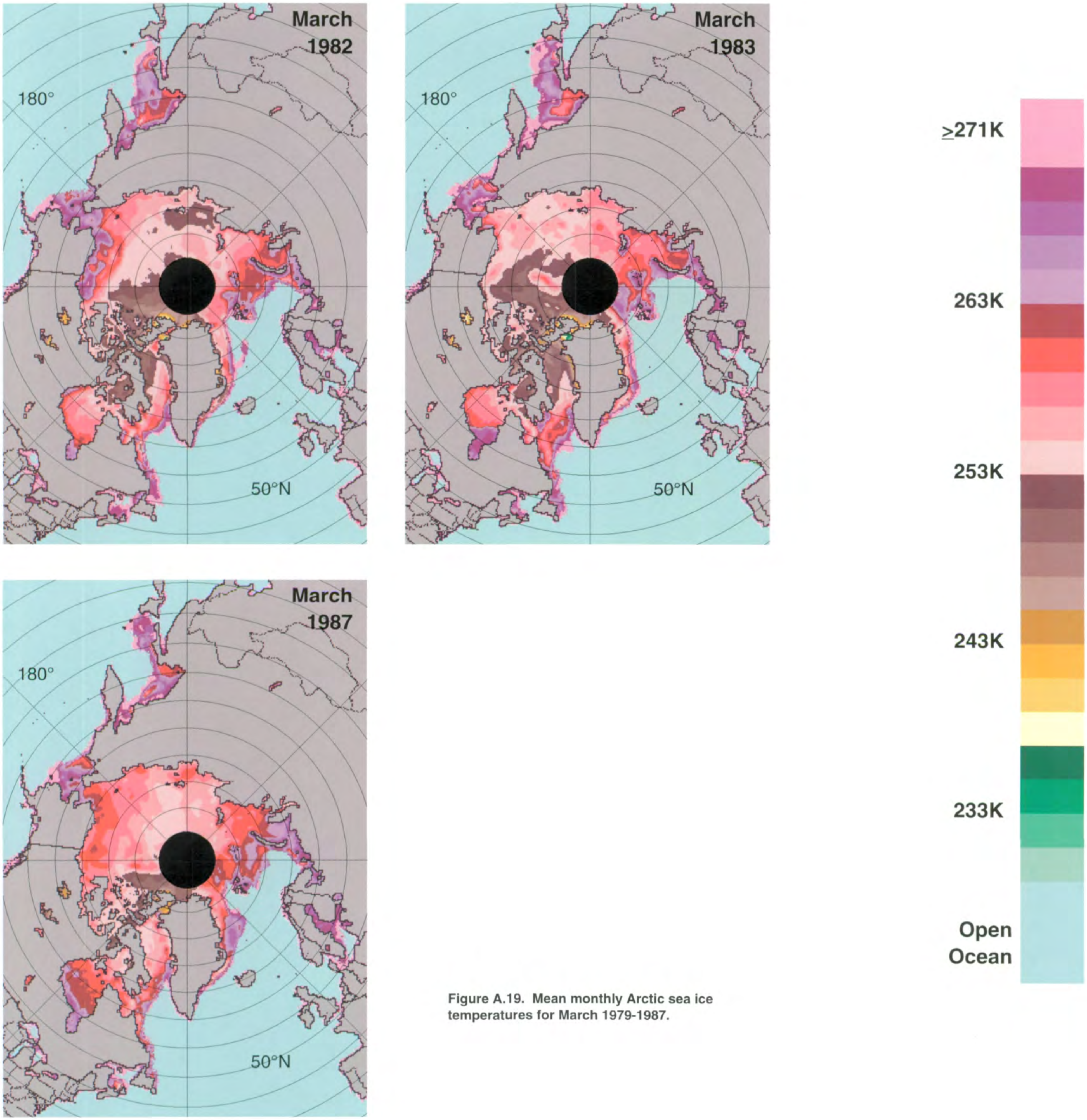

Figure A.19. Mean monthly Arctic sea ice temperatures for March 1979-1987.

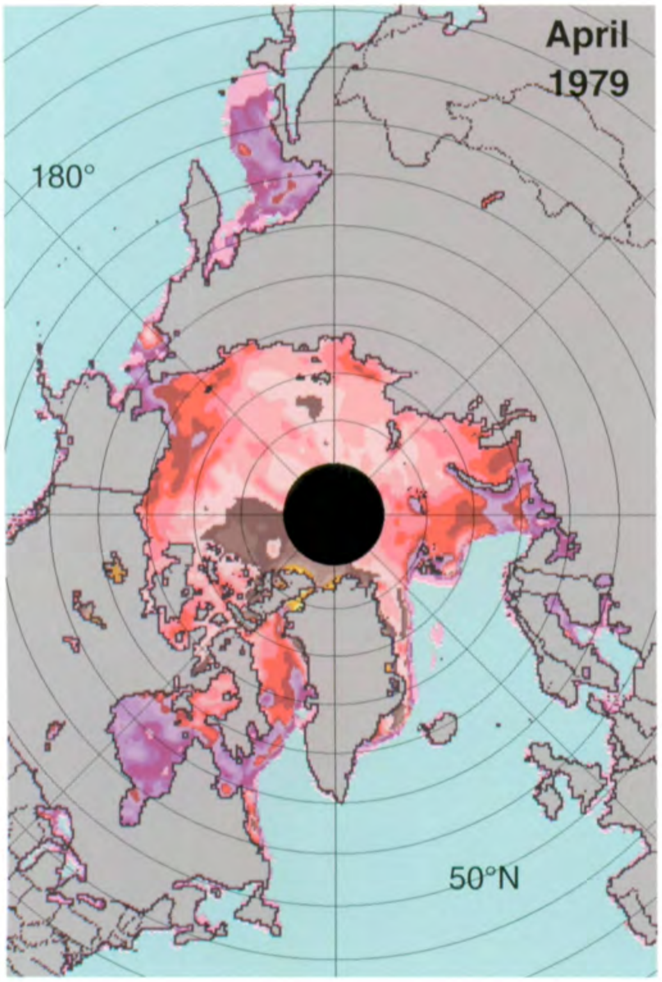
April
1979
180°
50°N

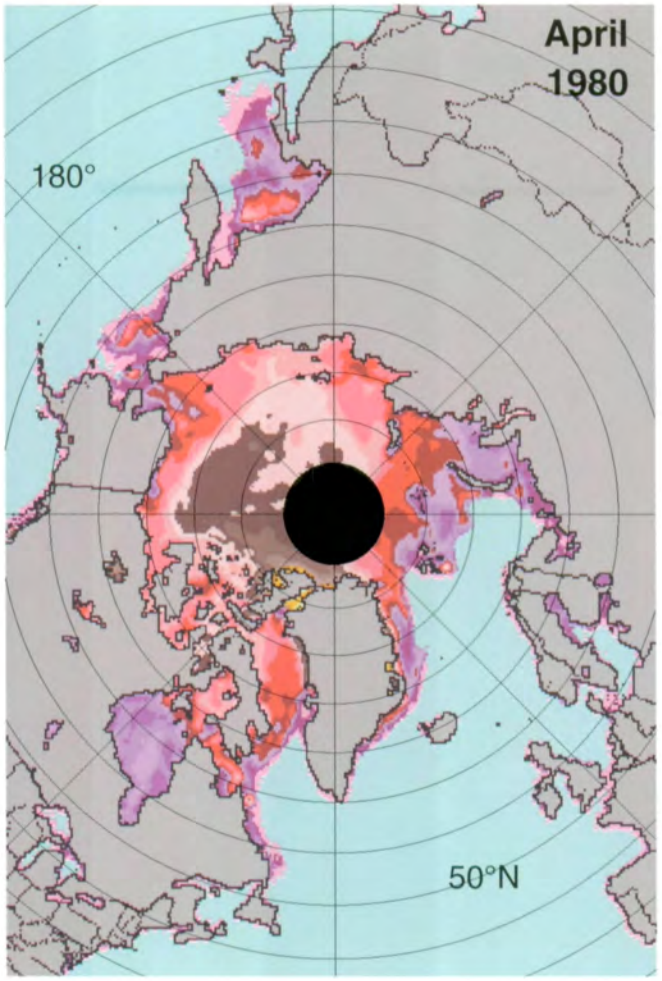
April
1980
180°
50°N

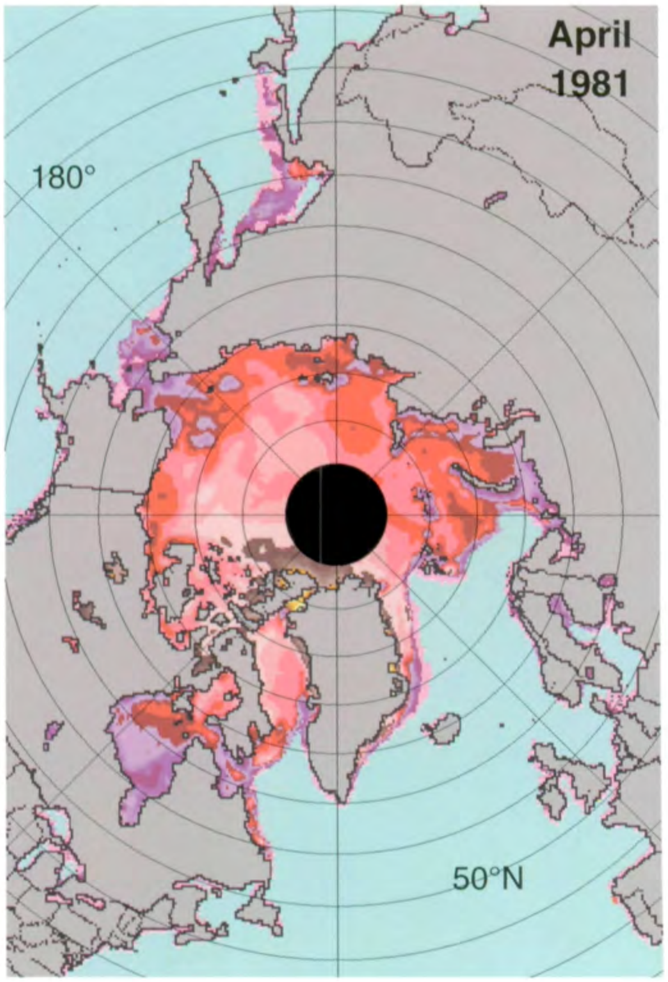
April
1981
180°
50°N

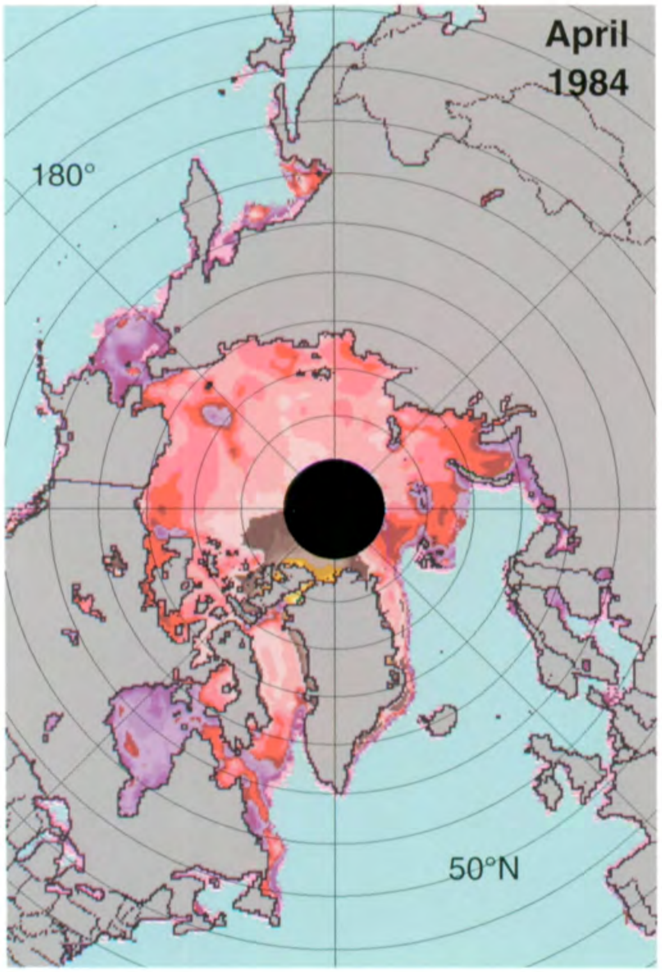
April
1984
180°
50°N

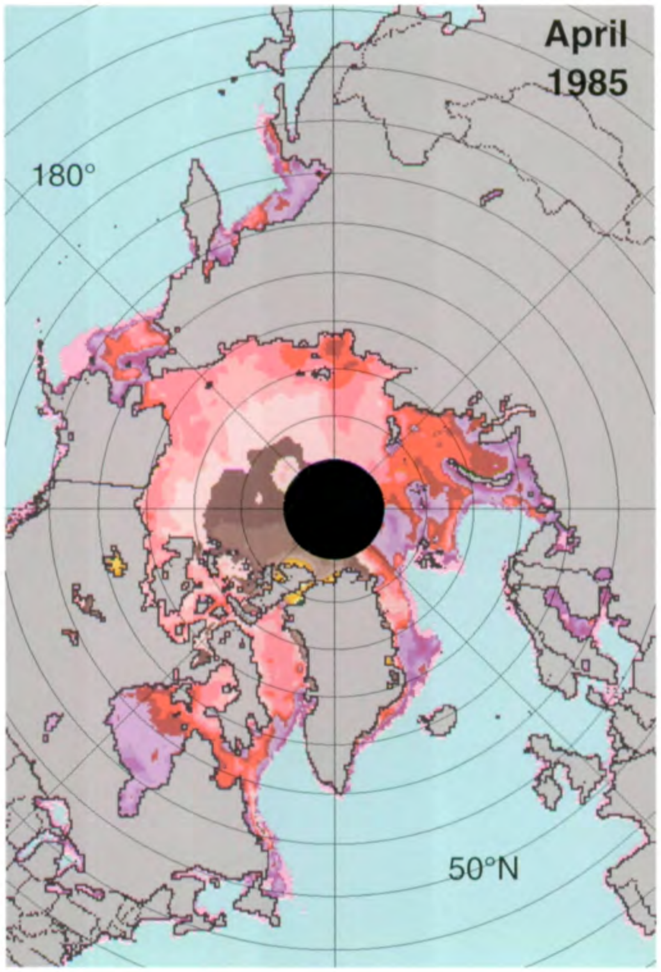
April
1985
180°
50°N

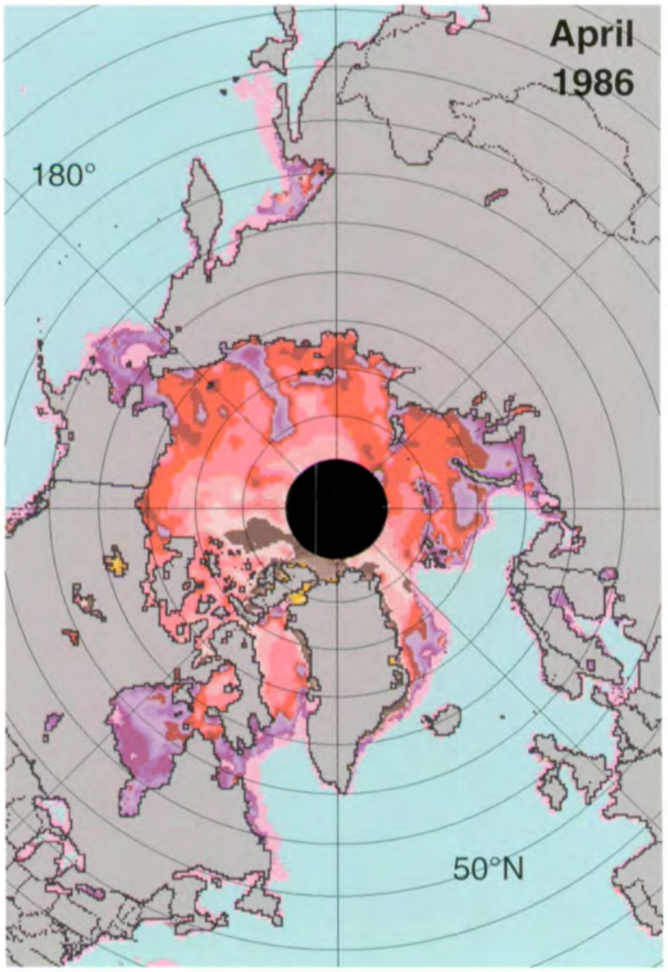
April
1986
180°
50°N

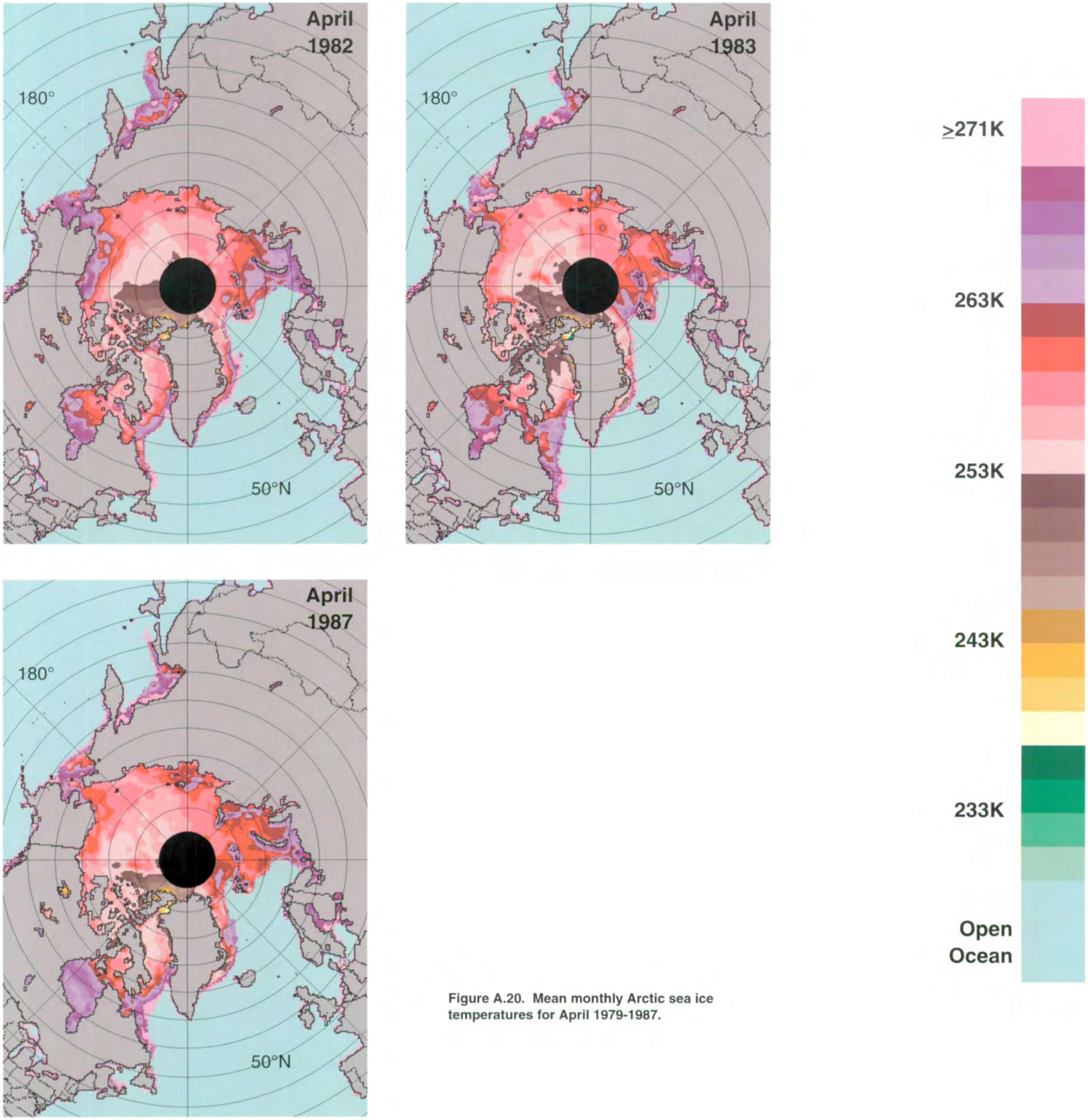

Figure A.20. Mean monthly Arctic sea ice temperatures for April 1979-1987.

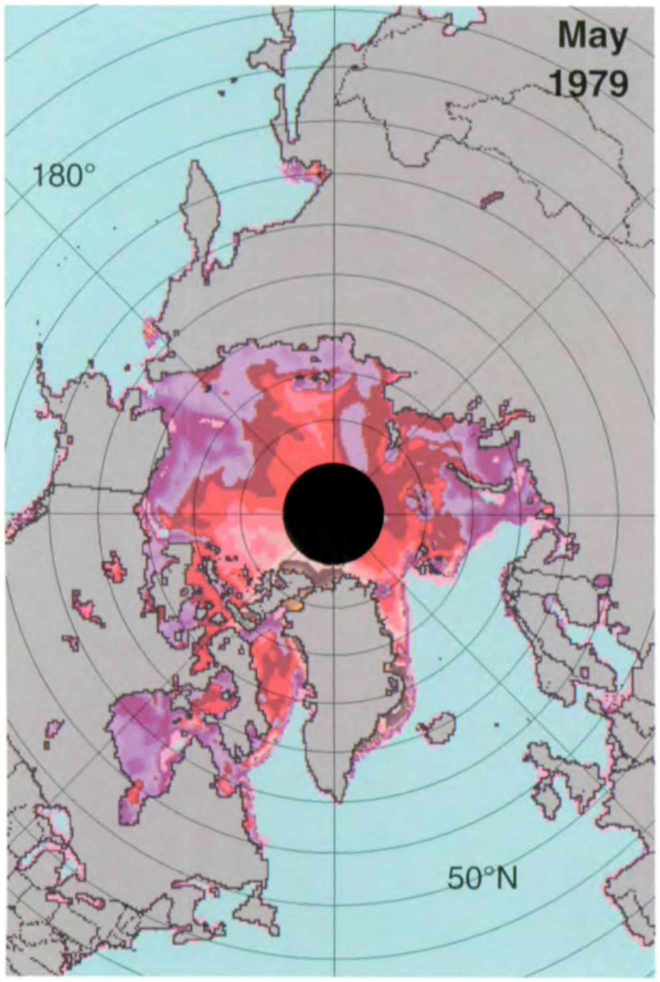
May
1979
180°
50°N

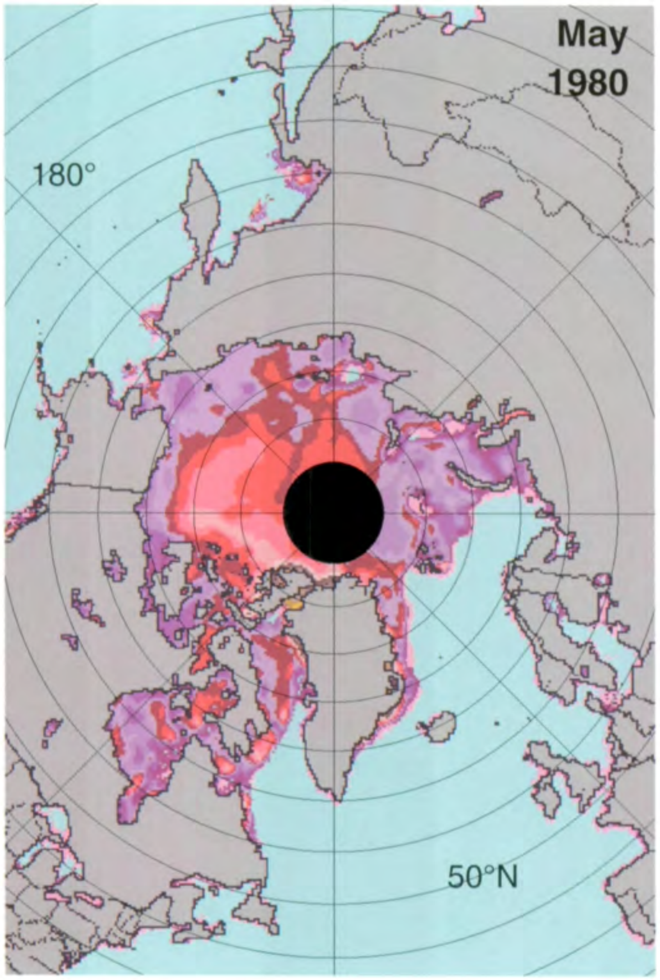
May
1980
180°
50°N

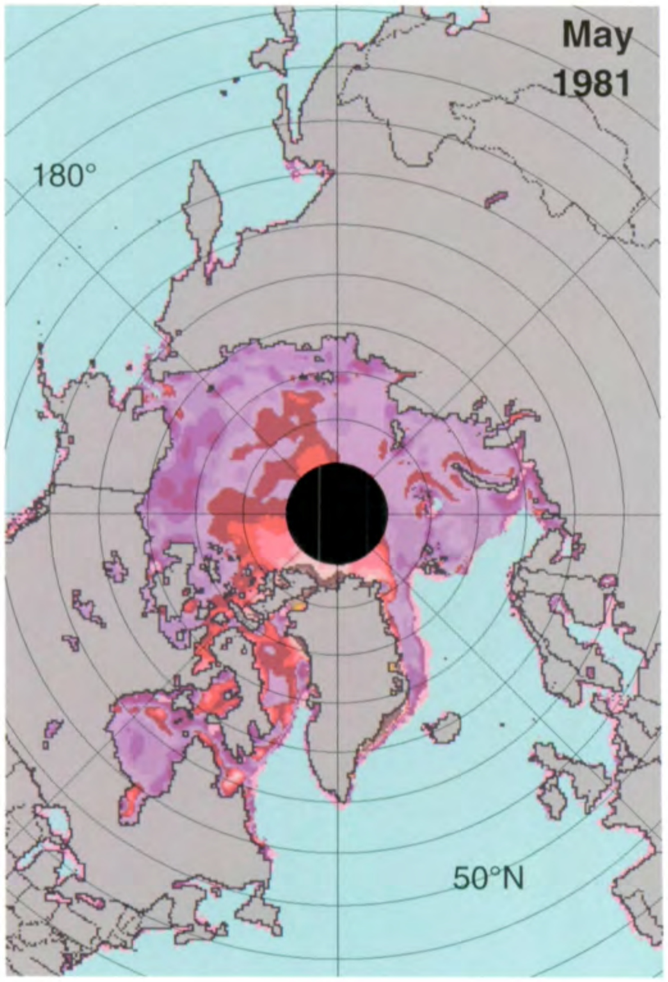
May
1981
180°
50°N

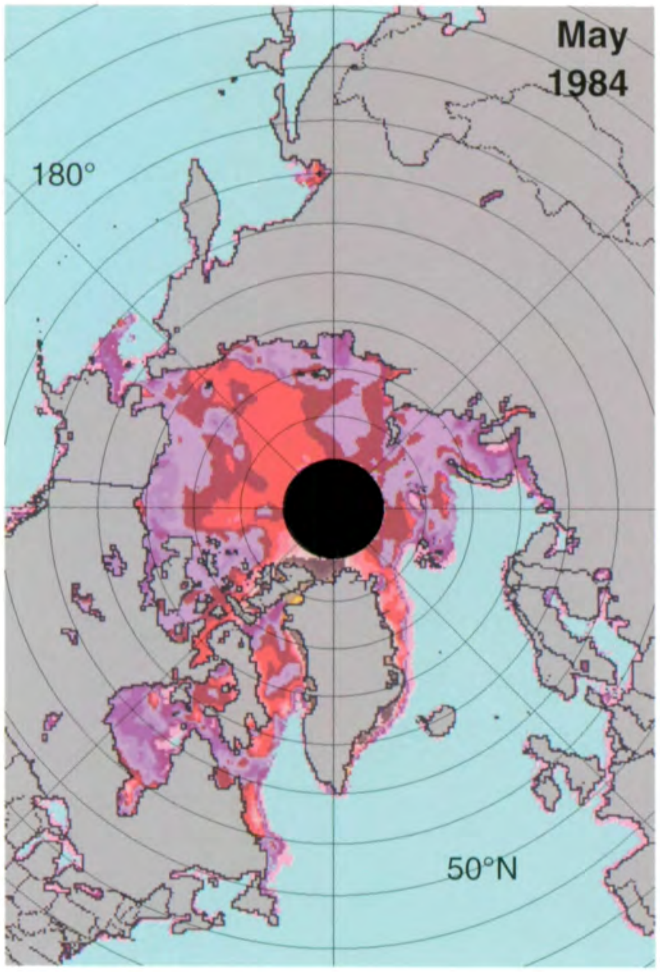
May
1984
180°
50°N

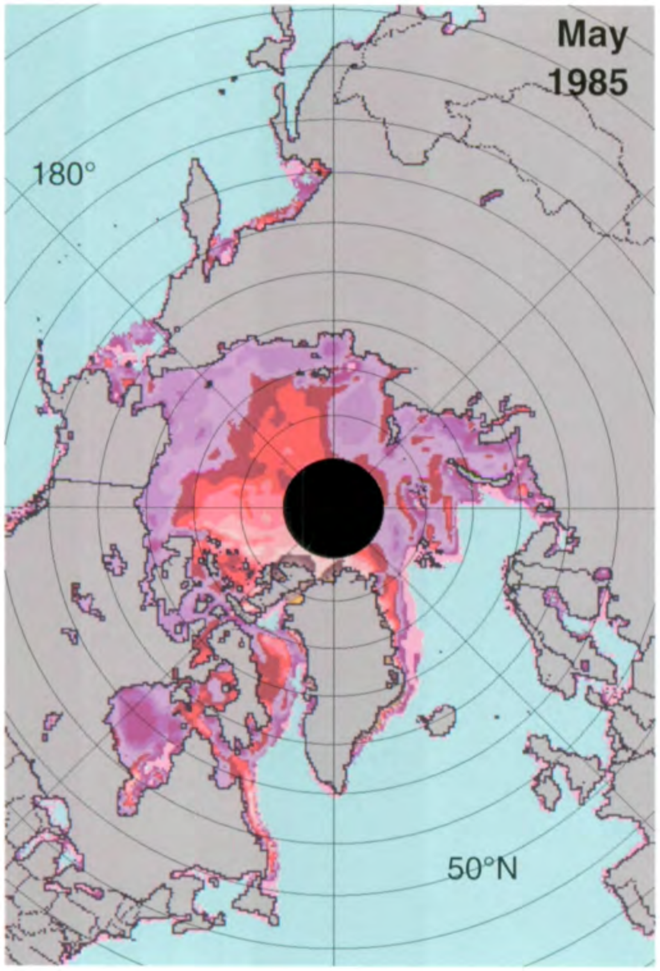
May
1985
180°
50°N

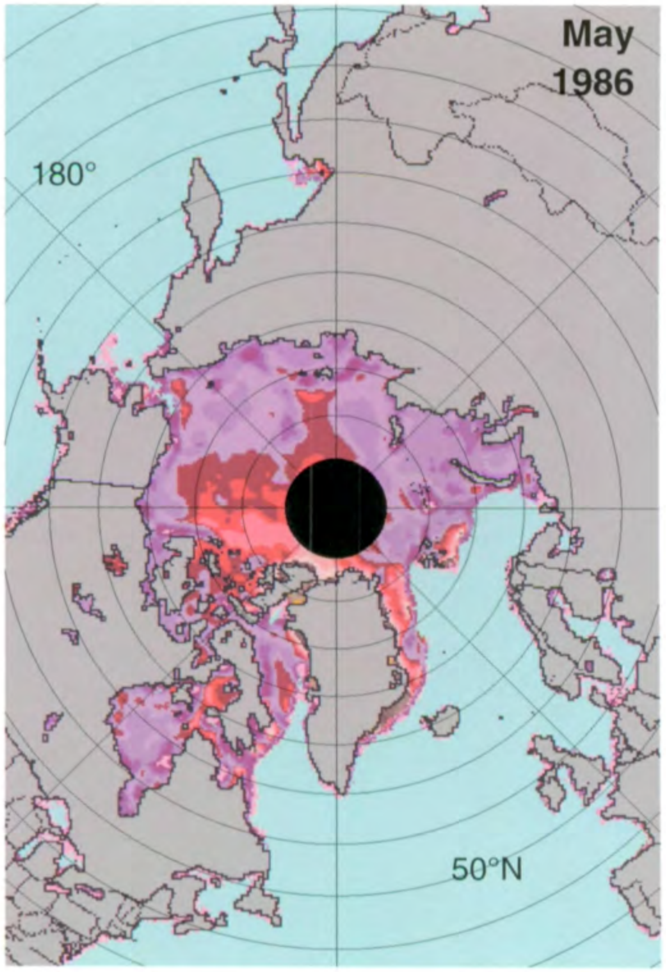
May
1986
180°
50°N

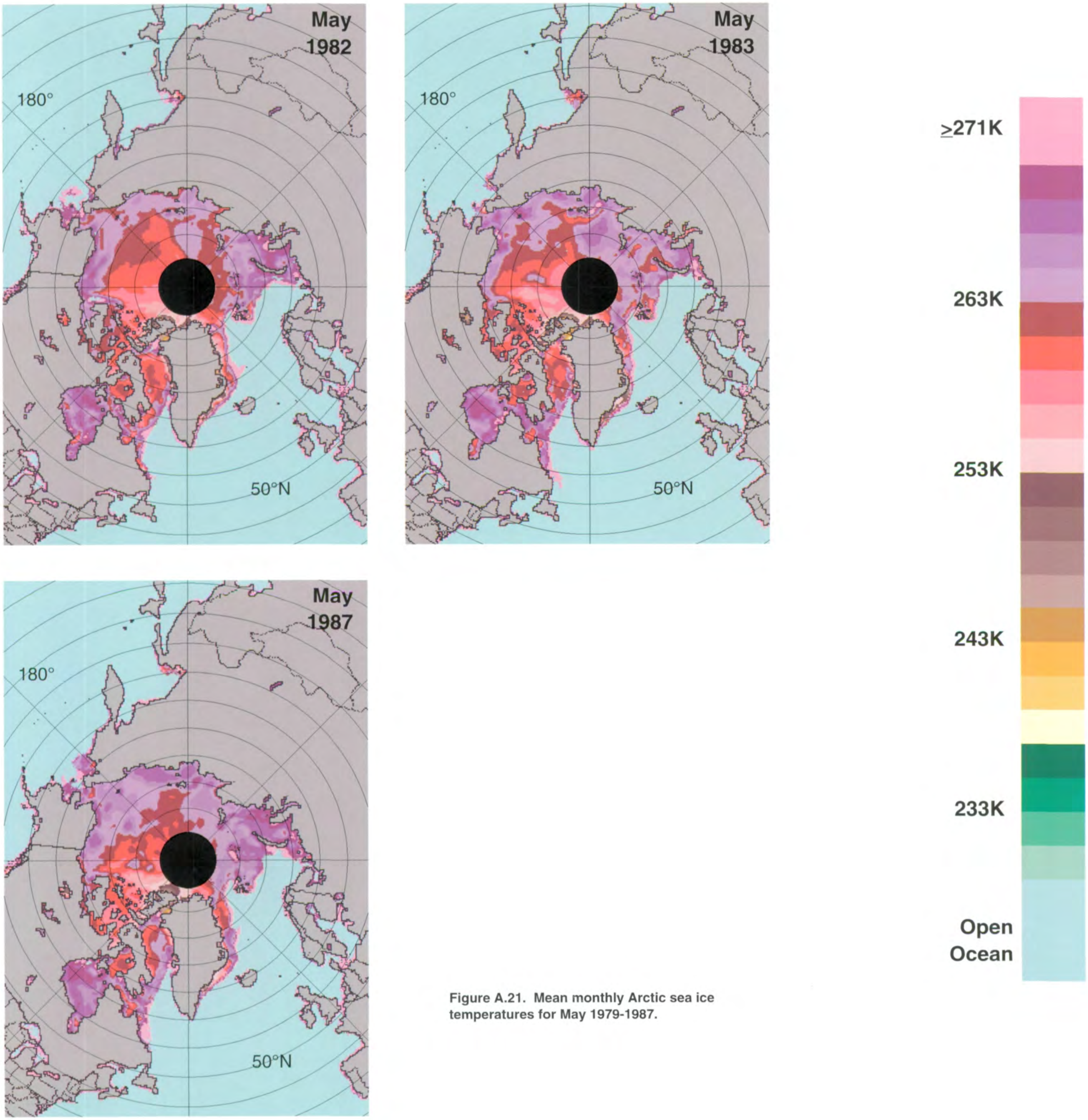

Figure A.21. Mean monthly Arctic sea ice temperatures for May 1979-1987.

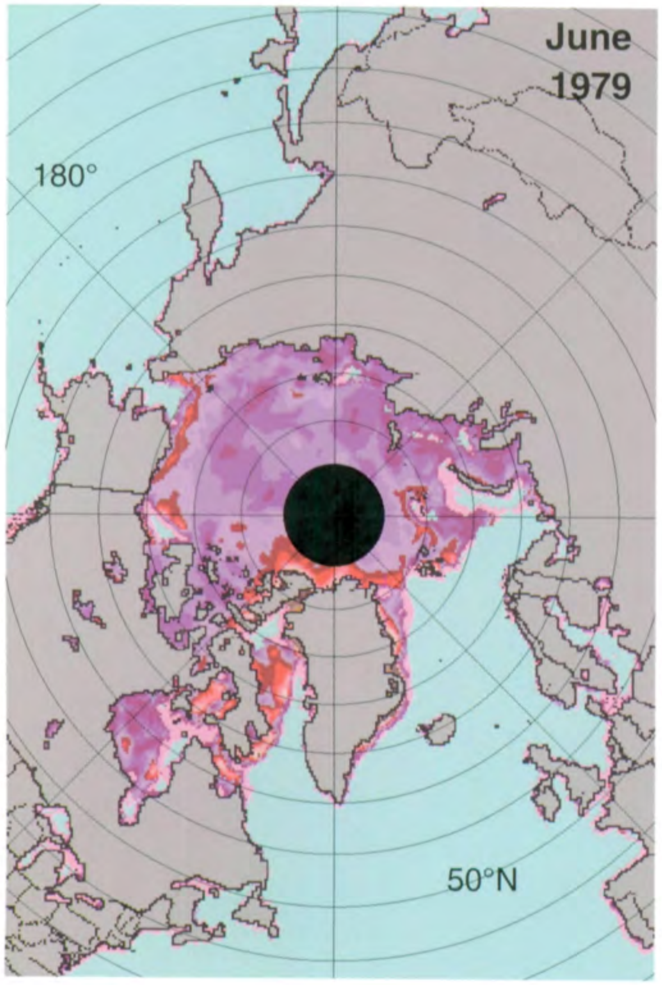
June
1979
180°
50°N

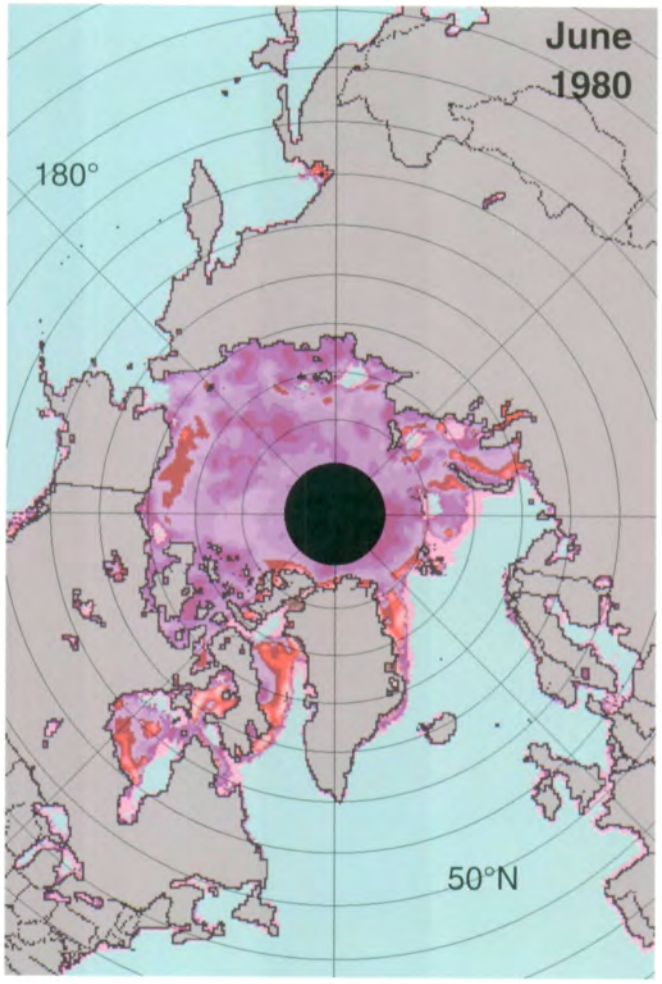
June
1980
180°
50°N

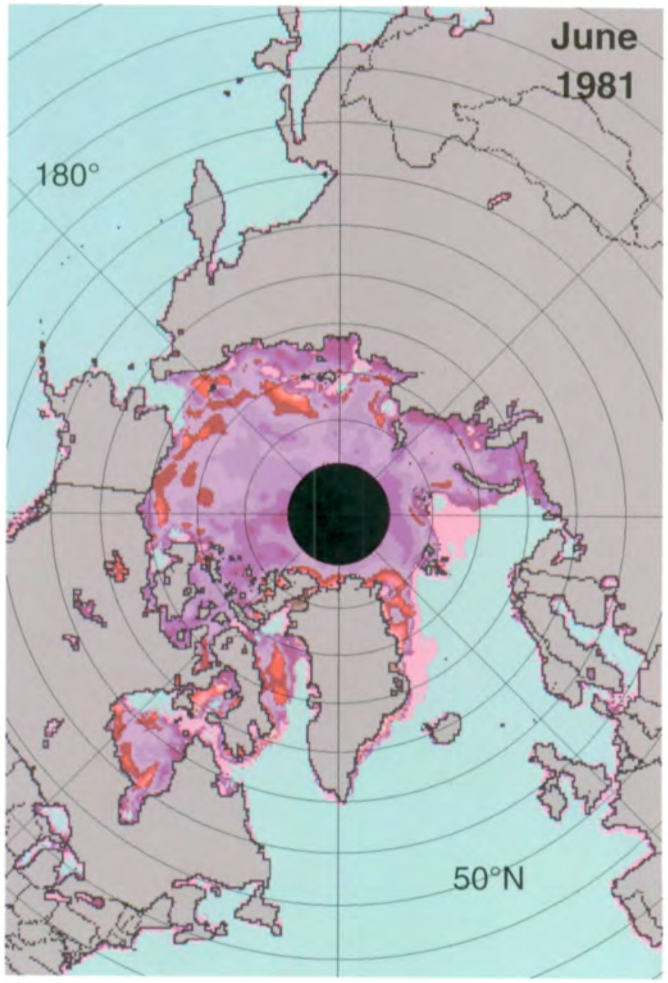
June
1981
180°
50°N

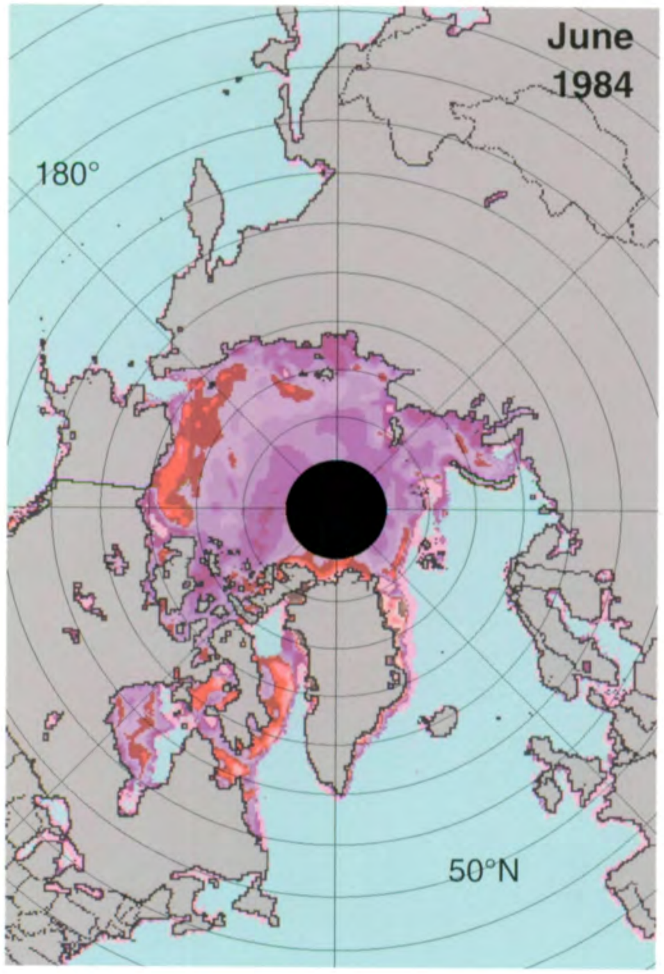
June
1984
180°
50°N

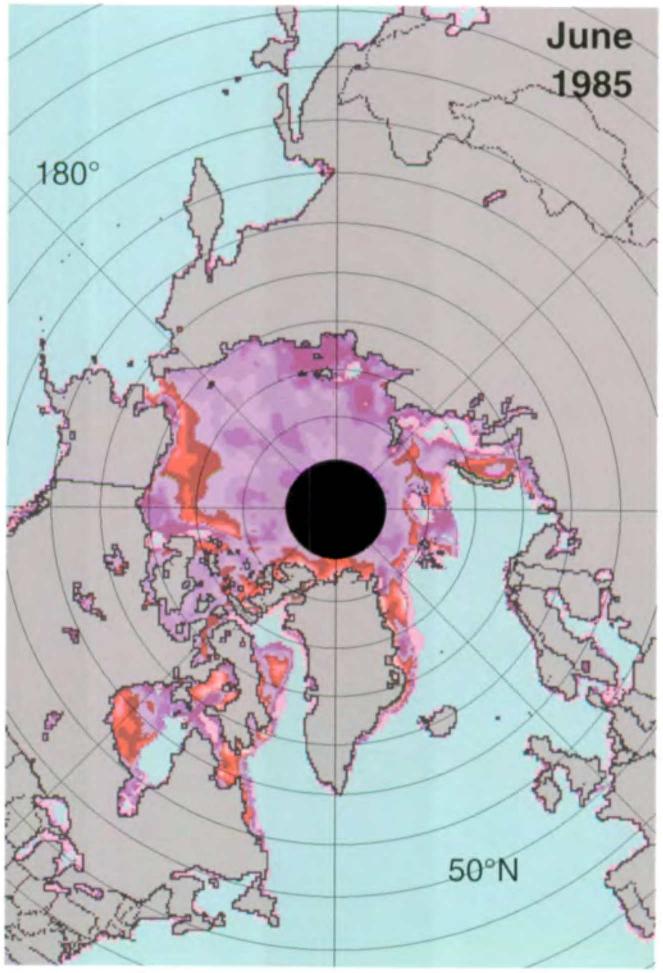
June
1985
180°
50°N

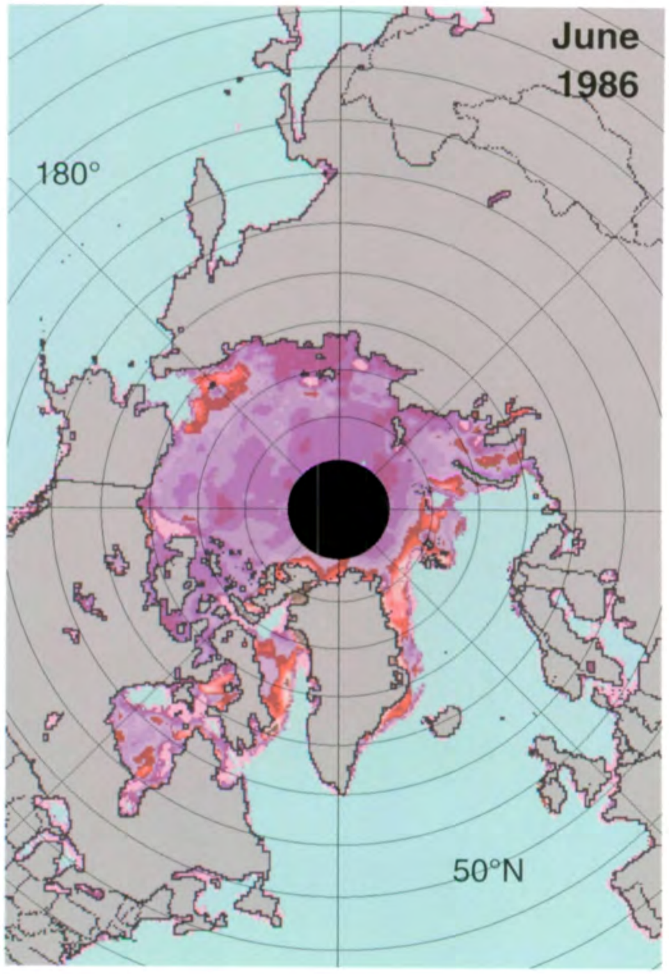
June
1986
180°
50°N

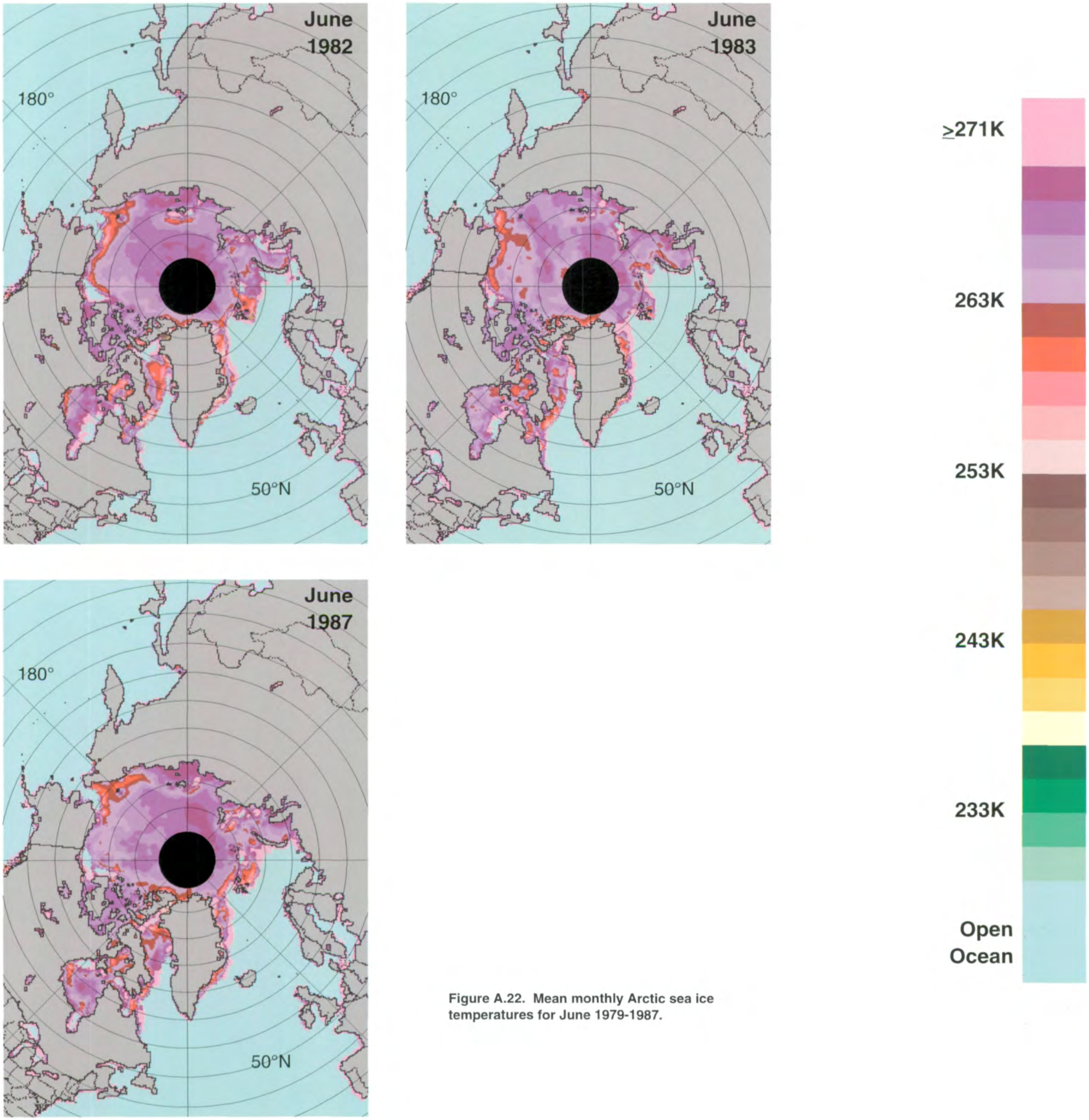

Figure A.22. Mean monthly Arctic sea ice temperatures for June 1979-1987.

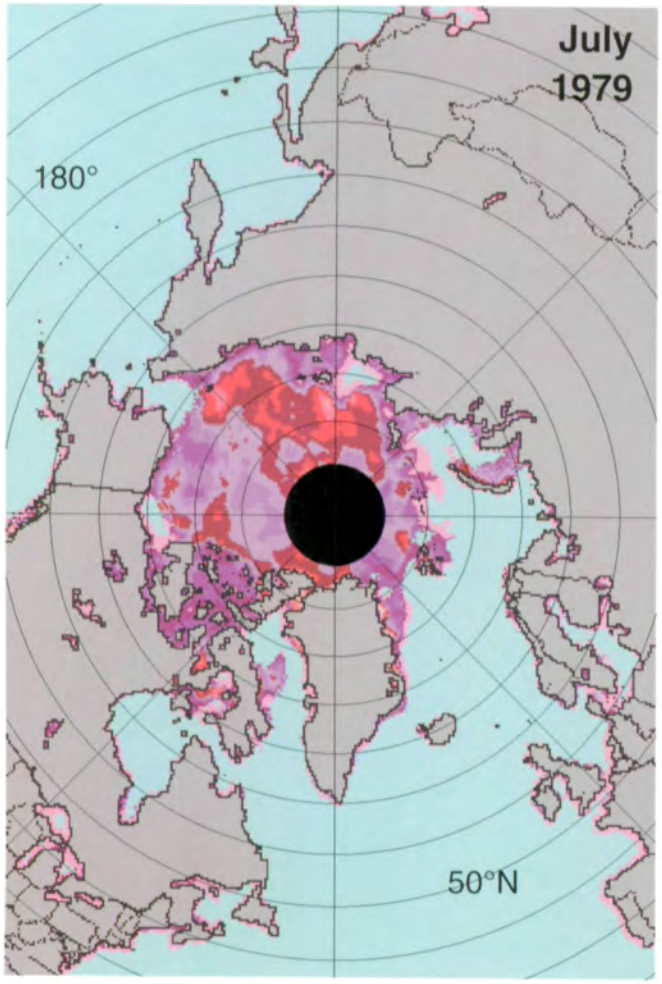
July
1979
180°
50°N

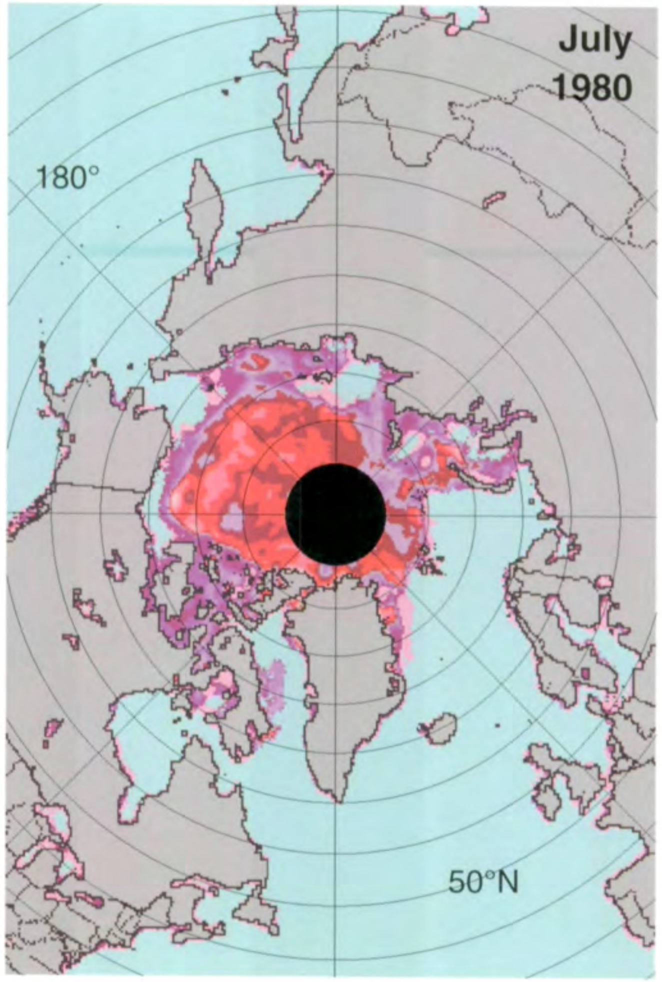
July
1980
180°
50°N

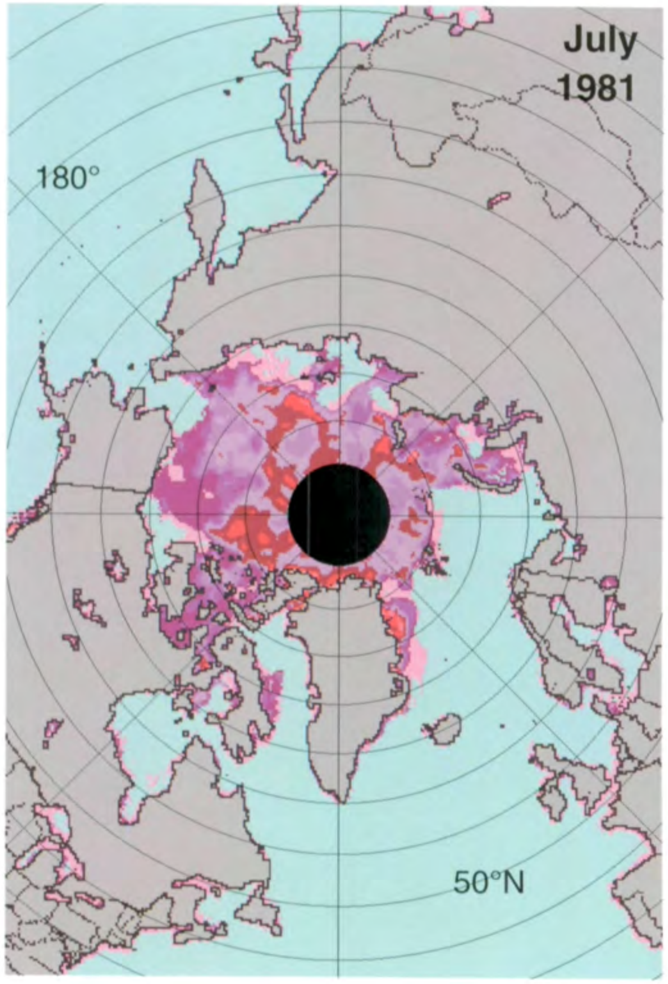
July
1981
180°
50°N

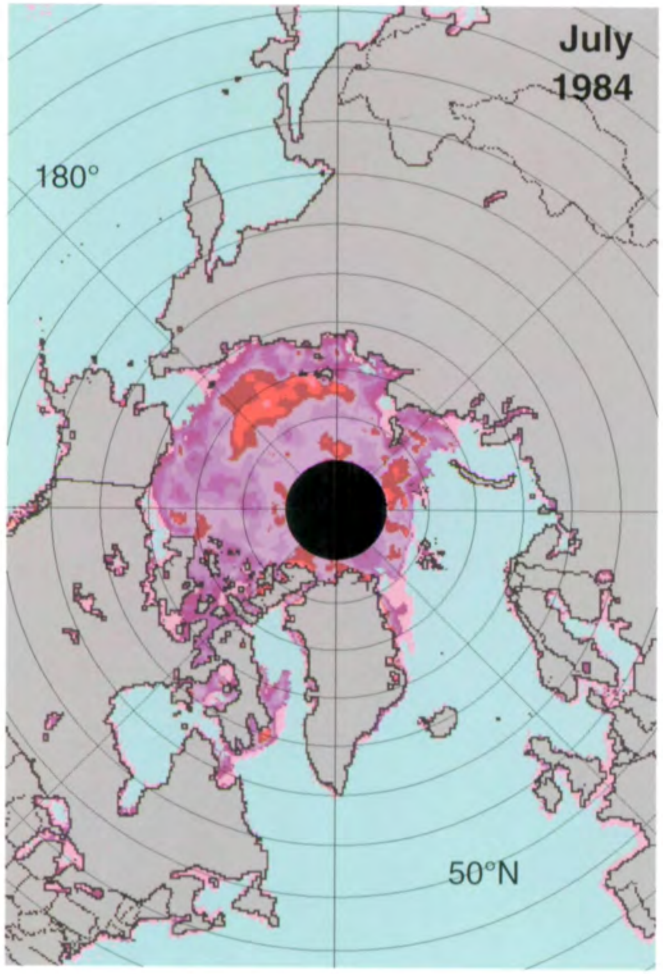
July
1984
180°
50°N

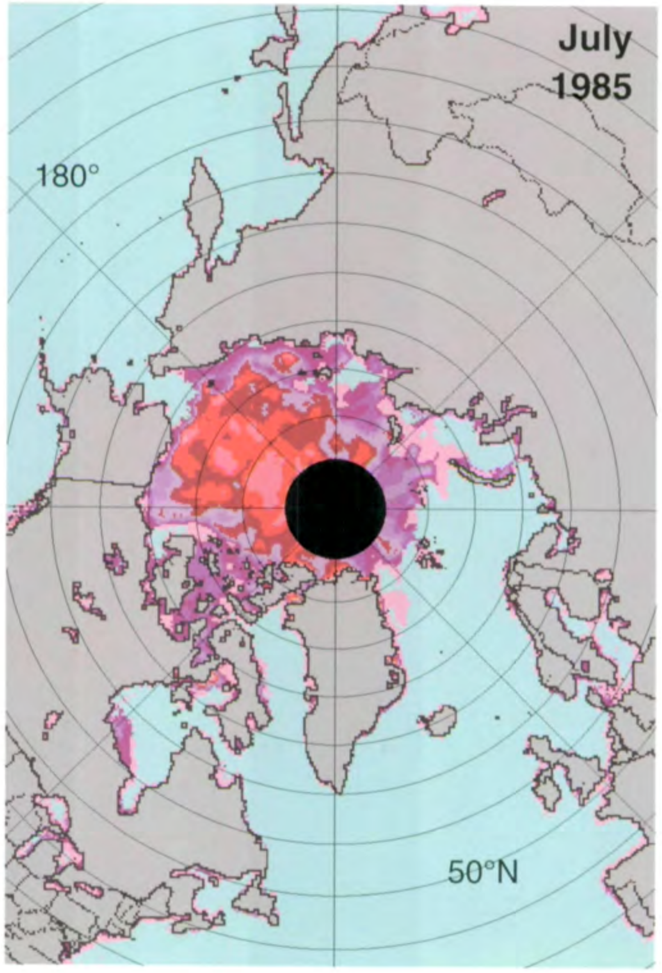
July
1985
180°
50°N

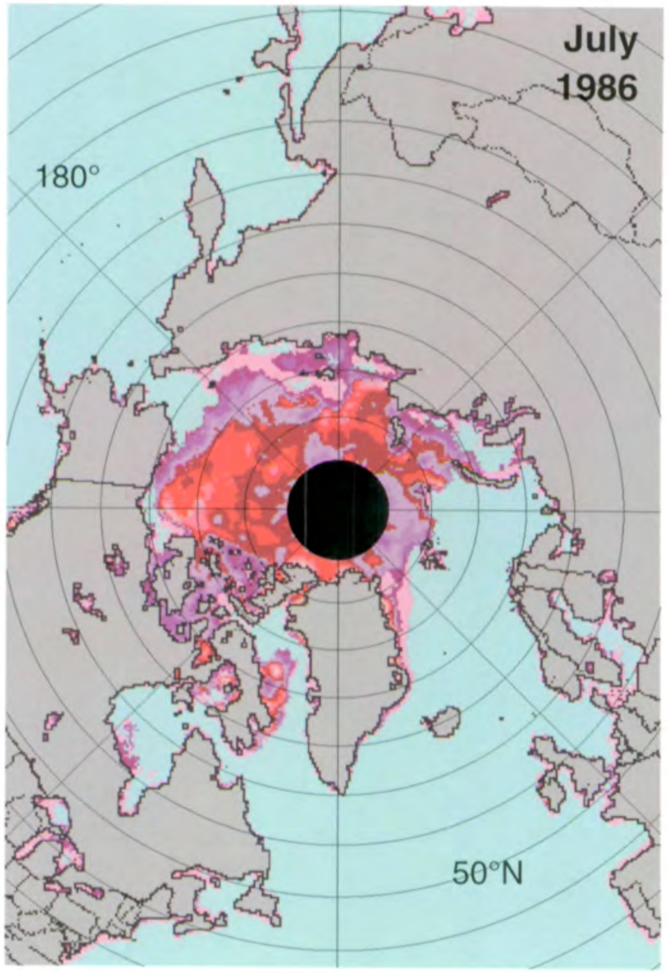
July
1986
180°
50°N

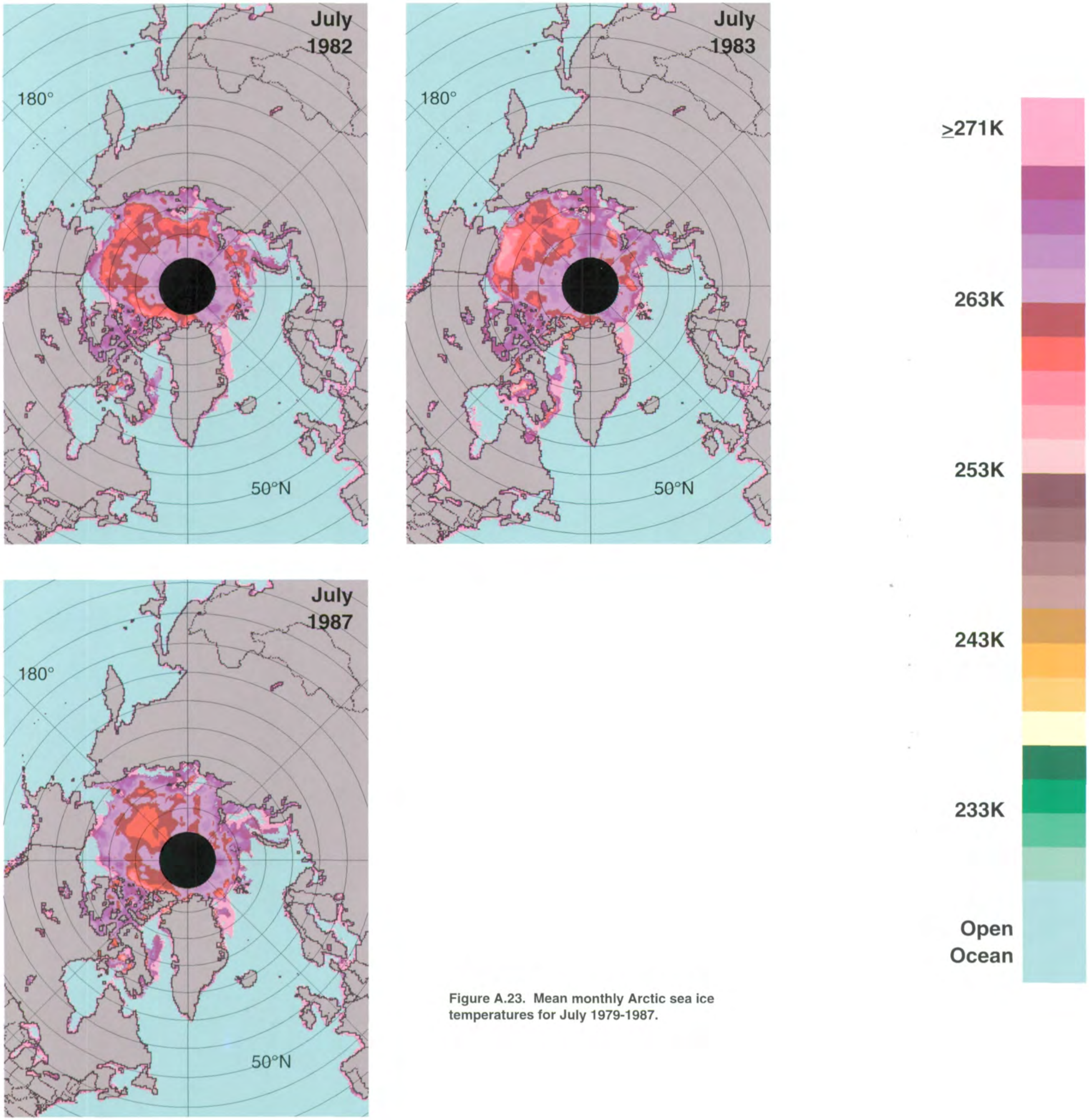

Figure A.23. Mean monthly Arctic sea ice temperatures for July 1979-1987.

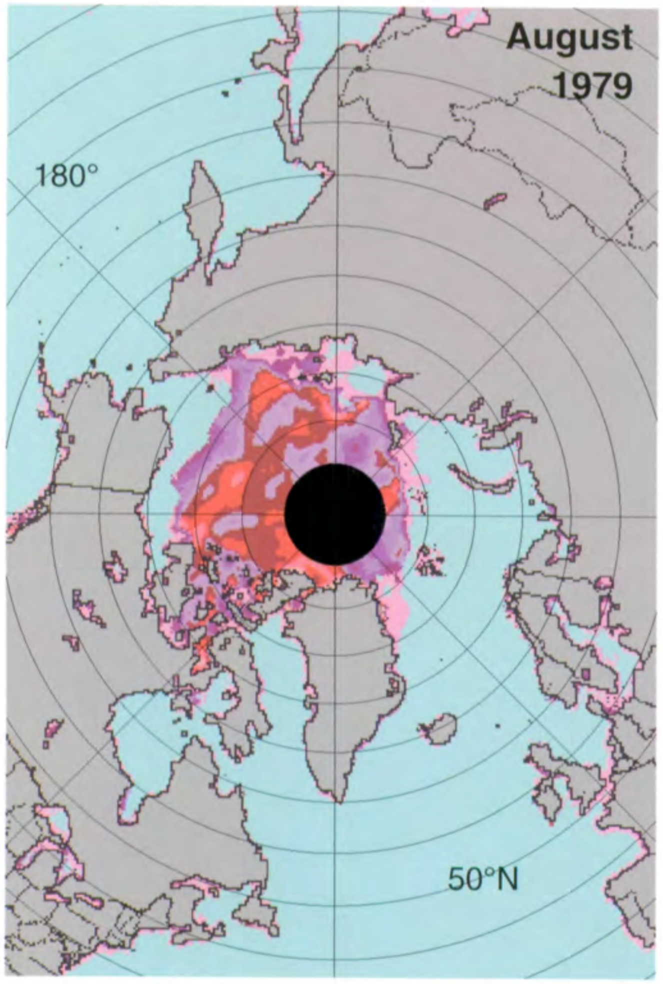
August
1979
180°
50°N

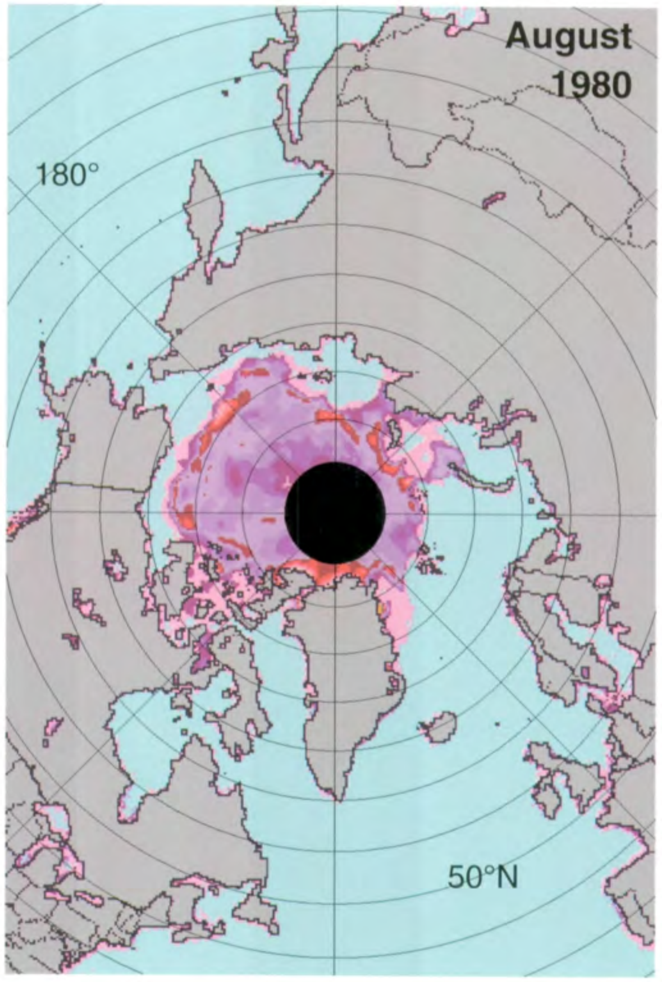
August
1980
180°
50°N

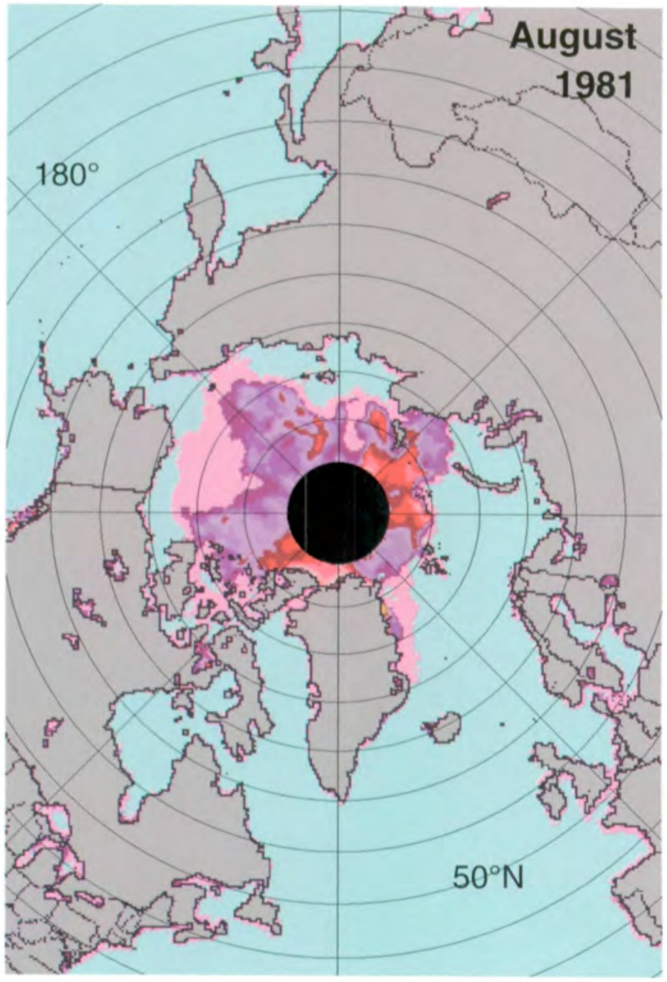
August
1981
180°
50°N

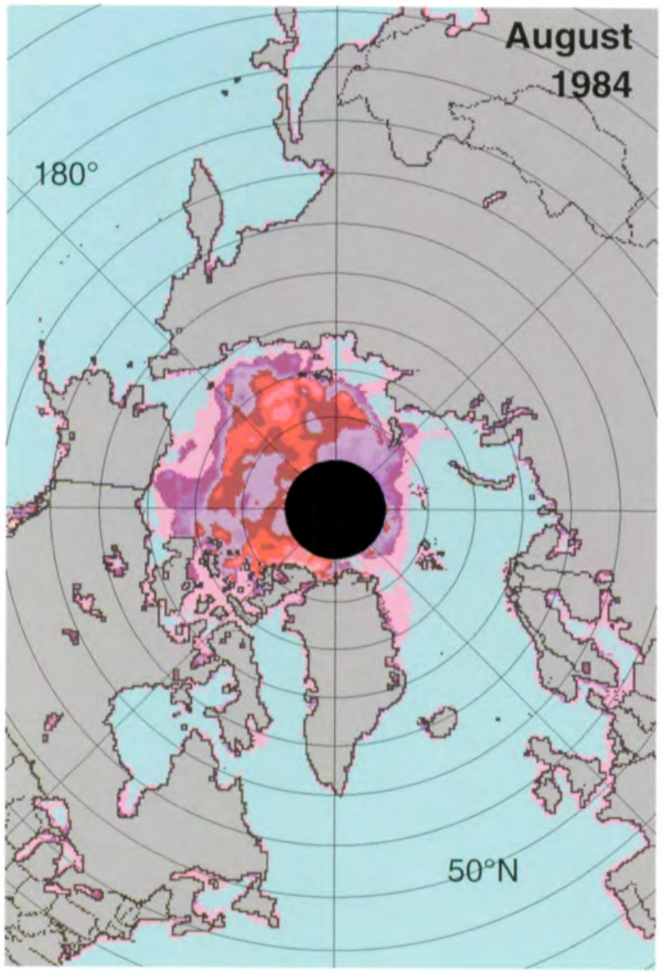
August
1984
180°
50°N

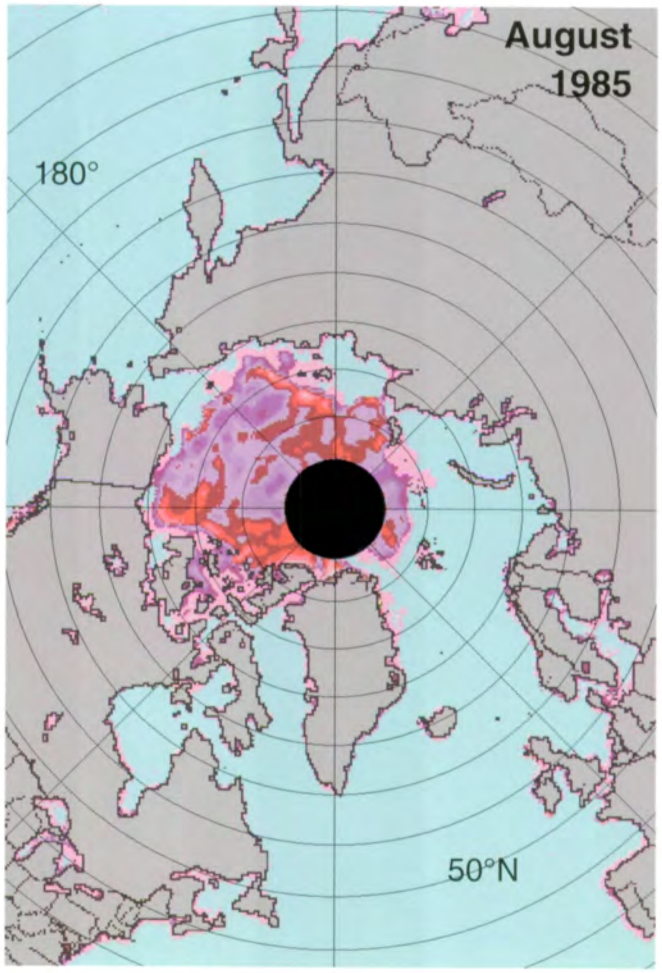
August
1985
180°
50°N

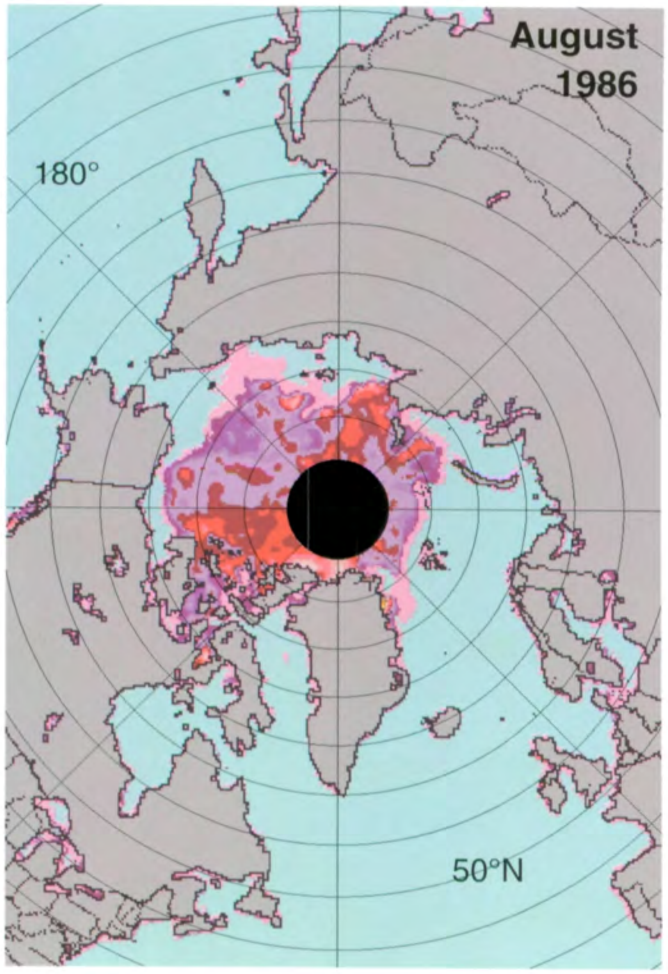
August
1986
180°
50°N

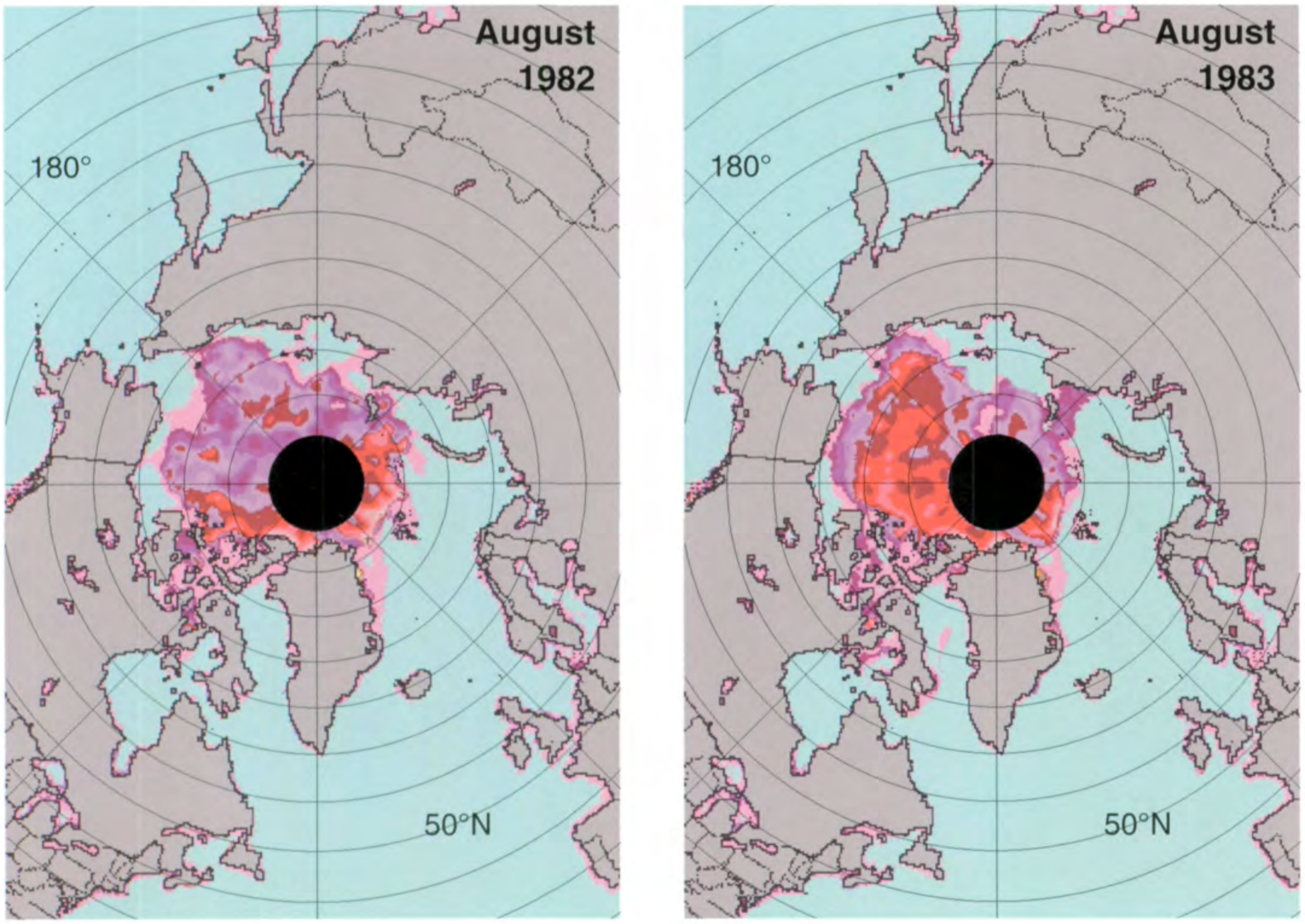

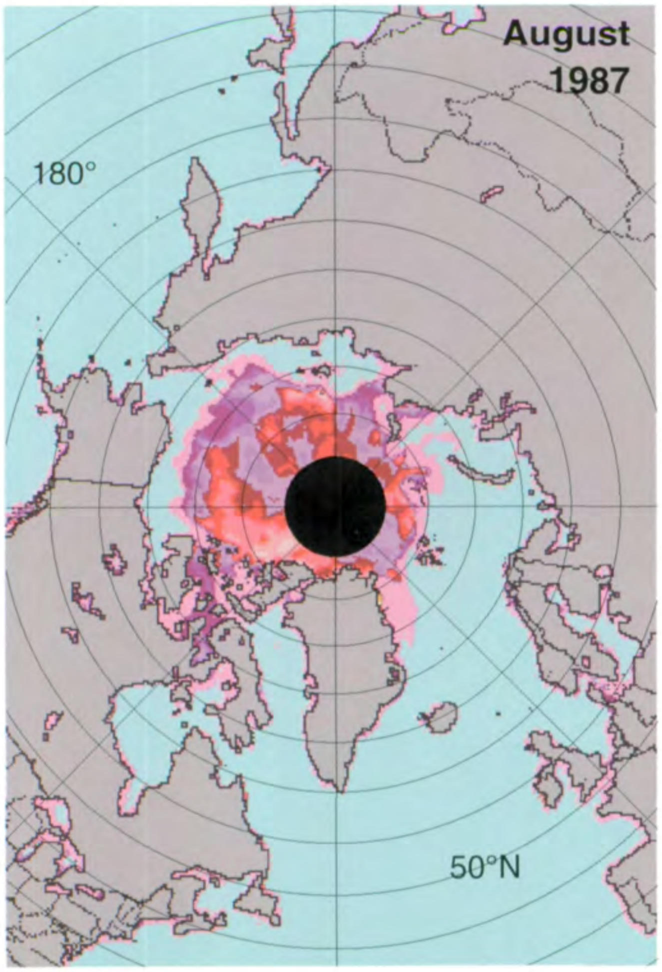

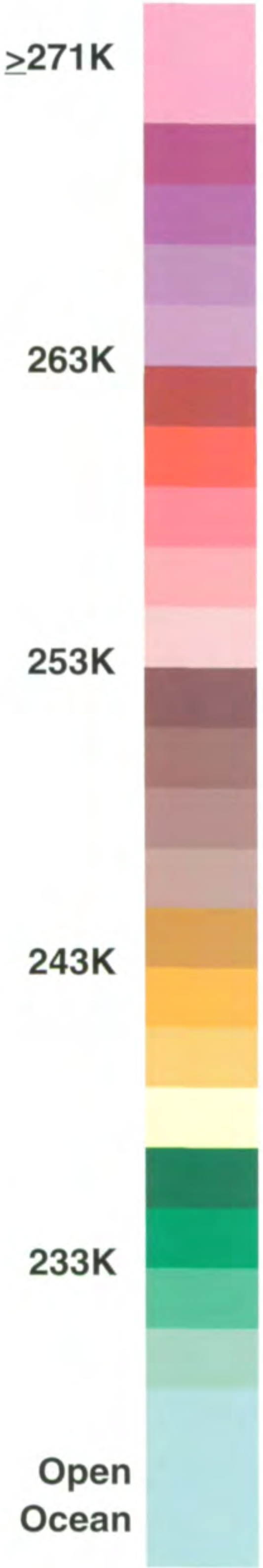

Figure A.24. Mean monthly Arctic sea ice temperatures for August 1979-1987.

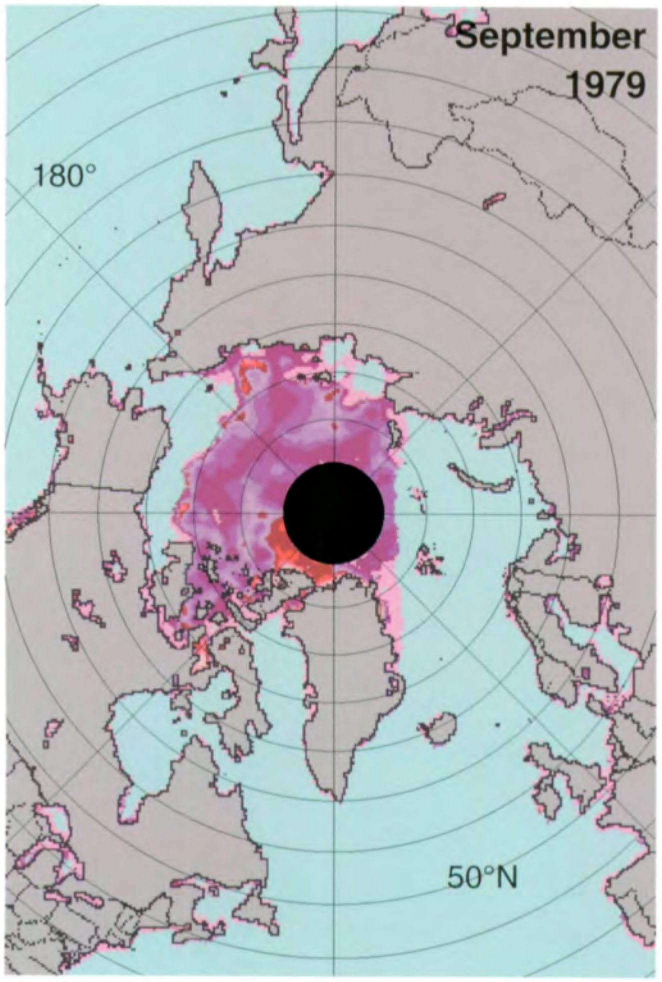
September
1979
180°
50°N

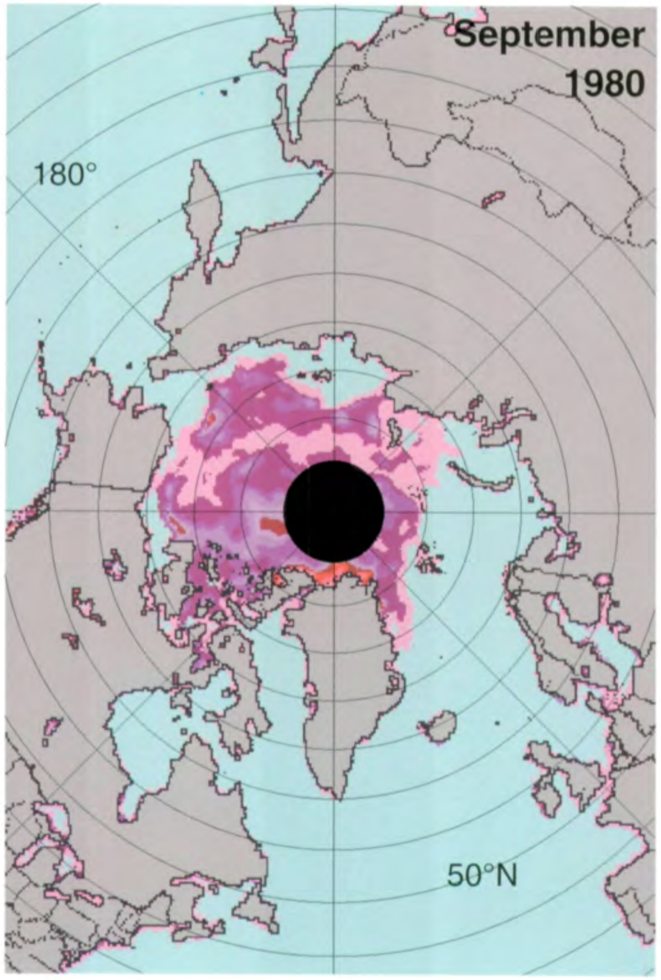
September
1980
180°
50°N

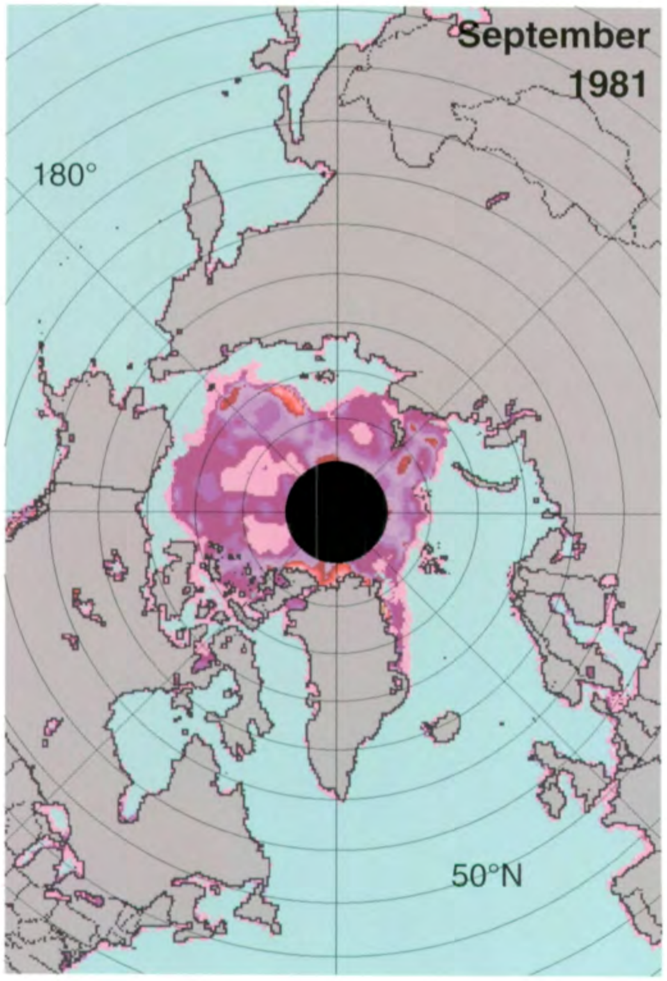
September
1981
180°
50°N

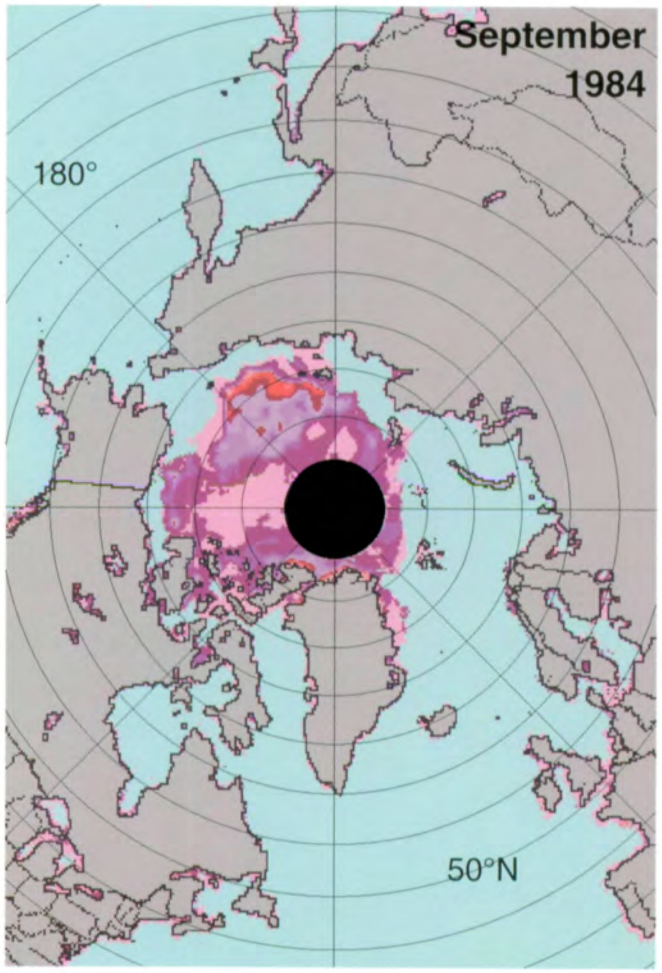
September
1984
180°
50°N

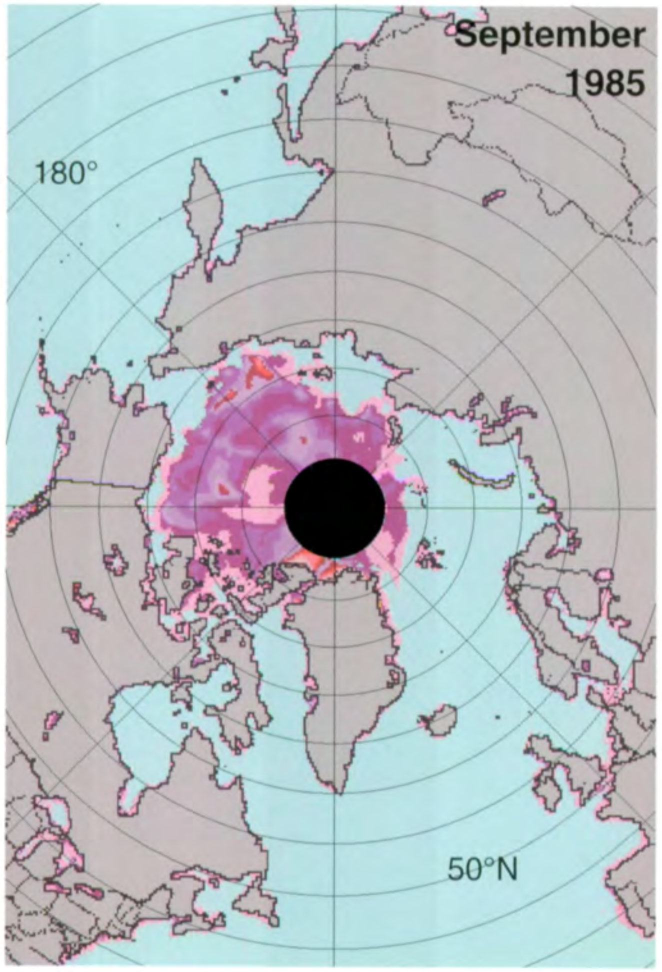
September
1985
180°
50°N

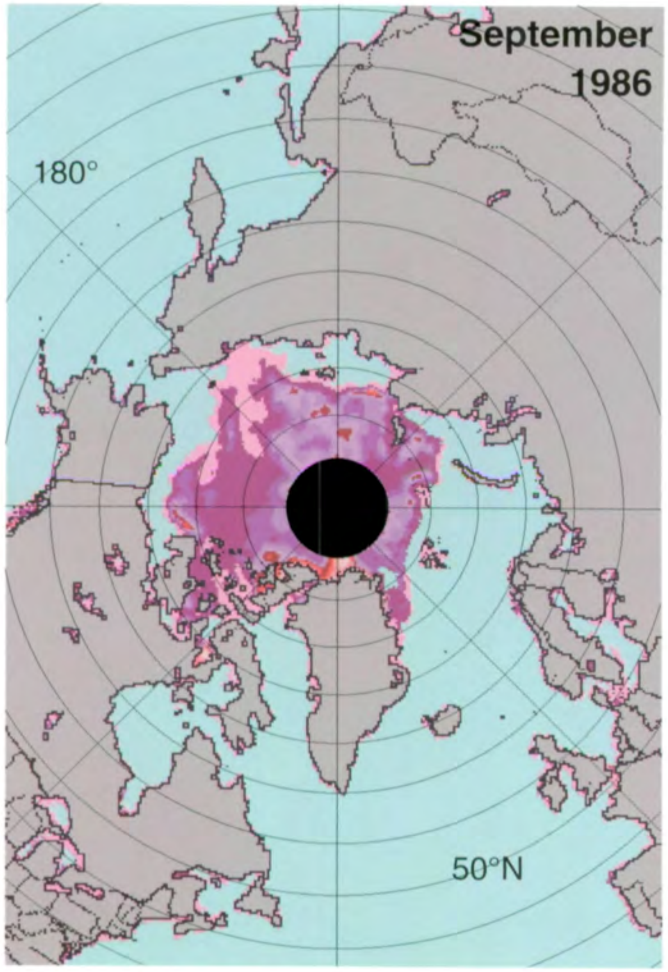
September
1986
180°
50°N

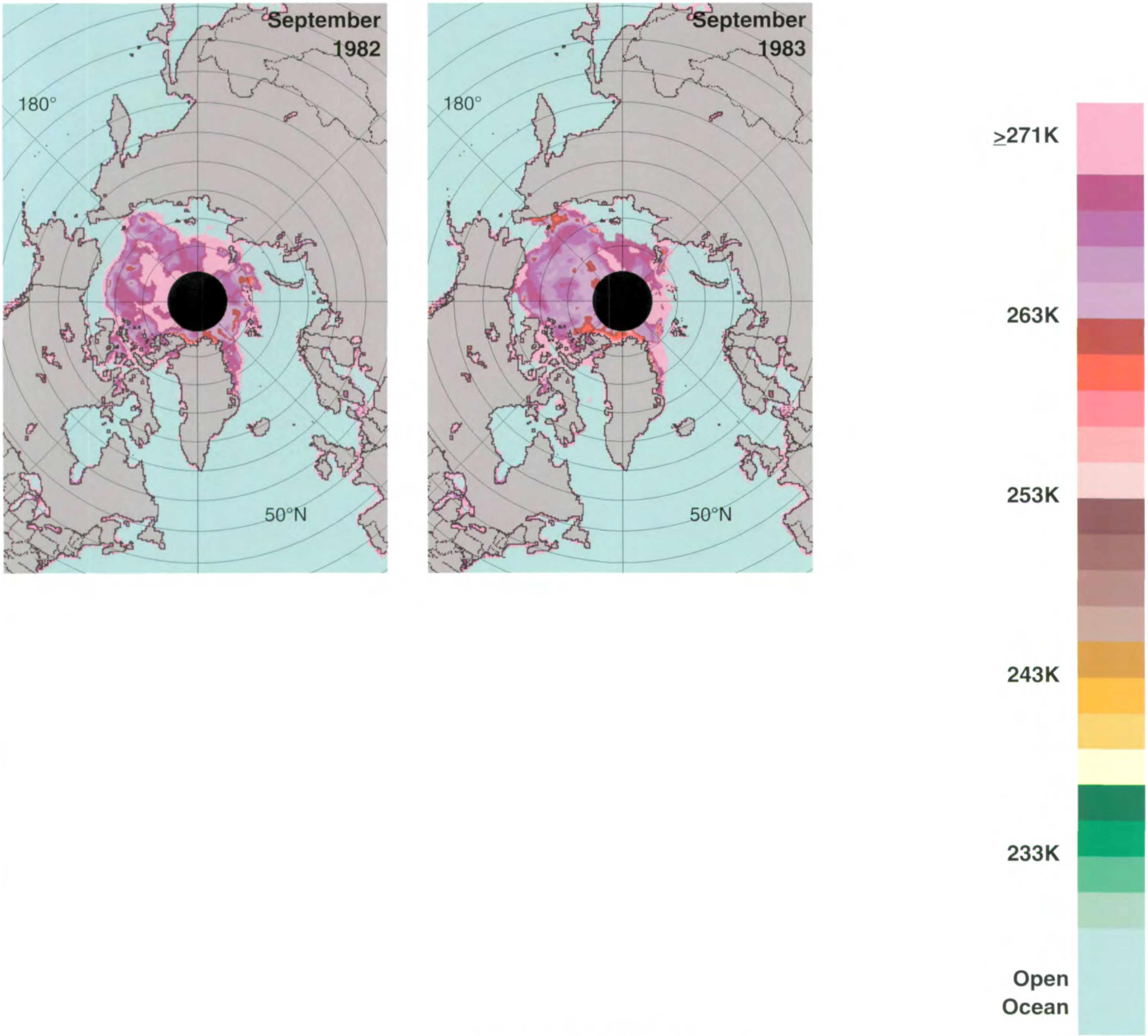

Figure A.25. Mean monthly Arctic sea ice temperatures for September 1979-1986.

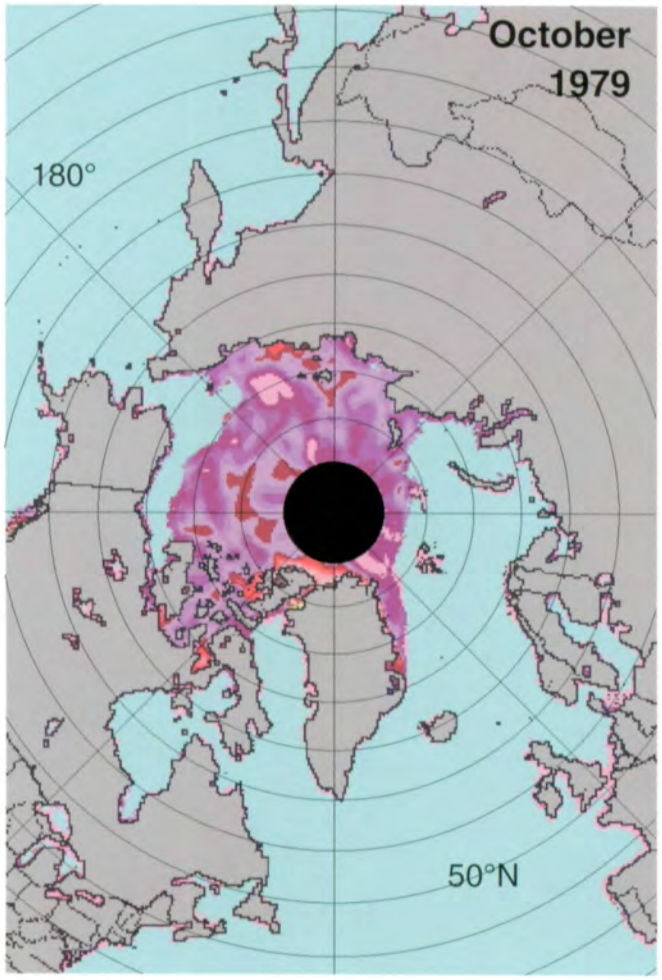
October
1979
180°
50°N

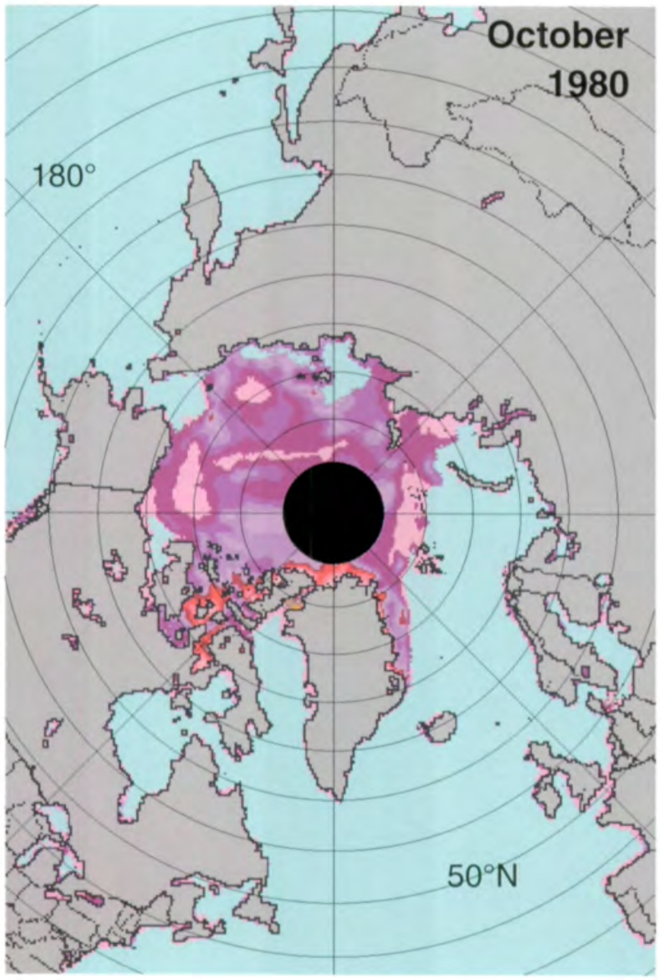
October
1980
180°
50°N

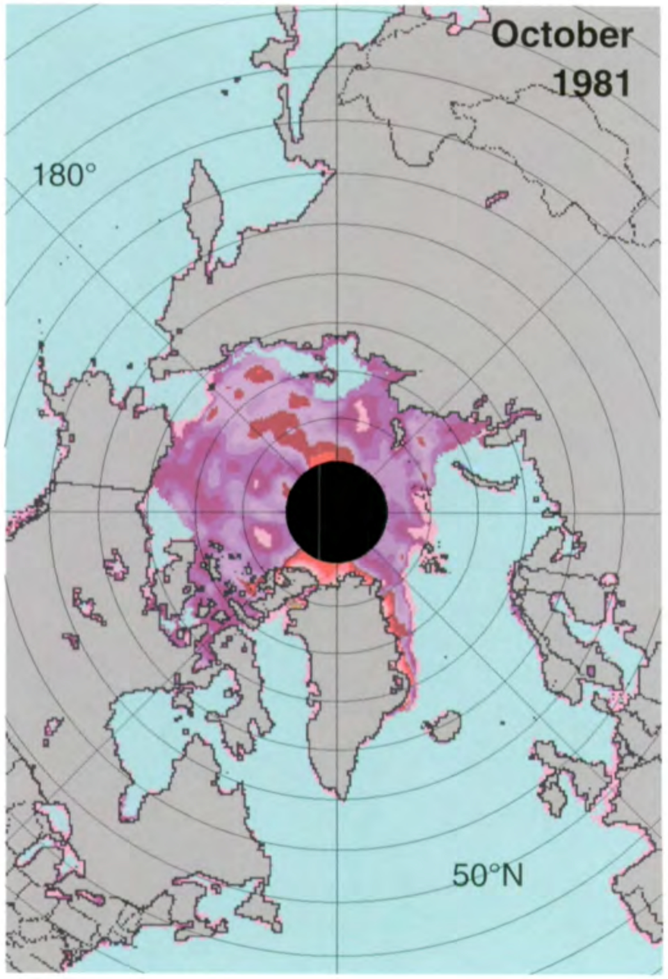
October
1981
180°
50°N

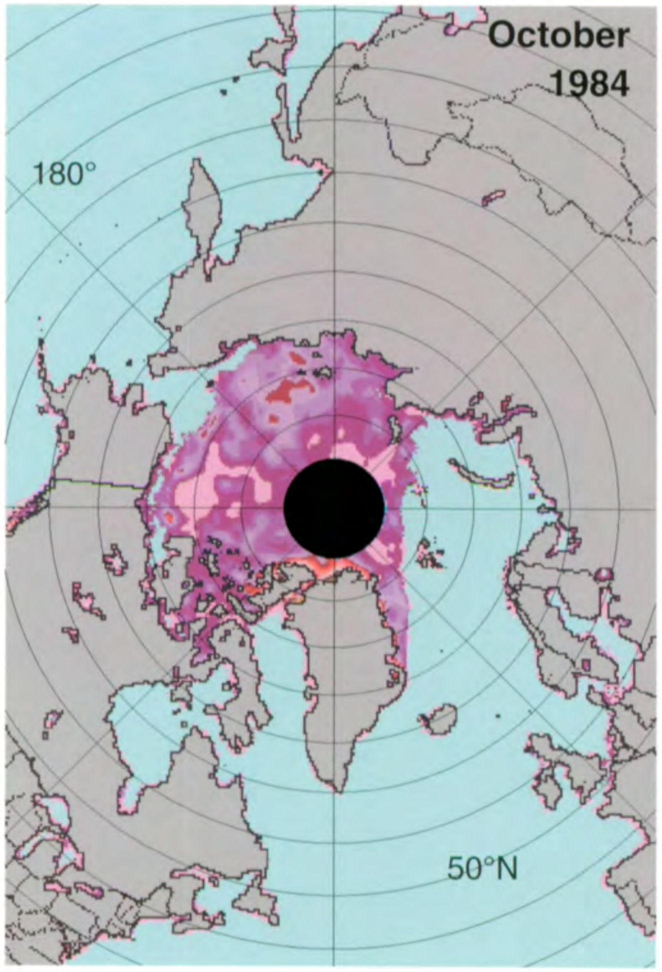
October
1984
180°
50°N

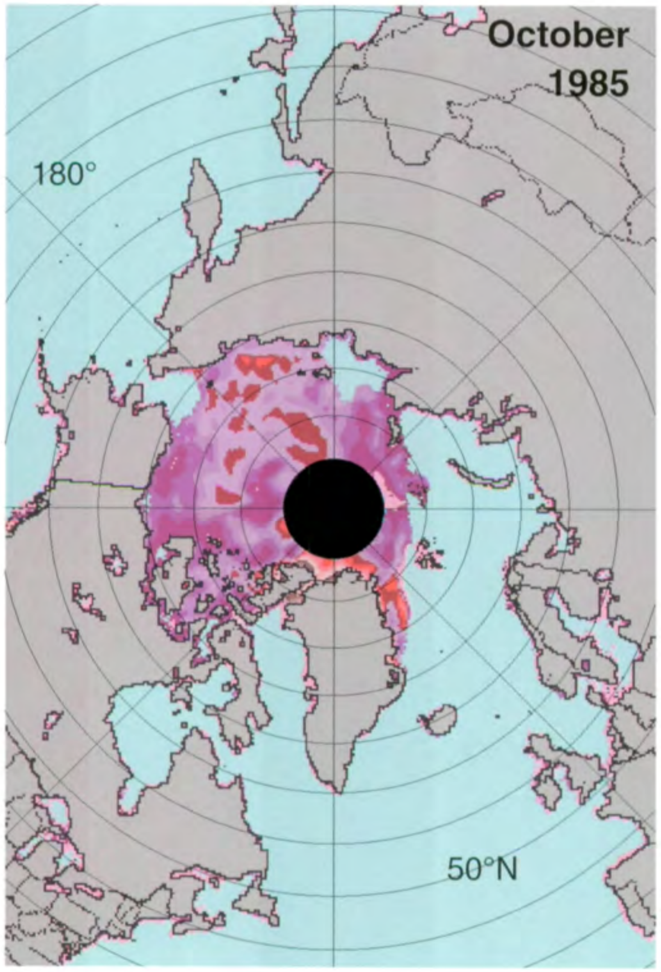
October
1985
180°
50°N

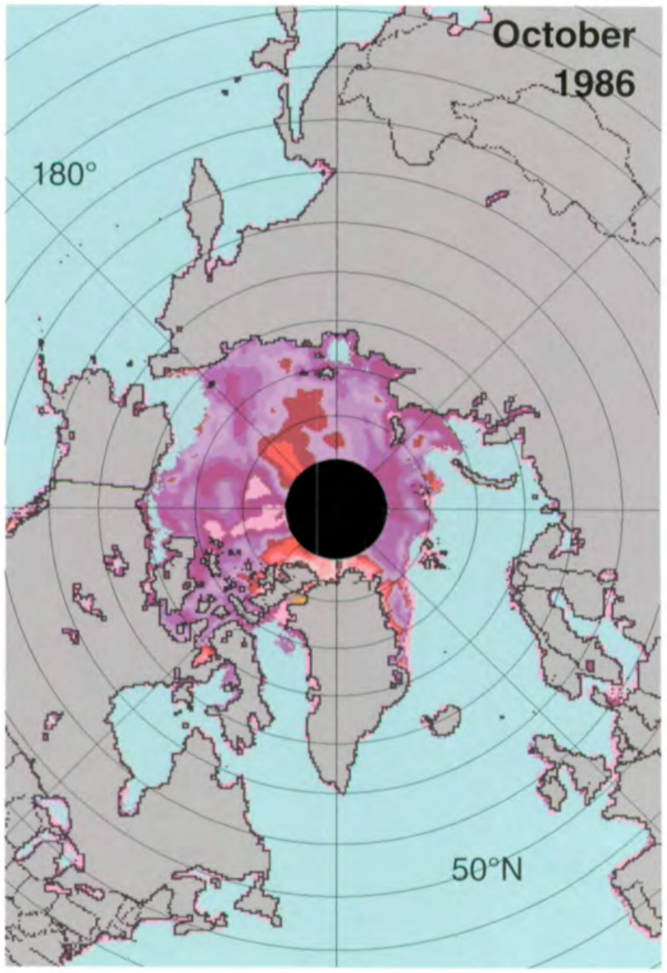
October
1986
180°
50°N

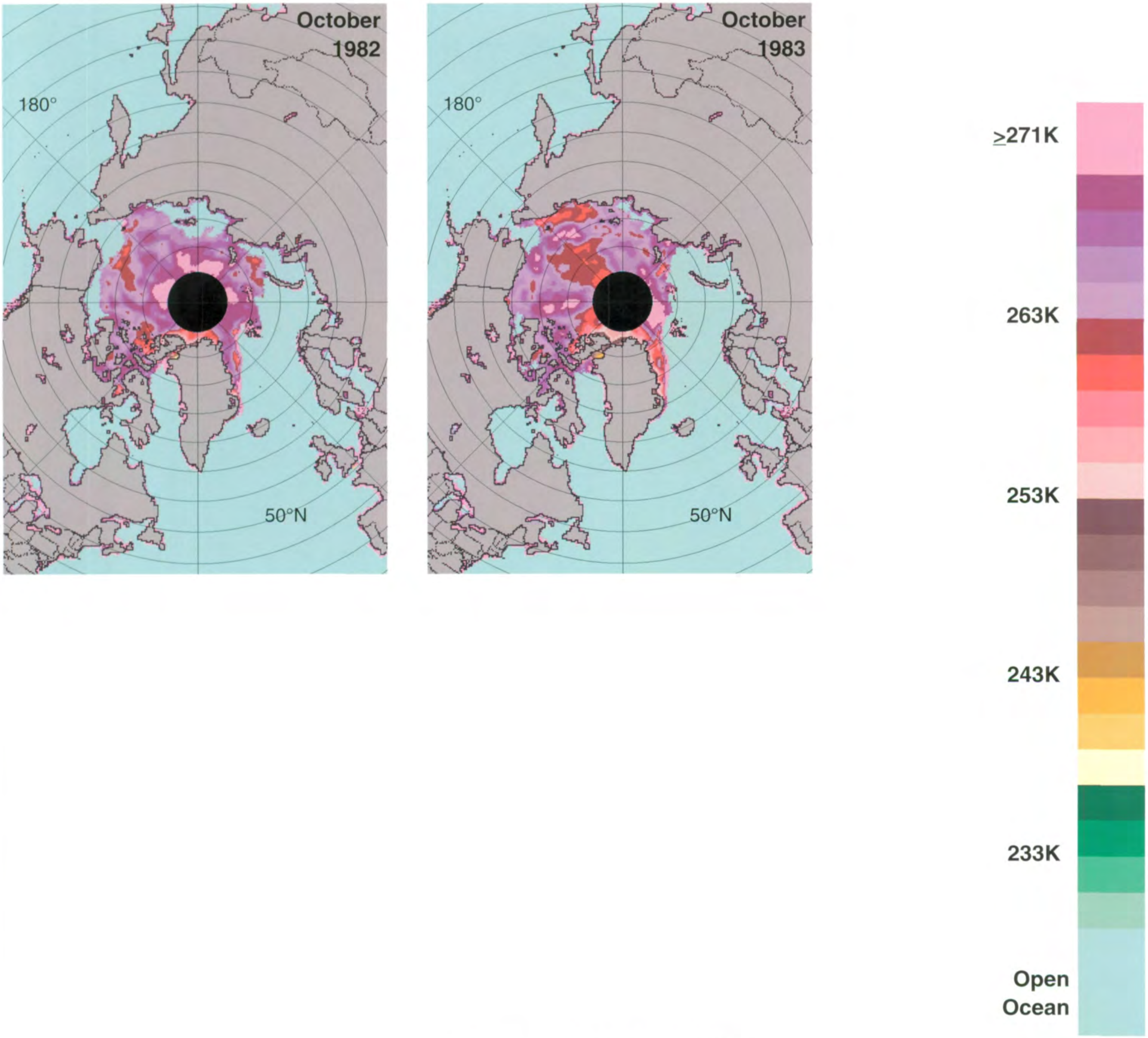

Figure A.26. Mean monthly Arctic sea ice temperatures for October 1979-1986.

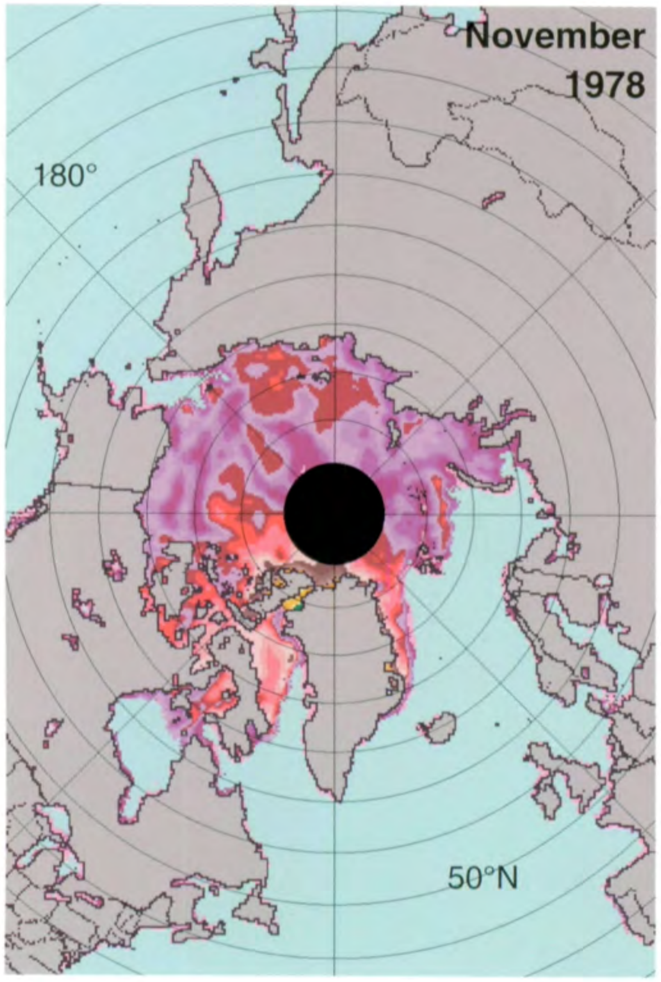
November
1978
180°
50°N

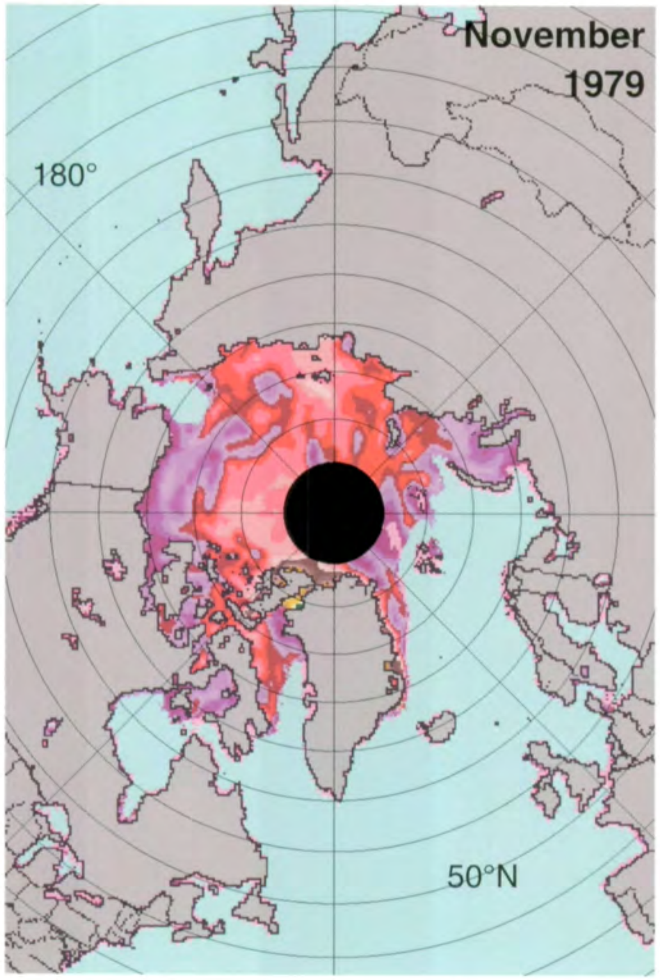
November
1979
180°
50°N

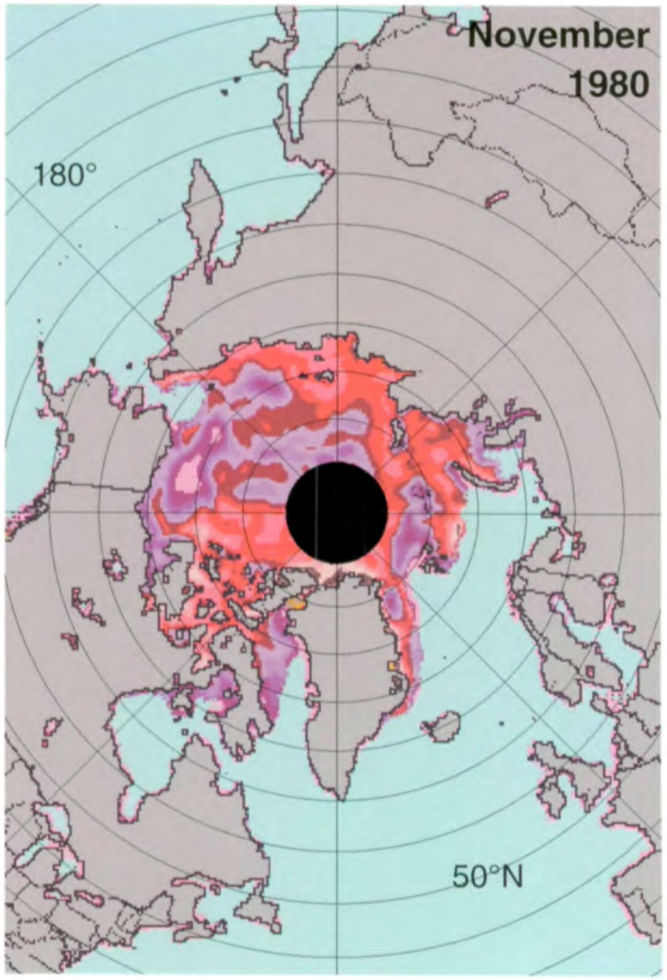
November
1980
180°
50°N

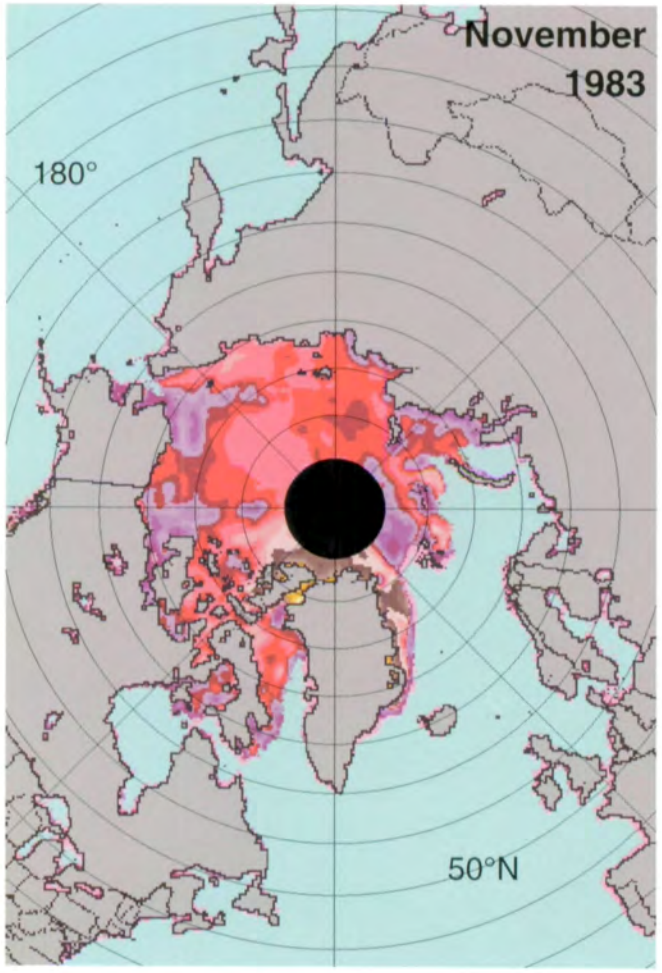
November
1983
180°
50°N

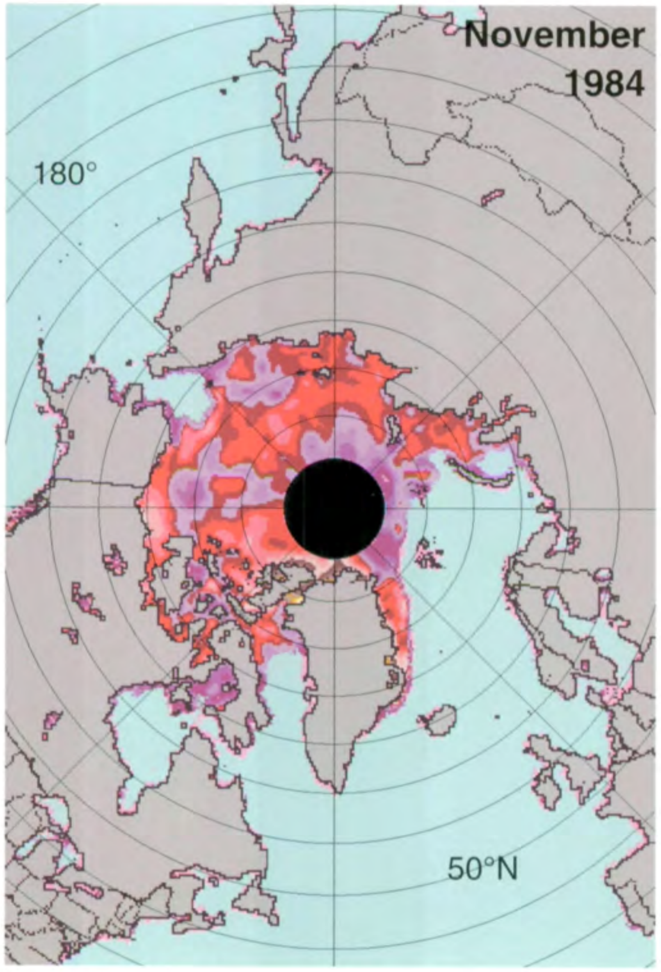
November
1984
180°
50°N

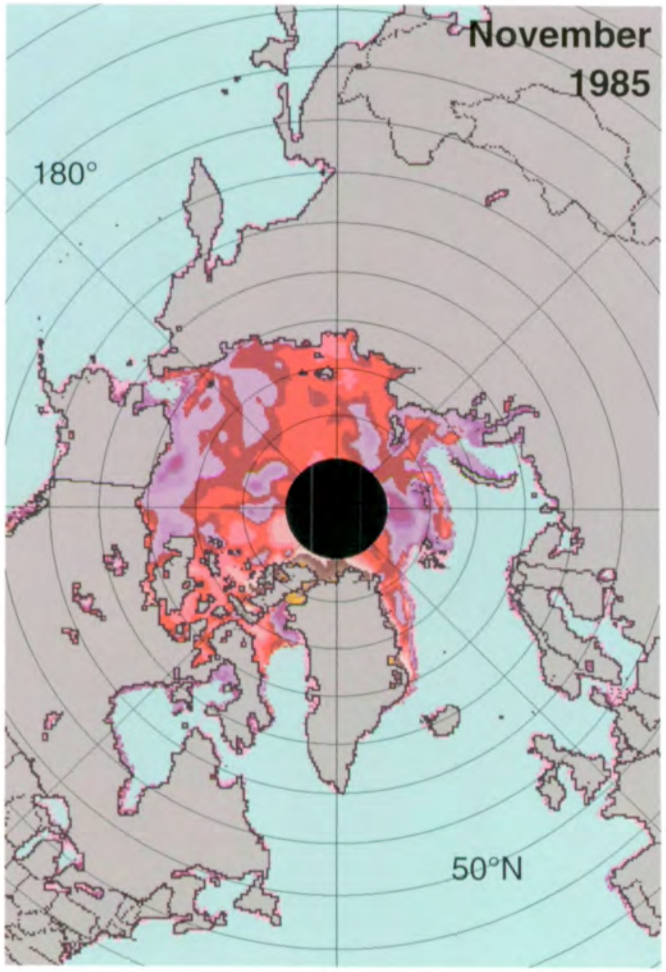
November
1985
180°
50°N

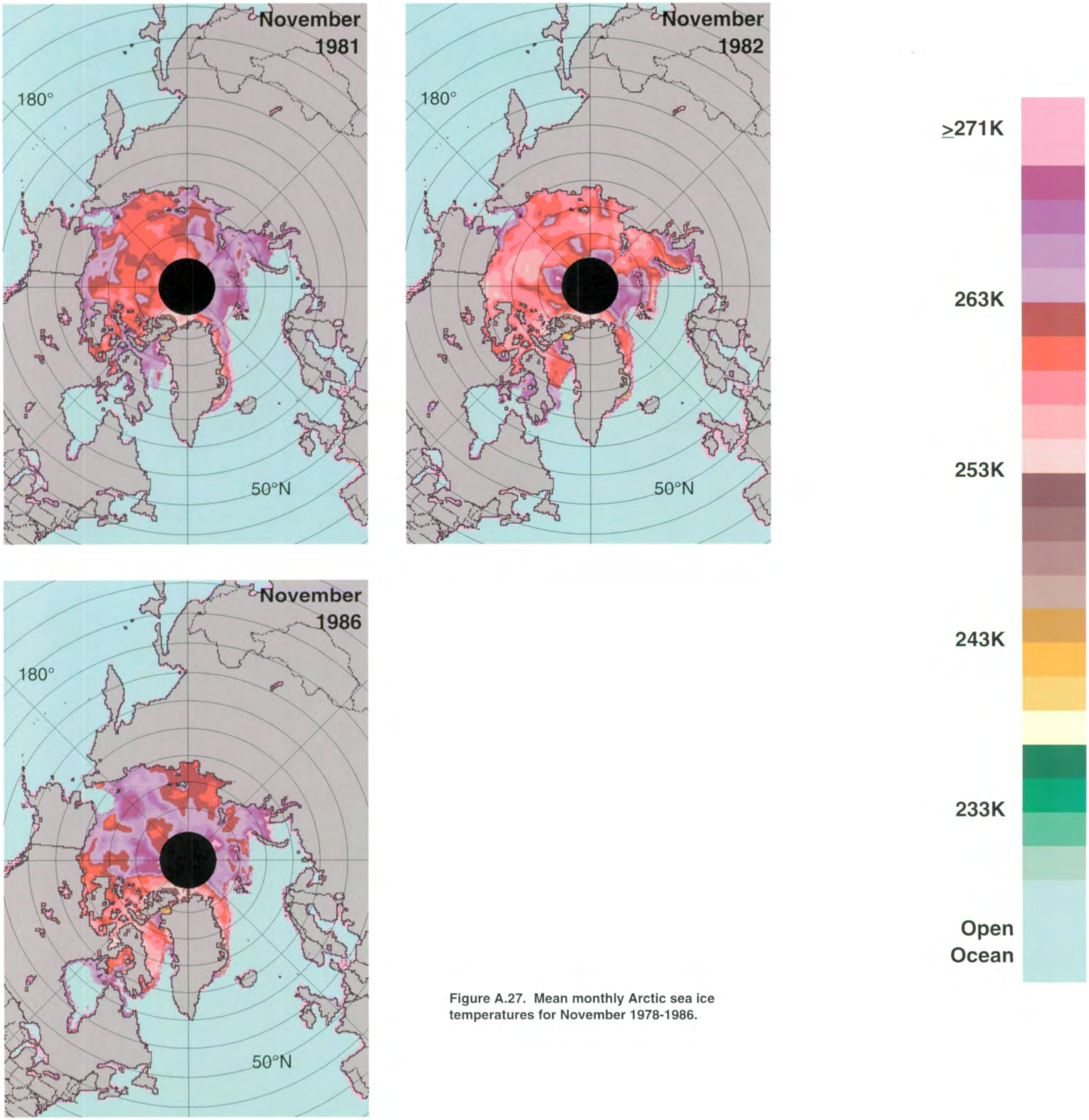

Figure A.27. Mean monthly Arctic sea ice temperatures for November 1978-1986.

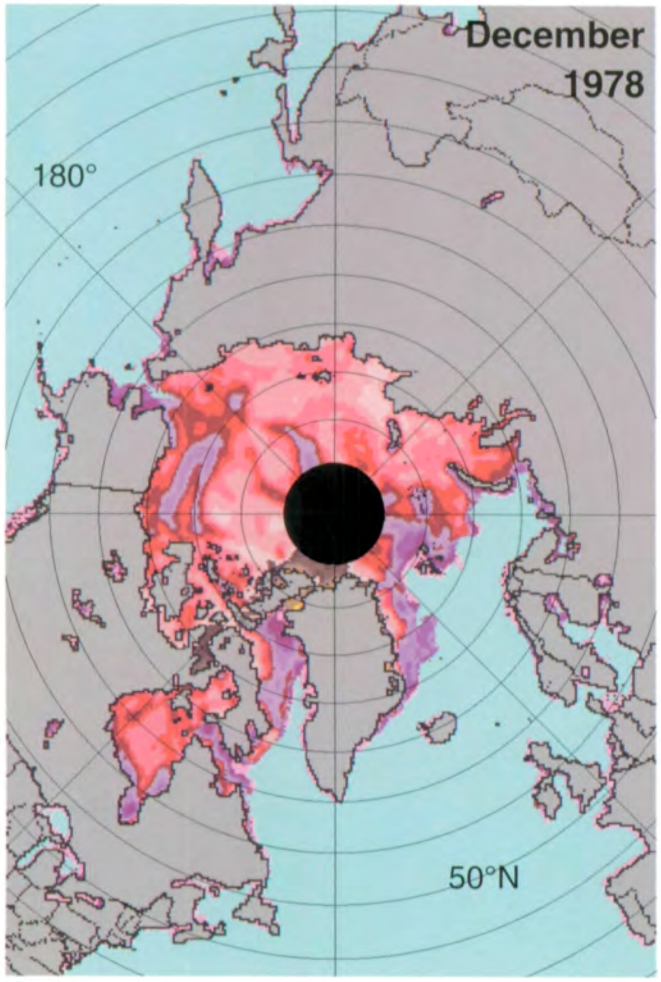
December
1978
180°
50°N

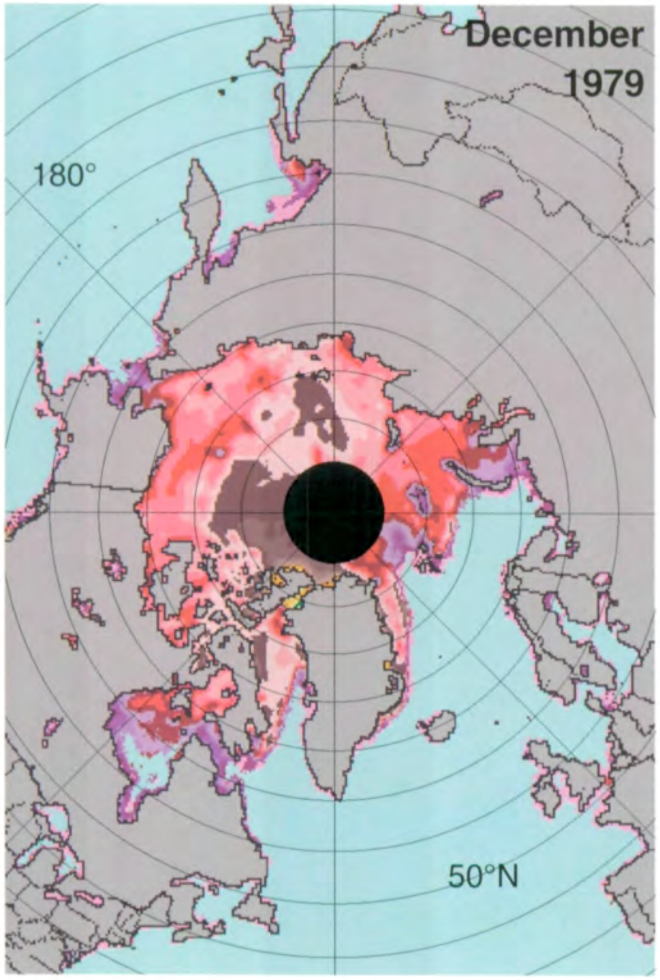
December
1979
180°
50°N

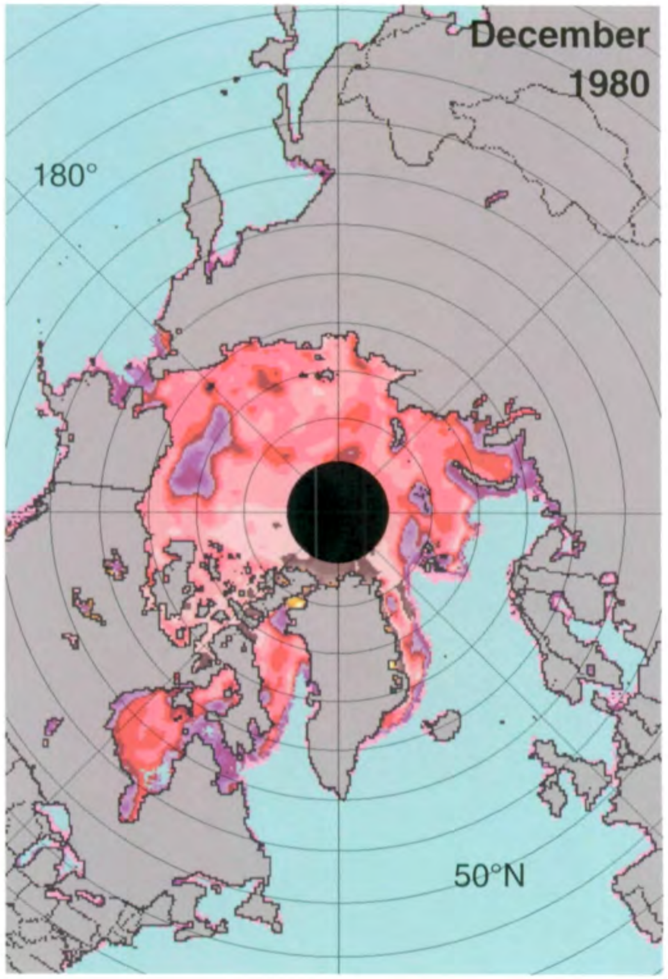
December
1980
180°
50°N

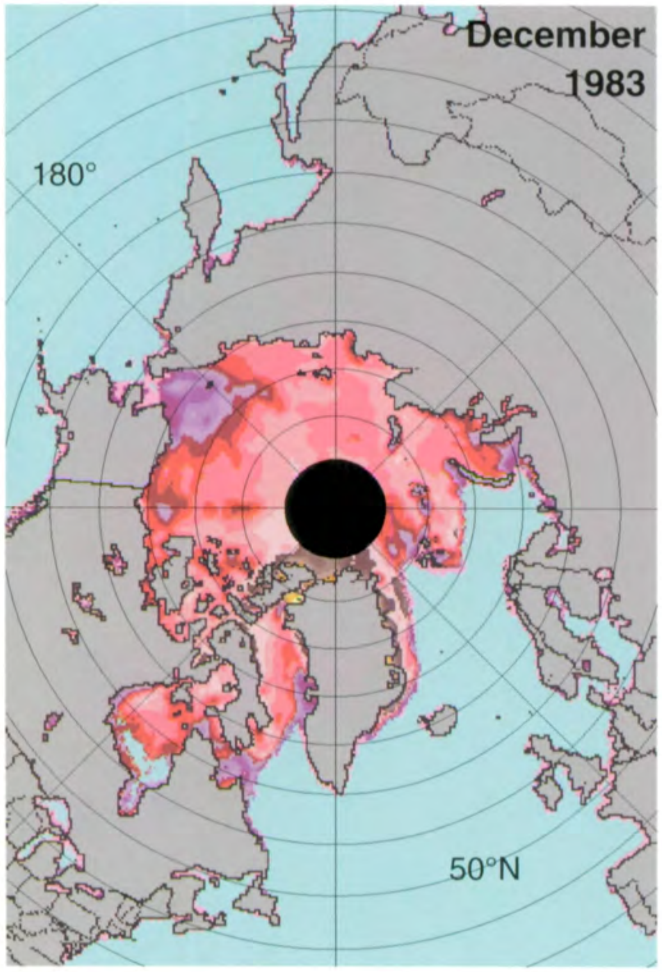
December
1983
180°
50°N

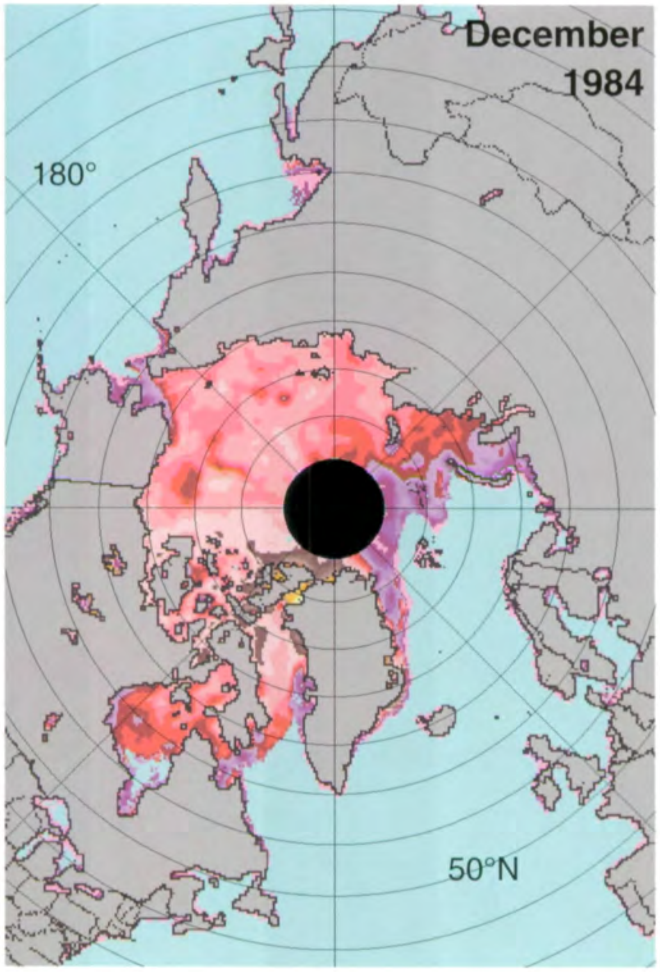
December
1984
180°
50°N

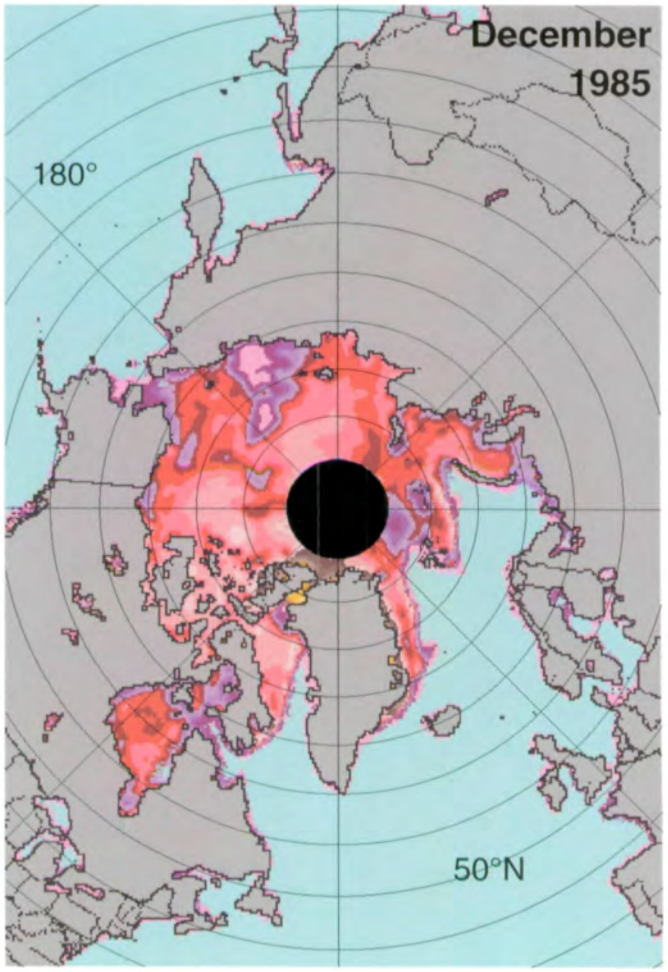
December
1985
180°
50°N

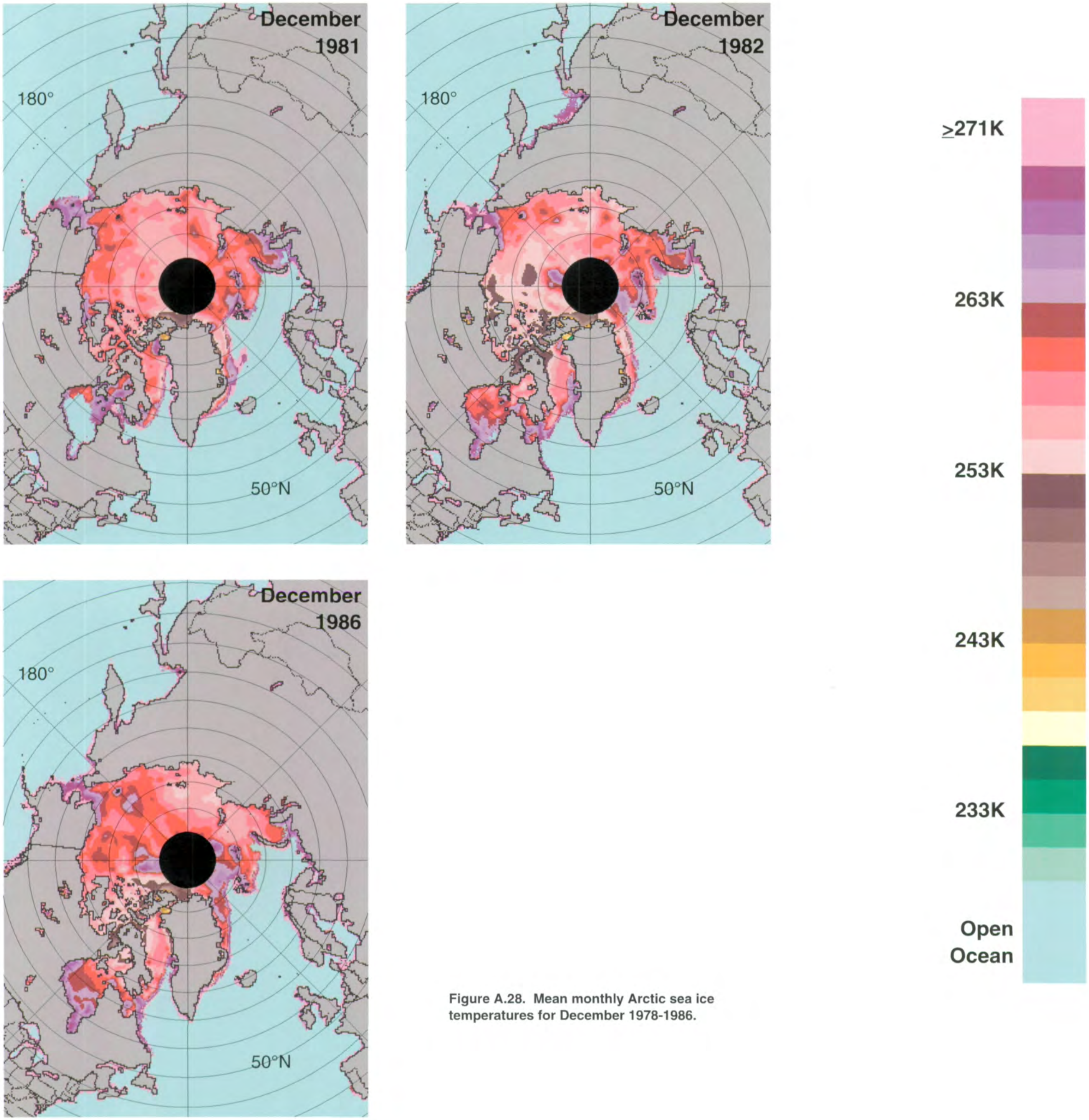

Figure A.28. Mean monthly Arctic sea ice temperatures for December 1978-1986.

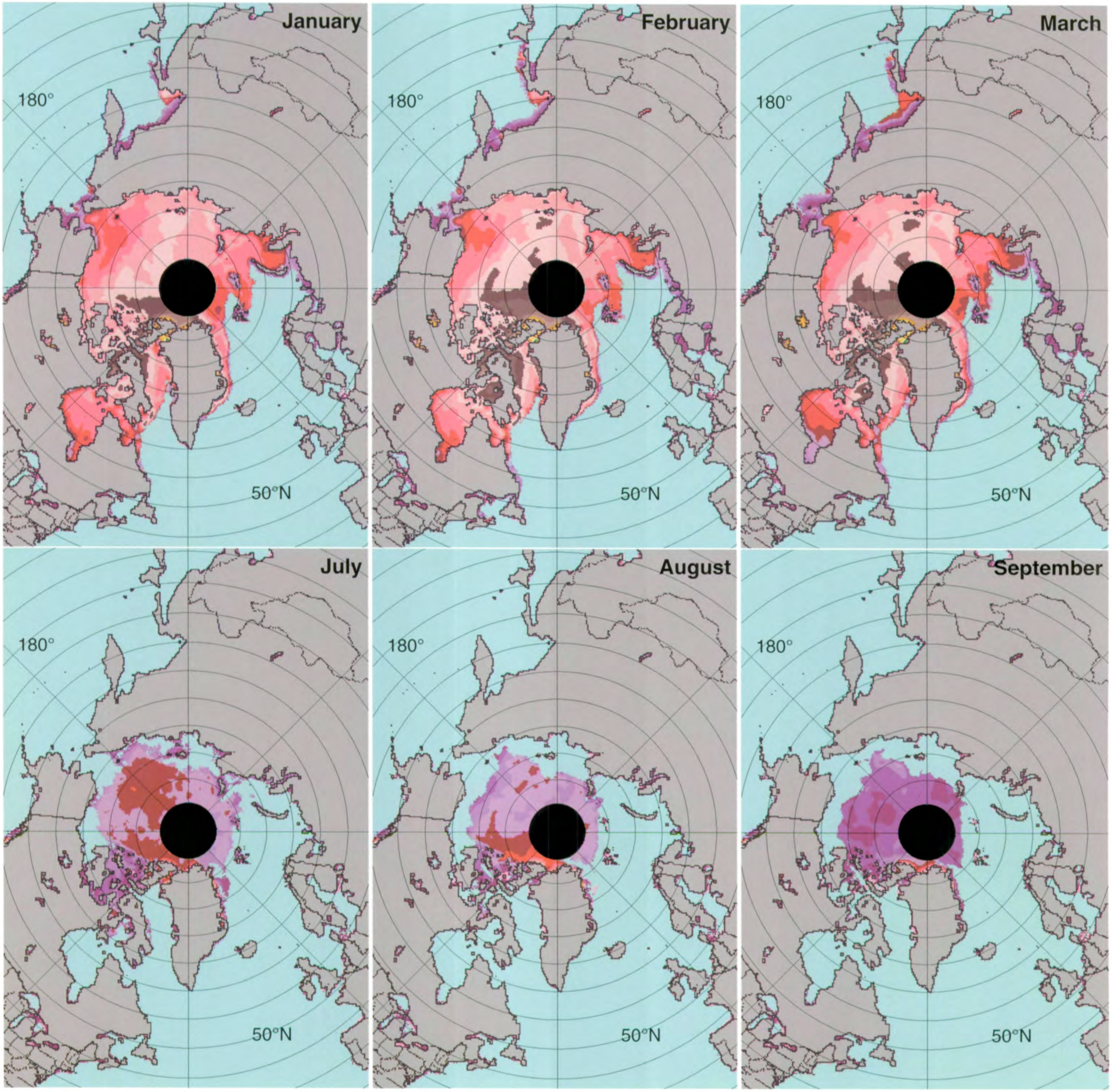
January
180°
50°N
February
180°
50°N
March
180°
50°N
July
180°
50°N
August
180°
50°N
September
180°
50°N

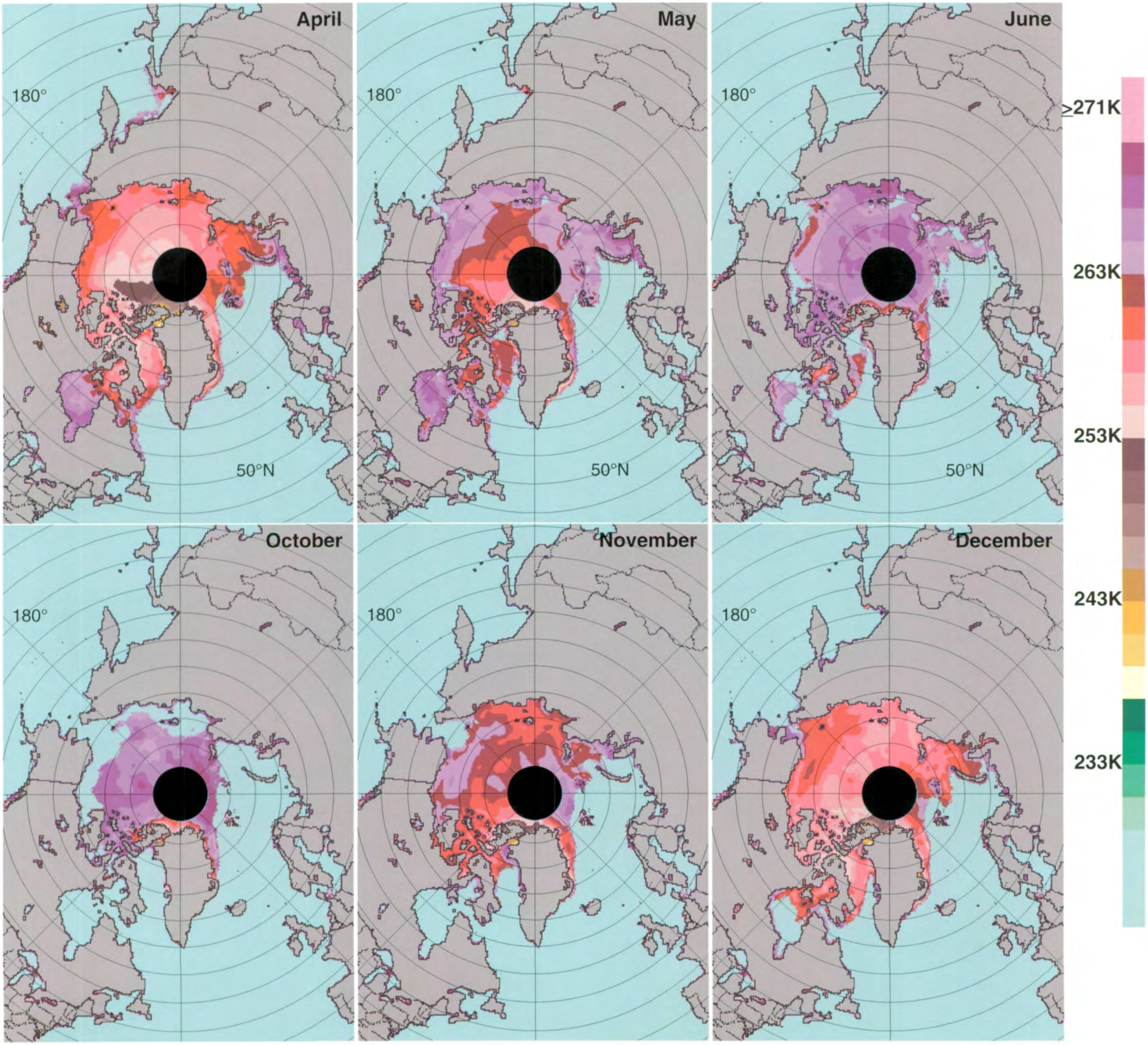

Figure A.29. Monthly Arctic sea ice temperatures averaged over the SMMR lifetime.

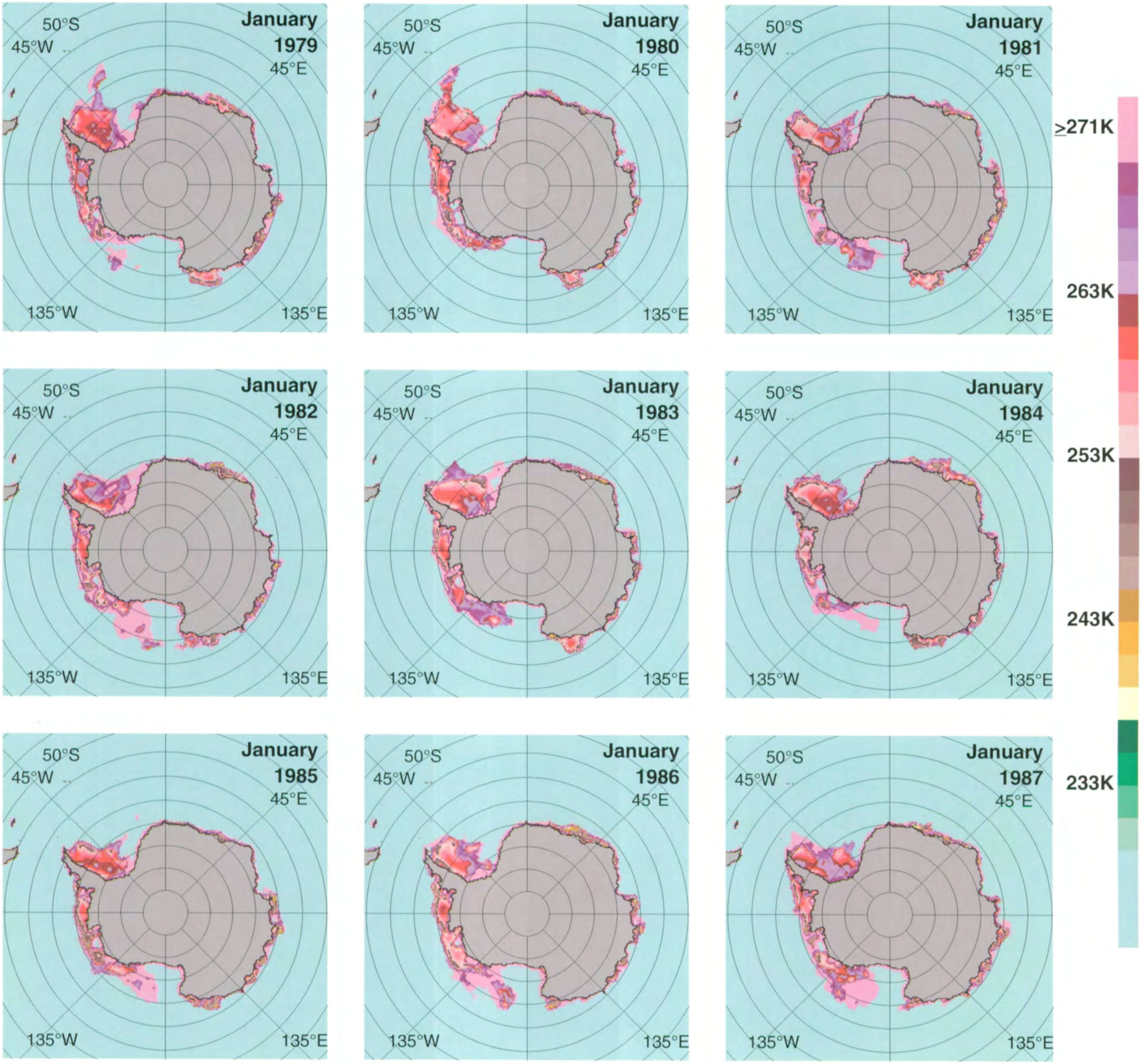

Figure A.30. Mean monthly Antarctic sea ice temperatures for January 1979-1987.

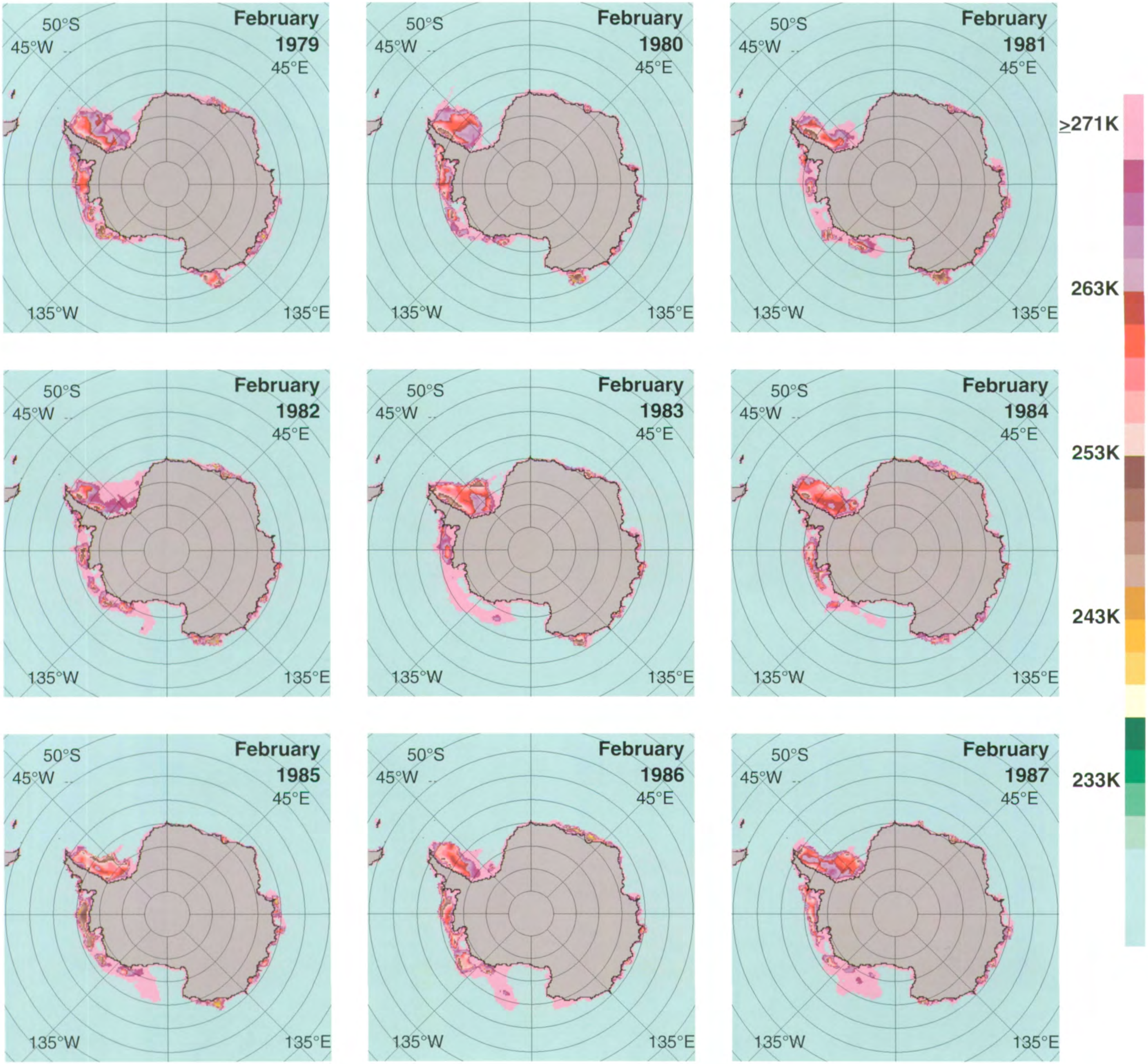

Figure A.31. Mean monthly Antarctic sea ice temperatures for February 1979-1987.

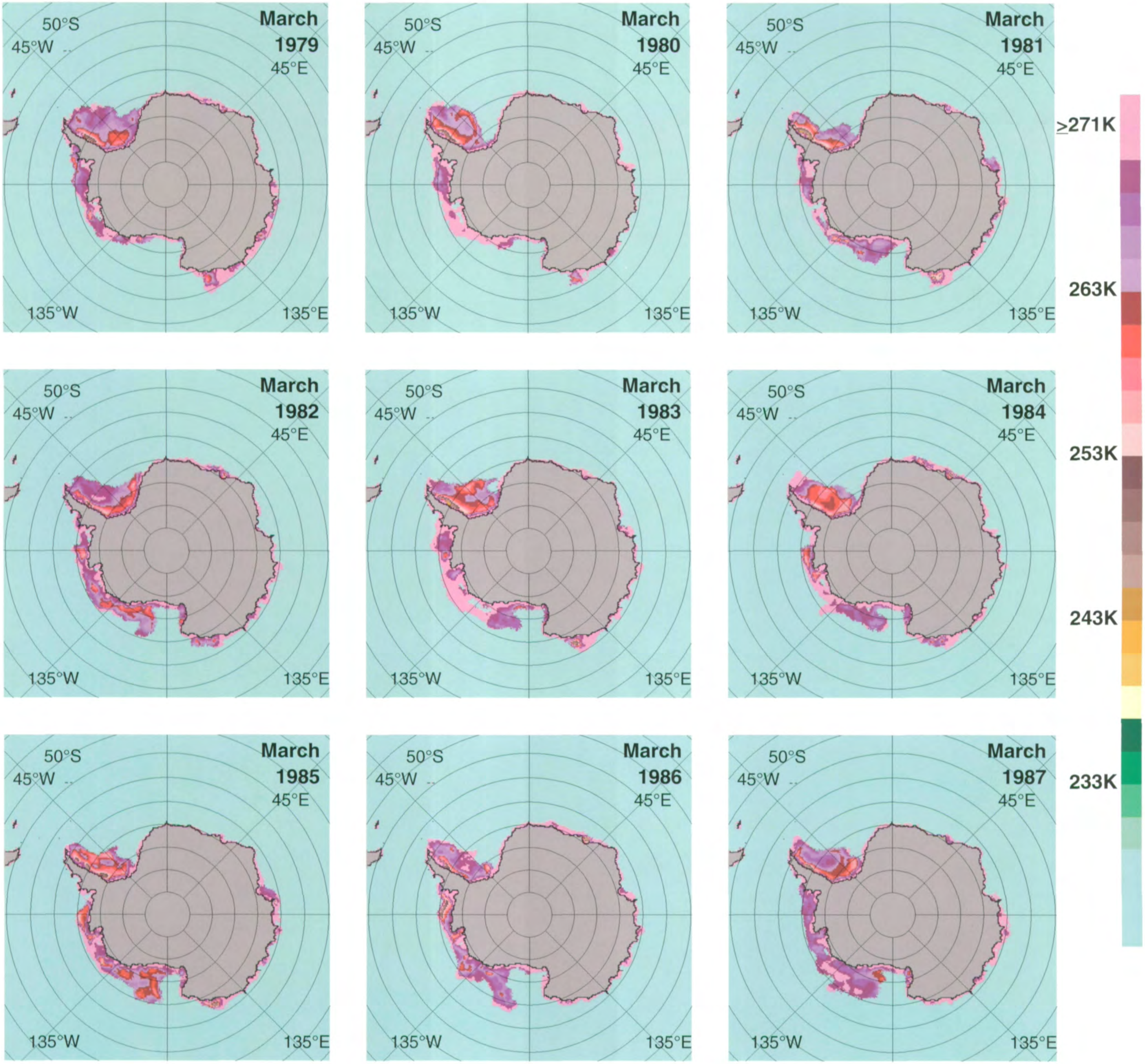

Figure A.32. Mean monthly Antarctic sea ice temperatures for March 1979-1987.

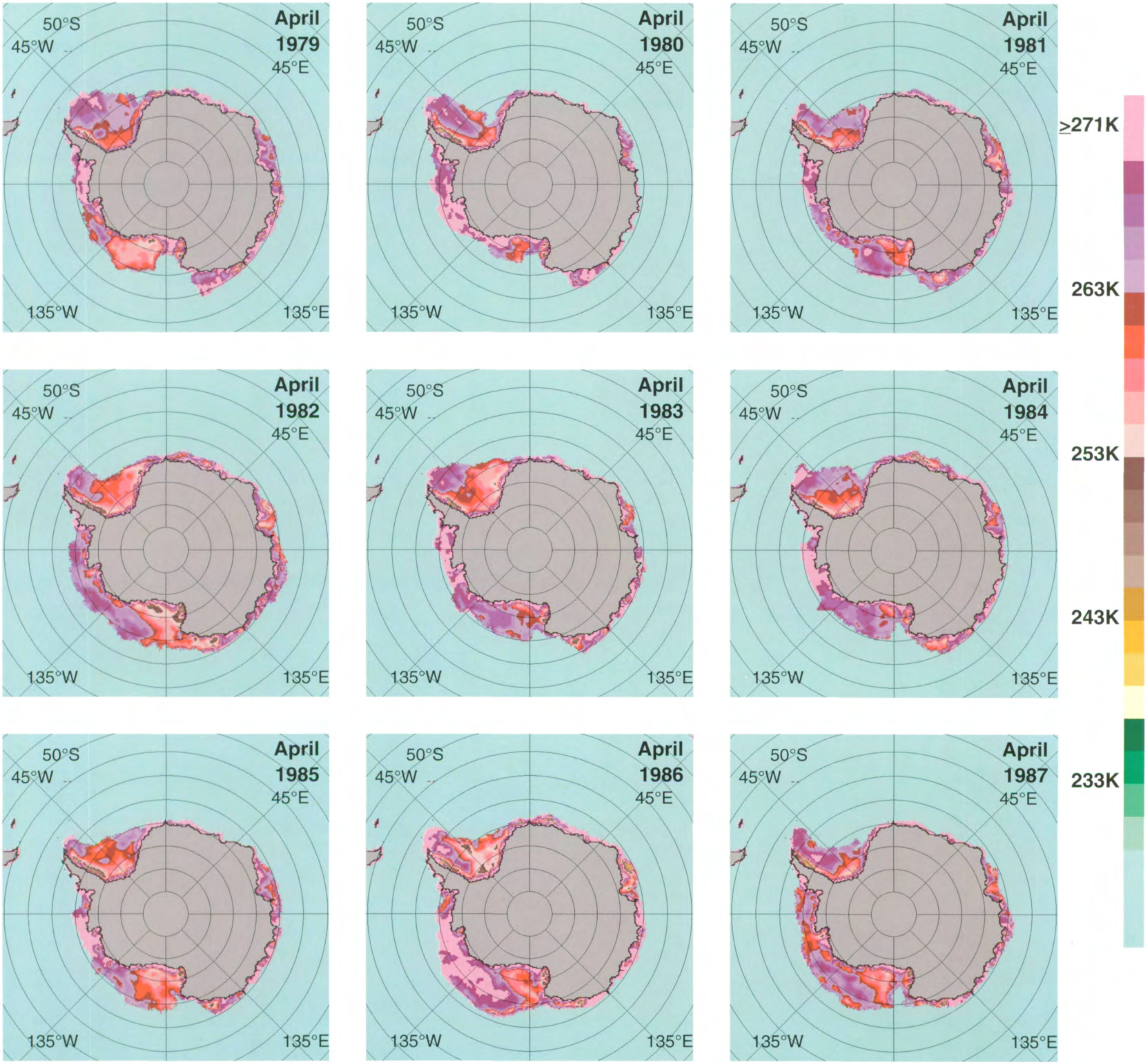

Figure A.33. Mean monthly Antarctic sea ice temperatures for April 1979-1987.

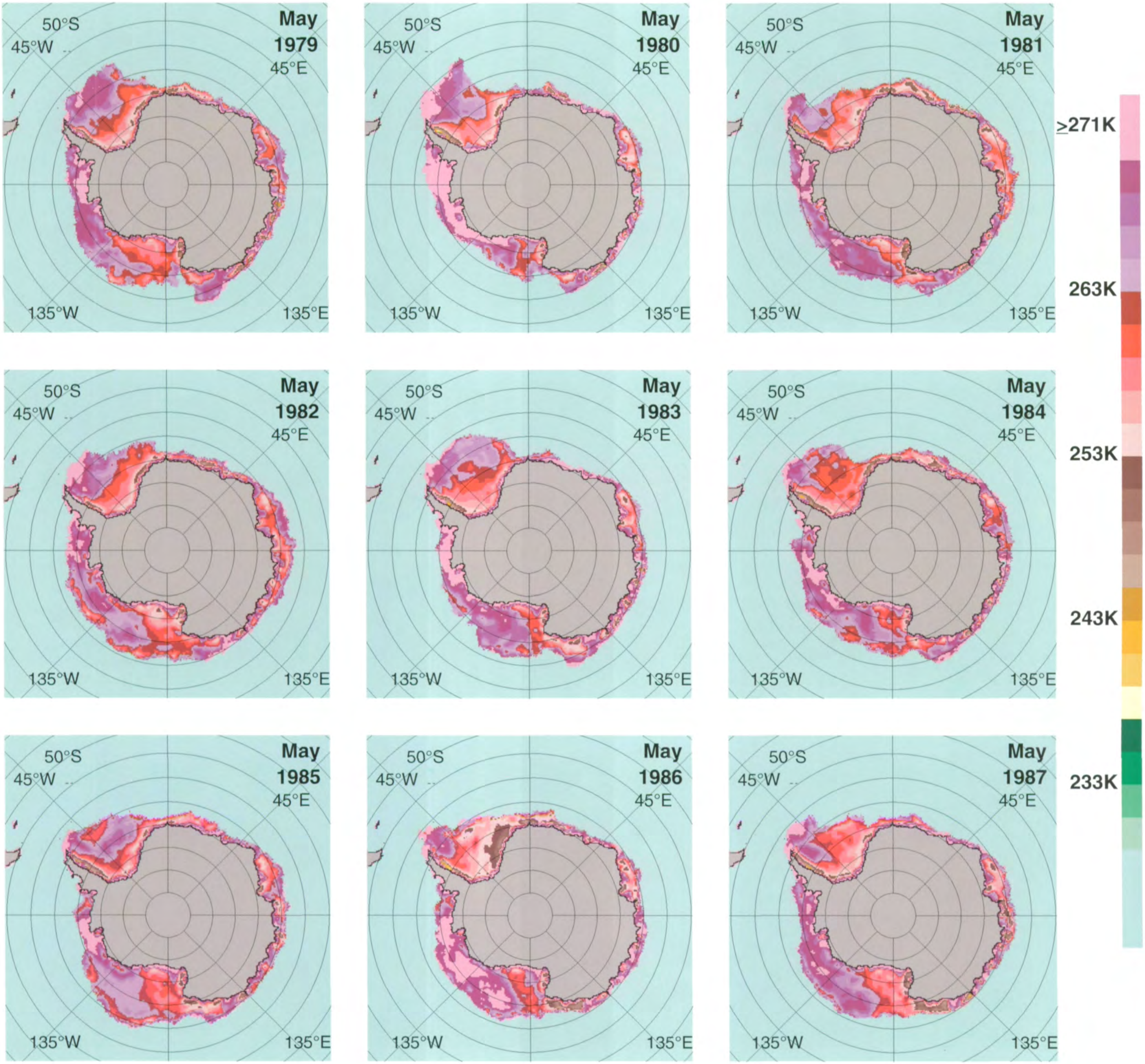

Figure A.34. Mean monthly Antarctic sea ice temperatures for May 1979-1987.

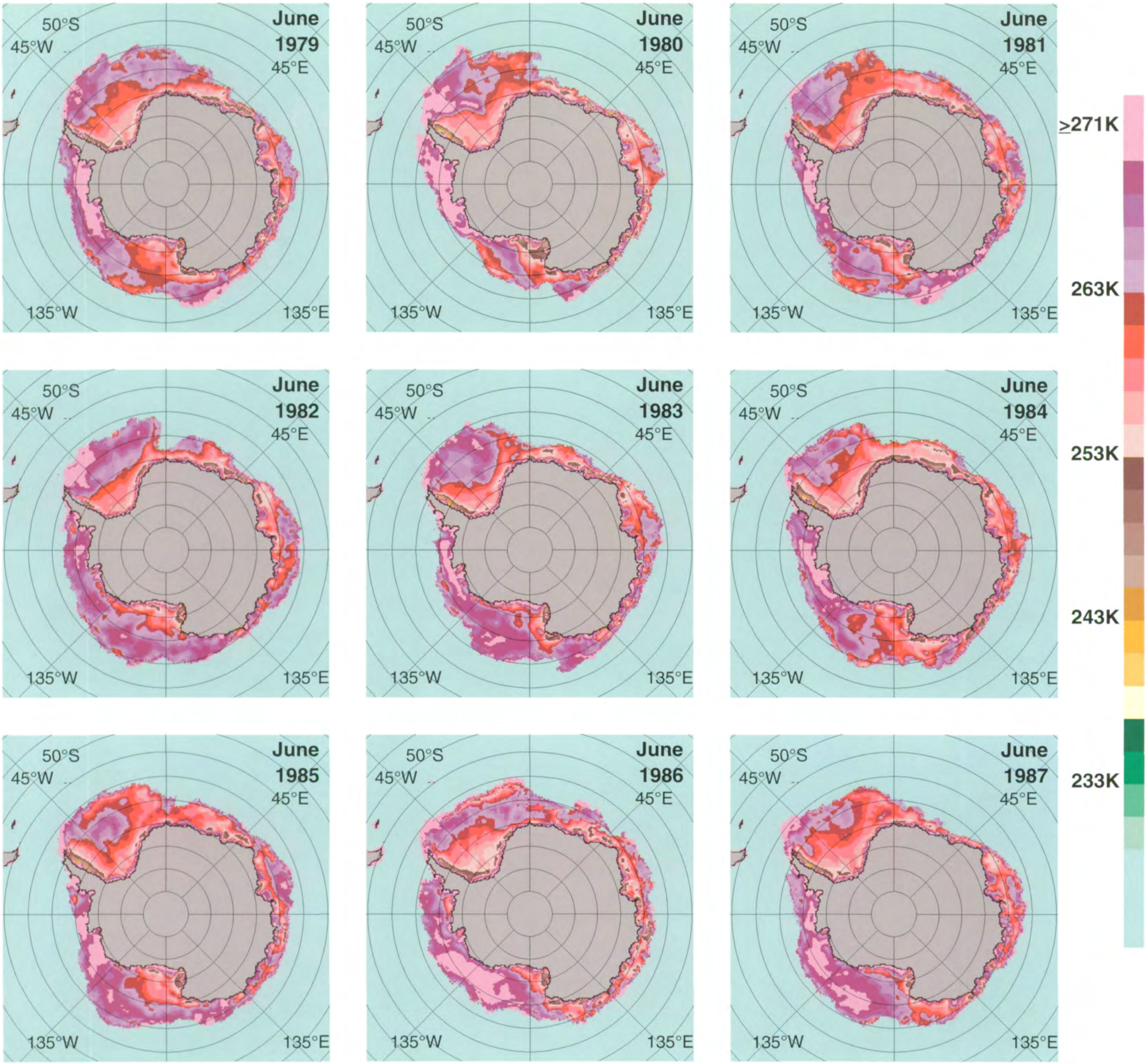

Figure A.35. Mean monthly Antarctic sea ice temperatures for June 1979-1987.

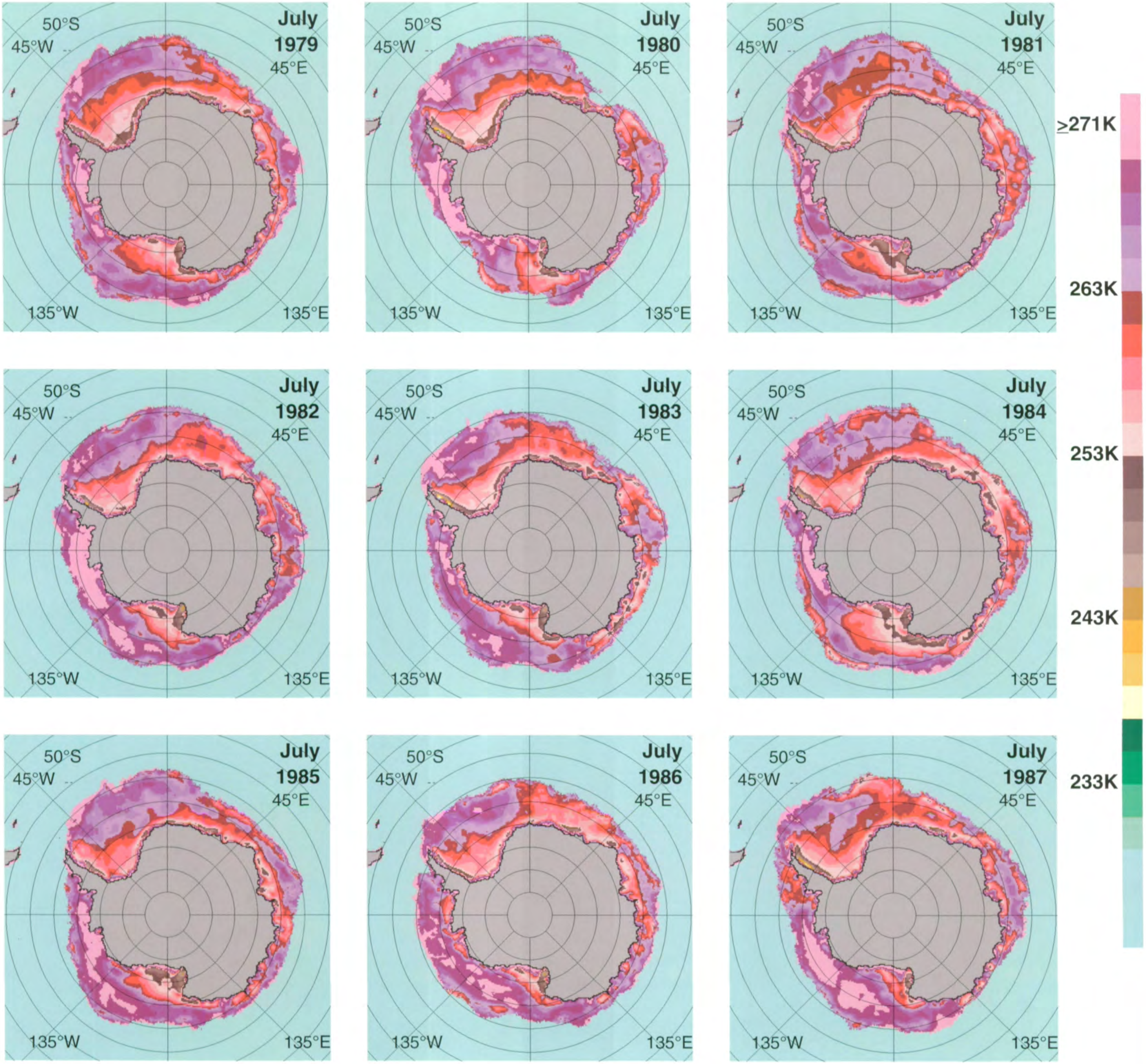

Figure A.36. Mean monthly Antarctic sea ice temperatures for July 1979-1987.

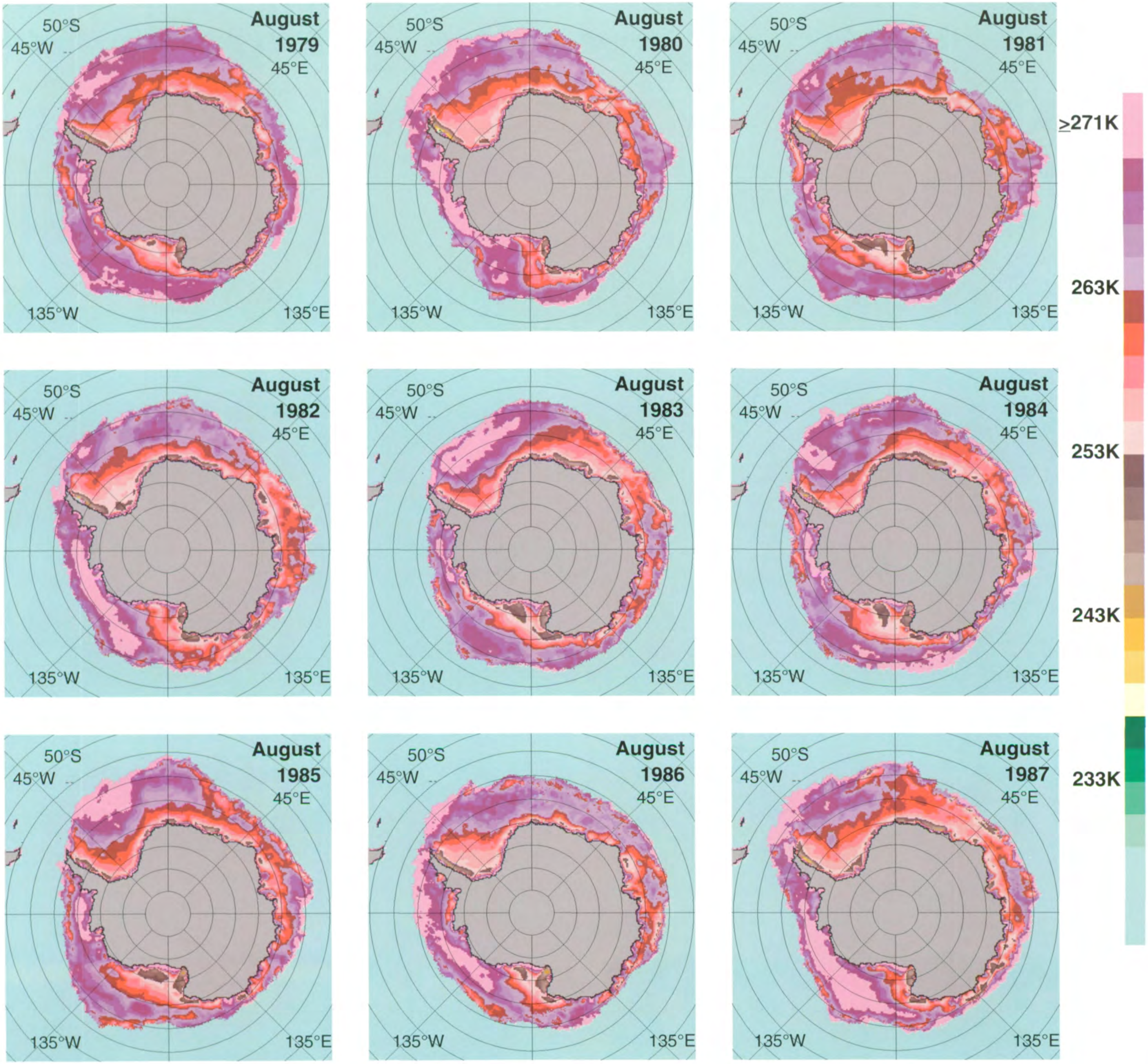

Figure A.37. Mean monthly Antarctic sea ice temperatures for August 1979-1987.

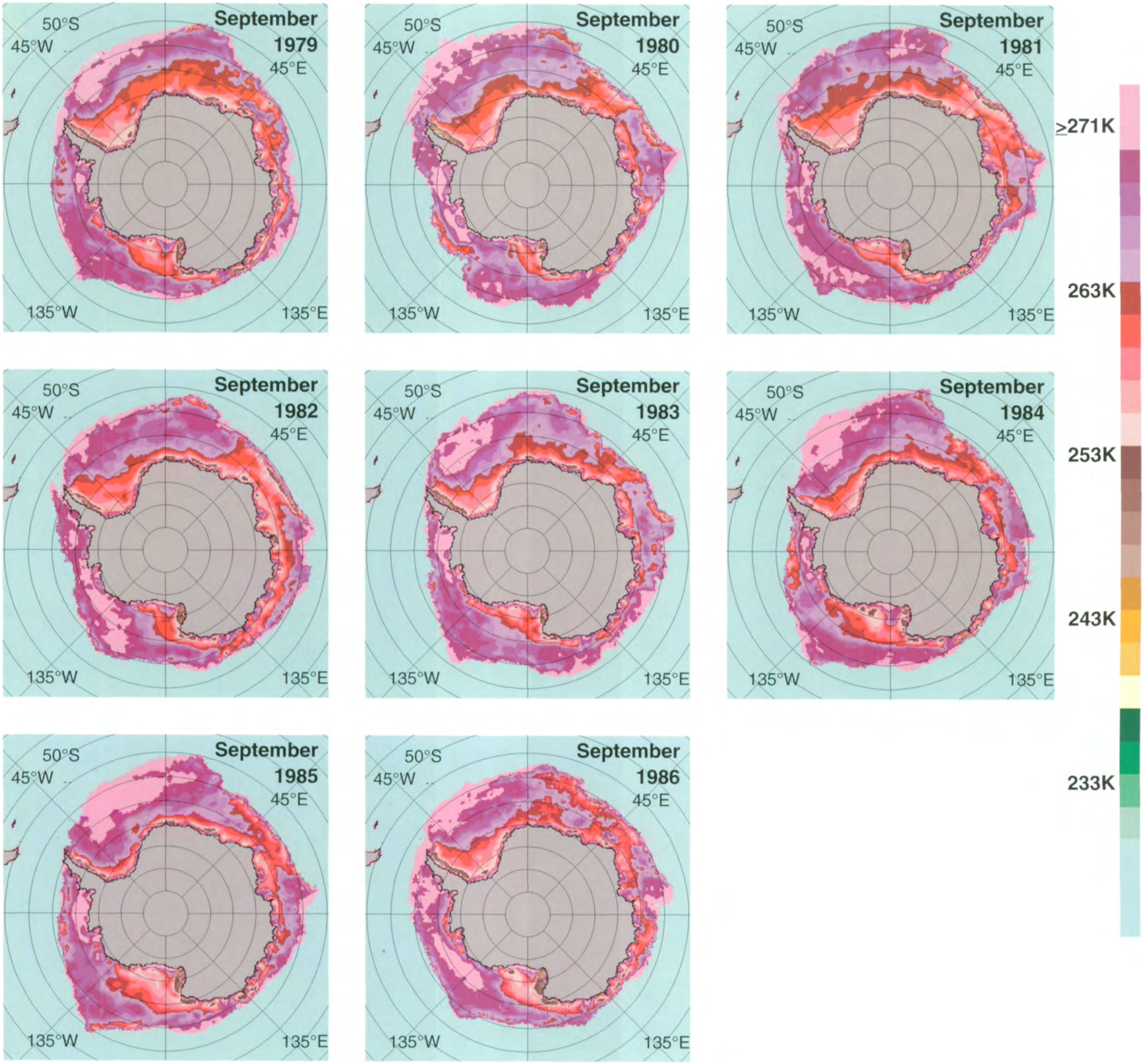

Figure A.38. Mean monthly Antarctic sea ice temperatures for September 1979-1986.

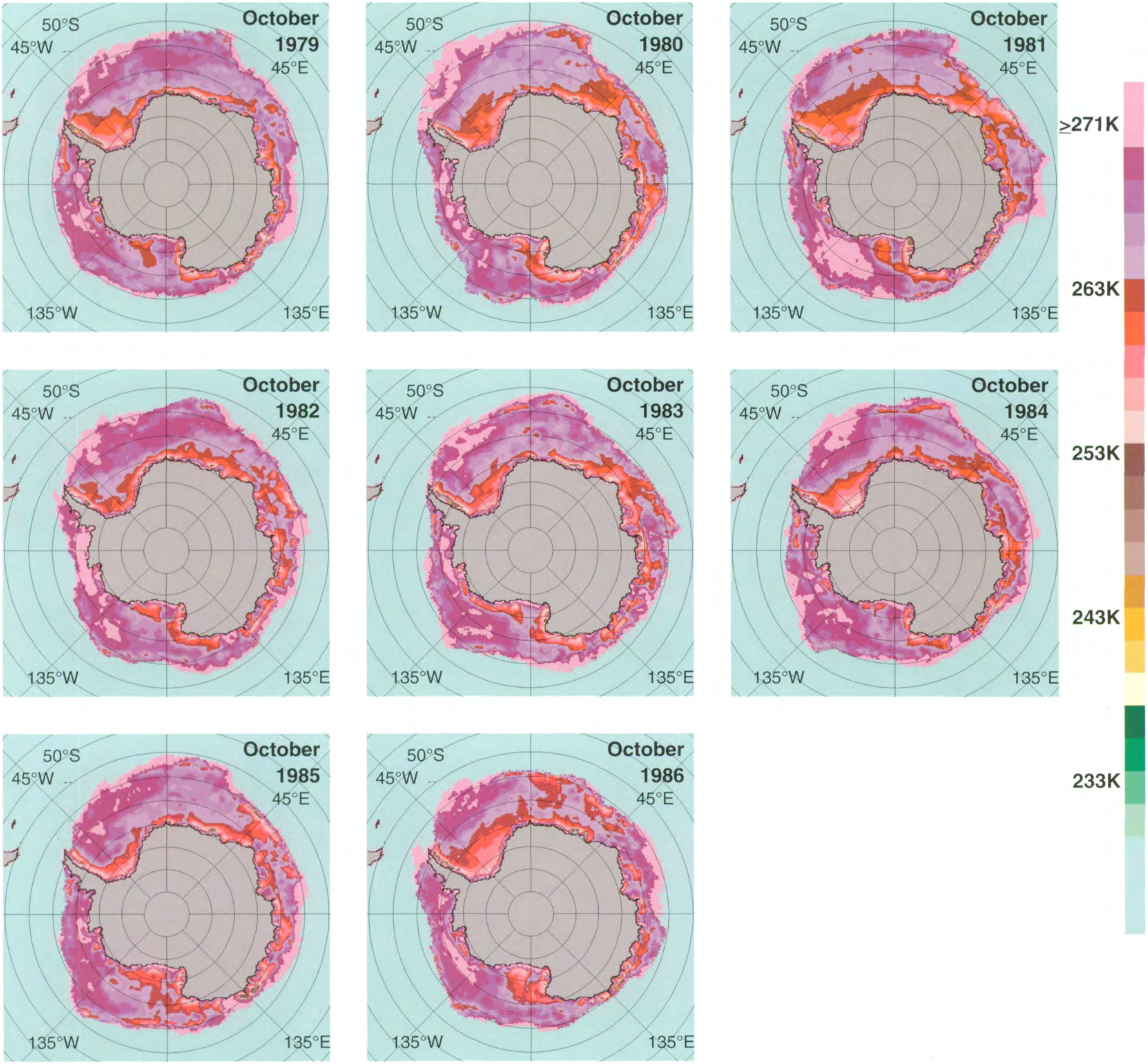

Figure A.39. Mean monthly Antarctic sea ice temperatures for October 1979-1986.

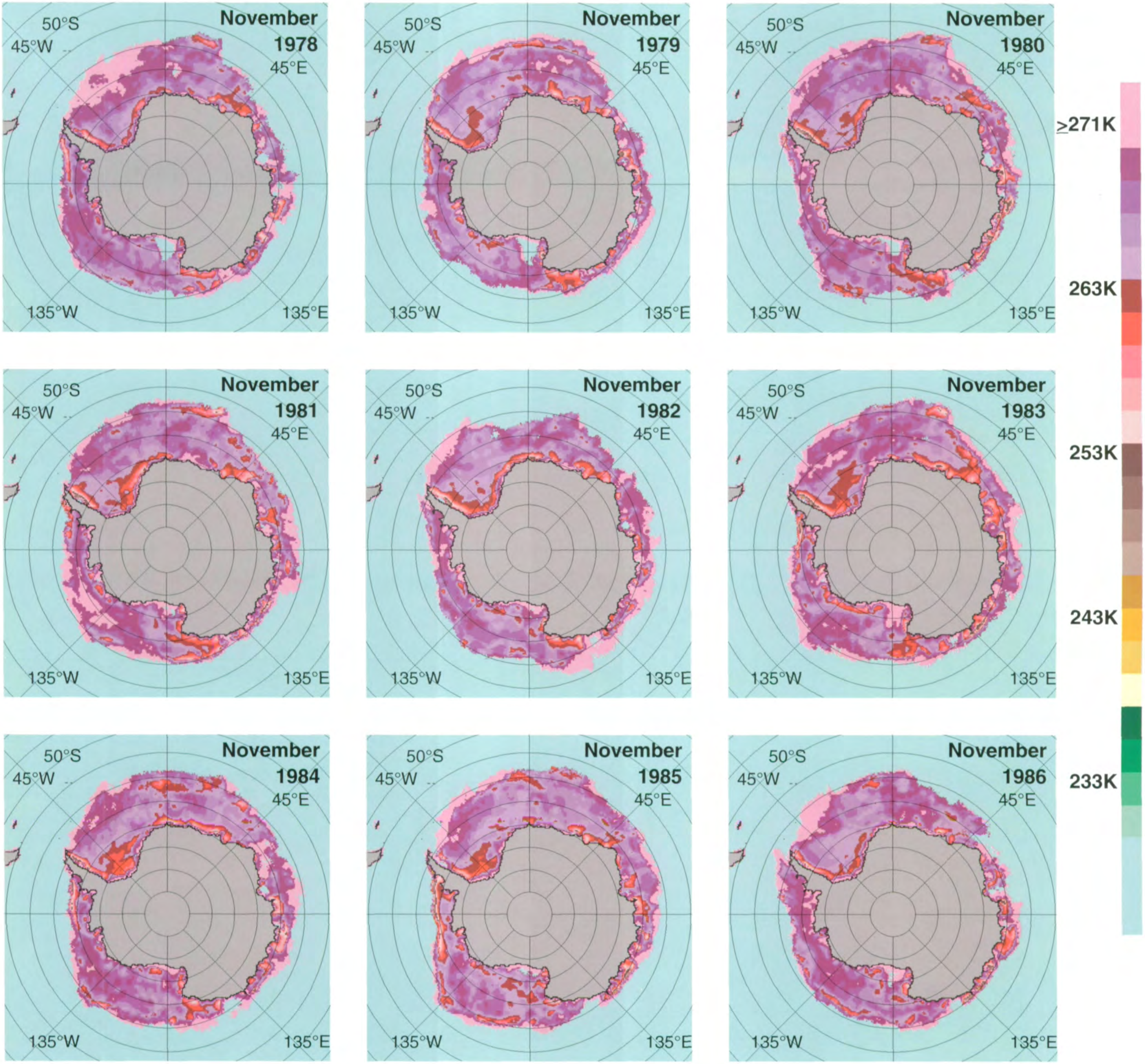

Figure A.40. Mean monthly Antarctic sea ice temperatures for November 1978-1986.

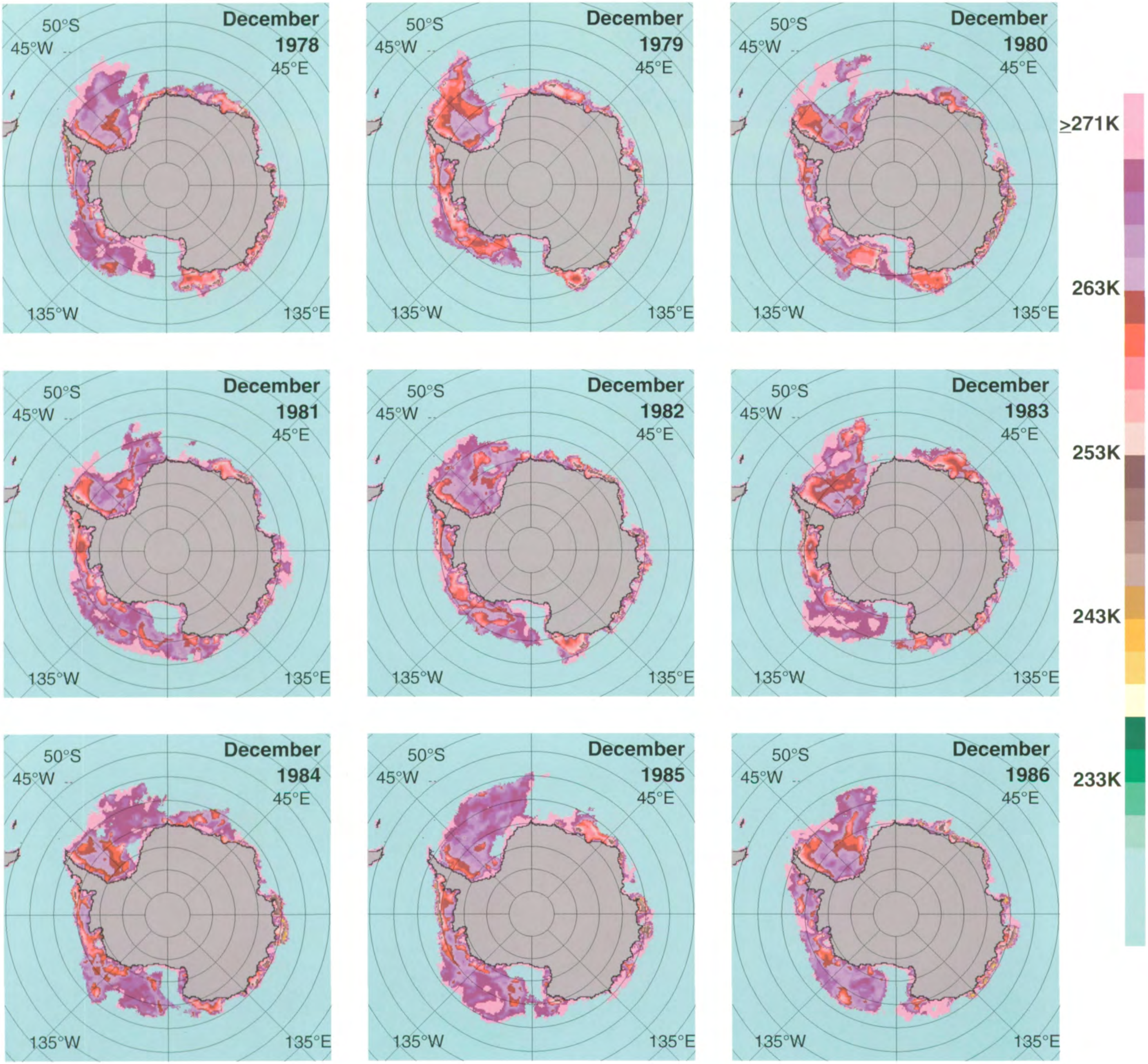

Figure A.41. Mean monthly Antarctic sea ice temperatures for December 1978-1986.

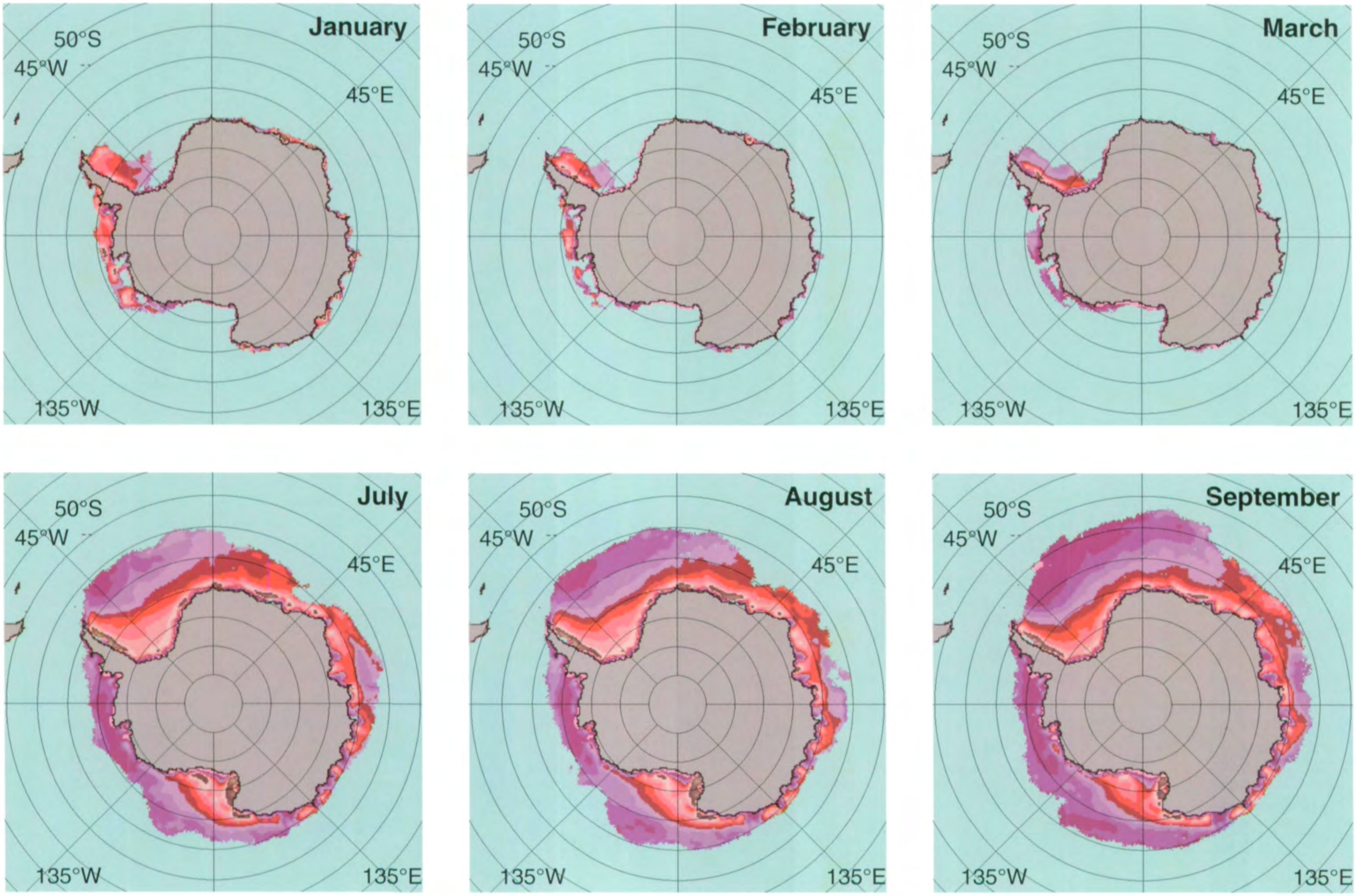
January
February
March
July
August
September
50°S
45°W
45°E
135°W
135°E

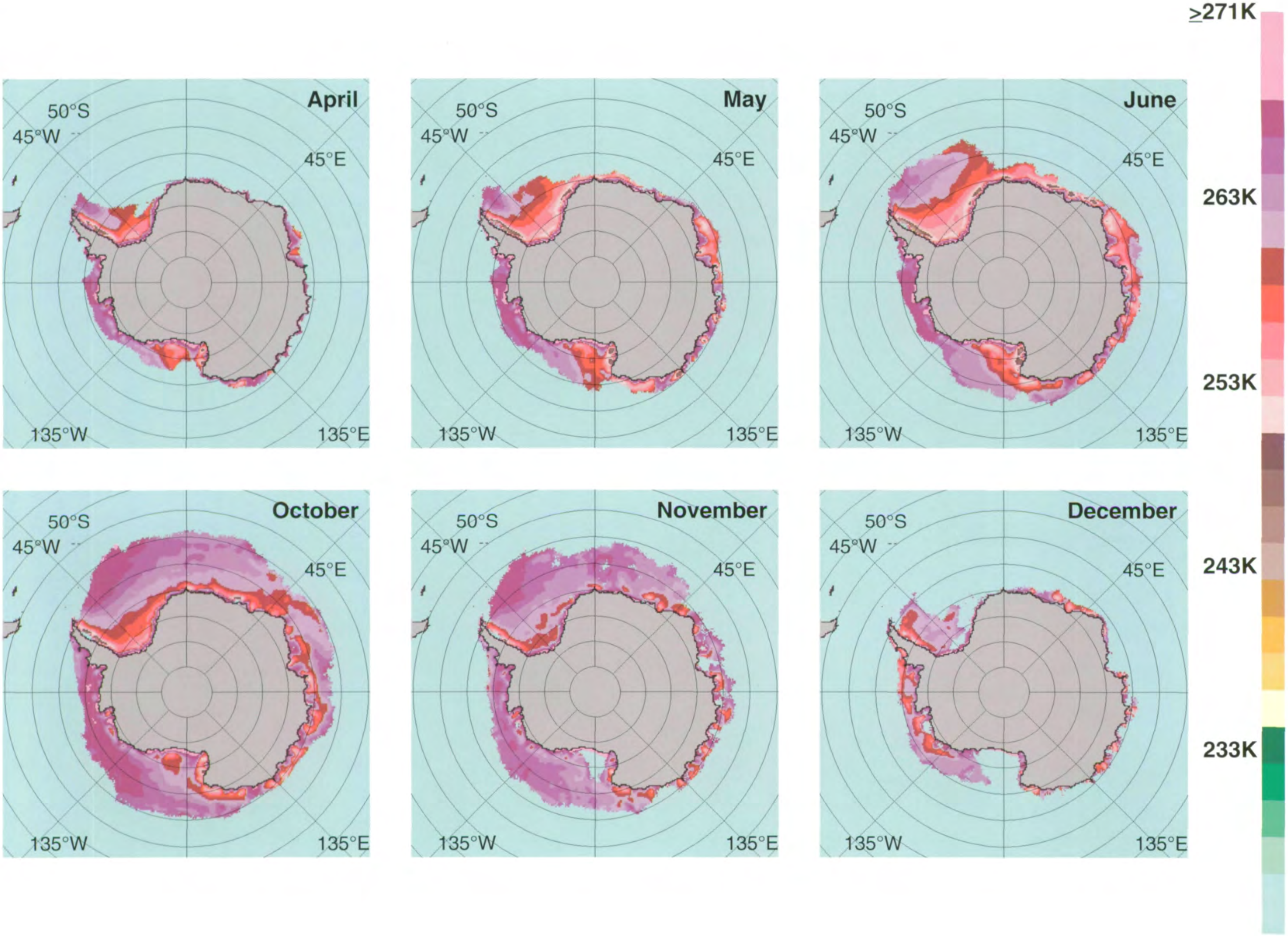

Figure A.42. Mean monthly Antarctic sea ice temperatures averaged over the SMMR lifetime.

Page Intentionally Left Blank

Appendix B

ACRONYMS AND ABBREVIATIONS

AIDJEX	Arctic Ice Dynamics Joint Experiment
AMMR	Airborne Multichannel Microwave Radiometer
AOBP	Arctic Ocean Buoy Program
ARLIS	Arctic Research Laboratory Ice Station
AVHRR	Advanced Very High Resolution Radiometer
BESEX	Bering Sea Experiment (Joint U.S.S.R./U.S.)
BLR	Band-limited regression
C_T	Total sea ice concentration (of all ice types)
C_{MY}	Multiyear sea ice concentration
CELL	A tape in which SMMR data have been remapped into cells of various sizes arranged perpendicular to the suborbital track on the Earth.
CIA	Central Intelligence Agency
CFC	Chlorofluorocarbon
DMSP	Defense Meteorological Satellite Program
ENSO	El Niño-Southern Oscillation
EOS	Earth Observing System
ERIM	Environmental Research Institute of Michigan
ERTS	Earth Resources Technology Satellite (Renamed Landsat 1)
ESMR	Electrically Scanning Microwave Radiometer
FFT	Fast Fourier Transform
FOV	Field of view
FY	First-year (sea ice)
GCM	General Circulation Model
GFDL	Geophysical Fluid Dynamics Laboratory
GHz	Gigahertz (frequency)
GR	Spectral gradient ratio
GSFC	Goddard Space Flight Center (NASA)
H	Horizontally polarized component
IF	Intermediate frequency
IFOV	Integrated field of view
IGY	International Geophysical Year
JD	Julian day
JIC	Joint Navy/NOAA Ice Center
JPL	Jet Propulsion Laboratory
K	Kelvins (absolute temperature)
KRMS	Ka-band Radiometer Mapping System
L	Cloud liquid water content
LTM	Local temporal minima (pertaining to ice concentrations)
MIZEX	Marginal Ice Zone Experiment
MSS	Multispectral Scanner
MY	Multiyear (sea ice)
NADC	Navy Air Development Command
NASA	National Aeronautics and Space Administration
NCAR	National Center for Atmospheric Research
NEMS	Nimbus E Microwave Spectrometer
NOAA	National Oceanographic and Atmospheric Administration
NOARL	Navy Oceanographic and Atmospheric Research Laboratory
NORSEX	Norwegian Remote Sensing Experiment
NSIDC	National Snow and Ice Data Center
NSW	Near-surface scalar wind
OLS	Ordinary least squares
OW	Open water
PR	Polarization
RF	Radio frequency
rms	Root-mean-square
SAR	Synthetic aperture radar
SCAMS	Scanning Microwave Sounder
SF	Space spillover fraction
SIR-B	Shuttle Imaging Radar-B
SMMR	Scanning Multichannel Microwave Radiometer
SSMI	Special Sensor Microwave/Imager
SST	Sea surface temperature
SURSAT	Surveillance Satellite
TAT	Antenna temperature (TA) tape (raw instrument counts; swath data)
TCT	A TAT that has been calibrated to give radiances as brightness temperatures, in kelvins.
THIR	Temperature-Humidity Infrared Radiometer
USGS	U.S. Geological Survey
V	Vertically polarized component
W	Water vapor amount
WMO	World Meteorological Organization

Page Intentionally Left Blank

INDEX

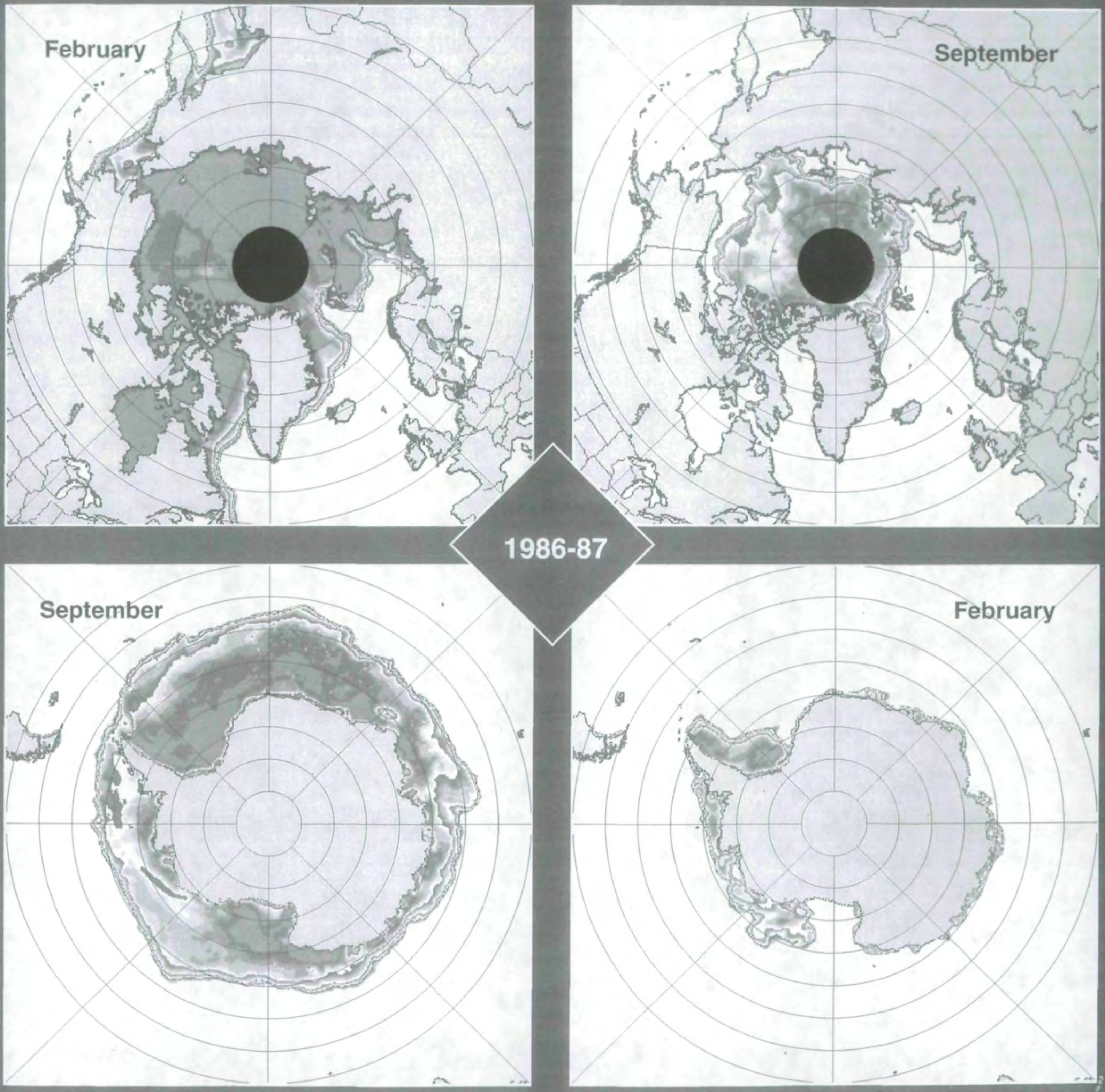
February
September
1986-87
September
February